Transactions of the ASME

Journal of Applied Mechanics (ISSN 0021-8936) is edited and published quarterly at the offices of The American Society of Mechanical Engineers, United Engineering Center, 345 E. 47th St., New York, N. Y. 10017. ASME-TWX No. 710-581-5267, New York. Second Class postage paid at New York, N. Y., and at additional mailing offices.

CHANGES OF ADDRESS must be received at Society headquarters seven weeks before they are to be effective. Please send old label and new address.

PRICES: To members, $25.00, annually; to nonmembers, $50.00. Single copies, $15.00 each. Add $1.50 for postage to countries outside the United States and Canada.

INDEXED by the Engineering Index, Inc.

Journal of Applied Mechanics

Published Quarterly by The American Society of Mechanical Engineers

VOLUME 47 • NUMBER 1 • MARCH 1980

TECHNICAL PAPERS

(Contents continued on Page 224)

CONTENTS (CONTINUED)

BRIEF NOTES

BOOK REVIEWS

(Contents continued on Inside Back Cover)

CONTENTS (CONTINUED)

ERRATA

T. Ota
Assistant Professor.

H. Motegi
Graduate Student.

Department of Mechanical Engineering,
Akita University,
Akita 010, Japan

Turbulence Measurements in an Axisymmetric Separated and Reattached Flow Over a Longitudinal Blunt Circular Cylinder

Turbulence measurements were made in the separated, reattached, and redeveloped regions of an axisymmetric incompressible airflow over a longitudinal circular cylinder with blunt leading edge. Three components of turbulent fluctuating velocity and the turbulent shear stress are presented. In the boundary layer downstream of the reattachment point, Prandtl's mixing length and turbulent kinetic energy length scale are estimated, and the correlation between the turbulent shear stress and the turbulent kinetic energy is described.

Introduction

The separation and reattachment of flow occurs in various engineering aspects and there have been many works on a wide variety of flow configurations, which were referred to papers by the present authors [1–3]. In addition, several papers have recently been published [4–10]. However there is still little published work on the incompressible separated and reattached flow past bodies of revolution.

In this standpoint, one of the present authors has reported an experimental study for the separated, reattached, and redeveloped regions of an axisymmetric flow over a longitudinal blunt circular cylinder [1], in which the boundary layer at the separation point can be considered to be very thin and its effects on the separation and reattachment to be small. The testing fluid was air and the speed was so slow as to regard the flow as an incompressible one. The flow pattern in the separated and reattached regions was measured and the boundary-layer characteristics of the flow downstream of reattachment have been discussed. The turbulence characteristics except the streamwise component of turbulent fluctuating velocity, however, were not measured.

The authors studied the turbulence characteristics in the separated, reattached, and redeveloped regions of a two-dimensional incompressible airflow over a flat plate of finite thickness having blunt leading edge [3]. In the redeveloped flow region downstream of reattachment, Prandtl's mixing length and turbulent kinetic energy length scale were described, and the correlation between the turbulent shear stress and the turbulent kinetic energy was discussed. Unfortunately the longitudinal distance examined was relatively short so as to clarify the development of the turbulence characteristics in the downstream direction, and the spanwise component of turbulent fluctuating velocity was not measured. Furthermore the previous studies noted before on the turbulence characteristics in the separated and reattached flow are mainly concerned with the two-dimensional flow and the internal flow in pipes or ducts.

The purpose of the present study was to investigate the turbulence characteristics such as three components of turbulent fluctuating velocity and the turbulent shear stress in the separated, reattached, and redeveloped regions of an axisymmetric incompressible airflow over a longitudinal circular cylinder with blunt leading edge. In the redevelopment region of the boundary layer downstream of reattachment, Prandtl's mixing length and turbulent kinetic energy length scale are estimated and the correlation between the turbulent shear stress and the turbulent kinetic energy is presented. In addition the present results for an axisymmetric flow are compared with the previous data for a two-dimensional flow over a blunt flat plate and for other flow configurations. The flow configuration treated in the present study is schematically shown in Fig. 1 where U_0, d, and l are

Contributed by the Applied Mechanics Division for publication in the JOURNAL OF APPLIED MECHANICS.

Discussion on this paper should be addressed to the Editorial Department, ASME, United Engineering Center, 345 East 47th Street, New York, N. Y. 10017, and will be accepted until June 1, 1980. Readers who need more time to prepare a discussion should request an extension from the Editorial Department. Manuscript received by ASME Applied Mechanics Division, November, 1978; final revision, July, 1979.

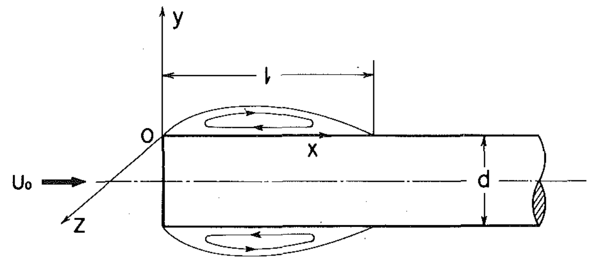

Fig. 1 Flow configuration and coordinate system

the velocity of upstream uniform flow, the cylinder diameter, and the distance from the leading edge to the reattachment point, respectively. The flow separates at the leading edge of the cylinder over the whole circumference and then reattaches onto the cylinder surface and subsequently develops to the downstream. The coordinate system employed is also included in Fig. 1.

Experimental Apparatus and Technique

The experiments were carried out in a low speed free-jet-type open wind tunnel which is the same as that used in the previous study [1] and accordingly its detail is neglected in this paper. The circular cylinder having smooth surface tested is 38 mm in diameter and 580 mm long, and its leading edge is sharply cut at an angle of 90 deg in order that the flow separates always there over the whole circumference. The cylinder was set at the center of the test section and was supported to a strut at the most downstream section, which is the same as that constructed in the earlier heat transfer study [11]. The laser Doppler anemometer has recently been employed in the studies on the separated and reattached flow [4–7]. It may be considered that the uncertainty of the data obtained using the hot-wire anemometer is larger in the separated and reattached flow regions than that measured employing the laser Doppler anemometer. However that uncertainty may become small in other flow region and furthermore the hot-wire anemometer is easy to handle and analyze the data. In the present study therefore the mean and turbulent fluctuating velocities were measured using a constant temperature hot-wire anemometer. The measuring technique was almost the same as that in the earlier study for the two-dimensional flow [3] and its detail is omitted here. The only difference is that z-component of turbulent fluctuating velocity was measured by rotating the hot-wire in the plane parallel to x-z plane, and its inclination angles to the mean flow direction were 60, 90, and 120 deg, which were equal to those in the measurements of other two components of turbulence (at that time, the prong and support of the hot-wire were aligned in the plane parallel to x-z plane).

In the previous study, the Reynolds number formed with the upstream uniform flow velocity U_0, the cylinder diameter d, and the kinematic viscosity of air ν; Re = $U_0 d/\nu$ was varied from 40,800–68,000, and the mean flow characteristics were found to be, in general, independent of the Reynolds number [1]. In accordance with it, the present experiments were conducted at a constant free stream velocity $U_0 = 16.2$ m/s and the corresponding Reynolds number Re = 42,100. The axisymmetry of the flow was confirmed to be satisfactory through the velocity profiles measured along three circumferential angles (say φ = 0, 90, and 180 deg) at three streamwise cross sections including the separated, reattached, and redeveloped flow regions (x/d = 0.7, 1.8, and 5.0). No corrections were made to values of mean and turbulent fluctuating velocities for nonlinear responses of the hot-wire and the tunnel wall effects.

The uncertainty of the present data shown in the following may be considered to be almost equal to that in the previous study [3]. That is: the uncertainty of nondimensional turbulence intensities $\sqrt{\overline{u^2}}/U$, $\sqrt{\overline{v^2}}/U$, and $\sqrt{\overline{w^2}}/U$ may be about ±8 percent and that of nondimensional turbulent shear stress $-\overline{uv}/U^2$ about ±9 percent, where U denotes the local mean velocity along the mean streamline and u and v are the components of turbulent fluctuating velocity along and normal to the mean streamline, and w that parallel to the peripheral direction of the cylinder. Their uncertainty may exceed ±10 percent near the wall where the local turbulence intensities are large and furthermore it may be higher than ±30 percent in the separated and reattached flow regions where the unsteadiness of the flow is very severe. The geometrical positions are accurate to within about ±0.15 mm.

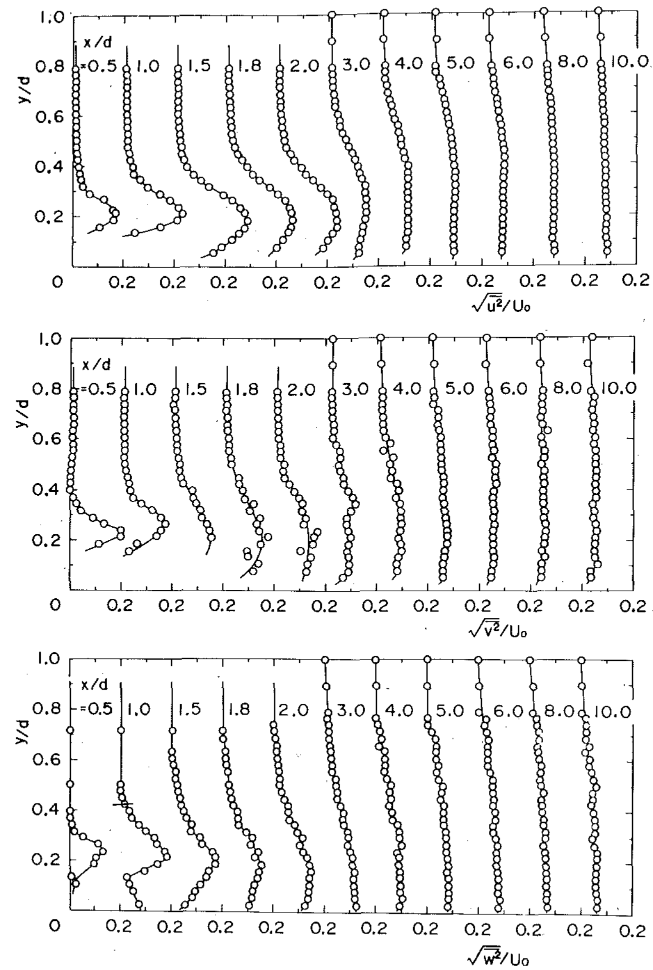

Fig. 2 Distributions of turbulent fluctuating velocities

Experimental Results and Discussion

Mean velocity profiles in the separated, reattached, and redeveloped flow regions are almost the same as those obtained in the previous work [1] and the boundary-layer characteristics of the flow downstream of reattachment are also in very good agreement with those of [1]. The point of zero skin friction (extrapolated value) occurred at about x/d = 1.3 which is nearly equal to those measured in the works [1, 11]. Accordingly these results are excluded from the present paper.

Three components of turbulent fluctuating velocity and the turbulent shear stress at various sections along the cylinder axis are shown in Figs. 2 and 3. In the separated and reattached regions, $\sqrt{\overline{u^2}}$ is larger than $\sqrt{\overline{v^2}}$ and $\sqrt{\overline{w^2}}$ and on the other hand, $\sqrt{\overline{v^2}}$ and $\sqrt{\overline{w^2}}$ are roughly equal to each other. It is clear that the maxima of $\sqrt{\overline{u^2}}$, $\sqrt{\overline{v^2}}$, and $\sqrt{\overline{w^2}}$ occur in the reattachment region and their values are about 30, 20, and 20 percent of the free-stream velocity. Quite large scatter is found in the data for $\sqrt{\overline{v^2}}$ in the entire field investigated in the present study. Similar feature also exists in the data for $\sqrt{\overline{w^2}}$. The flow in the reattachment region may be considered to resemble that impinging on the cylinder surface and moreover the

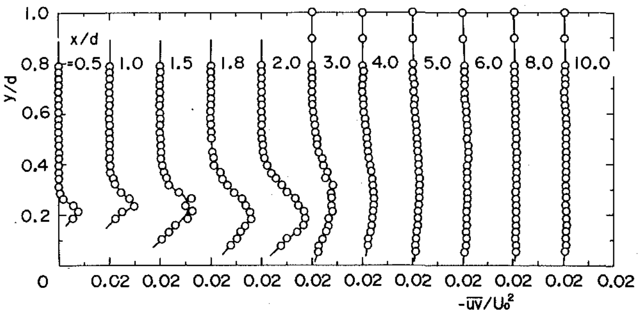

Fig. 3 Turbulent shear stress distribution

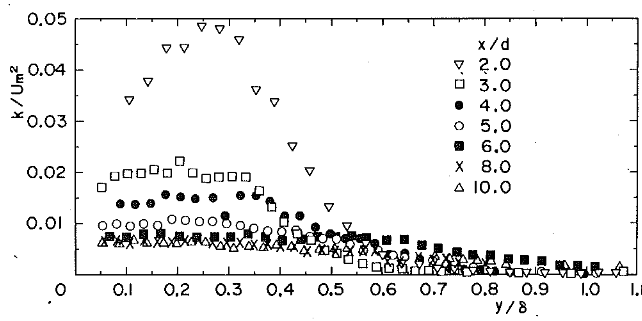

Fig. 5 Streamwise variation of turbulent kinetic energy in redeveloped flow region

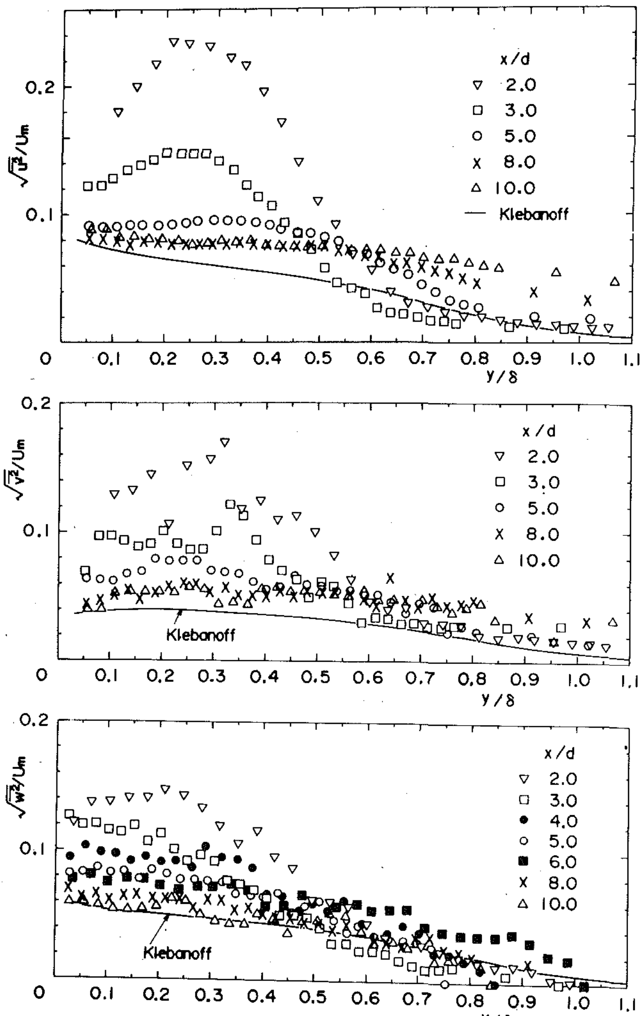

Fig. 4 Streamwise variations of turbulent fluctuating velocities in redeveloped flow region

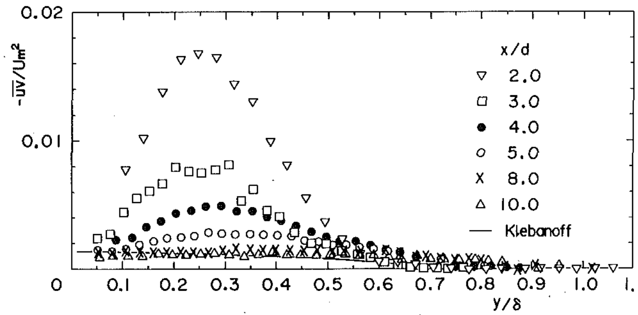

Fig. 6 Streamwise variation of turbulent shear stress in redeveloped flow region

position of reattachment fluctuates randomly with time. It may be presumed that the large scatter of $\sqrt{\overline{v^2}}$ data originates from this fluctuation and it continues for a long distance to some point quite far downstream from the reattachment point.

Nondimensional turbulent shear stress is very large in the separated and reattached regions and it attains a value of about 0.02 just after the reattachment point. The turbulence intensities and the turbulent shear stress decrease quite steeply in the region from about $x/d = 2$ to 3 and afterward they decrease gradually to the downstream.

In the separated and reattached flow regions, the flow direction is generally different from that of upstream uniform flow. Accordingly u and v are different from x and y-components of turbulent fluctuating velocity. Following the procedure by Bissonnette, et al., [12], x and y-components and their cross product were estimated from measured values of $\overline{u^2}$, $\overline{v^2}$, and $-\overline{uv}$ by

$$\overline{u_x{}^2} = \overline{u^2}\cos^2\alpha - \overline{uv}\sin 2\alpha + \overline{v^2}\sin^2\alpha \tag{1}$$

$$\overline{v_y{}^2} = \overline{u^2}\sin^2\alpha + \overline{uv}\sin 2\alpha + \overline{v^2}\cos^2\alpha \tag{2}$$

$$\overline{u_x v_y} = (\overline{u^2} - \overline{v^2})\sin 2\alpha/2 + \overline{uv}\cos 2\alpha \tag{3}$$

where u_x and v_y denote x and y-components of fluctuating velocity. α in the foregoing equations is the angle between x-axis and the flow direction in x-y plane. As already described in [3], $\sqrt{\overline{u_x{}^2}}$, $\sqrt{\overline{v_y{}^2}}$, and consequently $-\overline{u_x v_y}$ are quite different from $\sqrt{\overline{u^2}}$, $\sqrt{\overline{v^2}}$, and $-\overline{uv}$, respectively, in such flow regions, for example; in the present study $-\overline{u_x v_y}$ attains a maximum of about 0.025 at a cross section of $x/d = 1.8$ (that of $-\overline{uv}$ is about 0.015). However, in the redeveloped flow region downstream of reattachment, their difference becomes very small since the flow direction is nearly equal to that of upstream uniform flow.

In Figs. 4–6, streamwise variations of the turbulence characteristics in the boundary layer downstream of reattachment are shown. Klebanoff's data [13] for a turbulent boundary layer over a flat plate at zero incidence are included for reference. In these figures, δ is the nominal boundary-layer thickness defined as the distance from the wall to a point of $U/U_m = 0.99$, where U_m is the velocity outside the boundary layer. The turbulence intensities, turbulent kinetic energy, and turbulent shear stress generally attain maxima at some point quite far from the cylinder surface. They decrease rapidly in the region close to the reattachment point to the downstream; however their decreasing rate becomes very slow beyond that. Difference of the results at $x/d = 8.0$ and 10.0 is small as compared with those at the upstream positions. Therefore it may be concluded that a longitudinal distance longer than at least 10 times the cylinder diameter is needed to reach the turbulence characteristics of a fully developed turbulent

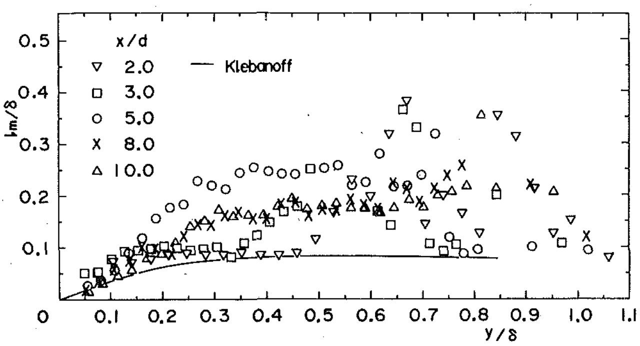

Fig. 7 Prandtl's mixing length

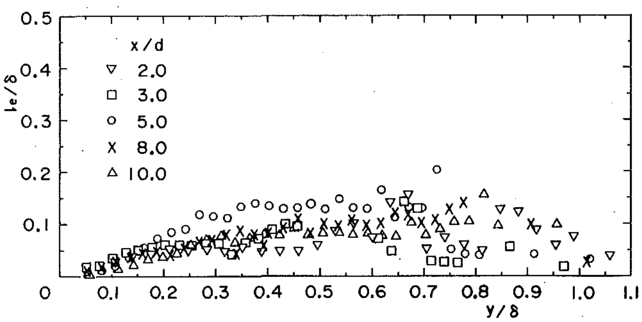

Fig. 8 Prandtl's turbulent kinetic energy length scale

boundary layer over a longitudinal circular cylinder. However their profiles are different from those of Klebanoff, especially in the outer part of the boundary layer, though the results for $\sqrt{\overline{w^2}}$ become relatively close to those of Klebanoff at $x/d = 10.0$.

It is very interesting to notice that the profile of turbulent shear stress is very similar to that of turbulent kinetic energy and also of streamwise component of turbulent fluctuating velocity, although a slight different feature is found in the region near the wall. As noted before, the data scatter is the largest for $\sqrt{\overline{v^2}}$ and it continues for a long distance.

In Figs. 7 and 8, Prandtl's mixing length l_m and turbulent kinetic energy length scale l_e are shown at several cross sections. The eddy kinematic viscosity is defined as

$$\epsilon_m = -\overline{uv}/(\partial U/\partial y) \tag{4}$$

and in terms of Prandtl's mixing length and turbulent kinetic energy length scale, ϵ_m can be written, respectively, as follows [14]:

$$\epsilon_m = l_m{}^2(\partial U/\partial y) \tag{5}$$

$$\epsilon_m = l_e\sqrt{k} \tag{6}$$

where k denotes the turbulent kinetic energy defined as $k = (\overline{u^2} + \overline{v^2} + \overline{w^2})/2$. The data for l_m by Klebanoff which were read from the book by Cebeci, et al., [15], are included for reference. Both l_m and l_e increase almost linearly from the wall to points near $y/\delta = 0.2$ to 0.3. It can be presumed from this fact that the mixing length and the turbulent kinetic energy length scale are approximated near the wall as

$$l_m = K_m y \quad \text{and} \quad l_e = K_e y \tag{7}$$

Though quite large scatter exists in the outer region, it may be said that l_m and l_e show no material change there. Accordingly it may be reasonable that the mixing length and the turbulent kinetic energy length scale are approximated by equation (7) near the wall and as constants C_m and C_e, respectively, in the outer region of the boundary

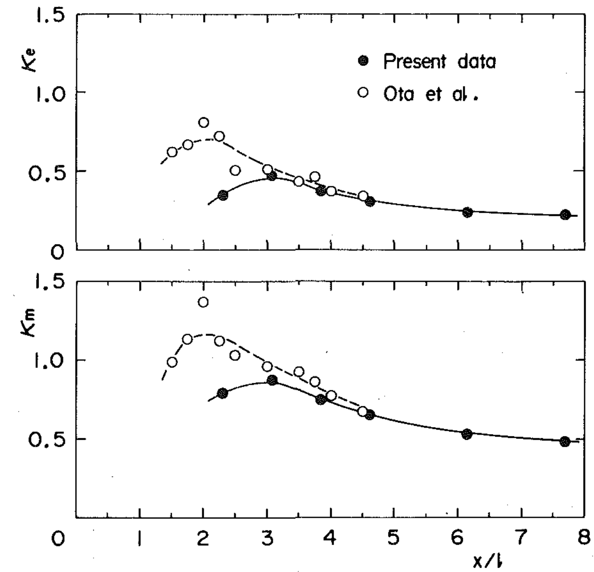

Fig. 9 Streamwise variation of K_m and K_e

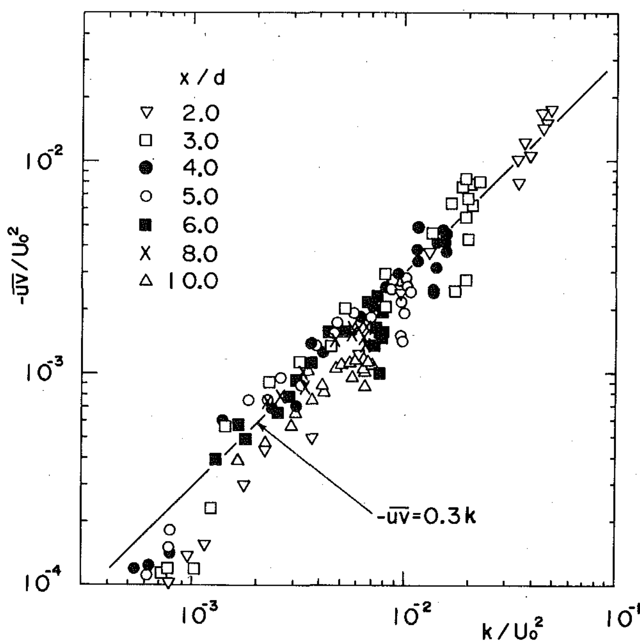

Fig. 10 Correlation between turbulent shear stress and turbulent kinetic energy

layer, where the turbulent shear stress estimated by assuming l_m or l_e constant may not be much different from measured one since the velocity gradient is very small. However values of K_m, K_e, C_m, and C_e vary with the axial distance, as already described in the earlier work [3].

It is interesting to note that the turbulent kinetic energy length scale is roughly half the mixing length, and they reach maxima around at $x/d = 5$ and afterward decrease monotonically in the downstream direction. These features are clearly shown in Fig. 9 which expresses the estimations of K_m and K_e in equation (7). The longitudinal distance is normalized with the reattachment length l, which is $1.3d$ in the present study as noted before. Included in the figure for comparison are the previous results for the two-dimensional flow over a blunt flat plate [3] in which the reattachment length is obtained as four times the plate thickness. Present values of K_m and K_e attain maxima at about $x/l = 3$, and on the other hand, the previous ones at

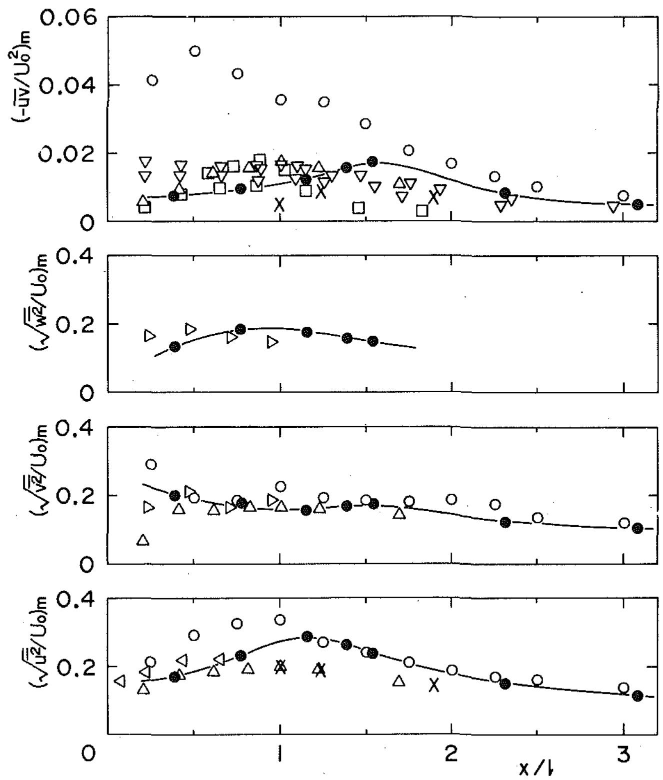

Fig. 11 Comparison of maximum values of turbulence intensities and turbulent shear stress, ●; present data, ○; Ota, et al., [3], ▷; Arie, et al., [17], □; Tani, et al., [18], ▽; Mueller, et al., [19], X; Wauschkuhn, et al., [20], ◁; Grant, et al., [21], △; Etheridge, et al., [7]

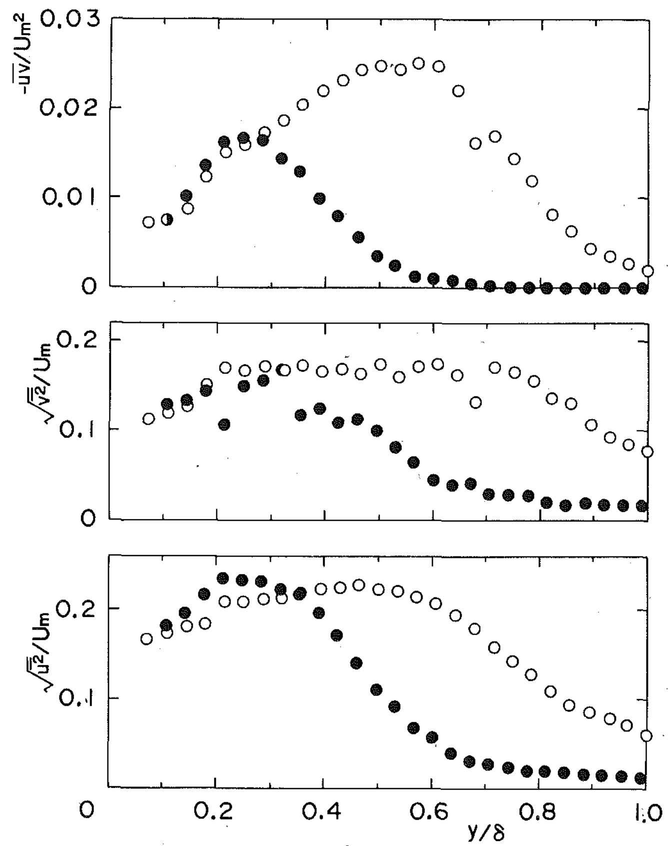

Fig. 12 Comparison of profiles of turbulance intensities and turbulent shear stress, ●; present data (x/l = 1.54), ○; Ota, et al., [3], (x/l = 1.50)

about $x/l = 2$. The latter is very large in the region close to the reattachment point as compared with the former. They however become nearly equal to each other at about $x/l = 3$.

Fig. 10 shows the correlation between the turbulent shear stress and the turbulent kinetic energy at several cross sections downstream from the reattachment point. That may be roughly described by an equation of the form

$$-\overline{uv}/U_0{}^2 = a(k/U_0{}^2)^n \tag{8}$$

where $n = 1$ corresponds to Bradshaw's model [14]. Values of a and n however vary with the axial distance. In general the present data deviate from the correlation given by equation (8) near the wall where the velocity gradient is large. However as shown in Fig. 10, it may be described that the turbulent shear stress is generally proportional to the turbulent kinetic energy and that an average line of the data is about $-\overline{uv} = 0.3k$, as included in the figure. The value of 0.3 is smaller than 0.4 shown in the previous study [3], in which the turbulent kinetic energy, however, does not include the contribution from the spanwise component $\overline{w^2}/2$. Recent results determined by including $\overline{w^2}/2$ into k for the two-dimensional flow [16] are almost described by the same equation as in the present study. In the outer part of the boundary layer (small values of k and $-\overline{uv}$), the data deviate from the aforementioned correlation. This may be originated from the low certainty of the data in such region since both k and $-\overline{uv}$ are very small.

In Figs. 11 and 12, the present results are compared with the previous works for different flow configurations [3, 7, 17–21] since there have been no appropriate data for the axisymmetric flow over bodies of revolution. Fig. 11 shows streamwise variations of maximum values of the turbulence intensities and the turbulent shear stress at each cross section. All the results show qualitatively same trends though the data for $(-\overline{uv}/U_0{}^2)_m$ by Ota, et al., [3], are a little different from others. The cross correlation between u and v may be much stronger in the two-dimensional flow than in the axisymmetric flow. However it is still not clear to the present authors why such high turbulent shear stress exists for the two-dimensional flow over a blunt flat plate. Previous data for $(\sqrt{\overline{u^2}}/U_0)_m$, which were already referred in the earlier paper [1], are not included. Only published data for $\sqrt{\overline{w^2}}$ in the separated and reattached flow may be those by Arie, et al., [17], for a flat plate with tail plate, and the present data are in good agreement with them.

Present data for $(\sqrt{\overline{u^2}}/U_0)_m$, $(\sqrt{\overline{w^2}}/U_0)_m$, and $(-\overline{uv}/U_0{}^2)_m$ reach maxima in the neighborhood of the reattachment point. On the other hand, there is no unobscured peak for $(\sqrt{\overline{v^2}}/U_0)_m$ there. The value of $(\sqrt{\overline{w^2}}/U_0)_m$ is not shown in the region of $x/l > 1.6$, since distinct maximum value of $\sqrt{\overline{w^2}}$ does not exist at cross sections far downstream from the reattachment point, as clearly understood from Fig. 2.

It is worth noting here that the data by Grant, et al., [21], and Etheridge, et al., [7], were obtained using the laser Doppler anemometer and others using the hot-wire anemometer. It may be more suitable to compare these results under the condition of normalizing them with the maximum velocity in the separated shear layer at each cross section in the separated and reattached flow regions and with U_m in the redeveloped region. It was however not easy to get their values from the papers published, and therefore the data are compared in the present form.

Fig. 12 compares the distributions of the turbulence intensities and the turbulent shear stress for the present axisymmetric flow and for the two-dimensional flow [3] at a cross section of about $x/l = 1.5$. Both of them indicate qualitatively the same trends, but the present data exhibit, as comparing with those for the two-dimensional flow, that the region affected by the separation and reattachment of flow is relatively small, that is; the turbulence intensities and the turbulent shear stress approach those of the main flow outside the boundary layer at about $y/\delta = 0.7$, and their approaching rate, on the other hand, is very slow for the two-dimensional flow.

Concluding Remarks

Turbulence characteristics in the separated, reattached, and redeveloped flow of air over a longitudinal circular cylinder having blunt leading edge were measured at Re = 42,100 with a constant temperature hot-wire anemometer. It is shown that the approach to those of a fully developed turbulent boundary layer needs a distance longer than at least ten times the cylinder diameter.

Prandtl's mixing length and turbulent kinetic energy length scale are presented in the boundary layer downstream of the reattachment point. They increase almost linearly near the cylinder surface and their gradients increase in the downstream direction from the point just downstream of reattachment to some point near $x/l = 3$(or $x/d = 4$) and subsequently decrease monotonically in the same direction. In the redeveloped flow region, the turbulent shear stress is roughly proportional to the turbulent kinetic energy, though quite large scatter is found to exist.

Present data for an axisymmetric flow are compared with the results for a two-dimensional flow over a blunt flat plate and for other flow configurations, and their differences are discussed.

Acknowledgments

The present authors express their thanks to Mr. Nobuhiko Kon and Mr. Yoshiaki Kuwamura for their assistance in the experiments.

References

1 Ota, T., "An Axisymmetric Separated and Reattached Flow on a Longitudinal Blunt Circular Cylinder," ASME JOURNAL OF APPLIED MECHANICS, Vol. 42, 1975, pp. 311–315.

2 Ota, T., and Itasaka, M., "A Separated and Reattached Flow on a Blunt Flat Plate," ASME *Journal of Fluids Engineering,* Vol. 98, 1976, pp. 79–86.

3 Ota, T., and Narita, M., "Turbulence Measurements in a Separated and Reattached Flow Over a Blunt Flat Plate," ASME *Journal of Fluids Engineering,* Vol. 100, 1978, pp. 224–228.

4 Durst, F., Melling, A., and Whitelaw, J. H., "Low Reynolds Number Flow Over a Plane Symmetric Sudden Expansion," *Journal of Fluid Mechanics,* Vol. 64, 1974, pp. 111–128.

5 Moon, L. F., and Rudinger, G., "Velocity Distribution in an Abruptly Expanding Circular Duct," ASME *Journal of Fluids Engineering,* Vol. 99, 1977, pp. 226–230.

6 Cherdron, W., Durst, F., and Whitelaw, J. H., "Asymmetric Flows and Instabilities in Symmetric Ducts With Sudden Expansions," *Journal of Fluid Mechanics,* Vol. 84, 1978, pp. 13–31.

7 Etheridge, D. W., and Kemp, P. H., "Measurements of Turbulent Flow Downstream of a Rearward-Facing Step," *Journal of Fluid Mechanics,* Vol. 86, 1978, pp. 545–566.

8 Badri Narayanan, M. A., Khadgi, Y. N., and Viswanath, P. R., "Similarities in Pressure Distribution in Separated Flow Behind Backward-Facing Steps," *Aeronautical Quarterly,* Vol. 25, 1974, pp. 305–312.

9 Honji, H., "The Starting Flow Down a Step," *Journal of Fluid Mechanics,* Vol. 69, 1975, pp. 229–240.

10 Hunt, J. C. R., et al., "Kinematical Studies of the Flows Around Free or Surface-mounted Obstacles; Applying Topology to Flow Visualization," *Journal of Fluid Mechanics,* Vol. 86, 1978, pp. 179–200.

11 Ota, T., and Kon, N., "Heat Transfer in an Axisymmetric Separated and Reattached Flow Over a Longitudinal Blunt Circular Cylinder," ASME *Journal of Heat Transfer,* Vol. 99, 1977, pp. 155–157.

12 Bissonnette, L. R., and Mellor, G. L., "Experiments on the Behavior of an Axisymmetric Turbulent Boundary Layer With a Sudden Circumferential Strain," *Journal of Fluid Mechanics,* Vol. 63, 1974, pp. 369–413.

13 Klebanoff, P. S., "Characteristics of Turbulence in a Boundary Layer With Zero Pressure Gradient," NACA Report 1247, 1955.

14 Launder, B. E., and Spalding, D. B., *Lectures in Mathematical Models of Turbulence,* Academic Press, London, 1972.

15 Cebeci, T., and Smith, A. M. O., *Analysis of Turbulent Boundary Layers,* Academic Press, New York, 1974.

16 Ota, T., and Kaneko, E., to be published.

17 Arie, M., and Rouse, H., "Experiments on Two-dimensional Flows Over a Normal Wall," *Journal of Fluid Mechanics,* Vol. 1, 1956, pp. 129–141.

18 Tani, I., Iuchi, M., and Komoda, H., "Experimental Investigation of Flow Separation Associated With a Step or a Groove," Aeronautical Research Institute, University of Tokyo, Report No. 364, 1961.

19 Mueller, T. J., and Robertson, J. M., "A Study of the Mean Motion and Turbulence Downstream of a Roughness Element," *Developments in Theoretical and Applied Mechanics,* Vol. 1, 1963, pp. 326–340.

20 Wauschkuhn, P., and Vasanta Ram, V. I., "Die Turbulente Grenzschicht Hinter Einem Ablösungsgebiet," *Zeitschrift für Flugwissenschaften,* Vol. 23, 1975, pp. 1–9.

21 Grant, I., Barnes, F. H., and Greated, C. A., "Velocity Measurements Using the Photon Correlation Technique in a Separated Boundary Layer," *The Physics of Fluids,* Vol. 18, 1975, pp. 504–507.

C.-Y. Wang

Professor,
Department of Mathematics,
Michigan State University,
East Lansing, Mich. 48824

Flow in Narrow Curved Channels

The flow through narrow, arbitrarily curved channels is formulated using intrinsic coordinates. An exact solution exists for constant curvature or circular arc boundaries. A perturbation scheme is used for the case of small, periodic curvature. The velocities and flow rates depend on both the curvature amplitude and the wave number. It is found that for a given pressure gradient per arc length, the flow may be larger for periodically curved channels than that of straight channels.

Introduction

The sheet flow in a curved, narrow channel is important in engineering and biological transport phenomena. For instance, the seepage flow through cracks and fissures of dams involve low Reynolds number flow through narrow channels. Also the pulmonary alveolar blood flow can be approximated by Stokes flow through narrow channels across which gasses are interchanged [1]. Fig. 1 shows such a channel in two dimensions. The position vector of the center line is given by

$$\mathbf{R} = X(s')\mathbf{i} + Y(s')\mathbf{j} \tag{1}$$

where s' is the arc length along the center line and $\mathbf{i}, \mathbf{j}, \mathbf{k}$ are unit vectors in the Cartesian directions x', y', z', respectively. The unit tangent $\mathbf{T}$ is defined by

$$\mathbf{T} = \frac{d\mathbf{R}}{ds'} = \frac{dX}{ds'}\mathbf{i} + \frac{dY}{ds'}\mathbf{j} \tag{2}$$

According to the Frenet formulas [2]

$$\frac{d\mathbf{T}}{ds'} = K'\mathbf{N}, \quad \frac{d\mathbf{N}}{ds'} = -K'\mathbf{T} \tag{3}$$

where $K'(s')$ is the curvature and $\mathbf{N}$ is the unit normal. The channel is bounded by two surfaces at a constant distance a from the center line and extended in the $\mathbf{k}$-direction indefinitely. For uniqueness we require $1/K' \geq a$. Any position inside the channel is given by

$$\mathbf{x}' = \mathbf{R}(s') + \eta\mathbf{N}(s') + z'\mathbf{k} \tag{4}$$

$$-a \leq \eta' \leq a \tag{5}$$

where η' is the distance from the center surface in $\mathbf{N}$-direction. The triad $\mathbf{T}, \mathbf{N}, \mathbf{k}$ constitutes an orthogonal coordinate system. From equations (2)–(4) we have

$$|d\mathbf{x}'|^2 = (1 - K'\eta')^2(ds')^2 + (d\eta')^2 + (dz')^2 \tag{6}$$

Contributed by the Applied Mechanics Division for publication in the JOURNAL OF APPLIED MECHANICS.

Discussion on this paper should be addressed to the Editorial Department, ASME, United Engineering Center, 345 East 47th Street, New York, N. Y. 10017, and will be accepted until June 1, 1980. Readers who need more time to prepare a discussion should request an extension from the Editorial Department. Manuscript received by ASME Applied Mechanics Division, January, 1979; final revision, July, 1979.

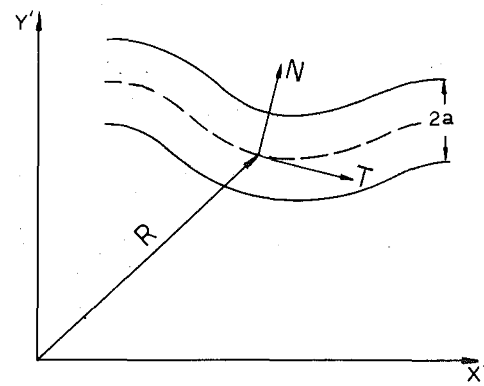

Fig. 1 The coordinate system

The scale factor in the s'-direction is thus $(1 - K'\eta')$. If the center line is straight, $K' = 0$ and the channel consists of two parallel flat planes. The purpose of the present paper is to investigate the effect of small but arbitrary curvature $K'(s')$ on the flow generated by a given pressure difference in the s' and z'-directions.

The Governing Equations

Due to geometry, we expect the velocities are independent of the z'-direction. We then normalize all lengths with respect to a, the pressure with respect to $\mu U/a$, the velocities with respect to U and K' with respect to $1/a$. Here μ is the viscosity and U is a velocity scale. In what follows the unprimed variables are nondimensionalized. Let u, v, w be velocity components in the s, η, z-directions, respectively. For a constant density fluid the continuity equation is

$$\frac{\partial}{\partial s}u + \frac{\partial}{\partial \eta}[(1 - K\eta)v] = 0 \tag{7}$$

The steady Navier-Stokes equations (see, e.g., [3]) give

$$\mathrm{Re}\left[\left(\frac{u}{1 - K\eta}\frac{\partial}{\partial s} + v\frac{\partial}{\partial \eta}\right)u - \frac{Kuv}{1 - K\eta}\right] = \frac{-1}{1 - K\eta}\frac{\partial p}{\partial s} - \frac{\partial}{\partial \eta}\left\{\frac{1}{1 - K\eta}\left[\frac{\partial v}{\partial s} - \frac{\partial}{\partial \eta}\langle(1 - K\eta)u\rangle\right]\right\} \tag{8}$$

$$\mathrm{Re}\left[\left(\frac{u}{1-K\eta}\frac{\partial}{\partial s}+v\frac{\partial}{\partial \eta}\right)v+\frac{Ku^2}{1-K\eta}\right]$$
$$=-\frac{\partial p}{\partial \eta}+\frac{1}{1-K\eta}\frac{\partial}{\partial s}\left\{\frac{1}{1-K\eta}\left[\frac{\partial v}{\partial s}-\frac{\partial}{\partial \eta}\left((1-K\eta)u\right)\right]\right\} \quad (9)$$

$$\mathrm{Re}\left[\left(\frac{u}{1-K\eta}\frac{\partial}{\partial s}+v\frac{\partial}{\partial \eta}\right)w\right]$$
$$=-\frac{\partial p}{\partial z}+\frac{1}{1-K\eta}\left\{\frac{\partial}{\partial s}\left(\frac{1}{1-K\eta}\frac{\partial w}{ds}\right)+\frac{\partial}{\partial \eta}\left[(1-K\eta)\frac{\partial w}{\partial \eta}\right]\right\} \quad (10)$$

Here Re is the Reynolds number $\rho Ua/\mu$. The boundary conditions are that the velocities vanish on $\eta = \pm 1$. Except in special cases, equations (7)–(10) are extremely difficult to solve exactly. In general, we shall assume the curvature, normalized by channel half width a, is small

$$K(s) = \epsilon k(s), \quad (11)$$

where $\epsilon \ll 1$ and k is of order unity. For narrow channels it is also reasonable to assume the Reynolds number is small, i.e.,

$$\mathrm{Re} = \epsilon\gamma = O(\epsilon) \quad (12)$$

The pressure, velocities are then expanded in terms of ϵ

$$p = p_0 + \epsilon p_1 + \epsilon^2 p_2 + \ldots \quad (13)$$

$$u = u_0 + \epsilon v_1 + \epsilon^2 v_2 + \ldots$$
$$v = v_0 + \epsilon v_1 + \epsilon^2 v_2 + \ldots$$
$$w = w_0 + \epsilon w_1 + \epsilon^2 w_2 + \ldots \quad (14)$$

The order ϵ^0 terms from equations (7)–(10) are

$$\frac{\partial u_0}{\partial s}+\frac{\partial v_0}{\partial \eta}=0 \quad (15)$$

$$\frac{\partial p_0}{\partial s}=-\frac{\partial}{\partial \eta}\left(\frac{\partial v_0}{\partial s}-\frac{\partial u_0}{\partial \eta}\right) \quad (16)$$

$$\frac{\partial p_0}{\partial \eta}=\frac{\partial}{\partial s}\left(\frac{\partial v_0}{\partial s}-\frac{\partial u_0}{\partial \eta}\right) \quad (17)$$

$$\frac{\partial p_0}{\partial z}=\frac{\partial^2 w_0}{\partial s^2}+\frac{\partial^2 w_0}{\partial \eta^2} \quad (18)$$

Given a zeroth-order linear pressure gradient,

$$p_0 = 2\alpha s + 2\beta z + \text{constant} \quad (19)$$

where α, β are constants of order unity, we find

$$u_0 = \alpha(\eta^2 - 1), \quad v_0 = 0, \quad w_0 = \beta(\eta^2 - 1) \quad (20)$$

This is exactly Poiseuille's flow between flat parallel plates.

The first-order correction is governed by

$$\gamma\left(u_0\frac{\partial}{\partial s}+v_0\frac{\partial}{\partial \eta}\right)u_0$$
$$=-\frac{\partial p_1}{\partial s}-k\eta\frac{\partial p_0}{\partial s}-\frac{\partial}{\partial \eta}\left(\frac{\partial v_1}{\partial s}+k\eta\frac{\partial v_0}{\partial s}+ku_0-\frac{\partial u_1}{\partial \eta}\right) \quad (21)$$

$$\gamma\left(u_0\frac{\partial}{\partial s}+v_0\frac{\partial}{\partial \eta}\right)v_0$$
$$=-\frac{\partial p_1}{\partial \eta}+\frac{\partial}{\partial s}\left(\frac{\partial v_1}{\partial s}+ku_0+k\eta\frac{\partial v_0}{\partial s}-\frac{\partial u_1}{\partial \eta}\right)$$
$$+k\eta\frac{\partial}{\partial s}\left(\frac{\partial v_0}{\partial s}-\frac{\partial u_0}{\partial \eta}\right) \quad (22)$$

$$\gamma\left(u_0\frac{\partial}{\partial s}+v_0\frac{\partial}{\partial \eta}\right)w_0=-\frac{\partial p_1}{\partial z}+\frac{\partial}{\partial s}\left(\frac{\partial w_1}{\partial s}+k\eta\frac{\partial w_0}{\partial s}\right)$$
$$+\frac{\partial}{\partial \eta}\left(\frac{\partial w_1}{\partial \eta}-k\eta\frac{\partial w_0}{\partial \eta}\right)+k\eta\left(\frac{\partial^2 w_0}{\partial \eta^2}+\frac{\partial^2 w_0}{\partial s^2}\right) \quad (23)$$

$$\frac{\partial u_1}{\partial s}+\frac{\partial}{\partial \eta}(v_1 - k\eta v_0) = 0 \quad (24)$$

The boundary conditions are

$$u_1(\pm 1) = v_1(\pm 1) = w_1(\pm 1) = 0 \quad (25)$$

The first-order perturbation equations (21)–(25) can be solved in closed form for several special curvatures: $k(s)$ equals constant, cos (λs) and exp $(\pm\lambda s)$ (including cosh (λs) and sinh (λs)). We shall be concerned with the more important cases $k(s)$ = constant and $k(s) = \cos(\lambda s)$ only.

Constant Curvature

In this case the Navier-Stokes equations, equations (7)–(10), admit an exact solution. Although this solution may also be obtained from cylindrical polar coordinates, for consistency of notation we shall use the present intrinsic s, η, z coordinates.

Let the pressure be linear in η and z. The solution to equations (7)–(10) is

$$v = 0 \quad (26)$$

$$u=\frac{-1}{2K^2}\frac{\partial p}{\partial s}\left\{\frac{(1-K^2)^2}{4K}\ln\left(\frac{1-K}{1+K}\right)\frac{1}{(1-K\eta)}\right.$$
$$-\frac{1}{4K}\left[(1-K)^2\ln(1-K)-(1+K)^2\ln(1+K)\right](1-K\eta)$$
$$\left.-(1-K\eta)\ln(1-K\eta)\right\} \quad (27)$$

$$w=\frac{-1}{4K}\frac{\partial p}{\partial z}\left\{\frac{4}{\ln\left(\frac{1-K}{1+K}\right)}\ln\left(\frac{1-K}{1-K\eta}\right)-2(1-\eta)+K(1-\eta^2)\right\}$$
$$(28)$$

Fig. 2 shows the velocity profiles u and w for various K. It is seen that the maxima of velocities shift toward $\eta = 1$ or toward the wall which has larger local curvature. Let the flow in the s-direction, per unit z, be F_s.

$$F_s=\int_{-1}^{1}u\,d\eta=\frac{1}{8K^4}\frac{\partial p}{\partial s}\left\{(1-K^2)^2\left[\ln\left(\frac{1-K}{1+K}\right)\right]^2-4K^2\right\} \quad (29)$$

The flow in the z-direction, per unit s, is

$$F_z=\int_{-1}^{1}w(1-K\eta)\,d\eta$$
$$=\frac{1}{K^2}\frac{\partial p}{\partial z}\left\{K-\left[2K\ln(1-K)+K+\frac{1}{2}(1-K)^2\ln(1-K)\right.\right.$$
$$\left.\left.-\frac{1}{2}(1+K)^2\ln(1+K)\right]\Big/\ln\left(\frac{1-K}{1+K}\right)\right\} \quad (30)$$

These functions are plotted in Fig. 3. We see that increased curvature decreases the azimuthal flow F_s but increases the axial flow F_z. In the limit of $K \to 0$

$$F_s \to -\frac{2}{3}\frac{\partial p}{\partial s}, \quad F_z \to -\frac{2}{3}\frac{\partial p}{\partial z} \quad (31)$$

These are the flow rates for plane Poiseuille flow. In the limit of $K \to 1$, which approximates a circular cylinder with a thin wire at the center,

$$F_s \to -\frac{1}{2}\frac{\partial p}{\partial s}, \quad F_z \to -\frac{\partial p}{\partial z} \quad (32)$$

Although the results of this section is valid for $0 \le K \le 1$, end effects should be considered when K is not small.

Sinusoidal Curvature

The geometries of the center line for $K = \epsilon \cos \lambda s$ are shown in Fig. 4. Notice these curves are periodic but not simple harmonic. We shall limit to $\lambda \ge 0.472$, in order to avoid cross overs of the center line.

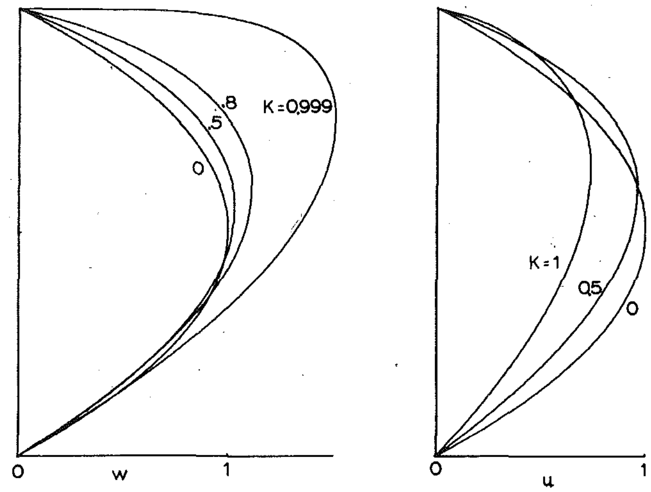

Fig. 2 Velocity profiles for constant curvature

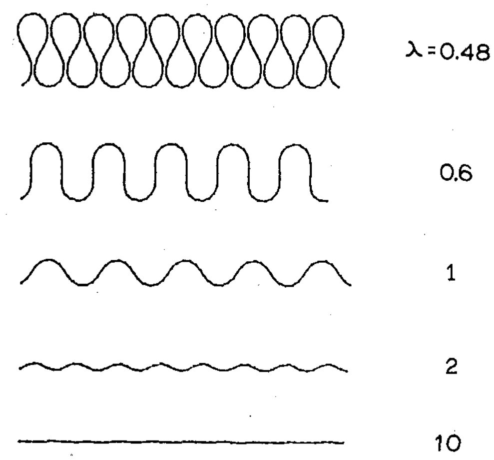

Fig. 4 Center-line geometries for sinusoidal curvature

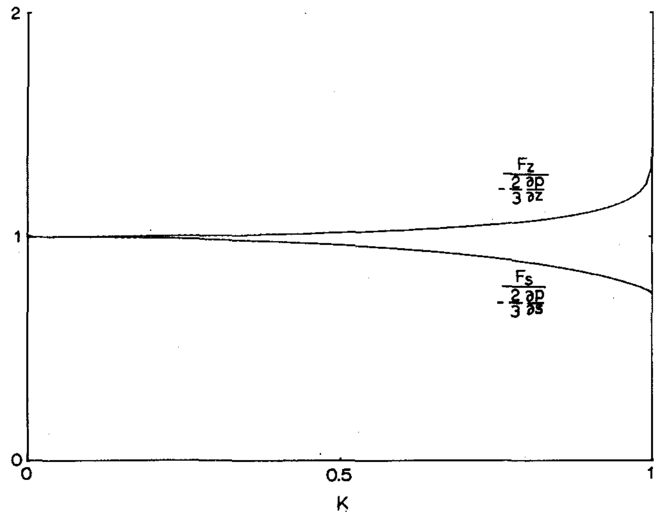

Fig. 3 Axial and azimuthal flow rates for constant curvature

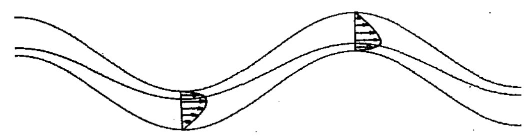

Fig. 5 Schematic diagram of the flow in a periodically curved channel

For small curvature the zeroth-order solution is given by equation (20). We assume the mean pressure gradient is given by equation (19). The first-order equations, equations (21)–(24), reduce to

$$\frac{\partial}{\partial \eta}\left(\frac{\partial v_1}{\partial s} - \frac{\partial u_1}{\partial \eta}\right) + \frac{\partial p_1}{\partial s} = -4\alpha k \eta \tag{33}$$

$$-\frac{\partial}{\partial s}\left(\frac{\partial v_1}{\partial s} - \frac{\partial u_1}{\partial \eta}\right) + \frac{\partial p_1}{\partial \eta} = \alpha \frac{dk}{ds}(\eta^2 - 1) \tag{34}$$

$$\frac{\partial^2 w_1}{\partial s^2} + \frac{\partial^2 w_1}{\partial \eta^2} = 2\beta k \eta \tag{35}$$

$$\frac{\partial u_1}{\partial s} + \frac{\partial v_1}{\partial \eta} = 0 \tag{36}$$

If $k = \cos \lambda s$, we set

$$u_1 = f'(\eta)\cos\lambda s, \quad v_1 = f(\eta)\lambda \sin \lambda s \tag{37}$$

$$w_1 = g(\eta)\cos \lambda s, \quad p_1 = \varphi(\eta)\sin\lambda s \tag{38}$$

Equations (33)–(36) reduce further to

$$f''' - \lambda^2 f' - \lambda\varphi = 4\alpha\eta \tag{39}$$

$$\lambda f'' - \lambda^3 f - \varphi' = \lambda\alpha(\eta^2 - 1) \tag{40}$$

$$g'' - \lambda^2 g = 2\beta\eta \tag{41}$$

with the boundary conditions

$$f'(\pm 1) = f(\pm 1) = g(\pm 1) = 0 \tag{42}$$

The solutions are

$$f = \frac{2\alpha \cosh \lambda}{\lambda^2(\sinh\lambda\cosh\lambda + \lambda)} \times (\eta \sinh \lambda\eta - \tanh\lambda \cosh \lambda\eta) - \frac{\alpha}{\lambda^2}(\eta^2 - 1) \tag{43}$$

$$g = \frac{2\beta}{\lambda^2}\left(\frac{\sinh\lambda\eta}{\sinh\lambda} - \eta\right) \tag{44}$$

$$\varphi = \frac{4\alpha\cosh\lambda \sinh\lambda\eta}{\lambda(\sinh\lambda\cosh\lambda + \lambda)} - \frac{2\alpha}{\lambda}\eta \tag{45}$$

As in the case of constant curvature, we find the velocities increase toward the side of larger local curvature. The stream lines shift from side to side, seeking a less tortuous path than those described by the walls. The pressure, 90° out-of-phase, is maximum on the "windward" side of the walls (Fig. 5).

The first-order solutions are periodic in s and do not contribute to the mean flow through the channel. Let us use a bar to denote the nonperiodic part (in s) of a variable. The nonperiodic, order ϵ^2 terms of equations (7)–(10) are

$$0 = -\overline{k^2}\eta^2\frac{\partial p_0}{\partial s} - \frac{\partial}{\partial \eta}\left[\overline{ku_1} + \eta\left(\overline{k\frac{\partial v_1}{\partial s}} + \overline{k^2}u_0\right) - \frac{\partial \overline{u_2}}{\partial \eta}\right] \tag{46}$$

$$0 = \overline{\eta\frac{\partial}{\partial s}\left(k\frac{\partial w_1}{\partial s}\right)} + \frac{\partial}{\partial \eta}\left(\frac{\partial \overline{w_2}}{\partial \eta} - \eta\overline{k\frac{\partial w_1}{\partial \eta}}\right) + \overline{k^2}\eta^2\frac{\partial^2 w_0}{\partial \eta^2} + \eta\left[\overline{k\frac{\partial^2 w_1}{\partial s^2}} + \overline{k\frac{\partial^2 w_1}{\partial \eta^2}} - \overline{k^2}\frac{\partial}{\partial \eta}\left(\eta\frac{\partial w_0}{\partial \eta}\right)\right] \tag{47}$$

$$\frac{\partial \overline{p_2}}{\partial \eta} = 0, \quad \frac{\partial \overline{v_2}}{\partial \eta} = \frac{\partial}{\partial \eta}(\eta\overline{kv_1}) \tag{48}$$

After integration we find

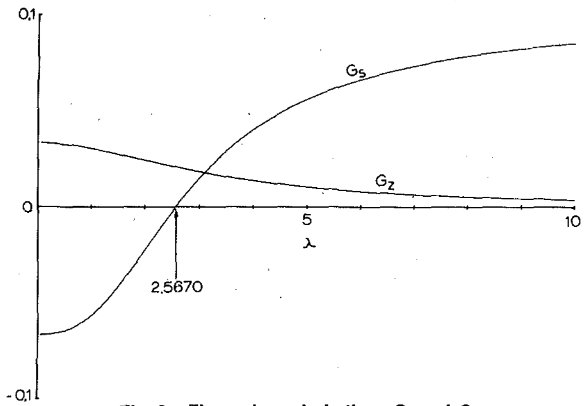

Fig. 6 Flow rate perturbations G_s and G_z

$$\overline{u}_2 = \frac{\alpha}{12}(\eta^4 - 1) - \frac{\alpha}{2\lambda^2}(\eta^2 - 1) + \frac{\alpha}{\lambda^2(\sinh\lambda\cosh\lambda + \lambda)}\left[\frac{2}{\lambda}\cosh\lambda\cosh\lambda\eta + (\lambda\cosh\lambda)\eta^2\cosh\lambda\eta - (\cosh\lambda + \lambda\sinh\lambda)\eta\sinh\lambda\eta - \frac{2}{\lambda}\cosh^2\lambda + \sinh\lambda\cosh\lambda - \lambda\right] \quad (49)$$

$$\overline{w}_2 = \frac{\beta}{\lambda^3\sinh\lambda}(\lambda\eta\sinh\lambda\eta - \cosh\lambda\eta - \lambda\sinh\lambda + \cosh\lambda) - \frac{\beta}{2\lambda^2}(\eta^2 - 1) \quad (50)$$

$$\overline{p}_2 = \overline{v}_2 = 0 \quad (51)$$

The mean flows per unit width are

$$\overline{F}_s = \int_{-1}^{1}(u_0 + \epsilon^2\overline{u}_2 + \ldots)d\eta = \frac{-4\alpha}{3}[1 + \epsilon^2 G_s(\lambda) + O(\epsilon^4)] \quad (52)$$

$$G_s \equiv -\frac{3}{2\lambda^2}\left\{\frac{1}{3} - \frac{\lambda^2}{15} + \frac{1}{(\sinh\lambda\cosh\lambda + \lambda)} \times\left[\cosh\lambda\sinh\lambda\left(\frac{5}{\lambda^2} + 1\right) - \frac{4}{\lambda}\cosh^2\lambda - \frac{1}{\lambda} - \lambda\right]\right\} \quad (53)$$

$$\overline{F}_z = \int_{-1}^{1}\overline{(w_0 + \epsilon w_1 + \epsilon^2 w_2 + \ldots)(1 - \epsilon k\eta)}d\eta = \frac{-4\beta}{3}[1 + \epsilon^2 G_z + O(\epsilon^4)] \quad (54)$$

$$G_z \equiv \frac{1}{2\lambda^2} + \frac{3}{2\lambda^4} - \frac{3\cosh\lambda}{2\lambda^3\sinh\lambda} \quad (55)$$

Fig. 6 shows G_s and G_z as a function of λ. G_z is always positive, indicating an increase in axial flow due to curvature. As λ increases, G_z decreases to zero. The function G_s, however, behaves differently. There is a decrease in flow for $0.472 \leq \lambda < 2.567$ and an increase in flow for $\lambda > 2.567$. As λ approaches infinity G_s approaches 1/10. The foregoing conclusions are for a given nonzero curvature amplitude ϵ. If the channel were straight, we have $\epsilon = 0$ and $\overline{F}_s, \overline{F}_z$ both reduce to the correct Poiseuille flow rate. We arrive at the important result: For a given pressure gradient, the mean flow in a periodically curved channel may be larger or smaller than that of a straight channel.

Discussion

The flow in symmetrical channels with slowly varying curvature of the walls has been studied by Langlois [4] and Fraenkel [5]. The center line is straight while the channel width varies. Both authors used wedge flows to approximate local flow distributions. In the present paper the channel width is the same and the curvature of the center line varies slowly. This kind of problem can be studied only through the use of the intrinsic coordinate system developed here.

By assuming the curvature is much smaller than the channel width, we are able to solve for the fluid flow in arbitrarily periodically curved channels. Although the Reynolds number is assumed to be of order ϵ, the inertial terms affected neither the first-order solution nor the second-order mean flow in periodically curved channels.

We have studied one Fourier component of the curvature of a periodically curved channel. Since the Navier-Stokes equations has been linearized by the perturbation scheme, one can superpose other Fourier components. In the current analysis, the wave number λ is assumed to be of order unity. This assumption may be relaxed since large λ does not alter the order of magnitude of the results.

The straight channel is still the most efficient for the delivery of fluid between a given distance. However, in this paper, the pressure gradient is not based on direct distance, but based on unit arc length s, or unit surface area. We found that for given surface area (a condition used in transport processes) the periodically curved channel may be more efficient.

For the s-direction flow this phenomenon can partially be explained as follows. The flow rate decreases as the fluid turns a curve as indicated by our constant curvature result. However, the flow also tends to increase for periodically curved channels since, from Fig. 5, the bulk of the fluid takes a more direct path than the pressure gradient (which is based on the longer center-line arc length). For large λ the latter reason prevails and we have a net increase in flow.

The z-direction flow is parallel. The only other paper which considers parallel flow between wavy plates is due to Wang [6]. In that paper the maximum curvature is assumed to be much larger than (mean distance between the plates)$^{-1}$, while the present paper assumes the opposite, that the curvature is much smaller than (mean distance)$^{-1}$. However, in [6], it was noted that the flow rate may be increased by increasing the phase shift of the plates, while both the cross-sectional area and the wetted perimeter remain the same.

The present paper yields a similar result. While the curvature changes neither the cross-sectional area nor the boundary surface area (wetted perimeter), the z-direction flow per unit s is larger for curved channels (whether the curvature is constant or periodic) than that of the straight channel. We, therefore, make the following conjecture. In the set of all parallel flows with same cross-sectional area and the same wetted perimeter, the minimum flow rate occurs with the geometry which yields the least variation in surface shear. This situation corresponds to the in phase flow of [6] and the straight channel of the present paper.

References

1 Fung, Y. C., and Sobin, S. S., "Pulmonary Alveolar Blood Flow," *Bioengineering Aspects of the Lung*, ed., West, J. B., Dekker, 1977, Chapter 4.

2 Sokolnikoff, I. S., *Tensor Analysis—Theory and Applications to Geometry and Mechanics of Continua*, Wiley, 1964, Chapter 3.

3 Batchelor, G. K., *An Introduction to Fluid Dynamics*, Cambridge University Press, 1970, Appendix 2.

4 Langlois, W. E., "Creeping Viscous Flow Through a Two-Dimensional Channel of Varying Gap," *Proceedings, 3rd U. S. National Congress of Applied Mechanics*, 1958, pp. 777–783.

5 Fraenkel, L. E., "Laminar Flow in Symmetrical Channels With Slightly Curved Walls," *Proceedings of the Royal Society*, Series A, Vol. 272, 1963, pp. 406–428.

6 Wang, C. Y., "Parallel Flow Between Corrugated Plates," *Journal of the Engineering Mechanics Division*, ASCE, Vol. 102, No. EM6, 1976, pp. 1088–1090.

K. S. Kim
Research Fellow
Department of Aeronautics
California Institute of Technology,
Pasadena, Calif. 91125

R. J. Clifton
Professor of Engineering,
Division of Engineering,
Brown University,
Providence, R. I. 02912

Pressure-Shear Impact of 6061-T6 Aluminum[1]

Experimental results are presented for impact of two parallel plates of 6061-T6 Aluminum, skewed at an angle of 26.6° from the axis of the projectile. A transverse displacement interferometer (TDI) [1] with a 200 lines/mm grating is used to monitor the transverse motion of the rear surface of the aluminum target plate. Two first-order diffracted laser beams are used for this TDI with a resulting sensitivity of 2.5 μm per fringe. In addition the normal motion of the rear surface is monitored simultaneously by means of a velocity interferometer [2] in which the zeroth-order diffracted beam is used as the beam reflected from a moving mirror. Comparison of the velocity-time profiles of the target rear surface with those predicted by the analysis given by Abou-Sayed and Clifton [17] indicates that the computed transverse velocity-time profiles have regions of steeper slope than observed in the experiments. This discrepancy appears to be mainly due to the inadequacy of the assumption of isotropic hardening and the Huber-Mises yield function in the analysis [17]. The sensitivity of the transverse velocity profiles to the plastic flow characteristics of the material suggests that the pressure-shear impact experiment, when used with a TDI, is a good technique for the study of material properties at very high strain rates ($10^4 \sim 10^5$ sec^{-1}) and under postshock conditions.

Introduction

Plastic wave problems of combined compression and shear in solids have been an interest of many investigators in the past two decades [3–19]. One-dimensional plane wave problems involving combined stresses have received primary attention, since these waves provide varied stress paths for probing the flow characteristics of solids, yet the analysis is relatively simple. While considerable theoretical work has been done on the problem [10–17], relatively few experimental studies have been attempted. Although a technique for an oblique impact experiment was introduced by Abou-Sayed and Clifton [18, 19], lack of sensitivity in the dynamic Moirè technique [18] used for monitoring transverse displacements has discouraged further use of this technique. Recently, the authors and Kumar have developed a new transverse displacement interferometer (TDI) [1] that allows the transverse motion of a surface to be measured with satisfactory sensitivity for such experiments. The normal component of the surface motion can be monitored by means of standard laser interferometer techniques that have been developed and used for the usual plate impact experiments at normal incidence. These optical techniques could also prove to be useful in the shear wave experiments employing nonparallel impact faces [20, 21] since they would allow simultaneous monitoring of normal and transverse motion and would not be limited to nonmetallic materials.

Many research workers have investigated the behavior of aluminum at high strain rates and tried to establish constitutive relations that model its behavior as an elastic/viscoplastic material [22, 23]. Most investigations have depended on normal plate impact experiments for determining values of parameters in the models. However, the longitudinal wave profiles appear to be less sensitive to the dynamic flow relations than transverse wave profiles because the hydrostatic pressure makes the longitudinal wave profile depend largely on the elastic compressibility of the material, except for a region of small plastic strains near the wave front.

In this work, a TDI is used together with a normal velocity interferometer (NVI), to monitor simultaneously, and at one point, the normal and transverse components of the particle velocity of the free rear surface of a 6061-T6 Aluminum target subjected to symmetric, skewed (26.6° from normal impact) impact at a projectile velocity of approximately 0.22 mm/μsec. The experimental results are compared to theoretical predictions based on an elastic/viscoplastic model for 6061-T6 Aluminum [17]. Results show that the experimental transverse velocity-time profile following the elastic precursor rises

[1]This work was supported by the National Science Foundation, including support provided through the Brown University Materials Research Laboratory. It is part of the research carried out by the first author in partial fulfillment of the requirements for a PhD degree from Brown University.

Contributed by the Applied Mechanics Division and presented at the Winter Annual Meeting, New York, N. Y., December 2–7, 1979, of THE AMERICAN SOCIETY OF MECHANICAL ENGINEERS.

Discussion on this paper should be addressed to the Editorial Department, ASME, United Engineering Center, 345 East 47th Street, New York, N. Y. 10017, and will be accepted until June 1, 1980. Readers who need more time to prepare a discussion should request an extension from the Editorial Department. Manuscript received by ASME Applied Mechanics Division, October, 1978; final revision, July, 1979. Paper No. 79-WA/APM-39.

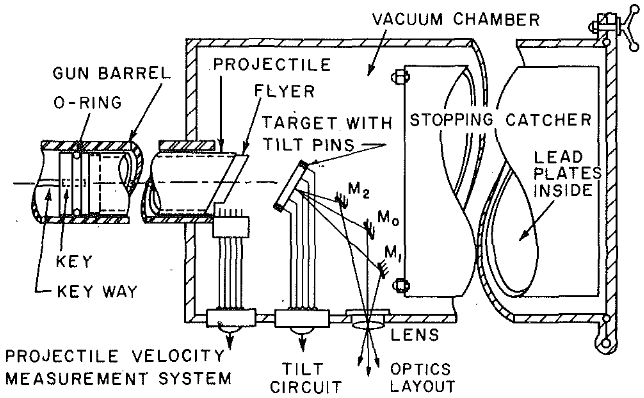

Fig. 1 Schematic of pressure shear experiment

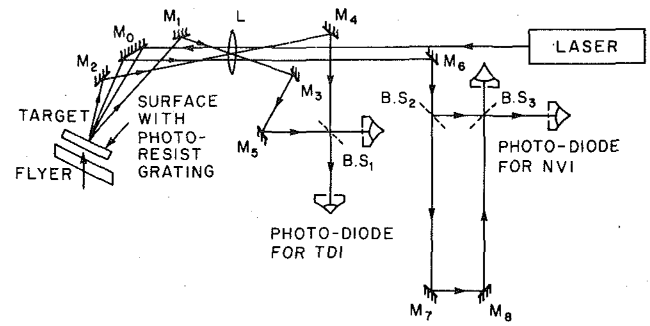

Fig. 2 Schematic of traverse displacement interferometer with normal velocity interferometer

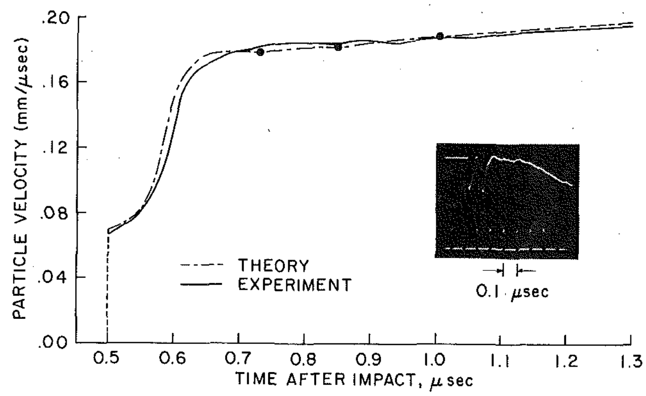

Fig. 3 Normal velocity-time profile at the rear surface

initially more slowly than predicted by the analysis. This discrepancy appears to be due primarily to the analysis using a model that does not account adequately for the stress path dependence of plastic flow.

Experimental Procedure

Plane waves of combined compression and shear were generated by impact of two skewed flat plates of 6061-T6 Aluminum as shown in Fig. 1. A disk (50.80-mm dia, 3.20 or 6.35-mm thick) of 6061-T6 Aluminum was used as a target specimen. The disk contained four 5-mm-dia holes, equally spaced on a circle of 38.10-mm dia. Each of these holes contained a 3-mm-dia contact pin held in place by epoxy resin. The fronts of the pins were set in the plane of the front surface of the specimen within a tolerance of 0.2 μm. The specimen and the flyer plates were lapped flat to better than 1 μm over the width of the plates. Surface roughness was approximately 0.03 μm.

A 63.5-mm single-stage gas gun capable of launching projectiles at velocities up to 0.3 mm/μsec was used to accelerate the flyer. Details of the gun have been described by Abou-Sayed and Clifton [18]. The target was mounted in a chamber evacuated to a pressure of 50 μm Hg before the shot in order to minimize the air cushion between flyer target. The velocity of the projectile was measured by recording the times at which a series of voltage-biased thin wires were shorted out by contacting the flyer as shown schematically in Fig. 1. Angular misalignment between the flyer and target at impact was determined by recording the times at which the four voltage-biased contact pins make contact with the flyer. Initial alignment of the target impact face parallel to the impact face of the flyer is accomplished by an optical technique developed by Kumar and Clifton [24]. This technique insures initial parallelity to an accuracy of 2×10^{-5} rad, which is considerably better than required. The transverse and normal components of the motion of the target rear surface were monitored, respectively, by means of the TDI and NVI as shown in Fig. 2. The diffraction grating on the rear surface of the target specimen was obtained by copying a 200 lines/mm ruled glass grating directly onto the mirrorized surface using a photo-resist process with Kodak 747 negative photo-resist.

For the TDI the two first-order diffracted beams were used for shots 1–8; the two second-order diffracted beams were used for shot No. 9. The resulting sensitivity, $d/2n$ [1], where d is the pitch of the grating and n is the order of the diffracted beams, was 2.5 μm of transverse displacement per fringe for shots 1–8 and 1.25 μm per fringe for shot No. 9. The incident and reflected beams are aligned to lie in the plane perpendicular to the grating and parallel to the grating lines. This alignment eliminates the need for correcting the recorded displacement due to non-normal incidence of the laser beam [1], since the diffracted beams are perfectly symmetric and unaffected by the normal motion of the surface.

The zeroth-order reflected beam was used for the NVI. The delay leg length was 1745 mm, which corresponds to a delay time $\tau = 5.82$ ns. The light source used for the TDI and NVI was an argon ion laser with a maximum output of 1.5 watts of single mode, single frequency light at a wavelength of $\lambda = 5.145 \times 10^{-4}$ mm. With these values for delay time and wavelength the sensitivity, $\lambda/2\tau$ [25], is 0.0442 mm/μs per fringe. The diameter of the laser beam was 1.3 mm. Monsanto MD-2 photo diodes were used as detectors, and the detected signals were recorded on Tektronix 7704 and 7904 oscilloscopes for the TDI and NVI, respectively. Both scopes were triggered, after a preset delay, by the first step output of the logic circuit used in measuring the tilt. Data from photographs of the oscilloscope traces were reduced by reading the times between the phases of the traces by means of a traveling microscope. For the NVI, the velocity-time relation measured at 30 points using the aforementioned technique was displayed on a graph and interpolated graphically. Since the TDI gives a displacement-time relation, the displacement was differentiated with respect to time by means of a cubic spline interpolation method which is described in the Appendix. The standard deviation of the error in the recorded displacement at a given time is estimated to be approximately 1.0×10^{-2} μm; the corresponding error in the transverse velocity is expected to be less than 1.0×10^{-3} mm/μsec.

Experimental Results

A summary of the experiments is given in Table 1. The two low velocity impacts, shots 1 and 2, were carried out to determine whether or not slip occurs at the interface between the flyer and the target. In these shots the target remains nearly elastic. The TDI record in shot No. 2 indicates that the transverse velocity reached the transverse component of the projectile velocity, demonstrating that no slip occurred at the impact face.

A velocity-time profile of the normal component of particle velocity at the target rear surface is shown in Fig. 3 for one of the higher velocity shots—shot No. 7 with a projectile velocity $V_0 = 0.215$ mm/μsec. The oscilloscope trace of the normal velocity interferometer (NVI)

Table 1 Summary of pressure-shear impact experiments on 6061-T6 Aluminum

Shot No.	Target Thickness (mm)	Projectile vel. (mm/μsec)	Skew Angle (degrees)	Tilt Angle (radians)	Laser Power (mW)	Remarks on Oscilloscope Traces
1	6.35	0.074	26.6	0.5×10^{-4}	700	Poor traces due to mode transition of laser
2	6.35	0.076	26.6	2.0×10^{-4}	700	Poor NVI trace due to poor surface reflectivity
3	6.35	0.214	26.6	-	700	Projectile velocity pin squeezed between impact faces
4	6.35	0.213	26.6	1.0×10^{-4}	200	Excellent traces
5	6.35	0.214	26.6	1.0×10^{-4}	800	Poor TDI trace due to poor surface reflectivity
6	3.20	0.214	26.6	6.0×10^{-4}	200	No NVI trace due to late trigger
7	3.20	0.215	26.6	0.5×10^{-4}	200	Excellent traces
8	6.15	0.215	26.6	12.6×10^{-4}	200	No NVI trace
9	6.15	0.168	26.6	12.2×10^{-4}	200	Excellent traces 2nd order beam used for TDI

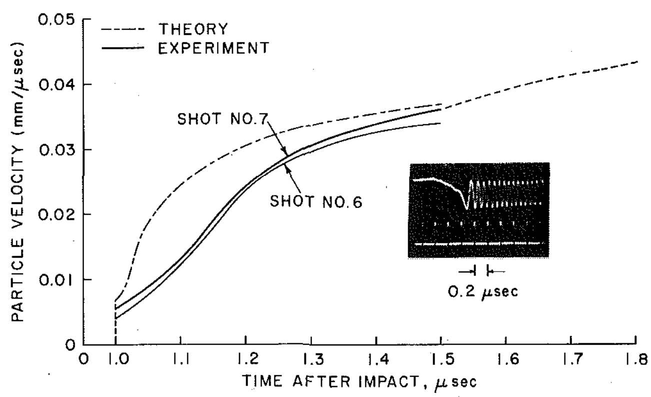

Fig. 4 Transverse velocity-time profile at the rear surface

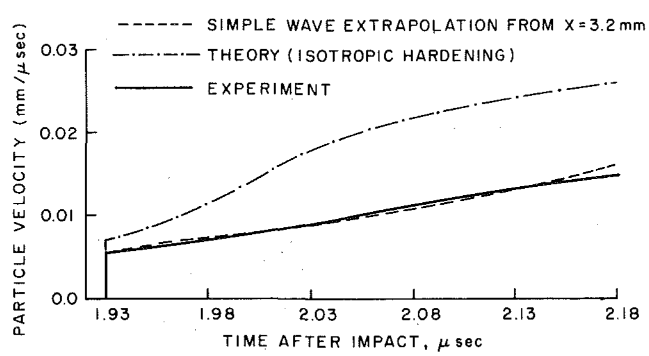

Fig. 5 Transverse velocity-time profile at the rear surface (specimen thickness 6.2 mm)

is as clean as usually obtained when a grating is not used. The projectile velocity for shot No. 7 produces normal and transverse components of the particle velocity at the impact face of 0.096 mm/μsec, and 0.048 mm/μsec, respectively. These particle velocities correspond to initial tractions at the impact face of 1.65 GPa normal stress and 0.41 GPa shear stress, assuming instantaneous elastic response of the flyer and target.

Velocity-time profiles of transverse components of particle velocity at the target rear surface are shown in Figs. 4 and 5. Recorded profiles for two shots (6 and 7) on 3.2-mm-thick targets are shown in Fig. 4 in order to give an indication of the reproducibility of the results. A recorded profile for one shot (No. 8) on a 6.15-mm-thick target impacted at a comparable projectile velocity is shown in Fig. 5 in order to show the change in wave profile with distance of propagation.

The oscilloscope trace shown in the insert in Fig. 4 is from shot No. 6 due to the better photographic quality obtained by using the Tektronix 7904 oscilloscope for the TDI in this shot. The toe at the front of the oscilloscope trace for the TDI presumably corresponds to transverse displacement resulting from an oblique reflection of the longitudinal wave at the free surface. The oblique incidence of the longitudinal wave is due to the tilt between the impact faces of the flyer and target. This tilt was measured to be approximately 0.6 mrad, which would cause the normal to the longitudinal wave front to deviate from the normal to the rear surface by approximately 0.018 rad (1.03°). For a longitudinal plane wave of this angle of incidence the predicted ratio of transverse to longitudinal velocity is 0.015, which gives a peak transverse velocity of 0.003 mm/μsec. This value compares favorably with the peak transverse velocity in the toe region in Fig. 4. The dashed line beyond 1.5 μsec in Fig. 4 indicates the recorded transverse motion after the longitudinal wave reflected from the rear surface has made a round trip in the target. Since the effect of this reflected wave is not included in the theoretical curve, comparison between theoretical and experimental profiles is not meaningful beyond 1.5 μsec after impact.

The experimental results have been compared with computed velocity-time profiles [17], although the thicknesses of the targets for these experiments are different from that (2 mm) used in the analysis [17]. Such comparisons are possible, however, since the solution [17] shows that a simple wave pattern develops at distances remote from the impact face. Thus the comparison is made by extrapolating the computed solution to the thicknesses of 3.2 mm and 6.15 mm by assuming that the solution remains constant along lines x/t = constant where x is distance from the impact plane and t is time from impact.

Fig. 3 shows that the extrapolated and recorded normal velocity profiles agree reasonably well. However, the extrapolated solution does not account for elastic precursor decay between 2.0 and 3.2 mm, and the observed main plastic wave profile is slightly more spread out than obtained by the simple wave extrapolation. In Fig. 3 the dots on the theoretical profile denote arrival times of wavefront-like features. The first dot corresponds to a reflection from the elastic plastic boundary shown in Fig. 8 of [17]. The second dot is the arrival time of an elastic longitudinal wave emanating from the interaction of the reflected longitudinal wave front and the oncoming shear wave front. The third dot represents the arrival time of the elastic shear wave. In the experiment, the first two arrival times are consistently observable although the second one is not as distinguishable to noise that is presumably related to inhomogeneous deformation on the scale of grain sizes. The arrival time indicated by the first dot is consistently a few nanoseconds earlier than expected from the theoretical analysis.

Figs. 4 and 5 show that there are significant discrepancies between the theoretical and experimental transverse velocity-time profiles at early times after the arrival of the front of the shear wave. The discrepancy in the precursor decay of the transverse wave may be due to the lack of precursor decay beyond 2.0 mm in the extrapolated solution. However, the discrepancy behind the wave front suggests a fundamental inadequacy of the theory. This discrepancy persists for longer durations in the case of thicker targets—presumably because of the spreading of the wave with distance of propagation. The dashed curve in Fig. 5 shows that the spreading of the observed velocity-time profiles between 3.2 mm and 6.15 mm is essentially the same as for centered simple waves in which a given level of particle velocity propagates along a line x/t = constant.

The discrepancy at early times after arrival of the shear wave front is believed to be due primarily to the loading history dependence of plastic deformation. The analysis [17] shows that the loading path follows the axis of the normal stress, say σ_{11}, until the shear wave arrives and then turns at essentially a right angle to proceed in the direction of the axis of the shear stress, say σ_{12}. Since the latter direction is tangent to the locus of states of constant equivalent plastic strain rate (second invariant of the plastic strain rate tensor), it follows that the analysis predicts only a small increase in strain rate when the shear wave arrives. On the other hand, experiments on path-dependence of plastic deformation in polycrystalline aluminum [26, 27] show that the yield surface tends to elongate in the direction of loading and develop a higher curvature segment at the intersection of the loading trajectory with the current yield surface. Such experiments indicate that a right angle change in direction of the stress trajectory would initially cause a higher rate of plastic deformation than predicted by an isotropic hardening model. This higher plastic strain rate would cause greater attenuation of the plastic wave in regions corresponding to the early stages of loading in the direction σ_{12}. Such changes in the computed wave profile in Figs. 4 and 5 would tend to improve agreement between theory and experiment. In related work, Güldenpfennig and Clifton [28] found that use of a self-consistent slip model for trajectories involving right angle changes in loading direction gave better agreement with experimental results on combined longitudinal and torsional plastic waves than were obtained using models which employ smooth yield surfaces that do not sharpen in the direction of loading.

Concluding Remarks

The oblique plate impact experiment, employing a TDI, appears to be a useful technique for studying material behavior at high strain rates. The results show that the transverse velocity profile is clearly more sensitive to the constitutive relations than is the longitudinal velocity profile. In addition, the transverse velocity profile gives the relatively long time history of the flow characteristics of solids, whereas the longitudinal one does not because the plastic strain rate decreases as the stress state becomes more nearly that of hydrostatic pressure.

Improved agreement between theoretical predictions and results of pressure shear impact experiments appears to require improved constitutive models for plastic flow. Comparisons presented here suggest that models are required which characterize plastic flow characteristics accurately along loading trajectories with sharp changes in direction.

As an extension of the present work it should be possible to use the pressure-shear configuration in a reverberation experiment [29] designed to study stress-strain relations at very high strain rates, say 10^4–10^5 sec^{-1}. In such experiments a thin specimen would be sandwiched between two hard elastic disks and subjected to pressure-shear impact by a hard flyer plate. Then, the longitudinal wave generated at the impact face would arrive at the specimen and build up hydrostatic pressure; the following shear wave could be used to measure the flow stress of the material at high pressure and high strain rate.

Further development of the pressure-shear technique should determine whether or not a window material can be placed behind a grating on the rear surface of a target and whether a grating will remain bonded to a free surface for high velocity shots, say above 1.0 mm/μsec. If not it may be necessary to use a TDI based on scattered light from a rough surface instead of a grating. This possibility is discussed briefly in [1].

Acknowledgment

The authors are pleased to acknowledge the contribution of Amos Gilat, a graduate student at Brown, who carried out the experiments reported as shots 8 and 9.

References

1 Kim, K.-S., Clifton, R. J., and Kumar, P., "A Combined Normal and Transverse Displacement Interferometer With An Application to Impact of Y-Cut Quartz," *Journal of Applied Physics*, Vol. 48, No. 10, 1977, pp. 4132–4139.

2 Barker, L. M., "Fine Structure of Compressive and Release Wave Shapes in Aluminum Measured by the Velocity Interferometer Technique," *Behavior of Dense Media Under High Dynamic Pressures*, Gordon and Breach, New York, 1968, pp. 483–505.

3 Clifton, R. J., "An Analysis of Combined Longitudinal and Torsional Plastic Waves in a Thin-Walled Tube," *Proceedings of the Fifth U.S. National Congress of Applied Mechanics*, ASME, New York, 1966, pp. 465–480.

4 Lipkin, J., and Clifton, R. J., "An Experimental Study of Combined Longitudinal and Torsional Plastic Waves in a Thin-Walled Tube," *Proceedings of the 12th International Congress of Applied Mechanics*, Stanford University, 1968, pp. 292–304.

5 Cristescu, N., "Dynamic Plasticity Under Combined Stress," *Mechanical Behavior of Materials Under Dynamic Loads*, ed., Lindholm, U. S., Springer-Verlag, 1968, pp. 329–342.

6 Lipkin, J., and Clifton, R. J., "Plastic Waves of Combined Stresses Due to Longitudinal Impact of a Pretorqued Tube, Part 1: Experimental Results and Part 2: Comparison of Theory With Experiment," ASME JOURNAL OF APPLIED MECHANICS, Vol. 37, 1970, pp. 1107–1120.

7 Clifton, R. J., "Plastic Waves: Theory and Experiment," *Mechanics Yearbook*, ed., Nemat-Nasser S., Pergamon Press, 1972, pp. 102–167.

8 Hsu, J. C. C., and Clifton, R. J., "Plastic Waves in a Rate-Sensitive Material, II: Waves of Combined Stress," *Journal of Mechanics and Physics of Solids*, Vol. 22, 1974, pp. 255–266.

9 Banerjee, A. K., and Malvern, L. E., "Plastic Waves of Combined Stress From the Longitudinal Impact of a Pretorqued Tube, Analysis by Rate-Dependent Theory," ASME JOURNAL OF APPLIED MECHANICS, Vol. 41, 1974, pp. 615–618.

10 Rakhmatulin, Kh. A., "On the Propagation of Elastic-Plastic Waves Owing to Combined Loadings," *Journal of Applied Mathematics and Mechanics (Prikladnaya Matematika i Mekhanika)*, Vol. 22, 1958, pp. 1079–1088.

11 Cristescu, N., "On the Propagation of Elastic-Plastic Waves for Combined Stresses," *Journal of Applied Mathematics and Mechanics (Prikladnaya Matematika i Mekhanika)*, Vol. 23, 1959, pp. 1605–1612.

12 Bleich, N. N., and Nelson, I., "Plane Waves in an Elastic-Plastic Half Space Due to Combined Surface Pressure and Shear," ASME JOURNAL OF APPLIED MECHANICS, Vol. 33, 1966, pp. 149–158.

13 Kalisky, S., Nowacki, W. K., and Wlodarczyk, E., "Plane Biwaves in Elastic-Viscoplastic Semispace," "Propagation of Plane Loading and Unloading Biwaves in an Elastic-Viscoplastic Semi-Infinite Body, Part I: Theory and Part II: Numerical Analysis," *Proceedings of Vibration Problems*, Vol. 8, 1967, pp. 175–190 and pp. 293–331.
14 Ting, T. C. T., and Nan, N., "Plane Waves Due to Combined Compressive and Shear Stresses in a Half Space," ASME JOURNAL OF APPLIED MECHANICS, Vol. 36, 1969, pp. 1389–1397.
15 Goel, R. P., and Malvern, L. E., "Elastic-Plastic Plane Waves With Combined Compressive and Two Shear Stresses in a Half Space," ASME JOURNAL OF APPLIED MECHANICS, Vol. 38, 1971, pp. 895–898.
16 Abou-Sayed, A. S. and Clifton, R. J., "Pressure-Shear Waves in Fused Silica," *Journal of Applied Physics*, Vol. 47, No. 5, 1976, pp. 1762–1770.
17 Abou-Sayed, A. S., and Clifton, R. J., "Analysis of Combined Pressure-Shear Waves in an Elastic/Viscoplastic Material," ASME JOURNAL OF APPLIED MECHANICS, Vol. 44, 1977, pp. 79–84.
18 Abou-Sayed, A. S., Clifton, R. J., and Herman, L., "The Oblique-Plate Impact Experiment," *Experimental Mechanics*, Vol. 16, No. 4, 1976, pp. 127–132.
19 Abou-Sayed, A. S., and Clifton, R. J., "Pressure-Shear Waves in 6061-T6 Aluminum Due to Oblique Plate Impact," ASME JOURNAL OF APPLIED MECHANICS, Vol. 44, 1977, pp. 85–88.
20 Gupta, Y. M., "Shear Measurements in Shock Loaded Solids," *Applied Physics Letters*, Vol. 29, No. 11, 1976, pp. 694–697.
21 Koller, L. R., and Fowles, G. R., "Simultaneous Generation and Measurement of Longitudinal and Shear Waves in Shock-Compressed Media," Sixth AIRAPT International High Pressure Conference, University of Colorado, July 1977.
22 Barker, L. M., and Lundergen, C. D., "Dynamic Response of Aluminum," *Journal of Applied Physics*, Vol. 35, No. 4, 1964, pp. 1203–1212.
23 Johnson, J. N., and Barker, L. M., "Dislocation Dynamics and Steady Plastic Wave Profiles in 6061-T6 Aluminum," *Journal of Applied Physics*, Vol. 40, No. 11, 1969, pp. 4321–4334.
24 Kumar, P., and Clifton, R. J., "Optical Alignment of Impact Faces for Plate Impact Experiments," *Journal of Applied Physics*, Vol. 48, No. 3, 1977, pp. 1366–1367.
25 Clifton, R. J., "Analysis of the Laser Velocity Interferometer," *Journal of Applied Physics*, Vol. 41, No. 13, 1970, pp. 5335–5337.
26 Naghdi, P. M., Essenburg, F., and Koff, W., "An Experimental Study of Initial and Subsequent Yield Surfaces in Plasticity," ASME JOURNAL OF APPLIED MECHANICS, Vol. 25, 1958, pp. 201–209.
27 Bertsch, P. K., and Findley, W. N., "An Experimental Study of Subsequent Yield Surfaces–Corners, Normality, Bauschinger and Allied Effects," *Proceedings of the Fourth U. S. National Congress of Applied Mechanics*, Vol. 2, ASME, New York, 1962, pp. 893–907.
28 Guldenpfennig, J., and Clifton, R. J., "An Application of Self-Consistent Slip Models to Plastic Waves of Combined Stress," *Proceedings of International Congress of Applied Mechanics*, Delft, Holland, 1976.
29 Lysne, P. C., et al., "Determination of Release Adiabats and Recentered Hugoniot Curves by Shock Reverberation Techniques," *Journal of Applied Physics*, Vol. 40, No. 9, 1969, pp. 3786–3795.

APPENDIX

Michelson-type displacement interferometers have been used for the measurement of the motion of a surface. However, the output of the interferometer gives displacement-time relations whereas velocity-time relations are required. The recorded information is the finite set of data points $(t_i, u_i; i = 0,1,\ldots,n)$ where t_i, u_i are, respectively, the time and displacement coordinates of the ith point. If we define the measured average velocity during an interval from t_i to t_{i+1} as $v_i = (u_{i+1} - u_i)/(t_{i+1} - t_i)$, then v_i tends to oscillate or be scattered in a broad band since errors in recorded values of u_i and t_i cause v_{i-1} and v_i to deviate in opposite directions. To reduce such scatter it is better to ominimize the average curvature of the interpolated displacement-time profile under a side condition that constrains deviations from the recorded values. This condition can be written as

$$\text{minimize} \int_{t_0}^{t_n} [\ddot{u}(t)]^2 dt \qquad (1a)$$

under the side condition

$$\sum_{i=0}^{n} [u(t_i) - u_i]^2 = (n+1)\sigma^2 \qquad (1b)$$

where $u(t)$ represents the interpolated displacement function and σ is the standard deviation. The problem can be solved by minimizing the functional

$$J[u] \equiv \int_{t_0}^{t_n} [\ddot{u}(t)]^2 dt + \alpha \sum_{i=0}^{n} [u(t_i) - u_i]^2 \qquad (2)$$

where α is a Lagrangian multiplier. The first variation of (2) becomes, after integration by parts,

$$\delta J[u] = 2\left\{ \sum_{i=1}^{n} [\ddot{u}\delta\dot{u} - \dddot{u}\delta u]\Big|_{t_{i-1}}^{t_i} + \int_{t_0}^{t_n} \ddddot{u}\delta u dt + \alpha \sum_{i=0}^{n} [u(t_i) - u_i]\delta u(t_i) \right\}. \qquad (3)$$

We seek the function $u(t)$ for which the variation $\delta J[u]$ vanishes for all trial functions $u(t) + \delta u(t)$ that are continuous and have continuous first and second derivatives on the interval (t_0, t_n).

In order for the integral in (3) to vanish the function $u(t)$ must satisfy $\ddddot{u}(t) = 0$ everywhere in the interval (t_0, t_n). Thus $u(t)$ must have the form

$$u(t) = a_i + b_i(t - t_{i-1}) + c_i(t - t_{i-1})^2 + d_i(t - t_{i-1})^3 \quad \text{for} \quad t_{i-1} \leq t < t_i, \quad i = 1, \ldots, n \qquad (4)$$

where a_i, b_i, c_i, d_i are constants to be determined from the continuity of u, $\dot{u}$, and $\ddot{u}$ at $t = t_i$ and consideration of independent variations of $\delta u(t)$ and $\delta\dot{u}(t)$ at data points $t = t_i$.

The continuity of $\ddot{u}(t)$ reduces the sum in (3) involving $\delta\dot{u}$ to

$$-\ddot{u}(t_0)\delta\dot{u}(t_0) + \ddot{u}(t_n)\delta\dot{u}(t_n).$$

This variation is made to be zero by restricting the admissible class of trial functions to those which satisfy $\delta\dot{u}(t_0) = 0$ and $\delta\dot{u}(t_n) = 0$. That is, the initial and final velocities, $\dot{u}(t_0)$ and $\dot{u}(t_n)$ are specified. The specified values are obtained by least-squares interpolation near $t = t_0$ and $t = t_n$. Then, two conditions on the coefficients in (4) are obtained from

$$b_1 = \dot{u}_0 \qquad (5a)$$

$$b_n + 2c_n(t_n - t_{n-1}) + 3d_n(t_n - t_{n-1})^2 = \dot{u}_n \qquad (5b)$$

where $\dot{u}_0$ and $\dot{u}_n$ denote the independently determined values of $\dot{u}(t_0)$ and $\dot{u}(t_n)$.

The conditions on the constants in (4) arising from independent variations $\delta u(t_i)$ are

$$-\dddot{u}(t_i^-) + \dddot{u}(t_i^+) + \alpha[u(t_i) - u_i] = 0 \quad i = 1, \ldots, n-1 \qquad (6a)$$

$$\dddot{u}(t_0^+) + \alpha[u(t_0) - u_0] = 0 \qquad (6b)$$

$$-\dddot{u}(t_n^-) + \alpha[u(t_n) - u_n] = 0 \qquad (6c)$$

where, for example, $\dddot{u}(t_i^-)$ and $\dddot{u}(t_i^+)$ denote the limiting values of $\dddot{u}(t)$ as t_i is approached with $t < t_i$ and $t > t_i$, respectively. Substitution of (4) in (6) gives

$$6(d_{i+1} - d_i) + \alpha a_{i+1} = \alpha u_i \quad i = 1, \ldots, n-1 \qquad (6a)'$$

$$6d_1 + \alpha a_1 = \alpha u_0 \qquad (6b)'$$

$$-6d_n + \alpha[a_n + b_n(t_n - t_{n-1}) + c_n(t_n - t_{n-1})^2 + d_n(t_n - t_{n-1})^3] = \alpha u_n \qquad (6c)'$$

The remaining conditions on the undetermined constants are obtained from imposing the continuity of u, $\dot{u}$, and $\ddot{u}$ at $t = t_i$, $i = 1, \ldots, n-1$. These continuity conditions give

$$a_i - a_{i+1} + b_i(t_i - t_{i-1}) + c_i(t_i - t_{i-1})^2 + d_i(t_i - t_{i-1})^3 = 0 \qquad (7a)$$

$$b_i - b_{i+1} + 2c_i(t_i - t_{i-1}) + 3d_i(t_i - t_{i-1})^2 = 0 \qquad (7b)$$

$$c_i - c_{i+1} + 3d_i(t_i - t_{i-1}) = 0 \qquad (7c)$$

Equations (5), (6)′, (7) constitute $4n$ linear algebraic equations in the $4n$ unknowns a_i, b_i, c_i, d_i, $i = 1, \ldots, n$. For a prescribed value of the parameter α, these equations can be solved for the $4n$ unknowns. Since α is not known *a priori*, but is obviously related to the standard deviation σ^2 in (1b), the solution is obtained in an iterative manner by adjusting α until the value of σ^2 obtained from (1b) agrees with an estimated value, say $\bar{\sigma}^2$, obtained using displacement differences resulting from repeated reading of a representative oscilloscope trace to calculate the sum in (1b). An initial choice for α, say $\alpha^{(1)}$, is the value for which the two terms in (2) are comparable in magnitude. This selection gives

$$\alpha^{(1)} = \frac{\overline{(\ddot{u})^2 \Delta t}}{\bar{\sigma}^2} \tag{8}$$

where

$$\overline{(\ddot{u})^2 \Delta t} \equiv \frac{1}{n-1} \sum_{i=1}^{n-1} \frac{2}{t_{i+1} - t_{i-1}} \left\{ \frac{u_{i+1} - u_i}{t_{i+1} - t_i} - \frac{u_i - u_{i-1}}{t_i - t_{i-1}} \right\}^2. \tag{9}$$

Experience shows that (8) provides quite a good first approximation of α. Since σ^2 increases monotonically with decreasing α it is a relatively easy matter to choose successive approximations for α so that σ^2 converges to $\bar{\sigma}^2$. Once a set $(a_i, b_i, c_i, d_i, \alpha)$ is found that satisfies (5), (6)′, (7) and provides a satisfactory value of σ^2 in (1b), then the velocity-time profile $\dot{u}(t)$ that is sought is

$$\begin{aligned} v(t) = \dot{u}(t) = b_i + 2c_i(t - t_{i-1}) \\ + 3d_i(t - t_{i-1})^2, \quad t_{i-1} \le t \le t_i, \quad i = 1, \ldots, n \end{aligned} \tag{10}$$

M. J. Forrestal
Systems Development Department III.
Mem. ASME

B. W. Duggin
Simulation Technology Department.

R. I. Butler
Nuclear Safety Department.

Sandia Laboratories,
Albuquerque, New Mex. 87185

An Explosive Loading Technique for the Uniform Expansion of 304 Stainless Steel Cylinders at High Strain Rates[1]

A new explosive loading technique is applied to study the uniform plastic expansion and fracture initiation of 304 stainless steel cylinders. An annular layer of dry PETN high explosive is placed in contact with the inner diameter of the cylinder and surface-initiated with an array of etched copper bridgewires. This technique produces a simultaneous detonation of the explosive and a nearly uniform expansion of the stainless steel cylinders.

Introduction

Development programs concerned with the simulation of radiation-induced impulse loads [1–4], the containment of high explosives [5], and safety problems in the nuclear industry [6] have created a need for new experimental methods which examine the response of structures at high strain rates. Data from the rapid expansion of thin rings [7] and cylinders [8] have provided basic information on rate effects, shear banding and fracture. The referenced loading techniques, however, are limited in impulse magnitudes and a new loading technique with a larger magnitude capability was developed to examine the expansion of thicker walled cylinders.

A simultaneous loading technique with sufficient impulse magnitude to study the plastic expansion and fracture of 6.35mm (0.25 in.) thick, stainless steel cylinders is presented. Thin (3.0 to 4.3 mm or 0.12 to 0.17 in.) annular layers of dry PETN high explosive are surface-initiated with arrays of etched copper bridgewires. This technique produces a simultaneous detonation of the explosive, rather than a sweeping load [9], and a nearly uniform expansion of the stainless steel cylinders. In addition, loading with low density PETN does not spall or cause other material damage through the thickness of the test cylinders.

Three stainless steel cylinders were expanded to strain rates up to 4100 s^{-1}. The plastic expansion and strain rate to cause fracture are compared with other data in the literature.

[1] This work was supported by the U.S. Department of Energy.

Contributed by the Applied Mechanics Division for publication in the JOURNAL OF APPLIED MECHANICS.

Discussion on this paper should be addressed to the Editorial Department, ASME, United Engineering Center, 345 East 47th Street, New York, N. Y. 10017, and will be accepted until June 1, 1980. Readers who need more time to prepare a discussion should request an extension from the Editorial Department. Manuscript received by ASME Applied Mechanics Division, January, 1979; final revision, July, 1979.

Experiments

Loading Technique. A simplified section through the test setup is shown in Fig. 1. Mylar insulation located on the inner surface of the steel cylinder and on the surfaces of the phenolic tube is omitted from the sketch. The phenolic tube between the mesh and copper return provides a uniform low inductance circuit to all current paths and the desired thickness for the PETN is obtained by varying the tube thickness. PETN is packed between the copper mesh supported by the phenolic tube and the inner walls of the test specimen and guard rings. Additional photographs of a similar test setup for a specific scale model test are given in [10].

The mesh pattern shown in Fig. 2 is 18 μm (0.7 mil) thick copper foil bonded to Mylar and chemically etched by the techniques used to manufacture printed circuits. A 15 μF capacitor bank is connected to the mesh pattern, and when the bank is switched at 20 kV the individual bridgewires are electrically exploded by the discharge current.[2] The bridgewires detonate the PETN with a high density of initiation points (2.5×10^4 m^{-2} or 16 $in.^{-2}$) and produce a uniform internal loading on the stainless steel test cylinder and guard rings.

Specimens. Test specimens were cut to 0 127 m (5.0 in.) lengths from a 304 stainless steel seamless tube (specification ASTM-A511) with outer diameter 0.127 m (5.0 in.) and wall thickness 6.35 mm (0.25 in.). Two guard rings of length 38.1 mm (1.5 in.) were also cut for each specimen and glued to the ends of the test cylinders. The uniformly detonated explosive loads the test cylinder and guard rings over the total length 0.203 m (8.00 in.).

Cylinder Expansion Experiments. Three tests were conducted and some of the experimental parameters and results are given in Table 1. Early time response of the cylinders (less than 100 μs) was monitored with high-speed photography and pulsed X-rays. Test

[2] Impulse loads from the electrically exploded mesh pattern without high explosives have been used for a recent application [11].

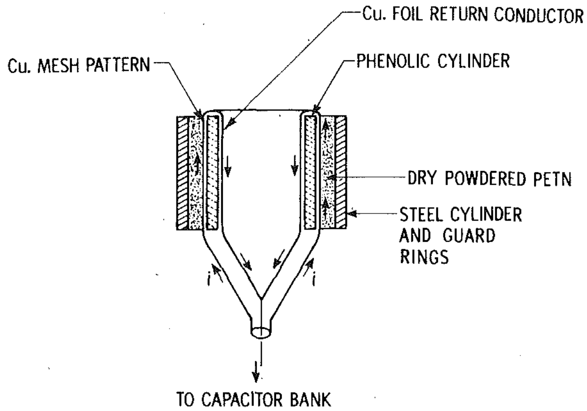

Fig. 1 Experimental arrangement

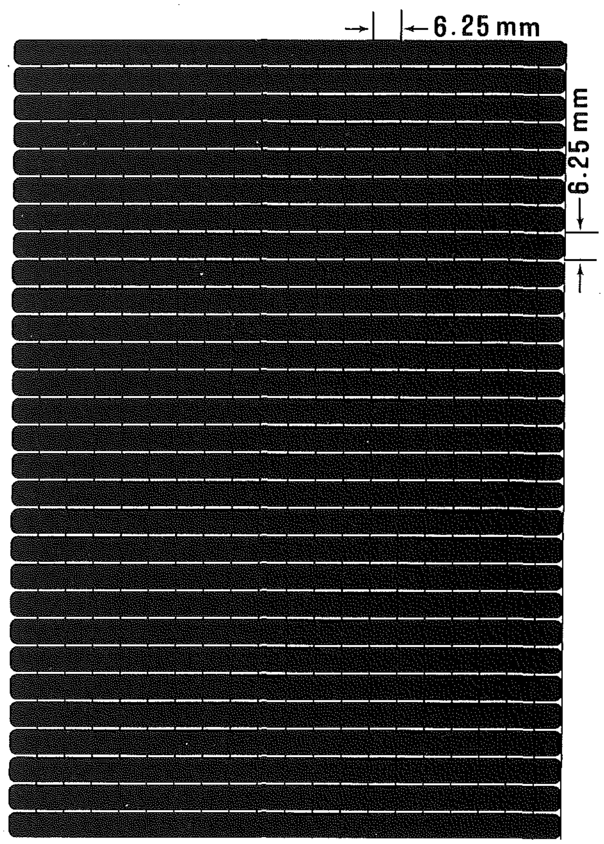

Fig. 2 Mesh pattern; the small connecting black lines are the bridgewires

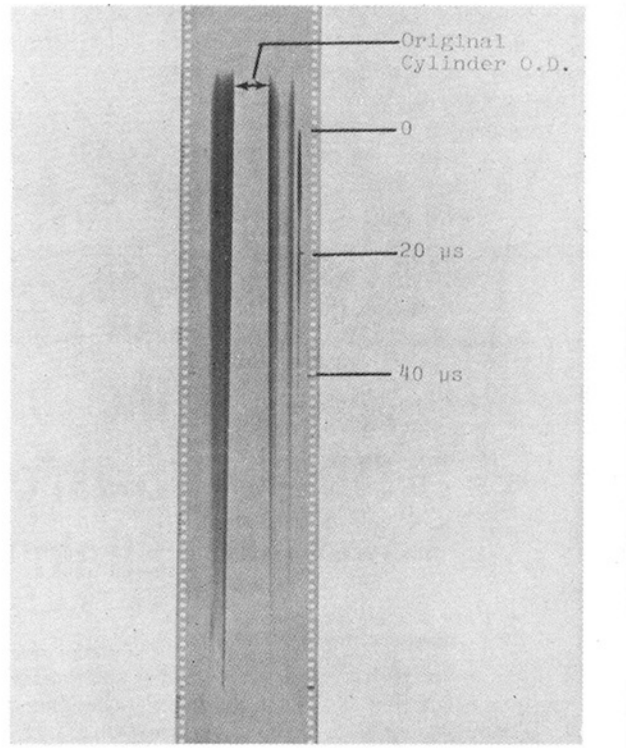

Fig. 3 Streak record of the expanding diameter at the cylinder midlength for Test Number 3

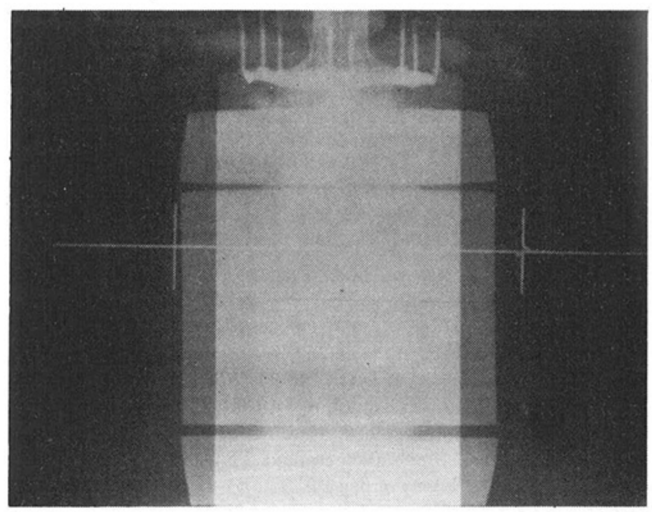

Fig. 4 Superimposed flash X-ray photographs of the test cylinder and guard rings at $t = 0$ and 85 μs for Test Number 3

Number 1 used a 119 Cordin framing camera with a rate of 1.2 μs per frame and Tests Numbers 2 and 3 used a 132 Cordin, 70 mm streaking camera with a rate of 3 mm/μs. Both cameras measured the early time motion consisting of the initial acceleration phase and peak wall velocity. A streak record of the expanding diameter at the cylinder midlength and a pulsed X-ray photograph of the expanded cylinder and guard rings at t = 85 μs for Test Number 3 are shown in Figs. 3 and 4. Plots of the early time response from the camera data for all tests are presented in Fig. 5 along with several points of discrete data from the pulsed X-ray diagnostics. These curves were used to obtain the peak wall velocities listed in Table 1. The maximum engineering strain in this table was obtained from complete circumferential midlength measurements.

In order to obtain post-test diagnostics, square grids of 25.4 mm (1.0 in.) were drawn on the outer surfaces of the test cylinders. Five grids were located along axes of the cylinders and at 90-deg angular intervals. A post-test photograph of the specimens and an undeformed cylinder cut from the tube are shown in Fig. 6. This photograph indicates that expansion is maximum at the cylinder midlength and perhaps the expansion would have been more uniform with longer guard rings. A summary of the final engineering strains (change in length divided by the original length) in the axial x, circumferential θ, and thickness z-directions are given in Table 2. In Table 2, x is measured from the cylinder midlength and gives the center of the axial location of the grid location.

The incompressibility condition [12] commonly used in plasticity analyses, namely,

Table 1

Test Number	PETN Thickness	PETN Mass	Maximum Wall Velocity	Maximum Strain Rate	Maximum Final Engineering Strain
1	3.15 mm	0.116 kg	0.17 mm/μs	2680 s^{-1}	0.41
2	3.51 mm	0.131 kg	0.20 mm/μs	3150 s^{-1}	0.49
3	4.24 mm	0.177 kg	0.26 mm/μs	4090 s^{-1}	0.80

Table 2

	Axial Location	Test No. 1 Angular Locations				Test No. 2 Angular Locations				Test No. 3 Angular Locations			
		0	π/2	π	3/2π	0	π/2	π	3/2π	0	π/2	π	3/2π
ϵ_θ	x = 0	0.34	0.35	0.47	0.40	0.45	0.52	0.53	0.48	0.91	0.77	0.67	0.80
$-\epsilon_x$		0.12	0.11	0.15	0.12	0.13	0.14	0.15	0.13	0.21	0.20	0.17	0.20
$-\epsilon_z$		0.14	0.17	0.27	0.22	0.20	0.27	0.29	0.25	0.37	0.32	0.25	0.32
ϵ_θ	x = 25.4 mm (1.0 in.)	0.33	0.35	0.45	0.42	0.46	0.51	0.55	0.51	0.88	0.78	0.67	0.80
$-\epsilon_x$		0.12	0.12	0.14	0.13	0.13	0.15	0.14	0.14	0.21	0.19	0.18	0.20
$-\epsilon_z$		0.14	0.16	0.28	0.21	0.19	0.25	0.28	0.26	0.36	0.32	0.25	0.32
ϵ_θ	x = -25.4 mm (-1.0 in.)	0.36	0.38	0.46	0.46	0.43	0.47	0.51	0.47	0.87	0.76	0.65	0.77
$-\epsilon_x$		0.12	0.12	0.15	0.13	0.14	0.13	0.14	0.14	0.22	0.18	0.16	0.20
$-\epsilon_z$		0.15	0.18	0.25	0.22	0.19	0.25	0.28	0.24	0.38	0.31	0.24	0.31
ϵ_θ	x = 50.8 mm (2.0 in.)	0.31	0.35	0.44	0.41	0.44	0.48	0.49	0.49	0.83	0.72	0.64	0.74
$-\epsilon_x$		0.12	0.12	0.14	0.13	0.14	0.16	0.15	0.16	0.23	0.21	0.19	0.21
$-\epsilon_z$		0.12	0.16	0.24	0.22	0.16	0.22	0.24	0.22	0.35	0.30	0.23	0.30
ϵ_θ	x = -50.8 mm (-2.0 in.)	0.36	0.39	0.45	0.42	0.39	0.43	0.44	0.46	0.83	0.74	0.62	0.71
$-\epsilon_x$		0.13	0.13	0.14	0.13	0.14	0.14	0.14	0.15	0.22	0.21	0.18	0.20
$-\epsilon_z$		0.14	0.18	0.24	0.20	0.14	0.20	0.23	0.21	0.33	0.30	0.22	0.29

$$(1 + \epsilon_x)(1 + \epsilon_\theta)(1 + \epsilon_z) = 1 \quad (1a)$$

$$\bar{\epsilon}_x + \bar{\epsilon}_\theta + \bar{\epsilon}_z = 0 \quad (1b)$$

where ϵ_i is engineering strain and $\bar{\epsilon}_i$ is effective or logarithmic strain, was checked for the grids at $x = 0$ and good agreement was observed. In particular, only two of the 12 grids for the three tests differed by more than 5 percent from the predictions of equation (1).

Discussion

A novel high explosive loading technique was applied to examine the expansion of stainless steel cylinders. The technique produces a simultaneous detonation of the explosive, rather than a sweeping load [9], and provides reasonably fundamental data on the expansion process. The cylinder of Test Number 3 was expanded to a maximum strain rate of 4090 s^{-1} and showed signs that fracture initiation had begun. This data point for the strain rate or wall velocity to cause incipient fracture is in agreement with previous data on thinner (0.51 mm or 0.020 in.) cylindrical shells [13] expanded with magnetic pressure pulses. However, the thicker shells examined in this study expanded to ~80 percent circumferential engineering strain at incipient fracture; whereas, the thinner shells only expanded to ~25 percent.

In [9], aluminum shells were driven radially inward to examine the plastic flow buckling from impulse loads. These authors defined the parameter

$$k = -(\bar{\epsilon}_x/\bar{\epsilon}_\theta) \quad (2)$$

and experimentally determined k as a function of the cylinder length to diameter ratio L/D. Results from this study on the expansion of

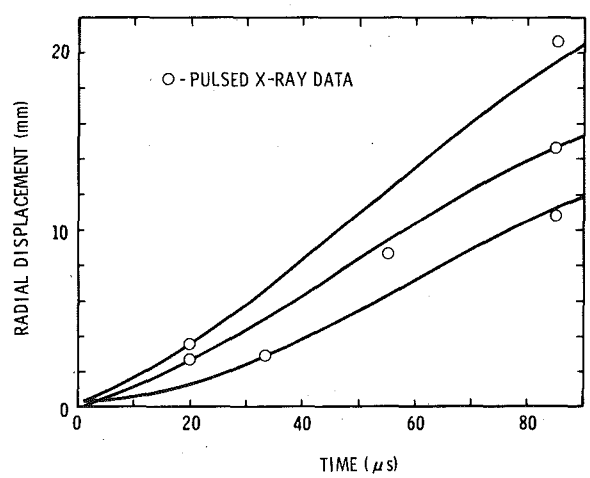

Fig. 5 **Early time radial wall response at the cylinder midlength from high speed photography and pulsed X-ray data**

stainless steel cylinders with $L/D = 1$ are in close agreement with the data presented in Fig. 7 of [9]. It should also be pointed out that some of our colleagues at Sandia Laboratories [14] have observed that aluminum shells with large L/D ratios fail at lower circumferential fracture strains than rings or shells with small L/D ratios. Equations (1) and (2) can be combined to give

$$\bar{\epsilon}_\theta = -\bar{\epsilon}_z/(1 - k); \quad k = -\bar{\epsilon}_x/\bar{\epsilon}_\theta$$

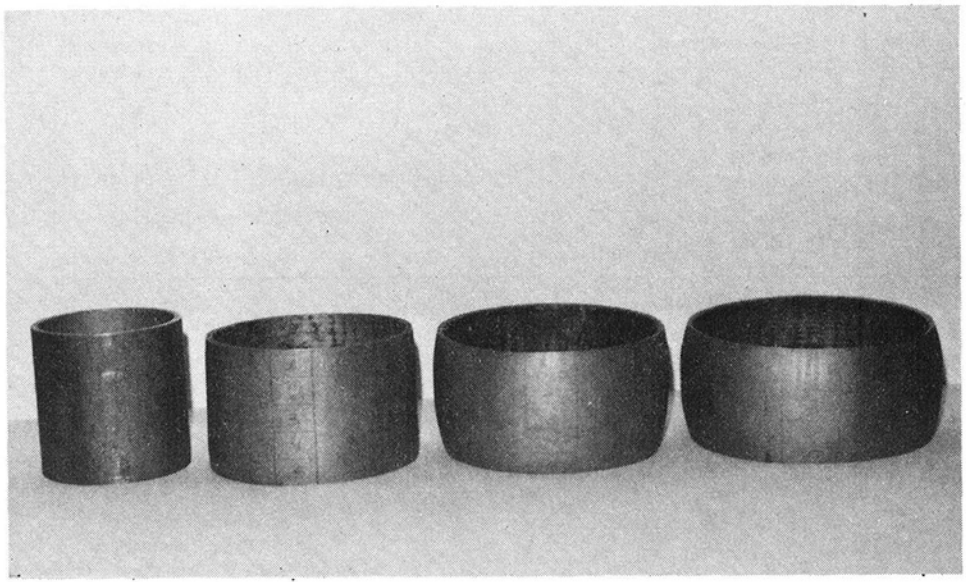

Fig. 6 Post-test cylinders compared with an undeformed cylinder

As pointed out in [9] $k = 0$ for plane strain or very long cylinders and $k = 1/2$ for plane stress or rings. If one speculates that incipient fracture occurs when the thickness strain of the specimen diminishes to a critical value, circumferential ring strains would be twice as large as circumferential strains for long cylinders at incipient fracture. The authors hoped to perform additional tests at other L/D ratios to examine the foregoing hypothesis; however, the program ended before we could complete this task.

Acknowledgment

The authors thank M. J. Sagartz and M. Perra for some helpful suggestions and R. R. Gallegos for assisting with the experiments.

References

1 Butler, R. I., "Initiation of Explosive Films With Electrically Exploded Etched Copper Mesh," *Proceedings of the 12th Annual Symposium of the New Mexico Section of the ASME*, eds., Davison, L., and Kennedy, J. E., 1972, pp. 215–223.

2 Forrestal, J. J., Tucker, W. K., and Von Riesemann, W. A., "Impulse Loading of Finite Cylindrical Shells," *AIAA Journal*, Vol. 13, No. 10, Oct. 1975, pp. 1396–1398.

3 Wenzel, A., "Use of Light Initiated Explosives for Impulsive Loading of Structures," *Proceedings of the 16th Annual Technical Meeting of the Institute of Environmental Sciences*, Boston, Mass., April 12–16, 1970.

4 Benham, R. A., and Mathews, F. H., "X-ray Simulation With Light-Initiated Explosive," *The Shock and Vibration Bulletin*, Bulletin 45, Oct. 1974, pp. 21–22.

5 Davison, L. W., "Explosive Containment Devices: Design Considerations," SAND74-0218, Sandia Laboratories, Albuquerque, New Mex., Dec. 1974.

6 Forrestal, M. J., and Sagartz, M. J., "Elastic-Plastic Response of 304 Stainless Steel Beams to Impulse Loads, ASME JOURNAL OF APPLIED MECHANICS, Vol. 34, No. 3, Sept. 1978, pp. 685–687.

7 Hoggatt, C. R., and Recht, R. F., "Stress-Strain Data Obtained at High Rates Using an Expanding Ring," *Experimental Mechanics*, Oct. 1969, pp. 441–448.

8 Wesenberg, D. L., and Sagartz, M. J., "Dynamic Fracture of 6061-T6 Aluminum Cylinders," ASME JOURNAL OF APPLIED MECHANICS, Vol. 44, No. 4, Dec. 1977, pp. 643–646.

9 Vaughn, H., and Florence, A. L., "Plastic Flow Buckling of Cylindrical Shells Due to Impulsive Loading," ASME JOURNAL OF APPLIED MECHANICS, Vol. 37, No. 1, Mar. 1970, pp. 171–179.

10 Butler, R. I., Duggin, B. W., and Forrestal, M. J., "Explosive Technique for Axisymmetric Expansion of Cylinders at High Strain Rates," SAND78-2393, Sandia Laboratories, Albuquerque, New Mex., Jan. 1979.

11 Duggin, B. W., Forrestal, M. J., and Butler, R. I., "Impulse From an Electrically Exploded Etched Copper Mesh," *AIAA Journal*, Vol. 16, No. 8, Aug. 1978, pp. 856–857.

12 Johnson, W., and Mellor, P. B., *Engineering Plasticity*, Von Nostrand Reinhold Co., London, 1973, pp. 4–6.

13 Wesenberg, D. L., and Forrestal, M. J., "Dynamic Expansion and Fracture of Stainless Steel Cylindrical Shells," *Proceedings of the 4th International Conference on Structural Mechanics in Reactor Technology*, August 15–19, 1977, San Francisco, Calif., Paper No. L8/1.

14 Cnare, E. C., et al., "PULSAR—The Experimental Program," Sixth Symposium on Engineering Problems in Fusion Research, San Diego, Calif., Nov. 1975, Paper No. 75, CHI, 097-5NPS.

J. S. Lai
Associate Professor,
School of Civil Engineering,
Georgia Institute of Technology,
Atlanta, Ga. 30332

W. N. Findley
Professor of Engineering,
Division of Engineering,
Brown University,
Providence, R. I. 02912
Fellow ASME

Creep of 2618 Aluminum Under Step Stress Changes Predicted by a Viscous-Viscoelastic Model

Nonlinear constitutive equations are developed and used to predict from constant stress data the creep behavior of 2618 Aluminum at 200°C (392°F) for tension or torsion stresses under varying stress history including stepup, stepdown, and reloading stress changes. The strain in the constitutive equation employed includes the following components: linear elastic, time-independent plastic, nonlinear time-dependent recoverable (viscoelastic), nonlinear time-dependent nonrecoverable (viscous) positive, and nonlinear time-dependent nonrecoverable (viscous) negative. The modified superposition principle, derived from the multiple integral representation, and strain-hardening theory were used to represent the recoverable and nonrecoverable components, respectively, of the time-dependent strain in the constitutive equations. Excellent-to-fair agreement was obtained between the experimentally measured data and the predictions based on data from constant-stress tests using the constitutive equations as modified.

Introduction

The creep behavior of metals under changing stress—especially changes in state of combined stress and stress reversal—has received little experimental observation. Mathematical expressions employed, such as strain hardening or viscoelastic models, usually are unable to describe the detail of creep behavior under changes such as just mentioned. References to prior work in this area are given in [1].

In a previous paper [1] the authors described a viscous-viscoelastic model in which the strain was resolved into five components: elastic ϵ^e, time-independent plastic ϵ^p, positive nonrecoverable (viscous) ϵ^v_{pos}, negative nonrecoverable (viscous) ϵ^v_{neg}, and recoverable (viscoelastic) ϵ^{ve} components. From creep and recovery experiments under combined tension and torsion, the time and stress dependence of these components were evaluated for constant stresses. Constitutive relations for changes in stress state also were discussed in [1].

In the present paper, constitutive equations for changes in state of combined tension and torsion are developed and used to predict, from the relations determined from constant stress tests in [1], the creep behavior under abrupt stepup and stepdown changes in tension or torsion. The results are compared with experiments reported in [2] and with new experiments described in the following pages. Future work will consider abrupt changes in the state of combined tension and torsion, stress reversal, relaxation and simultaneous creep, and relaxation.

Contributed by the Applied Mechanics Division for publication in the JOURNAL OF APPLIED MECHANICS.

Discussion on this paper should be addressed to the Editorial Department, ASME, United Engineering Center, 345 East 47th Street, New York, N. Y. 10017, and will be accepted until June 1, 1980. Readers who need more time to prepare a discussion should request an extension from the Editorial Department. Manuscript received by ASME Applied Mechanics Division, April, 1979; final revision, August, 1979.

Material and Specimens

An aluminum forging alloy 2618-T61 was employed in these experiments. Specimens were taken from the same lot of 2 ½-in-dia forged rod as used in [1] and the same lot as specimens D through H in [2]. Specimens were thin-walled tubes having outside diameter, wall thickness, and gage length of 1.00, 0.060, and 4.00 in., respectively. A more complete description of material and specimens is given in [1].

Experimental Apparatus and Procedure

The combined tension and torsion creep machine used for these experiments was described in [3] and briefly in [1]. The temperature control and measurement employed was described in [1,2]. Stress was produced by applying dead weights at the end of levers. These weights were applied by hand at the start of a test by lowering them quickly but without shock. Strain was measured by a mechanical device [3] whose sensitivity was 1×10^{-6} for axial strain and 1.5×10^{-6} for tensor shear strain. The time of the start of the test was taken to be the instant at which the load was fully applied. In the present experiments changes in loading were made at intervals during the creep tests. The load changes were accomplished by hand in the same manner. Strain was recorded at the following intervals following a load change: every 0.01 h to 0.05 h; every 0.02 h to 0.1 h; every 0.05 h to 0.5 h; every 0.1 h to 1.0 h; and every 0.2 h to 2.0 H. All experiments were performed at 200°C (392°F).

Constitutive Equations for Constant Stress

In this paper as in the previous one [1] the strain was resolved into five components: ϵ^e, ϵ^p, ϵ^v_{pos}, ϵ^v_{neg}, and ϵ^{ve} as defined in the Introduction. The elastic strain ϵ^e was determined from the elastic constants at the test temperature. In [1] the elastic constants at 200°C (392°F) were determined indirectly from creep test data with the following results:

$$E = 6.5 \times 10^4 \text{ MPa } (9.43 \times 10^6 \text{ psi}),$$
$$G = 2.46 \times 10^4 \text{ MPa } (3.57 \times 10^6 \text{ psi}),$$
$$\nu = 0.321,$$

where E, G, and ν are the elastic modulus, shear modulus, and Poisson's ratio, respectively.

As noted in [1] plastic strains ϵ^p were essentially zero in the creep tests performed and creep at constant stress was well represented by a power function of time

$$\epsilon_{ij} = \epsilon^0_{ij} + \epsilon^+_{ij} t^n, \quad (1)$$

where the time-independent strain ϵ^0_{ij} and the coefficient of the time-dependent strain terms ϵ^+_{ij} were functions of stress and n was a constant. It was also shown in [1] that the nonrecoverable $\epsilon^v(t)$ and recoverable $\epsilon^{ve}(t)$ components of time-dependent strain could each be represented by a power function of time with the same exponent n. Also it was shown that the ratio R of the coefficient of the recoverable time-dependent strains could be taken as a constant. Thus, under a constant stress,

$$\epsilon^v_{ij} = [1/(1 + R)]\, \epsilon^+_{ij} t^n, \quad (2)$$

$$\epsilon^{ve}_{ij} = [R/(1 + R)]\, \epsilon^+_{ij} t^n. \quad (3)$$

In the previous work [1], the authors found the time-dependent strain of the material under single step loading and recovery to be well described by the following two equations for time-dependent pure axial strain ϵ^+_{11} and pure shear strain ϵ^+_{12}.

$$\epsilon^+_{11}(\sigma) = F(\sigma) = F^+_1(\sigma - \sigma^*) + F^+_2(\sigma - \sigma^*)^2 + F^+_3(\sigma - \sigma^*)^3, \quad (4)$$

$$\epsilon^+_{12}(\tau) = G(\tau) = G^+_1(\tau - \tau^*) + G^+_2(\tau - \tau^*)^3. \quad (5)$$

The nonlinear relationship of σ, and τ in ϵ^+_{11} and ϵ^+_{12} was derived from a third-order multiple integral representation [4,5]. In (4) and (5) σ^*, τ^* are the creep limits in pure tension and pure torsion, respectively, where $\sigma - \sigma^*$ or $\tau - \tau^*$ are zero for $-\sigma^* \leqslant \sigma \leqslant \sigma^*$ or $-\tau^* \leqslant \tau \leqslant \tau^*$, respectively. The creep limit defines a stress below which creep appears to be zero or very small.[1]

Separating nonrecoverable ϵ^v and recoverable ϵ^{ve} strain components according to (2) and (3) and using (4) and (5) the time-dependent parts ϵ^v and ϵ^{ve} for creep under constant tension σ and torsion τ can be represented by the following equations:

$$\epsilon^{ve}_{11}(t) = \left(\frac{R}{1 + R}\right) F(\sigma - \sigma^*)\, t^n, \quad (6)$$

$$\epsilon^{ve}_{12}(t) = \left(\frac{R}{1 + R}\right) G(\tau - \tau^*)\, t^n, \quad (7)$$

$$\epsilon^{v}_{11}(t) = \left(\frac{1}{1 + R}\right) F(\sigma - \sigma^*)\, t^n, \quad (8)$$

$$\epsilon^{v}_{12}(t) = \left(\frac{1}{1 + R}\right) G(\tau - \tau^*)\, t^n, \quad (9)$$

where F^+_i, G^+_i, σ^*, τ^*, R, and n are the values determined from constant tension and torsion creep tests as reported earlier [1] and shown in Table 1.

The rationale for separating the time-dependent strains into nonrecoverable strain ϵ^v and recoverable strain ϵ^{ve} was based on the assumption that recovery resulted from recoverable strain accumulated during creep. Thus ϵ^{ve} was determined from recovery data for the material in a set of constant stress creep and recovery tests as reported in [1]. ϵ^v was determined from creep tests by subtracting strains due to ϵ^{ve} as described in [1]. Under time-dependent stress inputs, including step changes, other considerations are required in addition to (6)–(9) for predicting ϵ^v and ϵ^{ve}. These considerations will be presented in the next section.

Table 1 Constants for equations (2)–(5)

F^+_i, G^+_i
F^+_1 = 6.084×10^{-12}, per Pa-hr^n (0.004195, % per ksi-hr^n)
F^+_2 = -7.431×10^{-20}, per Pa^2-hr^n (-0.0003533, % per ksi^2-hr^n)
F^+_3 = 7.596×10^{-28}, per Pa^3-hr^n (0.0000249, % per ksi^3-hr^n)
σ^* = 9.143×10^7, Pa (13.26, ksi)
G^+_1 = 7.170×10^{-12}, per Pa-hr^n (0.004944, % per ksi-hr^n)
G^+_2 = 2.703×10^{-28}, per Pa^3-hr^n (0.00000886, % per ksi^3-hr^n)
τ^* = 4.571×10^7, Pa (6.630, ksi)

Note: $n = 0.270$, $R = 0.55$.

Constitutive Equations for Variable Stress

Creep behavior is dependent on the past history of stress (or strain). History dependence can be incorporated in the multiple integral representation [4,5] for a recoverable-type material. Unfortunately, the experimental difficulty of determining F_i, G_i to completely characterize a given material is almost insurmountable [5]. Furthermore, as pointed out by Wang and Onat [6,7], higher-order terms beyond the third order of the multiple integral representation appeared to be required to describe creep of metals under multiple step loadings with sufficient accuracy. In the following, constitutive equations are developed to describe ϵ^v and ϵ^{ve} under time-dependent stress history.

Constitutive Equation for ϵ^{ve}. In [5], it was shown that the multiple integral representation and various simplified forms can be used to describe creep behavior of recoverable type material under variable stress. Among the various simplified forms, the modified superposition principle (MSP) [5] has been shown to yield satisfactory results. Thus the modified superposition principle will be used here to describe the time-dependent recoverable strain ϵ^{ve}.

The modified superposition principle has the effect of reducing multiple integrals to single integrals. The modified superposition principle considers that following the first change in stress at time t_1 from σ_1 to σ_2 the creep strain is the sum of: the strain which would have resulted had the original stress σ_1 continued unchanged; plus the strain (negative) which would have resulted from an equal but opposite stress ($-\sigma_1$) applied at t_1 to an untested specimen; plus the strain which would have resulted from applying the new stress σ_2 at t_1 to an untested specimen. Thus, if the strain at constant stress is given by

$$\epsilon = f(\sigma, t) \quad (10)$$

the strain from N step changes in stress from σ_{i-1} to σ_i at time t_i is given by

$$\epsilon(t) = \sum_{i=0}^{N} [f(\sigma_i, t - t_i) - f(\sigma_{i-1}, t - t_{i-1})]. \quad (11)$$

The modified superposition principle for a continuously varying stress may be expressed as follows by considering the limiting case as the

[1] Information obtained after completion of this work indicated that there was creep below the creep limit, but at a much lower rate than above the creep limit.

steps in (11) tend to an infinite number of infinitesimal steps of stress,

$$\epsilon(t) = \int_0^t \frac{\partial f[\sigma(\xi), t-\xi]}{\partial \sigma(\xi)} \dot{\sigma}(\xi)\, d\xi. \tag{12}$$

Applying (11) to the following series of three steps in tension σ (or torsion τ) stress: $\sigma_1(\tau_1)$ for $0 < t < t_1$, $\sigma_2(\tau_2)$ for $t_1 < t < t_2$, and $\sigma_3(\tau_3)$ for $t_2 < t$ yields the following by inserting (6) and (7) in (11). The time-dependent recoverable strain ϵ^{ve} following the third step is given by

$$\begin{aligned}\epsilon_{11}^{ve}(t) = \left(\frac{R}{1+R}\right)\{F(\sigma_1)[t^n - (t-t_1)^n] \\ + F(\sigma_2)[(t-t_1)^n - (t-t_2)^n] \\ + F(\sigma_3)(t-t_2)^n\}, \quad t_2 < t,\end{aligned} \tag{13}$$

$$\begin{aligned}\epsilon_{12}^{ve}(t) = \left(\frac{R}{1+R}\right)\{G(\tau_1)[t^n - (t-t_1)^n] \\ + G(\tau_2)[(t-t_1)^n - (t-t_2)^n] \\ + G(\tau_3)(t-t_2)^n\}, \quad t_2 < t,\end{aligned} \tag{14}$$

where the stress functions $F(\sigma_i)$ and $G(\tau_i)$ represent $F(\sigma_i - \sigma^*)$ and $G(\tau_i - \tau^*)$ and are given in (4) and (5).

For a series of m steps in stress the shearing strain ϵ_{12}^{ve}, for example, following the mth step, has the form:

$$\begin{aligned}\epsilon_{12}^{ve}(t) = \left(\frac{R}{1+R}\right)\{G(\tau_1)[t^n - (t-t_1)^n] + \ldots \\ + G(\tau_{m-1})[(t-t_{m-2})^n - (t-t_{m-1})^n] \\ + G(\tau_m)(t-t_{m-1})^n\}, \quad t_{m-1} < t.\end{aligned} \tag{15}$$

Now, if σ_1, σ_2 (or τ_1, τ_2) are greater than σ^* (or τ^*), respectively, and if σ_3 (or τ_3) in the third step is less than the stresses σ_2 (or τ_2), respectively, in the second step, then according to (13) [or (14)] both ϵ_{11}^{ve} and ϵ_{12}^{ve} will show partial recovery if $\sigma_3 > \sigma^*$ (or $\tau_3 > \tau^*$). Also, whenever $\sigma_3 \leqslant \sigma^*$ (or $\tau_3 \leqslant \tau^*$) (including $\sigma_3 = \tau_3 = 0$), then the time-dependent strains will exhibit the same recovery as from complete unloading. The validity of this prediction will be explored later in this paper.

Constitutive Equation for ϵ^v. Strain hardening is taken to be applicable to the nonrecoverable strain. The relations employed were derived as follows. Consider the axial strains as an example. The derivative of (8) yields the axial strain rate $\dot{\epsilon}_{11}^v(t)$

$$\dot{\epsilon}_{11}^v(t) = \frac{n}{1+R} F(\sigma)\, t^{n-1}. \tag{16}$$

Eliminating t between (8) and (16) yields

$$\frac{\epsilon_{11}^v(1+R)}{F(\sigma)} = \left[\frac{\dot{\epsilon}_{11}^v(1+R)}{nF(\sigma)}\right]^{n/(n-1)},$$

from which

$$\frac{\dot{\epsilon}_{11}^v}{(\epsilon_{11}^v)^{1-(1/n)}} = n\left[\frac{F(\sigma)}{1+R}\right]^{1/n} \tag{17}$$

Multiplying both sides of (17) by dt and integrating yields

$$\epsilon_{11}^v(t) = \frac{1}{1+R}\left[\int_0^t \{F[\sigma(\xi)]\}^{1/n}\, d\xi\right]^n. \tag{18}$$

In (18) it has been assumed, in accordance with the usual strain-hardening concept, that the same function $F(\sigma)$ applies for variable stress $F[\sigma(\xi)]$ as for constant stress $F[\sigma]$.

For step changes in stress, such as the series of three steps given in the foregoing the axial strain in the third step may be found from (18) by employing the Dirac delta function as follows:

$$\begin{aligned}\epsilon_{11}^v(t) = \frac{1}{1+R}\{[F(\sigma_1)]^{1/n}(t_1) + [F(\sigma_2)]^{1/n}(t_2 - t_1) \\ + [F(\sigma_3)]^{1/n}(t-t_2)\}^n, \quad t_2 < t.\end{aligned} \tag{19}$$

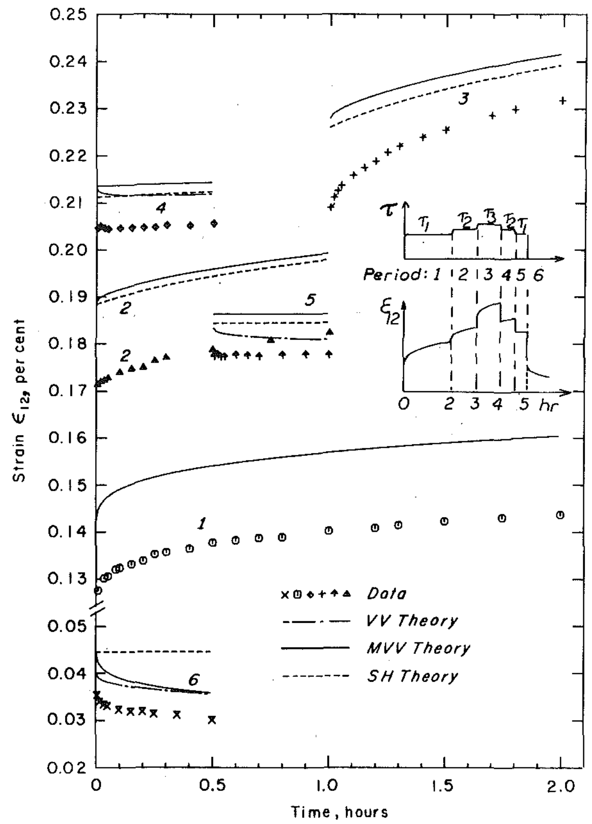

Fig. 1 Creep of 2618AL at 200°C under step loading. Where a theory is not shown it is the same as the (MVV) theory. Numbers indicate periods; τ_1 = 69.0 MPa (10 ksi), τ_2 = 82.7 MPa (12 ksi), τ_3 = 96.5 MPa (14 ksi).

Similarly the shearing strain $\epsilon_{12}^v(t)$ may be found as follows:

$$\begin{aligned}\epsilon_{12}^v(t) = \frac{1}{1+R}\{[G(\tau_1)]^{1/n}(t_1) + [G(\tau_2)]^{1/n}(t_2 - t_1) \\ + [G(\tau_3)]^{1/n}(t-t_2)\}^n, \quad t_2 < t.\end{aligned} \tag{20}$$

For a series of m steps in stress, the shearing strain ϵ_{12}^v, for example, has the form

$$\begin{aligned}\epsilon_{12}^v(t) = \frac{1}{1+R}\{[G(\tau_1)]^{1/n}(t_1) + \ldots \\ + [G(\tau_{m-1})]^{1/n}(t_{m-1} - t_{m-2}) \\ + [G(\tau_m)]^{1/n}(t - t_{m-1})^n\}, \quad t_{m-1} < t.\end{aligned} \tag{21}$$

where $F(\sigma_i)$ and $G(\tau_i)$ represent $F(\sigma_i - \sigma^*)$ and $G(\tau_i - \tau^*)$, see (4) and (5).

Total Strain. The total strain following a series of steps or jumps in stress is found by adding to the elastic strain corresponding to the stresses existing at the time of interest the recoverable strain given by (13) or (15) and the nonrecoverable strain (19) or (21) for axial strain or shear strain, respectively.

The aforementioned approach [the viscous-viscoelastic theory (VV)] was employed to calculate the creep behavior corresponding to several complex stress histories and compared with actual results in the following section.

In addition, the strain-hardening theory alone (SH) as described by (21) was employed also to predict the total creep strain. In this case the coefficient $1/1 + R$ in (21) was replaced by unity and ϵ^{ve} was taken to be zero.

Experimental Results and Comparisons

Using the material constants in (2)–(5) determined from constant stress creep and recovery tests as described in [1] and given in Table

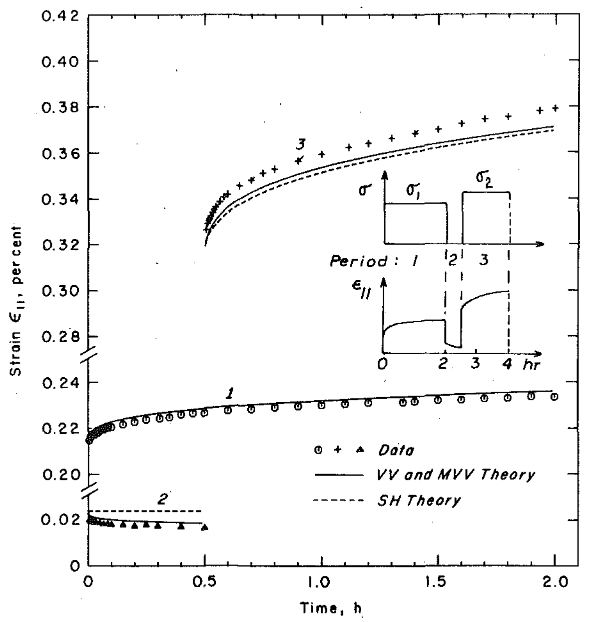

Fig. 2 Creep of 2618AL at 200°C under complete unloading and reloading to a higher stress. Where a theory is not shown it is the same as the (MVV) theory. Numbers indicate periods; σ_1 = 137.9 MPa (20 ksi), σ_2 = 193.1 MPa (28 ksi).

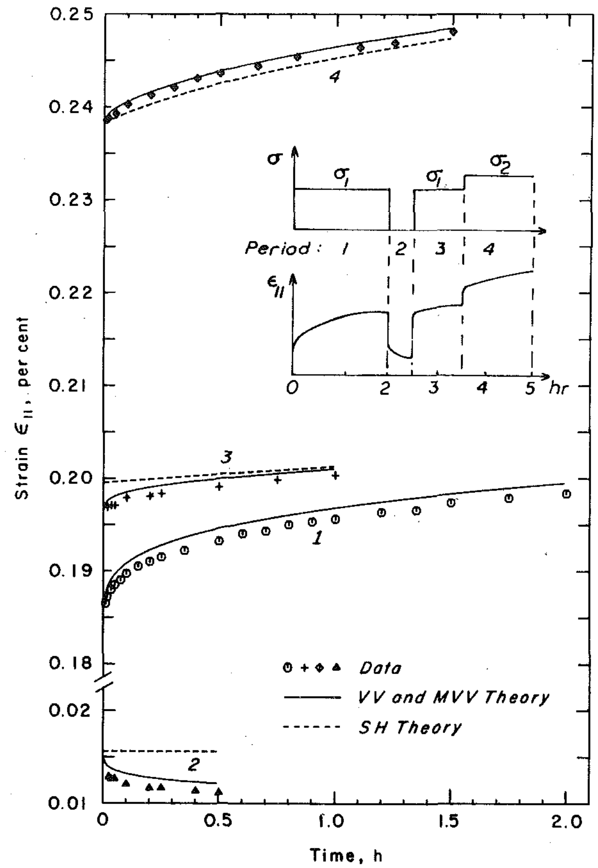

Fig. 3(a) Creep of 2618AL at 200°C under complete unloading, reloading, and stepup. Where a theory is not shown it is the same as the (MVV) theory. Numbers indicate periods. σ_1 = 119.5 MPa (17.33 ksi), σ_2 = 143.4 MPa (20.8 ksi).

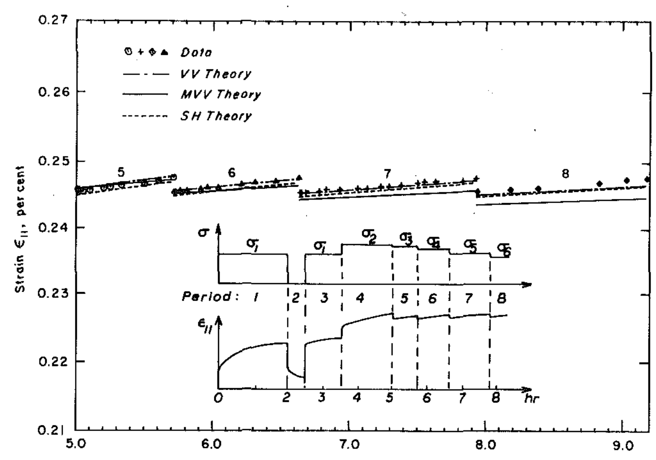

Fig. 3(b) Creep of 2618AL at 200°C under very small unloading steps. Numbers indicate periods; σ_1 = 119.5 MPa (17.33 ksi), σ_2 = 143.4 MPa (20.8 ksi), σ_3 = 142.0 MPa (20.6 ksi), σ_4 = 140.7 MPa (20.4 ksi), σ_5 = 139.3 MPa (20.2 ksi), σ_6 = 137.9 MPa (20.0 ksi).

1, creep resulting from stepup, stepdown, and recovery stress change experiments were predicted using the procedures just described. The results were then compared with corresponding experimental results as shown in Figs. 1–4. The experiments consisted of tension or torsion creep tests in which abrupt changes in load were made at intervals. Several types of load changes often were made in the same experiment. In the following the predictions for similar types of load changes are compared with experiments rather than discussing the results of each testing sequence. The predictions based on (13), (14), (19), and (20), the viscous-viscoelastic (VV) theory, are shown as dot-dash lines. The short-dash lines represent the predictions based on strain hardening (SH) alone. The solid lines represent the predictions based on modifications of the viscous-viscoelastic (MVV) theory which are discussed in later paragraphs. In Fig. 1–4 omission of the dot-dash line or the dash line for any period indicates that the prediction based on the omitted theory is the same as that represented by the solid lines.

Stepup Experiments. Stepup experiments are shown in Fig. 1–4. In Fig. 1 there is a sequence of two upward steps following the first period of creep. An upward step was preceded by a downward step to zero stress in Figs. 2 and 3. A small stress reduction preceded the stepup in Fig. 4.

(VV) Theory. Except for a vertical displacement, the agreement between experiment and creep predicted by the (VV) theory is excellent for the second period in Fig. 1. During the third period the actual creep rate was somewhat greater than predicted by the (VV) theory and there was more of a "primary"-type creep (greater rate of change of slope) than predicted.

The third period in Fig. 2 (involving reloading to a higher stress than the first loading) shows excellent agreement between the prediction of the (VV) theory and the test data taken from [2]. The third and fourth periods in Fig. 3(a) consist of reloading to the same stress as the first after a period at zero stress and then a stepup in stress. Again there is excellent agreement between data and prediction of the (VV) theory. The experiment in Fig. 4 involves creep at one stress followed by a small reduction in stress and then a reapplication of the same stress. In the third period the character of the creep curve and that predicted by the (VV) theory differ in that the primary-type behavior predicted at the start of the period was not observed. Also, the rate of creep was greater than predicted.

(SH) Theory. For stepup experiments the predictions using the strain-hardening (SH) theory are about the same as that of the viscous-viscoelastic (VV) theory. For the first period of loading, both theories yielded identical results. In Fig. 1, periods 2 and 3, and Fig. 4, period 3, the results from the strain-hardening (SH) theory are somewhat closer to the test data than the (VV) theory. In Fig. 2, period

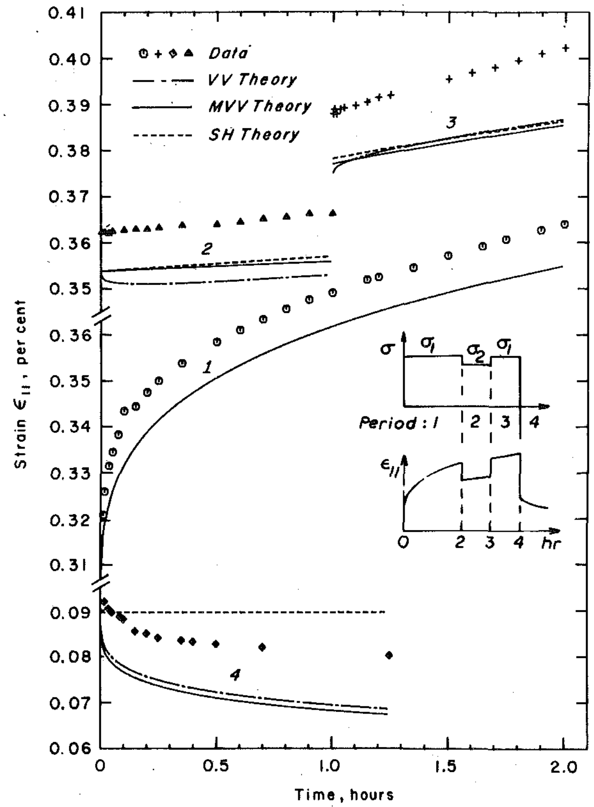

Fig. 4 Creep of 2618AL at 200°C with small unloading and reloading. Numbers indicate periods; σ_1 = 193.1 MPa (28 ksi), σ_2 = 179.4 MPa (26 ksi).

3, and Fig. 3(a), period 4, the reverse is true. In Fig. 1 the primary-type behavior of the (VV) theory at the start of the period is not found in the (SH) theory.

Recovery (Complete Unloading). Recovery following unloading to zero stress is shown in Fig. 1–4. Agreement between the experimental data and the prediction of the (VV) theory is very good for all experiments except for small vertical shifts in Figs. 1 and 4. In all cases the shape is satisfactorily predicted.

Similar results were also found for recovery following three tests having complex histories of combined tension and torsion (to be reported later). The recovery data in the second period of Figs. 2 and 3 is not a prediction, however, as these data were used in [1] as input in obtaining the constants in Table 1. In Figs. 1 and 4 the recovery shown in periods 6 and 4, respectively, followed a complicated history of changes in magnitude of stress.

Predictions of recovery from the strain-hardening (SH) theory in all cases are incorrect. The strain-hardening theory predicts no recovery upon complete unloading, although the experimental data in all cases show time-dependent recovery as predicted by the viscous-viscoelastic (VV) theory.

Stepdown Stress Change (Partial Unloading). Stepdown experiments involving partial unloading are shown in Fig. 1 at periods 4 and 5, Fig. 3(b) at periods 5–8, and Fig. 4 at period 2. The changes in stress are about 17 percent in Fig. 1, 10 percent in Fig. 3, and 7 percent in Fig. 4. In all of these cases the prediction based on the (VV) theory showed a recovery-type of behavior, that is, a negative slope of the creep curve with a gradually reducing rate. In Fig. 4. at period 2 the gradually reducing rate was reversed in the middle of the period. However, in every instance the observed creep behavior showed no negative rate, but a nearly constant small positive rate. On the other hand, as just noted, complete unloading to zero stress resulted in a recovery-type curve (negative creep rate) in both the observed recovery and the prediction from the (VV) theory.

The prediction based on the (SH) theory for the stepdown experiments showed a small positive rate which was quite similar to the form of the observed creep behavior. In Fig. 3 periods 5–8 the prediction for both (VV) and (SH) theories were about the same.

Discussion. The following features of the foregoing results were noted. (a) The strain-hardening (SH) theory did not predict the recovery observed on complete removal of a stress component. (b) The creep rate following an increase in stress in all cases was somewhat greater than predicted. Since the contribution of the nonrecoverable component was about twice that of the recoverable component for the (VV) theory, it may be concluded that this is a defect of the work-hardening approach used in computing the nonrecoverable component of strain. (c) In the third period of Fig. 1, the data showed more of a primary-type behavior than predicted. However, there is no such defect under similar circumstances in period 4 of Fig. 3(a). This may also be a defect of the work-hardening concept. (d) In the stepup tests and recovery at zero stress, there is no ambiguity as to how the creep limit enters into the calculation. However, on partial unloading the role of the creep limit is less clear.

Modification of Constitutive Equations, (MVV) Theory

Some of the features of the stepdown and recovery experiments not properly described by the (VV) or (SH) theories are better described by assuming that the behavior with regard to the creep limits is different for the nonrecoverable strain ϵ^v than for the recoverable strain ϵ^{ve} as follows:

(A) For the *nonrecoverable strain* component, the strain-hardening rule is still applicable. Upon reduction of stress, this strain rate $\dot{\epsilon}^v$ continues at the reduced but increasing rate prescribed by the strain-hardening rule, (19)–(21) for example, until the current stress σ_a equals or is less than the creep limit σ^*. When $\sigma_a \leqslant \sigma^*$, $\dot{\epsilon}^v$ is zero as prescribed by (19)–(21). Upon reloading to a stress above the creep limit, the nonrecoverable strain rate $\dot{\epsilon}^v$ resumes at the rate prescribed by the same equations as though there had been no interval t_x for which $\sigma_a \leqslant \sigma^*$.

(B) For the *recoverable strain* components ϵ^{ve}, on *partial unloading*, the recoverable strain rate $\dot{\epsilon}^{ve}$ becomes and remains zero for all reductions of stress until the total change in stress from the highest stress $\sigma_{\max}$ previously encountered to the current stress σ_a equals in magnitude the creep limit σ^*. That is,

$$\dot{\epsilon}^{ve} = 0 \quad \text{when} \quad (\sigma_{\max} - \sigma_a) \leqslant \sigma^*. \tag{22}$$

Equation (22) can be considered as meaning that for a small unloading, the recoverable strain component is "frozen" until the stress differential is greater than σ^* before the recovery mechanism is activated.

Besides the response that $\dot{\epsilon}^{ve} = 0$ under the stress condition described by (22) for the (MVV) theory, there are two other possible responses for $\dot{\epsilon}^{ve}$ under the stress condition given by (22): (a) $\dot{\epsilon}^{ve} < 0$ (this has been covered by the (VV) theory) and (b) $\dot{\epsilon}^{ve} > 0$ (for small partial unloading this is not admissible).

(C) For *large partial unloading*, $(\sigma_{\max} - \sigma_a) > \sigma^*$, the recovery mechanism becomes active and the recoverable strain component ϵ^{ve} may be computed as if the previous stress continued to cause creep and a reverse stress equal to $(\sigma_{\max} - \sigma_a)$ was applied to the specimen. The recoverable strain may be computed by the modified superposition principle except that the stress is replaced by the stress difference minus σ^* when the stress is reduced. This satisfies the requirement of complete recoverability of ϵ^{ve} upon complete unloading for one step loading only. Further load changes may involve difficulties because of nonlinearity.

(D) *Upon increasing the stress* to σ_b, $(\sigma_b \geqslant \sigma_a)$ following a period t_x (a dead zone) for which $(\sigma_{\max} - \sigma_a) < \sigma^*$ and $\dot{\epsilon}^{ve} = 0$ as discussed in (B), the recoverable strain component ϵ^{ve} continues in accordance with the viscoelastic behavior (12) as though the period t_x never occurred. Thus, in computing the behavior for situations described in (B) and (D), it is necessary to introduce a time shift in equations (13)–(15) to eliminate the appropriate period t_x when ϵ^{ve} is "frozen."

Thus the new time t' subsequent to a period $t_x = (t_b - t_a)$, becomes $t' = t - (t_b - t_a)$, where t is the real time and t_a, t_b are the times when σ_a, and σ_b are applied.

(E) Of course it is possible if not probable that the *creep surface in stress space* defining the creep limit changes size, shape, and position as a result of plastic and creep strains. However, the nature of such changes, if any, is not known at present.

The predictions of the modified viscous-viscoelastic (MVV) theory computed in accordance with A–D in the foregoing are shown as solid lines in Figs. 1–4. These predictions are in accord with the experimental data in Figs. 1, 2, 3(a), and 4, and are generally better representations of the material behavior than either the (VV) or (SH) theories.

However, the small stepdown experiments shown in Fig. 3(b) are best represented by the (VV) theory with the (SH) theory yielding the next best description of the data. The data in Fig. 3(b) are an approximation of stress relaxation in that the stress was held constant at each step until the strain had returned to its previous value before the stress was reduced again. Also the shape of the actual recovery curve resulting from complete unloading following a series of unloading steps (Fig. 1 period 6) is better described by the (VV) than the (MVV) theory. A similar result was also observed in the recovery following complete unloading in a creep test under variable combined tension and torsion (to be reported later).

All the partial stepdown tests shown in Figs. 1 and 4 are in the range where the change in stress is less than the magnitude of the creep limit (hence there was no contribution from ϵ^{ve}) and the stress following the change was greater than the creep limit (hence $\dot{\epsilon}^{v}$ would continue at a reduced rate). As shown for partial stepdown tests there was no "recovery"-type behavior and the creep rate was positive or approaching zero, which was in accord with the (MVV) theory. Additional stepdown tests in which the change in stress is greater than the magnitude of the creep limit are needed to explore further the role of the creep limit.

Reproducibility

Five creep tests were performed at 172.4 MPa (25 ksi) tension and 200°C. Four of these creep tests were followed by recovery at zero stress. All specimens were taken from the same lot of material. The results of all tests were similar. When (1) was fitted to the creep data with $n = 0.270$ the values of ϵ_{11}^{0} and ϵ_{11}^{+} were as follows for tests F,[2] 13, 14, 15, and 16,[2] respectively: ϵ_{11}^{0}—0.2627,0.2617, 0.2735, 0.2638, and 0.2659; ϵ_{11}^{+}—0.0401, 0.0390, 0.0365, 0.0361, and 0.0416. The duration of these creep tests was 2, 0.1, 6, 0.8, and 0.1 h, respectively. These results suggest that the variability of the material and experimental errors were small.

Aging

The possibility that aging may have affected the results of the experiments was investigated further. A tension creep test was performed at 25 ksi stress at 200°C (392°F) after aging at the same temperature for 95 hr. The results showed a small increase in creep rate compared to the results of Tests $F1$ and 16 reported in [1] at the same stress but aged for 18 hr. Analysis of the data yielded the following values of the constants in (1) for the test which was aged for 95 hr.: For best fit $n = 0.237$, $\epsilon^0 = 0.2668$ percent, $\epsilon^+ = 0.0557$ percent/hr^{-n}; for $n = 0.270$, $\epsilon^0 = 0.2716$, $\epsilon^+ = 0.0508$. The creep rate $\dot{\epsilon}$ at 1 hr is given by $n\epsilon^+$. Making this computation for the three ages available yielded the following creep rates: Aged 18 hr, the average of Tests $F1$ and 16 yielded $\dot{\epsilon} = 0.0085$ percent/hr; aged 95 hr $\dot{\epsilon} = 0.0132$ percent/hr, aged 1103 hr, $\dot{\epsilon} = 0.230$ percent/hr. Interpolating these values on the basis of either a log-log relation or linear time-log strain-rate relation yielded an increase of creep rate from 18–30 hr of about 7 percent for either interpolation. Thus, during the testing time of the experiments reported, the creep rate increased about ½ percent per hr, which is considered negligible over the time span of the experiments.

[2] Previously reported in [1].

Results and Conclusions

Analysis of results of creep tests of 2618 Aluminum under a variety of changes in stress during creep in the nonlinear range show that a strain-hardening (SH) theory does not properly describe the behavior on unloading or reloading; but a viscous-viscoelastic theory with certain modifications (MVV) theory predicts most of the features of the observed creep behavior quite well.

Among the conclusions are the following:

1 The behavior may be represented by resolving the time-dependent strain into recoverable and nonrecoverable components having the same time-dependence.

2 The material behaves as though there was a creep limit such that creep is very small or zero unless the stress is greater than a limiting value.

3 On partial unloading the material behaves as though the nonrecoverable strain component ϵ^{v} continued to creep in accordance with strain hardening unless the stress became less than the creep limit; whereas the recoverable strain component ϵ^{ve} remained constant unless the decrease in stress exceeded the magnitude of the creep limit.

4 On reloading following an interval t_x of partial unloading involving no further change in ϵ^{ve} the component ϵ^{ve} resumed creep as though the interval t_x did not exist.

5 *Very* small reductions of stress are best represented by the viscous-viscoelastic (VV) theory, which is inconsistent with the behavior under small stress reductions.

6 Recovery on complete unloading following a history of step changes in stress is reasonably represented by the (VV) or (MVV) theories, but best represented by the (VV) theory.

Acknowledgment

This work was supported by the Office of Naval Research and the Army Research Office, Research Grant No. DAAG29-78-G-0185. The material was contributed by the Aluminum Company of America. The authors are grateful to: U. W. Cho for helpful discussion and recomputation of theory; R. M. Reed for performing some of the experiments, and M. C. Gingrich for typing the manuscript.

Data

The authors will supply the numerical data for tests reported in [1–2] and the present paper to those having need for their research.

References

1 Findley, W. N., and Lai, J. S., "Creep and Recovery of 2618 Aluminum Alloy Under Combined Stress With a Representation by a Viscous-Viscoelastic Model," ASME JOURNAL OF APPLIED MECHANICS, Vol. 45, 1978, pp. 507–514; also Findley, W. N., Cho, U. W., and Ding, J. L., "Creep of Metals and Plastics Under Combined Stresses, A Review," ASME *Journal of Engineering Materials and Technology*, Vol. 101, 1979, p. 365.

2 Blass, J. J., and Findley, W. N., "Short-Time Biaxial Creep of an Aluminum Alloy With Abrupt Changes of Temperature and State of Stress," ASME JOURNAL OF APPLIED MECHANICS, Vol. 38, 1971, pp. 489–501.

3 Findley, W. N., and Gjelsvik, A., "A Biaxial Testing Machine for Plasticity, Creep or Relaxation Under Variable Principal-Stress Ratios," *Proceedings, American Society for Testing and Materials*, Vol. 62, 1962, pp. 1103–1118.

4 Green, A. E., and Rivlin, R. S., "The Mechanics of Nonlinear Materials With Memory—Part I," *Archive for Rational Mechanics and Analysis*, Vol. 1, 1957, p. 1.

5 Findley, W. N., Lai, J. S., and Onaran, K., *Creep and Relaxation of Nonlinear Viscoelastic Materials*, North-Holland Publishers, Amsterdam, 1976.

6 Onat, E. T., and Wang, T. T., "Integral Representation of Creep and Rate Sensitivity in Metals," Division of Engineering, Brown University, Providence, R. I., 1965.

7 Wang, T. T., and Onat, E. T., "Nonlinear Mechanical Behavior of 1100 Aluminum at 300°F," *Acta Mechanica*, Vol. 5, 1968, p. 54.

Norman Jones[1]
Professor.
Mem. ASME

J. Gomes de Oliveira
Assistant Professor.

Department of Ocean Engineering,
Massachusetts Institute of Technology,
Cambridge, Mass. 02139

Dynamic Plastic Response of Circular Plates With Transverse Shear and Rotatory Inertia

The response of a simply supported circular plate made from a rigid perfectly plastic material and subjected to a uniformly distributed impulsive velocity is developed herein. Plastic yielding of the material is controlled by a yield criterion which retains the transverse shear force as well as bending moments and the influence of rotatory inertia is included in the governing equations. Various equations and numerical results are presented which may be used to assess the importance of transverse shear effects and rotatory inertia for this particular problem.

1 Introduction

The rigid-plastic idealization of a ductile material considerably simplifies theoretical investigations into the dynamic response of structures subjected to large dynamic loads which cause inelastic behavior [1–4, etc.]. These analyses can give surprisingly accurate yet simple predictions for a wide range of practical problems. However, it turns out that transverse shear effects can exercise an important influence on the dynamic plastic behavior of various structural members as discussed in reference [4].

Two recent theoretical studies on beams loaded dynamically [5, 6] have examined the effect of rotatory inertia in the governing equations and the influence of transverse shear force as well as bending moment in the yield condition for a rigid perfectly plastic material. References [4–6] contain citations to earlier work which explore the influence of transverse shear effects on the dynamic plastic response of beams, while various yield criteria are discussed in reference [7].

The influence of transverse shear forces on the static plastic collapse of circular plates has been examined by several authors [8–12], but no papers appear to have been published for any dynamic loading case. Moreover, the influence of rotatory inertia on the dynamic plastic response of circular plates has not been examined, despite the fact that many authors have explored its effect for linear elastic plates [13, 14, etc.].

Reference [15] contains a review of many of the theoretical solutions on the dynamic response of circular plates which have been obtained since the publication of reference [16]. However, the analyses were developed for plates made from rigid perfectly plastic materials which were controlled by a yield criterion relating the circumferential and radial bending moments, while the influence of transverse shear forces were disregarded. Wang [17] examined the behavior of a rigid perfectly plastic circular plate which was simply supported around the outer boundary and subjected to a uniformly distributed impulsive velocity V_0. It may be shown that the transverse shear force in this analysis is infinitely large at the supports immediately after the start of motion. It is the purpose of the work in Section 3 of this article to seek the behavior of Wang's problem when the circular plate is made from a rigid perfectly plastic material with a finite transverse shear strength. The simultaneous influence of transverse shear and rotatory inertia effects is then examined in Section 4.

2 Basic Equations

The equilibrium equations for the dynamic behavior of the element of an axisymmetrically loaded circular plate shown in Fig. 1 may be written in the form

$$\partial M_r/\partial r + (M_r - M_\theta)/r + Q_r = I_r \partial^2\psi/\partial t^2 \tag{1a}$$

and

$$\partial Q_r/\partial r + Q_r/r = -p + \mu \partial^2 w/\partial t^2, \tag{1b}$$

where $I_r = \rho H^3/12$, $\mu = \rho H$, $\partial w/\partial r = \psi + \gamma$, ψ is the rotation of lines which were originally perpendicular to the initial midplane ($z = 0$) due to bending and

$$\gamma = \partial w/\partial r - \psi, \quad \kappa_r = \partial\psi/\partial r, \quad \kappa_\theta = \psi/r \tag{2a–c}$$

are the transverse shear strain, radial curvature change, and circumferential curvature change, respectively.

The dynamic continuity condition across a discontinuity front, which travels from region 1 to region 2 with a velocity c in a continuum with a constant density ρ, may be written [18, 19]

$$[\sigma_{i1}] = -\rho c[\partial u_i/\partial t], \tag{3}$$

[1] Presently, Professor, Department of Mechanical Engineering, The University of Liverpool, P. O. Box 147, Brownlow Hall, Liverpool L69 3BX, England.

Contributed by the Applied Mechanics Division for publication in the JOURNAL OF APPLIED MECHANICS.

Discussion on this paper should be addressed to the Editorial Department, ASME, United Engineering Center, 345 East 47th Street, New York, N. Y. 10017, and will be accepted until June 1, 1980. Readers who need more time to prepare a discussion should request an extension from the Editorial Department. Manuscript received by ASME Applied Mechanics Division, December, 1978.

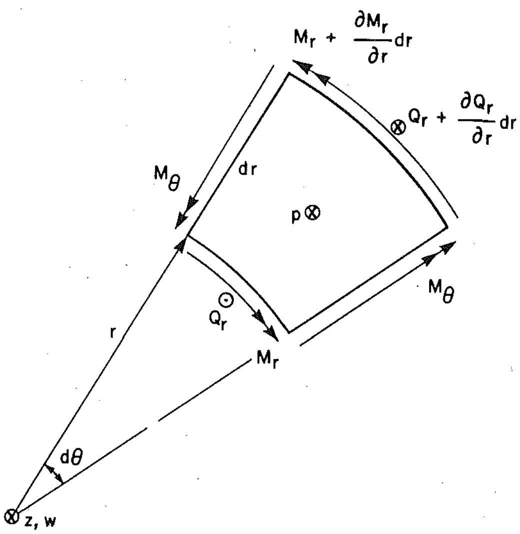

Fig. 1 Element of a circular plate

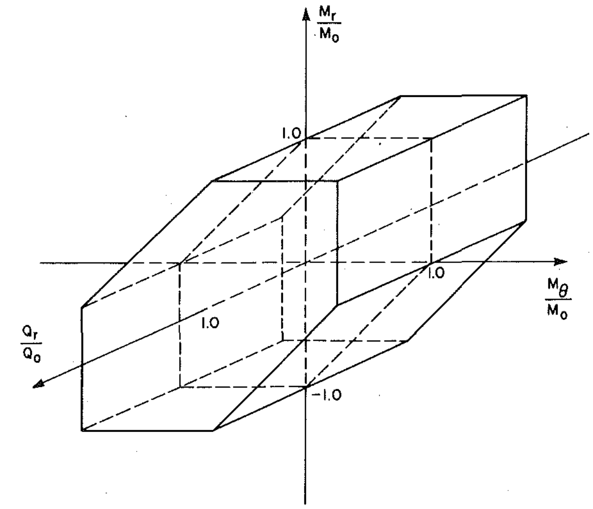

Fig. 2 Yield surface

where $[X] = X_2 - X_1$, and when the particle velocity $(\partial u_1/\partial t)$ in region 1, which is normal to the discontinuity front, is negligible compared with c. The displacements u_i act along the x_i-axes with x_1 directed from region 1 to region 2 and normal to the discontinuity front.

Now, $x_1 = r$, $x_2 = r\theta$, $x_3 = z$, $\sigma_{11} = \sigma_r$, $\sigma_{21} = 0$, $\sigma_{31} = \sigma_{\theta z}$, $u_1 = -z\psi$, $u_2 = 0$, and $u_3 = w$ for the particular case of an axisymmetrically loaded circular plate with the variables defined in Fig. 1 and in the Nomenclature. Thus, if equation (3) with $i = 1$ is multiplied by z and integrated with respect to z then

$$[M_r] = -cI_r[\dot{\psi}], \tag{4a}$$

while equation (3) with $i = 3$ when integrated with respect to z gives

$$[Q_r] = -c\mu[\dot{w}]. \tag{4b}$$

The kinematic continuity condition associated with equation (3) is [18, 19]

$$[\partial u_i/\partial t] = -c[\partial u_i/\partial x_1], \tag{5}$$

which using the variables appropriate for an axisymmetrically loaded circular plate predicts

$$[\dot{\psi}] = -c[\partial\psi/\partial r] \tag{6a}$$ [2]

and

$$[\dot{w}] = -c[\partial w/\partial r]. \tag{6b}$$

3 Impulsive Loading of a Circular Plate With Transverse Shear

It was remarked in the Introduction that the transverse shear force at the simply supported edge of the impulsively loaded circular plate examined in reference [17] is infinitely large at the start of motion. A theoretical analysis of the same problem is presented in this section but for a plate made from a rigid perfectly plastic material with a finite transverse shear strength. Plastic flow is controlled by the simplified yield criterion shown in Fig. 2 which was used by Sawczuk and Duszek [8] to examine the static loading of circular plates. Q_0 and M_0 are the respective values of the transverse shear force per unit length and bending moment per unit length required for independent plastic yielding of the plate cross section.

3.1 Class I Plates, $0 < \nu \leq 3/2$. The dimensionless transverse velocity profile for this class of plates subjected to a uniformly distributed initial impulsive velocity V_0 is

[2] This condition may also be obtained from the equivalent postulate $[\psi] = 0$ which was used in references [5, 20] for beams.

Nomenclature

a = defined by equation (46a)
$m_r, m_\theta = M_r/M_0, M_\theta/M_0$
p = lateral pressure
$q = Q_r/Q_0$
r, θ = polar coordinates
t = time
w = transverse displacement
$\overline{w}$ = dimensionless transverse displacement (equation (10g))
z = coordinate through plate thickness (Fig. 1)
H = plate thickness
I = dimensionless rotatory inertia defined by equation (46b)
$I_r = \rho H^3/12$
M_r, M_θ = radial and circumferential bending moments per unit length defined in Fig. 1
M_0 = magnitude of bending moment per unit length required for plastic flow of cross section
Q_r = transverse shear force per unit length defined in Fig. 1
Q_0 = magnitude of Q_r required for plastic flow of cross section
R = outside radius of plate
R_B, R_S = bending and shear energies divided by the initial kinetic energy
T = dimensionless time defined by equation (10f)
V_0 = initial impulsive velocity
$\overline{W}$ = dimensionless transverse displacement defined by equation (10g)
$\alpha = r/R$
β = dimensionless radius of an axisymmetric interface
γ = transverse shear strain
κ_r, κ_θ = radial and circumferential curvature changes
$\mu = \rho H$
$\nu = Q_0R/2M_0$
ρ = density of material
σ_0 = uniaxial yield stress
ψ = rotation of midplane due to bending
$[X] = X_2 - X_1$
$(\dot{\ }) = \partial(\ )/\partial t$ or $\partial(\ )/\partial T$.

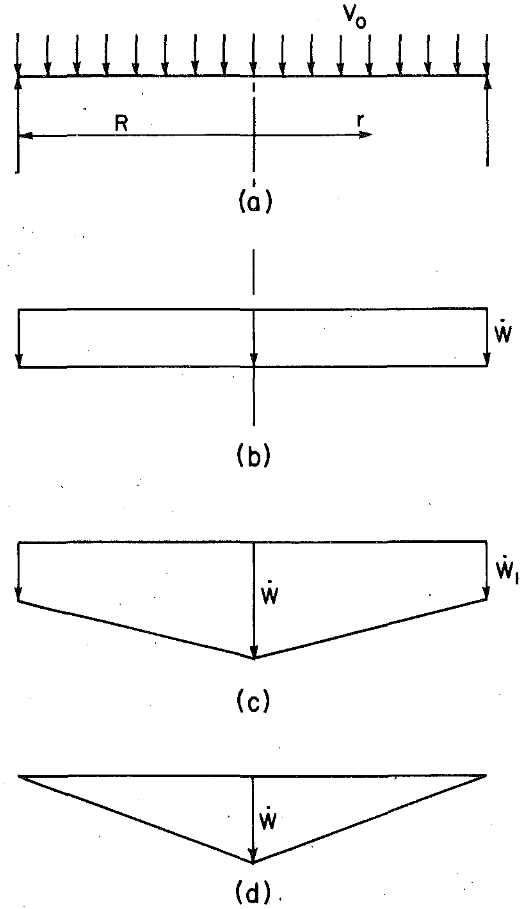

Fig. 3 (*a*) **Impulsively loaded circular plate;** (*b*) **Velocity profile for Class I plates;** (*c*) **Velocity profile for the first phase of motion for Class II Plates;** (*d*) **Velocity profile for the second phase of motion for Class II plates**

$$\dot{\overline{w}} = \dot{\overline{W}} \quad \text{for} \quad 0 \le \alpha \le 1, \tag{7}$$

which gives a circumferential shear hinge at the supports as indicated in Fig. 3(*b*). Thus, if M_θ is assumed constant in the rigid region $0 \le \alpha < 1$, then equations (1*a*, *b*) with $I_r = 0$, and $p = 0$, and equation (7) give

$$\ddot{\overline{W}} = -\nu/3, \quad q(\alpha) = -\alpha, \tag{8a, b}$$

$$m_r(\alpha) = -2\nu(1-\alpha^2)/3, \quad m_\theta(\alpha) = -2\nu/3 \tag{9a, b}$$

when satisfying $q(1) = -1$, and $m_r(1) = 0$, where

$$\alpha = r/R, \quad \nu = Q_0R/2M_0, \quad q = Q_r/Q_0, \quad m_r = M_r/M_0,$$
$$m_\theta = M_\theta/M_0, \quad T = 12M_0t/\mu V_0R^2,$$
$$\overline{W} = 12M_0W/\mu V_0^2R^2, \dot{\overline{W}} = \dot{W}/V_0. \tag{10a–h}$$

Now, equation (8*a*) predicts

$$\overline{W}(T) = T - \nu T^2/6 \tag{11}$$

since $\dot{\overline{W}}(0) = 1$ and $\overline{W}(0) = 0$. Thus motion ceases when

$$T_1 = 3/\nu \tag{12}$$

and the associated maximum permanent transverse displacement is

$$\overline{W}_f = 3/2\nu. \tag{13}$$

This transverse displacement is manifested as a shear slide at the supports which must not therefore become too large to avoid failure of the plate. A suitable failure criterion for engineering purposes was developed in reference [21] for beams and may be written for the present case in the form

$$W_f \le kH, \tag{14}$$

where $0 < k \le 1$ and H is the plate thickness.

The generalized stress fields given by equations (8*b*) and (9) are statically admissible provided $0 < \nu \le 3/2$.

3.2 Class II Plates, $3/2 \le \nu \le 2$. If $\nu \ge 3/2$, then equation (9) shows that m_θ violates the yield condition throughout a plate and m_r penetrates the yield surface in a central region. Thus the first stage of motion for the present case is governed by the velocity profile sketched in Fig. 3(*c*) which gives plastic bending throughout a plate with a stationary shear hinge at the supports. This phase of motion is completed when shear sliding ceases at the supports and is followed by a final stage of motion with the velocity profile illustrated in Fig. 3(*d*).

3.2.1 First Phase of Motion, $0 \le T \le T_1$. The transverse velocity profile in Fig. 3(*c*) is

$$\dot{w}(r,t) = \dot{W}(t) + \{\dot{W}_1(t) - \dot{W}(t)\}r/R, \tag{15}$$

which predicts $\dot{\kappa}_r = 0$ and $\dot{\kappa}_\theta \le 0$ if $\dot{\overline{W}} > \dot{\overline{W}}_1$ according to equations (2) with $\gamma = 0$ in the region $0 \le \alpha < 1$. Thus the normality rule of plasticity requires

$$m_\theta = -1, \quad -1 \le m_r \le 0, \quad -1 \le q \le 1. \tag{16a–c}$$

Equations (15), (16*a*), and (1*a*, *b*) with $I_r = p = 0$ give

$$\ddot{\overline{W}}_1 = 1 - \nu, \quad \ddot{\overline{W}} = \nu - 2, \tag{17a, b}$$

$$q(\alpha) = \alpha\{2(3-2\nu)\alpha + 3(\nu-2)\}/\nu,$$

and

$$m_r(\alpha) = -1 - (3-2\nu)\alpha^3 - 2(\nu-2)\alpha^2, \tag{18a, b}$$

since $q(1) = -1$, $m_r(1) = 0$, and $m_r(0) = -1$. Thus

$$\overline{W}_1 = T + (1-\nu)T^2/2, \quad \overline{W} = T + (\nu-2)T^2/2 \tag{19a, b}$$

because $\dot{\overline{W}}(0) = 1$, $\dot{\overline{W}}_1(0) = 1$, $\overline{W}(0) = 0$, and $\overline{W}_1(0) = 0$. This phase of motion terminates at

$$T_1 = 1/(\nu - 1) \tag{20}$$

when $\dot{\overline{W}}_1 = 0$, and the associated shear sliding at the supports is

$$\overline{W}_1(T_1) = 1/\{2(\nu-1)\}. \tag{21}$$

The total energy dissipated due to shearing deformations is

$$R_S = \nu/\{3(\nu-1)\} \tag{22}$$

when nondimensionalised with respect to the initial kinetic energy $\mu\pi R^2V_0^2/2$.

It is straightforward to show that the generalized stress fields (18) are statically admissible provided $3/2 \le \nu \le 2$.

3.2.2 Second Phase of Motion, $T_1 \le T \le T_f$. The equilibrium equations (1*a*, *b*) together with equation (15) with $\dot{W}_1 = 0$ and equations (16*a*–*c*) predict

$$\ddot{\overline{W}} = -1, \quad q(\alpha) = -\alpha(3-2\alpha)/\nu, \tag{23a, b}$$

and

$$m_r(\alpha) = 2\alpha^2 - \alpha^3 - 1 \tag{23c}$$

since $m_r(1) = 0$, and $m_r(0) = -1$. Now, integrating equation (23*a*) and making the displacements and velocities continuous at T_1 with equations (19) gives

$$\overline{w}(\alpha, T) = (2 - T/2)(1-\alpha)T + (\alpha - 1/2)/(\nu - 1). \tag{24}$$

Finally, motion ceases at

$$T_f = 2 \tag{25}$$

when $\dot{\overline{W}} = 0$ and

$$\overline{w}(\alpha, T_f) = (4\nu - 5)/\{2(\nu - 1)\} + (3 - 2\nu)\alpha/(\nu - 1). \quad (26)$$

The ratio of the energy dissipated in bending to that dissipated in shear is

$$R_B/R_S = 2 - 3/\nu. \quad (27)$$

3.3 Class III Plates, $\nu \geq 2$. It is evident from equation (18b) that $\partial^2 m_r(0, T)/\partial\alpha^2 \leq 0$ when $\nu \geq 2$, which leads to a yield violation at the plate center. These yield violations are avoided when a plate responds with the three phases of motion indicated in Fig. 4.

3.3.1 First Phase of Motion, $0 \leq T \leq T_1$. A stationary hinge circle forms at a dimensionless radius $\beta_1(\beta_1 = r_1/R)$ and transverse shear sliding develops at the plate supports as shown in Fig. 4(b). This transverse velocity field may be written

$$\dot{\overline{w}}(\alpha, T) = \dot{\overline{W}}(T) \quad \text{for} \quad 0 \leq \alpha \leq \beta_1, \quad (28a)$$

and

$$\dot{\overline{w}}(\alpha, T) = \dot{\overline{W}}_1(T)(\alpha - \beta_1)/(1 - \beta_1) + \dot{\overline{W}}(T)(1 - \alpha)/(1 - \beta_1), \quad \beta_1 \leq \alpha \leq 1. \quad (28b)$$

Equations (2) with $\gamma = 0$ and the flow rule of plasticity again give equations (16), which together with the equilibrium equations (1), equations (28), and $q(1) = -1$, $m_r(1) = 0$, $m_r(\beta_1) = -1$, $q(0) = 0$, $[q(\beta_1, T)] = [m_r(\beta_1, T)] = 0$ predict

$$\ddot{\overline{W}} = 0,\ \ddot{\overline{W}}_1 = -\{(1 - \beta_1)^2(1 + \beta_1)\}^{-1}, \quad (29a, b)$$

$$q(\alpha) = 0, \quad m_\theta(\alpha) = m_r(\alpha) = -1 \quad \text{for} \quad 0 \leq \alpha \leq \beta_1, \quad (30a\text{–}c)$$

while

$$q(\alpha) = -(\alpha - \beta_1)^2(2\alpha + \beta_1)/\{\alpha(1 - \beta_1)^2(2 + \beta_1)\}, \quad m_\theta(\alpha) = -1,$$

and

$$m_r(\alpha) = \nu(\alpha - \beta_1)^3(\alpha + \beta_1)/\{\alpha(1 - \beta_1)^2(2 + \beta_1)\} - 1$$

when

$$\beta_1 \leq \alpha \leq 1, \quad (31a\text{–}c)$$

where

$$\beta_1 = \{(4\nu^2 - 8\nu + 1)^{1/2} - 1\}/2\nu. \quad (32)$$

Equations (28) and (29) with the initial conditions $\dot{\overline{W}}(0) = \dot{\overline{W}}_1(0) = 1$, and $\overline{W}(0) = \overline{W}_1(0) = 0$ give

$$\overline{W}(\alpha, T) = T, \quad 0 \leq \alpha \leq \beta_1, \quad (33a)$$

and

$$\overline{W}(\alpha, T) = T - \nu T^2(\alpha - \beta_1)/\{2(2 + \beta_1)(1 - \beta_1)^2\}, \quad \beta_1 \leq \alpha \leq 1. \quad (33b)$$

This phase of motion terminates when $\dot{\overline{W}}_1 = 0$ which occurs at

$$T_1 = (1 + \beta_1)(1 - \beta_1)^2 \quad (34)$$

and the associated dimensionless transverse displacements are

$$\overline{w}(\alpha, T_1) = (1 + \beta_1)(1 - \beta_1)^2, \quad 0 \leq \alpha \leq \beta_1 \quad (35a)$$

and

$$\overline{w}(\alpha, T_1) = (1 - \beta_1{}^2)(1 - \beta_1/2 - \alpha/2), \quad \beta_1 \leq \alpha \leq 1, \quad (35b)$$

while the corresponding dimensionless energy dissipated due to transverse shear deformations is

$$R_S = (2 + \beta_1)(1 - \beta_1)/3. \quad (36)$$

3.3.2 Second Phase of Motion, $T_1 \leq T \leq T_2$. No transverse shear deformations occur during this phase of motion. The transverse velocity profile illustrated in Fig. 4(c) with a circumferential hinge traveling at speed $\dot{\beta}$ is given by equations (28) with $\dot{\overline{W}}_1 = 0$ and β_1 replaced by $\beta(T)$ and is similar to that used by Wang [17] during the first phase of motion of the bending only solution for a simply supported circular plate loaded impulsively. Thus, following a theoretical procedure similar to Wang [17] and matching the velocity and displacement fields at $T = T_1$ with equations (33), shows that this phase of motion ends at

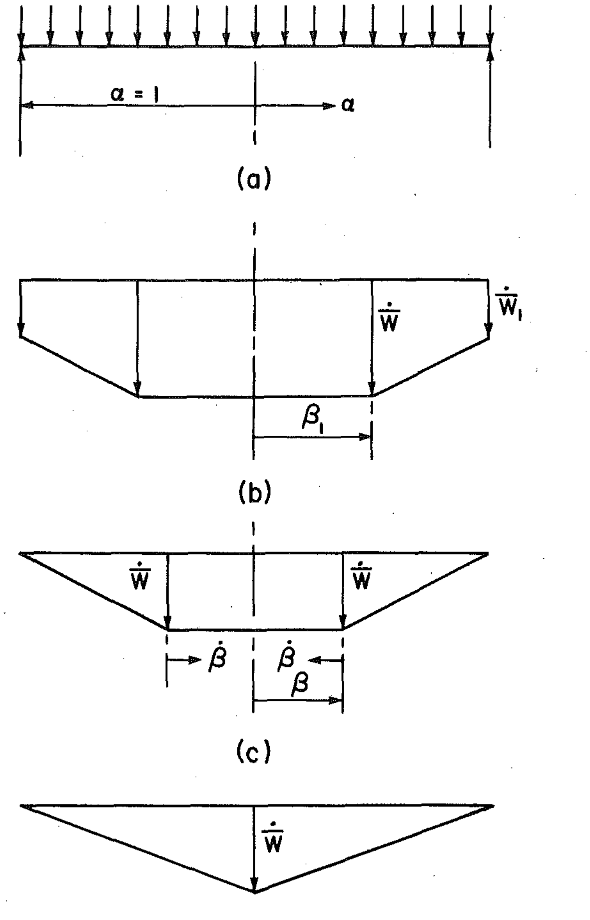

Fig. 4 (a) Impulsively loaded circular plate with $\nu \geq 2$; (b–d) are the dimensionless velocity profiles for the first, second, and third phases of motion for Class III plates

$$T_2 = 1 \quad (37)$$

when $\beta = 0$. The associated transverse displacements are

$$\overline{w}(\alpha, T_2) = 1 - \alpha^2/2 - \alpha^3/2, \quad 0 \leq \alpha \leq \beta_1 \quad (38a)$$

and

$$\overline{w}(\alpha, T_2) = (1 - \beta_1{}^2)(2 - \beta_1 - \alpha)/2 + \beta_1(1 + 3\beta_1/2)(1 - \alpha), \quad \beta_1 \leq \alpha \leq 1. \quad (38b)$$

It may be shown that the transverse shear force $q(\alpha, T)$ and the other generalized stresses are statically admissible.

3.3.3 Third Phase of Motion, $T_2 \leq T \leq T_f$. Again no transverse shear deformations develop during this final phase of motion which is governed by the transverse displacement profile in Fig. 4(d). Thus the theoretical procedure for this phase of motion is similar to that employed by Wang [17] for the final phase of motion in the bending only case and is also similar to the second phase of motion in Section 3.2.2 for Class II plates.

It may be shown that motion finally ceases when

$$T_f = 2, \quad (39)$$

and the final deflection profile is

$$\overline{w}(\alpha, T_f) = (1-\alpha)(\alpha^2 + 2\alpha + 3)/2 \quad \text{for} \quad 0 \le \alpha \le \beta_1, \quad (40a)$$

and

$$\overline{w}(\alpha, T_f) = (1-\alpha)(1 + 2\beta_1 + 3\beta_1{}^2)/2 + (1-\beta_1{}^2)(2-\beta_1-\alpha)/2$$

when

$$\beta_1 \le \alpha \le 1. \quad (40b)$$

The ratio of energy dissipated in bending to that dissipated in shear is

$$R_B/R_S = (1 + \beta_1 + \beta_1{}^2)/(2 - \beta_1 - \beta_1{}^2), \quad (41)$$

where β_1 is given by equation (32).

4 Impulsive Loading of a Circular Plate With Transverse Shear and Rotatory Inertia

4.1 Plates With $0 < \nu \le 3/2$. It is evident that the transverse velocity field illustrated in Fig. 3(*b*) and used to describe the behavior of the Class I simply supported circular plates in Section 3.1 does not involve any rotation of the plate elements. Thus $\psi = 0$ and the rotatory inertia term in equation (1*a*) is zero even when $I_r \neq 0$. The theoretical analysis in Section 3.1 therefore remains valid for the case when transverse shear and rotatory inertia effects are retained in the basic equations.

4.2 Plates With $\nu \ge 3/2$. It may be shown that the transverse velocity fields illustrated in Figs. 3(*c, d*) and 4 do not give statically admissible solutions when the influence of rotatory inertia is retained in equation (1*a*). For example, it may be shown that the solution of the equilibrium equations (1*a, b*) with the velocity field illustrated in Fig. 3(*c*) gives a yield violation near the plate center since $m_r = -1$ and $\partial m_r/\partial\alpha < 1$ at $\alpha = 0$. It turns out that in order to satisfy the kinematic and static requirements, plastic hinges do not develop in a plate, a circumstance which was also found in reference [5] for beams.

If $M_\theta = M_r = -M_0$ and $|Q_r| < Q_0$ throughout a plastic zone in a circular plate with $I_r \neq 0$, then equations (1*a, b*) give

$$\partial^2\dot{w}/\partial r^2 + r^{-1}\partial\dot{w}/\partial r - \mu\dot{w}/I_r = 0. \quad (42)$$

If $w(r, t)$ is written using the separation of variables, then the spatial dependence of w is governed by a modified Bessel equation of zero order. Thus

$$\ddot{w} = C_1(t) I_0\{(\mu/I_r)^{1/2} r\} \quad (43)$$

when disregarding the usual $K_0\{(\mu/I_r)^{1/2}r\}$ term to avoid a singularity at $r = 0$ and where $C_1(t)$ is an arbitrary function of time, and $I_0\{(\mu/I_r)^{1/2}r\}$ is a modified Bessel function of the first kind of order zero. Equation (43) therefore leads to a velocity field in the plastic zone

$$\dot{w} = C(t) I_0\{(\mu/I_r)^{1/2} r\} + D(r), \quad (44)$$

where $C(t)$ and $D(r)$ are found from the initial conditions and the boundary conditions at the interface.

The response of a simply supported circular plate which is subjected to a uniformly distributed impulsive velocity V_0 consists of the two phases of motion illustrated in Fig. 5.

4.2.1 First Phase of Motion, $0 \le T \le T_1$. The transverse velocity profile illustrated in Fig. 5(*b*), which has a central zone governed by equation (44) with a stationary axisymmetric interface at $\alpha = \beta_1$ and a stationary shear hinge at the supports ($\alpha = 1$), may be written in the form

$$\dot{\overline{w}}(\alpha, T) = 1 + \{\dot{\overline{W}}(T) - 1\} I_0(a\alpha)/I_0(a\beta_1), \quad 0 \le \alpha \le \beta_1, \quad (45a)$$

and

$$\dot{\overline{w}}(\alpha, T) = \dot{\overline{W}}_1(T)(\alpha - \beta_1)/(1-\beta_1) + \dot{\overline{W}}(T)(1-\alpha)/(1-\beta_1), \ \beta_1 \le \alpha \le 1, \quad (45b)$$

since

$$\dot{\overline{w}}(0,0) = 1 \quad \text{and} \quad \dot{\overline{W}}(0) = 1,$$

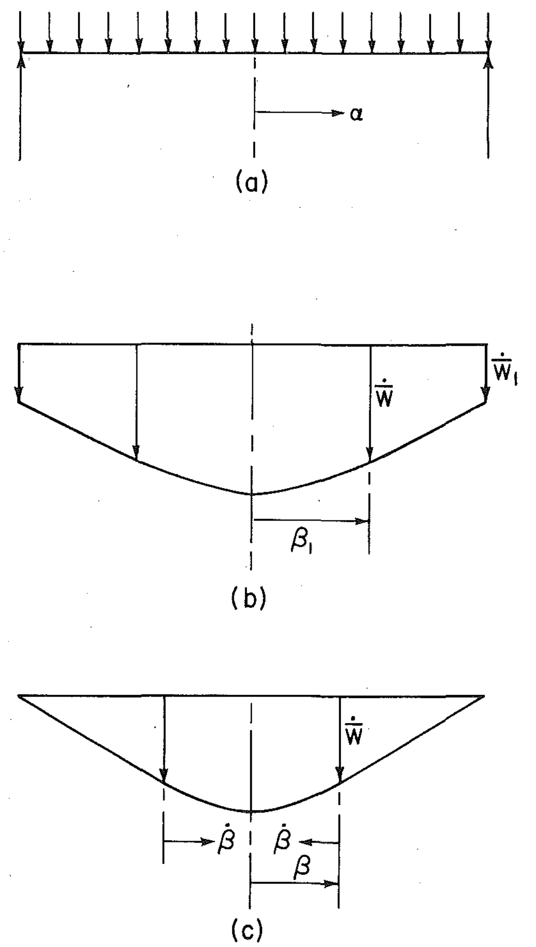

Fig. 5 (*a*) **Impulsively loaded circular plate with $\nu \ge 3/2$ and $I_r \neq 0$; (*b, c*), Velocity profiles for the first and second phases of motion**

and where

$$a^2 = 6/I \quad \text{and} \quad I = 6I_r/\mu R^2. \quad (46a, b)$$

Equations (45) give $[\dot{\overline{w}}(\beta_1, T)] = 0$ and $\partial\dot{\overline{w}}(0, T)/\partial\alpha = 0$. Furthermore, $\dot{\gamma} = 0$, $\dot{\kappa}_r \le 0$ and $\dot{\kappa}_\theta \le 0$ in the central plastic zone ($0 \le \alpha \le \beta_1$) with $\dot{\overline{W}} \le 1$ which is consistent with the normality requirements of plasticity associated with the portion $m_\theta(\alpha, T) = m_r(\alpha, T) = -1$ and $|q(\alpha, T)| < 1$ of the yield surface in Fig. 2, while in the outer region $\beta_1 \le \alpha \le 1$, $\dot{\gamma} = 0$, $\dot{\kappa}_r = 0$, and $\dot{\kappa}_\theta \le 0$ if $\dot{\overline{w}}_1 \le \dot{\overline{W}}$ and therefore $m_\theta(\alpha, T) = -1$, $-1 \le m_r(\alpha, T) \le 0$, and $|q(\alpha, T)| < 1$.

Now, it may be shown when substituting the foregoing generalized stresses and velocity fields (45) into the equilibrium equations (1*a, b*) and when insuring $q(0, T) = 0$, $q(1, T) = -1$, $m_r(1, T) = 0$, $[m_r(\beta_1, T)] = 0$, and $[\partial m_r(\beta_1, T)/\partial\alpha] = 0$[3] that

$$q(\alpha) = [\sqrt{6I}/\nu)\ddot{\overline{W}} I_1(a\alpha)/I_0(a\beta_1),$$

$$m_r(\alpha) = m_\theta(\alpha) = -1, \quad \text{for} \quad 0 \le \alpha \le \beta_1, \quad (47a\text{–}c)[4]$$

and

[3] It may be shown when using equation (1*a*) for the present case with $m_\theta = -1$ for $0 \le \alpha \le 1$ with β_1 time-independent that $[q(\beta_1, T)] = 0$ may be replaced by the requirement $[\partial m_r(\beta_1, T)/\partial\alpha] = 0$ provided $[\partial^2\psi(\beta_1, T)/\partial T^2] = 0$.

[4] $I_0(\ \ )$ and $I_1(\ \ )$ are modified Bessel functions of the first kind of orders zero and one, respectively.

$$q(\alpha) = (1-\alpha)\{(3\beta_1 + 3\alpha\beta_1 - 2\alpha^2 - 2\alpha - 2)\ddot{\overline{W}}_1 - (1-\alpha)(1+2\alpha)\ddot{\overline{W}}\}/\{\nu\alpha(1-\beta_1)\} - 1/\alpha,$$

$$m_r(\alpha) = -(1-\alpha)^2\{(3 - 4\beta_1 - 2\alpha\beta_1 + 2\alpha + \alpha^2)\ddot{\overline{W}}_1 + (1-\alpha^2)\ddot{\overline{W}}\}/\{\alpha(1-\beta_1)\} - I(1-\alpha^2)(\ddot{\overline{W}}_1 - \ddot{\overline{W}})/\{\alpha(1-\beta_1)\} - (1-\alpha)(2\nu-1)/\alpha,$$

$$m_\theta(\alpha) = -1$$

when

$$\beta_1 \le \alpha \le 1, \qquad (48a\text{–}c)$$

where

$$\ddot{\overline{W}} = -[(1-\beta_1)^2\{2+\beta_1 - \nu(1-\beta_1^2)\} + I\{\beta_1 + \nu(1-\beta_1)^2\}]/\Omega, \quad (49a)$$

$$\ddot{\overline{W}}_1 = [(1-\beta_1)^2(1+2\beta_1) - \nu(1-\beta_1)^3(1+3\beta_1) - I\{\beta_1 + \nu(1-\beta_1)^2\}]/\Omega, \quad (49b)$$

and

$$\Omega = (1-\beta_1)^2\{(1-\beta_1)^2(1+4\beta_1+\beta_1^2) + I(3+2\beta_1+\beta_1^2)\}. \quad (49c)$$

Thus equations (49) with $\dot{\overline{W}}_1(0) = \dot{\overline{W}}(0) = 1$ predict

$$\dot{\overline{W}} = 1 - [(1-\beta_1)^2\{2+\beta_1 - \nu(1-\beta_1^2)\} + I\{\beta_1 + \nu(1-\beta_1)^2\}]T/\Omega \quad (50a)$$

and

$$\dot{\overline{W}}_1 = 1 - [\nu(1-\beta_1)^3(1+3\beta_1) - (1-\beta_1)^2(1+2\beta_1) + I\{\beta_1 + \nu(1-\beta_1)^2\}]T/\Omega, \quad (50b)$$

so that the first stage of motion is completed at

$$T_1 = \Omega[I\{\beta_1 + \nu(1-\beta_1)^2\} - (1-\beta_1)^2\{1+2\beta_1 - \nu(1-\beta_1)(1+3\beta_1)\}]^{-1} \quad (51)$$

when $\dot{\overline{W}}_1 = 0$, and the associated dimensionless transverse displacement at the supports is

$$\overline{W}_1(T_1) = \Omega[2I\{\beta_1 + \nu(1-\beta_1)^2\} - 2(1-\beta_1)^2\{1+2\beta_1 - \nu(1-\beta_1)(1+3\beta_1)\}]^{-1}. \quad (52)$$

It was remarked previously that the flow rule of plasticity requires $\dot{\overline{W}}_1 - \dot{\overline{W}} \le 0$ and $\dot{\overline{W}} \le 1$ which leads to the restriction

$$3(1+\beta_1)/\{2(1-\beta_1)(1+2\beta_1)\} \le \nu \le \{(1-\beta_1)^2 \times (2+\beta_1) + I\beta_1\}/\{(1-\beta_1)^2(1-\beta_1^2 - I)\}. \quad (53)$$

The location of the stationary interface between the two plastic zones at $\alpha = \beta_1$ is obtained from the requirement that

$$[\partial^2\psi(\beta_1, T)/\partial t^2] = 0,^5 \quad \text{or} \quad I_1(a\beta_1)/I_0(a\beta_1) = a^{-1} \times (1-\beta_1)\{2\nu(1-\beta_1)(1+2\beta_1) - 3(1+\beta_1)\}[(1-\beta_1)^2 \times \{2+\beta_1 - \nu(1-\beta_1^2)\} + I\{\beta_1 + \nu(1-\beta_1)^2\}]^{-1}. \quad (54)$$

This equation may be evaluated numerically to predict the position of the interface β_1 as shown in Fig. 6. It turns out that the inequality (53) is satisfied up to at least $\nu = 50$ when the calculations were terminated.

4.2.2 Second Phase of Motion, $T_1 \le T \le T_f$. The transverse velocity is zero at the supports and the dimensionless radius β of the central plastic zone decreases with time during the second phase of motion which is governed by the transverse velocity profile in Fig. 5(c) which is described by equations (45) with $\dot{\overline{W}}_1 = 0$ and β_1 replaced by $\beta(T)$. This velocity profile gives $[\dot{\overline{w}}(\beta, T)] = 0$ and therefore $[q(\beta, T)] = 0$ is required according to equation (4b). Furthermore, if $[m_r(\beta, T)] = 0$, then from equation (4a), $[\dot{\psi}(\beta, T)] = 0$, which leads to the expression

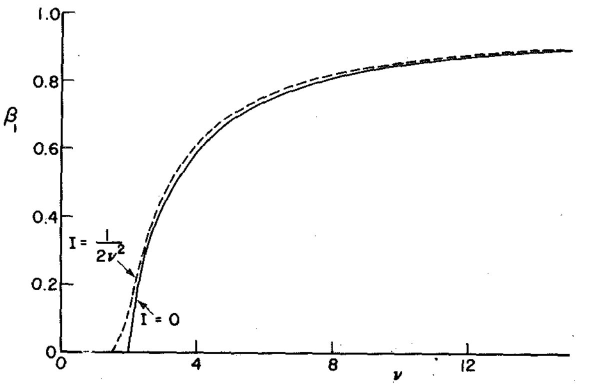

Fig. 6 Variation of β_1 with ν, where $I = 1/2\nu^2$ for a circular plate with a solid cross section; —— equation (32), - - - equation (54)

$$\dot{\overline{W}} = a(1-\beta)I_1(a\beta)/\{I_0(a\beta) + a(1-\beta)I_1(a\beta)\}. \quad (55)$$

Thus the equilibrium equations (1a, b) with $q(0, T) = 0$, $m_r(0, T) = m_\theta(0, T)$, $[m_r(\beta, T)] = 0$, $[q(\beta, T)] = 0$, and $m_r(1, T) = 0$ gives

$$q(\alpha, T) = (\sqrt{6I}/\nu)(1-\beta)\{I_1(a\alpha)/I_0(a\beta)\}(d/dT)\{\dot{\overline{W}}/(1-\beta)\},$$

$$m_r(\alpha, T) = m_\theta(\alpha, T) = -1 \quad \text{for} \quad 0 \le \alpha \le \beta, \qquad (56a\text{–}c)$$

and

$$q(\alpha, T) = \{4(\alpha^3 - \beta^3) - 6(\alpha^2 - \beta^2) - 12b\beta(1-\beta)\}[2\nu\alpha(1-\beta) \times \{(1-\beta)^2(1+3\beta) + I(1+\beta) + 12b\beta(1-\beta)\}]^{-1},$$

$$m_r(\alpha, T) = (1-\alpha)\{\beta(1+\beta-\beta^2) - \alpha(1+\alpha-\alpha^2) - I(\alpha-\beta)\} \times \{\alpha(1-\beta)^3(1+3\beta) + \alpha I(1-\beta^2) + 12\alpha b\beta(1-\beta)^2\}^{-1} - \beta(1-\alpha)/\{\alpha(1-\beta)\},$$

and

$$m_\theta(\alpha, T) = -1 \quad \text{when} \quad \beta \le \alpha \le 1, \qquad (57a\text{–}c)$$

where

$$b = I_1(a\beta)/\{aI_0(a\beta)\}, \qquad (58a)$$

and

$$(d/dT)\{\dot{\overline{W}}/(1-\beta)\} = -\{(1-\beta)^3(1+3\beta) + I(1-\beta^2) + 12b\beta(1-\beta)^2\}^{-1}. \quad (58b)$$

Equations (55) and (58b) may be solved to give the velocity of propagation ($\dot{\beta}$) of the interface at $\alpha = \beta$

$$\dot{\beta} = -\beta\{1 + a^2b(1-\beta)\}^2[a^2b(1+c\beta)\{(1-\beta)^3(1+3\beta) + I(1-\beta^2) + 12b\beta(1-\beta)^2\}]^{-1}, \quad (59a)$$

where

$$c = aI_2(a\beta)/I_1(a\beta), \qquad (59b)$$

and $I_2(\ )$ is a modified Bessel function of the first kind of order two.

It is evident from equation (55) that when $\beta = 0$ and $T = T_f$ then $\dot{\overline{W}} = 0$ and the motion of the plate ceases. The duration of the second phase of motion may be obtained numerically from the expression

$$T_f - T_1 = \int_{\beta(T_1)}^{0} d\beta/\dot{\beta} \qquad (60)$$

according to equation (59a), where $\beta(T_1)$ is calculated from equation (54). It turns out that a numerical evaluation of equation (60) up to $\nu = 25$ when the calculations were terminated gives a total duration of response $T_f = 2$.

[5] It was remarked in a previous footnote that the requirement $[q(\beta_1, T)] = 0$ may be replaced by $[\partial m_r(\beta_1, T)/\partial\alpha] = 0$ provided $[\partial^2\psi(\beta_1, T)/\partial T^2] = 0$.

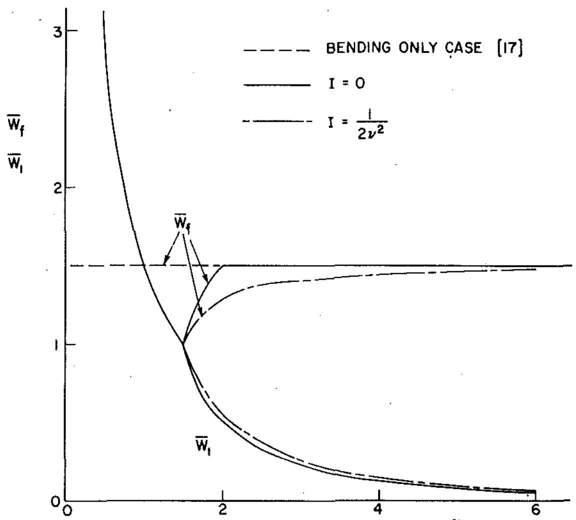

Fig. 7 Variation of permanent transverse displacements at plate center ($\overline{W}_f$) and plate supports ($\overline{W}_1$)

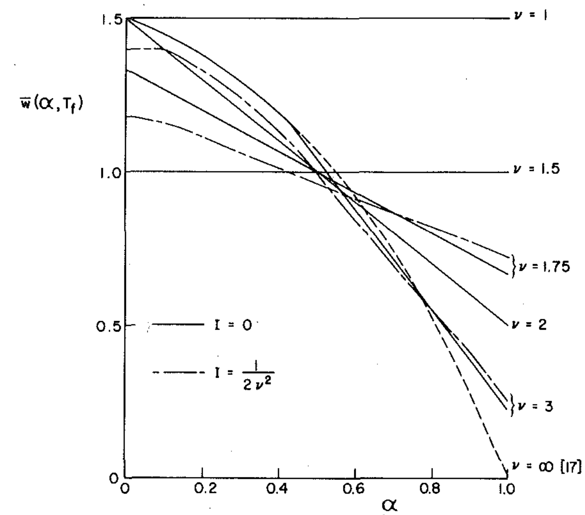

Fig. 8 Permanent deformed profiles of circular plates ($0 \le \alpha \le 1$)

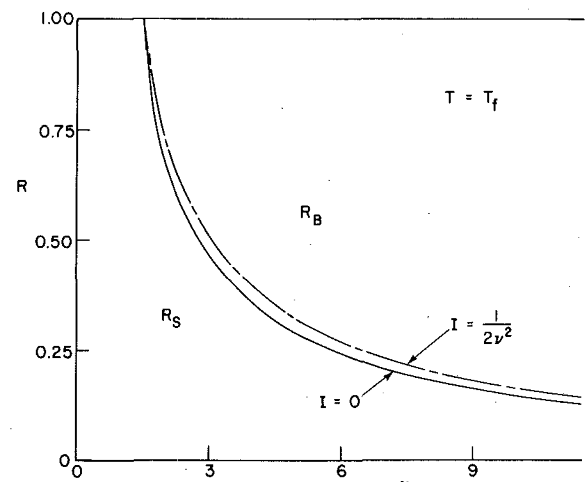

Fig. 9 Proportion of initial kinetic energy absorbed due to shearing (R_S) and bending (R_B) deformations

The maximum permanent transverse displacement at $\alpha = 0$ when $T = T_f$ may be evaluated numerically from the expression

$$\overline{w}(0, T_f) = \overline{w}(0, T_1) + \int_{\beta(T_1)}^{0} \dot{\overline{w}}(0, T)d\beta/\dot{\beta}, \qquad (61a)$$

where

$$\dot{\overline{w}}(0, T) = 1 + (\dot{\overline{W}} - 1)/I_0(a\beta) \qquad (61b)$$

from equation (45a) (with β_1 replaced by $\beta(T)$), and

$$\overline{w}(0, T_1) = T_1 - [(1 - \beta_1)^2\{2 + \beta_1 - \nu(1 - \beta_1{}^2)\} + I\{\beta_1 + \nu(1 - \beta_1)^2\}]T_1{}^2/\{2\Omega I_0(a\beta_1)\} \qquad (61c)$$

according to the integral of equation (45a) with $\alpha = 0$ and where T_1 is given by equation (51).

5 Discussion

It may be shown that the theoretical analyses presented in Sections 3 and 4 are kinematically and statically admissible and therefore exact within the setting of classical plasticity for the yield surface in Fig. 2. The amount of shear sliding at the plate supports in these analyses should satisfy the criterion represented by equation (14) as discussed in reference [21]. In addition, the material is assumed to be strain-rate insensitive, and in order to remain consistent with an infinitesimal theory the difference between the maximum transverse displacements at the plate center and the transverse shear sliding at the supports should be less than the plate thickness, approximately.

The theoretical analysis in Section 3 with $I = 0$ and a finite transverse shear strength ($\nu < \infty$) is compared in Figs. 7 and 8 with the theoretical predictions of Wang [17] which retains neither transverse shear ($\nu = \infty$) nor rotatory inertia ($I = 0$) effects. Incidentally, the various equations in Section 3 with $\nu \to \infty$ reduce to the corresponding theoretical predictions in reference [17]. It is evident from Figs. 7 and 8 that transverse shear effects play an important role when ν is small, as expected. However, the results in Figs. 7 and 8 with $I = 0$ and $\nu > 5$, approximately, are similar to those of Wang, although Fig. 9 reveals that a significant portion of the initial kinetic energy is dissipated through shearing deformations at the supports for larger values of ν. The theoretical solution in reference [8] for a simply supported circular plate subjected to a uniformly distributed static pressure indicates that transverse shear effects do not influence the static collapse behavior for the yield surface in Fig. 2 when $\nu \geq 3/2$. Thus the present study demonstrates that transverse shear effects are more important for the dynamic case than for the corresponding static problem as also found in reference [20] for beams and discussed in references [4, 5]. It should be noted that $\nu = R/H$ for the particular case of a circular plate having a solid homogeneous cross section with $Q_0 = \sigma_0 H/2$ and $M_0 = \sigma_0 H^2/4$.

On the other hand, if a circular plate is constructed with a sandwich cross section, then an inner core of thickness h and a shear yield stress τ_0 supports a maximum transverse shear force $Q_0 = \tau_0 h$ (per unit length), while thin exterior sheets of thickness t can independently carry a maximum bending moment $M_0 = \sigma_0 t(h + t)$, where σ_0 is the corresponding tensile yield stress. In this circumstance $\nu = Q_0 R/2M_0$ gives

$$\nu = \left(\frac{R}{H}\frac{\tau_0}{\sigma_0/2}\right)\left\{\frac{h/H}{1 - (h/H)^2}\right\}$$

when $H = h + 2t$. Thus a sandwich plate with $2R/H = 15$, $\sigma_0/2\tau_0 = 8$, and $h/H = 0.735$ (e.g., a 0.5-in-thick core with 0.1-in. sheets gives $h/H = 0.714$) gives $\nu = 1.5$ for which transverse shear effects are very important according to the results in Fig. 7.

It is evident from Fig. 7 that the inclusion of rotatory inertia in the governing equations and the retention of transverse shear as well as bending effects in the yield criterion leads to an increase in the permanent transverse shear sliding at the plate supports and a decrease in the maximum final transverse displacement which occurs at the plate center. However, the inclusion of I gives rise to respective changes in these quantities of approximately 11.5 and 14.2 percent at most. Thus the simpler theoretical analysis in Section 3 with $I = 0$ would probably suffice for most practical purposes. If greater accuracy is required, then it is only necessary to include I for circular plates with $1.5 \le \nu \le 4$, approximately.

The duration of response $T_f = 3/\nu$ is independent of rotatory inertia effects when $\nu \le 3/2$. Furthermore, $T_f = 2$ is independent of both I and ν when $\nu \ge 3/2$.

It turns out that the theoretical analysis for the impulsively loaded simply supported circular plate presented herein has many features in common with the corresponding theoretical solution for an impulsively loaded simply supported beam which was discussed in references [5, 22]. A beam with $I = 0$ has three classes of motion $\nu \le 1$, $1 \le \nu \le 1.5$, and $\nu \ge 1.5$ and transverse velocity profiles associated with each of these regions are similar to those in Figs. 3 and 4 here for the three classes of plate behavior examined in Section 3. Two classes of behavior occur for impulsively loaded simply supported beams with $\nu \le 1$ and $\nu \ge 1$ and $I \neq 0$ [5]. The corresponding transverse velocity profiles are similar to those found in Section 4 here.

6 Conclusions

A theoretical solution for an impulsively loaded circular plate made from a rigid perfectly plastic material has been developed when the transverse shear force as well as bending moments are retained in the yield condition and the influence of rotatory inertia is included in the governing equations. Transverse shear effects are important for small values of $\nu(Q_0R/2M_0)$, as expected, while rotatory inertia can further decrease the maximum permanent transverse displacement up to about 14 percent when $\nu > 1.5$. Thus the simple theoretical analysis with $I = 0$ in Section 3 should suffice for most practical purposes, except possibly for circular plates with $1.5 \le \nu \le 4$, approximately, when greater accuracy is required.

Acknowledgments

The authors are indebted to the Structural Mechanics Program of O.N.R. who supported this work through Contract Number N00014-76-C-0195, Task NR 064-510.

References

1 Symonds, P. S., "Survey of Methods of Analysis for Plastic Deformation of Structures Under Dynamic Loadings," Brown University Report BU/NSRDC/1-67, 1967.

2 Johnson, W., *Impact Strength of Materials*, Arnold, London, and Crane Russak, U.S., 1972.

3 Jones, N., "A Literature Review of the Dynamic Plastic Response of Structures," *The Shock and Vibration Digest*, Vol. 7, No. 8, 1975, pp. 89–105.

4 Jones, N., "Recent Progress in the Dynamic Plastic Behavior of Structures," *The Shock and Vibration Digest*, Part I, Vol. 10, No. 9, pp. 21–33 and Part II, Vol. 10, No. 10, 1978, pp. 13–19.

5 Jones, N., and Gomes de Oliveira, J., "The Influence of Rotatory Inertia and Transverse Shear on the Dynamic Plastic Behavior of Beams," ASME JOURNAL OF APPLIED MECHANICS, Vol. 46, 1979, pp. 303–310.

6 Gomes de Oliveira, J., and Jones, N., "A Numerical Procedure for the Dynamic Plastic Response of Beams With Rotatory Inertia and Transverse Shear Effects," *Journal of Structural Mechanics*, Vol. 7, No. 2, 1979, pp. 193–230.

7 Gomes de Oliveira, J., and Jones, N., "Some Remarks on the Influence of Transverse Shear on the Plastic Yielding of Structures," *International Journal of Mechanical Sciences*, Vol. 20, No. 11, 1978, pp. 759–765.

8 Sawczuk, A., and Duszek, M., "A Note on the Interaction of Shear and Bending in Plastic Plates," *Archiwum Mechaniki Stosowanej*, Vol. 15, No. 3, 1963, pp. 411–426.

9 Oschatz, A., "Bestimmung der Traglast von Kreis und Kreisringplatten mit Berücksichtigung der Querkraftschubspannungen," *ZAMM*, Vol. 48, No. 5, 1968, pp. 325–332.

10 Haydl, H. M., and Sherbourne, A. N., "Limit Loads of Variable-Thickness Circular Plates Accounting for Transverse Shear," *Journal of Strain Analysis*, Vol. 8, No. 2, 1973, pp. 108–112.

11 Mohaghegh, M. M., and Coon, M. D., "Plastic Analysis of Thick Circular Plates," *International Journal of Mechanical Sciences*, Vol. 15, 1973, pp. 935–942.

12 Dinno, K. S., and Robinson, M., "Limit Analysis of Thick and Thin Circular Plates Subjected to Transverse Pressure," World Conference on Space Enclosures, Montreal, 1976.

13 Krieg, R. D., "On the Behavior of a Numerical Approximation to the Rotatory Inertia and Transverse Shear Plate," ASME JOURNAL OF APPLIED MECHANICS, Vol. 40, No. 4, 1973, pp. 977–982.

14 Rao, S. S., and Prasad, A. S., "Vibrations of Annular Plates Including the Effects of Rotatory Inertia and Transverse Shear Deformation," *Journal of Sound and Vibration*, Vol. 42, No. 3, 1975, pp. 305–324.

15 Jones, N., et al., "The Dynamic Plastic Behavior of Shells," *Dynamic Response of Structures*, eds., Herrmann, G., and Perrone, N., Pergamon Press, 1972, pp. 1–29.

16 Hopkins, H. G., and Prager, W., "On the Dynamics of Plastic Circular Plates," *Journal of Applied Mathematics and Physics, (ZAMP)*, Vol. 5, No. 4, 1954, pp. 317–330.

17 Wang, A. J., "The Permanent Deflection of a Plastic Plate Under Blast Loading," ASME JOURNAL OF APPLIED MECHANICS, Vol. 22, 1955, pp. 375–376.

18 Thomas, T. Y., *Plastic Flow and Fracture in Solids*, Academic Press, 1961.

19 Nowacki, W. K., *Stress Waves in Nonelastic Solids*, Pergamon Press, 1978.

20 Symonds, P. S., "Plastic Shear Deformations in Dynamic Load Problems," *Engineering Plasticity*, eds., Heyman, J., and Leckie, F. A., C.U.P., 1968, pp. 647–664.

21 Jones, N., "Plastic Failure of Ductile Beams Loaded Dynamically," ASME *Journal of Engineering for Industry*, Vol. 98, No. 1, 1976, pp. 131–136.

22 Nonaka, T., "Shear and Bending Response of a Rigid-Plastic Beam to Blast-Type Loading," *Ingenieur-Archiv*, Vol. 46, 1977, pp. 35–52.

Y. Weitsman

Professor,
Mechanics and Materials Research Center, Civil Engineering Department, Texas A & M University, College Station, Texas 77843

Optimal Cool-Down in Linear Viscoelasticity

An optimal temperature path is derived for a thin viscoelastic plate which is cooled from a stress-free state against geometric constraints. The optimal path, which minimizes the final residual stress due to cool down, is shown to possess discontinuities at the initial and final times and to be smooth and continuous during all intermediate times. An iterative convergent scheme is provided for a wide class of linear viscoelastic responses and typical paths are determined for two specific cases. In addition, a time-temperature path which maintains constant stress values during cool-down is derived. The problem is motivated by the cooling process of composite materials.

1 Introduction

This paper presents an analytical scheme for the optimal temperature path which minimizes residual thermal stresses in linear, thermorheologically simple, viscoelastic thin plates. The plates are assumed to be stress-free at an elevated temperature and are cooled down against geometric constraints to a prerequisite temperature level during a prescribed time-span. The optimal path is shown to possess jump discontinuities at the initial and final times and to decrease smoothly and continuously during the intermittent time-interval.

The problem is related to the determination of the optimal cool down in fiber-reinforced, epoxy-resin composite materials where excessive residual stresses within the viscoelastic resin are detrimental to the load-carrying capacity of the composite laminates. In particular, graphite fibers possess a null coefficient of thermal expansion, so that the shrinkage of the relatively soft epoxy is severely inhibited during cool-down.

Discontinuous paths were shown to exist in several viscoelasticity problems [1–4]. In the present problem the initial discontinuity can be explained intuitively by the fact that it introduces instantaneous residual stresses which undergo relaxation during subsequent times. The magnitude of this jump cannot be excessive because the time-temperature shift property dictates that high temperature levels, subsequent to the initial drop, would relax the instantaneous stresses in a most efficient manner.

The present problem was treated previously [3, 4], by an iterative numerical scheme. The main deficiency of that scheme was that, in the absence of a clear method to select an appropriate initial guess, it was not obvious under what circumstances convergence was assured.

In addition, consideration is given to the cool-down temperature-time path which maintains a constant value of the thermal stress during the cooling process. This path also contains initial and final temperature discontinuities.

2 Analysis

Consider a thin isotropic viscoelastic slab, whose circumferential boundary is bonded to rigid walls.[1] The slab is stress-free at a certain elevated temperature T_I and subjected to a fluctuating ambient temperature $T(t)$. Due to the thinness of the slab and the relatively high value of its heat conduction coefficient we neglect transient temperature states across the thickness and assume that the entire plate is subjected to spatially uniform temperatures $T = T(t)$. Consequently, the only stresses within the plate are the spatially uniform, in-plane normal stresses which are denoted by $\sigma = \sigma(t)$, while all in-plane and shear strains vanish.

Consider a thermorheologically simple viscoelastic response and assume that the coefficient of thermal expansion α and Poisson's ratio ν are constants. Elementary considerations then yield [3]

$$-\frac{1-\nu}{\alpha}\sigma(t) = \int_{0^-}^{t} E[\xi(t)-\xi(\tau)]\frac{d[T(\tau)-T_I]}{d\tau}d\tau \qquad (1)$$

In (1) $E(t)$ is the relaxation modulus and

$$\xi(u) = \int_0^u \frac{ds}{a[T(s)]}$$

is the reduced time where $a(T)$ is the "shift factor" function.

Consider now the case of cool-down, where the temperature T_I is dropped to a prescribed final value of T_F during a time span t_f. The purpose of the subsequent analysis is to determine the optimal cool-down path $T(t)$, $0 \le t \le t_f$, which minimizes the stress $\sigma(t)$ at $t = t_f^+$. We shall hypothesize that the optimal cool-down path $T(t)$ possesses discontinuities at times $t = 0$ and $t = t_f$. The validity of this hypothesis

Contributed by the Applied Mechanics Division for publication in the JOURNAL OF APPLIED MECHANICS.

Discussion on this paper should be addressed to the Editorial Department, ASME, United Engineering Center, 345 East 47th Street, New York, N. Y. 10017, and will be accepted until June 1, 1980. Readers who need more time to prepare a discussion should request an extension from the Editorial Department. Manuscript received by ASME Applied Mechanics Division, May, 1979; final revision, September, 1979.

[1] Alternatively we could consider a quasi-isotropic laminate of a fiber-reinforced composite where the fibers—being much stiffer than the viscoelastic resin and possessing a negligible coefficient of thermal expansion—provide the in-plane geometric constraint.

will be proven *a posteriori*. It may be recalled that for a special, simple form of $E(t)$ it was already shown that no continuous optimal path exists [3].

Denote $T(0^+) = T_0$ and $T(t_f^-) = T_f$ then (1) yields

$$-\frac{1-\nu}{\alpha}\sigma(t_f^+) = \int_{0^-}^{t_f^+} E[\xi(t_f) - (\xi(\tau)]\frac{d[T(\tau) - T_I]}{d\tau}d\tau$$
$$= E[\xi(t_f)](T_0 - T_I) + E(0)(T_F - T_f) + I(t_f^-) \quad (2)$$

where

$$I(t_f^-) = \int_{0^+}^{t_f^-} E[\xi(t_f) - \xi(\tau)]\frac{d[T(\tau) - T_I]}{d\tau}d\tau \quad (3)$$

Let $T(t)$ be the optimal path and $\tilde{T}(t) = T(t) + \epsilon\eta(t)$ be an adjacent path, then

$$-\frac{1-\nu}{\alpha}\tilde{\sigma}(t_f^+) = E\left[\int_0^{t_f}\frac{ds}{a(T+\epsilon\eta)}\right](T_0 + \epsilon\eta_0 - T_I)$$
$$+ E(0)(T_F - T_f - \epsilon\eta_f) + \tilde{I} \quad (4)$$

where

$$\tilde{I} = \int_{0^+}^{t_f^-} E\left[\int_\tau^{t_f}\frac{ds}{a(T+\epsilon\eta)}\right]\frac{d[T(\tau) + \epsilon\eta(\tau) - T_I]}{d\tau}d\tau \quad (5)$$

Fundamental considerations of the calculus of variations require that

$$\frac{d}{d\epsilon}\left[-\frac{1-\nu}{\alpha}\tilde{\sigma}(t_f)\right]_{\epsilon=0} = 0$$

whereby

$$(T_0 - T_I)E'\left[\int_0^{t_f}\frac{ds}{a(T(s))}\right]\int_0^{t_f} -\frac{a'(T(t))}{a^2(T(t))}\eta(t)dt$$
$$+ \eta_0 E\left[\int_0^{t_f}\frac{ds}{a(T(t))}\right] - \eta_f E(0) + \frac{d\tilde{I}}{d\epsilon}\bigg|_{\epsilon=0} = 0 \quad (6)$$

where

$$\frac{d\tilde{I}}{d\epsilon}\bigg|_{\epsilon=0} = \int_{0^+}^{t_f^-}\left\{E'\left[\int_t^{t_f}\frac{ds}{a(T(s))}\right]\left[\int_t^{t_f^-} -\frac{a'(T(s))}{a^2(T(s))}\eta(s)ds\right]\frac{dT}{dt}\right.$$
$$\left.+ E\left[\int_t^{t_f}\frac{ds}{a(T(s))}\right]\frac{d\eta}{dt}\right\}dt \quad (7)$$

In equations (6), (7) and the sequel primes indicate derivatives with respect to the argument.

Denote

$$M(t) = \int_0^t E'\left[\int_p^{t_f}\frac{ds}{a(T(s))}\right]T'(p)\,dp \quad (8)$$

then

$$M'(t) = E'\left[\int_t^{t_f}\frac{ds}{a(T(s))}\right]T'(t)$$

Integration by parts of (7) yields

$$\frac{d\tilde{I}}{d\epsilon}\bigg|_{\epsilon=0} = M(t)\int_t^{t_f^-} -\frac{a'(T(s))}{a^2(T(s))}\eta(s)ds\bigg|_{t=0^+}^{t=t_f}$$
$$-\int_{0^+}^{t_f^-}\left\{\int_0^t E'\left[\int_p^{t_f}\frac{ds}{a(T(s))}\right]T'(p)dp\right\}\frac{a'(T(t))}{a^2(T(t))}\eta(t)dt$$
$$+ E\left[\int_t^{t_f}\frac{ds}{a(T(s))}\right]\eta(t)\bigg|_{t=0^+}^{t=t_f^-}$$
$$+ \int_{0^+}^{t_f^-} E'\left[\int_t^{t_f}\frac{ds}{a(T(s))}\right]\frac{\eta(t)}{a(T(t))}dt \quad (9)$$

The first term on the right side of (9) vanishes at both limits. Combining the remainder of (9) with (6) we obtain

$$\int_{0^+}^{t_f^-}\left\{\frac{E'(t,t_f)}{a(T(t))} - \frac{a'(T(t))}{a^2(T(t))}\left[\int_0^t E'(p,t_f)\,T'(p)dp\right.\right.$$
$$\left.\left.+ (T_0 - T_I)E'(0,t_f)\right]\right\}\eta(t)dt = 0 \quad (10)$$

Hence Euler's equation for our problem is

$$E'(t,t_f) - \frac{a'(T(t))}{a(T(t))}\left[\int_0^t E'(p,t_f)\,T'(p)dp\right.$$
$$\left.+ (T_0 - T_I)E'(0,t_f)\right] = 0 \quad (11)$$

In (10) and (11) $E'(t_1, t_2)$ denotes

$$E'\left[\int_{t_1}^{t_2}\frac{ds}{a(T(s))}\right].$$

We can now observe that if no initial discontinuity were assumed, i.e., $T_0 = T_I$, then equation (11) would yield the contradictory result $E'(0,t_f) = 0$. This proves the existence of the initial discontinuity.

The magnitude of $T_0 - T_I$ is determined by setting $t = 0$ in (11) which yields

$$T_0 - T_I = \frac{a(T_0)}{a'(T_0)} \quad (12)$$

Since $a > 0$ and $a' < 0$ for all T, the temperature undergoes an initial *drop*. Expression (12) is a transcendental equation for T_0.

Multiplying (11) by $a(T(t))\,T'(t)$, we obtain

$$a(T(t))\,M'(t) - [M(t) + k]\,a'(T)T'(t) = 0 \quad (13)$$

where $M(t)$ is defined in (8) and $k = (T_0 - T_I)\,E'(0,t_f)$.

However, (13) can be written as

$$a^2(T)\frac{d}{dt}\left[\frac{M(t) + k}{a(T)}\right] = 0$$

consequently, we get

$$M(t) + k = C_0 a(T(t)) \quad (14)$$

The constant C_0 can be determined by the conditions at $t = 0$ which, together with (12), give

$$C_0 = \frac{(T_0 - T_I)\,E'(0,t_f)}{a(T_0)} = \frac{E'(0,t_f)}{a'(T_0)}$$

Differentiation of (14) with respect to t yields

$$E'(t,t_f) = C_0 a'(T(t)) \quad (15)$$

Expression (15) represents the Euler's equation for our problem over the interval $0 < t < t_f$.

Another version of the Euler's equation can be obtained by differentiating (11) with respect to t, then substituting the result back into (11) to eliminate the integral there. These operations yield

$$\frac{dT}{dt} = -\frac{E''(t,t_f)}{E'(t,t_f)}\frac{a'(T(t))}{a(T(t))a''(T(t))} \quad (16)$$

Note that if (15) is differentiated with respect to t then the result, in combination with (15), leads to (16).

Data on polymeric resins [5–7] indicate that in most cases $a'/aa'' < 0$, while $E''/E' < 0$ in view of thermodynamic considerations [8]. Consequently, equation (16) shows that the temperature T continues to drop monotonically over the interval $(0, t_f)$. The value of $T_f = T(t_f^-)$ as determined from (16) would generally differ from the prescribed value of T_F. We thus conclude that the optimal path would undergo a second jump discontinuity of magnitude $T_f - T_F$ at the final time.

3 An Iterative Scheme for the Determination of the Optimal Path—Positive-Definite Values of $\sigma(t)$

Consider the optimization problem posed in Section 2 with prescribed temperatures T_I and T_F and for a given time t_f.

The temperature T_0 is determined by (12).

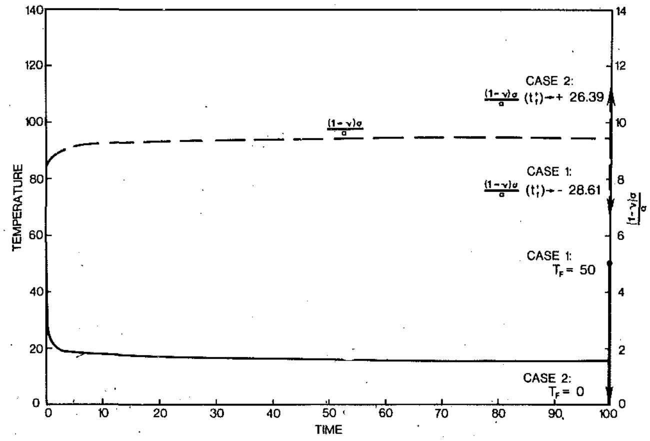

Fig. 1 Optimal temperature path $T(t)$ (solid line) and the associated stress $(1-\nu)\sigma(t)/\alpha$ (dashed line) for the three-element model with $A = 1$, $B = 20$, $T_I = 100$, $A_0 = 0.1$, $B_0 = 1$, and $\lambda = 1$ for two cases of $T_F = 50$ and $T_F = 0$. Note the scale of T, $0 < T < 100$, and of $(1-\nu)\sigma(t)/\alpha$ between 0 and 10. When $T_F = 50$ the value of $(1-\nu)\sigma(t_f^+)/\alpha$ is -28.61. While for $T_F = 0$, $(1-\nu)\sigma(t_f^+)/\alpha = 26.39$.

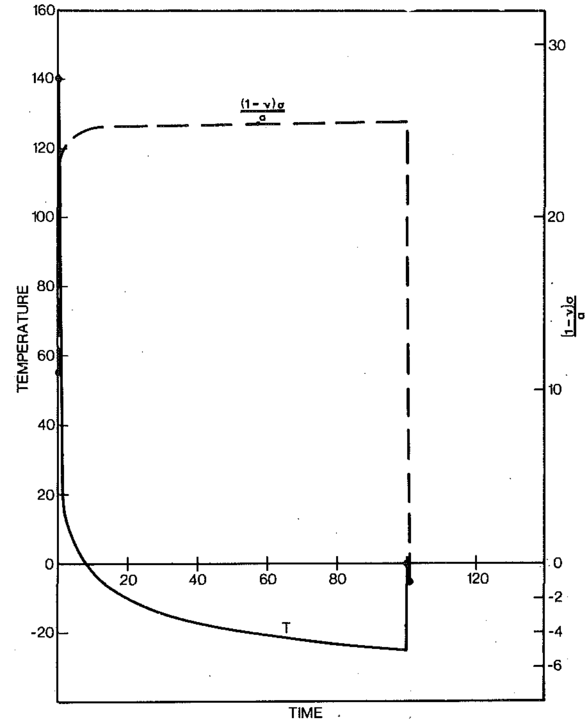

Fig. 2 Optimal temperature path $T(t)$ (solid line) and the associated stress $(1-\nu)\sigma(t)/\alpha$ (dashed line) for the three-element model with $A = 10$, $B = 2$, $T_I = 150$, $T_F = 0$, $A_0 = 0.1$, $B_0 = 1$, $\lambda = 1$ and $t_f = 100$. Note the scale of T, $-26 < T < 150$, and of $(1-\nu)\sigma/\alpha$ between -1 and 26.

To obtain the optimal path for $0 \le t < t_f$ guess $T_f^{(1)}$ and employ (16) to obtain all preceding temperatures by numerical integration. Carrying the integration backward to time $t = 0$ yields a value $T(0)$ which in general will differ from T_0. In view of the aforementioned properties of a'/aa'' and E''/E' we note that if $T_0 < T(0)$ a new guess value $T_f^{(2)} < T_f^{(1)}$ should be tried, and vice versa. The procedure can be repeated, with subsequent guesses obtained through interpolation or extrapolation of previous values, until a value T_f is found for which $T_0 = T(0)$.

Obviously, to each guess value T_f there corresponds a unique path $T(t)$ and a unique $T(0)$. Consequently, the optimal path, which is obtained by integration of (16) and passes through T_0 at $t = 0^+$, is unique.

It is worth noting that insertion of (16) into (2) yields, for $0 \le t < t_f$:

$$\frac{1-\nu}{\alpha}\sigma(t) = \int_{0^+}^{t} \frac{E(\tau,t_f)\,E''(\tau,t_f)}{E'(\tau,t_f)} \frac{a'(T(\tau))}{a(T(\tau))\,a''(T(\tau))} d\tau + E(0,t)\,(T_I - T_0) \quad (17)$$

In view of the aforementioned properties of EE''/E' and a'/aa'' the integrand in (17) is always positive, implying that $\sigma(t) > 0$ along the optimal path. If $T_f > T_F$ then $\sigma(t)$ remains positive at all subsequent times. However, if $T_f < T_F$ then it is possible to obtain negative stresses σ for $t \ge t_f$.

If for any specific case it also happens that $\sigma'(t) > 0$ for $0 < t < t_f$ then the knowledge of $\sigma(t_f^-)$ may suffice for assessing the detrimental effects of the thermal stresses. For the three element model considered in the next section it was observed that $\sigma'(t) > 0$ and $\sigma''(t) > 0$ for wide ranges for t_f, but this property does not hold in general.

4 The Optimal Path for a Three-Element Model

Consider a three-element model for which the relaxation function is given by

$$E(t) = A_0 + B_0 \exp(-t/\lambda) \quad (18)$$

where

$$A_0 = E_\infty > 0, \quad B_0 = E_0 - E_\infty > 0$$

Substitution in (15), and integration yield

$$t = \lambda \int_{T_0}^{T} \frac{d\theta}{F(\theta)} \quad (19)$$

where $F(T) = a'(T)/a(T)a''(T)$.

Assume now

$$a(T) = \exp\left(-\frac{T}{A} + B\right) \quad (20)$$

Straightforward manipulations yield

$$T(t) = A[B - \ln \phi(t)] \quad (21)$$

where $\phi(t) = t/\lambda + \exp C$, $C = B + 1 - T_I/A$.

The instantaneous jumps in $T(t)$, which occur at $t = 0$ and $t = t_f$ are given by

$$\begin{aligned} T(0) - T_I &= -A \\ T(t_f^-) - T(t_f^+) &= A[B - \ln \phi(t_f)] - T_F \end{aligned} \quad (22)$$

The ensuing stresses are

$$\begin{aligned} \frac{1-\nu}{\alpha}\sigma(t) &= A\,\{A_0[\ln \phi(t) + 1 - C] + B_0\} \\ \frac{1-\nu}{\alpha}\sigma(t_f^-) &= A\{A_0[\ln \phi(t_f) + 1 - C] + B_0\} \\ \frac{1-\nu}{\alpha}\sigma(t_f^+) &= A_0(T_I - T_F) + B_0\{A\,[B + 1 - \ln \phi(t_f)] - T_F\} \end{aligned} \quad (23)$$

Results based upon equations (21) and (23) are plotted in Figs. 1 and 2. In Fig. 1 $A = 1$, $B = 20$, $T_I = 100$ and T_F takes the values of 0 and 50, respectively. In Fig. 2, $A = 10$, $B = 2$, $T_I = 150$, and $T_F = 0$. In both figures $A_0 = 0.1$, $B = 1$, $\lambda = 1$, and $t_f = 100$.

Both figures show the optimal temperature path $T(t)$ (in solid lines) and the consequent stress path $\sigma(t)$ (in dashed lines). Observe the abrupt changes in the temperature at time t_f. In addition, the temperature paths contain sudden drops at $t = 0$, of magnitudes $T_I - T(0) = A$. The stress paths $\sigma(t)$ also exhibit abrupt changes at $t = 0$ and $t = t_f$. Note that the trend of $\sigma(t)$ is always in an opposite direction to $T(t)$.

The three-element model affords an analytical check on the nature of the optimal path. For instance, if we consider the path

$$\tilde{T}(t) = A[B - \ln \phi(t)] + \epsilon\eta_0 \ (\eta_0 = \text{constant}),$$

then a somewhat laborious calculation shows that the stationary value provided by (21) corresponds to a minimum for $\sigma(t_f^+)$.

5 The Optimal Path for "Power Law" Response

Consider the relaxation function

$$E(t) = A_1 + A_2 (t + t_0)^{-n} \tag{24}$$

which is widely utilized to describe the response of resins. Also, let $a(T)$ be given by (20). Substitution in (16) yields

$$T' = -(n+1)A \exp(T/A - B)\left\{\int_t^{t_f} \exp[T(\tau)/A - B]d\tau + t_0\right\}^{-1} \tag{25}$$

Differentiating (25) with respect to t we get

$$C_1(T')^2 = T'' \tag{26}$$

where

$$C_1 = \frac{n}{(n+1)A}$$

The solutions of (26) is

$$T = \frac{1}{C_1}\ln\frac{L}{K + C_1 t} \qquad L, K > 0 \tag{27}$$

where K and L are arbitrary constants.

Insertion of (27) into (25) gives

$$L = \left[\frac{t_0(K + C_1 t_f)^{1/n} e^B}{(n+1)A}\right]^{n/n+1} \tag{28a}$$

and the initial condition $T_0 = (1/C_1)\ln(L/K)$ yields

$$L = Ke^{C_1 T_0} \tag{28b}$$

Equations (28) result in a transcendental equation for K (and L). In view of (28a) we note that for a power law response the optimal path depends on the cooling time t_f.

The initial drop is again given by $(22)_1$, while the final temperature drop is now

$$T(t_f^-) - T(t_f^+) = \frac{1}{C_1}\ln\frac{L}{K + C_1 t} - T_F \tag{29}$$

6 Constant-Stress Temperature Paths

Consider now a different aspect of the cool-down problem. Instead of an optimal value for $\sigma(t_f^+)$ let us search for a temperature path $T(t)$ which maintains $\sigma(t) = \sigma_0$ during $0 < t < t_f$, with σ_0 a prescribed constant.

In view of (1) we have

$$-\frac{1-\nu}{\alpha}\sigma_0 = E(0)\,(T_0 - T_I)$$

or

$$T_0 - T_I = -\frac{1-\nu}{\alpha}\frac{\sigma_0}{E(0)} \tag{30}$$

Substitution into (1) yields an integral equation for $T(t)$

$$\int_{0^+}^t E[\xi(t) - \xi(\tau)]\frac{dT}{d\tau}d\tau - \frac{1-\nu}{\alpha}\frac{\sigma_0}{E(0)}\{E[\xi(t)] - E(0)\} = 0 \tag{31}$$

Equation (31) can be solved by numerical iteration which is omitted here.

We shall restrict consideration to the three-element model for which

$$E(t) = A_0 + B_0 e^{-\mu t} \tag{32}$$

Setting (32) into (31) gives

$$A_0 T + B_0 \int_{0^+}^t \exp\{-\mu[\xi(t) - \xi(\tau)]\}\frac{dT}{d\tau}d\tau - \frac{1-\nu}{\alpha}\frac{\sigma_0 B_0}{A_0 + B_0}\{\exp[-\mu\xi(t)] - 1\} = 0 \tag{33}$$

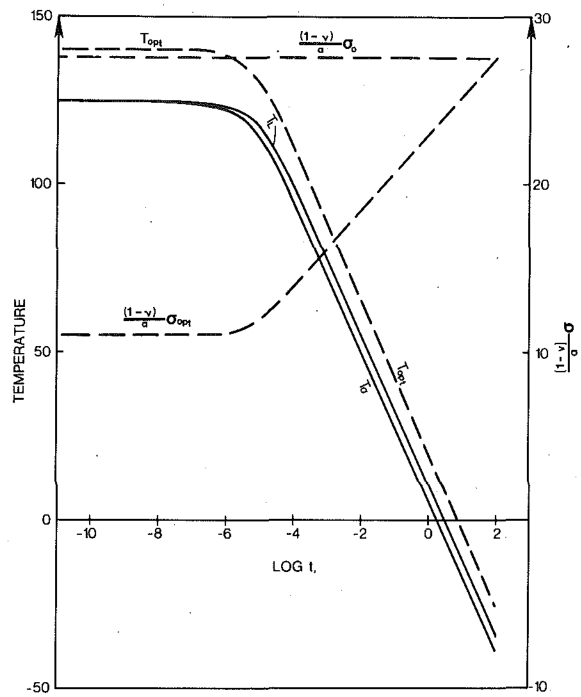

Fig. 3 Constant-stress cool down temperature paths. T_L for the linear case and T_σ for the nonlinear case, versus log t, for $A_0 = 0.1$, $B_0 = 1$, $\mu = 1$, $A = 10$, $B = 2$, $T_I = 150$ and $(1-\nu)\sigma_0/\alpha = 27.61$. In the nonlinear case $\sigma_0/s_0 = 1/2$. The optimal temperature path T_{opt} and the associated values of $(1-\nu)\sigma_{opt}/\alpha$ are shown in dashed lines for comparison. Note the different scales for temperature, $-50 < T < 150$, and for $(1-\nu)\sigma/\alpha$ between 0 and 30.

Differentiating (33) with respect to t, then subtracting from (33) multiplied by μ we obtain

$$\frac{dT}{dt} = -\frac{\mu}{A_0 + B_0}\frac{A_0 T + B_0(T_I - T_0)}{a(T)} \tag{34}$$

Note that since $a(T) > 0$, T drops monotonically with t.

Select $a(T) = \exp(-T/A + B)$ as in (20).

Substitution in (34) and integration yield

$$t = -\frac{A_0 + B_0}{\mu}\int_{T_0}^T \frac{\exp(-\theta/A + B)}{B_0(T_I - T_0) + A_0\theta}d\theta \tag{35}$$

where the initial condition $T(0) = T_0$ was employed.

Denote $\hat{C} = (T_I - T_0)B_0/A_0$, $m = \hat{C}/A + B$, $k = (\hat{C} + T)/A$, $k_0 = (\hat{C} + T_0)/A$. Performing the integration indicated in (35) we get

$$t = -\frac{A_0 + B_0}{\mu}\frac{e^m}{A_0}[E_i(-k) - E_i(-k_0)] \tag{36}$$

where $E_i(x)$ is the exponential integral function defined by

$$E_i(x) = \int_{-\infty}^x \frac{e^z}{z}dz \qquad (x < 0).$$

It is interesting to note that the constant-stress temperature paths for nonlinear viscoelastic response can be obtained without additional difficulty. For many resins [9, 10] the paramount nonlinear effects may be incorporated into the shift factor function, i.e., $a = a(T, \sigma)$. However, for a constant-stress path $\sigma = \sigma_0$ thereby $a = a(T, \sigma_0) = \hat{a}(T)$ and the computation of $T(t)$ remains essentially the same as in the linear case.

Consider the three element model and assume

$$a(T, \sigma) = \exp\left(-\frac{T}{A} - \frac{\sigma}{s_0} + B\right) \tag{37}$$

Then, the result presented in (36) remains valid provided we replace B with $B - \sigma_0/s_0$.

Results are exhibited in Fig. 3 where the temperature paths T_L for the linear response and T_σ for the nonlinear response are drawn versus $\log t$. The computations were performed for $A_0 = 0.1$, $B_0 = 1$, $\mu = 1$, $A = 10$, $B = 2$, $T_I = 150$, $(1 - \nu)\sigma_0/\alpha = 27.61$ and $\sigma_0/s_0 = 1/2$. For comparison purposes the optimal temperature path and the ensuing stresses $(1 - \nu)\sigma/\alpha$ along that path are shown in dashed lines in the figure. Note that all paths are of the same character, though the optimal path begins at a higher initial temperature T_0.

7 Concluding Remarks

This paper presented optimal cool-down paths which minimize the residual thermal stress at time $t = t_f^+$, i.e., immediately after termination of cooling. These temperature paths were shown to contain two jump discontinuities. The magnitude of the first jump, which occurs $t = 0$, depends strictly on the shift-factor function $a(T)$ and is always directed downward. The second jump, which occurs at the terminal time t_f, depends on the prescribed final temperature T_F as well as on t_f and $a(T)$.

It is to be noted that the paths presented herein provide only local optima, since the calculus of variations approach is valid only in that restricted sense. In some circumstances the lowest $\sigma(t_f^+)$ may be obtained from "extraneous" paths, not in the neighborhood of the optimal paths derived in this paper. If $T_f > T_F$ then obviously $\sigma(t) < \sigma(t_f^+)$ for $t > t_f$ because the stresses continue to relax with time. However, if $T_f < T_F$, so that the final jump in temperature points upward, it may happen that $\sigma(t) > \sigma(t_f^+)$ for $t > t_f$. A criterion for this circumstance was discussed in [3].

It should be emphasized that if $T_f \neq T_F$ then cooling along the optimal temperature path may result in intermediate stresses which exceed $|\sigma(t_f^+)|$, thus presenting a more severe condition than is apparent by the last value. However, if only T_F is specified (with $T_F < T_0$) then when this temperature is reached smoothly along the optimal path at $t = t_f$ all the intermediate stresses $\sigma(t)$, $t < t_f$, are minimal.

Finally, it was shown that for a constant stress during cool-down the temperature path contains initial and final discontinuities which resemble the optimal solution.

Acknowledgments

The author wishes to express his thanks to Prof. J. Walton for several illuminating discussions and to Prof. R. A. Schapery for a useful suggestion. This investigation was performed under Contract F-49620-78C-0034 from the Air Force Office of Scientific Research (AFOSR). This support is gratefully acknowledged.

References

1 Breuer, S., and Onat, E. T., "On Recoverable Work in Linear Viscoelasticity," *Journal of Applied Mathematics and Physics* (*ZAMP*). Vol. 15, 1964, pp. 12–21.

2 Gurtin, M. E., McCamy, R. C., and Murphy, L. F., "On Optimal Strain Paths in Linear Viscoelasticity," (forthcoming).

3 Weitsman, Y., and Ford, D., "On the Optimization of Cool-Down Temperatures in Viscoelastic Resins," "Recent Advances in Engineering Science" *Proceedings of the 14th Annual Meeting of SES*, Sih, G. C., ed., Nov. 1977, p. 323–339.

4 Weitsman, Y., "Residual Thermal Stresses due to Cool-Down of Epoxy-Resin Composites," ASME JOURNAL OF APPLIED MECHANICS, Vol. 46, No. 3, Sept. 1979, pp. 563–567.

5 Beckwith, S. W., "Viscoelastic Characterization of a Nonlinear Glass/Epoxy Composite Including the Effect of Damage," PhD dissertation, Texas A&M University, Dec. 1974.

6 Renton, W. J., and Ho, T., "The Effect of Environment on the Mechanical Behavior of AS/3501-6 Graphite Epoxy Material," final report, Vought Corp., Aug. 1978.

7 Ferry, J. D., *Viscoelastic Properties of Polymers*, Wiley, 1961; see WLF equation on page 212.

8 Schapery, R. A., "Viscoelastic Behavior and Analysis of Composite Materials," Vol. 2, *Mechanics of Composite Materials*, Sendeckj, G. P., ed., Academic Press, 1974, pp. 86–165.

9 Lou, Y. C., and Shapery, R. A., "Viscoelastic Characterization of Nonlinear Fiber-Reinforced Plastics," *Journal of Composite Materials*, Vol. 5, 1971, pp. 208–234.

10 Cartner, J. S., Jr., and Brinson, H. F., "The Nonlinear Viscoelastic Behavior of Adhesives and Chopped Fiber Composites," V.P.I. & S.U. Report VPI-E-7821, Aug. 1978.

J. L. Bogdanoff
Professor,
School of Aeronautics and Astronautics,
Purdue University,
West Lafayette, Ind. 47907
Fellow ASME

F. Kozin
Professor,
Department of Electrical Engineering,
New York Polytechnic,
Brooklyn, N. Y. 11201

A New Cumulative Damage Model—Part 4

Application of the new cumulative damage model to two sets of fatigue crack growth data is presented. It is shown that the model can describe the statistical features of crack growth including mean and variance of time to reach a specified crack length, cumulative distribution of time to reach a specified crack length, and sample function behavior. Moreover, this is done with very little effort.

Introduction

Fatigue crack growth is a random cumulative damage phenomena which has and continues to attract a great deal of attention. The usual approach in the literature [1–4] is through a deterministic differential equation; since the phenomena is random in nature, there exists the problem of how randomness is to be introduced. It is thus fitting to close this four-part series on a new random cumulative damage model with a presentation of how this model applies to the crack growth problem in metals under cyclic loading.

Part 1 presented the basic elements of the model. Part 2 illustrated some of the potential of the model and demonstrated the use of the model in describing and analyzing some life data from fatigue and wear. Part 3 showed that life data does not characterize the damage accumulation process, that without knowledge of the details of the process, accuracy in life prediction under a change in condition is limited, and that data can be collected to improve the definition of the details of the process. To conserve space, we refer the reader to these papers [5–7] for the notation used and a description of the model. Suffice it to say that the model is an embedded Markoff process with discrete states and discrete time; thus the mathematics is in terms of Markoff chains.

The purpose of this paper is to demonstrate, using two sets of data, how the model can be used to describe and analyze these data in a simple manner. We also shall show that the precrack phase of fatigue can be combined easily with the crack growth phase.

We shall contrast in a future paper the results obtained by our model with the results obtained by the usual deterministic approach.

The Data

We shall use two sets of data [8, 9]. An aluminum tension specimen with a central slit perpendicular to the tension axis is employed in [8], with 68 replications. A steel compact tension specimen is used in [9], with data from 23 replications used in our analysis.

The data in [8] consist of the times in cycles to reach the same specified crack length for each specimen; 164 crack lengths are used ranging from 9 mm to 49.8 mm for half length. From these data, moments of times to reach the specified crack length are estimated, sample functions can be plotted by connecting adjacent data points with segments of a straight line, empirical distribution functions of the times to reach specified crack lengths can be obtained, etc. The distribution of time to reach a specified crack length is unknown and not normal; thus we cannot give precise confidence intervals. However, some idea of *relative* size of the confidence intervals for mean and variance can be obtained by assuming the distribution is normal; we find, with confidence coefficient equal to 0.90 and equal tails, sample size n,

$$\begin{aligned} \text{Mean:} \quad & (\hat{x}_n - 0.2022\,\hat{\sigma}_n,\ \hat{x}_n + 0.2022\,\hat{\sigma}_n), \\ \text{Variance:} \quad & (0.7338\,\hat{\sigma}_n{}^2,\ 1.3001\,\hat{\sigma}_n{}^2). \end{aligned}$$

The estimated values of mean $\hat{x}_n$ and variance $\hat{\sigma}_n{}^2$ of time to reach a specified crack length and relative confidence interval are shown in Figs. 1 and 2. The mean is obviously well determined with 68 replications. The variance is statistically acceptable but shows the effects of sample variability. The signal to noise ratio, i.e. $\hat{x}_n/\hat{\sigma}_n$ (reciprocal of coefficient of variation) rapidly becomes large (>5) for these carefully controlled laboratory experiments. The effects of sample variability rendered the third and fourth central moment estimates unacceptable for any practical use.

The data gathered in [9] came from a number of different laboratories. Time records started at, ended at, and were recorded at different crack lengths. To avoid extrapolation problems, the crack length interval (22.9 mm, 50.8 mm) is used in this paper; 23 specimens have records that encompass this interval. We adjusted all records to start at time = 0 at 22.9 mm. The times to reach specified crack lengths are obtained by straight line interpolation between adjacent points. Thus we have performed two smoothing operations in these data that we did not use in the data of [8]. We find the moments of time to reach specified crack lengths, etc., from these smoothed data. The relative confidence intervals based upon the normal assumption corresponding to the aforementioned are

Contributed by the Applied Mechanics Division for publication in the JOURNAL OF APPLIED MECHANICS.

Discussion on this paper should be addressed to the Editorial Department, ASME, United Engineering Center, 345 East 47th Street, New York, N. Y. 10017, and will be accepted until June 1, 1980. Readers who need more time to prepare a discussion should request an extension from the Editorial Department. Manuscript received by ASME Applied Mechanics Division, July 1979; final revision, October, 1979.

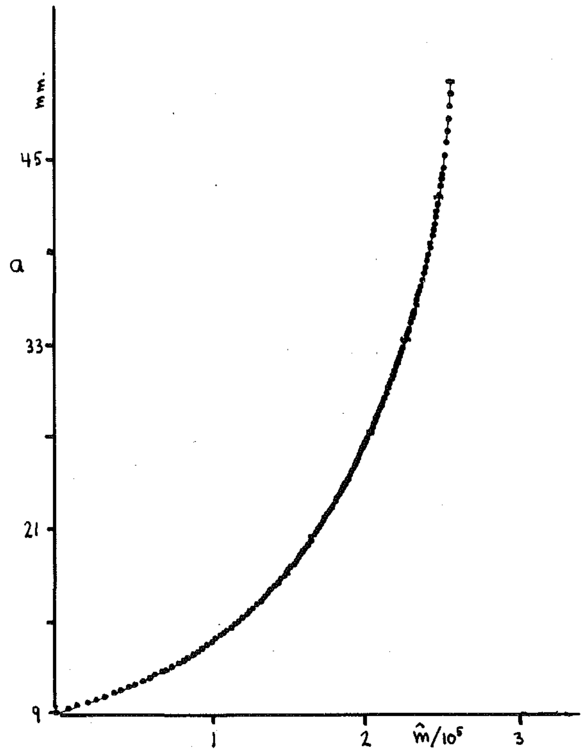

Fig. 1 Estimated mean $\hat{m}_n$ versus a for data of [8]

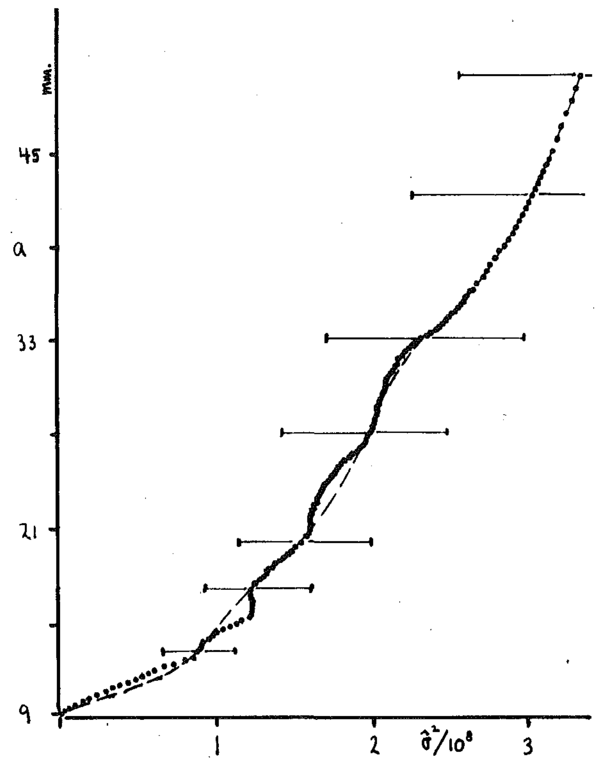

Fig. 2 Estimated variance $\hat{\sigma}_n{}^2$ versus a for data of [8]

Table 1

a	$\hat{x}_n(a)/10^2$	$\hat{\sigma}_n(a)/10^2$	$\hat{x}_n(a)/\hat{\sigma}_n(a)$
9	0	0	
11	557	65.8	8.47
13	911	93.5	9.74
17	1394	111.4	12.51
20	1639	124.0	13.22
26	1988	138.3	14.38
33	2265	152.1	14.89
42.4	2485	174.3	14.26
49.8	2512	183.1	14.05

Table 2

j	$r_j = p_j/q_j$
$1, \ldots, 63$	7.813
$64, \ldots, 90$	12.174
$91, \ldots, 149$	7.186
$150, \ldots, 166$	13.412
$167, \ldots, 196$	10.631
$197, \ldots, 214$	14.389
$215, \ldots, 221$	30.429
$222, \ldots, 224$	42.500
with $p_{225} = 1$	

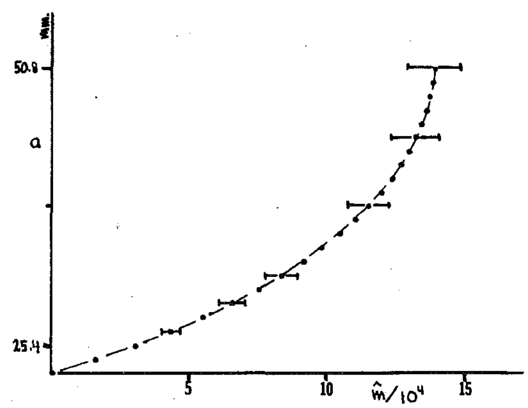

Fig. 3 Estimated mean $\hat{m}_n$ versus a for data of [9]

$$\text{Mean:} \quad (\hat{x}_n - 0.3580\,\hat{\sigma}_n, \hat{x}_n + 0.3580\,\hat{\sigma}_n),$$
$$\text{Variance:} \quad (0.5608\,\hat{\sigma}_n{}^2, 1.5420\,\hat{\sigma}_n{}^2);$$

these intervals are much larger than those for [8] as is expected. Figs. 3 and 4 shows the estimated mean and variance of time to reach a specified crack length. The effect of the smoothing operations is apparent. Again we do not use third and fourth central moments because of sample variability. The signal to noise ratio $\hat{x}_n/\hat{\sigma}_n$ does not exceed 5.5; this is indicative of variability encountered among several laboratories.

The two sets of data yield statistically acceptable estimates only for mean and variance of time to reach a specified crack length, due to restrictions imposed by the small number of replications. Therefore, model building also is restricted to the use of these two estimates.

The Model

Data From [8]. The model can be made to describe the data in as much detail as is desired. However, there is little point in pushing the detail too far since only mean and variance are available. We therefore shall only use the data shown in Table 1.

Following the procedures given in [7], we find the description of the model listed in Table 2. A comparison of Tables 1 and 2 reveals that state $s = 1$ corresponds to crack length 9 mm, $s = 64 \rightarrow a = 11$ mm, $s = 91 \rightarrow a = 13$, $s = 150 \rightarrow a = 17$ mm, $s = 167 \rightarrow a = 20$ mm, $s = 197 \rightarrow a = 27$ mm, $s = 215 \rightarrow a = 33$ mm, $s = 222 \rightarrow 42.11$ mm, and $s = 225 \rightarrow a = 49.8$ mm. The correspondence between other s and a is obtained by finding the two values that have the same mean value.

Data From [9]. Table 3 gives the data used to construct the model

Table 3

a	$\hat{x}_n(a)/10^2$	$\hat{\sigma}_n(a)/10^2$	$\hat{x}_n(a)/\hat{\sigma}_n(a)$
22.6	0	0	4.57
26.7	434	95	4.76
29.2	657	138	4.76
31.6	837	171	4.89
38.1	1151	221	5.21
44.5	1321	252	5.24
50.8	1394	273	5.11

Table 4

j	$r_j = p_j/q_j$
$1, \ldots, 20$	20.7
$21, \ldots, 25$	44.0
26, 27, 28	59.0
$29, \ldots, 33$	61.8
34, 35, 36	84.0
row 37 has 0.315 in column 37 and 0.6851 in column 45	
$37, \ldots, 46$ with $p_{47} = 1$	$\frac{68.3}{j} - 1$

for this case. This table leads to Table 4. We find by comparing tables that $s = 1 \rightarrow a = 22.6$ mm, $s = 21 \rightarrow a = 26.7$ mm, $s = 26 \rightarrow a = 29.2$ mm, $s = 20 \rightarrow a = 31.6$ mm, $s = 34 \rightarrow a = 38.1$ mm, $s = 28 \rightarrow a = 44.5$ mm, $s = 47 \rightarrow a = 50.8$ mm.

We note that the model as specified by Table 4 differs from the model specified by Table 2. This difference is traceable to the fact that in going from $a = 1.75$ in. to $a = 2.00$ in., the ratio $\Delta\hat{x}/\Delta\hat{\sigma}$ becomes less than 1, necessitating a slight change in procedure to obtain the needed r_j.

Results

Results are similar for the two cases. Because [8] contains 68 replications, most of our remarks apply to that case.

Let $W_{1,s}$ denote number of cycles to reach state s given specimen in state 1 at time zero. $EW_{1,s}$ and Var $W_{1,s}$ agree with the data in the two cases at the states (and corresponding crack lengths) listed in Tables 1 and 3. The correspondence between state s and crack length a is established by means of the equation

$$\hat{x}_n(a) = EW_{1,s} \tag{1}$$

This correspondence is illustrated in Fig. 5. Using this correspondence, we find that the curve

$$EW_{9,a} \text{ versus } a$$

lies on top of the curve of $\hat{x}_n(a)$ as is shown in Fig. 1. We also find that the curve

$$\text{Var } W_{9,a} \text{ versus } a,$$

shown as the dashed curve in Fig. 2, provides a reasonable fit to the curve $\hat{\sigma}_n(a)$ versus a supplied by the data. Thus, as far as the first two moments of the time to reach a given crack length are concerned, the model defined in Table 2 is very good. The corresponding results for the model defined in Table 4 are comparable.

The model generates the cumulative distribution function (cdf) $F_w(x;9,a)$ of the time $W_{9,a}$ to reach a given crack length a. We can construct from the data the corresponding empirical distribution function (edf) $F(x;9,a)$. Fig. 7 shows a comparison of these two distribution functions at the crack length where the model and data fit and where the fit was worst.

Fig. 8 shows the two distributions at a crack length where the model was not made to fit the data. The fit in this case is better than shown in Fig. 7. Thus there is no reason to reject the model based upon these results.

The model also generates sample functions. Sixty-eight sample

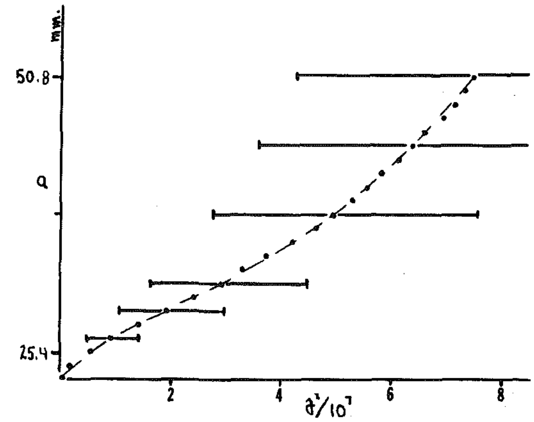

Fig. 4 Estimated variance $\hat{\sigma}_n{}^2$ versus a for data of [9]

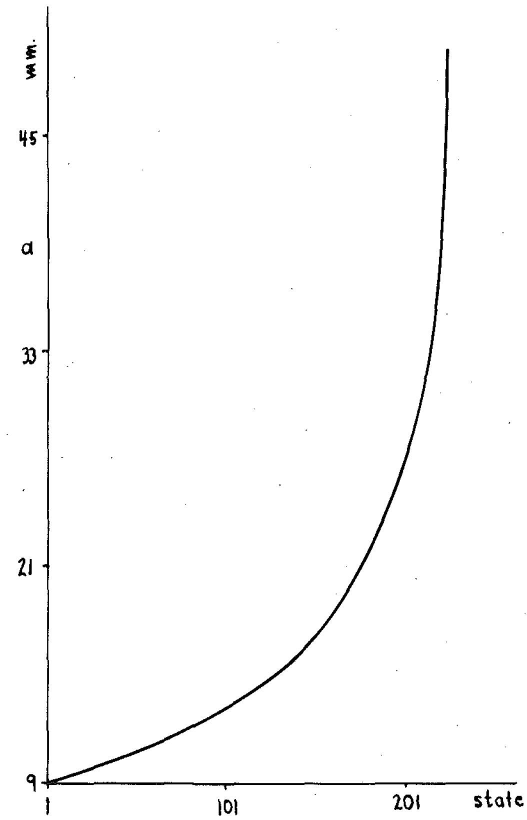

Fig. 5 Model state s versus a for data of [8]

functions are shown in Fig. 8. The 68 sample functions of the data are shown in Fig. 9. The sample functions from the model are somewhat rougher than those from the data, primarily because the model only matches the data at 9 values of a. They both show considerable intermingling.

Discussion

The first point to observe is that the models are second-order models, namely, only the first two moments are used in their construction. The data only provide statistically acceptable estimates of the mean and variance of the number of cycles to reach a given crack length, with the latter having large confidence intervals. (With only the first two moments acceptable, the models are restricted to the second order.) If more replications are available to supply acceptable estimates of moments to higher order, the model can be adjusted to

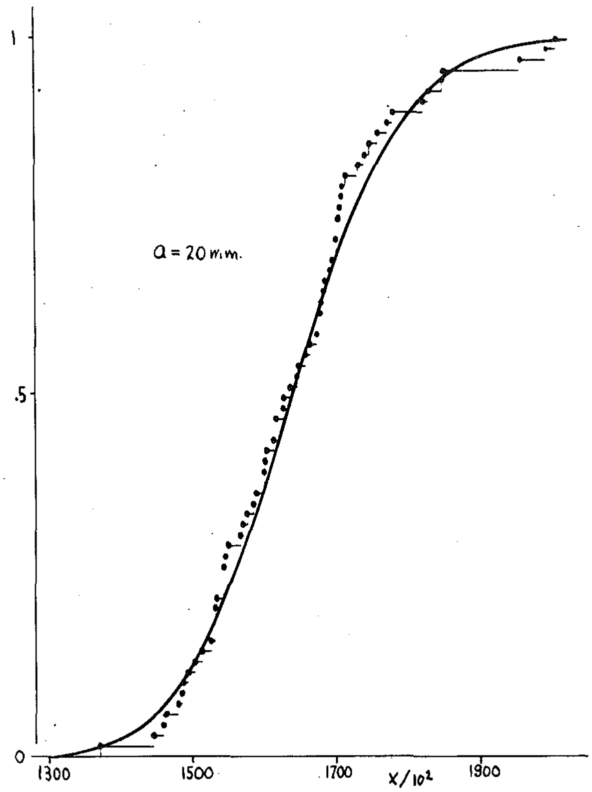

Fig. 6 Model generated cdf of time to reach crack length a = 20 mm and and corresponding edf from data of [8]

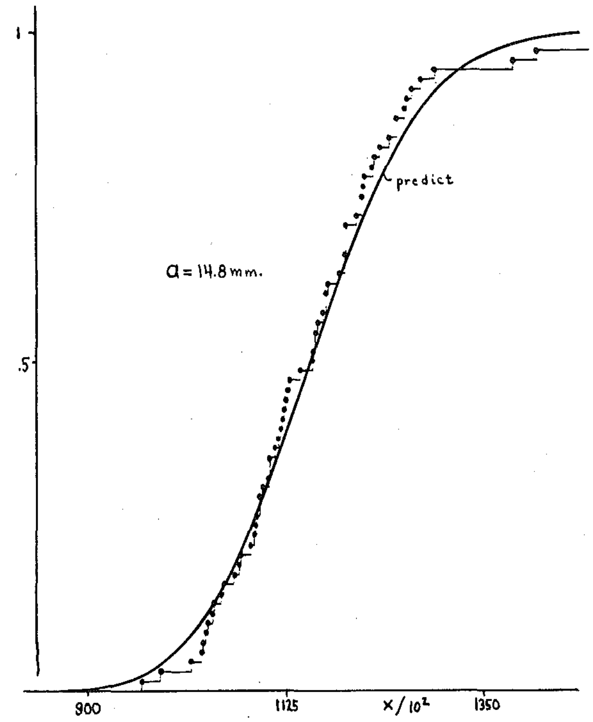

Fig. 7 Model generated cdf of time to reach crack length a = 14.8 mm and corresponding edf from data of [8]

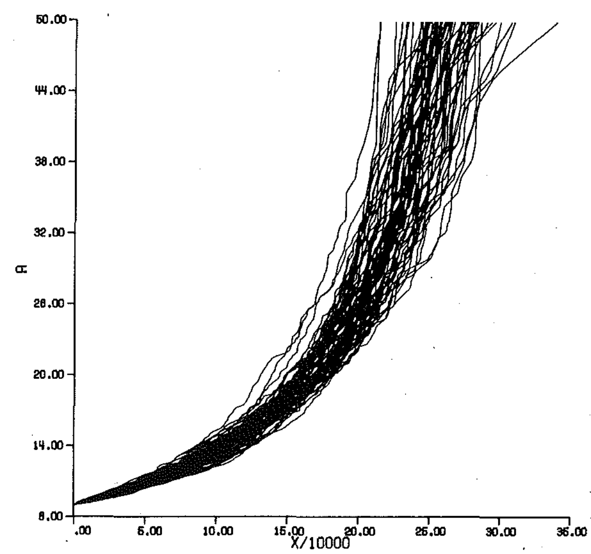

Fig. 8 68 sample functions generated by model for data of [8]

take account of this additional information. Thus the choice of the order of the models is dictated by what the data will support.

The second point to observe is that the fineness of the models used was arbitrarily selected. For example, in Table 1 we used nine values of crack length at which the model was made to fit mean and variance. More or less values or different values of crack length could have been selected. Nine values were chosen so that the curve mean versus a of the model would fit the corresponding curve of the data with considerably accuracy. Going to more values of crack length would smooth the sample functions. However, in view of the large magnitudes of the approximate confidence intervals for the variance, it could be argued that too many values have already been used. At this time, we have not used a measure that would permit us to decide the "best" number of values to use. Thus the fineness of the model is an open question. But we wish to point out that recent techniques such as the Akaike Information Criterion [10] might be used to judge the best value of fineness that should be used.

The third point to observe is that the models are not unique. We have used one-jump models, which are the simplest. However, we could have used two-jump models, for example. However, among one-jump models, based upon the data of Table 1, the model defined by Table 2 is unique. The one-jump model defined in Table 4 and based upon the data of Table 3, is unique up to the last stage; in the last stage, a choice of the form of the r_j is made. Uniqueness is not a requirement here any more than it is in the construction of finite-element models.

The fourth point to note is the ease with which the models are constructed. We need only calculate the first two moments of the time to reach a specified crack length; this is a trivial task. The construction of the models based upon these data is almost as easy to obtain. Not only does the model describe mean and variance, but it provides distributions on time to reach a specified crack length. This effort contrasts in our model's favor with the effort required in [8] to use the da/dn approach which provides less information.

Finally and most importantly, these crack growth models can easily be combined with appropriate models of fatigue damage accumulation *before a crack can be* detected. Let P_1 denote the probability transition matrix for the constant severity precrack phase, and let P_2 denote the probability transition matrix for the constant severity crack growth phase. Then, the constant severity probability transition matrix P for the combined phases is defined by

$$P = \left\{ \begin{array}{c|c} P_1' & O_{b_1-1,b_2-1} \\ \hline O_{b_2,b_1-1} & P_2 \end{array} \right\}, \tag{2}$$

where in P_1' the last row has been deleted from P_1. The change when either or both phases are nonstationary also can be handled. Thus our model can easily combine all phases of fatigue into one simple form that can then be used to predict behavior under a wide variety of conditions.

Conclusion

We have demonstrated in the foregoing that our new model can easily assemble into one simple structure crack growth data. The crack growth phase also can easily be combined with the precrack phase. No other model known to us can do this. The model also provides information on the probability a crack will reach a specified length at a specified time; thus there is no need to use *da/dn* scatter to obtain information on early crack growth. A question that naturally arises is, how does the model apply to other stress conditions, materials, geometry, environment, etc.? It is a straightforward task to construct a test program that will relate model parameters to such changes; this will be commented upon elsewhere.

A few final comments on this series of papers are in order.

The discretization of state and time, makes the computational procedure easy to use, and in this respect is similar to what finite-element techniques have done in continuum mechanics.

In confrontation with data from fatigue, crack growth, and wear the model has shown its ability to describe and analyze data and has demonstrated its diagnostic ability.

The general structure of the model makes it possible for the first time to view the cumulative damage process in a comprehensive and coherent manner. The model assembles into a single structure the specification of material and manufacturing defects and storage degradation, severity, and order of DC's and environmental and changing material properties effects, failure and/or replacement criteria, and inspection standards and replacement policy. From the view point provided by this general structure, much of what occurs in cumulative damage phenomena takes on meaning which can be readily interpreted; limits on accuracy of life prediction can be assessed, life cycle costs can be assessed, and suitable test programs designed to achieve a given accuracy. We know of no other model that has these features. Obviously, the model can be generalized in a number of directions if this should prove necessary.

Acknowledgment

Support from an A.F.O.S.R. Contract with Kozin-Bogdanoff and Associates, Inc., Dr. I. N. Shimi Contract Monitor, is gratefully acknowledged. Computational assistance from J. Sprandel and J. Modrey is acknowledged with pleasure. Finally, the authors wish to thank Drs. B. Hillbery and R. P. Wei for providing tapes and cards containing the raw data.

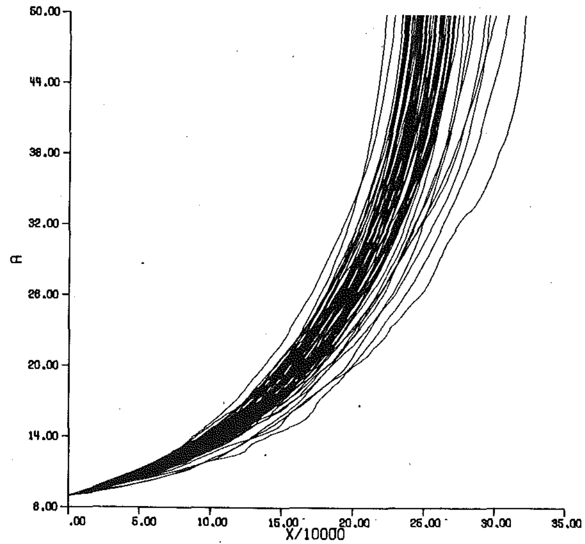

Fig. 9 The 68 sample functions from data of [8]

References

1 Hoeppner, D. W., and Krupp, W. E., "Prediction of Component Life by Application of Fatigue Crack Growth Knowledge," *Eng. Fact. Mech.*, Vol. 6, No. 1, 1974, pp. 47–70.

2 McCartney, L. N., and Gale, B., "Two Theoretical Models of Fatigue Crack Propagation," *Proceedings of the Royal Society, London*, Series A, Vol. 333, 1973, pp. 337–345.

3 McCartney, L. N., and Cooper, P. M., "A Numerical Method of Processing Fatigue Crack Propagation Data," *Eng. Fract. Mech.*, Vol. 9, No. 2, 1977, pp. 265–272.

4 McCartney, L. N., and Cooper, P. M., "A New Method of Analyzing Fatigue Crack Propagation Data," *Eng. Fract. Mech.*, Vol. 9, No. 2, 1977, pp. 273–290.

5 Bogdanoff, J. L., "A New Cumulative Damage Model—Part 1," ASME JOURNAL OF APPLIED MECHANICS, Vol 45, No. 2, June 1978, pp. 246–250.

6 Bogdanoff, J. L., and Krieger, W., "A New Cumulative Damage Model—Part 2," ASME JOURNAL OF APPLIED MECHANICS, Vol. 45, No. 2, June 1978, pp. 251–257.

7 Bogdanoff, J. L., "A New Cumulative Damage Model—Part 3," ASME JOURNAL OF APPLIED MECHANICS, Vol. 45, No. 4, Dec. 1978, pp. 733–739.

8 Virkler, D. A., Hillbery, B. M., and Goel, P. K., "The Statistical Nature of Fatigue Crack Propagation," AFFDL-TR-78-43, Apr. 1978.

9 Clark, W. G., Jr., and Hudak, S. J., Jr., Variability in Fatigue Crack Growth Rate Testing," *Journal of Testing and Evaluation*, Vol. 3, No. 6, Nov. 1975, pp. 454–476.

10 Akaike, H., "A New Look at Statistical Model Identification," IEEE, *Trans. Auto. Cont.*, Vol. AC-19, No. 6, Dec. 1974, pp. 717–723.

V. K. Kinra
Assistant Professor.
Mem. ASME

B. Q. Vu
Research Assistant.
Assoc. Mem. ASME

Department of Mechanical Engineering,
University of Colorado,
Boulder, Colo. 80309

Brittle Fracture of Plates in Tension

Virgin Waves and Boundary Reflections

Virgin waves emitted during tensile fracture of edge-notched brittle plates have been measured at points on and away from the crack path. The results are in excellent agreement with the analysis of Freund. Boundary reflections were also determined. Both the rear and the front edge reflections are small but not negligibly small; the former are tensile, the latter compressive. Unloading waves are propagated behind the crack tip, and are small compared to the loading waves, which are propagated ahead of the tip. The front edge reflections were also examined near the edge; these are compressive and large. Finally, for an embedded crack, the field scattered by the stationary crack tip was found to be negligibly small.

Introduction

Dynamic stress fields in the vicinity of a rapidly propagating crack were recently studied by Kinra and Bowers [1] who used single-edge-notched (SEN) glass specimens subjected to fracture in tension. The recorded signals contained, of necessity, reflections from the edge containing the crack-initiating notch and hence were not truly "virgin" in nature. The purpose of the present work is

1 To study these waves prior to the arrival of *any* reflections.
2 To measure the boundary reflections by isolating them from the virgin waves.

The arrival of the boundary reflection from the "rear" edge (see Fig. 1) was delayed by using specimens with very long notches. Following [1], stresses at a point lying on the prospective crack path were measured first. These are compared with the experimental results of [1] and the analytical results of [2]. Next, stresses at a point some small distance *away* from the crack plane were recorded; these are compared with the corresponding experimental results of [1]. Next, the reflections from the "front" and the rear edges are determined. The stress field scattered by the stationary crack tip when one tip of an embedded crack begins to propagate was also measured. Finally, waves traveling behind the crack tip have been recorded.

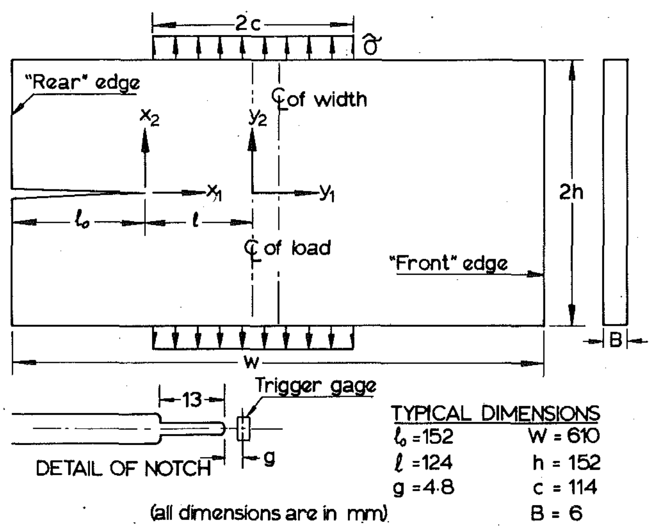

Fig. 1 Schematic of a typical "wide" specimen

Experimental Procedures

With reference to Fig. 1, the earliest boundary reflections are from the rear edge. These can be delayed only by making l_0 suitably large (the reflections from the other three boundaries could be easily delayed by increasing the size of the specimen). Now it would be more desirable to apply $\hat{\sigma}$ to the entire width W, for that would result in simplified expressions for the stresses in the plate. However, there are two considerations which prohibit this. First, in view of large l_0 (152 mm), crack initiation would have occurred at a low value of $\hat{\sigma}$. Since the amplitude of the emitted waves is proportional to $\hat{\sigma}$, our calculations revealed that the waves would have been too small to be measured satisfactorily using the strain gages (microvolt signals). Second, after a certain amount of extension the dynamic stress-intensity factor K_{ID} would have been large enough to cause branching or veering (hooking). Since we wish to compare our experimental results with the analysis of Freund [2] based on the assumption of rectilinear motion of the crack, branching or hooking could not be tolerated. Consequently $\hat{\sigma}$ was applied only to a fraction of the width.

Contributed by the Applied Mechanics Division and presented at the Winter Annual Meeting, New York, N.Y., December 2–7, 1979, of THE AMERICAN SOCIETY OF MECHANICAL ENGINEERS.

Discussion on this paper should be addressed to the Editorial Department, ASME, United Engineering Center, 345 East 47th Street, New York, N.Y. 10017, and will be accepted until June 1, 1980. Readers who need more time to prepare a discussion should request an extension from the Editorial Department. Manuscript received by ASME Applied Mechanics Division, October, 1978; final revision, July, 1979. Paper No. 79-WA/APM-36.

The value of $\hat{\sigma}$ required for crack extension could be made suitably large by placing the crack tip outside the loaded width (see Fig. 1). Further, with this type of loading the stress decreases rapidly as the crack tip extends beyond the center line of the load, thus branching could be avoided in most of the experiments. It is emphasized that all data reported in this paper are for those cases where a rectilinear motion of the crack was observed across the entire width of the specimen.

In addition to the "Wide" specimen shown in Fig. 1, two other types were also used in the investigation: "Intermediate" (254 mm wide with a 51 mm *embedded notch*) and "Narrow" (100 to 150 mm wide with 20 mm *edge notch*). In all cases the height ($2h$ = 305 mm) and the thickness (B = 6 mm) are the same. The specimens used in this work were from the same batch as those used in [1]. The properties of glass, as stated by the manufacturer, are: velocity of longitudinal waves c_1 = 5800 m/sec; velocity of shear waves c_2 = 3350 m/sec; Young's modulus $E = 70 \times 10^9$ N/m^2; Poisson's ratio $\nu = 0.25$, and density $\rho = 2.5$.

The rest of the experimental procedures have already been described in [1].

Theoretical Considerations

Consider the specimen shown in Fig. 1. The applied stress $\hat{\sigma}$ is increased quasi-statically until the static stress-intensity factor K_I barely exceeds the fracture toughness K_{IC}, and the crack begins to extend. We will assume here that the crack extends with a constant velocity v; justifications for this assumption may be found in [1]. The objective of this section is to derive expressions for $\sigma_{22}{}^*(x_1, 0, t)$—the *dynamic component* of the stress at any point ($x_1 > 0$, $x_2 = 0$) on the prospective crack plane.

The simple analysis starts with an expression for the stress in the *uncracked* plate, $\tilde{\sigma}_{22}(x_1, x_2 = 0)$. The necessary expressions for the stress in the *cracked* plate, $\sigma_{22}{}^0(x_1, 0)$ are derived next. These are substituted into equation (3) of [1] (which in turn was derived from equation (3.2) of [2]) to obtain the desired expressions for $\sigma_{22}{}^*(x_1, 0, t)$.

Let $\tilde{\sigma}_{\alpha\beta}$ be the (static) stress field in the specimen of Fig. 1 *if it had been uncracked*. It will be subsequently shown that $\tilde{\sigma}_{22}(y_1, 0) \to 0$ at the rear and front edges of the plate, hence we assume that plate is infinitely wide along y_1. Then from [3],

$$\tilde{\sigma}_{22}(y_1, 0) = \int_0^\infty d\beta F(\beta) \cos(\beta y_1), \tag{1}$$

where

$$F(\beta) = \frac{2\hat{\sigma}\sin(\beta c)}{\pi\beta}\left[\frac{Sh(\beta h) + \beta h Ch(\beta h)}{\beta h + Sh(\beta h)Ch(\beta h)}\right]. \tag{2}$$

We now introduce the edge crack $y_2 = 0^\pm$, $-\infty > y_1 < -l$. By the familiar argument of superposition, the stresses in the *cracked* plate, $\sigma_{\alpha\beta}{}^0$, may be written as $\sigma_{\alpha\beta}{}^0 = \tilde{\sigma}_{\alpha\beta} + \sigma_{\alpha\beta}{}^c$, where $\sigma_{\alpha\beta}{}^c$ are the stresses *due only to* the tractions $-\tilde{\sigma}_{22}(y_1\, 0^\pm)$ acting on the crack faces. An expression for $\sigma_{22}{}^c$, which can easily be derived from [4], is

$$\sigma_{22}{}^c = -\frac{1}{\pi\sqrt{x_1}}\int_{-\infty}^0 \frac{(-s)^{1/2}}{(s - x_1)}ds \int_0^\infty \frac{F(\beta)}{\sqrt{\beta}}\cos\beta(s - l)d\beta. \tag{3}$$

where we have substituted $y_1 = x_1 - l$ and used equation (1) for $\tilde{\sigma}_{22}(y_1, 0)$. Let

$$I_1 = \int_0^\infty \frac{\sqrt{s}\cos\beta s}{s + x_1}ds \quad \text{and} \quad I_2 = \int_0^\infty \frac{\sqrt{s}\sin\beta s}{s + x_1}ds, \tag{4}$$

then

$$\sigma_{22}{}^c = \frac{1}{\pi\sqrt{x_1}}\int_0^\infty d\beta F(\beta)\{I_1\cos\beta l - I_2\sin\beta l\}. \tag{5}$$

In order to calculate I_1 and I_2, consider the contour integral $\oint_C f(z)dz$, $f(z) = e^{i\beta z}\sqrt{z}/(z + x_1)$, $z = t + iu$, and $C = C_1 + C_R + C_2 + C_\rho$, where C_1: $z = te^{i\epsilon}$, ϵ is an infinitesimally small positive real number, and $\rho \le t \le R$, where ρ and R are, respectively, small and large positive real numbers; C_R: $z = \mathrm{Re}^{i\theta}$, $\epsilon < \theta \le \pi/2$; C_2: $z = ue^{i\pi/2}$, $\rho \le u \le R$; C_ρ: $\rho e^{i\theta}$, $\epsilon < \theta \le \pi/2$, and C is traversed in the counterclockwise direction. The integrand is rendered single-valued by introducing a branch cut along the positive real axis. Using the standard techniques of the residue theory, it can be readily shown that in the limit as $\rho \to 0$, $R \to \infty$, and $\epsilon \to 0$,

$$\int_{C_1} f(z)dz = -\int_{C_2} f(z)dz = e^{i\pi/4}\int_0^\infty \frac{\sqrt{u}}{u + x_1 e^{-i\pi/2}}e^{-\beta u}du.$$

The integral is recognized as a Laplace transform, and from [5],

$$\int_{C_1} f(z)dz = e^{i\pi/4}(\pi/\beta)^{1/2} - \pi(x_1)^{1/2}e^{-i\beta x_1}\,\mathrm{erfc}\,\{e^{-i\pi/4}(x_1\beta)^{1/2}\}. \tag{6}$$

To evaluate erfc ( ), the contour of integration is chosen along a straight line from $z = e^{-i\pi/4}(x_1\beta)^{1/2}$ to $z = 0$, and from $z = 0$ to $z = \infty$ along the positive real axis:

$$\mathrm{erfc}\,\{e^{-i\pi/4}(x_1\beta)^{1/2}\} = 1 - (1 - i)[C(x_1\beta) + iS(x_1\beta)], \tag{7}$$

where $C(\ )$ and $S(\ )$ are Fresnel integrals [6] defined by,

$$C(x) = \left(\frac{2}{\pi}\right)^{1/2}\int_0^{(x)^{1/2}} \cos(t^2)dt,$$

$$S(x) = \left(\frac{2}{\pi}\right)^{1/2}\int_0^{(x)^{1/2}} \sin(t^2)dt. \tag{8}$$

Substituting (7) into (6) and taking real and imaginary parts,

$$I_1 = \left(\frac{\pi}{2\beta}\right)^{1/2} - \pi(x_1)^{1/2}\cos(\beta x_1) + \pi(x_1)^{1/2}[\cos(\beta x_1)\{C(\beta x_1) + S(\beta x_1)\} + \sin(\beta x_1)\{S(\beta x_1) - C(\beta x_1)\}], \tag{9}$$

$$I_2 = \left(\frac{\pi}{2\beta}\right)^{1/2} + \pi(x_1)^{1/2}\sin(\beta x_1) + \pi(x_1)^{1/2}[\cos(\beta x_1)\{S(\beta x_1) - C(\beta x_1)\} - \sin(\beta x_1)\{S(\beta x_1) + C(\beta x_1)\}]. \tag{10}$$

From equations (9), (10), (5), (1), and $\sigma_{22}{}^0 = \tilde{\sigma}_{22} + \sigma_{22}{}^c$ we obtain,

$$\sigma_{22}{}^0(x_1, 0) = \int_0^\infty d\beta F(\beta)\left[\frac{\cos\beta l - \sin\beta l}{(2\pi\beta x_1)^{1/2}} + \cos\beta(x_1 - l)\{C(\beta x_1) + S(\beta x_1)\} + \sin\beta(x_1 - l)\{S(\beta x_1) - C(\beta x_1)\}\right]. \tag{11}$$

From equation (3) of [1],

$$\sigma_{22}{}^*(x_1, 0, t) = \frac{1}{\pi(x_1 d - t)^{1/2}}\int_0^{x_{0cr}} \frac{\sigma_{22}{}^0(x_0, 0)[x_0(d - c) - (t - cx_1)]dx_0}{(x_1 - x_0)[(t - ax_1) - x_0(d - a)]^{1/2}}, \tag{12}$$

for $ax_1 < t < dx_1$ and $\sigma_{22}{}^*(x_1, 0, t) = 0$ otherwise. Here $t = 0$ is the instant of crack initiation and a, b, c, and d are, respectively, the slownesses (i.e., inverse of the speed) of dilatational, distortional, and Rayleigh waves, and the crack tip; and $x_{0\,cr} = (t - ax_1)/(d - a)$. Finally, the total stress (static plus dynamic) is given by,

$$\sigma_{22}(x_1, 0, t) = \sigma_{22}{}^0(x_1, 0) + \sigma_{22}{}^*(x_1, 0, t). \tag{13}$$

Now the expression (12) for $\sigma_{22}{}^*(x_1, 0, t)$, in view of equation (11) for $\sigma_{22}{}^0$, is a very complicated double integral to evaluate. However, considerable reduction in the numerical effort could be achieved by making the following observations. $\tilde{\sigma}_{22}$ (equation (1)) and $\sigma_{22}{}^0$ (equation (11)) are plotted in Fig. 2. The range of x_1 for which $\sigma_{22}{}^0$ enters into equation (12) is from $x_1 = 0$ (crack tip) to $x_1 = 57$ mm (strain gage location, see Fig. 3) or $0 < x_1/h < 0.375$. Over this range $\sigma_{22}{}^0$ is shown in the inset. With the obvious exception of the crack-tip singularity, it appears that $\sigma_{22}{}^0$ may be adequately approximated by

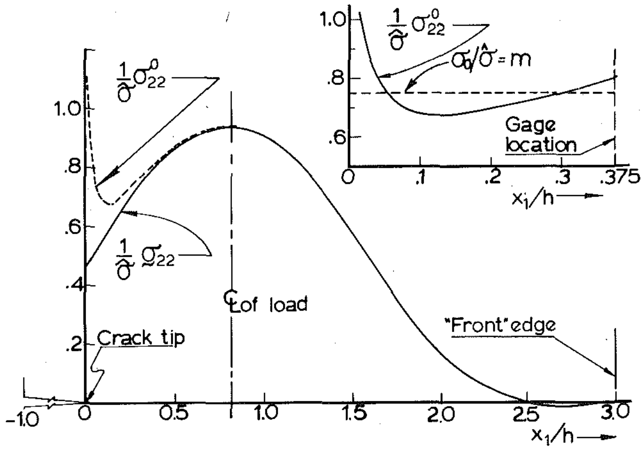

Fig. 2 Stress distribution on the crack plane for the specimen of Fig. 1

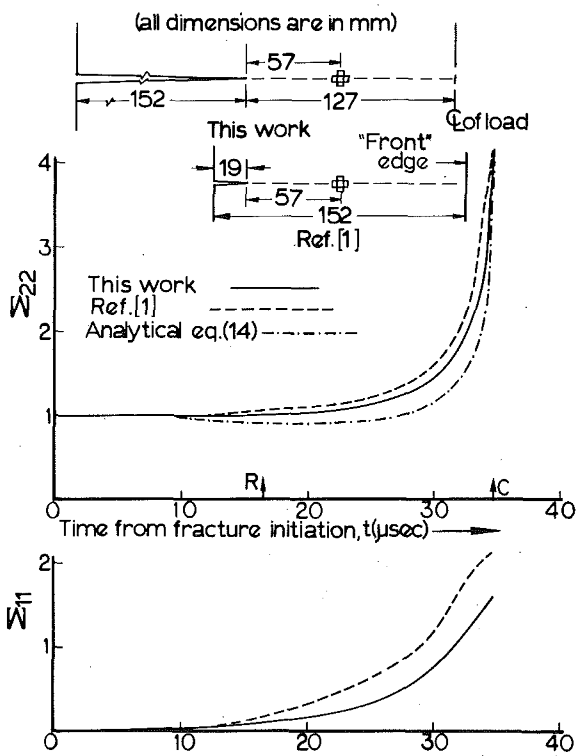

Fig. 3 Virgin waves emitted during fracture of the specimen shown; comparison with experiments of [1] and analysis, equation (14)

a constant value: let $\sigma_{22}{}^0 = m\hat\sigma = \sigma_0$ (say); for the *particular* geometry of Fig. 1, $m = 0.75$. It is noted that by neglecting the singularity, we are neglecting the discontinuity in stress propagated with the dilatational wavefront. However, as reported in [1] and further confirmed in this investigation, the discontinuity is not observed experimentally because in reality the stress at the crack tip is finite. Also note that $\tilde\sigma_{22}/\hat\sigma$ becomes negligibly small near the plate boundaries, justifying the assumption made in deriving the foregoing equations that the plate is infinitely wide. Setting $\sigma_{22}{}^0 = \sigma_0$ in (12), substituting the result in (13), and defining $\Sigma_{\alpha\beta} = \sigma_{\alpha\beta}/\sigma_0$, $\Sigma^*{}_{\alpha\beta} = \sigma^*{}_{\alpha\beta}/\sigma_0$, one obtains

$$\Sigma_{22}(x_1, 0, t) = 1 + \Sigma^*{}_{22}(x_1, 0, t),$$

$$\Sigma^*{}_{22}(x_1, 0, t) = \frac{-1}{\pi(x_1 d - t)^{1/2}} \int_0^{x_{0cr}} dx_0 \frac{x_0(d-c) - (t - cx_1)}{(x_1 - x_0)[(t - ax_1) - x_0(d-a)]^{1/2}} \quad (14)$$

It is emphasized that equation (14) is valid only for (1) points with $x_2 = 0$, and (2) for time before the arrival of *any* boundary reflections. These are consequences of the fact that Freund's analysis [2] is for rectilinear motion of a semi-infinite crack in an infinite medium.

Results and Discussions

1 Virgin Waves at a Point on the Crack Plane. The specimen of Fig. 1 was used to record the emitted waves. At the top of Fig. 3 we have included a schematic which shows the location of the strain gages. The stresses Σ_{11} and Σ_{22} are shown as solid lines. The average crack velocity over $0 < x_1 < 57$ mm was found to be 1.695 mm/μsec or 0.067 in./μsec; equivalently $bv = 0.51$. The earliest boundary reflections arrive at 53 μsec, hence the recorded signals are virgin for the entire time shown and may, therefore, be compared with the analytical results, equation (14). (The analytical results for Σ_{11} are not yet available.) The comparison between the theory and the experiment is considered excellent, particularly in view of the fact that the analysis [2] is based on the plane strain assumption while our experiments were conducted in *essentially* plane-stress conditions. This is an encouraging result because much of the analytical work concerning (opening) Mode 1 dynamic crack propagation is based on the assumption of plane strain. It cannot be directly applied to laboratory specimens or real life structures because, in these, plane-strain conditions are seldom realized. The excellent comparison just mentioned suggests that the plane-strain analyses may very well be applicable to plane-stress failures. This conclusion is drawn with the appropriate caution that our results are for a particular specimen geometry and loading conditions.

In Fig. 3 we have also reproduced the corresponding experimental results obtained in reference [1] using a "narrow" specimen (152 mm wide) as well as the geometry of that specimen. Due to the proximity of the rear edge to the crack tip (19 mm) these results contain rear edge reflections (RER) in addition to the virgin waves for $t > 16.5$ μsec. The arrival time of the reflection and of the crack tip at the strain gages is indicated by arrows labeled R and C, respectively. (Similar notation will be used throughout this work to indicate arrival time.) The results of the present investigation (solid lines) are virgin waves alone. Note also that the gages are located at $x_1 = 57$ mm, $x_2 = 0$ in both specimens. Therefore, the difference—dashed lines minus solid lines—are the RER in the narrow specimen at $x_1 = 57$ mm, $x_2 = 0$ for $t > 16.5$ μsec. Both Σ_{11} and Σ_{22} component of the RER are tensile, and small but not negligibly small compared to the virgin waves. Some implications of this observation will be discussed in Section 3.5 when the discussion concerning the boundary reflections is complete.

2 Virgin Waves at a Point Away From the Crack Plane ($x_2 \neq 0$). For the problem under consideration the exact analytical solution for the stresses $\Sigma_{\alpha\beta}$ at a generic point (i.e., with $x_2 \neq 0$) does not appear to be in sight. We have measured these stresses and reported them here with a twofold purpose:

1 For comparison with the results of approximate models if and when they appear in literature.

2 We hope that our results may provide some useful insight to a theoretical mechanician considering an approximate model.

A wide specimen (Fig. 1) was used in this experiment. The strain gage location is shown in Fig. 4(a) and the measured stresses are shown as *solid* lines. These are virgin until 53 μsec when reflections from the loading grips arrive (indicated by arrow G). The crack velocity $v = 1.75$ mm/μsec ($bv = 0.52$) for this experiment. In [1], similar results were obtained with the same (x_1, x_2) gage location. Since "narrow" specimens were used, the recorded signals contained rear-edge reflections. For use in a subsequent section, the specimen geometry is reproduced in Fig. 4(b), and the $\Sigma_{\alpha\beta}$ are shown as *chain*

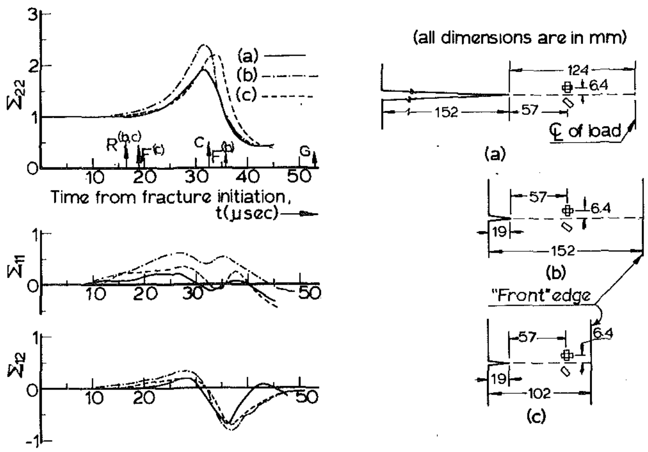

Fig. 4 Virgin waves emitted during fracture of specimen (*a*); determination of boundary reflections by comparison with other experiments

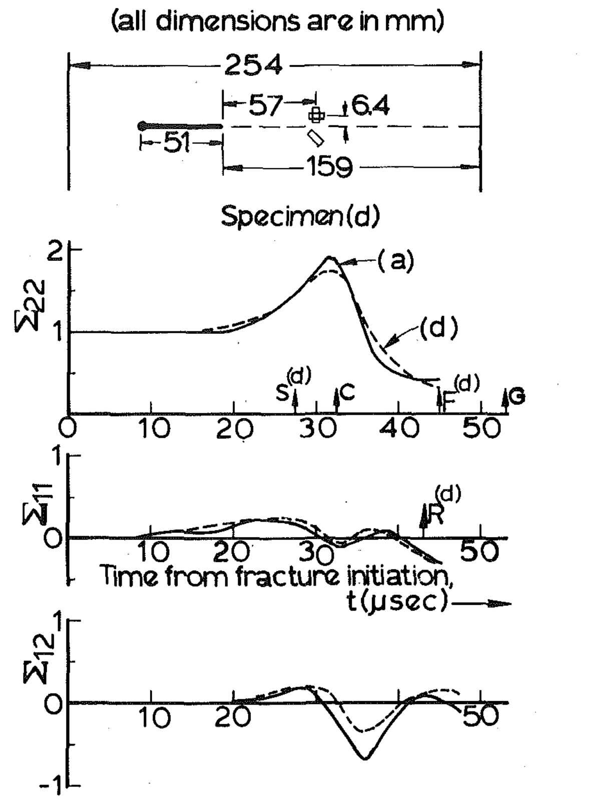

Fig. 5 Determination of field scattered by the stationary tip of the specimen shown

lines. Evidently, the general features of the two sets of data are quite similar; these have been discussed in [1]. Here discussion is limited to a specific observation of interest. Let t_c be the time when the tip occupies $x_1 = 57$ mm. For $t > t_c = 32.5$ μsec, the gages have traction-free surfaces in their immediate vicinity, hence one would expect the stresses Σ_{12} and Σ_{22} to drop off rapidly to zero thereafter. Instead, Σ_{22} appears to approach a nonzero plateau and Σ_{12} attains rather large magnitudes for $t > t_c$, although it does approach zero eventually. (This phenomenon was observed in all similar experiments with "narrow," "intermediate," or "wide" specimens.) It is *conjectured* that these phenomena may be due to the emitted Rayleigh waves which propagate along the crack surfaces without suffering attenuation. Finally, Σ_{11} exhibits two maxima surrounding $t = t_c$, corroborating similar observations in [1].

3 **Boundary Reflections.** There are a number of situations where the boundary reflections may play an important role:

1 Most analytical solutions of Mode 1 dynamic crack problems are for semi-infinite cracks in infinite media, hence they are valid only up to the time when the first reflection from either the boundaries or the stationary crack tip (in case of embedded cracks) arrives at the running crack tip.

2 Frequently in photoelastic investigations of K_{ID}, measurements are made after the boundary reflections have impinged upon the crack tip.

3 In experiments dealing with crack arrest problems (a number of articles may be found in [8]) the duration of the experiment is usually large compared to the transit time of the waves. The dynamic effects may, therefore, influence the crack-arrest process in relatively smaller specimens.

These are some of the reasons for undertaking the experiments described in the following, in which the boundary reflections are determined. It was found that the reflections are *small but not negligibly small* compared to the virgin waves. It is emphasized that these measurements are for only one particular geometry and loading conditions and for extremely fast fracture: bv $\simeq 0.5$.

3.1 Rear Edge Reflections (*RER*). These reflections were determined by comparing the results of two different experiments. Recall that $\Sigma_{\alpha\beta}$ measured with the specimen 4(*a*) are virgin (solid lines). However, due to close proximity of the rear edge to the notch-tip in specimen 4(*b*), these measurements (chain lines) contain RER for $t > 16.5$ μsec, indicated by $R^{(b)}$. (Note that x_1, x_2 coordinates of the gage are identical in specimens (*a*), (*b*), (*c*) of Fig. 4 and (*d*) of Fig. 5. Thus the virgin waves alone are identical in all four cases.) Therefore, the difference—chain lines minus solid lines—is due to the RER in specimen (*b*) at $x_1 = 57$ mm, $x_2 = 6.4$ mm for $16.5 < t < 36$ μsec; the upper limit corresponds to the front edge reflection whose arrival time is indicated by $F^{(b)}$. The subtraction has not been explicity carried out for reasons deferred to the Appendix.

Discussion. Σ_{22}: the RER is *tensile* throughout the period of observation, the maximum amplitude is about 0.5, and it goes to zero at about 35 μsec; recall that $t_c = 32.5$ μsec. Σ_{11}: again the RER is tensile and the peak amplitude is about 0.5. Σ_{12}: the RER is quite small and changes sign at about $t = t_c$. In conclusion, rear edge reflections are *tensile,* and for the particular specimen (*b*), are *small but not negligibly small* compared to the virgin waves.

3.2 Front Edge Reflections (*FER*). These were determined in a similar manner. The front edge reflections in specimen (*b*) arrive at $t = 36$ μsec, indicated by $F^{(b)}$. Now compare specimens (*b*) and (*c*); with the exception that the front edge in (*c*) is 50 mm closer to the strain gages, the two are exactly identical. Thus, in specimen (*c*), the FER begins to arrive at $t = 18.5$ μsec, indicated by $F^{(c)}$. Thus the difference—dashed lines minus chain lines—is due to the front edge reflections in specimen (*c*) for $18.5 < t < 36$ μsec.

Discussion. Σ_{22}: Note that the peak in (*c*) is shifted significantly to the right relative to the peak in (*b*), implying that the reflected wave is *compressive.* The maximum amplitude is 0.5. Σ_{11}: again, the reflection is *compressive.* (Since the stress field radiated in front of the crack was found to be tensile (Section 1), one would expect that the reflection from the traction-free front edge will be compressive.) The peak amplitude is about 0.5. Σ_{12}: clearly the shear stress associated with the front edge reflection is quite small ($\sim$0.2) throughout. In conclusion, front edge reflections are *compressive,* and *small but not negligibly small* compared to the virgin waves.

3.3 Waves Scattered by the Stationary Crack Tip. Attention is now drawn to Fig. 5, where the "intermediate" sized specimen (*d*) used in these experiments is shown schematically. Note that the specimen has an *embedded* (rather than edge) notch. A very small hole was drilled at the left tip of the notch with an ultrasonic drill and filled with an epoxy adhesive; the purpose was to ensure that only the right tip propagated when the specimen was eventually subjected to fracture by applying a remote uniform tension σ_0 (see Figs. 1 and 2

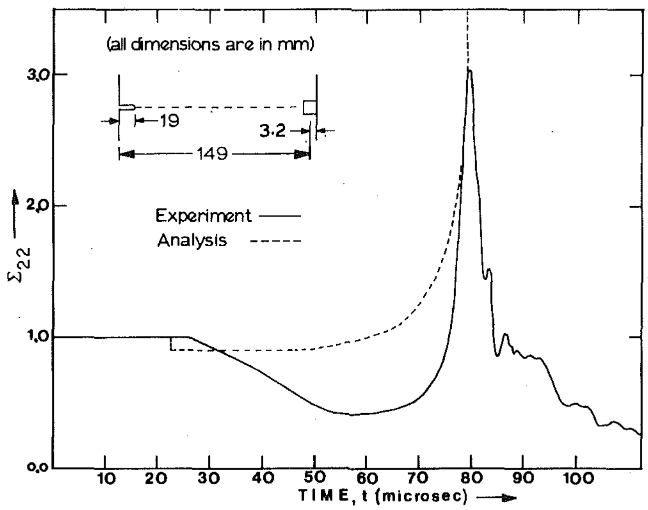

Fig. 6 Determination of front edge reflection by comparison of experimental and analytical results

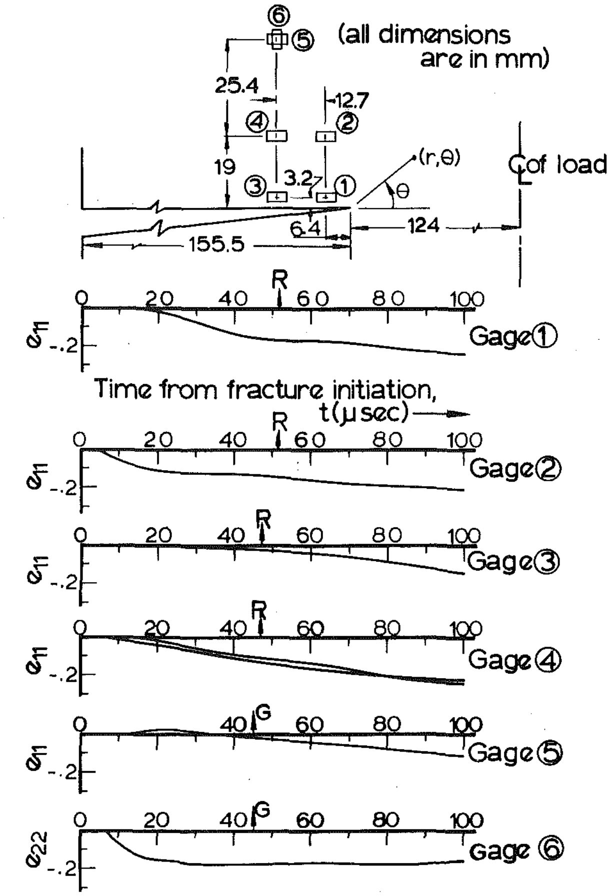

Fig. 7 Rear-going waves for the fracture of specimen shown

of [1] for experimental details). Note also that the location of the strain gages is identical in specimens (a) and (d). A fourth strain gage was mounted immediately to the left of the blunted notch tip and its output during the fracture showed that this tip remained stationary throughout the period of observation. The stresses recorded during the fracture of specimen (d) are shown as dashed lines in Fig. 5; here $\Sigma_{\alpha\beta} = \sigma_{\alpha\beta}/\sigma_0$. In addition to the virgin waves these contain the stress field scattered by the stationary tip for $t > 27$ μsec indicated by $S^{(d)}$. For easy comparison, the *virgin* waves obtained with the use of specimen (a) have also been reproduced here as solid lines. Thus the difference—dashed lines minus the solid lines—is the stress field scattered by the stationary tip. *Clearly, the scattered field may be considered negligibly small compared to the virgin waves.*

3.4 Front Edge Reflections at the Edge. The limitations of the foregoing experimental procedures in yielding precise measurements of the boundary reflections are discussed in the Appendix. In view of that, it was considered desirable to use an *independent* technique to obtain corroborative results. To this end, narrow specimens shown in Fig. 6 were used; these were fractured in simple tension, σ_0 (see reference [1] for details). The crack velocity $v = 1.63$ mm/μsec or 0.064 in/μsec. Now if the specimen had been infinitely wide along its width, then the stress Σ_{22} ($= \sigma_{22}/\sigma_0$) at the strain gage location would have been given by equation (3) of reference [1]; this is plotted as the dashed line in Fig. 6. As it is, the measured Σ_{22} contains the front edge reflection from the very instant (22.5 μsec) the dilatational wave front arrives at the strain gage; this is shown as the solid line. Therefore, the difference—experimental trace minus the analytical trace—is the front edge reflection *at the edge.* It is compressive and its peak amplitude is about 0.75. This qualitatively corroborates the compressive Σ_{22} in the FER discussed earlier in Section 3.2. Similar results were obtained by Kinra and Kolsky [7] in their experiments with the fracture of glass plates in *pure bending.* They observed a monotonic increase in the magnitude of the compressive stress at the front edge (which was in compression prior to fracture). Thus it appears that a crack will have a tendency to slow down as it approaches a traction-free edge.

Finally, in Fig. 6 there is a rapid reversal of slope at about 70 μsec. A simple calculation shows that at about this time the tensile crack-tip stress field (the so-called singular term) begins to dominate the stress at the strain gage location.

3.5 Concluding Remarks on Boundary Reflections. At the beginning of Section 3 a number of situations were mentioned in which the boundary reflections may be expected to play a significant role. Briefly, these are: analytical solutions of semi-infinite cracks; photoelastic measurements of K_{ID}, and experimental measurements of crack-arrest parameters. From the experimental results presented in Sections 3.1, 3.2, and 3.4, it is clear that the boundary reflections *may not be considered negligibly small—at least for the particular* range of specimen widths used (100 to 150 mm) and the particular crack velocity (bv $\simeq$ 0.5) observed. Although a quantitative estimate of the errors due to the reflections is beyond the scope of this work, it is hoped that our measurements will be of some help to other experimentalists concerned about the magnitude of the reflections; for any particular specimen size and geometry some estimate could be obtained by extrapolating our results on the basis of geometric attenuation ($1/\sqrt{x}$) associated with cylindircal expansion.

On the other hand, the results regarding the stress field scattered by the stationary crack-tip (Section 3.3) suggest that in all of the situations previously listed, the presence of the stationary crack tip may be ignored for all practical purposes.

Finally, on the basis of the foregoing experimental results, the following *qualitative* assertions can be made:

1 The tensile rear edge reflections will tend to increase K_{ID}

2 The compressive front edge reflections will tend to decrease K_{ID}.

3 The effect of the stress field scattered by the stationary crack tip on K_{ID} can be ignored for all practical purposes.

4 Waves Radiated Behind the Crack Tip. To complete the *experimental investigation of the virgin stress field radiated* by a suddenly propagating crack, strains were also measured at points *behind* the crack tip. The geometry of the wide specimen used is shown in Fig. 1; the strain gage locations are schematically shown in Fig. 7. The measured strains, $\epsilon_{\alpha\beta}$, have been normalized relative to $\hat{\epsilon} = \hat{\sigma}/E$ (Fig. 1), i.e., $e_{\alpha\beta} = \epsilon_{\alpha\beta}/\hat{\epsilon}$. The two traces appearing in the record for Gage 4 are the result of a "reproducibility" test. The single arrow on each record indicates the end of the virgin period: R implies rear edge reflection; G implies reflections from the grips.

Discussion. Gages 1 and 3 (e_{11}): one would expect that upon crack initiation a very strong field will be radiated in *all* directions. Surprisingly, a very weak signal is radiated behind the crack tip as evidenced by the signals recorded by Gages 1 and 3. In fact, there is no discernible signal at Gage 1 until about 20 μsec and at Gage 3 until about 40 μsec, which is nearly the entire virgin period. Gages 2 and 4 (e_{11}): here the records are as expected. At Gage 2 there is a rapid initial drop corresponding to the arrival of the dilatational wave front. Subsequently, as the tip moves further away, the slope decreases. The same remarks apply to the record of Gage 4 with the expected difference that the initial drop is more gradual because the gage is located farther away. Gage 5 (e_{11}): throughout the virgin period, $e_{11} \sim 0$. This may be attributed to the large distance (45 mm) between the gage and the notch tip. Gage 6 (e_{22}): again the signal is very much as expected. A rapid initial drop in strain corresponds to the arrival of the dilatational wave front, suggesting that the emitted wave is relatively stronger along the ray $\theta = \pi/2$. Together, these records show that for *the initial motion of a crack, the stress field in the vicinity of the tip is strongly dependent upon the angle* θ. Another interesting observation is that while loading (or tensile) waves of relatively large magnitude ($\Sigma_{\alpha\beta} \sim 1.0$) are propagated ahead of the crack tip (Sections 1 and 2), unloading (or compression) waves of relatively small magnitude ($e_{\alpha\beta} \sim 0.2$) are propagated behind it.

Conclusions

The foregoing investigation of stress waves emitted during fracture and their boundary reflections has led to the following conclusions.

1 For a point on the crack plane, the virgin waves compare remarkably well with the predictions of Freund [2]. The comparison was better than in [1], where the recorded signals also contained the rear edge reflections.

2 At a point away from the crack plane ($x_2 \neq 0$), the complete stress field in its virgin state has been recorded.

3 The reflections from the rear edge are tensile, and their maximum amplitudes $(\Sigma_{\alpha\beta})_{\max} \sim 0.5$.

4 The reflections from the front edge are generally compressive, and their maximum amplitude $(\Sigma_{\alpha\beta})_{\max} \sim 0.5$.

5 At a point on the crack plane and near the front edge, the front edge reflections are compressive and $(\Sigma_{22})_{\max} = 0.75$.

6 For the case of an embedded crack, the stress field scattered by the stationary crack tip is negligibly small for the particular geometrical configuration tested.

7 The waves propagated behind the crack tip are considerably smaller than those propagated ahead of the crack tip.

8 For the initial motion of a crack tip, the stress field radiated behind the crack tip and measured in its immediate vicinity was found to be very small, which is contrary to expectations. It appears, therefore, that the radiated field has very strong angular dependence.

9 Loading waves are propagated ahead of the crack tip, whereas unloading waves are propagated behind the tip.

Acknowledgments

The authors thank Prof. W. E. Jahsman and S. K. Datta for many helpful discussions. Thanks are due to K. Rupp and R. Cowgill for technical assistance, to Nickie Ashley for a careful preparation of the manuscript, and to Dr. Howard Swift of Libbey-Owens-Ford Company for supplying the glass. The encouragement of Dr. Clifford Astill and the financial support of the National Science Foundation under Grant ENG 76-09613 to the University of Colorado is gratefully acknowledged.

References

1 Kinra, V. K., and Bowers, C. L., "Brittle Fracture of Plates in Tension. Stress Field Near the Crack," submitted to the ASME JOURNAL OF APPLIED MECHANICS.

2 Freund, L. B., "Crack Propagation in an Elastic Solid Subjected to General Loading—I. Constant Rate of Extension," *Journal of Mechanics and Physics of Solids*, Vol. 20, 1972, pp. 129–140.

3 Little, R. W., *Elasticity*, Prentice-Hall, Englewood Cliffs, N. J., 1973.

4 Rice, J. R., "Mathematical Analyses in the Mechanics of Fracture," *Fracture. An Advanced Treatise*, ed., Liebowitz H., Vol. 2, Academic Press, New York, 1968, pp. 191–311.

5 Roberts, G. E., and Kaufman, H., *Tables of Laplace Transforms*, W. B. Saunder Company, Philadelphia, 1968, p. 318.

6 Jahnke, E., Emde, F., and Lösch, F., *Tables of Higher Functions*, McGraw-Hill, New York, 1960, p. 26.

7 Kinra, V. K., and Kolsky, H., "The Interaction Between Bending Fractures and the Emitted Stress Waves," *Engineering Fracture Mechanics*, Vol. 9, 1977, pp. 423–432.

8 *Fast Fracture and Arrest*, ASTM STP 627, Hahn, G. T., and Kanninen, M. F., eds., American Society for Testing and Materials, 1977.

APPENDIX

1 $\hat{\sigma}$ changed somewhat from one experiment to another. The terminal crack velocity may also be expected to change accordingly. Since the emitted waves are velocity dependent, the two experiments cannot be considered as exact replicated measurements.

2 A typical oscillographic measurement is in error by about 5 percent; the *difference* of the two experiments would be in error by about 10 percent.

3 The *maximum* deviation of the crack from its assumed straight-ahead path was found to be about one (1) mm. The consequent errors in the measured stresses can be shown to be negligibly small for the most part except near $t = t_c$ where the maximum error was estimated to be about 10 percent.

4 As discussed in *Experimental Procedures*, the time-delay can be determined only to the accuracy of ± 1 μsec. Let $\Sigma_{\alpha\beta}{}^a$ and $\Sigma_{\alpha\beta}{}^b$ denote, respectively, the stresses obtained with specimens (a) and (b) of Fig. 4. A quick examination of these traces reveals that if they are displaced by ± 1 μsec relative to each other, the rear edge reflection, $\Sigma_{\alpha\beta}{}^b - \Sigma_{\alpha\beta}{}^a$, will be significantly affected. (This difficulty led to the following procedure for fixing $t = 0$. For $0 < t < 16.5$ μsec both data are virgin and hence should be identical, except for measurement errors. Choosing $\Sigma_{\alpha\beta}{}^a$ arbitrarily as the reference, $t = 0$ in $\Sigma_{\alpha\beta}{}^b$ was fixed by minimizing the difference between $\Sigma_{\alpha\beta}{}^a$ and $\Sigma_{\alpha\beta}{}^b$ over the duration $0 < t < 16.5$ μsec.)

H. J. Petroski
Mem. ASME

J. L. Glazik[1]
Engineering Mechanics Program,
Reactor Analysis and Safety Division,
Argonne National Laboratory,
Argonne, Ill. 60439

J. D. Achenbach
Professor,
Department of Civil Engineering,
The Technological Institute,
Northwestern University,
Evanston, Ill. 60201
Fellow ASME

Construction of a Dynamic Weight Function From a Finite-Element Solution for a Cracked Beam

An elastodynamic weight function for a cracked beam is shown to be determined by the elastodynamic stress intensity factor corresponding to a single crack-face loading of the beam. This weight function suffices to determine the time-dependent stress intensity factor corresponding to other dynamic loadings of the same cracked beam. The example of a center-cracked pinned-pinned beam serves to illustrate and verify the technique. The weight function is constructed from finite element results for the case of a step pressure distributed uniformly along the beam, and the case of a step load concentrated at the crack plane serves as an illustration of the efficacy of the weight function so constructed.

Introduction

A problem of considerable interest in linear elastic fracture mechanics is the determination of the dynamic stress-intensity factor for a cracked body of finite dimensions which is subjected to time varying loads. Since purely analytical techniques are usually inapplicable to problems concerning finite bodies (whether static or dynamic loads are applied), the major work in this area has been performed using the finite-element method. This form of analysis, however, can have several severe drawbacks which make its widespread use impractical. The large requirements for computer storage and/or running time can be quite prohibitive, especially when performing parametric studies to determine the effects of different loading conditions and crack lengths.

For statically loaded bodies, the weight function technique is an excellent method for determining stress-intensity factors with a minimum of computational effort. Bueckner [1] and Rice [2] have shown that if the displacement field and Mode I stress-intensity factor are known for a symmetrically loaded cracked body, then the stress-intensity factor for the same body under another symmetric load system can be obtained by the evaluation of simple integrals. A computational scheme which eliminates the need for knowledge of the displacement field has been presented by Petroski and Achenbach [3] for edge-cracked bodies.

The elastodynamic counterpart of the Bueckner-Rice weight-function principle has been derived by Freund and Rice [4], but the elastodynamic principle does not appear to have been applied to cracked bodies with finite boundaries. In this paper we demonstrate a technique whereby the principle is applied to the dynamic analysis of cracked beams.

The result of Freund and Rice applies to a linear elastic solid containing a planar crack under conditions of plane strain. The body is assumed to be symmetrical with respect to the crack plane and only loading systems which give rise to Mode I deformation are permitted. For time $t < 0$, the material is stress free and at rest. At time $t = 0$, a traction distributed on the boundary Γ begins to act. If, for a system of reference loads, the elastodynamic stress-intensity factor $k(l;t)$ is known as a function of the crack length parameter l and time t and the displacement $\mathbf{u}(l;\mathbf{x},t)$ is also known on the boundary as a function of l,t and position $\mathbf{x}$, then for any second symmetric system of time-dependent loads, the Laplace transform of the elastodynamic stress-intensity factor can be expressed as

$$\hat{k}^{(2)}(l;p) = \int_\Gamma \hat{\mathbf{T}}^{(2)}(\mathbf{x},p) \cdot \hat{\mathbf{h}}(l;\mathbf{x},p) d\Gamma. \tag{1}$$

The caret herein denotes the Laplace transform with respect to time, and p is the Laplace transform parameter. In equation (1), $\hat{\mathbf{T}}^{(2)}(\mathbf{x},p)$ is the Laplace transform of the traction distribution for the second problem and $\hat{\mathbf{h}}(l;\mathbf{x},p)$ is the transform of a weight function given by

$$\hat{\mathbf{h}}(l;\mathbf{x},p) = \frac{1}{2} H[\hat{k}(l;p)]^{-1} \frac{\partial}{\partial l} \hat{\mathbf{u}}(l;\mathbf{x},p) \tag{2}$$

where the constant H is related to Young's modulus and Poisson's ratio by

$$H = E/(1 - \nu^2). \tag{3}$$

Equation (1) can be used in two ways. In the first application, $\hat{\mathbf{T}}^{(2)}(\mathbf{x},p)$ is the actual surface traction, which is often zero on the crack faces. For the reference problem, the displacement $\hat{\mathbf{u}}(l;\mathbf{x},p)$ must be known at points where the surface tractions of the second problem

[1] Presently, Bell Telephone Laboratory, Naperville, Ill. 60540.

Contributed by the Applied Mechanics Division and presented at the Winter Annual Meeting, New York, N. Y., December 2–7, 1979, of THE AMERICAN SOCIETY OF MECHANICAL ENGINEERS.

Discussion on this paper should be addressed to the Editorial Department, ASME, United Engineering Center, 345 East 47th Street, New York, N. Y. 10017, and will be accepted until June 1, 1980. Readers who need more time to prepare a discussion should request an extension from the Editorial Department. Manuscript received by ASME Applied Mechanics Division, December 1978; final revision, July, 1979. Paper No. 79-WA/APM-37.

are applied. In the second application, which exploits the principle of superposition, one first computes the stresses across the crack plane in an uncracked body subjected to the surface tractions of the second problem. The crack faces of the cracked body are then loaded with equal but opposite surface tractions. The displacement $\hat{\mathbf{u}}(l;\mathbf{x},p)$ then needs to be known only on the crack faces of the reference problem if the body is subject to the same displacement boundary conditions in both cases.

Although equation (1) is conceptually very interesting, it is not practically useful in its present form. For the reference problem, both $k(l;t)$ and $\mathbf{u}(l;\mathbf{x},t)$ must be computed, e.g., by the finite-element method. The Laplace transform must be taken, the integral in equation (1) must be evaluated, and, finally, the inverse Laplace transform must be calculated. This sequence of steps must be performed numerically and can give rise to accumulative errors, and an accurate description of the crack-opening displacement $\mathbf{u}(l;\mathbf{x},t)$ might require a very refined finite-element grid.

Our purpose here is to present significant simplifications to this procedure for beamlike bodies with edge cracks. Finite-element results suggest that the time-dependence of the crack opening displacement may be taken as approximately the same as that of the elastodynamic stress-intensity factor. In addition, the spatial variation of the crack opening displacement appears to be proportional to the one for the corresponding static problem. This suggests the use of the weight-function technique with crack face loading (the second application of equation (1) mentioned earlier). These assumptions, along with the representation for the Bueckner-Rice weight function made in reference [3], enable one to limit the input from the reference problem to simply the elastodynamic stress-intensity factor. The only other pieces of information necessary are the stresses across the crack plane in an uncracked beam subjected separately to the surface tractions of the reference and second problems.

To illustrate our procedure for applying equation (1), we consider two step loadings of a beam with an edge crack. In the reference problem, the beam is loaded uniformly and the elastodynamic stress-intensity factor is determined for different crack lengths by the finite-element method. In the second problem, a point load is applied at the crack plane and the elastodynamic stress-intensity factor is computed both by the weight function techniques of this paper and by the finite-element method. The results show excellent agreement. It is also demonstrated that the technique can easily accommodate an input of discrete values from finite-element computations.

Analytical Development

For the case of crack-face loading (to which all other loading conditions can be reduced by appealing to the principle of linear superposition), when both the reference and second problems involve the same displacement boundary conditions, equation (1) can be rewritten as an integral over the crack face only, yielding

$$\hat{k}^{(2)}(l;p) = H[\hat{k}(l;p)]^{-1} \int_0^l \hat{\sigma}^{(2)}(\gamma,p) \frac{\partial}{\partial l} \hat{u}(l;\gamma,p) d\gamma \tag{4}$$

where H is given by equation (3). In equation (4), γ and l are the dimensionless quantities

$$\gamma = \xi/d \quad \text{and} \quad l = a/d \tag{5a,b}$$

where ξ is a rectangular coordinate with origin at the crack mouth, d is a characteristic dimension of the body, e.g., its thickness, and a is the physical crack length. In equation (4), $\hat{u}(l;\gamma,p)$ is the crack-face displacement normal to the crack plane and $\hat{\sigma}^{(2)}(\gamma,p)$ is the negative of the normal stress across the plane of the crack when the uncracked body is loaded with the surface tractions of the second problem. If $\hat{\sigma}^{(2)}(\gamma,p)$ is taken to be the same as that for the reference problem, equation (4) reduces to the following identity:

$$[\hat{k}(l;p)]^2 = H \int_0^l \hat{\sigma}(\gamma,p) \frac{\partial}{\partial l} \hat{u}(l;\gamma,p) d\gamma. \tag{6}$$

For the elastodynamic reference problem, we can write

$$k(l;t) = K(l) f_k(l;t) \tag{7}$$

where $K(l)$ is the stress-intensity factor for the corresponding static problem. For the cracked-beam problems we will consider, we make the following assumptions:

$$u(l;\gamma,t) = U(l;\gamma) f_u(l;t) \tag{8}$$

$$f_u(l;t) \simeq f_k(l;t) \tag{9}$$

In equation (8), $U(l;\gamma)$ is the crack opening displacement for the corresponding static problem. These assumptions are valid for all beamlike structures in which the vibrational response is dominant. Any diffracted waves from the crack tip will only add slight perturbations to the basic modal response. Since these wave propagation effects are minimal, large time steps may be used in the finite-element calculations without fear of filtering out significant contributions.

For edge cracks, the static stress-intensity factor can generally be expressed in the form

$$K(l) = g_K(l) H d^{1/2} \tag{10}$$

and the corresponding crack opening displacement may be written

$$U(l;\gamma) = g_U(l;\gamma) d. \tag{11}$$

The static equivalent of equation (4) is

$$g_K{}^{(2)}(l) = [g_K(l)]^{-1} \int_0^l \Sigma^{(2)}(\gamma) \frac{\partial}{\partial l} g_U(l;\gamma) d\gamma \tag{12}$$

and the dimensionless functions $g_K(l)$ and $g_U(l)$ are related by the static equivalent of equation (6) (cf. equation (3) of reference [3]),

$$[g_K(l)]^2 = \int_0^l \Sigma(\gamma) \frac{\partial}{\partial l} g_U(l;\gamma) d\gamma \tag{13}$$

where $H\Sigma(\gamma)$ is the static stress across the plane of the crack in the uncracked body. As shown in reference [3], for given $g_K(l)$ and $\Sigma(\gamma)$ this relation allows the determination of the following approximate representation for $g_U(l;\gamma)$

$$g_U(l;\gamma) = 2(2/\pi)^{1/2} g_K(l)(l-\gamma)^{1/2} + G(l) l^{-1/2} (l-\gamma)^{3/2} \tag{14}$$

where

$$G(l) = [I_1(l) - 2(2/\pi)^{1/2} g_K(l) I_2(l)] l^{1/2} / I_3(l) \tag{15}$$

$$I_1(l) = \int_0^l [g_K(\tau)]^2 d\tau \tag{16}$$

$$I_2(l) = \int_0^l \Sigma(\gamma)(l-\gamma)^{1/2} d\gamma \tag{17}$$

$$I_3(l) = \int_0^l \Sigma(\gamma)(l-\gamma)^{3/2} d\gamma \tag{18}$$

By employing the well-known limiting value

$$g_K(l) = 1.1215\, \Sigma(0) \sqrt{\pi l} \quad \text{as} \quad l \to 0 \tag{19}$$

and using the mean-value theorem to evaluate the integrals (16)–(18), $G(0)$ may be determined to be

$$G(0) = -0.34758\, \Sigma(0) \tag{20}$$

Hence $g_U(l;\gamma)$ is known completely from the quasi-static stress-intensity factor $g_K(l)$ and corresponding crack-face loading for the reference problem. The weight function may now be derived.

Inversion of the Transformed Equations

Assumptions (8) and (9) may be employed to provide the following expression for $\partial \hat{u}/\partial l$ in transform space:

$$\frac{\partial \hat{u}}{\partial l} = \hat{f}_k(l;p) \frac{\partial}{\partial l} U(l;\gamma) + \frac{\partial}{\partial l} \hat{f}_k(l;p) U(l;\gamma). \tag{21}$$

If the order of spatial integration and inversion of the Laplace transform can be interchanged, then we may formally invert equation (4) after substituting equation (21). This formal inversion will always be possible if the product

$$\hat{\sigma}^{(2)}(\gamma;p)\,\frac{\partial}{\partial l}\,\hat{u}(l;\gamma,p)$$

is separable into a sum of products of functions of γ only and functions of p only. The representation (21) shows this separation to be the case for $\partial\hat{u}/\partial l$.

When $\sigma^{(2)}(\gamma,t)$ is known only at discrete points, as is the case when a finite-element solution is the source of the stress field, then at each discrete point $\gamma_n = (n - 1/2)\Delta\gamma$, where $\Delta\gamma$ is the element length and $N(l)\Delta\gamma = l$, we have for $n = 1, 2, 3, \ldots, N$

$$\sigma^{(2)}(\gamma_n,t) = \sigma_n{}^{(2)}(t) \tag{22}$$

a function of time only. Hence for each γ_n we have the integrand of equation (4) represented properly for formal inversion of the Laplace transform. Using a mean-value theorem and the convolution theorem then gives

$$k^{(2)}(l;t) = d^{1/2}[g_K(l)]^{-1}\sum_{n=1}^{N(l)}[J_{1n}(l;t) + J_{2n}(l;t)] \tag{23}$$

where

$$J_{1n}(l;t) = \sigma_n{}^{(2)}(t)\int_{(n-1)\Delta\gamma}^{n\Delta\gamma}\frac{\partial}{\partial l}g_U(l;\gamma)d\gamma \tag{24}$$

$$J_{2n}(l;t) = \int_{(n-1)\Delta\gamma}^{n\Delta\gamma}g_U(l;\gamma)\int_0^t\sigma_n{}^{(2)}(s)F(t-s)ds\,d\gamma \tag{25}$$

and where $F(t)$ is the inverse Laplace transform

$$F(t) = \mathcal{L}^{-1}\left\{\frac{\partial}{\partial l}\hat{f}_k(l;p)/\hat{f}_k(l;p)\right\}. \tag{26}$$

In these expressions $g_U(l;\gamma)$ is given by equation (14), $f_k(l;t)$ is known from the reference problem, and the stress distribution $\sigma_n{}^{(2)}(t)$ is determined from a finite-element analysis of the uncracked body subjected to the load system of the second problem.

The ideal reference problem would have the body loaded with only a uniform crack-face pressure, so that the integrations (17) and (18) may be determined in closed form. However, when a finite-element program provides the solution in the reference problem, it is more convenient to not load the crack surfaces, and the case of a uniform step pressure applied to the boundary of the beam initially at rest is a logical choice. The resulting vibrational response of beamlike bodies dominates the response and generally has the approximate form

$$f_u(l;t) = f_k(l;t) = 1 - \cos[\omega(l)t] \tag{27}$$

where the frequency ω is a function of crack length. Any wave propagation effects that might be superimposed on this response may be ignored as a good first approximation, but for geometries other than beams a more complicated representation may be necessary.

At this point the finite-element results may be used directly to evaluate the integrals in equations (24) and (25) as shown in the next section.

There is a wide class of vibration-like problems for which the inversion of the Laplace transform may be performed analytically, and only the spatial integrations need be done numerically. These are problems for which the stress response for the second problem may be represented by a Fourier series of L terms

$$\sigma^{(2)}(\gamma,t) = \sum_{m=0}^{L}[A_m{}^{(2)}(\gamma)\cos\omega_m t + B_m{}^{(2)}(\gamma)\sin\omega_m t] \tag{28}$$

where $\omega_0 \equiv 0$ for notational convenience. Taking the Laplace transforms of the representations (27) and (28) and employing (7) and (8) in equation (4) gives

$$\begin{aligned}\hat{k}^{(2)}(l;p) = \frac{Hd}{K(l)}\sum_{m=0}^{L}\int_0^l [A_m{}^{(2)}(\gamma)\frac{\partial}{\partial l}g_U(l;\gamma)p(p^2+\omega_m{}^2)^{-1}\\ + 2A_m{}^{(2)}(\gamma)g_U(l;\gamma)\omega^{-1}\omega' p^3(p^2+\omega^2)^{-1}(p^2+\omega_m{}^2)^{-1}\\ + B_m{}^{(2)}(\gamma)\frac{\partial}{\partial l}g_U(l;\gamma)\omega_m(p^2+\omega_m{}^2)^{-1}\\ + 2B_m{}^{(2)}(\gamma)g_U(l;\gamma)\omega_m\omega^{-1}\omega' p^2(p^2+\omega^2)^{-1}(p^2+\omega_m{}^2)^{-1}]d\gamma\end{aligned} \tag{29}$$

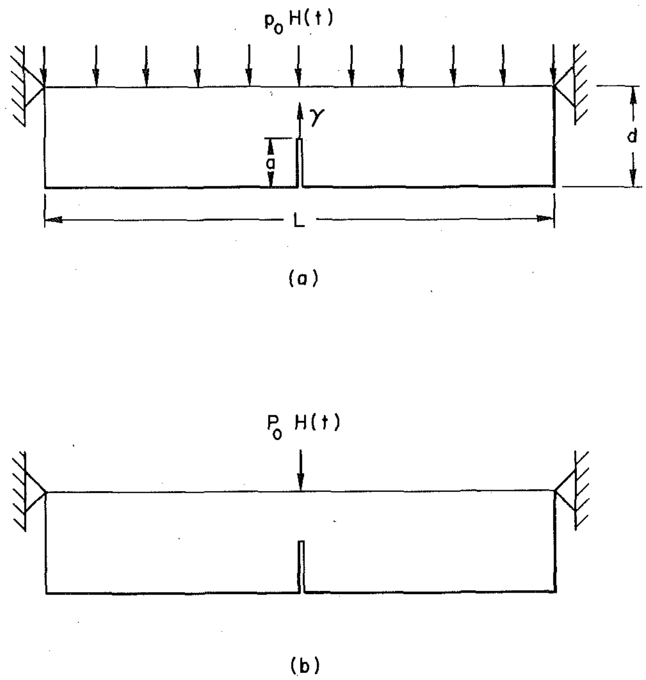

Fig. 1 Geometry and loading of (*a*) the reference problem and (*b*) the second problem employed as examples

where $\omega' = d\omega/dl$. This may now be inverted to give

$$\begin{aligned}k^{(2)}(l;t) = \frac{Hd}{K(l)}\sum_{m=0}^{L}\Bigg\{\frac{2\omega'}{\omega(1-r_m{}^2)}[G_m{}^{(2)}(l)\cos\omega t\\ + r_m H_m{}^{(2)}(l)\sin\omega t]\\ + \left[\frac{\partial G_m{}^{(2)}(l)}{\partial l} - \frac{2\omega' r_m{}^2}{\omega(1-r_m{}^2)}G_m{}^{(2)}(l)\right]\cos\omega_m t\\ + \left[\frac{\partial H_m{}^{(2)}(l)}{\partial l} - \frac{2\omega' r_m{}^2}{\omega(1-r_m{}^2)}H_m{}^{(2)}(l)\right]\sin\omega_m t\Bigg\}\end{aligned} \tag{30}$$

where

$$G_m{}^{(2)}(l) = \int_0^l A_m{}^{(2)}(\gamma)g_U(l;\gamma)d\gamma \tag{31}$$

$$H_m{}^{(2)}(l) = \int_0^l B_m{}^{(2)}(\gamma)g_U(l;\gamma)d\gamma \tag{32}$$

$$r_m = r_m(l) = \omega_m/\omega(l). \tag{33}$$

Examples of Technique

To illustrate the practical application of the procedures just outlined, we consider the plane-strain elastodynamic response of an edge-cracked beam which is rigidly supported at two points as shown in Fig. 1. The reference problem consists of loading the upper surface of the beam with a uniform pressure $p_0H(t)$, where $H(t)$ is the Heaviside step function. In the second problem, which is depicted in Fig. 1(*b*), a concentrated load $P_0H(t)$ is applied to the upper surface of the beam in the crack plane. For the finite-element calculations, the following values were chosen:

d = 2.54 cm (1 in.)
L = 12.7 cm (5 in.)
p_o = 6.89 MPa (1000 lb/in.^{2})
P_o = 1750 N/cm (1000 lb/in.)
E = 207 GPa (3.0×10^7 lb/in.^{2})
ρ = 0.0298 g/cm^3 (mass density = 0.00075 lb/in.^{3})
ν = 0.3.

One half of the symmetric beam was modeled with a 10 by 25 element grid of 0.254 cm sq finite elements. In order to obtain an estimate of

Table 1 Dimensionless quasi-static stress-intensity factors for the reference problem

ℓ	0.1	0.2	0.3	0.4	0.5	0.6	0.7	0.8
$K/p\sqrt{\pi a}$	14.23	14.75	16.02	18.27	22.04	28.56	40.97	69.50

Table 2 Dimensionless quasi-static stresses across crack plane for the *second problem*

n	1	2	3	4	5	6	7	8	9	10
$\Sigma^{(2)} \times 10^4$	1.542	1.220	0.935	0.672	0.423	0.180	−0.065	−0.329	−0.637	−1.629

Table 3 Dimensionless quasi-static stress-intensity factors for the second problem

	$K^{(2)}h/P_o\sqrt{\pi a}$		
ℓ	Finite Element	Eq. (34)	Eq. (12)
0.1	5.85		5.64
0.2	5.96	5.97	5.98
0.3	6.42		6.39
0.4	7.29	7.28	7.28
0.5	8.78		8.77
0.6	11.38	11.35	11.36
0.7	16.34		16.38
0.8	27.78	27.60	27.15

Table 4 Values of ω for the reference problem

ℓ	0	0.2	0.4	0.6	0.8
ω(rad/sec)	29361	27083	21969	14960	7480

the accuracy to be expected from the weight function technique, we first consider the static problem.

Static Problems. The finite-element computer code CHILES [5] was acquired for the static analysis of the reference and test problems. The CHILES program, which utilizes a singular element formulation to represent the state of stress immediately surrounding the crack tip, is a two-dimensional solid finite-element code in which linear isotropic stress-strain material properties and small-strain theory are assumed. Isoparametric quadrilateral elements are employed, and compatibility between singular and ordinary elements is maintained by transition elements, thereby ensuring monotone convergence. The singular element is constructed by enriching a bilinear displacement assumption with only the first-order terms of the asymptotic near-tip field which give the proper singularity at the crack tip. From studies conducted with several test problems, it appears that CHILES gives excellent results except for very deep crack situations in which the uncracked ligament is represented by only a few elements. For all cases, the finite-element results tend to underestimate the exact solution with the error increasing with crack depth.

Table 1 shows values of the stress-intensity factor computed by the finite-element method for the reference problem and Table 2 gives the crack-plane normal tractions corresponding to the second problem. One can observe from this latter table that $\Sigma^{(2)}(\gamma)$ is computed only at discrete points, viz., the centroids of the finite elements adjoining the crack plane. The crack must extend over an integer number N of finite elements, and, therefore, $\Sigma^{(2)}(\gamma)$ is known only at N points along the crack surface. In the present problem there are 10 elements across the thickness and thus N ranges from one to nine. Using the notation $\Sigma_n{}^{(2)}$ to denote $\Sigma^{(2)}(\gamma)$ at position $\gamma = (n - 1/2)\Delta\gamma$, corresponding to element n, the integration in equation (12) can be approximated by the following summation:

$$g_K{}^{(2)}(l) = [g_K(l)]^{-1} \sum_{n=1}^{N} a_n \Sigma_n{}^{(2)} \tag{34}$$

where

$$a_n = \int_{(n-1)\Delta\gamma}^{n\Delta\gamma} \frac{\partial}{\partial l} g_U(l;\gamma) d\gamma \tag{35}$$

and $g_U(l;\gamma)$ is given by equation (14). The integration in equation (35) can thus be carried out semianalytically. The computations of $g_K{}^{(2)}(l)$ and the subsequent comparison with independent finite-element results for $K^{(2)}(l)$ provide a good check on the crack-opening representation (14) and on the discretization of the integration over γ introduced in equation (34). The results are listed in Table 3. The agreement between weight-function and finite-element results is seen to be very satisfactory.

An alternative procedure for computing $K^{(2)}(l)$ employs least-squares polynomial fits of the finite-element data to represent $K(l)$ and $\Sigma(\gamma)$ for the reference problem. Then equations (16)–(18) may be integrated numerically to determine values of the function $G(l)$, which also may be fit with a polynomial. If the polynomial representations for $K(l)$ and $G(l)$ are well behaved, they may be differentiated term by term to provide the weight function for equation (12). A polynomial representation for $\Sigma^{(2)}(\gamma)$ then enables one to integrate equation (12) numerically to obtain the corresponding stress-intensity factor $K^{(2)}(l)$. The results of this technique are also good, as shown in Table 3.

Dynamic Problems. In order to provide input information for and verification of the weight-function technique under dynamic loading conditions, the CHILES code was modified. The program was given dynamic capabilities through the inclusion of a consistent mass matrix for the singular as well as transition and ordinary finite elements. The time integration scheme employed for the equations of motion was Anderson and Gupta's [6] version of Newmark's β method. This algorithm calculates the displacement increment over the time steps Δt rather than the total displacement at the end of the time step. Several other minor programming changes were necessary to create an efficient code, and the program was then verified by several test problems. The same finite-element mesh as for the static analysis was employed to handle the step loading conditions. Time steps of 10 μs were used in order to pick up all significant modes of response. For the reference problem, the elastodynamic stress-intensity factor as a function of l and t is shown in Fig. 2, where the symbols represent the finite-element results.

Fig. 2 suggests that the representation given in equation (27), and shown here as a solid curve, may be assumed for $f_u(l;t)$ and $f_k(l;t)$, where $\omega(l)$ may be estimated from the maxima or minima of the finite-element data. Table 4 lists values of $\omega(l)$ used. The value of $\omega(0)$ was estimated from the finite-element results for the uncracked beam.

First we shall describe a technique that utilizes the finite-element results directly. Taking the Laplace transform of equation (27) yields

$$\hat{f}_k(l;p) = [\omega(l)]^2 p^{-1}\{p^2 + [\omega(l)]^2\}^{-1} \tag{36}$$

Employing equation (36), the inverse Laplace transform indicated by equation (26) can be evaluated

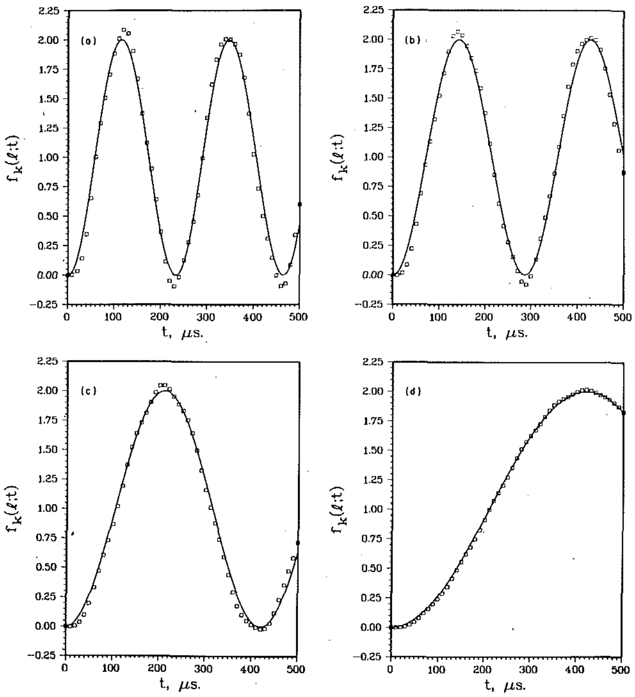

Fig. 2 Normalized stress-intensity factor $f_k(l;t) = k(l;t)/K(l)$ as a function of time for the reference problem for cases (a) $l = 0.2$, (b) $l = 0.4$, (c) $l = 0.6$, (d) $l = 0.8$. Data points are finite-element results; curves are approximations employed in constructing the weight function.

$$F(t) = 2[\omega(l)]^{-1}\omega'(l)\delta(t) - 2\omega'(l)\sin[\omega(l)t] \tag{37}$$

With equation (37), the expression for $J_{2n}(l;t)$, equation (25), reduces to

$$J_{2n}(l;t) = 2[\omega(l)]^{-1}\omega'(l)J_{3n}(l;t) - 2\omega'(l)J_{4n}(l;t) \tag{38}$$

where

$$J_{3n}(l;t) = \sigma_n{}^{(2)}(t)\int_{(n-1)\Delta\gamma}^{n\Delta\gamma} g_U(l;\gamma)d\gamma \tag{39}$$

$$J_{4n}(l;t) = \int_{(n-1)\Delta\gamma}^{n\Delta\gamma} g_U(l;\gamma)\int_0^t \sigma_n{}^{(2)}(s)\sin[\omega(l)(t-s)]ds\,d\gamma \tag{40}$$

The integrations in (24), (39), and (40) may now be carried out semianalytically. If we use the notation

$$\sigma_{mn}{}^{(2)} = \sigma_n{}^{(2)}(m\Delta t) \tag{41}$$

where $m = 0, 1, 2, \ldots, M$, and $M\Delta t = t$, then the sums of the integrals in equations (24), (39), and (40) may be approximated by

$$J_1(l;t) = \sum_{n=1}^{N} J_{1n}(l;t) = \sum_{n=1}^{N} a_n\sigma_n{}^{(2)}(t) \tag{42}$$

$$J_3(l;t) = \sum_{n=1}^{N} J_{3n}(l;t) = \sum_{n=1}^{N} b_n\sigma_n{}^{(2)}(t) \tag{43}$$

$$J_4(l;t) = \sum_{n=1}^{N} J_{4n}(l;t) = \sum_{n=1}^{N} a_n \sum_{m=1}^{M} \frac{1}{2}(\sigma_{mn-1}{}^{(2)} + \sigma_{mn}{}^{(2)})\alpha_m \tag{44}$$

where a_n is defined by equation (35), and

$$b_n = \int_{(n-1)\Delta\gamma}^{n\Delta\gamma} g_U(l;\gamma)d\gamma \tag{45}$$

$$\alpha_m = \int_{(m-1)\Delta t}^{m\Delta t} \sin[\omega(l)(M\Delta t - s)]ds$$

and, using equation (38), $k^{(2)}(l;t)$ follows from equation (23) as

$$k^{(2)}(l;t) = d^{1/2}\{J_1(l;t) + 2[\omega(l)]^{-1}\omega'(l)J_3(l;t) - 2\omega'(l)J_4(l;t)\}/g_K(l). \tag{46}$$

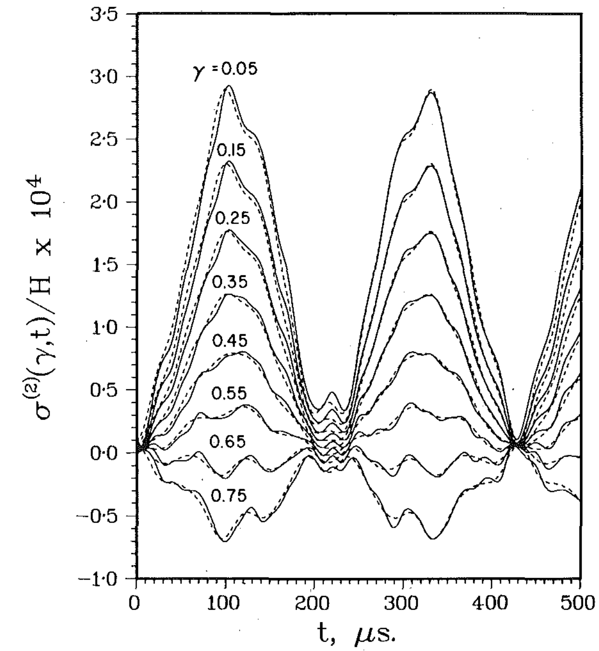

Fig. 3 Dimensionless stresses across the plane under the load as a function of time for the uncracked beam loaded as in the second problem. Solid curves are finite-element results; dashed curves are the Fourier representations employed.

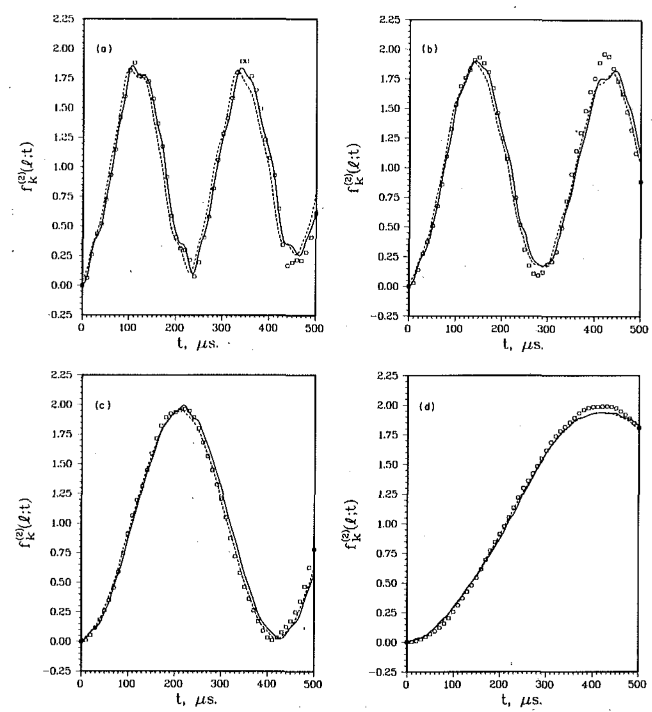

Fig. 4 Normalized stress-intensity factor as a function of time for the second problem for cases (a) $l = 0.2$, (b) $l = 0.4$, (c) $l = 0.6$, (d) $l = 0.8$. Data points are finite-element results; the curves are weight-function results. The solid curve results from using finite-element stresses directly; the dashed curve results from using the Fourier representations of Fig. 3.

The second technique employs the Fourier series representation (28) for the stress field of problem 2, which is shown in Fig. 3. This figure also shows the approximation to the stress field given by a three-term (plus one constant term) Fourier cosine series. The integrations (31) and (32) were carried out numerically and $k^{(2)}(l;t)$ was determined from equation (30).

The behavior of the stress-intensity factor for the second problem as predicted by the weight-function analyses is compared in Fig. 4 with the finite-element results. In this figure, the dashed curves represent the formulations expressed in equation (30), while the solid curves represent that in equation (46). Both predictions are in good agreement with each other and with the finite-element solution. The differences that show up may be explained as due to several causes.

The principal reason that the weight-function results fall short of the peaks and do not drop as low as the valleys of the finite-element results may be attributed to this same inadequacy in the approximation of the reference problem response by the simple expression for $f_k(l;t)$ given by equation (27) and plotted in Fig. 2. Since this representation for f_k was chosen precisely for its simplicity and the resulting simplification of the derivation of the weight function, it was not felt a better fit was necessary or desirable. The maximum error in the approximation of f_k is less than 5 percent at the first peak, and this error decreases with crack depth.

The differences in the results of the two weight-function formulations may be attributed to the manner in which the stresses $\sigma^{(2)}(\gamma;t)$ of the second problem are used. In the formulation which uses the finite-element results directly, there is no alteration of the stress field represented except insofar as the integration scheme uses mean stress values at discrete time steps only. The second formulation, which fits the finite-element stresses with a few Fourier terms does alter the stress field slightly, as exhibited in Fig. 3. We see in this figure that the Fourier representation gives a nonzero stress at zero time, gives lower stresses at the first peak, and initially leads the finite-element stress field in time. These shortcomings of the representation are reflected in the stress-intensity factor response predicted for the second problem. These predictable shortcomings may be removed by using a closer Fourier representation for the stress field $\sigma^{(2)}(\gamma;t)$.

Conclusion

We have demonstrated the efficacy of a dynamic weight-function technique that provides an efficient means of extending a single set of finite-element results for a cracked beam to other dynamic loading conditions of the same cracked beam. The simplicity of the weight-function technique and the accuracy of its predictions depend primarily upon the wise choice and careful modeling of the reference problem from which the weight function is constructed.

Acknowledgment

This work was performed under the Engineering Mechanics Program of the Reactor Analysis and Safety Division, Argonne National Laboratory, and was supported by the U. S. Department of Energy.

References

1 Bueckner, H. F., "A Novel Principle for the Computation of Stress Intensity Factors," *Zeitschrift für angewandte Mathematik und Mechanik*, Vol. 50, 1970, pp. 529–546.

2 Rice, J. R., "Some Remarks on Elastic Crack-Tip Stress Fields," *International Journal of Solids and Structures*, Vol. 8, 1972, pp. 751–758.

3 Petroski, H. J., and Achenbach, J. D., "Computation of the Weight Function from a Stress Intensity Factor," *Engineering Fracture Mechanics*, Vol. 10, 1978, pp. 257–266.

4 Freund, L. B., and Rice, J. R., "On the Determination of Elastodynamic Crack-Tip Stress Fields," *International Journal of Solids and Structures*, Vol. 10, 1974, pp. 411–417.

5 Benzley, S. E., and Beisinger, Z. E., "CHILES—A Finite Element Computer Program That Calculates the Intensities of Linear Elastic Singularities," Report SLA-73-0894, Sandia Laboratories, Albuquerque, 1973.

6 Anderson, J. C., and Gupta, R. P., "Earthquake Resistant Design of Unbraced Frames," *Journal of the Structural Division, Transactions of the ASCE*, Vol. 98, 1973, pp. 2523–2539.

K. J. Chang
Assistant Professor of Engineering Mechanics,
Senior Research Investigator of Rock Mechanics
and Explosives Research Center,
University of Missouri-Rolla,
Rolla, Mo. 65401
Assoc. Mem. ASME

H.-C. Wu
Associate Professor,
Division of Materials Engineering,
University of Iowa,
Iowa City, Iowa 52242
Mem. ASME

Angled Elliptic Notch Problem Under Biaxial Loading

The strain failure criterion proposed by the second author is applied to obtain general solutions for the angled elliptic notch problem subject to uniform biaxial loading. The solutions can be reduced to those for uniaxial tension, uniaxial compression, or pure shear as special cases. The solution for the case of pure shear is compared with experimental data found in literature. It is remarked that the present theory involves material parameters and predicts that fracture behavior is dependent on materials being investigated.

Introduction

The "angled elliptic notch problem" (also known as the "angled crack problem") has received extensive attention from investigators in the field of fracture mechanics for many years. In this problem a small traction-free elliptic notch or open crack, in the middle of a thin isotropic, homogeneous, linear elastic plate or cylindrical shell, is subjected to uniformly distributed inplane edge load. The load at which new cracks are initiated and the direction of the crack initiation are of interest in this investigation.

Both experimental and analytical work on this subject can be found in the literature [1–28]. Uniaxial *compressive* experiments were performed by Brace and Bombolakis [3] and Hoek and Bieniawski [4] on glass plates with an angled slit crack, and by Cotterell [6] on plates of annealed glass with an elliptical notch. Experiments in uniaxial *tension* were conducted by Erdogan and Sih [1] and Williams and Ewing [7] on PMMA, Palaniswamy and Knauss [24] on toluene swollen polyurethane, and by Pook [5] on aluminum plates with a slit crack; and by Wu, et al. [18], on PMMA plates with an angled elliptical notch. Furthermore, in the study of angled crack extension under pure shear, Ewing and Williams [11] presented experimental results obtained from torsionally loaded thin-walled cylindrical PMMA tubes with an angled slit crack; and Liu [27] performed tests on center-cracked aluminum panels with a special picture frame jig.

Theoretical work abounds on this subject, each using a different assumption and a different criterion for fracture. Erdogan and Sih [1] proposed that "the crack will start to grow from the tip in the direction along which the tangential stress σ_θ is maximum and the shear stress $\tau_{\gamma\theta}$ is zero" (the slit model of maximum stress criterion). They analyzed the problem under a uniform uniaxial tensile load. The implication resulting from the inclusion of higher-order terms in the eigenfunction expansion of the stress components near the crack tip on the maximum stress criterion was discussed by Williams and Ewing [7], Finnie and Saith [8], and Ewing and Williams [9]. McClintock [2] discussed Erdogan and Sih's [1] paper considering maximum stress on the boundary of the elliptic notch as a criterion (the elliptic model of maximum stress criterion). Cotterell [6] studied the problem under uniform compression utilizing the maximum stress criterion.

Sih [12, 13], Kipp and Sih [15], and Kassir and Sih [16] introduced the strain-energy density theory (the S-theory) and studied both tension and compression cases. Later, Ewing and Williams [11] investigated the pure shear case utilizing the maximum stress criterion as well as the S-theory. Wang [19] modified the S-theory and examined the tension case. Eftis and Subramonian [20] applied the maximum stress criterion of Erdogan and Sih [1] to the study of the biaxial tension case. Labourdette and Pellas [21] proposed the stress gradient criterion which is based on an energy balance, Tirosh [22] employed the energy-momentum tensor criterion, and both examined the tension case of the problem. Wu [23] and Palaniswamy and Knauss [24] applied the maximum-energy-release-rate criterion to the investigation of both tension and compression cases. Moreover, Coughlan and Barr [25] and Ingraffea [26] have utilized finite-element technique in the study of the crack initiation problem.

Recently, the present authors have looked into the angled elliptic notch problem [17, 18, 28]. Experimentally, Wu, et al. [18], have obtained data on elliptically notched PMMA plate under uniaxial tension. Theoretically, Wu and Chang [28] have applied the strain failure criterion proposed by Wu [29] combined with the concept of an outer contour of the critical neighborhood (or an effective notch) in their studies of the problem under both tension and compression. Their results have shown good correlation with experimental data presented by Wu, et al. [18], and Cotterell [6]. In the present paper, the authors apply Wu's [29] strain failure criterion to analyze the angled elliptic notch problem under biaxial tension and compression. Discussion of the present analytical results in comparison with those of Ewing and Williams [11], Eftis and Subramonian [20], and Liu [27] is also presented.

Contributed by the Applied Mechanics Division for publication in the JOURNAL OF APPLIED MECHANICS.

Discussion on this paper should be addressed to the Editorial Department, ASME, United Engineering Center, 345 East 47th Street, New York, N. Y. 10017, and will be accepted until June 1, 1980. Readers who need more time to prepare a discussion should request an extension from the Editorial Department. Manuscript received by ASME Applied Mechanics Division, November, 1978; final revision, August, 1979.

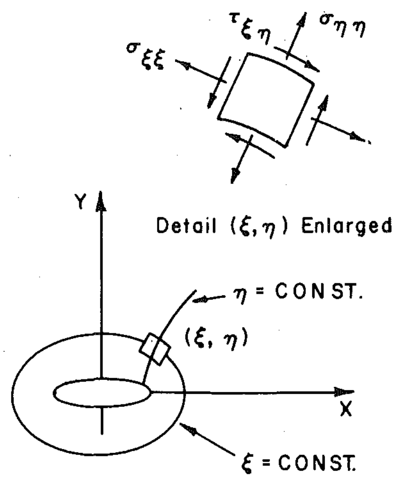

Fig. 1 The elliptic coordinate system

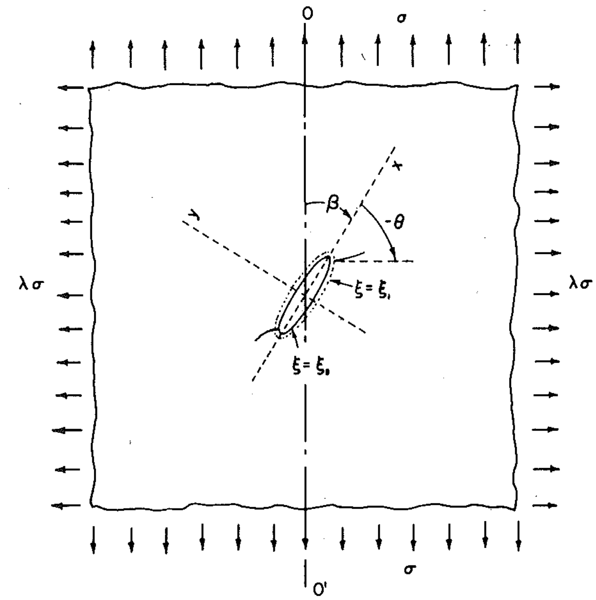

Fig. 2 Plate with an angled elliptic notch under uniformly distributed biaxial edge loads

Strain Failure Criterion

The strain failure criterion proposed by Wu [29] can be stated as: *the failure of a macroelement in a continuum is governed by a set of scalar failure criteria and a set of vector quantities which determine, respectively, the failure conditions and the directions of the crack or failure plane. For brittle fracture, which is the nature of the initial crack extension of the angled elliptic notch problem [6, 18], the criterion assumes that the material fails at the point when a scalar-valued function of the strain tensor, $\boldsymbol{\epsilon}$, reaches a critical value κ^2, i.e., when*

$$f(\boldsymbol{\epsilon}) = \kappa^2 \tag{1}$$

and the crack plane is normal to the direction of the maximum tensile strain at the point.

In the case of an isotropic material under small deformation, $f(\boldsymbol{\epsilon})$ must be a function of the principal invariants of $\boldsymbol{\epsilon}$ [32]. Using Taylor's expansion and ignoring higher-order terms, equation (1) may be written as

$$m\epsilon_{\rm I} + n\epsilon_{\rm I}^2 + \bar{\epsilon}_{\rm II} = \kappa^2 \tag{2}$$

in which m, n, and κ are material constants to be determined by experiments [29]; $\epsilon_{\rm I}$ and $\epsilon_{\rm II}$ are the first and second principal invariants of the strain tensor, $\boldsymbol{\epsilon}$; $\bar{\epsilon}_{\rm II} \equiv \epsilon_{\rm I}^2 - 2\epsilon_{\rm II}$ is the equivalent strain. It is remarked that failure of materials is thus dependent upon the equivalent strain and the hydrostatic strain.

It is convenient to express the foregoing criterion in terms of stresses. In the case of linear elasticity, equation (2) reduces to

$$\frac{1}{K}\left\{\frac{\sigma_{\rm I}}{\sigma_T}\right\}^2 + \frac{K-1}{K}\left\{\frac{\sigma_{\rm I}}{\sigma_T}\right\} - \frac{1}{{\tau_c}^2}\sigma_{\rm II} = 1 \tag{3}$$

in which $\sigma_{\rm I}$ and $\sigma_{\rm II}$ are the first and second principal invariants of the stress tensor, $\boldsymbol{\sigma}$. The constant $K = \sigma_c/\sigma_T$ is greater than 1 for brittle materials; σ_T and σ_c are, respectively, the tensile and compressive strength for brittle fracture of a macroelement;[1] and τ_c is the critical shear stress at brittle fracture of a thin-walled cylinder under torsion. These constants replacing m, n, and κ of equation (2) represent material properties and are considered known in the analysis of the angled elliptic notch problem. The relations between m, n, κ and σ_T, τ_c, σ_c have been derived by Wu [29].

The constants σ_T, σ_c, and τ_c are easily determined for materials that exhibit linearly elastic behavior prior to fracture in tension. For materials which experience yielding prior to fracture in tension, such as cast iron, equation (3) is then not valid. A suitable constitutive equation needs to be substituted into equation (2) to obtain a fracture criterion in stress. The latter has been discussed by Valanis and Wu [33, 34].

The Angled Elliptic Notch Problem

In the present work, the elliptic coordinates shown in Fig. 1 are used. The configuration of the angled elliptic notch problem under biaxial loading is shown in Fig. 2, in which β is the angle from the main loading axis, 0–0′, to the major axis of the elliptic notch measured positive clockwise, this will be called the "notch angle;" θ is the angle from the major axis of the notch to the direction of the crack initiation measured positive counterclockwise, as will be called the "fracture angle." *The notch surfaces are free of traction* and a uniformly distributed edge load is applied to the plate at a large distance from the notch.

The concept of a critical neighborhood[2] used by Wu and Chang [28] has been utilized in the analysis. They assumed that fracture is not governed by the stress at a point along the boundary of the notch, but by the stress state (equivalent to the analysis based on the strain state for linearly elastic materials) at a point on the outer contour of a critical neighborhood surrounding the notch. The introduction of the concept of critical neighborhood is necessitated by the technical difficulty involved in the machining of a notch. Local irregularities and microcracks are known to exist along the boundary of a machined notch. Although Wu, et al. [18], showed that small local irregularities do not affect the site and direction of crack initiation and the crack initiation strength (i.e., the critical $\sigma_{\rm cr}$ for a crack to initiate on the boundary of the notch), the effective size of the notch is still different than the nominal size of the notch, and the idealized continuum solution stops short at the immediate neighborhood of the nominal notch boundary.

In the analysis, the critical neighborhood is chosen as a confocal

[1] The second author has performed uniaxial compressive experiments using cubic PMMA specimens sandwiched between two heads in a setup discussed in Wu [29]. The results indicated that under very slow loading rate, the specimens failed by plastic deformation. However, at higher loading rates, brittle vertical cracks developed and the specimen failed in brittle mode. The strength of the aforementioned brittle fracture was very close to the measured yield strength under slow loading rate.

[2] The concept of critical neighborhood is not new. Similar ideas have been used by Erdogan and Sih [1], Williams and Ewing [7], Kipp and Sih [15]. However, it should be mentioned that the critical neighborhood used here represents the effective notch boundary and is not stress level dependent.

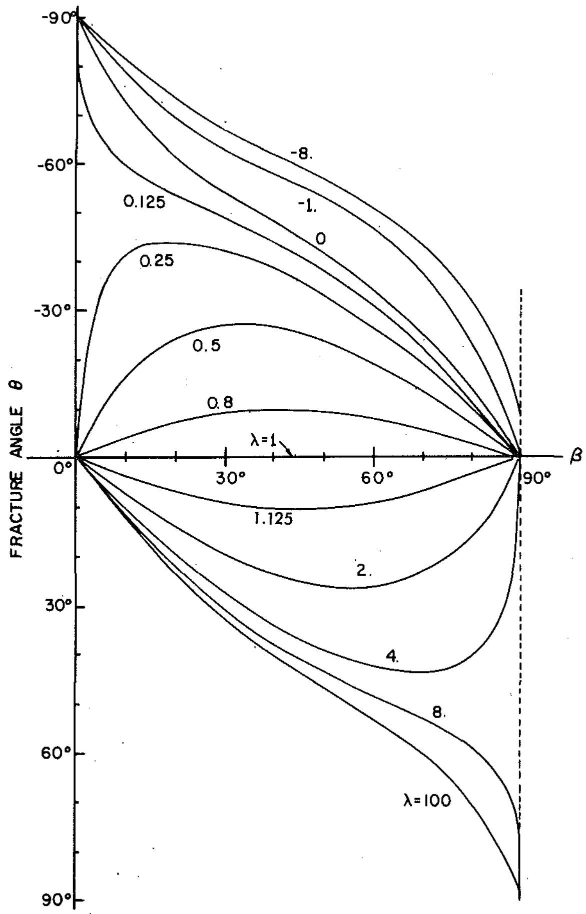

Fig. 3(a) Direction of crack initiation

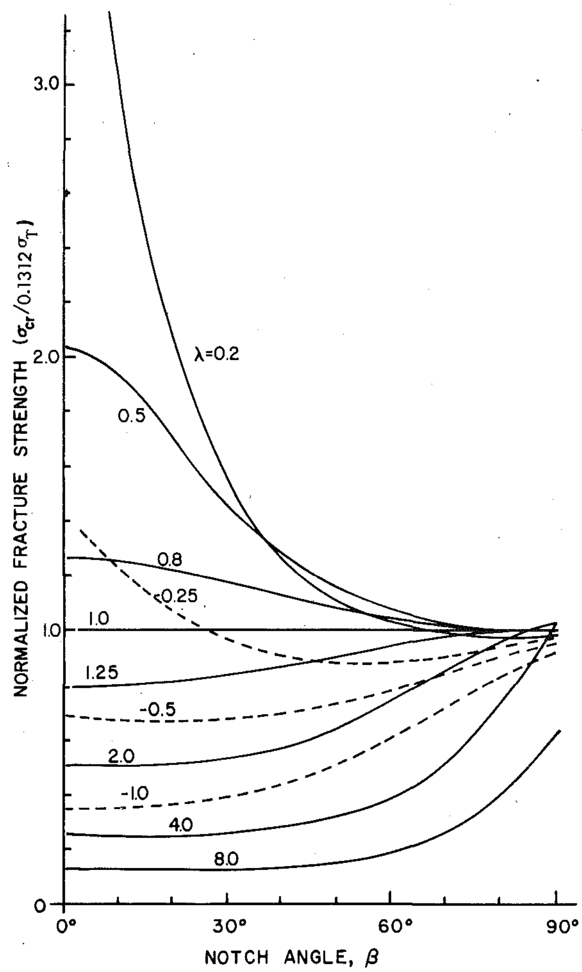

Fig. 3(b) Crack initiation strength

Fig. 3 Theoretical results for biaxial tension, with $K = 2$, $\sigma_T/\tau_c = 1.15$, $\xi_0 = 0.1$, $\xi_1 = 0.2$, and λ varies

ellipse, $\xi = \xi_1$, at the outer boundary of the elliptic notch, $\xi = \xi_0$, as shown in Fig. 2. For each loading case, the iteration procedures[3] check the stress state at points along $\xi = \xi_1$ and find the location and the magnitude of the maximum value of the scalar-valued function $f(\epsilon)$. Crack initiation is predicted to occur at the particular point of maximum $f(\epsilon)$ when the stress state at the point satisfies equation (3). The direction of the crack initiation is perpendicular to the direction of the maximum principal strain at that point. In the present work, since the experimental data of Ewing and Williams [11] on thin-walled PMMA tubes is compared with analytical results obtained for the case of pure shear, material parameters, and the critical outer boundary previously used by Wu and Chang [28] for PMMA in tension are again used in the calculation. These parameters are $K = 2$, $\sigma_T/\tau_c = 1.15$, $\xi_0 = 0.1$, and $\xi_1 = 0.2$.

Further analyses are presented in the following paragraphs.

A The Angled Elliptic Notch Problem Under Biaxial Loading. A graphical description of the angled elliptic notch problem under biaxial loading is given in Fig. 2, in which σ is the "main axial load" which is positive for biaxial tension and negative for biaxial compression; $\lambda\sigma$, the other axial load perpendicular to the direction of the major axial load σ, where λ can be either positive or negative, β, the notch angle, and θ, the fracture angle, have been defined previously.

An exact solution of the elastic stress field can be obtained by superposition of the solutions found in Wu and Chang [28] for the uniaxial loading cases. As a result, the stress field becomes

$$\sigma_{\xi\xi} + \sigma_{\eta\eta} = n\sigma e^{2\xi_0}\cos 2\beta + \alpha\sigma[\sinh 2\xi\,(m - ne^{2\xi_0}\cos 2\beta) - n\,e^{2\xi_0}\sin 2\beta\sin 2\eta] \quad (4)$$

$$\begin{aligned}\sigma_{\xi\xi} - \sigma_{\eta\eta} = \alpha^2\sigma[&-\sinh 2\xi\,(m\cosh 2\xi_0 - n\cos 2\beta)\\ &+ \sinh 2\xi\cos 2\eta(m - ne^{2\xi_0}\cos 2\beta)\\ &- n\,e^{2\xi_0}\sin 2\beta\sin 2\eta\cosh 2\xi\\ &- n\,e^{2\xi_0}\sinh 2\xi\sinh 2(\xi-\xi_0)\cos 2(\eta-\beta)\\ &- n\,e^{2\xi_0}\sin 2\eta\cosh 2(\xi-\xi_0)\sin 2(\eta-\beta)]\\ &+ 2n\alpha\sigma e^{2\xi_0}\cosh 2(\xi-\xi_0)\cos 2(\eta-\beta) \end{aligned} \quad (5)$$

$$\begin{aligned}\tau_{\xi\eta} = \frac{1}{2}\alpha^2\sigma\,[&(m - n\,e^{2\xi_0}\cos 2\beta)\sin 2\eta\cosh 2\xi\\ &- \sin 2\eta(m\cosh 2\xi_0 - n\cos 2\beta)\\ &+ n\,e^{2\xi_0}\sin 2\beta\cos 2\eta\sinh 2\xi\\ &+ n\,e^{2\xi_0}\sinh 2\xi\cosh 2(\xi-\xi_0)\sin 2(\eta-\beta)\\ &- n\,e^{2\xi_0}\sin 2\eta\sinh 2(\xi-\xi_0)\cos 2(\eta-\beta)]\\ &- n\alpha\sigma e^{2\xi_0}\sin 2\,(\eta-\beta)\sinh 2(\xi-\xi_0) \end{aligned} \quad (6)$$

[3] An arbitrary stress σ is assumed to start the calculation in order to find the max $f(\sigma)$ along the contour of the critical neighborhood; where

$$f(\sigma) = \frac{1}{K}\left\{\frac{\sigma_I}{\sigma_T}\right\}^2 + \frac{K-1}{K}\left\{\frac{\sigma_I}{\sigma_T}\right\} - \frac{1}{{\tau_c}^2}\sigma_{II}$$

The value of σ is then adjusted until such $\sigma = \sigma_{cr}$ is found at a point on the contour where $\max f(\sigma) = 1$. This determines both the strength and the direction of the crack initiation.

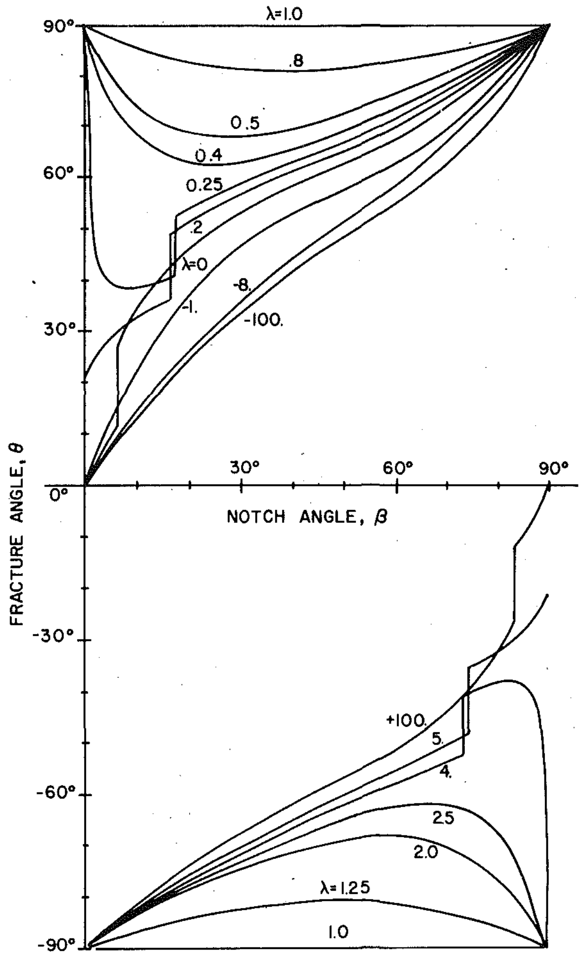

Fig. 4(a) Direction of crack initiation

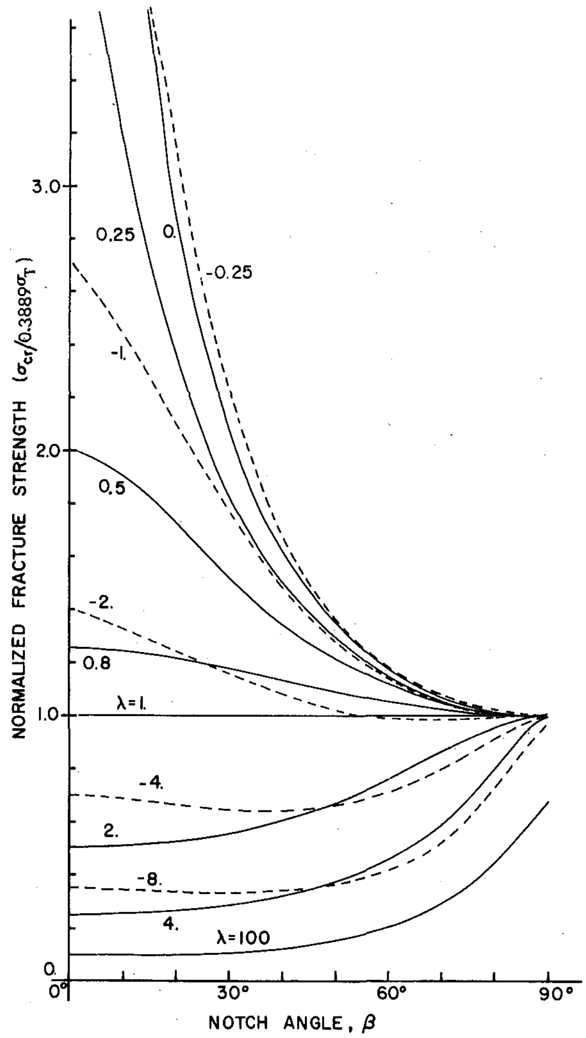

Fig. 4(b) Crack initiation strength

Fig. 4 Theoretical results for biaxial compression, with $K = 2$, $\sigma_T/\tau_c = 1.15$, $\xi_0 = 0.1$, $\xi_1 = 0.2$, and λ varies

in which $\alpha = (\cosh 2\xi - \cos 2\eta)^{-1}$, $m = 1 + \lambda$, and $n = 1 - \lambda$. The aforementioned solution applies to biaxial tension when σ is positive, and to biaxial compression when σ is negative.

Fig. 3(a) shows the theoretical curves relating the fracture angle to the notch angle for biaxial tension (where λ varies from -8 to $+100$). These curves are comparable with those presented by Eftis and Subramonian [20] using the maximum stress theory on the angled crack problem under biaxial tension. It is noted that, in Fig. 3(a), the fracture angle for $\lambda = \omega$ at notch angle β is equal but opposite in sign to the fracture angle for $\lambda = 1/\omega$ at notch angle $(90° - \beta)$, where $\omega > 0$. This correlation can be expected analytically because the biaxial loading configuration (Fig. 2) implies that at failure the stress states for the above two cases are antisymmetric with respect to the elliptical coordinate η. The same correlation can also be expected if one uses the maximum stress theory. However, no such correlation can be obtained by checking the results for $\lambda = 0.5$ and $\lambda = 2$ in Fig. 20 of reference [20].

For the case of $\lambda = 1$, the same stress is applied in all directions at the edge of the plate. Therefore, the stress state in terms of (ξ, η) is the same for all values of β, i.e., independent of β; thus the fracture angle as well as the fracture strength must be the same for all values of β. The foregoing argument applies under both biaxial tension and compression. In the case of biaxial tension, with $\lambda = 1$, the constant fracture angle, as shown in Fig. 3(a) is 0° (the same result is obtained by Eftis and Subramonian [20]) with the crack growth initiating at the tip of the notch, and the corresponding fracture strength is $\sigma_{cr} = 0.1312\ \sigma_T$. Fig. 3($b$) shows the fracture strength versus the notch angle for the case of biaxial tension, in which the fracture strengths have been normalized by dividing by $0.13121\ \sigma_T$, the fracture strength for $\lambda = 1$ in biaxial tension.

Based on the same analysis, the angled elliptic notch problem under biaxial compression has also been studied. Figs. 4(a and b) show, respectively, the corresponding fracture angle and fracture strength as functions of the notch angle β for λ varying from -100 to $+100$. The correlation of the fracture angles between $\lambda = \omega$ and $\lambda = 1/\omega$, where $\omega > 0$, is the same as for biaxial tension. For the case of $\lambda = 1$, the fracture strength and fracture angle are independent of the notch angle β as in the case of biaxial tension. The constant fracture strength is $\sigma_{cr} = 0.3889\ \sigma_T$, which has been used to normalize the fracture strength shown in Fig. 4(b). The constant fracture angle has two values, $\pm 89.36°$, as shown in Fig. 4(a). Because of the symmetry of the stress distribution, fracture initiation occurs at two locations symmetrically disposed to the major axis near each end of the elliptic notch. The point with a positive η coordinate leads to a fracture angle of $+89.36°$ and represents a limiting case as λ increases from 0 to 1. The other point leads to a fracture angle of $-89.36°$ and represents the limiting case as λ decreases from 100 to 1.

It is remarked that a general analysis of the angled elliptic notch

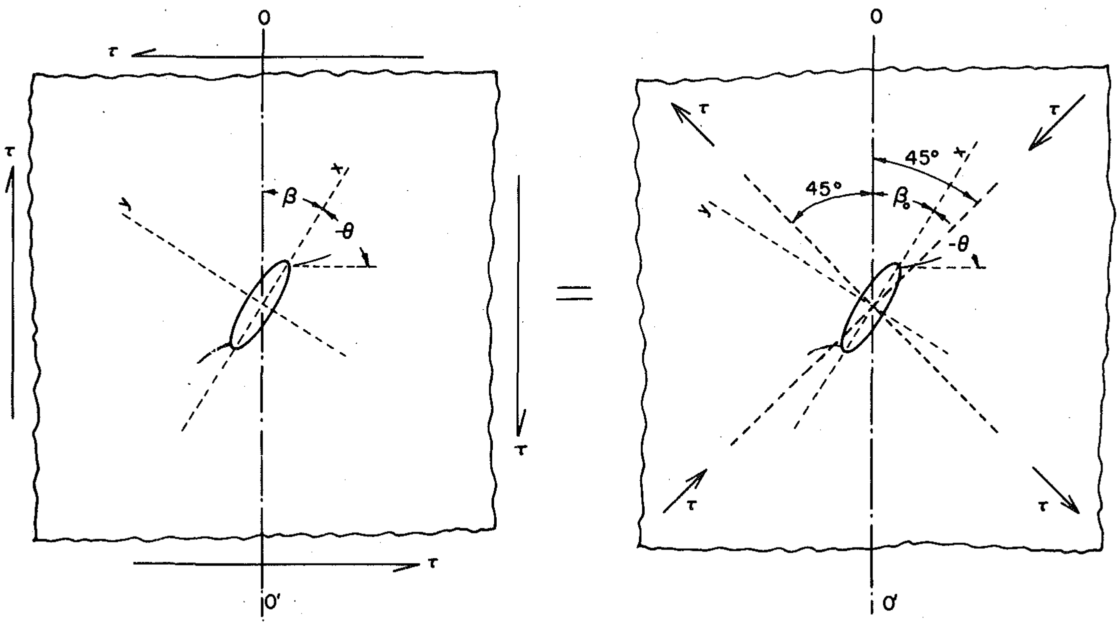

Fig. 5 Loading consideration for the angled elliptic notch problem in pure shear; (*a*) Notch geometry and loading condition; (*b*) Equivalent loading system considered in calculation

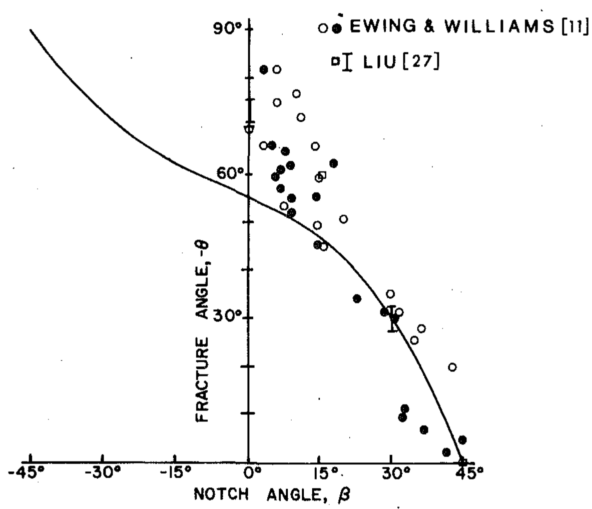

Fig. 6(*a*) Direction of crack initiation

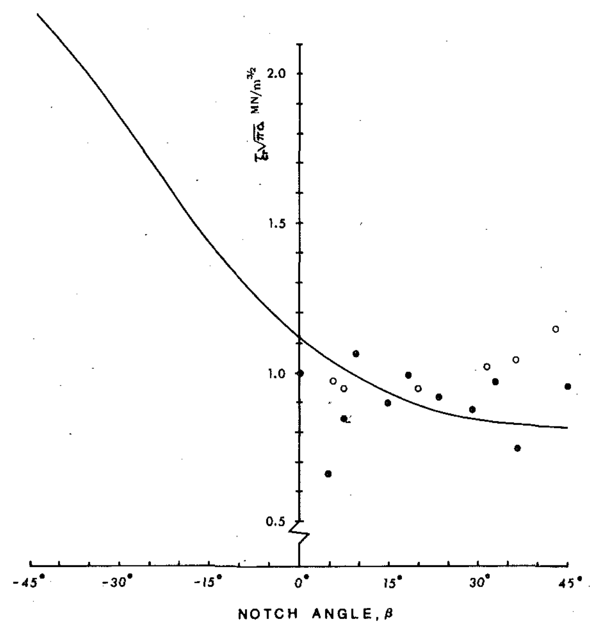

Fig. 6(*b*) Crack initiation strength

Fig. 6 Theoretical results for pure shear case compared with the experimental data of Ewing and Williams [11] and Lin [27]

problem using Wu's [29] theory has been presented in the foregoing. The results for the cases of uniaxial tension and compression, which have been shown previously by the authors [28] to provide good agreement with experimental data, can be obtained by setting $\lambda = 0$ and using appropriate material parameters, $K(= \sigma_c/\sigma_T)$, and σ_T/τ_c. A special case called "the angled elliptic notch problem in pure shear" can also be deduced by setting $\lambda = -1$. Further discussion of this case is presented in the following section.

B **The Angled Elliptic Notch Problem in Pure Shear.** The configuration of the angled elliptic notch problem in pure shear is shown in Fig. 5(*a*), in which the uniformly distributed edge load at infinity is a pure shearing stress τ. Under the principle of superposition, it can easily be shown that the resulting stress field for the condition of pure shear is analytically equivalent to that of the condition of biaxial tension or compression with $\lambda = -1$.[4] In fact, the case of $\beta = \beta_0$ in pure shear is equivalent to the case of $\beta = 45° + \beta_0$ in biaxial tension with $\lambda = -1$ or to the case of $\beta = \beta_0 - 45°$ in biaxial compression with $\lambda = -1$. This is clearly illustrated in Fig. 5(*b*). Therefore, the prediction of the fracture angle and fracture strength as functions of the notch angle, β, for the case of pure shear can be obtained directly from the appropriate curves presented in Figs. 3 or 4.

A comparison of the present analysis with Ewing and Williams' [11] results is now presented. Fig. 6(*a*) shows the theoretical fracture angle

[4] The expressions for the stress field can be obtained by superposition of equations (4)–(6) or the Inglis solution [20].

θ as a function of the notch angle β together with the experimental data obtained by Ewing and Williams [11]. Ewing and Williams [11] only examined cases of β ranging from 0° to 45° in their studies of the angled crack problem in pure shear and declared that the solution is symmetric with respect to the case of $\beta = 45°$. However, it is noted here that consideration of values of β ranging from only 0° to 45° does not include all possible cases of pure shear. A complete analysis should cover β from −45° to +45° as shown by the curve in Fig. 6(a). This argument is substantiated by the fact that the stress solutions obtained for different values of β from −45° to 45° differs.

Fig. 6(a) shows that, for small positive values of β, the theoretical fracture angles are smaller than those obtained experimentally by Ewing and Williams [11]. It is noted that this is due to the fact that the present analysis is based on an elliptic notch rather than the slit crack used by Ewing and Williams [11]. The same tendency has also been observed both experimentally and analytically in the author's [17, 18] studies on the angled elliptic notch problem in tension. It is further remarked that, in the present calculation, the fracture angle θ is relatively insensitive to the choice of ξ_0.

The experimental data of Liu [27] using 7075-T-7651 Aluminum alloy specimens are also plotted in Fig. 6(a) for comparison. From the load-displacement traces presented by Liu [27], it is seen that linear elasticity is applicable in this case. Again, Liu's specimens were plates with slit cracks and the fracture angles θ at small β are larger than those predicted by the present calculation.

The theoretical fracture strength is represented by the curve of $\lambda = -1$ in Fig. 3(b) with β replaced by $\beta - 45°$. This curve is again plotted in Fig. 6(b), but it should be noted that this curve cannot be directly compared with the data obtained experimentally by Ewing and Williams [11] where $\tau_{cr}\sqrt{\pi a}$ rather than τ_{cr} was plotted, since the value of the crack length $2a$ was not given in that report. In that study, the fracture strength was a function of the crack length, $2a$, as a result of the stress state generated in the vicinity of a crack tip. In the present analysis, however, an angled elliptic notch rather than a slit crack is considered, and $\xi_0 = 0.1$, yielding a constant ratio of $b{:}a \approx 0.1$, which is used to represent the elliptic notch. As a result, the fracture strength is found to depend on the ratio b/a. Fig. 6(b) is presented to show merely the same trend the calculated curve and the test results have.

Caution must be exercised when the experimental results of Ewing and Williams [11] and Liu [27] are used to judge the validity of an analysis based on an infinite plate. The torsional experiments of Ewing and Williams [11] were performed on cylindrical tubes of PMMA of outside diameter 89 mm and thickness 6.35 mm. Since the crack length $2a$ was not included in the report, it suffices to mention that the size of the crack in the specimens must be sufficiently small that the effects of finite radius of curvature of the tube and finite size of the specimen can be neglected. Also, the effect of geometry should play a role in Liu's [27] data, since the crack length was quite large compared to the size of Liu's specimens.

Concluding Remarks

The angled elliptic notch problem under biaxial loading has been studied based on the strain failure criterion proposed by the second author [29]. Numerical results have been obtained for both biaxial tensile and compressive loading. Only in the case of pure shear, which is equivalent to biaxial loading with $\lambda = -1$, there is comparable experimental data available in the literature. Further experimental data are needed to investigate fracture phenomena under biaxial loading. When $\lambda = 0$, the present solution reduces to the case of uniaxial loading previously discussed [28].

Five parameters (σ_T, σ_c, τ_c, ξ_0, and ξ_1) are used in the analyses. The first three parameters are material constants which represent brittle fracture strengths under simple loadings. The last two parameters are dependent on the machining technique used to develop the notch and the material used for the specimen (see reference [28] for detailed discussion).

Discrepancies found between the theoretical and experimental results are attributed to the difference generated between the elliptic notch used in the present analysis and the slit crack used in the experimental work. It is believed that the critical neighborhood chosen for this analysis is reasonable for elliptic notched specimens. In reference [28], the authors have presented good correlation to experimental data of Cotterell [6] in uniaxial compression, and Wu, et al. [18], in uniaxial tension. For plates with sharp slit cracks, the degenerated solution with $\xi_0 = 0$ is not readily applicable due to the fact that under biaxial loadings, the notch surfaces are no longer free of traction.

Under a variety of loading conditions, i.e., for various λ's as β varies, the location of crack initiation moves smoothly along the notch boundary. Under certain conditions, however, with specific λ's and when β is close to a critical value, the location of crack initiation changes abruptly from close to the notch tip to a point away from it as β varies. This effect leads to the discontinuity of the fracture angle curves, for $\lambda = 0$, 0.2, 0.25, 4, 5, 100, as shown in Fig. 4(a). However, the values of the fracture strength does not discontinuously vary but rather varies smoothly as shown in Fig. 4(b).

Figs. 7(a and b) show, respectively, the analytical prediction of the variation in fracture angle for pure shear ($\lambda = -1$) and biaxial tension with $\lambda = 0$ (uniaxial), as the critical neighborhood ξ_1 varies. This il-

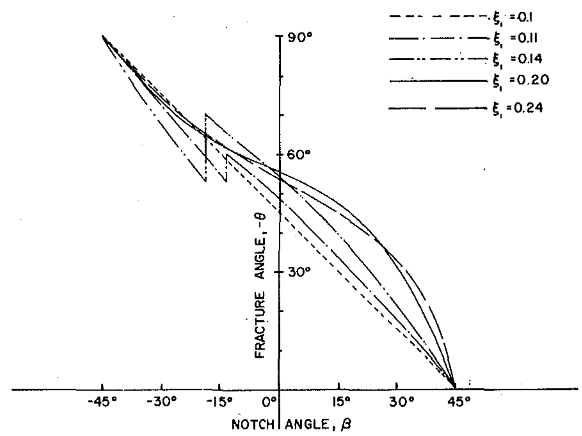

Fig. 7(a) Angled elliptic notch problem under uniaxial tension ($\lambda = 0$), with $K = 2.0$, $\sigma_T/\tau_c = 1.15$, $\xi_0 = 0.1$, and ξ_1 varies

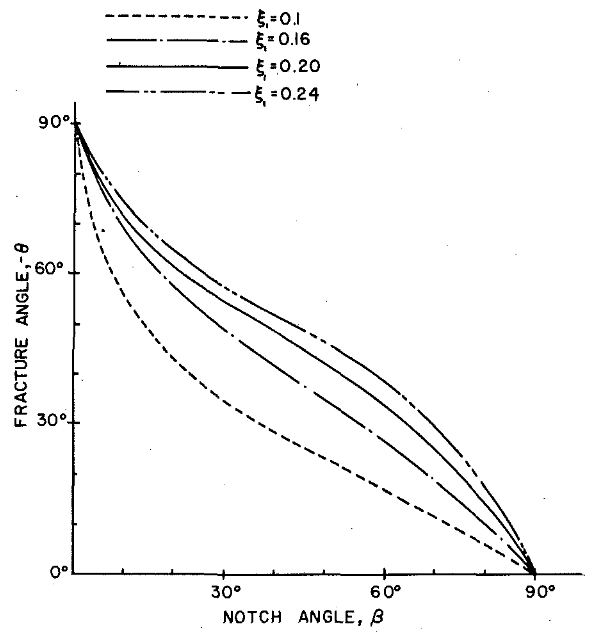

Fig. 7(b) Angled elliptic notch problem under pure shear ($\lambda = -1$) with $K = 2$, $\sigma_T/\tau_c = 1.15$, $\xi_0 = 0.1$, and ξ_1 varies

lustrates the dependence of the fracture angle on the choice of the contour, $\xi = \xi_1$. The value chosen for ξ_1 is related to the material and the technique used to create the notch.

In conclusion, the present theory predicts that under the same loading configuration, fracture initiation will be affected by material properties. This effect arises directly from the consideration that for different materials the values of the parameters σ_c, σ_T, and τ_c used in the theory are different. As an example for illustration, consider the case of biaxial compression with $\lambda = 1$. Earlier in the text a value of $K = 2$ yielded a fracture angle of $\pm 89.36°$. However, a value of $K = 6$, suitable for a different test material, will yield a fracture angle of $\pm 42.79°$ with fracture initiation located away from the tip of the elliptic notch.

References

1 Erdogan, F., and Sih, G. C., "On the Crack Extension in Plate Under Plane Loading and Transverse Shear," ASME *Journal of Basic Engineering*, Vol. 85, 1963, pp. 519–525.

2 McClintock, F. A., Discussion on "The Crack Extension in Plates Under Plane Loading and Transverse Shear" by Erdogan, F., and Sih, G. C., ASME *Journal of Basic Engineering*, Vol. 85, 1963, pp. 525–527.

3 Brace, W. F., and Bombolakis, E. G., "A Note on Brittle Crack Growth in Compression," *Journal of Geophysical Research*, Vol. 68, 1963, pp. 3709–3713.

4 Hoek, E., and Bieniawski, Z. T., "Brittle Fracture Propagation in Rock Under Compression," *International Journal of Fracture*, Vol. 1, 1965, pp. 137–155.

5 Pook, L. P., "The Effect of Crack Angle on Fracture Toughness," *Engineering Fracture Mechanics*, Vol. 3, 1971, pp. 205–218.

6 Cotterell, B., "Brittle Fracture in Compression," *International Journal of Fracture*, Vol. 8, 1972, pp. 195–208.

7 Williams, J. G., and Ewing, P. D., "Fracture Under Complex Stress—The Angled Crack Problem," *International Journal of Fracture*, Vol. 8, 1972, pp. 441–446.

8 Finnie, I., and Saith, A., "A Note on the Angled Crack Problem and the Directional Stability of Cracks," *International Journal of Fracture*, Vol. 9, 1973, pp. 484–486.

9 Ewing, P. D., and Williams, J. G., "Further Observations on the Angled Crack Problem," *International Journal of Fracture*, Vol. 10, 1974, p. 135.

10 Dudukolenko, V. V., and Romalis, N. B., "Direction of Crack Growth Under Plane-Stress-State Conditions," *Mechanics of Solids*, Vol. 8, 1973, pp. 109–115.

11 Ewing, P. D., and Williams, J. G., "The Fracture of Spherical Shells Under Pressure and Circular Tubes With Angled Cracks in Torsion," *International Journal of Fracture*, Vol. 10, 1974, pp. 537–544.

12 Sih, G. C., "Some Basic Problems in Fracture Mechanics and New Concepts," *Engineering Fracture Mechanics*, Vol. 5, 1973, pp. 365–377.

13 Sih, G. C., "Strain-Energy-Density Factor Applied to Mixed Mode Crack Problems," *International Journal of Fracture*, Vol. 10, 1974, pp. 305–321.

14 Sih, G. C., and Kipp, M. E., Discussion on "Fracture Under Complex Stress—The Angled Crack Problem," by Williams, J. G., and Ewing, P. D., *International Journal of Fracture*, Vol. 10, 1974, pp. 261–265.

15 Kipp, M. E., and Sih, G. C., "The Strain Energy Density Failure Criterion Applied to Notched Elastic Solids," *International Journal of Solids and Structures*, Vol. 11, 1975, pp. 153–173.

16 Kassir, M. K., and Sih, G. C., *Three-Dimensional Crack Problems*, Noordhoff International Publishing, Leyden, 1975.

17 Wu, H. C., and Chang, K. J., "Strain Failure Criterion and Its Application to Angled Elliptic Hole Problem in Compression," Report G378-DME-75-004, Division of Materials Engineering, University of Iowa, Iowa City, Iowa, 1975.

18 Wu, H. C., Yao, R. F., and Yip, M. C., "Experimental Investigation of the Angled Elliptic Notch Problem in Tension," ASME JOURNAL OF APPLIED MECHANICS, Vol. 44, 1977, pp. 455–461.

19 Wang, T. C., "Fracture Criteria for Combined Mode Cracks," Fourth International Conference on Fracture, June 1977, Waterloo, Canada, in *Advances in Research on the Strength and Fracture of Materials*, ed., Taplin, D. M. R., Vol. 4, 1977, pp. 135–154.

20 Eftis, J., and Subramonian, N., "The Inclined Crack Under Biaxial Load," *Engineering Fracture Mechanics*, Vol. 10, 1978, pp. 43–67.

21 Labourdette, R., and Pellas, J., "A New Approach to the Three-Dimensional Crack Growth Problem," *International Journal of Fracture*, Vol. 14, 1978, pp. R121–R124.

22 Tirosh, J., "Incipient Fracture Angle, Fracture Loci, and Critical Stress for Mixed Mode Loading," *Engineering Fracture Mechanics*, Vol. 9, 1977, pp. 607–616.

23 Wu, C. H., "Maximum-Energy-Release-Rate Criterion Applied to a Tension-Compression Specimen With Crack," *Journal of Elasticity*, Vol. 8, No. 3, 1978, pp. 235–257.

24 Palaniswamy, K., and Knauss, W. G., "On the Problem of Crack Extension in Brittle Solids Under General Loading," *Mechanics Today*, ed., Nemat-Nasser, S., Vol. 4, 1976, pp. 87–148.

25 Coughlan, J., and Barr, B. I. G., "Fracture Path Prediction," Report, Department of Civil Engineering and Building, Glamorgan Polytechnic, U.K., 1974.

26 Ingraffea, A. R., "On Discrete Fracture Propagation in Rock Loaded in Compression," *Proceedings, First International Conference on Numerical Methods in Fracture Mechanics*, Swansea, 1978, pp. 235–248.

27 Liu, A. F., "Crack Growth and Failure of Aluminum Plate Under In-Plane Shear," *AIAA Journal*, Vol. 12, 1974, pp. 180–185.

28 Wu, H. C., and Chang, K. J., "Angled Elliptic Notch Problem in Compression and Tension," ASME JOURNAL OF APPLIED MECHANICS, Vol. 45, 1978, pp. 258–262.

29 Wu, H. C., "Dual Failure Criterion for Plane Concrete," *Journal of the Engineering Mechanics Division*, ASCE, Vol. 100, 1974, pp. 1167–1181.

30 Inglis, C. E., "Stress in a Plate Due to the Presence of Cracks and Sharp Corners," *Trans. Institute of Naval Architects*, London, Vol. LV, 1913, pp. 219–230.

31 *Plexiglass Design and Fabrication Data PL-229K*, Rohm and Haas Co., Philadelphia, Pa., 1971.

32 Truesdell, C., "The Nonlinear Field Theories of Mechanics," *Encyclopedia of Physics*, Vol. III/3, ed., Flügge, S., Springer-Verlag, 1965.

33 Valanis, K. C., and Wu, H. C., "Fracture of Plastic Materials Under Proportional Strain, Part I: Theoretical Foundation," *Journal de Mechanique*, Vol. 15, 1976, pp. 543–556.

34 Valanis, K. C., and Wu, H. C., "Fracture of Plastic Materials Under Proportional Strain, Part II: Application to Gray Cast Iron," *Journal de Mechanique*, Vol. 15, 1976, pp. 557–577.

S. S. Wang

Assistant Professor,
Department of Theoretical
and Applied Mechanics,
University of Illinois,
Urbana, Ill. 61801
Assoc. Mem. ASME

An Analysis of Delamination in Angle-Ply Fiber-Reinforced Composites[1]

A study of the mechanics and failure modes of delamination initiated from a surface flaw in angle-ply fiber-reinforced composites is presented. The analysis employs a hybrid-stress finite-element method including a crack-tip singular element with its field variables expressed by Muskhelishvili's complex stress functions. Solutions are obtained for the delaminated composites with various laminate parameters. The results elucidate unique and important characteristics of delamination crack-tip response and interlaminar stress transfer mechanisms. Of particular interest are the mixed-mode stress-intensity factors associated with the delamination crack. The influence of ply orientation on K_I and K_{II} and their effects on subsequent crack extension are discussed.

Introduction

Among various kinds of damage in fiber-reinforced composites, delamination often causes greatest concern. It is one of the most frequently encountered types of damage during service and may introduce serious failure problems in composite structures. The presence of delamination cracks may result in a progressive stiffness reduction, structural disintegration, and material degradation, which may lead to the final fracture of the composites. Examples of the delamination failure have been shown in many engineering applications of composite materials such as missile motor cases, composite engine fan blades, laminated pressure vessels, and aircraft composite components. Thus understanding the damage behavior of this kind is of fundamental importance in the analysis and design of composite structures.

Delamination has been observed as a matrix dominated failure mechanism occurring in resin-rich interlaminar regions. It takes the form of separation of plies and is commonly initiated at geometric boundaries, manufacturing defects, and service-induced damage. Since the interlaminar strength is very low and interlaminar stresses are usually high, failure in composites generally tend to develop in a delamination mode at a very low nominal stress level. The development of a through-the-thickness crack from a defect or flaw in a real composite laminate may be difficult in many cases. This is a phenomenon unique to composites and is not commonly found in metals and polymers. The consequence of delamination in the performance of fiber composite structures has long been recognized. But research progress has been relatively slow as unanticipated delamination cracking occurs in numerous cases. The major difficulties arise from the inherent heterogeneity and anisotropy of the material, the through-thickness variation of ply properties and lamination effects, the complex crack geometry, and the associated crack-tip stress singularity. Early work by Kies [1] and Kulkarni, et al. [2] employing a critical energy release rate approach based on the fracture mechanics concept studied the fundamental nature of the problem. Erdogan and Arin [3] and several others [4–7] conducted interface crack analyses to examine the complex interface crack-tip stress singularity. Experimental studies by Im, et al. [8], Pipes and Pagano [9], and Sendeckyj, et al. [10], found unique characteristics of the delamination behavior in composites. Recent results reported by Wang, et al. [11, 12] provided further information of the crack-tip stresses and growth of a delamination under static and cyclic loading. However, many fundamental problems associated with delamination still remain unclear, especially in the cases of a delamination crack initiated from a service or manufacturing-induced flaw, since these real-life cracks in composites are characteristically difficult to analyze.

This paper presents an investigation of delamination emanating from a surface notch in angle-ply laminates subjected to in-plane nominal loading. The objective of this study is to examine the basic failure mechanics and mechanisms of delamination in the composites. Due to the aforementioned complexities of the problem, a numerical method, based on advanced hybrid-stress finite-element formulation, is introduced. This method, pioneered by Pian, et al. [13], can over-

[1] Presented in the session on Aerospace Composite Materials at the 1978 ASME Winter Annual Meeting in San Francisco, Calif., December 12–15, 1978.

Contributed by the Applied Mechanics Division for publication in the JOURNAL OF APPLIED MECHANICS.

Discussion on this paper should be addressed to the Editorial Department, ASME, United Engineering Center, 345 East 47th Street, New York, N. Y. 10017, and will be accepted until June 1, 1980. Readers who need more time to prepare a discussion should request an extension from the Editorial Department. Manuscript received by ASME Applied Mechanics Division, August, 1978; final revision, June, 1979.

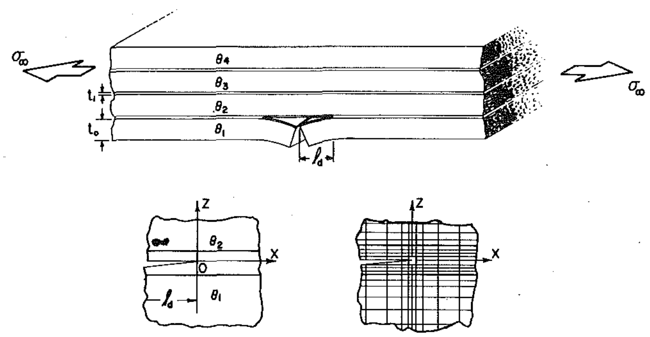

Fig. 1 Delamination crack geometry, coordinate system and hybrid-stress F.E.M. mesh configuration in $(\underline{\theta_1}//\theta_2/\theta_3/\theta_4)$ composite

come these difficulties and provide accurate solutions with rapid rates of convergence. It also enables an accurate description of the crack-tip response by incorporating a singular hybrid crack-tip element into the analysis to model more precisely the delamination crack. The crack-tip element is formulated by Muskhelishvili's complex stress functions, including the singular and higher-order terms. The analysis is capable of solving very complicated composite crack problems and is particularly suitable for the current study. Typical results, illustrating the fundamental behavior of a delamination crack in the angle-ply composites, are presented and discussed in the paper.

Mathematical Model and Assumptions

Since microscopic observations indicated that delamination is a matrix-dominated, progressive failure mechanism occurring in an interlaminar resin region, the composite laminate is modeled as an assembly of anisotropic plies bonded by thin layers of interply resin. Each fiber-reinforced ply of thickness t_0 has its material axis oriented with an angle θ_i from the loading direction. The resin interlayer is assumed to be isotropic and to have a uniform thickness t_1. The plies are perfectly bonded in the laminate everywhere except in the region where a delamination is initiated from the surface notch tip. The crack geometry and the laminate configuration are conveniently expressed by $(\underline{\theta_1}//\theta_2/\theta_3/\theta_4 \ldots)$, where the double solidus and the underline represent the location of the delamination and the penetrated depth by the surface notch, respectively. The delamination crack of length l_d is modeled as a flaw completely embedded in the resin interlayer as shown in Fig. 1. Studies on other extreme cases such as a crack located in a vanishing interlayer or at a ply-interlayer interface, giving a more complicated oscillating three-dimensional stress singularity, are reported elsewhere [14].

Method of Analysis

The general procedure of analyzing the plane delamination crack problem in composites is described briefly in this section. Details of formulation for the crack-tip superelement and surrounding nonsingular hybrid elements can be found elsewhere [13, 15] and are not repeated here. Briefly, the formulation of the crack-tip element is based on the variational principle of modified complementary energy. The functional to be minimized has the form expressible in terms of both unknown displacement and stress fields in the element and prescribed boundary tractions and displacements along segments of the element boundary. Following Muskhelishvili's formulation [16], the stress and displacement fields are expressed in terms of two stress functions, $\phi(z)$ and $\psi(z)$, of a complex variable $z = x + iy$ by

$$\sigma_{yy} + \sigma_{xx} = 2[\phi'(z) + \overline{\phi'(z)}] \tag{1}$$

$$\sigma_{yy} - \sigma_{xx} + 2i\sigma_{xy} = 2[\bar{z}\phi''(z) + \psi'(z)] \tag{2}$$

and

$$2G(u + iv) = \eta\phi(z) - z\overline{\phi'(z)} - \overline{\psi(z)}, \tag{3}$$

where G is the shear modulus, and η is a plane stress or a plane strain parameter. A function $w(\xi)$ is then introduced to map the singular crack domain to an analytical plane, where $z = w(\xi) = \xi^2$. The functions $\phi(\xi)$ and $\psi(\xi)$ are analytical and can be interrelated through traction boundary conditions along crack surfaces. In the crack-tip superelement formulation, $\phi(\xi)$ is assumed to have the form

$$\phi(\xi) = \sum_{j=1}^{n} b_j\xi^j \tag{4}$$

and the function $\psi(\xi)$ may be obtained as

$$\psi(\xi) = -\sum_{j=1}^{n}\left[\bar{b}_j(-1)^j + \frac{1}{2}jb_j\right]\xi^j, \tag{5}$$

where $b_j = \beta_j$ for a symmetric case or $b_j = \beta_j + i\beta_{n+j}$ for a nonsymmetric case and βs are real constants to be determined. Using equations (4) and (5), the stress and displacement fields in equations (1)–(3) may be expressed in terms of the stress coefficients βs. The boundary traction $\mathbf{T}$ can be calculated by $T_i = \sigma_{ij}\nu_j$. Interpolating boundary displacements $\tilde{\mathbf{u}}$ by nodal displacements $\mathbf{q}$ and inserting $\boldsymbol{\sigma}$ and $\mathbf{T}$ into the variational formulation, the crack-tip element stiffness matrix can be obtained.

Stiffness matrices of surrounding nonsingular elements are formulated by a conventional hybrid-stress finite-element method [17] through the variational principle of minimum complementary energy. Anisotropic elastic properties of each composite lamina are considered in the analysis by introducing an appropriate compliance matrix in the element stiffness formulation. Since boundary displacement functions are independently assumed for the crack-tip superelement and for the nonsingular elements, interelement compatibility can be insured by a suitable choice of interpolation functions.

The assembled governing equations for the whole system may be written as

$$\mathbf{Kq} = \mathbf{Q}, \tag{6}$$

where $\mathbf{K}$ is the global stiffness matrix, and $\mathbf{Q}$, the consistent loading vector. After solving $\mathbf{q}$ from equation (6) by an appropriate solution scheme, the stress field can be determined from material constitutive equations. Stress-intensity factors, K_{I} and K_{II}, for a given delamination crack geometry may be found from

$$K_{\mathrm{I}} = \sqrt{2\pi}\beta_1 \tag{7a}$$

and

$$K_{\mathrm{II}} = \sqrt{2\pi}\beta_{n+1}. \tag{7b}$$

The associated elastic energy release rates G_{I} and G_{II} can be obtained by a standard computational scheme.

Accuracy and Convergence of Solutions

Accuracy and convergence assessments of solutions are complicated by several unusual features of the problem and of the method of analysis due to the singular nature of the delamination crack. A study of the accuracy and convergence of the analysis and the solution stability has been conducted by testing cases for which independent solutions are available. Excellent agreements between the results obtained from the current analysis and existing closed-form solutions were observed. Current results indicate that accuracy within approximately one percent of the converged solutions of K_{I} and K_{II} can be achieved by the optimum mesh arrangements used in the present study. Details of this information can be found in [15].

Results and Discussion

Solutions for symmetric four-ply $(\underline{\theta}//-\theta/-\theta/\theta)$ composites are reported in this section to elucidate fundamental mechanics and mechanisms of the delamination and to illustrate the complex effects introduced by ply (or fiber) orientations. The results are compared with the reference solution obtained for a delaminated unidirectional composite. Studies on the composites consisting of more plies and/or with more complicated laminate configurations were conducted also and were reported elsewhere [12, 18]. Material elastic constants typical

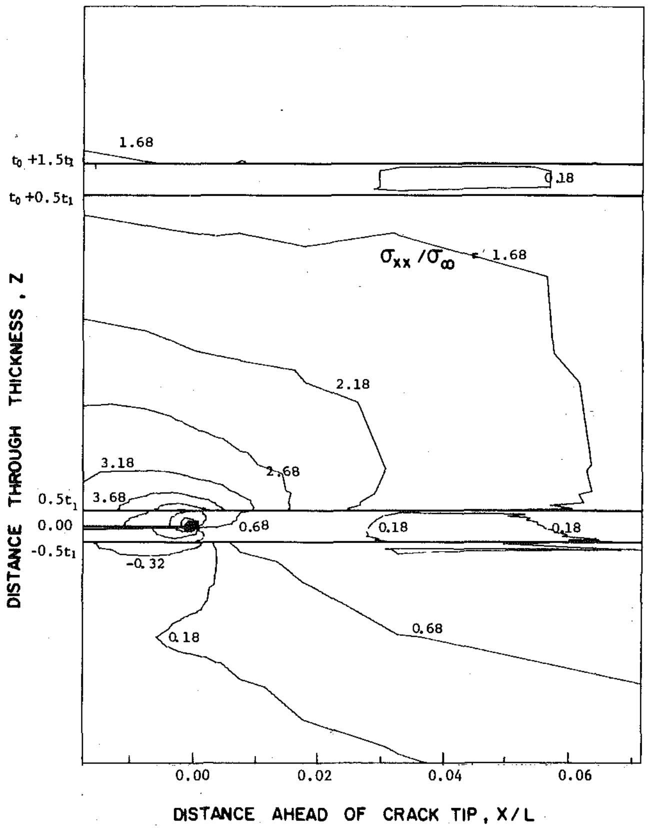

Fig. 2 **Longitudinal stress contours $\sigma_{xx}/\sigma_\infty$ near delamination crack tip in ($\underline{30}$°//−30°/−30°/30°) graphite/epoxy**

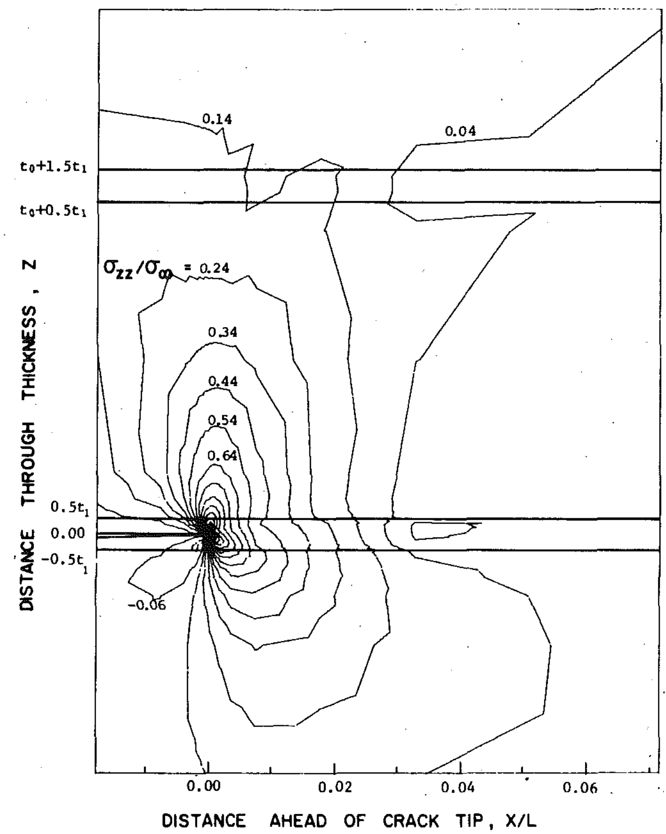

Fig. 3 **Transverse normal stress contours $\sigma_{zz}/\sigma_\infty$ near delamination crack tip in ($\underline{30}$°//−30°/−30°/30°) graphite/epoxy**

Table 1 **Materials elastic constants used in analysis**

a. Graphite/Epoxy Lamina

E_{LL} = 138 GPa (20.00 x 10^6 psi)

$E_{TT} = E_{ZZ}$ = 14.5 GPa (2.10 x 10^6 psi)

$G_{LZ} = G_{TL}$ = 5.87 GPa (0.85 x 10^6 psi)

$\nu_{TL} = \nu_{LZ} = \nu_{TZ}$ = 0.21

b. Interlaminar Epoxy Layer

E_m = 3.45 GPa (0.50 x 10^6 psi)

G_m = 1.28 GPa (0.185 x 10^6 psi)

ν_m = 0.35

of high modulus graphite/epoxy systems for aerospace applications are used in the present computation (Table 1). The graphite/epoxy lamina in the analytical modeling has a dimension of 0.01 in. The interlaminar resin layer has a uniform thickness of one-tenth of the individual ply thickness as observed under the microscope. The length of the delamination crack is assumed to be three times the ply thickness. The surface notch penetrates through one ply thickness from the outside, as shown in Fig. 1.

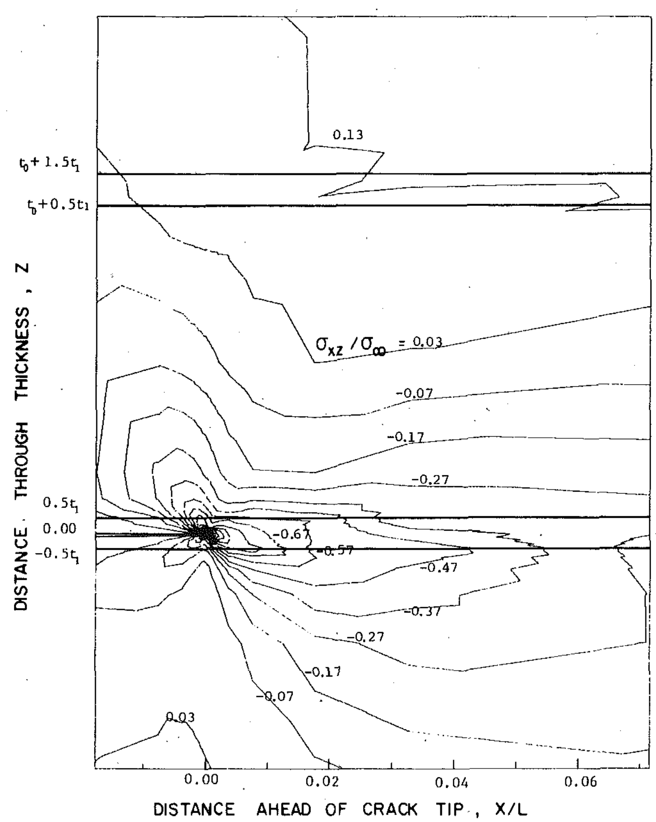

Fig. 4 **Interlaminar shear stress contours $\sigma_{xz}/\sigma_\infty$ near delamination crack tip in ($\underline{30}$°//−30°/−30°/30°) graphite/epoxy**

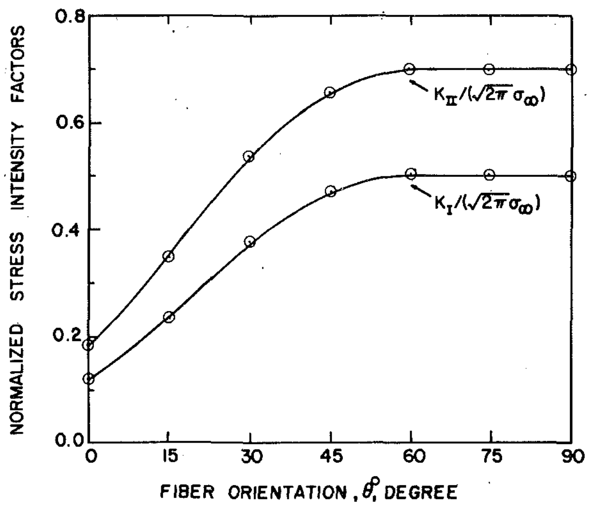

Fig. 5 Effect of fiber orientation on stress-intensity factors in ($\underline{\theta}//-\theta/-\theta/\theta$) graphite/epoxy

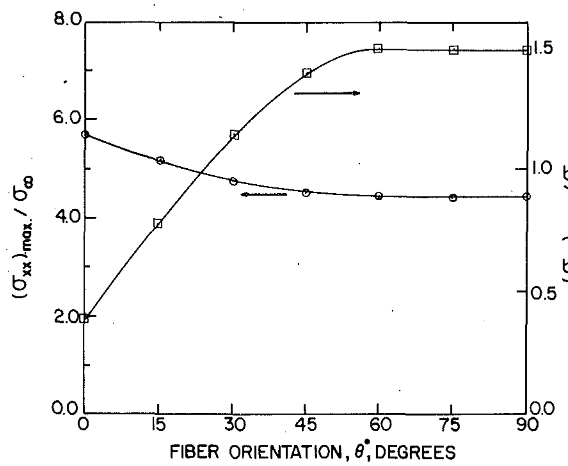

Fig. 6 Effect of fiber orientation on stress-concentration factors adjacent to crack tip at $x = 0$ and $z = 0.5t_1$, in ($\underline{\theta}//-\theta/-\theta/\theta$) graphite/epoxy

The response of the composite subjected to delamination may be best illustrated by examining the crack-tip stress field. The computer-plotted isostress contours, shown in Fig. 2, give the in-plane longitudinal stress distribution $\sigma_{xx}/\sigma_\infty$ around the delamination crack tip in a commonly used ($\underline{30°}//-30°/-30°/30°$) graphite/epoxy. The plot provides a graphic representation of the numerical solution and reveals several important features of the problem: the localized and intensified crack-tip stress field within the interlaminar region, the high stress concentration in adjacent plies, and the complex transfer mechanisms of interlaminar stresses in the delaminated composite. Figs. 3 and 4 show the distributions of interlaminar shear and transverse normal stresses near the crack tip. Both stress components reach extremely high levels within the thin interlaminar layer as the crack tip is approached. They extend continuously through the laminate thickness and attenuate gradually in the neighboring plies. A more accurate description of the near-field stresses may be achieved by plotting the stresses versus the distance away from the crack tip on logarithmic coordinates. Straight lines with a slope of $-1/2$ are obtained, indicating a classical fracture mechanics $1/\sqrt{r}$ singularity. Amplitudes of the near field stresses may be characterized by the mixed-mode stress-intensity factors computed from equations 7(a and b).

For a given loading condition and crack length, K_I and K_{II} are related directly to the ply configuration and the laminate geometry. Fig. 5 provides quantitative information of K_I and K_{II} in ($\underline{\theta}//-\theta/-\theta/\theta$) composites. A rapid increase in the stress intensity factors is observed as the ply orientation changes from the unidirectional configuration. K_I and K_{II} for the laminates with θs greater than 45° are found to be approximately three times larger than those obtained from a unidirectional case. Also note that the opening mode stress-intensity factors are of the same order of magnitude as those of the shearing mode. The stress-intensity factor solutions are of particular importance in characterizing and controlling the delamination fracture behavior of high-strength brittle composite laminates such as the graphite/epoxy system, since they may dominate subsequent crack extension in the composites subjected to a monotonically increasing load or a cyclic fatigue condition. It is essential to obtain accurate information of K_I and K_{II} for the analysis and prediction of mixed-mode interlaminar crack extension in multilayered composites. Using the stress-intensity solutions obtained from the current analysis and an appropriate mixed-mode fracture criterion such as the critical energy release rate criterion,

$$G_I + G_{II} = G_c \tag{8}$$

which can be expressed in terms of the delamination crack-tip stress-intensity factors [19, 20] as

$$\left(\frac{K_I}{K_{Ic}}\right)^2 + \left(\frac{K_{II}}{K_{IIc}}\right)^2 = 1, \tag{9}$$

where K_{Ic} and K_{IIc} are the critical mode I and II stress-intensity factors, it has been shown [21] that the delamination crack growth behavior in a unidirectional glass/epoxy composite can be predicted accurately. Moreover, mixed-mode cyclic stress-intensity ranges for a laminate subjected to fatigue loading can be determined by the analysis also and have been used successfully [21] in the study of fatigue crack propagation of delamination in the composite.

The redistribution of laminate stresses caused by the interlaminar crack has a significant effect on the deformation and fracture of the composite. For example, the compressive in-plane stress developed in the lower crack flank may introduce severe local buckling of the delaminated plies in the vicinity of the surface notch. This surface buckling phenomenon has been observed and reported in [10]. The nonuniform stress distributions through the laminate thickness, shown in Figs. 2–4, suggest that the classical laminate theory may be inapplicable in the region near the delamination crack. Numerical results indicate that maximum stress concentrations almost always occur at the interlayer/ply interface adjacent to the delamination crack, i.e., at $x = 0$ and $z = 0.5t_1$, for all ply configurations studied. Fig. 6 gives the change of stress-concentration factors $(\sigma_{ij})_{max}/\sigma_\infty$ as a function of the fiber orientation. While the ply logitudinal strength decreases rapidly as the fiber orientation θ is altered, the in-plane stress concentration at the noted position remains relatively the same. The spontaneous but opposite changes in ply strength and stress concentration may introduce a transition of failure modes from interlaminar to intralaminar fracture in the composite during crack growth. This behavior has been noted by several investigators [12, 22, 23]. Furthermore, the presence of the delamination may be detrimental to the durability of the material in an adverse environment, such as moisture and corrosive chemicals, because not only does the delamination crack reduce the structural stiffness, but also the stress concentration near the crack surfaces enhances the rate-dependent degradation process in the composites [24].

Effects of lamination of composites on stress transfer mechanisms around the delamination crack can be depicted also by examining crack-tip stress contours in the composites with various fiber orientations. Figs. 7(a and b) give a clear description of the in-plane longitudinal stress for two different cases, ($\underline{0}°//0°/0°/0°$) and ($\underline{45}°//-45°/-45°/45°$) graphite/epoxy. The difference between stress distribution patterns as shown in the figures delineates the distinct responses of the material to the delamination crack when the fiber orientation is altered. Figs. 8 and 9 provide better pictures of the ply orientation effects on the interlaminar stress transfer mechanisms. The interlaminar stresses exhibit higher values through the laminate thickness near the delamination in the angle-ply composite and ex-

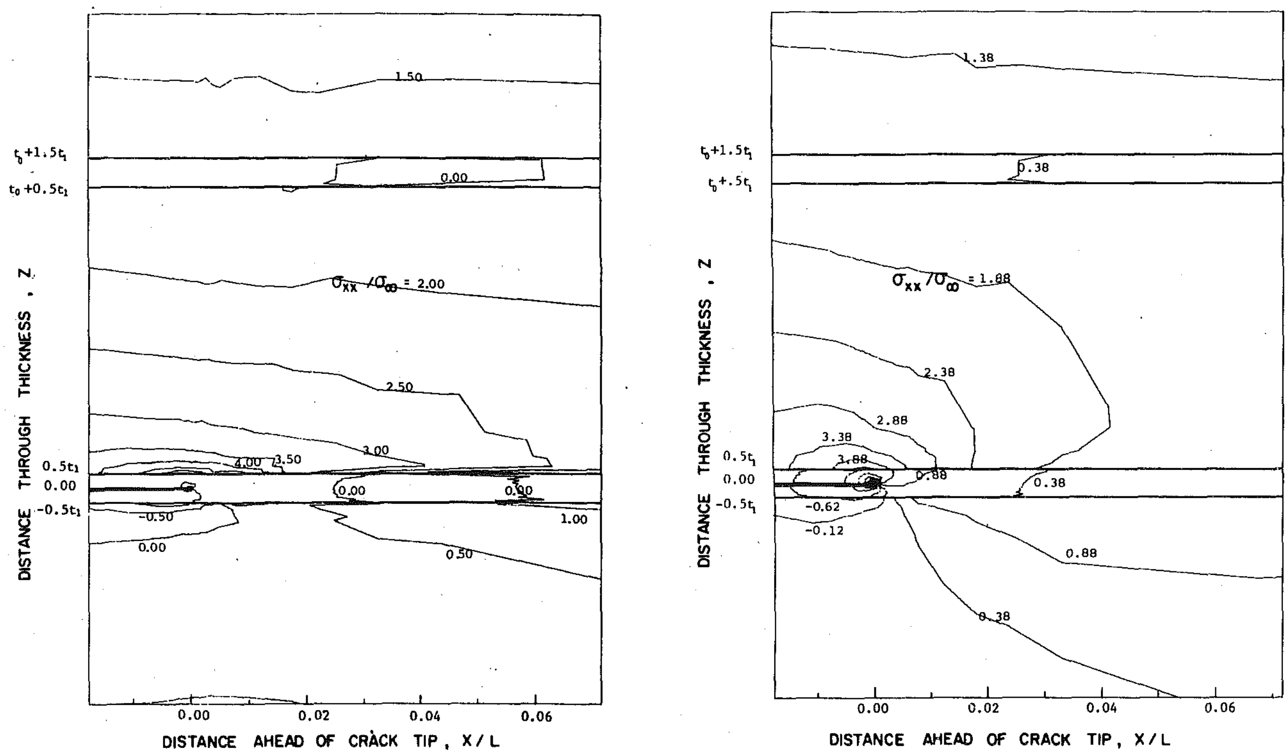

a) $(\underline{0}^\circ // 0^\circ / 0^\circ / 0^\circ)$ b) $(\underline{45}^\circ // -45^\circ / -45^\circ / 45^\circ)$

Fig. 7 Effect of ply orientation on longitudinal stress distribution $\sigma_{xx}/\sigma_\infty$ near delamination crack tip in graphite/epoxy composites

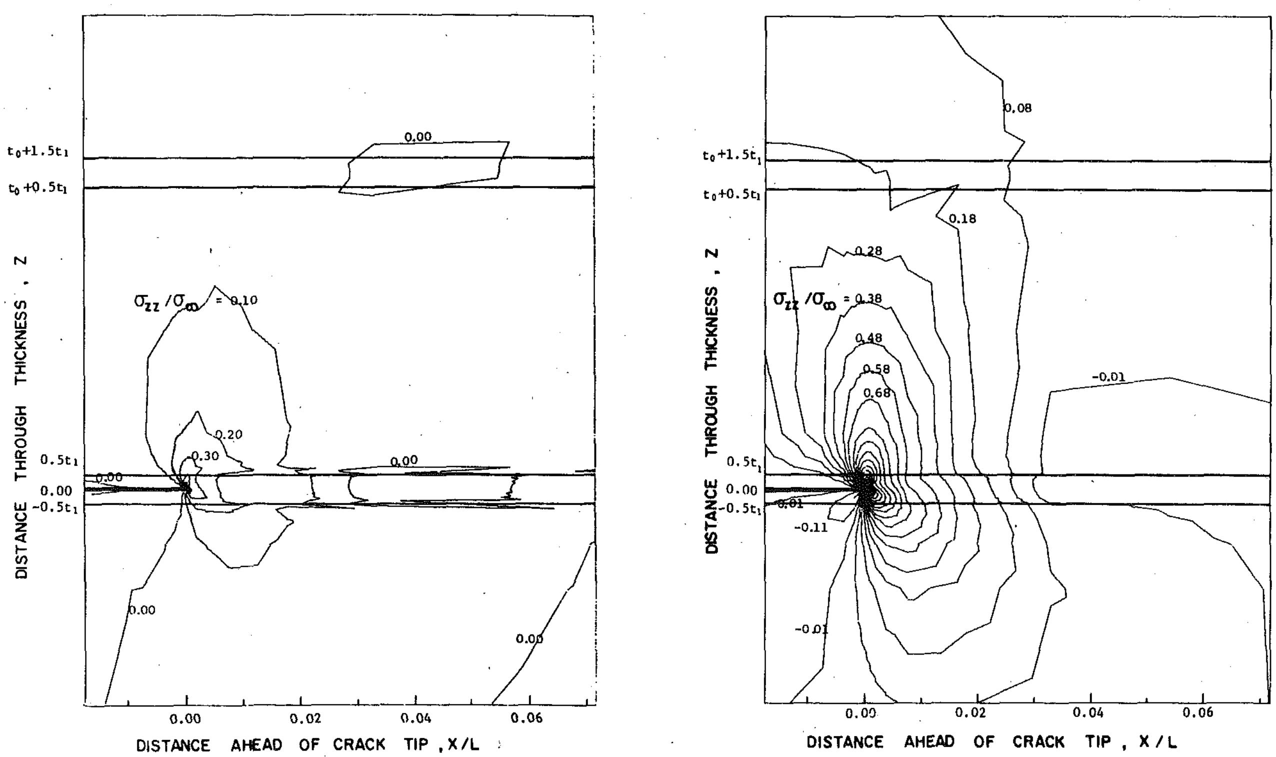

a) $(\underline{0}^\circ // 0^\circ / 0^\circ / 0^\circ)$ b) $(\underline{45}^\circ // -45^\circ / -45^\circ / 45^\circ)$

Fig. 8 Effect of ply orientation on transverse normal stress distribution $\sigma_{zz}/\sigma_\infty$ near delamination crack tip in graphite/epoxy composites

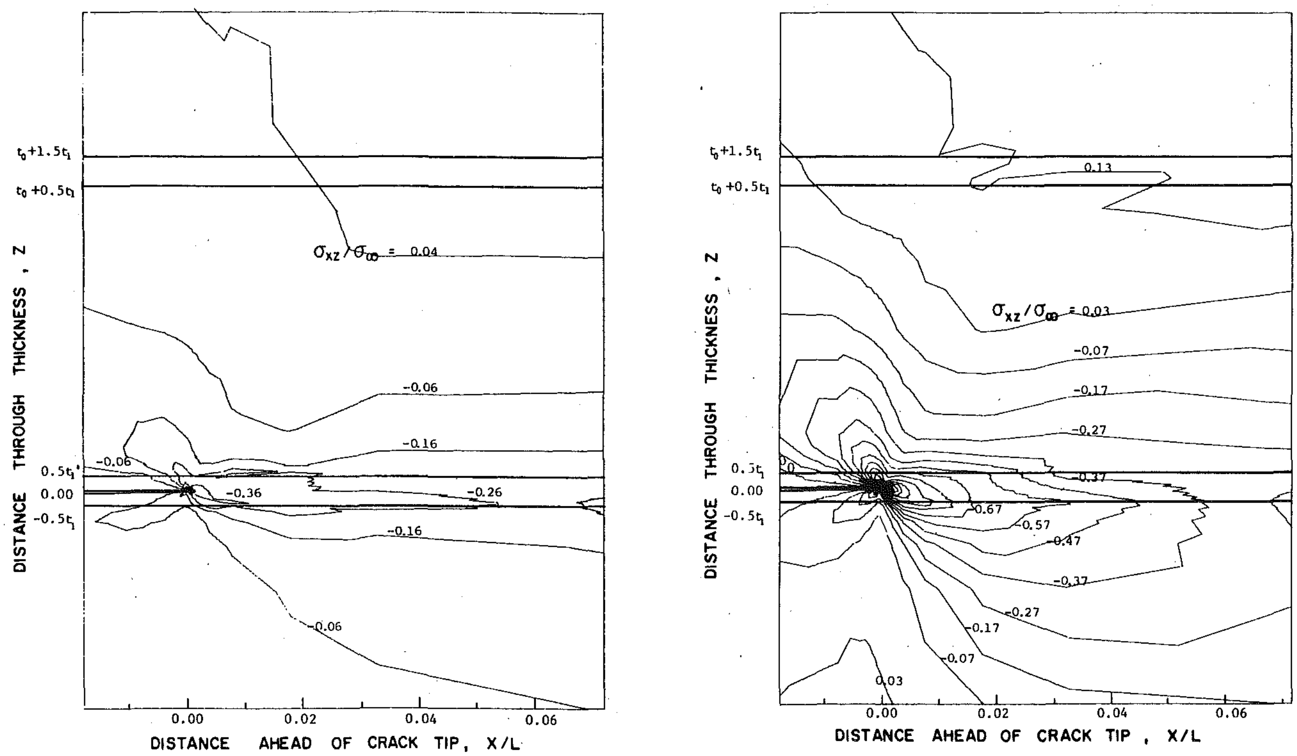

a) ($\underline{0^\circ}$//0°/0°/0°) b) ($\underline{45^\circ}$//−45°/−45°/45°)

Fig. 9 Effect of ply orientation on interlaminar shear stress distribution $\sigma_{xz}/\sigma_\infty$ near delamination crack tip in graphite/epoxy composites

tend farther in neighboring plies than those observed in a unidirectional case. The results also indicate that interlaminar stresses in the unidirectional composite are more localized within the interlaminar region than those in the perturbed domain of angle-ply laminates. Furthermore, the complicated stress transfer mechanisms reveal that failure modes and subsequent growth of the delamination crack may be more complex in nature in angle-ply composites.

Limitations of Current Study

It should be noted here that several geometric and material complications in the composites have not been included in the current analytical modeling, such as the nonuniformity of the thickness of interlaminar resin regions, the heterogeneity of fiber and matrix phases, and other kinds of defects (e.g., voids, inclusions, etc.). These complications are statistical in nature and almost always exist in the material. Their presence may have significant effects on the delamination behavior, but this has not been fully explored yet. The antiplane mode of deformation and fracture (mode III), which may have an important contribution to the progressive failure of the composites, especially in angle-plied laminates, has not been examined in this work. A recent study on edge delamination [14] revealed that the mode III component of the crack-tip deformation is indeed very significant and that it may be primarily responsible for the interlaminar failure of the composites.

Summary and Conclusions

An analysis for investigating delamination in angle-ply composites has been developed. The composite laminate was modeled as an assembly of anisotropic homogeneous plies bonded by thin resin interlayers. The delamination crack was assumed to be initiated from a surface notch in the form of broken plies and located in an interlaminar region. A hybrid-stress finite-element analysis, including a special crack-tip element formulated by Muskhelishvili's complex stress functions, was used to examine the failure mechanics and mechanisms of the delamination. Convergence and accuracy of the analysis were affirmed by comparing current results with existing closed-form solutions.

Solutions for the delaminated ($\underline{\theta}//-\theta/-\theta/\theta$) graphite/epoxy composites were obtained. The results reveal the fundamental nature of delamination in fiber-reinforced composite laminates: a localized singular stress field in the delamination crack-tip region, large stress gradients in the adjacent unbroken plies, complex interlaminar stress distributions and transfer mechanisms through the laminate thickness, and the comparable and relatively high magnitudes of $K_{\rm I}$ and $K_{\rm II}$ associated with the delamination. The change in fiber orientation significantly alters the mixed-mode stress-intensity factors and the stress concentrations by a factor of approximately three. The rapid decrease in the ply axial strength coupled with the increase in interlaminar stresses and the relatively constant in-plane stress component due to the alternation of fiber orientation suggest a possible transition of failure modes in the subsequent growth of the delamination crack in angle-ply laminates. The highly nonuniform stress distributions through the laminate thickness indicate the inapplicability of the classical laminate theory near the delamination crack-tip region.

Acknowledgments

The work described in this paper was supported in part by NASA-Lewis Research Center, Cleveland, Ohio, under Grant NSG 3044. The author is grateful to Dr. C. C. Chamis for his encouragement and cooperation. Fruitful discussion with Dr. J. F. Mandell of the Massachusetts Institute of Technology is deeply acknowledged.

References

1 Kies, J. E., "The Strength of Glass Fibers and the Failure of Filament Wound Pressure Vessels," Report No. 6034, Naval Research Laboratory, Washington, D.C., 1964.

2 Kulkarni, S. V., and Frederick, D., "Propagation of Delamination in a

Layered Cylindrical Shell," *International Journal of Fracture,* Vol. 9, 1973, pp. 113–115.

3 Erdogan, F., and Arin, K., "A Sandwich Plate With a Part-Through and Debonding Crack," *Engineering Fracture Mechanics,* Vol. 4, 1972, pp. 449–458.

4 Clements, D. L., "A Crack Between Dissimilar Anosotropic Media," *International Journal of Engineering Science,* Vol. 9, 1971, pp. 257–265.

5 Cook, T. S., and Erdogan, F., "Stresses in Bonded Materials With a Crack Perpendicular to the Interface," *International Journal of Engineering Science,* Vol. 10, 1972, pp. 677–697.

6 Lin, K. Y., and Mar, J. W., "Finite Element Analysis of Stress Intensity Factors for Cracks at a Bimaterial Interface," *International Journal of Fracture,* Vol. 12, No. 4, 1976, pp. 521–532.

7 Goree, J. G., and Venezia, W. A., "Bonded Elastic Half Planes With an Interface Crack and a Perpendicular Intersecting Crack That Extends Into Adjacent Material—I," *International Journal of Engineering Science,* Vol. 15, 1977, pp. 1–17.

8 Im, J., et al., "Surface Crack Growth in Fiber Composites," NASA Technical Report NASA CR-135094, Sept. 1976.

9 Pipes, R. B., Kaminski, B. E., and Pagano, N. J., "Influence of the Free Edge Upon the Strength of Angle-Ply Laminates," *Analysis of the Test Methods for High Modulus Fibers and Composites,* ASTM STP 521, American Society for Testing and Materials, 1973, pp. 218–228.

10 Sendeckyj, G. P., Stalnaker, H. D., and Kleismit, R. A., "Effect of Temperature and Fatigue Response of Surface Notched $[(0°/\pm 45°/0)_s]_3$ Graphite-Epoxy Laminate," *Fatigue of Filamentary Composite Materials,* ASTM STP 636, Reifsnider, K. L., and Lauraitis, K. N., eds., American Society for Testing and Materials, 1977, pp. 123–140.

11 Wang, S. S., and Mandell, J. F., "Analysis of Delamination in Unidirectional and Crossplied Fiber-Reinforced Composites Containing Surface Cracks," NASA Technical Report NASA-CR-135248, May 1977.

12 Wang, S. S., and Wang, H. T., "Interlaminar Crack Growth in Fiber-Reinforced Composites During Fatigue," ASME *Journal of Engineering Materials and Technology,* Vol. 101, 1979, pp. 34–41.

13 Tong, P., Pian, T. H. H., and Lasry, S., "A Hybrid-Element Approach to Crack Problems in Plane Elasticity," *International Journal of Numerical Methods in Engineering,* Vol. 7, 1973, pp. 297–308.

14 Wang, S. S., "An Analysis of Edge Delamination Crack in Composite Laminate Under Uniform Axial Extension," ASTM STP, American Society for Testing and Materials, 1978, to appear.

15 Wang, S. S., Mandell, J. F., and McGarry, F. J., "An Analysis of the Crack Tip Stress Field in DCB Adhesive Fracture Specimens," *International Journal of Fracture,* Vol. 14, No. 1, 1978, pp. 39–58.

16 Muskhelishvili, N. I., *Some Basic Problems of Mathematical Theory of Elasticity,* P. Noordhoff, Groningen, The Netherlands, 1953.

17 Pian, T. H. H., "Derivation of Element Stiffness Matrix by Assumed Stress Distribution," *American Institute of Aeronautics and Astronautics Journal,* Vol. 2, 1964, pp. 1333–1336.

18 Wang, S. S., "Delamination Fracture From Surface Notch in $[(\pm 45°)/0°/90°]_s$ Graphite/Epoxy Composites," *Proceedings of the Second International Conference on Composite Materials,* (ICCM-II), TMS-AIME 1978, pp. 277–291.

19 Wu, E. M., "Application of Fracture Mechanics to Anisotropic Plates," ASME Journal of Applied Mechanics, Vol. 34, 1967, pp. 967–974.

20 Lauraitis, K. N., "Failure Modes and Strength of Angle-Ply Laminates," T.&A.M. Report No. 345, Department of Theoretical and Applied Mechanics, University of Illinois, Urbana, Ill., 1971, pp. 60–63.

21 Wang, S. S. "Delamination Crack Growth in Unidirectional Fiber-Reinforced Composites Under Static and Cyclic Loading," *Composite Materials: Testing and Design (Fifth Conference),* ASTM STP 674, Tsai, S. W., ed., American Society for Testing and Materials, 1979, pp. 642–663.

22 Reifsnider, K. L., Henneke, E. G., II, and Stinchcomb, W. W., "Delamination in Quasi-isotropic Graphite-Epoxy Laminates," *Composite Materials: Testing and Design (Fourth Conference),* ASTM STP 617, American Society for Testing and Materials, 1977, pp. 93–105.

23 Oplinger, D. W., Parker, B. S., and Grenis, A., "On the Three Dimensionality of Failure Modes in Angle-Ply Strips Under Tension," *Proceedings of the Army Symposium on Solid Mechanics, 1976—Composite Materials: The Influence of Mechanics of Failure on Design,* AMMRC MS 76-2, Army Mechanics and Materials Research Center, Watertown, Mass. 1976, pp. 263–286.

24 Mandell, J. F., "Origin of Moisture Effects on Crack Propagation in Composites," Research Report R77-4, Department of Materials Science and Engineering, M.I.T., Dec. 1977.

J. Christoffersen

Associate Professor,
Department of Solid Mechanics,
The Technical University of Denmark,
Lyngby, Denmark

Fabrics: Orthotropic Materials With a Stress-Free Shear Mode

A material model of elastic fabrics is proposed. In this, orthotropy and a vanishing shear rigidity is assumed. Full nonlinear equations are derived and simplifications valid for small material rotations are proposed. Even the simplified model is nonlinear, but it is demonstrated that, in certain instances, a linearization, leading to harmonic equations, is admissible. This is exemplified by the case of a crack in an infinite sheet.

Introduction

Fabric is applied as a structural material in many instances, tents, inflatable halls, and sails to mention a few. Also laminated cord-rubber as used in tires and hoses have a fabric-like structure. Nevertheless it seems that these materials have not been given much consideration from the point of view of applied mechanics. Certainly a number of papers to be found mainly in *Textile Research Journal* and *Journal of the Textile Institute* deal with mechanical aspects of deformation of textiles, but as far as the theoretical papers are concerned emphasis is generally on the complications involved in accounting for a maximum of material and geometrical nonlinearities rather than on stripping the material models of secondary effects in order to bring out clearly the distinguishing features of a simple, yet reasonably realistic, model. Furthermore, the interest seems to have been confined to macroscopically homogeneous modes of deformation, whereas formulating and solving boundary-value problems for textile structures has not yet been accomplished.

The prominent distinguishing feature of textiles when viewed as anisotropic materials is their almost total lack of rigidity in shear-mode deformations not involving stretching of the yarns. This property accounts for the willingness with which these materials adapt to three-dimensional double curvature surfaces such as those of the human body. It is obvious from simple theoretical considerations, and it is also acknowledged, although not always explicitly, by experimentalists. A substantial number of investigations reported have been concerned either with force-elongation relationships under stretching of the yarns or with the mechanical behavior in shear, e.g. Kawabata, Niwa, and Kawai [1], whereas investigations combining the two aspects are rather scarce. However, experiments of Hearle and Stevenson [2], mainly concerning nonwovens with more or less randomly laid fibers but including also a woven rayon fabric, of Sengupta, De, and Sarkar [3] on woven cotton fabrics, and of Clark [4] on cord-rubber laminates all confirm the expectation of a low shear rigidity.

Contributed by the Applied Mechanics Division for publication in the JOURNAL OF APPLIED MECHANICS.

Discussion on this paper should be addressed to the Editorial Department, ASME, United Engineering Center, 345 East 47th Street, New York, N. Y. 10017, and will be accepted until June 1, 1980. Readers who need more time to prepare a discussion should request an extension from the Editorial Department. Manuscript received by ASME Applied Mechanics Division, October, 1978; final revision, May, 1979.

We believe that a deformable orthotropic plane behaving elastically in stretching along the two orthotropic directions and capable of a stress-free deformation in shear along these directions provides a realistic model for deformation of a fabric with orthogonally disposed yarns. The displacement functions are monovalued in accordance with the assumption that no slippage occurs at yarn crossovers. This is realistic in wovens if a sufficient friction is available, in nonwovens with bonded orthogonal fibers, in PVC-clad fabrics, and in laminates of cord-reinforced rubber.

Such severe anisotropy is not encountered in current theories of elasticity, and, therefore, these materials require special consideration. Governing equations are derived in the present paper, and it is demonstrated that even if the material is linearly elastic (in some sense) a complete linearization of the problem is usually not permissible. A simplified, but still nonlinear, version of the governing equations is presented on the basis of an assumption of small yarn rotations, and it is demonstrated that problems in which constancy of the normal stress in one of the orthotropic directions is to be expected may be reduced to harmonic ones. This is very similar to the linearization involved in string and membrane problems, and it is illustrated by a simple example involving an infinite sheet with an isolated crack parallel with one of the orthotropic directions.

The General Theory

The structure of a material element in the stress-free reference state and in some deformed state is illustrated in Fig. 1. Warp and weft, labeled 1 and 2, respectively, are originally orthogonal and parallel to the axes of a fixed Cartesian coordinate system. Mutual sliding of yarns is prevented through friction, bonding, or otherwise.

Coordinates x_α ($\alpha = 1, 2$) of a material point in the undeformed configuration are changed to y_α through the deformation. Taking y_α to be functions of x_1 and x_2 a line element dx_α transforms into

$$dy_\alpha = F_{\alpha\beta} dx_\beta \quad (1)$$

where, with $\beta = 1, 2$, the summation convention is adopted, and the deformation gradient

$$F_{\alpha\beta} = y_{\alpha,\beta} \quad (2)$$

has the partial derivatives of y_α with respect to x_β as its components.

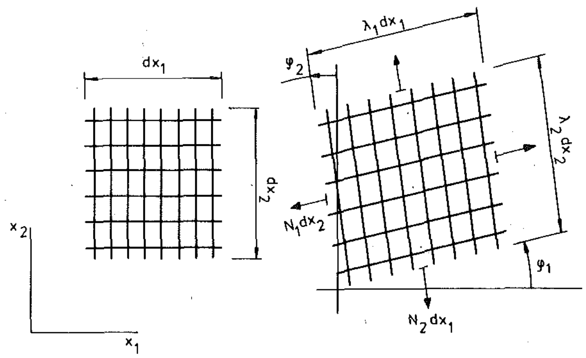

Fig. 1 Undeformed and deformed configurations of a material element

In the deformed configuration the yarns are rotated anticlockwise through angles ϕ_α and are stretched in ratios λ_α. Hence the deformation gradient has components

$$\begin{pmatrix} F_{11} & F_{12} \\ F_{21} & F_{22} \end{pmatrix} = \begin{pmatrix} \lambda_1 \cos\phi_1 & -\lambda_2 \sin\phi_2 \\ \lambda_1 \sin\phi_1 & \lambda_2 \cos\phi_2 \end{pmatrix}. \tag{3}$$

The fiber forces are statically equivalent to nominal tractions (i.e., forces per unit of length as measured in the undeformed configuration) of magnitude N_α directed along the yarns. Hence the components of Piola stress $S_{\alpha\beta}$ are

$$\begin{pmatrix} S_{11} & S_{12} \\ S_{21} & S_{22} \end{pmatrix} = \begin{pmatrix} N_1 \cos\phi_1 & N_1 \sin\phi_1 \\ -N_2 \sin\phi_2 & N_2 \cos\phi_2 \end{pmatrix}. \tag{4}$$

Balance of forces requires

$$S_{\alpha\beta,\alpha} = 0, \tag{5}$$

and this is identically satisfied with the introduction of stress functions H_α through

$$S_{\alpha\beta} = \epsilon_{\alpha\gamma} H_{\beta,\gamma} \tag{6}$$

where $\gamma = 1, 2$ and $\epsilon_{\alpha\gamma}$ is the two-dimensional permutation symbol. Physically, H_α is, at a given point, the α-th component of the internal force acting on any curve connecting the point in question with some fixed point, where H_α is preassigned the value zero. Balance of moments entails the symmetry relation

$$F_{\alpha\gamma} S_{\gamma\beta} = F_{\beta\gamma} S_{\gamma\alpha} \tag{7}$$

and is automatically satisfied.

Taking the material to be elastic, a stress potential $W(\lambda_1, \lambda_2)$ exists such that

$$N_\alpha = \frac{\partial W}{\partial \lambda_\alpha} \tag{8}$$

consistent with the expression, derivable from (3) and (4), for the rate of working per unit of original area

$$S_{\alpha\beta} \dot{F}_{\beta\alpha} = N_\alpha \dot{\lambda}_\alpha. \tag{9}$$

Eliminating $F_{\alpha\beta}$, $S_{\alpha\beta}$, and ϕ_α from equations (2)–(4), and (6) we arrive at the following set of equations:

$$H_{1,2} = \frac{N_1}{\lambda_1} y_{1,1}; \; H_{1,1} = -\frac{N_2}{\lambda_2} y_{1,2};$$

$$H_{2,2} = \frac{N_1}{\lambda_1} y_{2,1}; \; H_{2,1} = -\frac{N_2}{\lambda_2} y_{2,2}, \tag{10a–d}$$

where $N_\alpha = N_\alpha(\lambda_1, \lambda_2)$ (equation (8)) and

$$\lambda_1 = \sqrt{(y_{1,1})^2 + (y_{2,1})^2}; \quad \lambda_2 = \sqrt{(y_{1,2})^2 + (y_{2,2})^2} \tag{11a,b}$$

Alternatively we may take $\lambda_\alpha = \lambda_\alpha(N_1, N_2)$ and

$$N_1 = \sqrt{(H_{1,2})^2 + (H_{2,2})^2}; \quad N_2 = \sqrt{(H_{1,1})^2 + (H_{2,1})^2} \tag{12a, b}$$

Elimination of H_α or y_α from equations (10) results in a system of two 2nd-order partial differential equations, viz.,

$$\left(\frac{N_1}{\lambda_1} y_{1,1}\right)_{,1} + \left(\frac{N_2}{\lambda_2} y_{1,2}\right)_{,2} = 0;$$

$$\left(\frac{N_1}{\lambda_1} y_{2,1}\right)_{,1} + \left(\frac{N_2}{\lambda_2} y_{2,2}\right)_{,2} = 0, \tag{13a, b}$$

$$\left(\frac{\lambda_2}{N_2} H_{1,1}\right)_{,1} + \left(\frac{\lambda_1}{N_1} H_{1,2}\right)_{,2} = 0;$$

$$\left(\frac{\lambda_2}{N_2} H_{2,1}\right)_{,1} + \left(\frac{\lambda_1}{N_1} H_{2,2}\right)_{,2} = 0. \tag{14a, b}$$

Boundary conditions may be given in terms of displacements $(y_\alpha - x_\alpha)$ or tractions. It is recalled that H_α equals the resultant force acting on that part of the boundary which is contained between a fixed point (where we may set $H_\alpha = 0$) and the point where H_α is assigned its value. However, traction boundary conditions may be given in terms of y_α and displacement conditions in terms of H_α as

$$\frac{N_1}{\lambda_1} y_{1,1} n_1 + \frac{N_2}{\lambda_2} y_{1,2} n_2 = \frac{dH_1}{ds}; \tag{15a}$$

$$\frac{N_1}{\lambda_1} y_{2,1} n_1 + \frac{N_2}{\lambda_2} y_{2,2} n_2 = \frac{dH_2}{ds}, \tag{15b}$$

$$\frac{\lambda_2}{N_2} H_{1,1} n_1 + \frac{\lambda_1}{N_1} H_{1,2} n_2 = -\frac{dy_1}{ds}; \tag{16a}$$

$$\frac{\lambda_2}{N_2} H_{2,1} n_1 + \frac{\lambda_1}{N_1} H_{2,2} n_2 = -\frac{dy_2}{ds}. \tag{16b}$$

Here, ds is the line element of the undeformed boundary curve, and n_α is its outward unit normal. It is noted that dH_α/ds represents the nominal traction on the boundary.

Not addressing the question of existence of solutions directly we mention that boundary conditions for which no solution exists may easily be constructed, e.g., the specification $s_{11} \geq 0$, $s_{12} = 0$, $s_{21} = 0$, $s_{22} < 0$ is clearly inadmissible for a rectangular sheet with edges parallel with the coordinate axes. Taking $s_{22} = 0$ instead of $s_{22} < 0$ it is obvious that a solution exists but is nonunique. Apart from rigid-body motions, any shear field $y_1 = y_1(x_2)$ may be superposed on the solution.

To gain further insight in this aspect, consider the expression for the potential energy of the system,

$$F = \int_\Omega W(\lambda_1, \lambda_2) dS - \oint_{\Gamma_T} \frac{dH_\beta}{ds} y_\beta ds, \tag{17}$$

assuming for simplicity dead loading (i.e., dH_α/ds is constant during any deformation. Here, dS is the surface element of the undeformed configuration. The surface integral is extended over the region Ω occupied by the structure, and the line integral is taken over that part, Γ_T, of the boundary curve Γ, where tractions are prescribed. Displacements, and thereby y_β, are prescribed on the remaining part of the boundary curve $\Gamma_y = \Gamma - \Gamma_T$. Stationarity of F with respect to variations of y_β vanishing on Γ_y implies, and is implied by, the equilibrium conditions (13) and (15). Stability requires that F attains a minimum at the stationary point. Let the quantities introduced so far pertain to an equilibrium state, the stability of which is on trial, and let the corresponding quantities in any other configuration be denoted by starred symbols. The excess potential energy

$$F^* - F = \int \{W(\lambda_1^*, \lambda_2^*) - W(\lambda_1, \lambda_2)\} dS - \oint S_{\alpha\beta}(y_\beta^* - y_\beta) n_\alpha ds$$

may, with aid of the divergence theorem, be written as

$$\begin{aligned} F^* - F = \int \{ & W(\lambda_1^*, \lambda_2^*) \\ & - W(\lambda_1, \lambda_2) - N_1(\lambda_1^* - \lambda_1) - N_2(\lambda_2^* - \lambda_2) \\ & + N_1 \lambda_1^* [1 - \cos(\phi_1^* - \phi_1)] \\ & + N_2 \lambda_2^* [1 - \cos(\phi_2^* - \phi_2)]\} dS. \end{aligned} \tag{18}$$

The convexity condition

$$W(\lambda_1^*, \lambda_2^*) - W(\lambda_1, \lambda_2) - N_1(\lambda_1^* - \lambda_1) - N_2(\lambda_2^* - \lambda_2) \geq 0, \tag{19}$$

with equality only for $\lambda_\alpha^* = \lambda_\alpha$, is an expression of material stability. It is equivalent to positive-definiteness of the quadratic form

$$C_{\alpha\beta}\lambda_\beta\lambda_\alpha \geq 0 \tag{20}$$

(equality only for $\lambda_\alpha = 0$), where

$$C_{\alpha\beta} = \frac{\partial^2 W}{\partial\lambda_\alpha\partial\lambda_\beta} \tag{21}$$

are the instantaneous rigidities. The condition (20) is equivalent to

$$C_{11} > 0; \quad C_{22} > 0; \quad C_{11}C_{22} - (C_{12})^2 > 0. \tag{22a–c}$$

If these conditions are satisfied pointwise and if, furthermore, the solution has

$$N_1 > 0; \quad N_2 > 0 \tag{23a, b}$$

everywhere, except possibly for a region of zero measure, such as a boundary, then the solution is stable since in that case the functional (18) is positive definite.

It is emphasized that conditions (23) suffice to prevent in-plane buckling of the structure. It is likely that avoidance of out-of-plane buckling and buckling of single fibers is also insured by (23).

Approximate Equations

The approximation

$$\lambda_1 = y_{1,1}; \quad \lambda_2 = y_{2,2} \tag{24}$$

is justifiable if rotations ϕ_1 and ϕ_2 are small in the sense that $(\phi_1)^2 \ll 1$ and $(\phi_2)^2 \ll 1$. With (24) equations (10) simplify as follows:

$$H_{1,2} = N_1; \quad H_{1,1} = -\frac{N_2}{\lambda_2}y_{1,2};$$

$$H_{2,2} = \frac{N_1}{\lambda_1}y_{2,1}; \quad H_{2,1} = -N_2. \tag{25a–d}$$

A complete linearization leads to the somewhat trivial result that N_α should be constant along the respective fibers. It is obviously inadmissible if different stress boundary conditions are prescribed at both ends of the yarns. Equations (25) still bring out the crucial property of the material that forces can be transmitted between the yarns.

If the approximation (24) is admissible and the constitutive equations decouple with N_1 linear in λ_1,

$$N_1 = C_1(\lambda_1 - 1); \quad N_2 = N_2(\lambda_2), \tag{26a, b}$$

and if, furthermore, the boundary conditions admit

$$y_{2,1} = 0; \quad y_{2,2} = \lambda_2 = \text{constant}, \tag{27a, b}$$

hence

$$H_{2,2} = 0; \quad H_{2,1} = -N_2 = \text{constant}, \tag{28a, b}$$

then equations (25a, b) reduce to a set of linear differential equations in the unknowns y_1 and H_1, viz.,

$$H_{1,2} = C_1(y_{1,1} - 1); \quad H_{1,1} = -\frac{N_2}{\lambda_2}y_{1,2}. \tag{29a, b}$$

With the transformations

$$x_1 = x; \quad x_2 = \sqrt{\frac{N_2}{C_1\lambda_2}}y; \quad y_1 = x + u; \quad H_1 = \sqrt{\frac{C_1N_2}{\lambda_2}}v \tag{30a–d}$$

equations (29) reduce to the Cauchy-Riemann equations

$$\frac{\partial v}{\partial y} = \frac{\partial u}{\partial x}; \quad \frac{\partial v}{\partial x} = -\frac{\partial u}{\partial y}. \tag{31a, b}$$

Thus

$$z = x + iy, \tag{32}$$

where i is the imaginary unit, is the complex argument of a holomorphic function

$$w(z) = u(x, y) + iv(x, y). \tag{33}$$

A typical situation, if not the only one, in which this quasi-linearization is admissible, is one in which the yarns of system No. 2 have identical material properties and pass unbrokenly through the structure between straight, parallel boundaries where either equal, but oppositely directed, constant 2nd components of traction or constant 2nd components of displacements are prescribed.

An Extended Sheet With an Isolated Crack

Consider an infinite sheet of fabric with a crack of undeformed length $2l$ cutting the yarns of system No. 1. The crack tips are taken to be at $(x_1, x_2) = (0, \pm l)$. The tension is constant at infinity with rotations ϕ_1 and ϕ_2 tending to zero, hence

$$s_{11} \to N_1^\infty; \quad s_{12} \to 0; \quad s_{21} \to 0; \quad s_{22} \to N_2^\infty \quad \text{for} \quad (x_1, x_2) \to \pm\infty \tag{34a–d}$$

with N_1^∞ and N_2^∞ prescribed. The constitutive equations are assumed to be of the form (26).

Boundary conditions at $(x_1, x_2) = \pm\infty$ concerning $s_{2\alpha}$ are satisfied with (28), hence

$$N_2 = N_2^\infty \tag{35}$$

and the quasi-linear version of the theory described in the previous section is applicable. Since

$$H_1 \to N_1^\infty x_2; \quad y_1 \to \left(1 + \frac{N_1^\infty}{C_1}\right)x_1 \quad \text{for} \quad (x_1, x_2) \to \pm\infty \tag{36a b}$$

the holomorpic function $w(z)$ (equation (33)) must satisfy

$$w(z) \to \frac{N_1^\infty}{C_1}z \quad \text{for} \quad z \to \infty. \tag{37}$$

At the crack faces, $z = y^+$ and $z = y^-$, we take $H_1^- = H_1^+ = 0$ and, due to symmetry, $y_1^- = -y_1^+$. Hence

$$w(y^+) = u_0(y); \quad w(y^-) = -u_0(y)$$

$$\text{for} \quad x = 0 \quad \text{and} \quad |y| < \sqrt{\frac{N_2}{C_1\lambda_2}}l. \tag{38a, b}$$

where $u_0(y)$ is real. Adding equations (38a) and (38b) we find

$$w(y^+) + w(y^-) = 0 \quad \text{for} \quad x = 0 \quad \text{and} \quad |y| < \sqrt{\frac{N_2}{C_1\lambda_2}}l. \tag{39}$$

The solution of this very simple homogeneous Hilbert problem may be written down immediately, see, e.g., Muskhelishvili [5],

$$w(z) = P(z) \bigg/ \sqrt{z^2 + \frac{N_2}{C_1\lambda_2}l^2} \tag{40}$$

where $P(z)$ is a polynomium. Requiring $w(z)$ to be bounded everywhere we must insist that $P(z)$ has a factor $[z^2 + N_2l^2/(C_1\lambda_2)]$ and so, with the boundary conditions (37), the solution is

$$w(z) = \frac{N_1^\infty}{C_1}\sqrt{z^2 + \frac{N_2}{C_1\lambda_2}l^2}. \tag{41}$$

An example demonstrating the shape of the deformed grid of yarns is shown in Fig. 2. Fig. 3 displays curves of constant N_1 for one quadrant of the structure (referred to the undeformed state). The stresses on the extension of the crack is near the tip of the form

$$N_1 = K/\sqrt{r}; \quad K = N_1^\infty\sqrt{\frac{l}{2}}, \tag{42a, b}$$

where $r = x_2 - l$ is the distance from the crack tip. The maximum yarn

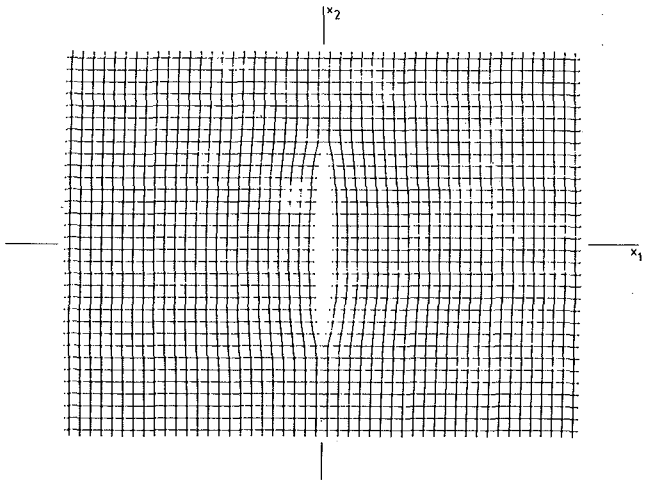

Fig. 2 A fabric crack (square grid when undeformed); stretch ratios at infinity: $\lambda_1^\infty = 1{,}05$; $\lambda_2^\infty = 1{,}20$; nominal stresses at infinity: N_1^∞; N_2^∞; $N_1^\infty = 0{,}25\, N_2^\infty$; number of fibers cut: $n = 16$

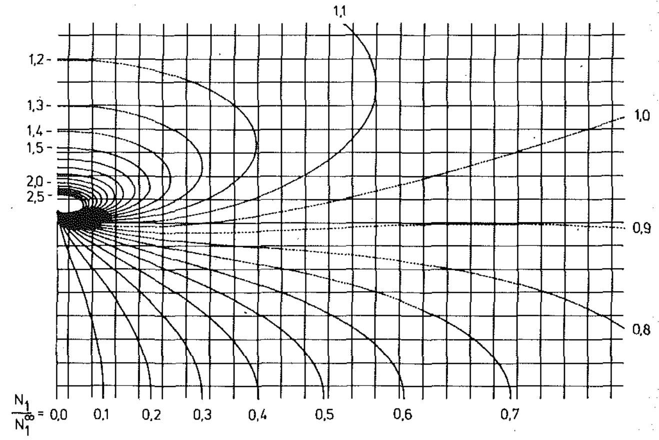

Fig. 3 Curves of constant N_1 for the situation illustrated in Fig. 2 (reference to the undeformed structure; only one quadrant is displayed)

force in the system cut by the crack appears in the yarns terminating the crack at the points of termination. Denoting this $P_1^{\max}$,

$$P_1^{\max} = H_1(0, l + \delta_2) - H_1(0, l) \tag{43}$$

where δ_2 is the spacing of the system No. 1 yarns in the undeformed grid. With (30*d*) and with

$$P_1^\infty = N_1^\infty \delta_2 \tag{44}$$

denoting the yarn force at infinity we find the simple formula

$$P_1^{\max} = \sqrt{n + 1} P_1^\infty \tag{45}$$

where

$$n = 2l/\delta_2 \tag{46}$$

is the number of yarns cut in forming the crack. The maximum yarn force and the stress-intensity factor K (equations (42)) are interrelated through

$$P_1^{\max} = 2K\sqrt{\delta_2} \tag{47}$$

where $n + 1$ has been replaced by n. Thus a condition of the type $P_1^{\max} < P_1^c$ is equivalent to a condition of the form $K < K^c$, and the material parameter with length as its dimension, inherent in fracture mechanics, may here be identified with the fiber spacing δ_2.

The case of a pin-shaped inclusion, rigid or elastic, parallel with the No. 1 yarns (e.g., a seam) leads to similar expressions. Further tractable problems are such in which the density of No. 1 yarns changes abruptly from one constant value to another across a boundary. These problems are of course less interesting than problems of holes and patches affecting both systems. However, this requires solution of the full nonlinear equations (10) or of some nonlinear approximation to them.

References

1 Kawabata, S., Niwa, M., and Kawai, K., "The Finite-Deformation Theory of Plain-Weave Fabrics—Part III: The Shear-Deformation Theory," *Journal of the Textile Institute*, Vol. 64, 1973, pp. 62–85.

2 Hearle, J. W. S., and Stevenson, P. J., "Nonwoven Fabric Studies—Part III: The Anisotropy of Nonwoven Fabrics," *Textile Research Journal*, Vol. 33, 1963, pp. 877–888.

3 Sengupta, A. K., De, D., and Sarkar, B. P., "Anisotropy in Some Mechanical Properties of Woven Fabrics," *Textile Research Journal*, Vol. 42, 1972, pp. 268–271.

4 Clark, S. K., "The Plane Elastic Characteristics of Cord-Rubber Laminates," *Textile Research Journal*, Vol. 33, 1963, pp. 295–313.

5 Muskhelishvili, N. I., *Singular Integral Equations*, Noordhoff, Groningen, 1953.

ADDENDUM

The author regrets having failed to reference the work by S. M. Genensky and R. S. Rivlin, "Infinitesimal Plane Strain in a Network of Elastic Cords," *Arch. Rational Mech.*, Vol. 4, 1960, pp. 30–44. The existence of this paper certainly invalidates the statement that elastic fabrics have not been given much attention from the point of view of mechanics.

While the scope and method of the two papers are parallel, the following differences may be noted.

In the paper of Genensky and Rivlin the case of a grid that is skewed when undeformed is considered. In a theory of small deflections this is essential, but when deformations of any magnitude are admitted it is only a matter of taking the fundamental state from which deformations are measured as one with orthogonal yarns. Such a state may be attained from any state with skewed yarns without applying forces to the fabric.

The two forms of the general theory are identical in essence, differing only in exposition. Emphasis on the stress measure of Piola, as in the case of the paper by this author, rather than on Cauchy stress, as in the paper by Genensky and Rivlin, appears to facilitate the discussion somewhat. In particular, the introduction of a vector of stress functions brings out nice duality properties of equilibrium and compatibility. Also the discussion on uniqueness appears to be new.

The "quadratic" approximation suggested in the paper by this author seems to be adequate in connection with some problems of practical importance, e.g., crack problems, where restrictions on boundary conditions, requisite for the linear theory, cannot be imposed.

In that paper the completely linearized form is dismissed as inadmissible. The thorough investigation of this case in the paper by Genensky and Rivlin clearly marks such a conjecture as premature: The cases treated there are most interesting.

R. T. Shield

Head,
Department of Theoretical and Applied Mechanics,
University of Illinois at Urbana-Champaign,
Urbana, Ill. 61801
Mem. ASME

An Energy Method for Certain Second-Order Effects With Application to Torsion of Elastic Bars Under Tension

When a mechanical system has a potential energy, it is a simple matter to show that if the generalized force corresponding to a coordinate p is known to first order in p for a range of the other coordinates of the system, then the other generalized forces can be found immediately to second order in p, without requiring a second-order analysis of the system. By this method the second-order change in the axial force when a finitely extended elastic cylinder is twisted is found from the first-order value of the twisting moment. Numerical results for a realistic form of the strain-energy function for an incompressible material suggest that the second-order expression for the axial force is very accurate for a wide range of twist for circular cylinders of rubber-like materials extended 100 percent or more.

1 Introduction

Approximations to exact solutions for nonlinear mechanical systems are often used because of the difficulty of obtaining exact solutions. A first-order approximation valid for a parameter, p say, approaching zero is usually determined by linear equations and so is often the first approximation to be found. In Section 2, we consider a system for which a potential energy exists. We show that if the generalized force corresponding to the parameter p is known to first order in p for a range of the other loading parameters of the system, then the generalized forces corresponding to the other parameters can be found immediately to second order in p, without requiring a second-order analysis of the system.

A simple illustration of the method is given in Section 2 but the main application of this paper is to the problem of an elastic cylinder which is first finitely extended and then twisted. Under certain conditions, the axial force and twisting moment on a section of the cylinder are proportional to the derivatives of the total strain energy with respect to the extension ratio λ and the twist ψ per unit initial length. This is true if the deformation is imposed through rigid end plates which remain parallel, and in Section 3 we show that it is also true if the state of strain is the same at each section of the cylinder (a natural extension of the Saint Venant torsion solution to finite elasticity). The solution derived by Green and Shield [1] for small twist superposed on finite extension of an isotropic cylinder provides the twisting moment M to first order in ψ, with an error of order ψ^3, for arbitrary λ and a general form for the strain-energy function. In Section 4 we use the approach of Section 2 to obtain directly the expression for the axial force L to second order in ψ, with an error of order ψ^4, for a general strain-energy function. By taking λ to be unity and using the five-constant form of Murnaghan [2] for the strain energy, we rederive the result of Rivlin [3] for the second-order fractional extension of a cylinder under small twist and zero axial force. Rivlin used the differential equations and the boundary conditions governing the second-order displacements in deriving his result, but his approach did not require an explicit solution for the second-order displacements. The method of this paper uses only the first-order value for the twisting moment M as a function of λ near $\lambda = 1$, without any consideration of second-order displacements.

Section 5 provides results for an incompressible isotropic material, again with a general form for the strain-energy function. Following Rivlin [3], Green [4] used the formulation of [1] for second-order torsion of an extended cylinder to derive the axial force to order ψ^2 for a cylinder composed of Mooney material, and the results of Section 5 agree with those of Green when specialized to a Mooney material. For a circular cylinder of Mooney material, M is proportional to ψ and L is linear in ψ^2 so that the second-order value derived here for L is exact in this case. When the material has the empirical form for the strain-energy function derived in [5] for a rubber-like material, the first-order value (37) for M and the second-order value (38) for L are found to be very accurate for circular cylinders extended 100 percent

Contributed by the Applied Mechanics Division for publication in the JOURNAL OF APPLIED MECHANICS.

Discussion on this paper should be addressed to the Editorial Department, ASME, United Engineering Center, 345 East 47th Street, New York, N. Y. 10017, and will be accepted until June 1, 1980. Readers who need more time to prepare a discussion should request an extension from the Editorial Department. Manuscript received by ASME Applied Mechanics Division, May, 1979; final revision, July, 1979.

or more ($\lambda \geqslant 2$) and twisted to values of ψa up to 3 rad (and above), where a is the initial radius.

Whether an extended cylinder will tend to elongate or shorten when given a small twist with the axial force held constant depends on the material, the geometry of the cross section of the cylinder and the amount of initial extension. Comparison is made in Section 5 between cylinders of Mooney material and cylinders composed of a material with the empirical form for the strain energy function.

Section 6 considers the small twist of an extended cylinder of transversely isotropic material and the first-order expression for the twisting moment is given for a general strain-energy function. The axial force can then be derived to second order in ψ but the calculations are omitted.

2 The Energy Method

Consider a mechanical system which can assume equilibrium states characterized by a range of values of the N loading parameters or generalized coordinates $q_1, \ldots, q_N$. The system is disturbed from a known state B with values q_I $(I = 1, \ldots, N)$ to another equilibrium state characterized by a parameter p in addition to q_I. The range of values for p includes $p = 0$ and p is 0 for the state B. We assume that a potential energy $V(q_1, \ldots, q_N; p)$ exists for the system and we suppose that the generalized forces Q_I and P defined by

$$Q_I = \frac{\partial V}{\partial q_I} \quad (I = 1, \ldots, N), \quad P = \frac{\partial V}{\partial p} \tag{1}$$

are of direct physical interest. From the definitions (1) it follows that

$$\frac{\partial Q_I}{\partial p} = \frac{\partial P}{\partial q_I} \quad (I = 1, \ldots, N), \tag{2}$$

assuming that V is twice continuously differentiable.

If $P(q; p)$ is determined, $V(q; p)$ can be found by integration of the system

$$\frac{\partial V}{\partial p} = P(q; p), \quad V(q; 0) = V_0(q), \tag{3}$$

where $V_0(q)$ is the energy for the state B. The forces Q_I can then be found from V. However, determination of $P(q; p)$ could be difficult, and it is unlikely that $P(q; p)$ will be known without it being possible to calculate V or Q_I directly. It may be that if p is considered small, it is a relatively simple matter to determine P to first order in p. We suppose that in this way we are led to

$$P = P_0(q) + pP_1(q) + O(p^2) \quad \text{as} \quad p \to 0, \tag{4}$$

where $P_0(q)$ and $P_1(q)$ are known functions. If P_0 is nonzero, it is a reaction for the configurations q_I $(p = 0)$. From (3) and (4) we obtain

$$V = V_0(q) + pP_0(q) + \frac{1}{2}p^2P_1(q) + O(p^3) \quad \text{as} \quad p \to 0. \tag{5}$$

The forces Q_I can be found by differentiation from (5) or by integration from (2), and we obtain

$$Q_I = Q_I{}^0(q) + p\frac{\partial P_0}{\partial q_I} + \frac{1}{2}p^2\frac{\partial P_1}{\partial q_I} + O(p^3) \quad \text{as} \quad p \to 0, \tag{6}$$

where $Q_I{}^0 = \partial V_0/\partial q_I$.

Thus the determination of P to first order in p for the disturbed system leads to values for V and Q_I correct to second order in p. The approach may be of particular interest for systems for which $P_0 = 0$ as in this case consideration of the disturbed system for small p will not predict changes in Q_I unless the analysis is carried out to second order in p. If P is found to a higher order in p, say to order p^n, then V and Q_I can be determined to order p^{n+1}.

As a simple illustration, consider a uniform thin strip of elastic material with its ends constrained by frictionless guides to lie on the same horizontal line. Opposing horizontal forces H applied to the ends of the strip hold the ends a distance $2\lambda a$ apart, where $2a$ is the unstretched length, inducing a tension $T(\lambda)$ in the strip. The midpoint of the strip is now displaced downward a distance pa by a vertical force P. In changes $\delta\lambda$, δp, the work done by the vertical and horizontal forces supplies the change in the strain energy U of the elastic strip,

$$\delta U = 2Ha\delta\lambda + Pa\delta p, \tag{7}$$

and it follows that

$$H = \frac{1}{2a}\frac{\partial U}{\partial \lambda}, \quad P = \frac{1}{a}\frac{\partial U}{\partial p}. \tag{8}$$

From statical equilibrium we have

$$P = 2T(\lambda)p/\lambda$$

to first order in p, and from (8) we now deduce that

$$H = T + \frac{1}{2}\frac{p^2}{\lambda}\left[\frac{dT}{d\lambda} - \frac{T}{\lambda}\right] \tag{9}$$

to second order in p, since $H = T$ when $p = 0$. Alternatively, the value (9) for H can be obtained by determining the tension in the strip to second order in p and taking the horizontal component.

In the following, we apply the method to an elastic cylinder of length l which is finitely extended to length λl and then twisted an amount ψl overall by end loads. Under appropriate end loading conditions (examples are given in the next section), the work of the end loads during changes $\delta\lambda$ and $\delta\psi$ is expressible as

$$Ll\delta\lambda + Ml\delta\psi, \tag{10}$$

where L is the axial force and M the twisting moment, and this in turn is equal to the change in the total strain energy $U(\lambda, \psi)$. The value of M to first order in ψ can be found from the solution to the boundary-value problem obtained by linearization of the governing differential equations and boundary conditions with respect to ψ. Assuming that this process leads to the first-order estimate

$$M = \psi m(\lambda),$$

we then have by the approach of this section

$$L = L_0(\lambda) + \frac{1}{2}\psi^2\frac{dm}{d\lambda},$$

where $L_0(\lambda)$ is the axial force under extension only, and the first-order solution has determined L to second order. The expression for L in terms of the deformation superposed on the finite extension will involve second-order displacements when third and higher-order terms are ignored. However, the preceding discussion shows that in those situations where the work on the ends in small changes in λ, ψ is expressible in the form (10), it must be possible, by use of the equations and boundary conditions governing the second-order displacements, to transform the expression for L to $O(\psi^2)$ into one involving the first-order displacements and boundary data only. Similarly, it must be possible to manipulate the expression for the total strain energy U to $O(\psi^2)$ so that it is in terms of the first-order displacements and boundary data without the necessity for solving for the second-order displacements.

Consider an elastic body in equilibrium in a deformed state B and denote the coordinates of a particle in the reference state and in B by x_i and $y_i(x)$, respectively. When the body is disturbed to a new equilibrium state for which a particle at y_i in B is now at the point

$$y_i + \epsilon u_i(x) + \epsilon^2 v_i(x) + \ldots,$$

the total strain energy U is given by

$$U = \int_{V_0}\left\{W(y_{i,k}) + \frac{\partial W}{\partial y_{i,k}}(\epsilon u_{i,k} + \epsilon^2 v_{i,k}) + \frac{1}{2}\epsilon^2\frac{\partial^2 W}{\partial y_{i,k}\,\partial y_{r,s}}u_{i,k}\,u_{r,s}\right\}dx_1dx_2dx_3$$

to second order in ϵ. Here V_0 is the region occupied in the reference state, and W is the strain energy per unit volume of V_0. With the equilibrium equations

$$\frac{\partial}{\partial x_k}\left(\frac{\partial W}{\partial y_{i,k}}\right) = 0 \tag{11}$$

for the state B, the use of the divergence theorem leads to

$$U = U_0 + \int_{S_0} T_i{}^0 (\epsilon u_i + \epsilon^2 v_i) dS + \frac{1}{2}\epsilon^2 \int_{V_0} \frac{\partial^2 W}{\partial y_{i,k}\, \partial y_{r,s}} u_{i,k}\, u_{r,s}\, dx_1 dx_2 dx_3,$$

where U_0 is the total strain energy for B, S_0 is the bounding surface of V_0 and $T_i{}^0$ are the known surface tractions for state B per unit area of S_0. We see that if u_i are known, U will be known to $O(\epsilon^2)$ without determining v_i if the second-order contribution from the surface integral is determinable from the boundary conditions for the superposed deformation.

3 Extension and Torsion of Cylinders

We consider a cylinder of elastic material which is extended so that its overall length l becomes λl and is twisted so that the ends suffer a relative rotation of amount ψl, the lateral surface being free from traction. The work done by the end tractions during small quasi-static changes in λ, ψ is equal to the change in the total strain energy $U(\lambda, \psi)$. In general, however, the end work depends on the details of the distribution of the surface traction, and not just on the resultant force and resultant moment applied to an end.

We choose the rectangular Cartesian coordinate system x_i so that the x_3-axis is the line of centroids of the cross sections of the cylinder in the reference state and so that the plane ends are in the planes $x_3 = 0$, $x_3 = l$. If the ends are assumed to be attached to rigid plates which remain parallel to each other, we can suppose that for the extended and twisted cylinder we have the displacement conditions

$$y_i = x_i \quad \text{on} \quad x_3 = 0,$$

$$y_i = (x_1 \cos \psi l - x_2 \sin \psi l, x_1 \sin \psi l + x_2 \cos \psi l, \lambda l) \quad \text{on} \quad x_3 = l. \tag{12}$$

Here x_i and y_i are the coordinates of a particle in the reference and deformed states, respectively. For homogeneous cylinders with sections having two axes of symmetry, the resultant load on each end will be an axial force L and a twisting moment M. For other sections, the "natural" axis of torsion will depend on the values of λ and ψ and on the material properties, and forces and moments other than L,M will be needed on the ends in order to maintain the end displacements (12).

Components of surface traction measured per unit area of the surface in the reference state are denoted by T_i. During changes in λ,ψ, the tractions on the fixed end $x_3 = 0$ do no work, while for the end $x_3 = l$ the work of the tractions is given by expression (10) to first order, because the end moves as a rigid surface. The form (10) is also obtained if we write the work as the integral of $T_i \delta y_i$ over the end $x_3 = l$, calculate δy_i from (12) and use the expressions

$$L = \int_{R_0} (T_3)_{x_3=l} dA, \quad M = \int_{R_0} (T_2 y_1 - T_1 y_2)_{x_3=l} dA, \tag{13}$$

where R_0 is the undeformed cross section. Thus, for the end conditions (12), we have

$$L = \frac{1}{l}\frac{\partial U}{\partial \lambda}, \quad M = \frac{1}{l}\frac{\partial U}{\partial \psi}. \tag{14}$$

For a long enough cylinder, end effects become negligible and (14) would then be expected to hold for other end conditions which impose the extension and twist. Poynting [6] has obtained experimental verification for long steel wires of the relation

$$\frac{\partial L}{\partial \psi} = \frac{\partial M}{\partial \lambda} \tag{15}$$

which follows from (14). More recent experimental work on torsion of wires under tension has been done by Allen and Saxl [7]. Houston [8] has shown that the reciprocal relation

$$\frac{\partial \lambda}{\partial M} = \frac{\partial \psi}{\partial L} \tag{16}$$

also holds.

For a homogeneous cylinder we can consider a state of extension and twist in which we have the same state of strain at each section, as in the classical Saint Venant solution. (The Cauchy strains $C_{ik} = y_{r,i}y_{r,k}$ are then independent of x_3.) For the portion of the cylinder initially between $x_3 = 0$ and $x_3 = l$, the section $x_3 = l$ will be rotated an amount ψl about the axis of torsion and displaced an amount $(\lambda - 1)l$ axially relative to the section $x_3 = 0$. Apart from an arbitrary superposed rigid displacement we can therefore write

$$(y_1, y_2)_{x_3=l} = (y_1 \cos \psi l - y_2 \sin \psi l, y_1 \sin \psi l + y_2 \cos \psi l)_{x_3=0},$$

$$(y_3)_{x_3=l} = (y_3)_{x_3=0} + \lambda l, \tag{17}$$

where $(y_i)_{x_3=0}$ are functions of x_1,x_2 which also depend on λ,ψ. These functions are determined by equilibrium and the condition of zero traction on the lateral surface. The line of particles which forms the axis of torsion is determined by the values of x_1, x_2 for which y_1 and y_2 on $x_3 = 0$ both vanish, and the axis location will vary with λ,ψ in general. We will also have the following relations between the tractions on the end surfaces $x_3 = 0$ and $x_3 = l$,

$$(T_1, T_2)_{x_3=l} = -(T_1 \cos \psi l - T_2 \sin \psi l, T_1 \sin \psi l + T_2 \cos \psi l)_{x_3=0},$$

$$(T_3)_{x_3=l} = -(T_3)_{x_3=0}. \tag{18}$$

In quasi-static changes $\delta\lambda$, $\delta\psi$ of the extension and twist the work of the tractions on $x_3 = 0,l$ will equal the change in the total strain energy $U(\lambda, \psi)$ of the portion of the cylinder, so that

$$\delta U = \int_{R_0} \{(T_i \delta y_i)_{x_3=0} + (T_i \delta y_i)_{x_3=l}\} dA$$

From (17) and (18), it is apparent that

$$(T_3 \delta y_3)_{x_3=0} + (T_3 \delta y_3)_{x_3=l} = (T_3)_{x_3=l}\, l \delta\lambda,$$

and a short calculation leads to

$$(T_1 \delta y_1 + T_2 \delta y_2)_{x_3=0} + (T_1 \delta y_1 + T_2 \delta y_2)_{x_3=0} = -(T_2 y_1 - T_1 y_2)_{x_3=0}\, l\delta\psi = (T_2 y_1 - T_1 y_2)_{x_3=l}\, l\delta\psi.$$

Thus we have

$$\delta U = Ll\delta\lambda + Ml\delta\psi,$$

where L and M are the resultant axial force and twisting moment acting on $x_3 = l$ (and on every other section). It follows that we again have (14), so that L and M are the partial derivatives of the strain energy per unit length of the undeformed cylinder.

4 Results for Cylinders of Isotropic Material

Green and Shield [1] considered the problem of a small twist superposed on the uniform finite extension of an isotropic cylinder, with the same state of strain at each section. They showed that to first order in the twist ψ per unit length of the undeformed cylinder,[1] the solution can be written in terms of the warping function of the classical Saint Venant solution for the unextended cylinder. Moreover to first order in ψ, the resultant force and moment on each section reduces to an axial force L and a twisting moment M when the axis of torsion is chosen to be the line of centroids of the cross sections.

From [1], the twisting moment M is, to first order in ψ, given by

$$M = 2\psi \frac{\lambda_1{}^2}{\lambda^2} (W_1 + \lambda_1{}^2 W_2)\, [\lambda^2 I_0 - \lambda_1{}^2 (I_0 - S_0)], \tag{19}$$

where the transverse extension ratio λ_1 is determined in terms of λ from

[1] In [1], ψ is used for the twist per unit length of the extended cylinder, so we replace ψ in [1] by ψ/λ to conform to the notation of this paper.

$$W_1 + (\lambda^2 + \lambda_1^2)W_2 + \lambda^2\lambda_1^2 W_3 = 0. \tag{20}$$

Here W_1, W_2, W_3 are the derivatives of the strain energy $W(I_1, I_2, I_3)$ per unit volume of the reference state with respect to the strain invariants, and they are evaluated for the values

$$I_1 = \lambda^2 + 2\lambda_1^2, \quad I_2 = 2\lambda^2\lambda_1^2 + \lambda_1^4, \quad I_3 = \lambda^2\lambda_1^4. \tag{21}$$

The geometry of the cross section enters in (19) through the moment of inertia I_0 of the unstrained cross section R_0 about the centroid and through the classical geometrical torsional rigidity S_0 of the unstrained cylinder.

From (14) and (19) we have for a portion of the cylinder initially of length l

$$\frac{1}{l} U(\lambda, \psi) = A_0 W(I_1, I_2, I_3) + \psi^2 \frac{\lambda_1^2}{\lambda^2}(W_1 + \lambda_1^2 W_2)[\lambda^2 I_0 - \lambda_1^2(I_0 - S_0)] \tag{22}$$

to second order in ψ, where A_0 is the initial cross-sectional area. Because of symmetry considerations, M is an odd function of ψ, so that (19) is in error by a term of order ψ^3 and the error in (22) is $O(\psi^4)$ as $\psi \to 0$.

The axial force L is obtained by differentiating (22) with respect to λ, and we obtain, with an error of $O(\psi^4)$,

$$\begin{aligned} L = A_0 t(\lambda) + 2\psi^2 \frac{\lambda_1}{\lambda^2}\Bigg\{&\frac{\lambda_1^3}{\lambda}(W_1 + \lambda_1^2 W_2)(I_0 - S_0) \\ &+ \frac{d\lambda_1}{d\lambda}[\lambda^2(W_1 + 2\lambda_1^2 W_2)I_0 - \lambda_1^2(2W_1 + 3\lambda_1^2 W_2)(I_0 - S_0)] \\ &+ \lambda_1[\lambda^2 I_0 - \lambda_1^2(I_0 - S_0)]\Bigg(\lambda[W_{11} + 3\lambda_1^2 W_{12} + \lambda_1^4 W_{13} \\ &+ 2\lambda_1^4 W_{22} + \lambda_1^6 W_{23}] + 2\lambda_1 \frac{d\lambda_1}{d\lambda}[W_{11} + (\lambda^2 + 2\lambda_1^2)W_{12} \\ &+ \lambda^2\lambda_1^2 W_{13} + \lambda_1^2(\lambda^2 + \lambda_1^2)W_{22} + \lambda^2\lambda_1^4 W_{23}]\Bigg)\Bigg\}, \end{aligned} \tag{23}$$

where we have written W_{ik} for $\partial^2 W/\partial I_i \partial I_k$. Here $t(\lambda)$ is the nominal stress in simple extension and

$$t(\lambda) = \frac{\partial W}{\partial \lambda} = \frac{2}{\lambda}(W_1 + \lambda_1^2 W_2)(\lambda^2 - \lambda_1^2) \tag{24}$$

if we use (20). The derivative $d\lambda_1/d\lambda$ can be determined by differentiation of (20) which leads to

$$\begin{aligned} &\frac{d\lambda_1}{d\lambda}[W_2 + \lambda^2 W_3 + 2W_{11} + 4(\lambda^2 + \lambda_1^2)W_{12} + 4\lambda^2\lambda_1^2 W_{13} \\ &\quad + 2(\lambda^2 + \lambda_1^2)^2 W_{22} + 4\lambda^2\lambda_1^2(\lambda^2 + \lambda_1^2)W_{23} + 2\lambda^4\lambda_1^4 W_{33}] \\ &= -\frac{\lambda}{\lambda_1}[W_2 + \lambda_1^2 W_3 + W_{11} + (\lambda^2 + 3\lambda_1^2)W_{12} + \lambda_1^2(\lambda^2 + \lambda_1^2)W_{13} \\ &\quad + 2\lambda_1^2(\lambda^2 + \lambda_1^2)W_{22} + \lambda_1^4(3\lambda^2 + \lambda_1^2)W_{23} + \lambda^2\lambda_1^6 W_{33}]. \end{aligned} \tag{25}$$

We note that equation (20), which expresses the condition that the transverse stress vanish during simple extension, can be written as

$$\frac{\partial W}{\partial \lambda_1} = 0, \tag{26}$$

in which, as before, W is evaluated for the values (21) of the strain invariants. An alternative expression for $d\lambda_1/d\lambda$ is therefore

$$\frac{d\lambda_1}{d\lambda} = -\frac{\partial^2 W}{\partial\lambda\partial\lambda_1}\Big/\frac{\partial^2 W}{\partial\lambda_1^2}. \tag{27}$$

Experiments on simple tension and compression can determine the dependence of the nominal stress $t(\lambda)$ and the transverse extension ratio λ_1 on λ, and the derivatives $dt/d\lambda$ and $d\lambda_1/d\lambda$ can then be estimated. It is therefore of some advantage to express M and L in terms of t and λ_1. From (19) and (24) we have, to first order in ψ,

$$M = \psi \frac{\lambda_1^2}{\lambda} t(\lambda)\left[I_0 + \frac{\lambda_1^2}{(\lambda^2 - \lambda_1^2)} S_0\right], \tag{28}$$

while to second order in ψ^2 we have

$$\begin{aligned} L &= A_0 t(\lambda) + \frac{1}{2}\psi \frac{dM}{d\lambda} \\ &= A_0 t(\lambda) + \frac{1}{2}\psi^2 \frac{\lambda_1}{\lambda}\Bigg\{\lambda_1 \frac{dt}{d\lambda}\left[I_0 + \frac{\lambda_1^2}{(\lambda^2 - \lambda_1^2)} S_0\right] \\ &\quad + t(\lambda)\Bigg(I_0\left(2\frac{d\lambda_1}{d\lambda} - \frac{\lambda_1}{\lambda}\right) \\ &\quad - \frac{\lambda_1^2 S_0}{\lambda(\lambda^2 - \lambda_1^2)^2}\left[\lambda_1(3\lambda^2 - \lambda_1^2) - 2\lambda\frac{d\lambda_1}{d\lambda}(2\lambda^2 - \lambda_1^2)\right]\Bigg)\Bigg\}. \end{aligned} \tag{29}$$

If λ is changed by an amount of $O(\psi^2)$, the axial force L will change by an amount of $O(\psi^2)$ (and the change in M will be of order ψ^3). If we change λ to $\lambda + \psi^2 h$, then the second-order change in L will be equal to

$$\begin{aligned} \psi^2 h A_0 \frac{dt}{d\lambda} = 2\psi^2 \frac{h}{\lambda} A_0 \Bigg\{&\frac{1}{\lambda}(\lambda^2 + \lambda_1^2)(W_1 + \lambda_1^2 W_2) - 2\lambda_1 \frac{d\lambda_1}{d\lambda} \\ &\times [W_1 + (2\lambda_1^2 - \lambda^2)W_2] + 2(\lambda^2 - \lambda_1^2)\Bigg(\lambda[W_{11} + 3\lambda_1^2 W_{12} \\ &+ \lambda_1^4 W_{13} + 2\lambda_1^4 W_{22} + \lambda_1^6 W_{23}] + 2\lambda_1 \frac{d\lambda_1}{d\lambda}[W_{11} + (\lambda^2 + 2\lambda_1^2)W_{12} \\ &+ \lambda^2\lambda_1^2 W_{13} + \lambda_1^2(\lambda^2 + \lambda_1^2)W_{22} + \lambda^2\lambda_1^4 W_{23}]\Bigg)\Bigg\}. \end{aligned} \tag{30}$$

By choosing h so that the right-hand side of (30) is equal to the negative of the second-order term on the right-hand side of (23), we can determine the second-order fractional extension $\psi^2 h$ which results when the cylinder is twisted with the axial force held constant.

When the reference state is unstressed, in order to include all second-order effects for deformations about the reference state it is sufficient, following Murnaghan [2], to take W to be given by

$$W = a_1 J_2 + a_2 J_1^2 + a_3 J_1 J_2 + a_4 J_1^3 + a_5 J_3, \tag{31}$$

where $a_1, a_2 \ldots a_5$ are material constants and

$$J_1 = I_1 - 3, \quad J_2 = I_2 - 2I_1 + 3, \quad J_3 = I_3 - I_2 + I_1 - 1.$$

The derivatives W_i, W_{ik} for the reference state are given by

$$\begin{gathered} W_1 = a_5 - 2a_1, \quad W_2 = a_1 - a_5, \quad W_3 = a_5, \\ W_{11} = 2(a_2 - 2a_3), \quad W_{12} = a_3, \quad W_{13} = W_{22} = W_{23} = W_{33} = 0. \end{gathered} \tag{32}$$

The constants a_1, a_2 are related to the first-order response of the material and in fact we have, when $\lambda = \lambda_1 = 1$,

$$\frac{dt}{d\lambda} = E = -8a_1 \frac{(a_1 + 3a_2)}{(a_1 + 4a_2)}, \quad \frac{d\lambda_1}{d\lambda} = -\sigma = -\frac{(a_1 + 2a_2)}{(a_1 + 4a_2)}, \tag{33}$$

where E and σ are Young's modulus and Poisson's ratio. By setting $\lambda = \lambda_1 = 1$ in (23) we can find the second-order axial force induced by twisting the cylinder with its initial length held fixed, and we obtain

$$L = \frac{2\psi^2}{(a_1 + 4a_2)}\{[a_5(a_1 + 2a_2) - a_1(2a_2 - a_3)]S_0 - 2a_1(a_1 + 3a_2)(I_0 - S_0)\}. \tag{34}$$

An extension of amount $\psi^2 h$ requires an axial force $\psi^2 h E A_0$ and if we choose h to be given by

$$h = \frac{1}{4A_0 a_1(a_1 + 3a_2)}\{[a_5(a_1 + 2a_2) - a_1(2a_2 - a_3)]S_0 - 2a_1(a_1 + 3a_2)(I_0 - S_0)\} \tag{35}$$

then the axial force will be of order ψ^4. This estimate for the fractional *extension of a cylinder under small twist and no axial force was first* obtained by Rivlin [3], who derived the result using the differential equations and boundary conditions governing the second-order displacements but without obtaining an explicit solution for the second-order displacments.

Green and Wilkes [9] considered the finite extension and torsion of a circular cylinder of isotropic material, and they obtained M correct to $O(\psi^3)$ and L correct to $O(\psi^2)$. With the method of Section 2, a value for L correct to $O(\psi^4)$ can be obtained from the value of M given in [9].

5 Incompressible Isotropic Materials

When the material can be treated as incompressible, there is some simplification of the results of the previous section. For no volume change $I_3 = 1$, and in simple tension this requires the transverse extension ratio λ_1 to be $1/\lambda^{1/2}$, with the hydrostatic pressure adjusting to make the transverse stresses zero. The strain energy W is a function of I_1 and I_2 which have the values

$$I_1 = \lambda^2 + 2/\lambda, \quad I_2 = 2\lambda + 1/\lambda^2 \tag{36}$$

for simple extension.

The twisting moment is

$$M = 2\frac{\psi}{\lambda}(W_1 + W_2/\lambda)[I_0 - (I_0 - S_0)/\lambda^3] \tag{37}$$

with an error of $O(\psi^3)$ and the axial force is

$$\begin{aligned} L = {} & 2A_0(W_1 + W_2/\lambda)(\lambda - 1/\lambda^2) \\ & + \frac{\psi^2}{\lambda^3}\{W_1[4(I_0 - S_0)/\lambda^2 - \lambda I_0] + W_2[5(I_0 - S_0)/\lambda^3 - 2I_0] \\ & + 2(\lambda^3 - 1)(W_{11} + 2W_{12}/\lambda + W_{22}/\lambda^2)[I_0 - (I_0 - S_0)/\lambda^3]\} \end{aligned} \tag{38}$$

with an error of $O(\psi^4)$. Alternatively we can write

$$M = \psi\frac{t(\lambda)}{\lambda^2}\left[I_0 + \frac{S_0}{(\lambda^3 - 1)}\right], \tag{39}$$

$$L = A_0 t(\lambda) + \frac{1}{2}\frac{\psi^2}{\lambda^2}\left\{\frac{dt}{d\lambda}\left[I_0 + \frac{S_0}{(\lambda^3 - 1)}\right] - \frac{t(\lambda)}{\lambda}\left[2I_0 + S_0\frac{(5\lambda^3 - 2)}{(\lambda^3 - 1)^2}\right]\right\}, \tag{40}$$

where

$$t(\lambda) = 2(W_1 + W_2/\lambda)(\lambda - 1/\lambda^2)$$

is the nominal stress in simple tension.

From (37) and (38), the ratio of the torsional stiffness M/ψ for a small twist superposed on simple extension to the force L_0 necessary to produce the simple extension is given by [1]

$$\frac{M/\psi}{L_0} = \frac{[I_0 - (I_0 - S_0)/\lambda^3]}{\lambda(\lambda - 1/\lambda^2)} \tag{41}$$

and it is independent of the particular form of the strain-energy function for the incompressible material. The result (41) was first obtained by Rivlin [10] for the special case of a circular cylinder and it has been verified experimentally for rods of rectangular section by Gent and Rivlin [11].

Second-order effects in torsion of an extended cylinder were considered by Green and Shield [1] for the case of a Mooney material, for which W_1 and W_2 are constants. Green [4] used the formulation of [1] to derive L to order ψ^2 without obtaining a solution of the boundary-value problem for the second-order displacements, and the results of [4] are in agreement with (38) if W_1 and W_2 are replaced by constants C_1 and C_2, so that $W_{\alpha\beta}$ are zero. (The symbol ψ of [4] corresponds to ψ/λ of this paper.)

The torsion and extension of a circular cylinder of incompressible isotropic material was treated by Rivlin [10] who derived the values

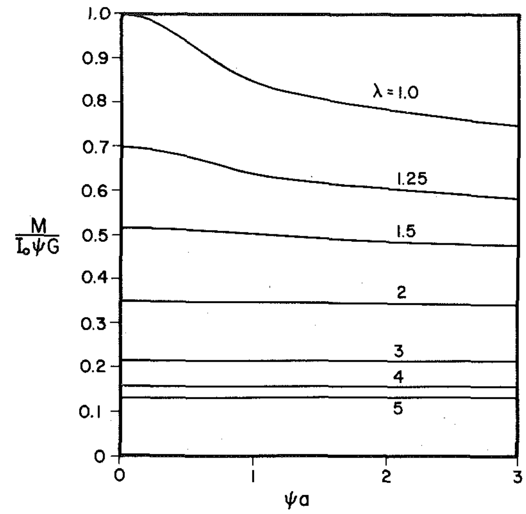

Fig. 1 Twisting moment for torsion of an extended circular cylinder with empirical strain energy

$$M = 4\pi\frac{\psi}{\lambda}\int_0^a (W_1 + W_2/\lambda)\rho^3 d\rho,$$

$$L = 2\pi\int_0^a \left\{2\left(\lambda - \frac{1}{\lambda^2}\right)(W_1 + W_2/\lambda) - \frac{\psi^2}{\lambda^2}(W_1 + 2W_2/\lambda)\rho^2\right\}\rho d\rho, \tag{42}$$

in which

$$I_1 = \lambda^2 + 2/\lambda + \psi^2\rho^2/\lambda, \quad I_2 = 2\lambda + 1/\lambda^2 + \psi^2\rho^2/\lambda^2$$

and a is the radius of the cylinder. When W_1 and W_2 are constants, M is linear in ψ and L is quadratic, so that (37) and (38) are exact for a circular cylinder (for which $S_0 = I_0$) of Mooney material.

Values for W_1 and W_2 were determined in [5] from experimental results of Treloar [12] for a latex rubber under the assumption that W_1 depends only on I_1 and W_2 only on I_2. The expressions

$$\begin{aligned} W_1/C_1 &= 1 + 2.49 \times 10^{-7}(I_1 - 3)^4 & 3 \leq I_1 \leq 56 \\ W_2/C_1 &= \begin{cases} 0.376 + 1.32 \times 10^{-2}(4.928 - I_2)^{4.864} & 3 \leq I_2 \leq 4 \\ 0.77/I_2 & 4 \leq I_2 \leq 200 \end{cases} \end{aligned} \tag{43}$$

provide a reasonable fit for the empirical values given in [5]. In contrast to the Mooney form, W_2 exhibits a sharp drop as I_2 increases from the value 3 for the reference state. By using (43) in (42), M and L can be found by numerical integration for a circular cylinder composed of a material with the empirical strain-energy function of [5]. Figs. 1 and 2 show the variation of $M/I_0\psi G$ and L/A_0G with ψa for values of λ from 1 to 5. Here G is the shear modulus for small strains,

$$G = 2(W_1 + W_2) \quad \text{for} \quad I_1 = I_2 = 3.$$

The value of M/ψ for $\lambda = 1.5$ varies less than 8 percent from the value given by (37) as ψa increases from 0 to 3 radians and the variation can be ignored for extension ratios greater than 2. For values of ψa between 1 and 3 the value of L departs significantly from the second-order value (38) for $\lambda = 1$, 1.25, and 1.5, but (38) is an excellent fit for $\lambda = 2$ and larger. (The larger values of ψa may be unrealistic for cylinders extended less than 100 percent.) For experimental results on circular cylinders made of rubber, see Rivlin and Saunders [13].

Fig. 3 shows the variation with λ of the torsional stiffness M/ψ for small twisting of an extended cylinder for $S_0/I_0 = 0$, 0.25, 0.5, 0.75, and 1. The values in Fig. 3 were derived from (37) using the empirical forms (43). The curves run together for larger values of λ and they have a minimum near $\lambda = 5.4$. The curves for $S_0/I_0 = 0$, 0.25, and 0.5

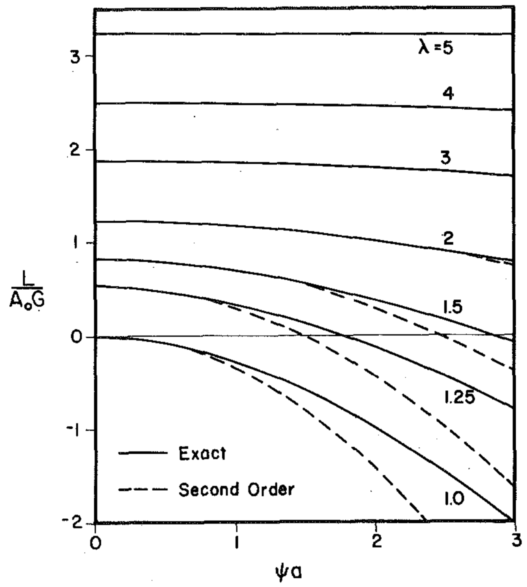

Fig. 2 Axial force for torsion of an extended circular cylinder with empirical strain energy, exact and second-order theory

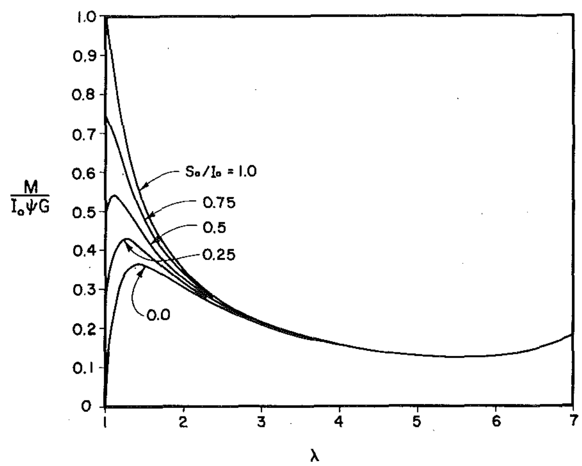

Fig. 3 Torsional stiffness for small twisting of an extended cylinder, empirical strain energy

also have a maximum between $\lambda = 1$ and $\lambda = 1.5$. The second-order term in expression (38) for L is proportional to $\partial M/\partial\lambda$ and the second-order term vanishes when

$$\frac{S_0}{I_0} = \frac{\{\lambda(4-\lambda^3)W_1 + (5-2\lambda^3)W_2 + 2(\lambda^3-1)^2(W_{11} + 2W_{12}/\lambda + W_{22}/\lambda^2)\}}{\{4\lambda W_1 + 5W_2 - 2(\lambda^3-1)(W_{11} + 2W_{12}/\lambda + W_{22}/\lambda^2\}}. \quad (44)$$

Thus (44) gives the location of the extremum of the torsional stiffness M/ψ for varying λ. Fig. 4 shows the value of S_0/I_0 given by (44) for λ increasing from unity for the empirical forms (43). For comparison the curves for a neo-Hookean material ($C_2/C_1 = 0$) and a Mooney material for which $C_2/C_1 = 0.6$ are also shown. The vertical scale on the right in the figure indicates the ratio b/a of the semiaxes of an ellipse corresponding to the values of S_0/I_0 on the left scale.

From (15), the axial force L will increase or decrease on twisting at constant extension according as $\partial M/\partial\lambda$ is positive or negative. The nominal stress $t(\lambda)$ in simple extension increases with λ for rubber-like materials so that the cylinder will tend to elongate or shorten on twisting when the axial force is held constant according as $\partial M/\partial\lambda$ is negative or positive. The tendency of an extended cylinder under constant axial force to elongate or shorten on twisting is indicated in

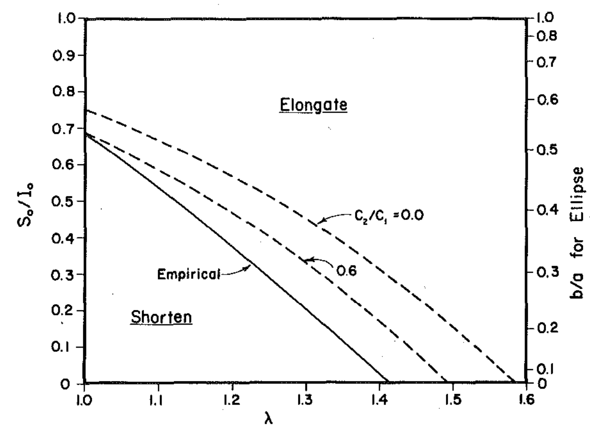

Fig. 4 Tendency of an extended cylinder to elongate or shorten when twisted, for empirical strain energy and Mooney material

Fig. 4 for extension ratios λ up to 1.6. All cylinders of material with the empirical strain-energy function tend to elongate on twisting for extension ratios λ between 1.6 and 5.4, where M has a minimum, and to shorten for larger extension ratios. Cylinders of Mooney material (with positive C_1 and C_2) all tend to elongate on twisting if stretched beyond 60 percent extension because $\partial M/\partial\lambda$ remains negative beyond $\lambda = 1.6$.

6 Transversely Isotropic Cylinder

When the material of the cylinder is transversely isotropic with respect to the x_3-axis (the cylinder axis), the strain energy is a function of the quantities

$$K_1 = \frac{1}{2}(C_{33} - 1), \quad K_2 = \frac{1}{4}(C_{13}^2 + C_{23}^2)$$

in addition to the invariants I_1, I_2, I_3 (see [14] for example). Here C_{ik} are the Cauchy strains $y_{r,i}y_{r,k}$ and K_1, K_2 are invariant with respect to rotations of the coordinate system about the x_3-axis. For the extended cylinder

$$K_1 = \frac{1}{2}(\lambda^2 - 1), \quad K_2 = 0, \quad (45)$$

and the transverse extension ratio λ_1 is given by (20) in which the derivatives W_i are evaluated for the values (21) and (45). The nominal axial stress $t(\lambda)$ is given by

$$t(\lambda) = \frac{\partial W}{\partial\lambda} = \frac{2}{\lambda}(W_1 + \lambda_1^2 W_2)(\lambda^2 - \lambda_1^2) + \lambda W_4$$

if we use (20), where $W_4 = \partial W/\partial K_1$.

We assume that after a small twist of the extended cylinder, the particle initially at x_i is at the point

$$y_i = \{\lambda_1(x_1 - \psi x_2 x_3),\ \lambda_1(x_2 + \psi x_1 x_3),\ \lambda(x_3 + \psi\phi(x_1, x_2))\} + O(\psi^2). \quad (46)$$

We can follow the approach of [1] to determine the warping function ϕ. Alternatively, we can introduce (46) into the equilibrium equations (11) and into the boundary conditions

$$T_i = \frac{\partial W}{\partial y_{i,k}} n_k = 0$$

on the lateral surface (n_k is the normal in the reference state), and then linearize in ψ. We find, as for the isotropic cylinder, that

$$\phi = \lambda_1{}^2 w(x_1, x_2)/\lambda^2,$$

where w is the classical warping function for the unextended cylinder. The twisting moment M is found to be given by

$$M = \psi \frac{\lambda_1{}^2}{\lambda} t(\lambda) I_0 + 2\psi \frac{\lambda_1{}^4}{\lambda^2} \left(W_1 + \lambda_1{}^2 W_2 + \frac{1}{4}\lambda^2 W_5\right) S_0$$

$$= 2\psi \frac{\lambda_1{}^2}{\lambda^2} (W_1 + \lambda_1{}^2 W_2)\{\lambda^2 I_0 - \lambda_1{}^2 (I_0 - S_0)\}$$

$$+ \psi \lambda_1{}^2 \left(W_4 I_0 + \frac{1}{2}\lambda_1{}^2 W_5 S_0\right) \quad (47)$$

to first order in ψ, where $W_5 = \partial W/\partial K_2$. The axial force L can be found from

$$L = t(\lambda) A_0 + \frac{1}{2}\psi \frac{dM}{d\lambda} + O(\psi^4), \quad (48)$$

but we omit the details of the calculation.

For an incompressible material, λ_1 is $1/\lambda^{1/2}$ and (47) becomes

$$M = 2\frac{\psi}{\lambda}(W_1 + W_2/\lambda)[I_0 - (I_0 - S_0/\lambda^3] + \frac{\psi}{\lambda}(W_4 I_0 + W_5 S_0/2\lambda). \quad (49)$$

References

1 Green, A. E., and Shield, R. T., "Finite Extension and Torsion of Cylinders," *Philosophical Transactions of the Royal Society*, Series A, Vol. 244, 1951, pp. 47–86; reprinted in *Problems in Nonlinear Elasticity*, Gordon and Breach, New York, 1965.

2 Murnaghan, F. D., "Finite Deformation of an Elastic Solid," *American Journal of Mathematics*, Vol. 59, 1937, pp. 235–260.

3 Rivlin, R. S., "The Solution of Problems in Second-Order Elasticity Theory," *Journal Rat. Mech. Anal.*, Vol. 2, No. 1, 1953, pp. 53–81.

4 Green, A. E., "A Note on Second-Order Effects in the Torsion of Incompressible Cylinders," *Proceedings, Cambridge Philosophical Society*, Vol. 50, Pt. 3, 1954, pp. 488–490.

5 Shield, R. T., "On the Stability of Finitely Deformed Elastic Membranes, Part I," *Journal of Applied Mathematics and Physics* (*ZAMP*), Vol. 22, No. 6, 1971, pp. 1016–1028.

6 Poynting, J. H., "On the Changes in the Dimensions of a Steel Wire When Twisted, and on the Pressure of Distortional Waves in Steel," *Proceedings of the Royal Society*, Series A, Vol. 86, 1912, pp. 534–561.

7 Allen, M., and Saxl, E. J., "Elastic Torsion in Wires Under Tension," *Journal of Applied Physics*, Vol. 40, No. 6, 1969, pp. 2505–2509.

8 Houston, R. A., "A Relation Between Tension and Torsion," *Philosophical Magazine*, Vol. 22, 1911, pp. 740–741.

9 Green, A. E., and Wilkes, E. W., "A Note on the Extension and Torsion of a Circular Cylinder of Compressible Elastic Isotropic Material," *Quarterly Journal of Mechanics and Applied Mathematics*, Vol. 6, Pt. 2, 1953, pp. 240–249.

10 Rivlin, R. S., "Large Elastic Deformations of Isotropic Material VI. Further Results in the Theory of Torsion, Shear and Flexure," *Philosphical Transactions of the Royal Society*, Series A, Vol. 242, 1949, pp. 173–195; reprinted in *Problems of Nonlinear Elasticity*, Gordon and Breach, New York, 1965.

11 Gent, A. N., and Rivlin, R. S., "Experiments on the Mechanics of Rubber III: Small Torsions of Stretched Prisms," *Proceedings of the Physical Society*, Vol. 65, 1952, pp. 645–648.

12 Treloar, L. R. G., "Stress-Strain Data for Vulcanized Rubber Under Various Types of Deformation," *Trans. Faraday Soc.*, Vol. 40, 1944, pp. 59–70.

13 Rivlin, R. S., and Saunders, D. W., "Large Elastic Deformations of Isotropic Materials, Part VII," *Philosophical Transactions of the Royal Society*, Series A, Vol. 243, 1951, pp. 251–288.

14 Green, A. E., and Adkins, J. E., *Large Elastic Deformations*, Oxford University, 2nd ed., 1970.

R. C. Batra

Associate Professor,
Department of Engineering Mechanics,
University of Missouri-Rolla,
Rolla, Mo. 65401
Mem. ASME

Rubber Covered Rolls—The Nonlinear Elastic Problem[1]

The problem of the indentation of a rubberlike layer bonded to a rigid cylinder and indented by another rigid cylinder is analyzed. The rubberlike layer is assumed to be made of a homogeneous Mooney-Rivlin material. The materially and geometrically nonlinear problem is solved by using the finite-element code developed by the author. Results computed and presented graphically include the pressure profile at the contact surface, stress distribution at the bond surface and the deformed shape of the indented surface.

Introduction

Traction in vehicles, the nip action in cylindrical rolls in the papermaking process and in the textile industry, and friction drives are some examples of the kind of problem studied herein. Each of these problems involves indentation, by a rigid cylinder, of the rubberlike layer bonded to a core made of a considerably harder material. Such problems have been studied analytically [1], experimentally [2], and numerically [3] by using the finite-element method. In [1] Hahn and Levinson solve the indentation problem on the assumption that the rubberlike layer is made of a Hookean material and its deformations are within the range of applicability of the linear theory. The problem is solved by using an Airy stress function and the solution is in terms of double infinite series one of which converges slowly. In the numerical study [3], Batra, et al., assume that the rubberlike layer is made of a thermorheologically simple material and its deformations are small so that the linear strain-displacement relations and a linear relation between stress and strain rate can be presumed. The experimental work [2] of Spengos is quite extensive and involves a wide range of loads, thicknesses of the rubber layer, and speed differences between the mating rollers. Other contact problems involving geometries different from the one considered here have been studied by Sve and Keer [4], Keer and Sve [5], Itou and Atsumi [6], Alblas and Kuipers [7–9], and Batra [10, 11].

A study of the results of Hahn and Levinson suggests that for moderate values of nip width, the value of the maximum principal strain is of the order of 20 percent. This observation is also confirmed by the experimental investigations of Spengos. It therefore appears that the maximum strain commonly encountered in practice is probably much higher than what is usually thought to be the range of applicability of the linear theory. Thus one needs to develop methods to solve the problem when the deformations are large and the material of the layer is nonlinear. In this paper we assume that the material of the rubberlike layer can be modeled as a Mooney-Rivlin material and solve the large deformation problem by the finite-element method.

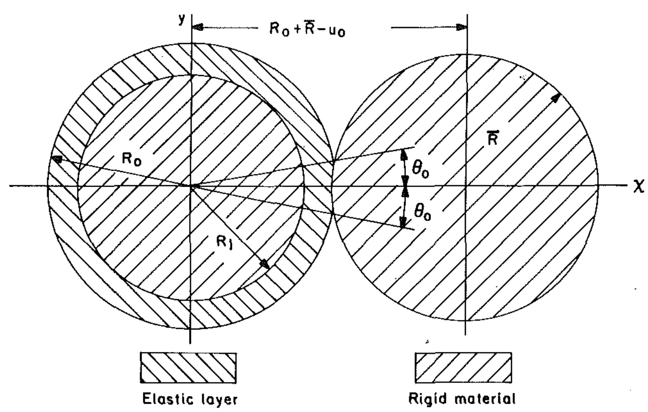

Fig. 1 System to be studied

A schematic diagram of the system studied is shown in Fig. 1. Since the length of rolls is considerably large as compared to their diameters, we assume that plane strain state of deformation prevails. Methodologies to solve finite plane strain problems for incompressible elastic materials have been given by Oden [12] and Scharnhorst and Pian [13]. Realizing that these authors had developed computer programs tailored to solving specific problems and illustrating the principles involved, the author developed a computer code capable of solving quasi-static, mixed boundary-value finite plane strain problems for Mooney-Rivlin materials. Results obtained for two sample problems by using this program compare favorably with those obtained from the analytical solution [14]. The indentation problem considered in this paper is solved by using this basic program and the techniques

[1] Dedicated to Clifford Truesdell on the occasion of his 60th birthday.

Contributed by the Applied Mechanics Division for publication in the JOURNAL OF APPLIED MECHANICS.

Discussion on this paper should be addressed to the Editorial Department, ASME, United Engineering Center, 345 East 47th Street, New York, N.Y. 10017, and will be accepted until June 1, 1980. Readers who need more time to prepare a discussion should request an extension from the Editorial Department. Manuscript received by ASME Applied Mechanics Division, May, 1979; final revision, October, 1979.

developed earlier [3, 10, 11] for solving contact problems numerically.

Formulation of the Problem

We use a fixed set of rectangular Cartesian axes with origin at the center of the roll with the rubberlike cover and denote the position of a material particle in the reference configuration by X^α and the position of the same material particle in the current configuration by x_i. Thus $x_i = x_i(X^\alpha, t)$ gives the current position, at time t, of the material particle that occupied place X^α in the reference configuration. Since the core and the mating cylinder are usually made of a material considerably harder than the material of the rubberlike layer, we regard these as being rigid and study only the mechanical deformations of the rubberlike layer. Neglecting the effect of body forces such as gravity on the deformations of the roll cover, equations governing the deformations of the rubberlike layer are

$$\det F_{i\alpha} = 1, \quad F_{i\alpha} \equiv x_{i,\alpha}, \tag{1}$$
$$\rho \ddot{x}_i = T_{i\alpha,\alpha}.$$

In (1) ρ is the present mass density, $T_{i\alpha}$ is the first Piola-Kirchoff stress tensor, a superimposed dot indicates material time differentiation, a comma followed by an index α indicates partial differentiation with respect to X^α, $F_{i\alpha}$ is the deformation gradient, and the usual summation convention is used. Equation $(1)_1$ is the continuity equation in referential description and signifies that the mass density stays constant. The first Piola-Kirchoff stress tensor $T_{i\alpha}$ and the Cauchy stress tensor σ_{ij} are related by

$$\sigma_{ij} = \frac{\rho}{\rho_0} T_{i\alpha} F_{j\alpha} \tag{2}$$

in which ρ_0 is the mass density in the reference configuration. For incompressible materials, $\rho = \rho_0$ and (2) simplies to $\sigma_{ij} = T_{i\alpha}F_{j\alpha}$. Equation (1) is to be supplemented by constitutive relation for $T_{i\alpha}$ and side conditions such as boundary conditions. Before we state these, we give the following assumptions to simplify the problem.

We assume that the material of the roll cover is homogeneous and can be modeled as a Mooney-Rivlin material, contact between the indentor and the roll cover is frictionless, and that the effect of all dynamic forces on the deformation of the roll cover is negligible. We note that the mass density of rubber is quite low (comparable to that of water). Therefore, for practical geometries and speeds in the range of 500 rpm, the effect of centrifugal force on the stress distribution is very small. Under these assumptions the indentation problem becomes quasi-static and equation (1) is replaced by

$$\det F_{i\alpha} = 1,$$
$$0 = T_{i\alpha,\alpha}$$
$$(F^{-1})_{\alpha i} T_{i\beta} = S_{\alpha\beta} = p(C^{-1})_{\alpha\beta} + 2C_1\delta_{\alpha\beta} + 2C_2(I_1\delta_{\alpha\beta} - C_{\alpha\beta}),$$
$$C_{\alpha\beta} = F_{i\alpha}F_{i\beta}, \quad I_1 = C_{\alpha\alpha}. \tag{3}$$

In these equations, $C_{\alpha\beta}$ is the right Cauchy-Green tensor, C_1 and C_2 are material constants, p is the hydrostatic pressure not determined by the deformation of the roll cover but can be found from the boundary conditions, $\delta_{\alpha\beta}$ is the Kronecker delta, I_1 is the first invariant of the strain tensor $C_{\alpha\beta}$ and $S_{\alpha\beta}$ is the second Piola-Kirchoff stress tensor.

In practice the length of the cylindrical rollers is significantly larger than their diameters so that it is reasonable to presume that plane strain state of deformation prevails. Thus $x_3 = \delta_{3\alpha}X^\alpha$ and equation $(3)_2$ for $i = 3$ is identically satisfied. Furthermore, deformations of the roll cover are symmetrical about the line joining the centers of the rollers. Because of this symmetry, we study the deformations of the upper half of the roll cover.

Equation $(3)_1$ and the set of equations obtained by substituting $(3)_3$ into $(3)_2$ are three equations for the three unknown fields p, x_1, and x_2. These equations are to be solved under the following boundary conditions. At the inner surface $X_\alpha X_\alpha = R_1$,

$$u_i = x_i - \delta_{i\alpha}X^\alpha = 0, \tag{4}$$

at the outer surface $X_\alpha X_\alpha = R_0$,

$$e_i T_{i\alpha} N_\alpha = 0, \tag{5}$$

$$n_i T_{i\alpha} N_\alpha = 0, \qquad \text{if } \theta = \arctan\left(\frac{X_2}{X_1}\right) \geq \theta_0,$$
$$= f(\theta), \quad \text{if } \arctan\left(\frac{X_2}{X_1}\right) \leq \theta_0, \tag{6}$$
$$f(\theta_0) = 0,$$

and at the plane through the center line of rollers,

$$u_2 = 0,$$
$$T_{12} = 0. \tag{7}$$

In equations (4)–(7), N_α is an outward unit normal to the surface in the reference configuration, e_i is an unit tangent vector to the surface in the current configuration, and n_i is an unit outward normal to the surface in the current configuration. The boundary condition (4) implies that there is perfect bonding between the core and the rubberlike layer, and the boundary conditions (5) and (6) signify that the part of the roll cover not in contact with the indentor is traction free whereas that in contact with the indentor has a normal pressure acting on it. Note that θ_0 defines half nip width in the reference configuration. The boundary condition $(6)_3$ insures that a contact problem rather than a punch problem is being solved.

We note that the half nip width θ_0 and the pressure $f(\theta)$ at the contact surface are unknown and are to be determined as a part of the solution. These two should assume values such that the deformed surface of the rubber like layer matches with the profile of the indentor. In practice the load P, given by

$$P = 2\int_0^{\theta_0} f(\theta) d\theta, \tag{8}$$

pressing the two rolls together is specified. However for ease in computation, we prescribe θ_0 and find the required load. Of course one could equally well prescribe the indentation u_0, as is done in [10], between the two rolls and compute the necessary load. Specification of P and then finding θ_0 and the indentation u_0, though feasible, results in significantly more computing time. The indentation u_0 equals the distance through which the two rolls move closer when loaded and is the value of the radial displacement of that point on the outermost surface of the roll cover that lies on the center line of the rollers.

The problem as just formulated is too difficult to solve analytically, so we solve it by the finite-element method.

Brief Description of the Finite-Element Formulation

We use the total Lagrangian formulation and the principle of stationary potential energy. That is, the potential energy

$$E = \int \left(W + \frac{p}{2}(I_3 - 1)\right) dV - \int h_\alpha u_\alpha \, dA \tag{9}$$

takes an extremum value [12, p. 253] for all admissible displacement fields that satisfy the displacement boundary condition. In (9), $\mathbf{h}$ is the surface traction acting on a unit area in the reference configuration, W is the strain-energy density and $I_3 = \det \mathbf{C}$ is the third invariant of $\mathbf{C}$. For Mooney-Rivlin materials

$$W = C_1(I_1 - 3) + C_2(I_2 - 3), \quad I_2 = I_3^{-1}(C^{-1})_{\alpha\alpha}. \tag{10}$$

$\delta E = 0$ gives

$$\int S_{\alpha\beta}\delta E_{\alpha\beta} dV = \int h_\alpha \delta u_\alpha dA, \quad \int \delta p(I_3 - 1) dV = 0, \tag{11}$$

in which $\mathbf{E} = (\mathbf{C} - \mathbf{1})/2$.

We assume that the load $f(\theta)$ at the contact surface is applied in M equal increments and denote the incremental change in the value of say $\mathbf{u}$ caused by the $(N + 1)$st load increment by $\Delta\mathbf{u}$, i.e.,

$$\mathbf{u}^{N+1} = \mathbf{u}^N + \Delta\mathbf{u}, \mathbf{E}^{N+1} = \mathbf{E}^N + \Delta\mathbf{E}. \tag{12}$$

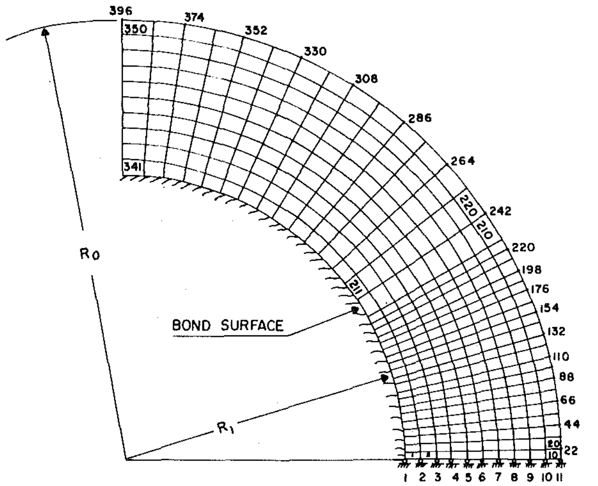

Fig. 2 Finite-element grid

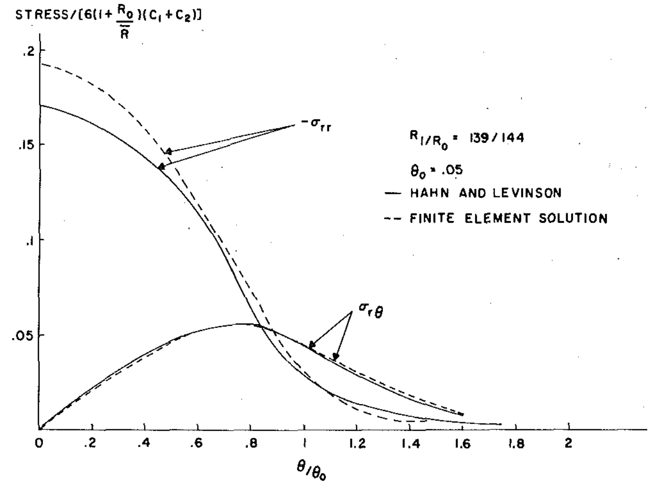

Fig. 3 Stress distribution at the bond surface; comparison of present results with those of Hahn and Levinson

From equations $(3)_4$, $(1)_2$, (4) and the definition of **E**, we obtain

$$\Delta E_{\alpha\beta} = \Delta e_{\alpha\beta} + \Delta\eta_{\alpha\beta}, \quad \Delta\eta_{\alpha\beta} = \tfrac{1}{2}\Delta u_{\gamma,\alpha}\Delta u_{\gamma,\beta},$$

$$\Delta e_{\alpha\beta} = \tfrac{1}{2}(\Delta u_{\alpha,\beta} + \Delta u_{\beta,\alpha} + u^N{}_{\gamma,\alpha}\Delta u_{\gamma,\beta} + u^N{}_{\gamma,\beta}\Delta u_{\gamma,\alpha}) \quad (13)$$

We note that $\Delta I_3 = 2(C^{-1})_{\alpha\beta}\Delta E_{\alpha\beta}$. The relation between $\Delta\mathbf{S}$, $\Delta\mathbf{E}$ and Δp is given in reference [13]. Setting $\delta E_{\alpha\beta} = \delta\Delta E_{\alpha\beta}$, $\delta u_\alpha = \delta\Delta u_\alpha$, and $\delta p = \delta\Delta p$ in (11) we obtain

$$\int (S_{\alpha\beta}{}^N + \Delta S_{\alpha\beta})\delta\Delta E_{\alpha\beta}dV = \int h_\alpha{}^{N+1}\delta\Delta u_\alpha dA, \quad (14)$$

$$\int \delta\Delta p(C^N)^{-1}{}_{\alpha\beta}\Delta E_{\alpha\beta}dV = -\tfrac{1}{2}\int \delta\Delta p(I_3{}^N - 1)dV. \quad (15)$$

We now make the assumption that the increment in the load is small so that

$$\Delta S_{\alpha\beta}\delta\Delta E_{\alpha\beta} \simeq \Delta S_{\alpha\beta}\delta\Delta e_{\alpha\beta},$$
$$(C^N)^{-1}_{\alpha\beta}\delta\Delta E_{\alpha\beta} \simeq (C^N)^{-1}_{\alpha\beta}\delta\Delta e_{\alpha\beta}, \text{etc.} \quad (16)$$

Hence an approximation to equations (14) and (15) is

$$\int \Delta S_{\alpha\beta}\delta\Delta e_{\alpha\beta}dV + \int S_{\alpha\beta}{}^N\delta\Delta\eta_{\alpha\beta}dV \simeq \int h_\alpha{}^{N+1}\delta\Delta u_\alpha dA - \int S_{\alpha\beta}{}^N\delta\Delta e_{\alpha\beta}dV \quad (17)$$

$$\int \delta\Delta p(C^N)^{-1}_{\alpha\beta}\Delta e_{\alpha\beta}dV \simeq -\tfrac{1}{2}\int \delta\Delta p(I_3{}^N - 1)dV. \quad (18)$$

We use equilibrium iterations [15], i.e., iterations within a load step, to insure that equations (17) and (18) are satisfied within a prescribed error.

A finite-element program based on equations (17) and (18) and employing 4-node isoparametric quadrilateral elements with 2×2 Gaussian integration rule has been written. The hydrostatic pressure p is assumed to be constant within an element. The pressure load between two surface nodal points a and b is replaced by lumped nodal loads given by

$$h_i{}^a = h_i{}^b = f(\theta^*)\epsilon_{3ij}(x_j{}^b - x_j{}^a).$$

Here ϵ_{ijk} is the permutation symbol and it equals 1 or -1 according as i, j, k form an even or an odd permutation of 1, 2, and 3 and is zero otherwise and θ^* is the value of θ for the midpoint of the line joining nodes a and b. The loads for the $(N + 1)$th load step are calculated based upon the positions of the nodes after the Nth load step.

The accuracy of the developed finite-element code has been established by comparing results for two sample problems with their analytical solution [14]. This program has been modified to solve the contact problem.

Computation and Discussion of Results

In order to solve the problem by the finite-element method, we consider the quarter of the roll cover lying in the first quadrant and assume that the surface along the vertical plane is traction-free. This assumption is motivated by previous studies on this problem in which it has been found that stresses decay rather rapidly with the distance from the contact region. This assumption is verified to be true in the present study too. This portion of the roll cover is divided into quadrilateral elements as shown in Fig. 2. The mesh is finer within approximately one and a half times the contact width.

Half nip width θ_0 and the form of the function $f(\theta)$ are assumed. The presumed load is divided into 30 equal steps and within each load step upto 15 equilibrium iterations [15] are performed to insure that displacements are accurate to within 1 percent of their values. The deformed surface of the roll cover is calculated and a check is made to insure that the deformed surface in the assumed contact zone matches, within a prescribed tolerance, with the circular profile of the indentor and that the nodal point just outside the assumed contact area has not penetrated into the indentor. If the second condition is not satisfied implying thereby that the nodal point outside the presumed contact width has penetrated into the indentor, either the value of θ_0 is increased or the total load is decreased. However, if the second condition is satisfied but the first is not, the form of $f(\theta)$ is suitably modified until both preceeding conditions are satisfied simultaneously. The deformed surface of the roll cover is taken to match with the profile of the indentor if the distance of each nodal point on the contact surface from the indentor is within 1 percent of the indentation u_0. Usually, with a little experience, one can make pretty good estimates of θ_0 and $f(\theta)$ so that the entire process converges in four or five iterations.

In order to insure that the modifications made in the program to solve contact problems are correct, we compare results computed from the present program with those given by Hahn and Levinson. As is clear from Fig. 3, the values of shear stress obtained by these two different methods are quite close. As for the difference in the values of the radial stress we remark that a similar difference exists between Hahn and Levinson's results and those of Betz and Levinson [16] who used the finite-element method to solve the problem. It should be added that Hahn and Levinson's solution is in the form of a double series and the computation of numerical results does involve convergence errors. However, the appreciable difference between the analytical solution and the finite-element solution can only be attributed to different methodologies.

Fig. 4 depicts the pressure profiles obtained by Spengos [3] and the present solution using the nonlinear theory. The two compare favorably. The difference between the two is possibly due to the fact that the assumption of plane strain state of deformation made in the present work is not quite valid for Spengos' experimental set up wherein the length-to-diameter ratio of rollers was of the order of one. Whereas Spengos reports that when the experimental contact widths are corrected by accounting for the finite size of the recording in-

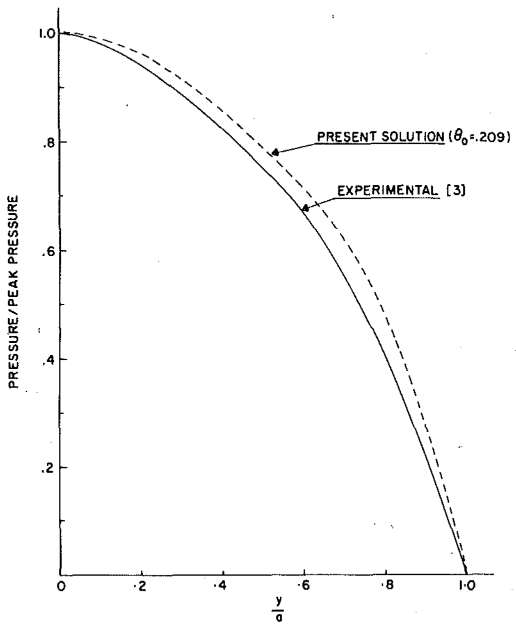

Fig. 4 Stress distribution at the contact surface; comparison of experimental and numerical results

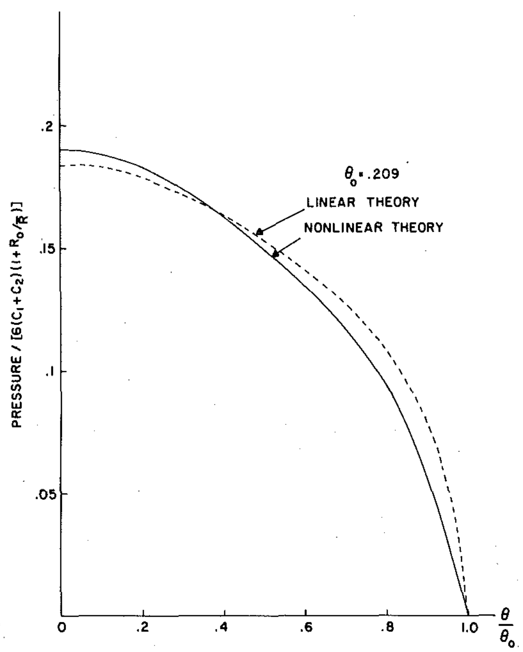

Fig. 5 Stress distribution at the contact surface; comparison of results from linear and nonlinear theories

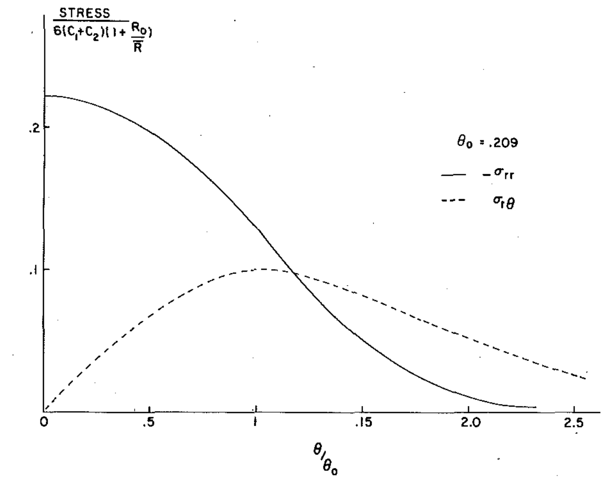

Fig. 6 Stress distribution at the bond surface

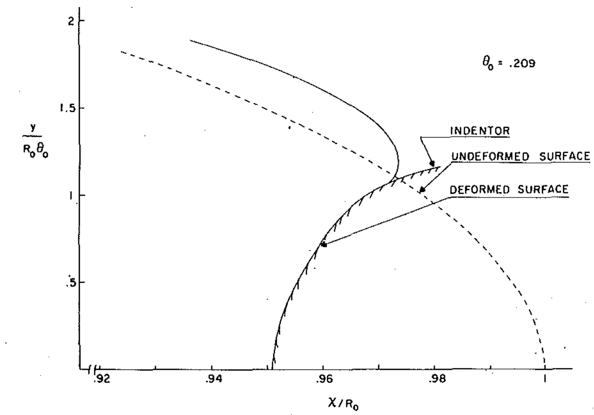

Fig. 7 Deformed surface of the rubberlike layer

struments, the pressure profiles for various nip widths match, we obtain slightly different pressure profiles for different contact widths. In the results presented in Figs. 4–7, the values of various geometrical parameters correspond to those for run number 30 of Spengos. (That is, R_1 = 47.2 mm, R_0 = 60.7 mm, $\overline{R}$ = 76.2 mm.) In Fig. 5 is shown the pressure profile obtained by using the linear and the nonlinear theory. In the linear theory entire load is applied in one step and no account is taken of the deformation of the surface on which the load is applied. Also the strain-displacement relation and the stress-strain relations are linear. In the nonlinear theory, the problem is solved incrementally and each increment in load is applied on the surface deformed up to the application of that load increment. We remark that in Fig. 5, the pressure profile at the contact surface represents the nondimensionalized Cauchy stress. It should be added that in the linear theory $6(C_1 + C_2)$ equals Young's modulus.

Results presented in Fig. 6 verify the assumption that stresses decay rapidly at points away from the contact zone. This insures that the assumption that the vertical surface of the quarter roll cover considered is traction-free does not introduce any significant error in the computed results.

Fig. 7 depicts the deformed surface of the roll cover. Because of symmetry, only half of the deformed surface is shown. Also due to different scales along the horizontal and vertical axes, the undeformed roll cover as well as the indentor plot as ellipses. The radius of curvature of the deformed surface changes near the point where rubber leaves the indentor.

For plane strain deformations of Mooney-Rivlin materials, one can show that [14] the values of displacement and components σ_{11}, σ_{22}, and σ_{12} of the Cauchy stress depend upon the material constants C_1 and C_2 only through their sum $C_1 + C_2$. Thus results presented herein are valid for all values of C_1/C_2 so long as the sum $C_1 + C_2$ is kept fixed. The values of the hydrostatic pressure p and the stress σ_{33} normal to the plane of deformation do depend upon C_1/C_2 even when $(C_1 + C_2)$ is constant.

Further extension of this work should involve the inclusion of the effects of friction at the contact surface, slipping at some points on the contact surface, and the deformations of the core and the indentor.

Acknowledgment

A slightly different version of this paper was presented at the

Second International Conference on Computational Methods in Nonlinear Mechanics held at the University of Texas-Austin in Mar. 1979.

References

1 Hahn, H. T., and Levinson, M., "Indentation of an Elastic Layer(s) Bonded to a Rigid Cylinder—I. Quasistatic Case Without Friction," *International Journal of Mechanical Science*, Vol. 16, 1974, pp. 489–502.

2 Spengos, A. C., "Experimental Investigation of Rolling Contact," ASME JOURNAL OF APPLIED MECHANICS, Vol. 32, 1965, pp. 859–864.

3 Batra, R. C., Levinson, M., and Betz, E., "Rubber Covered Rolls—The Thermoviscoelastic Problem. A Finite-Element Solution," *International Journal Num. Methods Engng.*, Vol. 10, 1976, pp. 767–785.

4 Sve, C., and Keer, L. M., "Indentation of an Elastic Layer by Moving Punches," *International Journal of Solids and Structures*, Vol. 5, 1969, pp. 795–816.

5 Keer, L. M., and Sve, C., "Indentations of an Elastic Layer by an Array of Punches Moving With Steady Velocity," ASME JOURNAL OF APPLIED MECHANICS, Vol. 38, 1971, pp. 92–98.

6 Itou, S. and Atsumi, A., "Indentations of an Elastic Layer by Moving Punches," *International Journal of Engineering Science*, Vol. 9, 1971, pp. 1209–1217.

7 Alblas, J. B., and Kuipers, M., "Contact Problems of a Rectangular Block on an Elastic Layer of Finite Thickness. Part I: The Thin Layer," *Acta Mechanica*, Vol. 8, 1969, pp. 133–145.

8 Alblas, J. B., and Kuipers, M., "Contact Problems of a Rectangular Block on an Elastic Layer of Finite Thickness. Part II: The Thick Layer," *Acta Mechanica*, Vol. 9, 1970, pp. 1–12.

9 Alblas, J. R., and Kuipers, M., "On the Two-Dimensional Problem of a Cylindrical Stamp Pressed Into a Thin Elastic Layer," *Acta Mechanica*, Vol. 9, 1970, pp. 292–311.

10 Batra, R. C., "Cold Sheet Rolling, The Thermoviscoelastic Problem, A Numerical Solution," *International Journal Num. Methods Engng.*, Vol. 11, 1977, pp. 671–682.

11 Batra, R. C., "Cold Rolling of a Laminated Composite Sheet—A Numerical Solution," *International Journal Num. Methods Engng.*, Vol. 12, 1978, pp. 429–435.

12 Oden, J. T., *Finite Elements of Nonlinear Continua*, McGraw-Hill, New York, 1972.

13 Scharnhorst, T., and Pian, T. H. H., "Finite-Element Analysis of Rubberlike Materials by a Mixed Model," *International Journal Num. Methods Engng.*, Vol. 12, 1978, pp. 665–676.

14 Batra, R. C., "Finite Plane Strain Deformations of Rubberlike Materials," *International Journal Num. Methods Engng.* (in press).

15 Hofmeister, L. D., Greenbaum, G. A. and Evensen, D. A., "Large Strain Elasto-Plastic Finite Element Analysis," *AIAA Journal*, Vol. 9, 1971, pp. 1248–1254.

16 Betz, E., and Levinson, M., "A Method for the Numerical Solution of Contact Problems," *Mechs. Res. Comm.*, Vol. 3, 1976, pp. 307–312.

G. B. Sinclair

Associate Professor,
Department of Mechanical Engineering,
Carnegie-Mellon University,
Pittsburgh, Pa. 15213
Assoc. Mem. ASME

On the Singular Eigenfunctions for Plane Harmonic Problems in Composite Regions

This paper is concerned with the singular behavior of harmonic functions at the vertex of a plane, composite, wedge region. Separable harmonic functions which include logarithmic terms are investigated for their possible existence in the vicinity of the vertex. The eigenequations governing existence are examined and explicit determination of the singular eigenvalues made for several combinations of boundary and interface conditions. The results enable an appreciation of the possible singular nature in such problems which aids any complete (numerical) analysis.

Introduction

Harmonic problems are capable of a number of physical interpretations, some of which may be set in composite regions. In this event the subregion interfaces, together with any abrupt changes in boundary conditions, can lead to functions which are unbounded in themselves or which have unbounded derivatives at the discontinuity. Such singular functions can prove troublesome in a numerical treatment—indeed it is quite reasonable to define singular behavior, with respect to a given numerical method, as that which gives rise to poor convergence. Hence it is advantageous in these situations to have an analytical understanding of the singularities present in order to devise numerical approaches with enhanced convergence and accuracy (see, for example, Strang and Fix [1, Chapter 8] or Jaswon and Symm [2, Chapter 12]).

In contrast to its biharmonic counterpart in elasticity which has been the subject of a considerable number of investigations (e.g., Bogy [3]), the derivation of singular eigenfunctions for harmonic problems in *composite* regions appears to have received little attention. Birkhoff [4], and some of the references contained therein, address related issues and Rao [5] and Fenner [6] determine singular eigenfunctions for a restricted range of geometries and boundary conditions. However, no explicit characterization of the singular harmonic nature for a general composite setting subjected to a full range of boundary conditions has been presented. Accordingly we seek to furnish this information here. In view of the variety of boundary conditions encountered therein, we consider heat transfer to be the physical application of our analysis and follow the approach initially developed by Williams [7] for the biharmonic problem to determine singular eigenfunctions for a range of composite harmonic problems.

Formulation

We begin by formulating the class of harmonic problems of concern, interpreting them within the context of steady-state heat transfer. To this end let (r,θ) denote the cylindrical polar coordinates of an arbitrary point P with respect to an origin O and within the composite, plane, wedge region $\mathcal{R}$ defined by

$$\mathcal{R} = \mathcal{R}_1 \cup \mathcal{R}_2, \qquad (1)$$

$$\left.\begin{aligned} \mathcal{R}_1 &= \{(r,\theta) \mid 0 < r < \infty, 0 < \theta < \alpha\}, \\ \mathcal{R}_2 &= \{(r,\theta) \mid 0 < r < \infty, -\beta < \theta < 0\}, \end{aligned}\right\} \qquad (2)$$

where $\mathcal{R}_1, \mathcal{R}_2$ are the two subregions comprising $\mathcal{R}$ and α,β are their respective vertex angles (Fig. 1). The equation governing the temperature distribution $\phi = \phi(r,\theta)$ throughout $\mathcal{R}$, under steady-state heat transfer, is

$$\nabla^2\phi = 0 \text{ on } \mathcal{R}, \qquad (3)$$

where $\nabla^2 = r^{-1}(\partial/\partial r(r\partial/\partial r)) + r^{-2}\partial^2/\partial\theta^2$ is the Laplacian operator in cylindrical polar coordinates.

On each of the wedge faces at $\theta = \alpha$ and $\theta = -\beta$, ϕ is to satisfy one of the following homogeneous boundary conditions:

A **Temperature Prescribed**

$$\phi = 0, \qquad (4)$$

B **Insulated Boundary**

$$\frac{\partial\phi}{\partial\theta} = 0, \qquad (5)$$

Contributed by the Applied Mechanics Division for publication in the JOURNAL OF APPLIED MECHANICS.

Discussion on this paper should be addressed to the Editorial Department, ASME, United Engineering Center, 345 East 47th Street, New York, N. Y. 10017, and will be accepted until June 1, 1980. Readers who need more time to prepare a discussion should request an extension from the Editorial Department. Manuscript received by ASME Applied Mechanics Division, May, 1978; final revision, September, 1979.

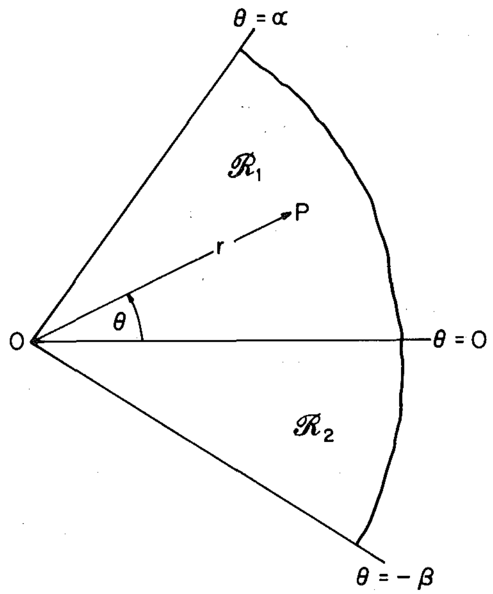

Fig. 1 Bimaterial wedge region

C **Convection Cooling**

$$\phi + \frac{k_e}{r}\frac{\partial \phi}{\partial \theta} = 0, \tag{6}$$

D **Radiation Condition**

$$\phi^4 + \frac{k_s}{r}\frac{\partial \phi}{\partial \theta} = 0. \tag{7}$$

Here k_e is the ratio of the conductivity of the material forming the wedge face to the exterior conductivity, and k_s is the material conductivity divided by the product of the Stefan-Boltzmann constant and the emissivity of the surface.[1] In what follows these boundary conditions are referred to merely by their associated letters.

The two subregions are in intimate contact along the interface at $\theta = 0$ so that the temperature and heat flux are to be matched there and consequently

$$\phi(r,0^+) = \phi(r,0^-), \quad K_1 \frac{\partial \phi}{\partial \theta}(r,0^+) = K_2 \frac{\partial \phi}{\partial \theta}(r,0^-), \tag{8}$$

where K_1,K_2 are the conductivities in $\mathcal{R}_1,\mathcal{R}_2$, respectively. Generally the two subregions have distinct conductivities. In the event that the wedge region $\mathcal{R}$ is closed and the faces at $\theta = \alpha$ and $\theta = -\beta$ coalesce to form a second interface, the boundary conditions on the wedge faces are replaced by a further pair of matching conditions, namely

$$\phi(r,\alpha) = \phi(r,-\beta), \quad K_1 \frac{\partial \phi}{\partial \theta}(r,\alpha) = K_2 \frac{\partial \phi}{\partial \theta}(r,-\beta). \tag{9}$$

Finally we adjoin the singularity requirements on ϕ in the vicinity of the wedge vertex which insist that

$$\phi = O(\ln r), \quad r/\phi = o(1), \quad \text{as} \quad r \to 0. \tag{10}$$

The first of these is physically motivated, precluding unbounded temperatures with the exception of an isolated heat source (sink) whereat the temperature becomes logarithmically infinite: the second insures that, except for the instance ϕ independent of r, $\partial\phi/\partial r$ is unbounded at $r = 0$ thus confining the extent of the eventual search for singular eigenvalues. Observe that, in the absence of any regularity requirements at infinity, or, without the insertion of an additional boundary away from $r = 0$ so as to render $\mathcal{R}$ bounded together with the specification of a boundary condition there, none of the 11 problems that may be drawn from the class described are completely formulated. However, the primary function of this class is to characterize the *possible local behavior* of ϕ, within the range admitted by (10), in the vicinity of the wedge vertex. Whether or not such behavior is present in a specific problem will depend upon the actual conditions remote from $r = 0$. Observe further that, if the local boundary conditions were to be *inhomogeneous*, then any behavior of ϕ determined for the analogous *homogeneous* problem is a candidate for inclusion in the complete ϕ for the inhomogeneous problem.

Separation-of-Variables Solutions—Conditions for Existence

Here we consider a set of separable harmonic functions and seek conditions for their satisfaction of a general combination of boundary and interface conditions. The set stems from the *basic separable solution* to (3),

$$\phi = r^\lambda(a_i \sin \lambda\theta + b_i \cos \lambda\theta) \quad \text{on} \quad \mathcal{R}_i \; (i = 1,2). \tag{11}$$

In (11), a_i,b_i $(i = 1,2)$ are constants and λ may be interpreted as a singularity parameter since it dictates the singular nature of ϕ as $r \to 0$. Letting $\lambda = \xi + i\eta$ in (11), ξ and η real, generates a *complex solution* the real and imaginary parts of which furnish an additional four independent solutions. For example

$$\phi = a_i r^\xi[\cos(\eta \ln r) \sin \xi\theta \cosh \eta\theta - \sin(\eta \ln r) \cos \xi\theta \sinh \eta\theta] \quad \text{on} \quad \mathcal{R}_i \; (i = 1,2). \tag{12}$$

With a view to examining *logarithmic* behavior we differentiate (11) with respect to λ to derive the last solution in the set,

$$\phi = r^\lambda[\ln r(a_i \sin \lambda\theta + b_i \cos \lambda\theta) + \theta(a_i \cos \lambda\theta - b_i \sin \lambda\theta)] \quad \text{on} \quad \mathcal{R}_i (i = 1,2). \tag{13}$$

Note that all of the foregoing solutions meet the singularity requirements (10) provided

$$0 \leqslant \operatorname{Re} \lambda < 1. \tag{14}$$

Now turning to the conditions under which these solutions fulfill an acceptable combination of boundary and interface conditions, we first treat solution (11): substituting from (11) into two boundary conditions from (4)–(7) and the two interface conditions (8), or substituting into the four interface conditions (8) and (9), yields a system of four homogeneous equations containing the vector of unknown constants $c = (a_1,b_1,a_2,b_2)$, viz.,

$$Bc = 0; \tag{15}$$

where B is a 4×4 matrix. For a nontrivial solution to (15) the determinant of $B,\mathcal{D}$, must satisfy

$$\mathcal{D} = 0. \tag{16}$$

For any specific problem, $\mathcal{D}$ is a function of λ alone and hence the particular value(s) of λ complying with (14) such that (16) holds determines the admissible solution(s) of type (11) to that problem. In this light λ, the singularity parameter, may be regarded as a singular eigenvalue of the eigenequation for the problem resulting from specializing (16).

Extension of the preceding argument to solutions of type (12) merely requires that we find a complex singular eigenvalue for (16) complying with (14). This pair of conditions is the harmonic counterpart to the conditions for the biharmonic problem established by Williams [7,9] within the context of plane elasticity.

For logarithmic solutions, we supplement (13) with a solution of type (11), distinguished from (13) by primed constants, substitute

[1] Boundary condition C, which has its genesis in both Newton's law for convection cooling and in an approximation to boundary condition D, is more usually termed the "radiation condition:" here, instead, the use of this description is reserved for D to distinguish it from C. For a full discussion of the various heat-transfer boundary conditions, see Carslaw and Jaegar [8, pp. 12–18].

in the boundary and interface conditions and exploit the fact that these conditions hold for all r to arrive at

$$Bc = 0, \quad \frac{dB}{d\lambda} c + Bc' = 0, \tag{17}$$

wherein $c' = (a_1', b_1', a_2', b_2')$. A logarithmic solution requires that $c \neq 0$; conditions for a nontrivial c for the system in (17) are derived in the Appendix of Dempsey and Sinclair [10] and are that

$$m < 4, \quad \frac{d^{4-m}\mathcal{D}}{d\lambda^{4-m}} = 0, \tag{18}$$

where m is the rank of the matrix B.

No attempt is made here to argue the ability of (11)–(13) to *completely* characterize the nature of ϕ in the vicinity of the wedge vertex within the limits defined by (10). Indeed a further possible solution can readily be devised from (13) by allowing λ to be complex therein. However the conditions for this last, and other similar solutions, contain those of (16) and (18), thus implying that the solution forms selected are the natural ones to pursue first. Moreover, significantly different solutions, such as ϕ of the form $r^{f(\theta)}g(\theta)$, cannot be easily constructed.

Eigenequations

By expanding the associated determinants we next establish eigenequations for the class of problems formulated earlier. Since all these problems contain the interface conditions (8), we can write

$$c_2 = Tc_1, \tag{19}$$

$$T = \lambda \begin{pmatrix} \kappa & 0 \\ 0 & 1 \end{pmatrix}, \tag{20}$$

where $c_i = (a_i, b_i)$ $(i = 1,2)$ are vectors, $\kappa = K_1/K_2$, and T may be interpreted as a transfer matrix in as much as it transfers information across the interface. On selecting two boundary conditions from (4)–(7), or on taking the additional interface conditions (9), and substituting for c_2 via (19), the boundary and interface conditions reduce to a 2×2 system hence facilitating the determinant expansion.[2] While this technique has only a marginal advantage over simply expanding the determinants of order four in bimaterial problems, extension of its application to n-material problems yields substantial simplification since then one can expand determinants of order two versus expanding determinants of order $2n$. Accordingly, as an aside here, we indicate how the extension to n-material problems proceeds:

$$c_n = \left(\prod_{i=n-1,\ldots}^{1} T_i \right) c_1, \tag{21}$$

$$T = \lambda \begin{pmatrix} \sin^2 \lambda\alpha_i + \kappa_i \cos^2 \lambda\alpha_i & (1-\kappa_i) \sin \lambda\alpha_i \cos \lambda\alpha_i \\ (1-\kappa_i) \sin \lambda\alpha_i \cos \lambda\alpha_i & \kappa_i \sin^2 \lambda\alpha_i + \cos^2 \lambda\alpha_i \end{pmatrix}, \tag{22}$$

wherein $\kappa_i = K_i/K_{i+1}$ and the interface between $\mathcal{R}_i$ *and* $\mathcal{R}_{i+1}$ occurs at $\theta = \alpha_i$.

Now returning to the class of problems at hand and applying the expansion technique to those involving boundary conditions A/B furnishes:

A-A

$$\mathcal{D} = \lambda[\sin \lambda\alpha \cos \lambda\beta + \kappa \sin \lambda\beta \cos \lambda\alpha], \tag{23}$$

B-B

$$\mathcal{D} = \lambda^3[\kappa \sin \lambda\alpha \cos \lambda\beta + \sin \lambda\beta \cos \lambda\alpha], \tag{24}$$

A-B

$$\mathcal{D} = \lambda^2[\kappa \sin \lambda\alpha \sin \lambda\beta - \cos \lambda\alpha \cos \lambda\beta]. \tag{25}$$

In the last, A holds on $\theta = -\beta$, B on $\alpha = \alpha$.

For problems entailing conditions C/D, the *inhomogeneity* in r of these boundary conditions requires an infinite sum of separable solutions of the form[3]

$$\phi = \sum_{j=0}^{\infty} r^{\lambda_j}[(\kappa(i-1) + 2 - i)a_j \sin \lambda_j\theta + b_j \cos \lambda_j\theta] \quad \text{on} \quad \mathcal{R}_i \ (i = 1,2), \tag{26}$$

where

$$\lambda_j = \lambda + j \quad \text{for} \quad C, \tag{27}$$

$$\lambda_j = 4^j\lambda + (4^j - 1)/3 \quad \text{for} \quad D. \tag{28}$$

On substituting (26) into the boundary conditions, the $r^{-1}\partial\phi/\partial\theta$ terms of (6) and (7) dominate and thus the determinant expansion is the same as that corresponding to boundary condition B. That is, th eigenequations for problems with boundary conditions C/D are *identical* to the eigenequations found on exchanging all the C and D conditions for B. However this is only true provided the higher-order terms in r satisfy the boundary conditions. Insisting that they do so generates the following set of requirements, which essentially insure the existence of a recurrence relation between the $j-1$ and j terms of (26):

For $A - C/D$

$$\left.\begin{array}{ll} \cot \lambda\alpha \cot \lambda\beta \neq \cot \lambda_j\alpha \cot \lambda_j\beta & (j = 1,2,\ldots), \\ 0 < |\cot \lambda_j\alpha \cot \lambda_j\beta| < \infty & (j = 0,1,\ldots), \end{array}\right\} \tag{29}$$

For $B/C - B/C$, $B/D - D$[4]

$$\left.\begin{array}{ll} \cot \lambda\alpha \tan \lambda\beta \neq \cot \lambda_j\alpha \tan \lambda_j\beta & (j = 1,2,\ldots), \\ 0 < |\cot \lambda_j\alpha \tan \lambda_j\beta| < \infty & (j = 0,1,\ldots). \end{array}\right\} \tag{30}$$

In some cases, relaxation of (29) and (30) is possible; in the interests of brevity we do not enumerate all such special cases here.[5]

Finally, expanding the determinant for the closed wedge (i.e., the wedge under (8) and (9)) gives

$$\mathcal{D} = \lambda^2[(\kappa^2 + 1) \sin \lambda\alpha \sin \lambda(2\pi - \alpha) + 2\kappa(1 - \cos \lambda\alpha \cos \lambda(2\pi - \alpha))]. \tag{31}$$

The determinants in (23)–(25) and (31), when set to zero, constitute the complete set of eigenequations for investigation next.

Singular Eigenvalues—Special Cases

We commence our study of the singular eigenvalues for the eigenequations derived thus far by analyzing the two special cases of a *homogeneous region* and a bimaterial region in which the two subregions have *equal vertex angles*—these two instances having simple expressions for the eigenvalues. First, the homogeneous case. Setting $\mathcal{D} = 0$, $\kappa = 1$ in (23)–(25) and selecting the eigenvalues satisfying the singularity requirements (10), or equivalently (14), yields:

$A - A$, $B/C - B/C$, $B/D - D$

$$\lambda = \pi/\gamma \ (\pi < \kappa \leqslant 2\pi), \tag{32}$$

$A - B/C/D$

$$\left.\begin{array}{l} \lambda = \pi/2\gamma \ (\pi/2 < \gamma \leqslant 2\pi), \\ \lambda = 3\pi/2\gamma \ (3\pi/2 < \gamma \leqslant 2\pi), \end{array}\right\} \tag{33}$$

[2] Notice that (20) has an extra λ multiplier over the expression resulting from rearranging (8) so as to insure exactly the same λ-power factor as the original 4×4 determinant.

[3] The ϕ of (26) satisfies the interface conditions (8).

[4] We do not permit problems containing both C and D since to date it has not been possible to construct infinite series which can satisfy both boundary conditions simultaneously.

[5] When (29) and (30), or their equivalents are not satisfied, separable solutions of the form (26) do not exist for problems with boundary conditions C/D. Vasil'ev [11] treats such a case for a homogeneous wedge subject to $C - C$ using the Mellin transform and finds it free from singular behavior.

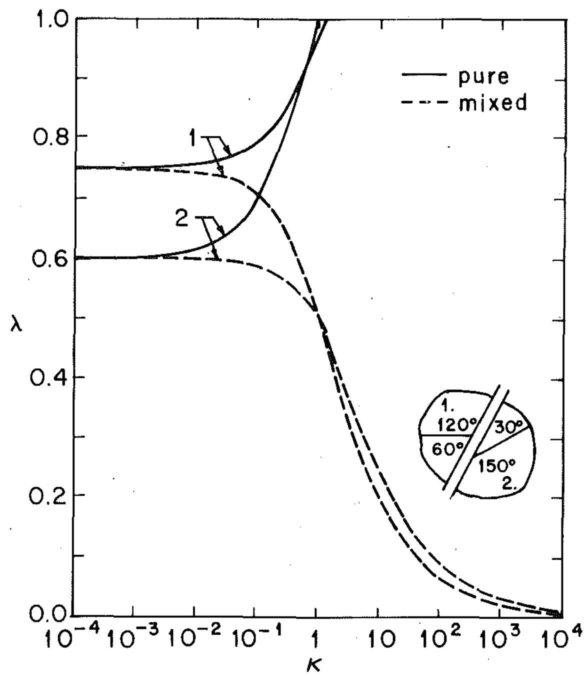

Fig. 2 Singular eigenvalues for the open wedge, $\alpha = 30°$, $60°$, $\alpha + \beta = 180°$

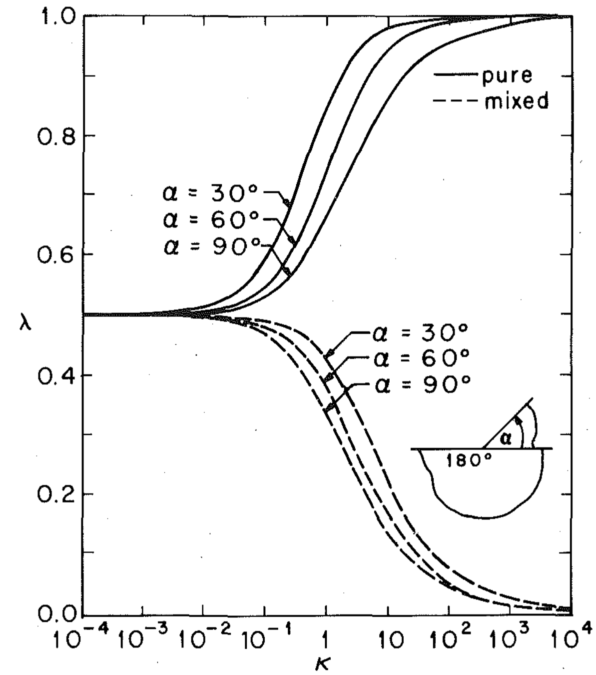

Fig. 3 Singular eigenvalues for the open wedge, $\alpha = 30°$, $60°$, $90°$, $\beta = 180°$

where $\gamma = \alpha + \beta$.[6] The second of these features two singularities within the range admitted by (14). The requirements for the existence of the infinite series such that boundary conditions C/D are met reduce to

$$\sin \lambda_j \gamma \neq 0 \ (j = 1,2,\ldots), \tag{34}$$

$$\cos \lambda_j \gamma \neq 0 \ (j = 1,2,\ldots). \tag{35}$$

for λ as in (32) and (33), respectively. The associated eigenfunctions are derived directly on introducing the eigenvalues into (11) and (26) with $\kappa = 1$ and choosing the constants appropriately.

There are no complex eigenvalues for the homogeneous region: this observation follows immediately on inspection of the real and imaginary parts of the $\mathcal{D}$ of (23)–(25) with $\kappa = 1$, $\lambda = \xi + i\eta$. Considering the possibility of a logarithmic multiplier, we note that none of (23)–(25) with $\kappa = 1$ have repeated roots away from $\lambda = 0$ so that there is no way of satisfying (18) for $\lambda \neq 0$. For the $\lambda = 0$ root, only $B/C - B/C$ and $B/D - D$ have sufficient multiplicity to fulfill (18) and thus allow the possibility of a logarithmic singularity.[7] Construction of such an eigenfunction is straightforward for $B - B$, and for $B/C - C$ proceeds on taking

$$\phi = \sum_{j=0}^{\infty} r^j[a_j(\ln r \cos j\theta - \theta \sin j\theta) + jb_j(\ln r \sin j\theta + \theta \cos j\theta) + a_j' \cos j\theta + b_j' \sin j\theta] \quad \text{on} \quad \mathcal{R}, \tag{36}$$

and complying with (34) for $\lambda_j = j$. However it is not apparent at this time how to construct a logarithmic eigenfunction for problems containing condition D.

For the second special case, setting $\mathcal{D} = 0$, $\alpha = \beta$ in (23)–(25) gives rise to the same admissible singular eigenvalues for $A - A$, $B/C - B/C$, $B/D - D$ as in (32), provided (30) holds when C/D is involved, but for $A - B/C/D$ gives

$$\left.\begin{aligned} \lambda &= \alpha^{-1} \cot^{-1} \kappa \ (\cot^{-1} \kappa < \alpha \leq \pi), \\ \lambda &= \alpha^{-1}(\pi - \cot^{-1}\kappa) \ (\pi - \cot^{-1}\kappa < \alpha \leq \pi), \end{aligned}\right\} \tag{37}$$

provided (29) holds when C/D is involved. Again no complex eigenvalues exist and logarithmic eigenfunctions are restricted to when $\lambda = 0$ in $B/C - B/C$ and in the closed wedge (see (31) with $\alpha = \pi$). The closed wedge in this case has no other singular eigenfunction.

Singular Eigenvalues—Numerical Results

To complete our investigation of the singular eigenvalues we treat a range of configurations which, in conjunction with the special cases already analyzed, exemplifies the possible singular character admitted here. Geometries in this range typically require numerical evaluation of the singular eigenvalues which is readily accomplished using an inverse approach; that is, by assuming a value of λ satisying (14) and determining the associated value of κ such that (23)/(24)/(25) are zero. Clearly, from the form of (23) and (24), the answers so determined for problem $A - A$ are the same as for $B - B$ if one interprets κ as K_2/K_1 in the latter instance. Thus, on recalling the equivalence of B, C, D, there are in essence two distinct combinations of boundary conditions which we designate as:

Pure

$$\left.\begin{aligned} A - A, \quad \kappa &= K_1/K_2, \\ B/C - B/C \text{ and } \ B/D - D, \ \kappa &= K_2/K_1, \end{aligned}\right\} \tag{38}$$

and *Mixed*

$$A - B/C/D, \left.\begin{aligned} \kappa &= K_1/K_2 \text{ if } A \text{ holds on } \theta = -\beta, \\ \kappa &= K_2/K_1 \text{ if } A \text{ holds on } \theta = \alpha. \end{aligned}\right\} \tag{39}$$

The term pure reflects the fact that (38) in effect involves the specification of ϕ *or* $\partial\phi/\partial\theta$ whereas the mixed conditions of (39) entail specifying ϕ *and* $\partial\phi/\partial\theta$. Figs. 2–6 present the singular eigenvalues for these two sets of boundary conditions delineated by solid and broken lines for the pure and mixed sets, respectively. Generally the mixed problems are more singular than the pure within the spectrum of singular character admitted by (10).

After a little algebra it may be proven that no complex eigenvalues

[6] The singular behavior characterized by (32) and (33) has been noted in conjunction with boundary conditions A/B by a number of investigators; see for example, Fox and Sankar [12].

[7] One expects a logarithmic singularity when basically the boundary conditions set $\partial\phi/\partial\theta = 0$ because heat sources (sinks) produce heat flow in the radial direction alone.

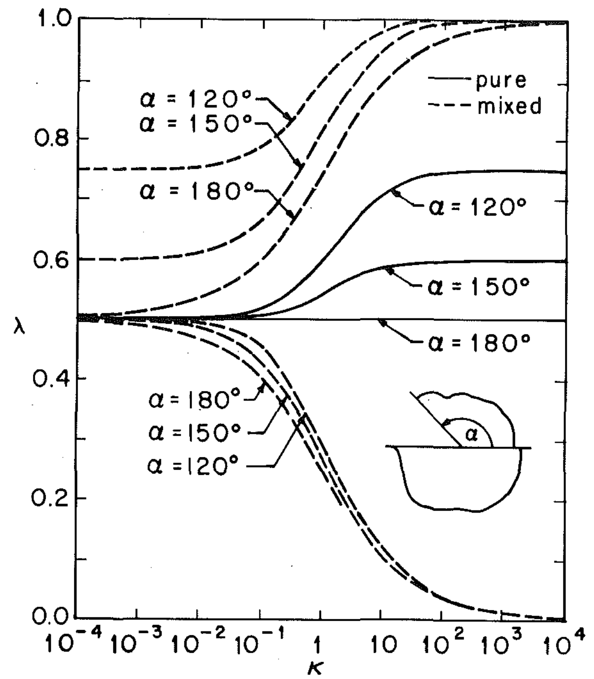

Fig. 4 **Singular eigenvalues for the open wedge, $\alpha = 120°, 150°, 180°, \beta = 180°$**

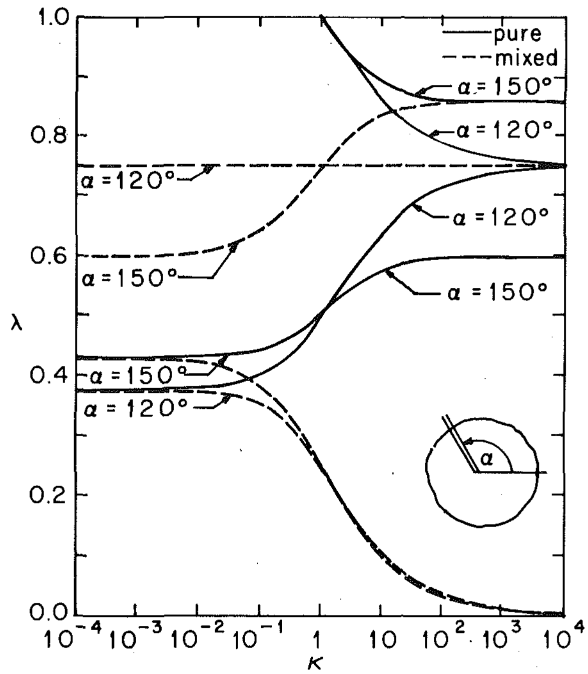

Fig. 6 **Singular eigenvalues for the open wedge, $\alpha = 120°, 150°, \alpha + \beta = 360°$**

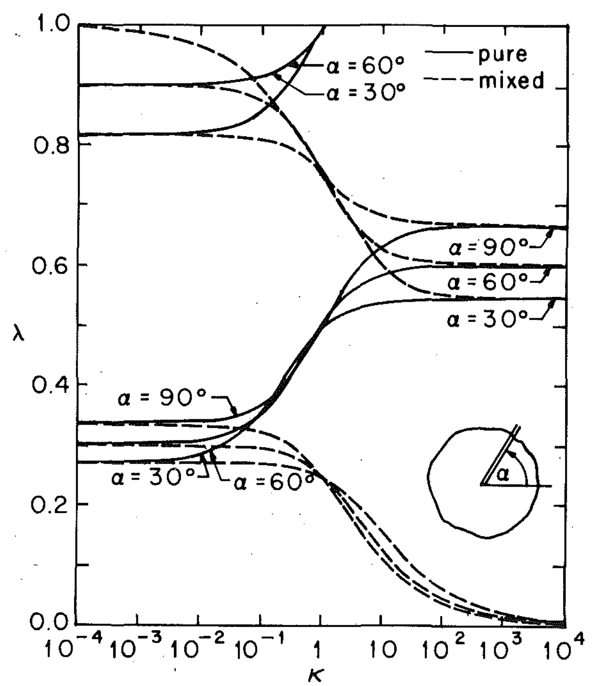

Fig. 5 **Singular eigenvalues for the open wedge, $\alpha = 30°, 60°, 90°, \alpha + \beta = 360°$**

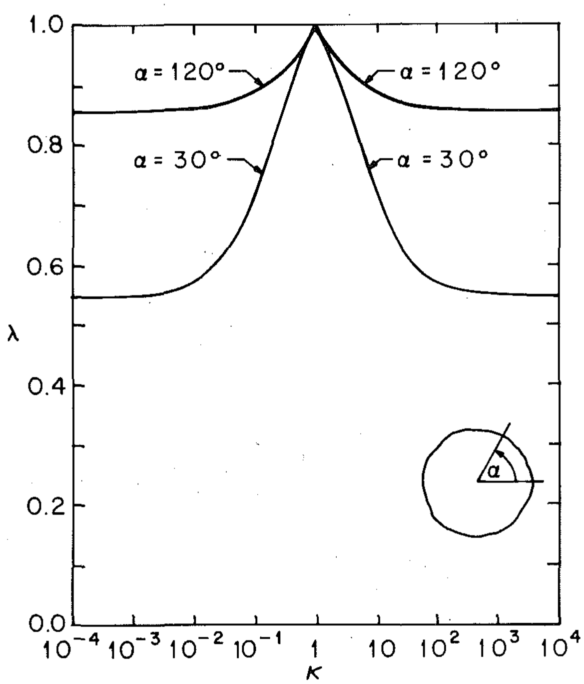

Fig. 7 **Singular eigenvalues for the closed wedge, $\alpha = 30°, 150°, \alpha + \beta = 360°$**

occur here and that the conditions for a logarithmic behavior are again solely met when $\lambda = 0$, giving rise to simple log singularities in $B/C - B/C$.

Fig. 7 demonstrates the variation of the singular eigenvalue for the closed wedge which also can have a simple log singularity.

Concluding Remarks

A number of singular eigenfunctions have been generated for harmonic problems in plane bimaterial wedges under a variety of boundary and interface conditions in the vicinity of the wedge vertex. It should be emphasized that whether or not these eigenfunctions are excited in a particular problem is governed by the conditions away from the vertex. Also, the completeness of the eigenfunctions found is not established, although it is anticipated that they probably embody most of the singular character possible in such problems.

Extension of the analysis presented to problems involving other boundary/interface conditions and to regions comprised of more than two materials is straightforward. Moreover, the eigenfunctions adapt to the *three-dimensional* wedge. To see this, let the origin of a three-dimensional cylindrical coordinate system (r,θ,z), occur at the wedge vertex with the wedge confined within $\theta = \alpha$, $\theta = -\beta$, and $z = 0$. Then if the additional boundary condition on the $z = 0$ plane is $\partial\phi/\partial z = 0$ the two-dimensional eigenfunction with corresponding conditions on $\theta = \alpha$, $\theta = -\beta$ is immediately applicable, while if the additional boundary condition is $\phi = 0$ it suffices to merely multiply the two-dimensional counterpart by z. Note, though, that such three-dimensional eigenfunctions are only appropriate in problems in which it is reasonable to expect no singular behavior as $z \to 0$, and even then are almost certain to possess a significant lack of completeness.

References

1 Strang, G., and Fix, G. J., *An Analysis of the Finite Element Method,* Prentice-Hall, Inc., New Jersey, 1973.

2 Jawson, M. A., and Symm, G. T., *Integral Equation Methods in Potential Theory and Elastostatics,* Academic Press, Inc., London, 1977.

3 Bogy, D. B., "Two Edge-Bonded Elastic Wedges of Different Materials and Wedge Angles Under Surface Tractions," ASME JOURNAL OF APPLIED MECHANICS, Vol. 38, 1971, pp. 377–386.

4 Birkhoff, G., "Angular Singularities of Elliptic Problems" *Journal of Approximation Theory,* Vol. 6, 1972, pp. 215–230.

5 Rao, A. K., "Stress Concentrations and Singularities at Interface Corners," *ZAMM,* Vol. 51, 1971, pp. 395–406.

6 Fenner, D. N., "Stress Singularities in Composite Materials With an Arbitrarily Oriented Crack Meeting an Interface," *International Journal of Fracture,* Vol. 12, 1976, pp. 705–721.

7 Williams, M. L., "Stress Singularities Resulting from Various Boundary Conditions in Angular Corners of Plates in Extension," ASME JOURNAL OF APPLIED MECHANICS, Vol. 19, 1952, pp. 526–528.

8 Carslaw, H. S., and Jaegar, J. C., *Conduction of Heat in Solids,* Oxford at the Clarendon Press, 1947.

9 Williams, M. L., "The Stresses Around a Fault or Crack in Dissimilar Media," *Bulletin of the Seismological Society of America,* Vol. 49, 1959, pp. 199–204.

10 Dempsey, J. P., and Sinclair, G. B., "On the Stress Singularities in the Plane Elasticity of the Composite Wedge," *Journal of Elasticity,* Vol. 9, 1979, to appear.

11 Vasil'ev, B. A., "Solution of a Stationary Heat-Conduction Problem for a Wedge-Shaped Body With a Boundary Condition of the Third Kind," *Differential Equations,* Vol. 6, 1970, pp. 410–415.

12 Fox, L., and Sankar, R., "Boundary Singularities in Linear Elliptic Differential Equations," *Journal of the Institute for Mathematics and Its Applications,* Vol. 5, 1969, pp. 340–350.

K. J. Bathe
Associate Professor.

C. A. Almeida
Graduate Student.

Department of Mechanical Engineering,
Massachusetts Institute of Technology,
Cambridge, Mass. 02139

A Simple and Effective Pipe Elbow Element—Linear Analysis

The formulation of a new, simple, and effective displacement-based pipe bend element is presented. The displacement assumptions are axial, torsional, and bending displacements that vary cubically along the axis of the elbow with plane sections remaining plane, and a generalization of the von Karman pipe radial displacement patterns to include the ovalization effects. The amount of ovalization varies cubically along the elbow with full compatibility between elbows. The pipe bend element has been implemented, and the results of various sample analyses are presented, which illustrate the effectiveness of the element.

1 Introduction

The structural integrity and cost of pipelines are of major concern in the nuclear, oil, and various other industries. Pipelines can be subjected to severe thermal, seismic, and other mechanical loads, and for these reasons, an increasing amount of attention has been given to their analyses [1].

In the analysis of pipelines it is convenient to distinguish between the straight and curved portions of the pipe. The straight portions of the pipeline can, in general, be adequately represented by simple beam elements with circular cross sections. However, the bend components of the pipe are much more difficult to analyze, because, in addition to undergoing the usual beam deformations, the pipe bends also ovalize. This ovalization affects the flexibility of a pipe bend a great amount and must be properly modeled in the analysis [2–8].

Because of the importance and the difficulties that lie in the analysis and design of pipe bends, much research has been devoted to the study of their structural behavior. In these investigations, during recent years, also various simple to complex finite-element models of pipe bends have been proposed. However, all these structural models have serious limitations either with regard to their accuracy in predicting pipe stresses and displacements or the cost of using them.

The simplest and widely used approach in the linear analysis of pipelines is to model a pipe bend using simple curved beam theory and scale the stiffness constants and calculated stresses using factors that account for the ovalization of the pipe cross section and the pipe internal pressure [5]. If the effect of the internal pressure can be neglected, the constants used in this analysis are, in essence, the von Karman flexibility and stress-intensification factors [6]. These constants were derived by von Karman for in-plane loading and later by Vigness using the von Karman analysis procedure for out-of-plane loading [2] with a number of assumptions. A major point is that von Karman considered a differential length of the elbow in which the internal bending moment is constant. Therefore, if the factors are applied to a complete elbow, it is assumed that the ovalization is constant along the pipe bend. The conditions of a varying magnitude in the internal bending moment and the fact that there may be no ovalization at the end of the elbow cannot be taken into account with accuracy.

Because of the limitations of the foregoing beam analysis of pipe bends various refined analytical and finite-element models have been proposed [5,7]. In essence, these models use shell theory to describe the behavior of the pipe bend. Clark and Reissner proposed equations that treat pipe bends as part of a torus and proposed an asymptotic solution for the stress and flexibility factors [8]. This approach removes some of the assumptions of the von Karman analysis but is not effective in the analysis of general pipelines. The greatest potential for the general analysis of pipe bends lies in the use of the finite-element method [9]. Pipe elbows are currently being modeled using three-dimensional elements, general shell elements, and special elbow-shell elements [10–13]. Using either three-dimensional or general shell elements, in theory, any elbow can be modeled very accurately by using a fine enough finite-element mesh. However, in practice, such an analysis of a simple elbow involves typically of the order of a thousand finite-element equilibrium equations that need be operated upon, which means that the linear analysis of a single elbow is very costly, the nonlinear analysis of a single elbow is prohibitively expensive and the nonlinear analysis of an assemblage of elbows is clearly beyond the current state-of-the-art of computational tools.

In order to reduce the number of finite-element variables special elbow-shell elements have been proposed [12]. Although these elements are more cost-effective in use, they still involve a relatively large

Contributed by the Applied Mechanics Division for publication in the JOURNAL OF APPLIED MECHANICS.

Discussion on this paper should be addressed to the Editorial Department, ASME, United Engineering Center, 345 East 47th Street, New York, N. Y. 10017, and will be accepted until June 1, 1980. Readers who need more time to prepare a discussion should request an extension from the Editorial Department. Manuscript received by ASME Applied Mechanics Division, April, 1979; final revision, July, 1979.

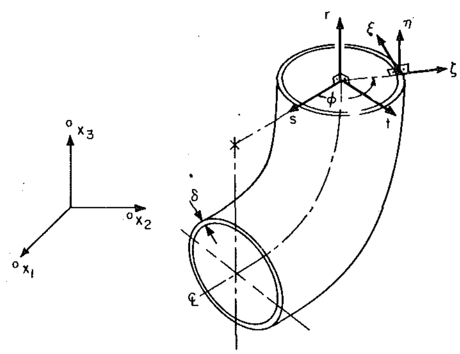

(a) COORDINATE SYSTEMS USED

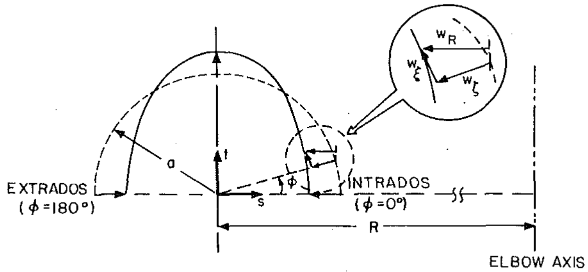

(b) DISPLACEMENTS OF DEFORMED CROSS SECTION (FIRST VON KARMAN MODE; w_ζ IS SHOWN NEGATIVE)

Fig. 1 Coordinate systems and displacements of elbow

number of solution variables and are subject to some major shortcomings, for example, the axial variation of the magnitude of ovalization is still neglected [12], or the rigid-body mode criterion is not satisfied [13].

The objective in this paper is to present the formulation of a new elbow element that is simple and effective and predicts accurately the significant deformations and stresses in various curved pipe segments. The elbow element is a four-node displacement-based finite element with axial, torsional, and bending displacements and the von Karman ovalization deformations all varying cubically along the elbow length. The formulation of the element is a very natural extension and generalization of von Karman's pioneering analysis [6]. In essence, von Karman analyzed in his work a differential length of pipe using the Ritz method to calculate the flexibility and stress-intensification factors. Because of the lack of the digital computer, von Karman could only consider in the Ritz analysis the hoop direction of the pipe, but it is interesting to note that von Karman "urges us engineers to become familiar with the Ritz method, because the method is simple and ideal to develop approximate solutions to complex practical problems" (quoted from reference [6]). The formulation of the new elbow element presented here extends the work of von Karman in that we use the Ritz method (the displacement-based finite-element method) to take also the axial variation of ovalization accurately into account, and relax some other von Karman assumptions. The actual analysis presented here is only possible because the digital computer is available and the analysis is performed efficiently using finite-element numerical procedures [9].

In this paper we consider only the linear analysis of piping systems. However, the full potential of the element lies in the geometric and material nonlinear analysis of pipes, because the element is very cost-effective and indeed allows an accurate nonlinear dynamic analysis of assemblages of pipe bends. The nonlinear formulation of the element, to be presented later, is based on the procedures given in [14, 15].

In the next section of this paper we briefly review the von Karman analysis with emphasis on the important concepts that we employ in the finite-element formulation of the new pipe elbow element. This formulation is presented in Section 3 of the paper. The elbow element has been implemented in the computer program ADINAP [16], and in Section 4 we present the analysis results of some problems that demonstrate the validity of the element.

2 The Theory of von Karman

The formulation of the pipe elbow element can be regarded as an extension of the von Karman analysis, the major concepts of which are for completeness briefly summarized in this section.

2.1 von Karman Assumptions. In his analysis of pipe elbows von Karman recognized that in addition to the usual curved beam theory strain components, two additional strain components also need be considered that are due to the ovalization of the cross section; see Fig. 1. These strain components are a pipe cross-sectional circumferential strain, $(\epsilon_{\xi\xi})_{ov}$, which is due to the deformation of the cross section, and a longitudinal strain, $(\epsilon_{\eta\eta})_{ov}$, which is due to the change in the curvature of the pipe itself. Corresponding to the usual strain components, the von Karman analysis is based on the following major assumptions.

1 Plane sections originally plane and normal to the neutral axis of the pipe are assumed to remain plane and normal to the neutral axis.

2 The longitudinal strains are assumed to be of constant magnitude through the pipe wall thickness.

3 The circumferential strains are assumed to vanish at the middle surface of the pipe wall, and are due to pure transverse bending of the pipe wall. Hence the pipe wall thickness is assumed to be small in comparison to the pipe external radius; i.e., $\delta/a \ll 1$.

4 The pipe external radius is assumed to be much smaller than the radius of the pipe bend; i.e., $a/R \ll 1$.

5 The effect of Poisson's ratio is neglected.

Using assumption 3, a relation can be written between the radial and circumferential displacements of the middle surface of the pipe wall,

$$w_\zeta = -\frac{dw_\xi}{d\phi} \tag{1}$$

where w_ζ is the radial displacement, w_ξ is the tangential displacement and ϕ measures the angular position considered as shown in Fig. 1.

2.2 von Karman Analysis. In his analysis von Karman established the strain energy in an element of pipe that is subjected to a constant bending moment, and used the Ritz method to estimate the amount of ovalization.

Using the assumptions previously summarized, the longitudinal strains due to the distortion of the cross section are

$$(\epsilon_{\eta\eta})_{ov} = \frac{w_R}{R} \tag{2}$$

where R is the pipe bend radius and w_R is the local displacement of the pipe wall in the bend radial direction, see Fig. 1. Also, the tangential strain component is

$$(\epsilon_{\xi\xi})_{ov} = -\frac{1}{a^2}\left[w_\zeta + \frac{d^2w_\zeta}{d\phi^2}\right]\zeta \tag{3}$$

where a is the radius of the pipe and ζ is the local coordinate in the pipe wall, see Fig. 1.

Using equations (1)–(3) and assumptions 1–5, the total strain energy of an elbow of angle α is

$$V = \frac{Ea\delta R}{2}\int_0^\alpha \times\left\{\int_0^{2\pi}\Big[\underbrace{-\left(\frac{\Delta\alpha}{R\alpha}\right)a\cos\phi}_{\text{TERM 1}} + \underbrace{\frac{1}{R}\left(w_\xi\sin\phi + \frac{dw_\xi}{d\phi}\cos\phi\right)}_{\text{TERM 2}}\Big]^2 d\phi, + \int_0^{2\pi}\underbrace{\left(\frac{\delta^2}{12}\right)\left[\frac{1}{a^2}\left(\frac{dw_\xi}{d\phi} + \frac{d^3w_\xi}{d\phi^3}\right)\right]^2}_{\text{TERM 3}} d\phi\right\} d\theta \tag{4}$$

Table 1 Number of ovalization shape functions to be used in Ritz analysis (and elbow formulation)

Geometric range	Number of functions N
$\lambda \geq 0.5$	1
$0.16 \leq \lambda < 0.5$	2
$0.08 \leq \lambda < 0.16$	3
$0.04 \leq \lambda < 0.08$	4

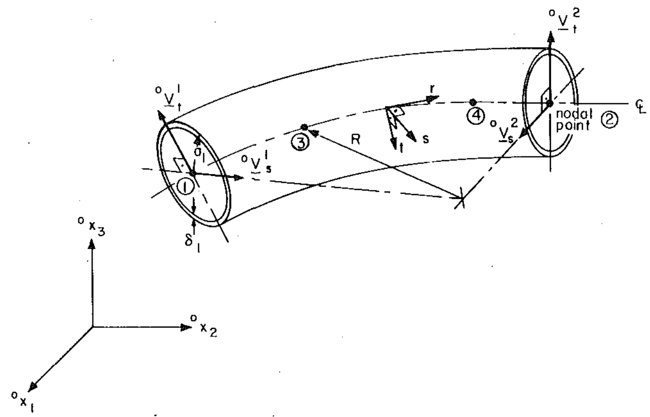

Fig. 2 Geometry of pipe elbow element

where δ is the pipe wall thickness, E is the Young's modulus of the material and $\Delta\alpha$ is the cross-sectional angular rotation. In equation (4) TERM 1 corresponds to the curved beam theory longitudinal strain, and TERM 2 and TERM 3 correspond to the straining that is due to ovalization.

The only variable in equation (4) is the displacement w_ξ. To estimate this displacement von Karman assumed for in-plane bending of the elbow

$$w_\xi = \sum_{n=1}^{N} c_i \sin 2n\phi \tag{5}$$

and performed a Ritz analysis to obtain the parameters c_i. The validity of the von Karman trial functions in equation (5) has been substantiated by experiments [2–4].

Considering the von Karman analysis, a geometric pipe factor λ, where $\lambda = R\delta/a^2$, plays an important role in the determination of the number of trial functions that should be included in the analysis. Table 1 summarizes the number of trial functions that need be used for different values of λ in order to obtain satisfactory results.

Considering the von Karman analysis, it may be noted that assumptions 2, 4, and 5 are not used in the formulation of the elbow element presented in the next section.

3 Finite-Element Formulation of the Elbow Element

The analysis of a general assemblage of finite elements consists in essence of the formulation of the equilibrium equations of each individual element and the subsequent application of general solution procedures that are independent of the type of element considered [9]. Therefore, in the following discussion, we only need to focus our attention on the derivation of the equilibrium equations of a typical elbow element.

Using the principle of virtual work (or principle of minimum total potential energy) to derive the equilibrium equations that govern the linear response of a general finite element, we obtain [9]

$$\mathbf{K}\,\mathbf{U} = \mathbf{R} \tag{6}$$

where $\mathbf{K}$ is the stiffness matrix of the finite element corresponding to the element nodal point degrees-of-freedom listed in $\mathbf{U}$,

$$\mathbf{K} = \int_V \mathbf{B}^T\,\mathbf{C}\,\mathbf{B}dv \tag{7}$$

and $\mathbf{R}$ is the effective nodal point load vector [9]. In equation (7) $\mathbf{B}$ is the strain-displacement matrix, and $\mathbf{C}$ is the corresponding stress-strain matrix [9]. Considering the pipe elbow element we therefore only need to establish the $\mathbf{B}$ matrix and discuss how the integration in equation (7) is performed efficiently.

3.1 Evaluation of the Strain-Displacement Matrix. Using the concepts of finite-element analysis, we need to describe the geometry and variations of internal element displacements of a typical pipe element in terms of its nodal point quantities. Fig. 2 shows a generic pipe elbow element with the assumed four nodal points. To establish the geometry and displacement interpolation functions of the element, assume first that the pipe cross section does not ovalize. In this case the coordinate and displacement interpolations are as used in the isoparametric finite-element formulations of beam, plate, and shell elements discussed in [15, 17–20]. For completeness of the formulation of the elbow element we briefly summarize first the isoparametric beam element formulation that does not include ovalization.

3.1.1 Element Geometry and Displacement Interpolations Assuming no Ovalization. The basic assumption in this formulation is that plane sections originally normal to the center-line axis of the pipe element remain plane but not necessarily normal to the center-line axis. Thus we can write the following equations for the coordinates of a point in the element before and after deformation:

$${}^lx_i(r,s,t) = \sum_{k=1}^{4} h_k\, {}^lx_i^k + t\sum_{k=1}^{4} a_k h_k\, {}^lV_{ti}^k + s\sum_{k=1}^{4} a_k h_k\, {}^lV_{si}^k$$

$$i = 1, 2, 3 \tag{8}$$

where

r, s, t = isoparameteric coordinates [9]
${}^lx_i$ = Cartesian coordinate of any point in the pipe element
$h_k(r)$ = isoparametric interpolation functions
${}^lx_i^k$ = Cartesian coordinate of nodal point k
a_k = outer radius of element at nodal point k
${}^lV_{ti}^k$ = component i of unit vector ${}^l\mathbf{V}_t^k$, in direction t at nodal point k
${}^lV_{si}^k$ = component i of unit vector ${}^l\mathbf{V}_s^k$, in direction s at nodal point k,

and the left superscript l denotes the configuration of the element; i.e., $l = 0$ denotes the original configuration, whereas $l = 1$ corresponds to the configuration in the deformed position.

The interpolation functions $h_k(r)$ used in equation (8) are derived in [9, pp. 127–130], and are summarized in Fig. 3. In the application of equation (8) it must be noted that the structural cross section considered is hollow, meaning that equation (8) is only applicable for the values of s and t that satisfy the equation

$$\left(1 - \frac{\delta_k}{a_k}\right)^2 \leq s^2 + t^2 \leq 1 \tag{9}$$

where δ_k and a_k are the wall thickness and the outside radius of the element at nodal point k. This fact is properly taken into account in the numerical integration to obtain the stiffness matrix of the element (see Section 3.3).

To obtain the displacement components at any point r, s, t in the pipe we have

$$u_i(r,s,t) = {}^1x_i - {}^0x_i \tag{10}$$

Thus, substituting from equation (8), we obtain

$$u_i(r,s,t) = \sum_{k=1}^{4} h_k u_i^k + t\sum_{k=1}^{4} a_k h_k V_{ti}^k + s\sum_{k=1}^{4} a_k h_k V_{si}^k \tag{11}$$

where

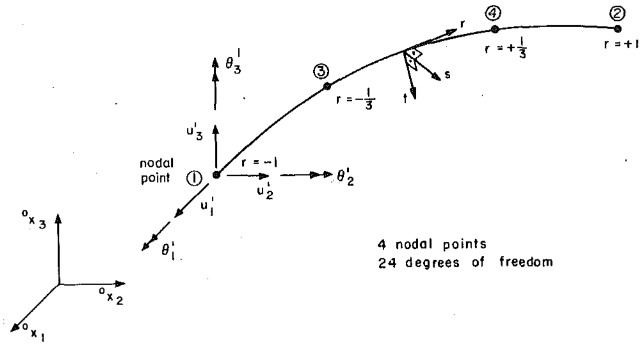

Fig. 3 Degrees-of-freedom and interpolation functions of pipe without ovalization

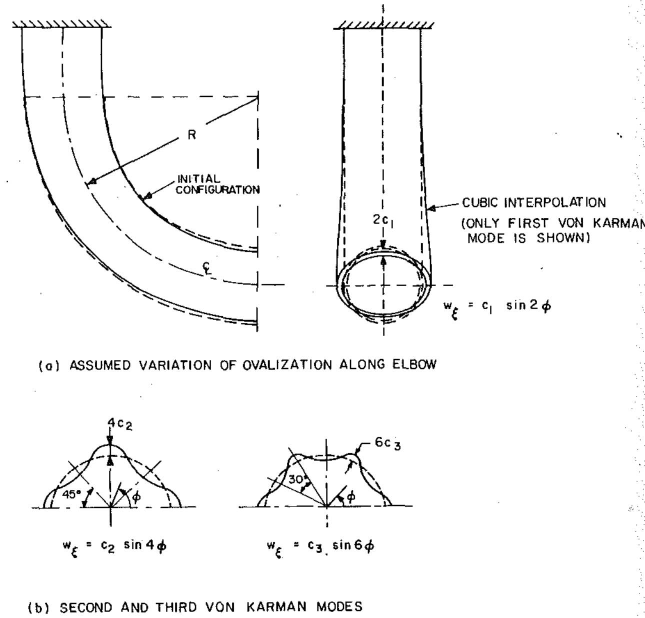

Fig. 4 Ovalization modes used in elbow formulation

$$V_{ti}^k = {}^1V_{ti}^k - {}^0V_{ti}^k$$
$$V_{si}^k = {}^1V_{si}^k - {}^0V_{si}^k \tag{12}$$

For the finite-element solution we express the components V_{ti}^k and V_{si}^k in terms of rotations about the global axes ${}^0x_i$, $i = 1, 2, 3$; namely, we have

$$\mathbf{V}_t^k = \boldsymbol{\theta}^k \times {}^0\mathbf{V}_t^k$$
$$\mathbf{V}_s^k = \boldsymbol{\theta}^k \times {}^0\mathbf{V}_s^k \tag{13}$$

where $\boldsymbol{\theta}^k$ is a vector listing the nodal point rotations at nodal point k, see Fig. 3,

$$\boldsymbol{\theta}^k = \begin{bmatrix} \theta_1^k \\ \theta_2^k \\ \theta_3^k \end{bmatrix} \tag{14}$$

Thus, substituting from equations (13) and (14) into equation (11), we obtain an equation that gives the displacement components $u_i(r, s, t)$ in terms of the nodal point displacements u_i^k and rotations θ_i^k, $i = 1, 2, 3$ and $k = 1, 2, 3, 4$.

3.1.2 Element Displacement Interpolations Including Ovalization. The displacement interpolations in equation (11) assume that the cross section of the pipe does not deform. To include the effect of ovalization we use the displacement patterns suggested by von Karman and others [2, 3, 5, and 6], and interpolate these displacement patterns cubically along the length of the elbow, see Fig. 4. Considering in-plane and out-of-plane action we use

$$w_\xi(r, \phi) = \underbrace{\sum_{m=1}^{N_c} \sum_{k=1}^{4} h_k c_m^k \sin 2m\phi}_{\text{in-plane bending}} + \underbrace{\sum_{m=1}^{N_d} \sum_{k=1}^{4} h_k d_m^k \cos 2m\phi}_{\text{out-of-plane bending}} \tag{15}$$

where the c_m^k and d_m^k, $k = 1, 2, 3, 4$, are the unknown generalized ovalization displacements. Depending on the pipe geometry, and the type of loading, it may be sufficient to include only the first, or first two, term(s) of one (or both) double summation(s) in equation (15), as discussed in Section 2.2 (see Table 1). In the implementation of the element we have allowed N_c to be 0 (no ovalization), 1, 2 or 3, and similarly for N_d.

The total pipe elbow displacements are the sum of the displacements given in equation (11) and equation (15). Thus a typical nodal point of a three-dimensional elbow element can have from 6 to 12 degrees of freedom at each node, depending on whether the ovalization displacements are included, and which ovalization patterns are used.

3.1.3 Displacement Derivatives. With the geometry and displacement interpolations given in equations (8), (11), and (15), in essence, standard procedures can be used to evaluate the appropriate displacement derivatives that constitute the elements of the strain-displacement matrix. Based on the discussion in Section 2.2 the complete strain-displacement relations for both in-plane and out-of-plane bending of the element can be written as

$$\begin{bmatrix} \epsilon_{\eta\eta} \\ \gamma_{\eta\xi} \\ \gamma_{\eta\zeta} \\ \epsilon_{\xi\xi} \end{bmatrix} = \sum_{k=1}^{4} \begin{bmatrix} \mathbf{B}^k & \mathbf{B}_{ov1}^k & \mathbf{B}_{ov3}^k \\ \mathbf{0} & \mathbf{B}_{ov2}^k & \mathbf{B}_{ov4}^k \end{bmatrix} \mathbf{u}^k \tag{16}$$

where

$$\mathbf{u}^{kT} = [u_1^k\, u_2^k\, u_3^k\, \theta_1^k\, \theta_2^k\, \theta_3^k \,|\, c_1^k\, c_2^k\, c_3^k \,|\, d_1^k\, d_2^k\, d_3^k] \tag{17}$$

In equation (16) all six ovalization patterns of equation (15) are included, but we could use less ovalization degrees of freedom.

The displacement derivatives in $\mathbf{B}^k$ correspond to the strains that are due to the beam bending nodal point displacements and rotations. Using equations (11)–(14) we have

$$\begin{bmatrix} u_{i,r} \\ u_{i,s} \\ u_{i,t} \end{bmatrix} = \sum_{k=1}^{4} \begin{bmatrix} h_{k,r}\ [1\ (g)_{1i}^k\ (g)_{2i}^k\ (g)_{3i}^k] \\ h_k\ [0\ (\hat{g})_{1i}^k\ (\hat{g})_{2i}^k\ (\hat{g})_{3i}^k] \\ h_k\ [0\ (\bar{g})_{1i}^k\ (\bar{g})_{2i}^k\ (\bar{g})_{3i}^k] \end{bmatrix} \begin{bmatrix} u_i^k \\ \theta_1^k \\ \theta_2^k \\ \theta_3^k \end{bmatrix} \tag{18}$$

where we employ the notation

$$(\hat{\mathbf{g}})^k = a_k \begin{bmatrix} 0 & -{}^0V_{s3}^k & {}^0V_{s2}^k \\ {}^0V_{s3}^k & 0 & -{}^0V_{s1}^k \\ -{}^0V_{s2}^k & {}^0V_{s1}^k & 0 \end{bmatrix} \tag{19}$$

$$(\bar{\mathbf{g}})^k = a_k \begin{bmatrix} 0 & -{}^0V_{t3}^k & {}^0V_{t2}^k \\ {}^0V_{t3}^k & 0 & -{}^0V_{t1}^k \\ -{}^0V_{t2}^k & {}^0V_{t1}^k & 0 \end{bmatrix} \tag{20}$$

and

$$(g)_{ij}^k = s(\hat{g})_{ij}^k + t(\bar{g})_{ij}^k \tag{21}$$

To obtain the displacement derivatives corresponding to the axes ${}^0x_i$, $i = 1, 2, 3$ we employ the Jacobian transformation

$$\frac{\partial}{\partial {}^0\mathbf{x}} = \mathbf{J}^{-1} \frac{\partial}{\partial \mathbf{r}} \tag{22}$$

where the Jacobian matrix, $\mathbf{J}$, contains the derivatives of the coordinates ${}^0x_i$, $i = 1, 2, 3$ with respect to the isoparametric coordinates r, s, and t [9]. Substituting from equation (18) into equation (22) we obtain

$$\begin{bmatrix} \dfrac{\partial u_i}{\partial {}^0x_1} \\ \dfrac{\partial u_i}{\partial {}^0x_2} \\ \dfrac{\partial u_i}{\partial {}^0x_3} \end{bmatrix} = \sum_{k=1}^{4} \begin{bmatrix} h_{k,1}\,(G1)_{i1}^k\,(G2)_{i1}^k\,(G3)_{i1}^k \\ h_{k,2}\,(G1)_{i2}^k\,(G2)_{i2}^k\,(G3)_{i2}^k \\ h_{k,3}\,(G1)_{i3}^k\,(G2)_{i3}^k\,(G3)_{i3}^k \end{bmatrix} \begin{bmatrix} u_i^k \\ \theta_1^k \\ \theta_2^k \\ \theta_3^k \end{bmatrix} \tag{23}$$

where

$$(Gm)_{in}^k = (J_{n1}^{-1}\,(g)_{mi}^k)h_{k,r} + (J_{n2}^{-1}\,(\hat{g})_{mi}^k + J_{n3}^{-1}\,(\bar{g})_{mi}^k)h_k \tag{24}$$

Using the displacement derivatives in equation (23) we can now directly calculate the elements of the matrix $\mathbf{B}^k$; namely, equation (23) is used to establish the global strain components (corresponding to the ${}^0x_i$, $i = 1, 2, 3$, axes), and these components are transformed to the local strain components $\epsilon_{\eta\eta}$, $\gamma_{\eta\xi}$, and $\gamma_{\eta\zeta}$ to obtain the elements of the matrix $\mathbf{B}^k$.

The elements of the matrices $\mathbf{B}_{ov1}^k$, $\mathbf{B}_{ov2}^k$, $\mathbf{B}_{ov3}^k$, and $\mathbf{B}_{ov4}^k$ correspond to the entries labeled TERM 2 and TERM 3 in equation (4).

Thus, using equation (15) to interpolate w_ξ, we have

$$\mathbf{B}_{ov1}^k = \frac{h_k}{R - a\cos\phi} \begin{bmatrix} a_1 & a_2 & a_3 \\ 0 & 0 & 0 \\ 0 & 0 & 0 \end{bmatrix} \tag{25}$$

where

$$a_l = m\cos(m\phi)\cos\phi + \sin(m\phi)\sin\phi$$
$$\phi = \text{angular position in the cross section; see Fig. 1}$$
$$m = 2l$$

and

$$\mathbf{B}_{ov2}^k = \frac{h_k}{a^2}[b_1\, b_2\, b_3] \tag{26}$$

where

$$b_l = -m(m^2 - 1)\cos(m\phi)\zeta \tag{27}$$

and

$$\mathbf{B}_{ov3}^k = \left(\frac{h_k}{R - a\cos\phi}\right) \begin{bmatrix} \tilde{a}_1 & \tilde{a}_2 & \tilde{a}_3 \\ 0 & 0 & 0 \\ 0 & 0 & 0 \end{bmatrix} \tag{28}$$

where

$$\tilde{a}_l = -m\sin(m\phi)\cos\phi + \cos(m\phi)\sin\phi, \tag{29}$$

and

$$\mathbf{B}_{ov4}^k = \frac{h_k}{a^2}[\tilde{b}_1\, \tilde{b}_2\, \tilde{b}_3] \tag{30}$$

where

$$\tilde{b}_l = m(m^2 - 1)\sin(m\phi)\zeta \tag{31}$$

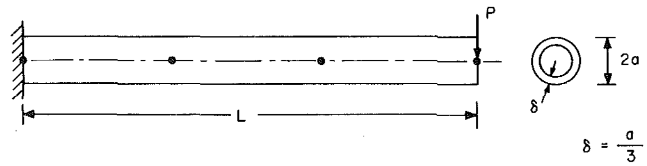

E = YOUNG'S MODULUS

I = MOMENT OF INERTIA

$$\delta_{TH} = \frac{PL^3}{3EI}$$

$$\phi_{TH} = \frac{PL^2}{2EI}$$

L/2a	$\dfrac{\delta - \delta_{TH}}{\delta_{TH}}$	$\dfrac{\phi - \phi_{TH}}{\phi_{TH}}$
10	.007042	.0000
100	.000071	.0000
1,000	.000001	.0000
10,000	.000000	.0000

Fig. 5 Analysis of cantilever straight pipe using a one element model

3.2 Stress-Strain Matrix. The stress-strain matrix used in the analysis corresponds to plane stress conditions in the $\xi - \eta$ plane, i.e., we use

$$\begin{bmatrix} \sigma_{\eta\eta} \\ \sigma_{\eta\xi} \\ \sigma_{\eta\zeta} \\ \sigma_{\xi\xi} \end{bmatrix} = \frac{E}{1-\nu^2} \begin{bmatrix} 1 & 0 & 0 & \nu \\ 0 & \dfrac{1-\nu}{2} & 0 & 0 \\ 0 & 0 & \dfrac{1-\nu}{2} & 0 \\ \nu & 0 & 0 & 1 \end{bmatrix} \begin{bmatrix} \epsilon_{\eta\eta} \\ \gamma_{\eta\xi} \\ \gamma_{\eta\zeta} \\ \epsilon_{\xi\xi} \end{bmatrix} \tag{32}$$

where E is the Young's modulus and ν the Poisson ratio of the material.

3.3 Numerical Integration. To evaluate the stiffness matrix in equation (7) we are using numerical integration. In linear analysis it may be possible and more effective to evaluate some of the integrations required in closed form, but in general nonlinear analysis numerical integration must be employed. Since our final objective is to use the element in nonlinear analysis, we choose to employ in all analyses numerical integration.

Much emphasis has been given in recent years to reduced numerical integration in the use of low-order beam and plate elements [17,21]. The use of reduced integration is necessary in those cases, because if the stiffness matrices of very thin low-order elements are evaluated accurately, the elements display much too stiff a behavior. Using reduced integration in the evaluation of the low-order element stiffness matrices can drastically improve some analysis results, but may also introduce spurious zero or very small eigenvalues that result in solution difficulties, and make it difficult to assess the reliability of the solution results in general (and particularly nonlinear) analysis. On the other hand, using the higher-order element presented in this paper reduced numerical integration is not needed for an accurate response prediction, and a reliable and effective solution is obtained using high-order integration (see also Section 4.1) [18,20].

Considering the assumed displacement distributions for the elbow element, the Newton-Cotes formulas can be employed for the numerical integration with the following integration orders: 3-point integration through the wall thickness, 5-point integration along the elbow, and, using the composite trapezoidal rule around the circumference, 12-point integration for in-plane loading, and 24-point integration for out-of-plane loading [9]. This integration order around the circumference assumes that all 3 ovalization patterns are included in the analysis; less integration stations can be employed if a smaller

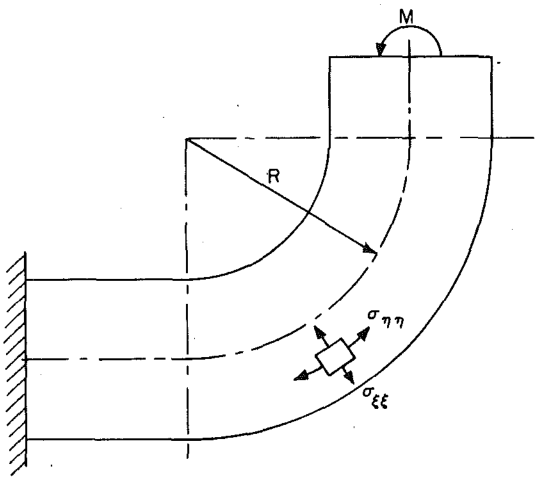

a) PIPE STRUCTURE; $R/a = 3.07$, $a/\delta = 20.8$, $\nu = .3$

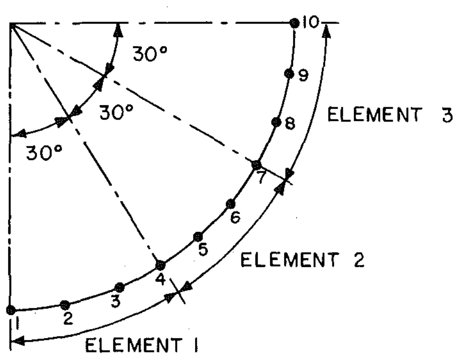

b) THREE ELEMENT MODEL (CENTRE LINE OF ELEMENTS AND NODAL POINTS ARE SHOWN)

Fig. 6 Pipe bend and finite-element model used

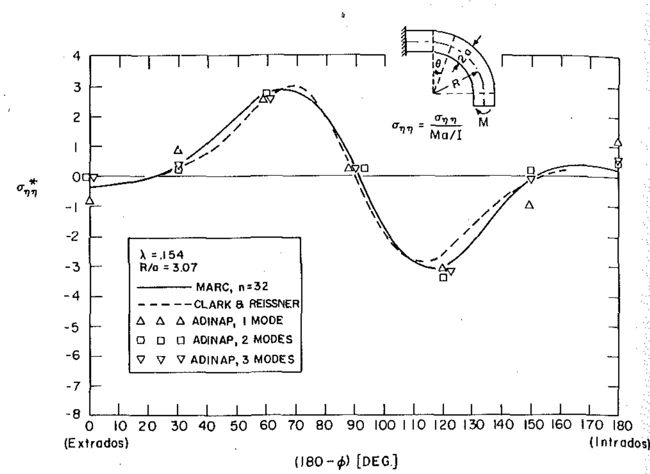

Fig. 7 Longitudinal stress at midsurface of bend in Fig. 6 (no end constraints)

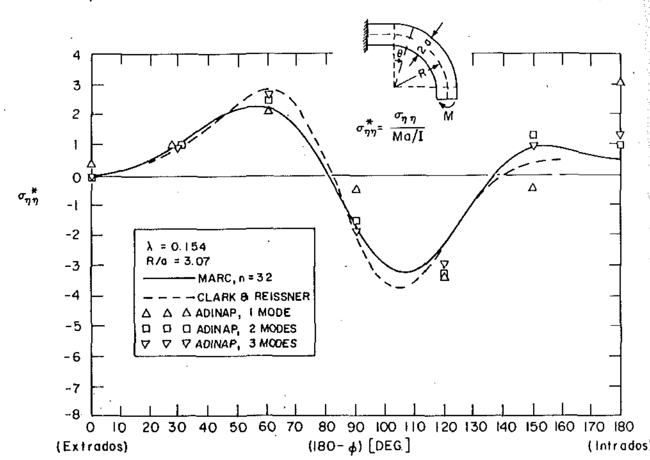

Fig. 8 Longitudinal stress at inside surface of bend in Fig. 6 (no end constraints)

number of ovalization degrees of freedom are used. Also, instead of the Newton-Cotes formulas, Gauss numerical integration could be employed. The choice of the integration scheme is particularly crucial in nonlinear analysis and we will be presenting more details on the numerical integration in future communications.

4 Sample Analyses

The elbow element has been implemented in the computer program ADINAP. The following analysis results are presented to indicate the applicability and effectiveness of the element. In all analyses the Newton-Cotes integration described in Section 3.3 was employed, and the pipe geometric factor used was $\lambda = R\delta/(a^2\sqrt{1-\nu^2})$ [12].

4.1 Analysis of a Straight Pipe. The straight cantilever pipe in Fig. 5 was analyzed to demonstrate the effectiveness of the element in the analysis of thin structural members. The element formulation includes shear deformations at a pipe cross section and it is instructive to evaluate this assumption in the solution of this problem. In the analysis one element was used to model the complete pipe.

Fig. 5 compares the analysis results obtained with the elementary beam theory solution for different length to diameter ratios. As expected, the displacements and stresses predicted using ADINAP are very close to those of elementary beam theory neglecting shear deformations for large length-to-diameter ratios, because in those cases the shear deformations contribute negligibly to the tip displacement of the pipe. Hence, it can be concluded that the element is effective when shear deformation effects can be neglected, which is the case in thin-walled pipes.

4.2 Analysis of a Pipe Bend. The pipe structure shown in Fig. 6 was analyzed using ADINAP because the analysis results could be compared with the results presented by Sobel [12]. Using ADINAP the pipe bend was modeled using three equal elbow elements as shown in Fig. 6.

In his work Sobel used the state-of-the-art tools provided in the MARC computer program to analyze the bend. Based on an extensive convergence study, Sobel concluded that 32 or 64 of the MARC pipe-bend segment elements need be used to model the bend.

In the first analysis using ADINAP the ovalization degrees of freedom at nodes 1 and 10 (and 2 to 9, see Fig. 6) were left free to simulate the conditions that were assumed in the analysis by Sobel. Figs. 7 to 9 show some stress components calculated using ADINAP and the corresponding results obtained by Sobel using the MARC program and the Clark and Reissner shell theory. The ADINAP analysis was performed using the 1, 2, and 3 in-plane bending ovalization terms of equation (15). Good correspondence between the ADINAP, MARC, and Clark and Reissner shell theory results is observed. It is also noted that in the ADINAP analysis all three terms of ovalization had to be included for an accurate response prediction, which corresponds to the recommendation given in Table 1. In the subsequent analysis of this bend we therefore included all the terms of ovalization.

In the second analysis using ADINAP the ovalization degrees of

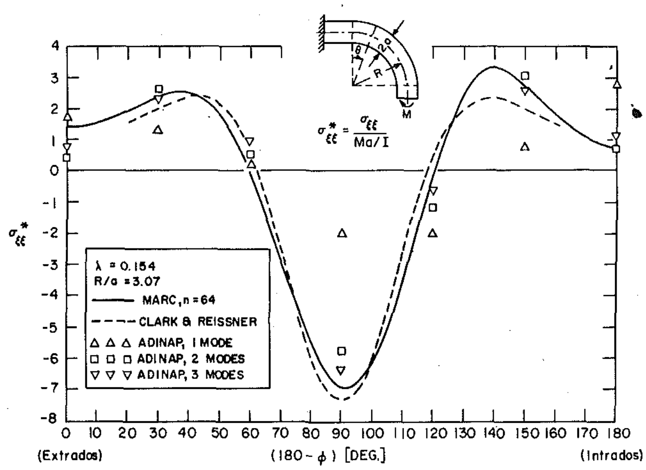

Fig. 9 Hoop stress at inside surface of bend in Fig. 6 (no end constraints)

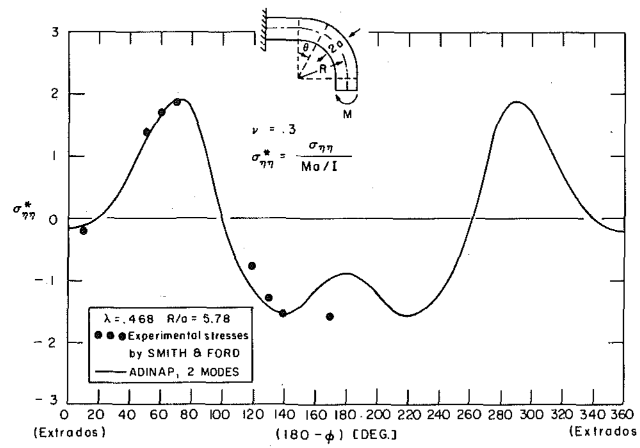

Fig. 12 Longitudinal stress at outside surface and at $\theta = 45°$ of Smith and Ford bend subjected to an in-plane bending moment

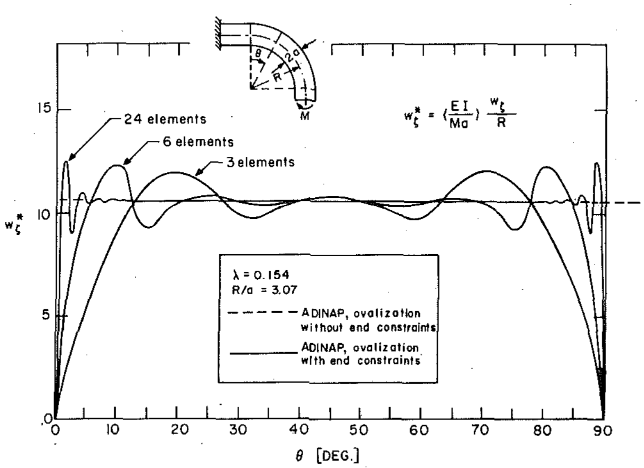

Fig. 10 Radial displacement w_ζ at $\phi = 90°$ of bend in Fig. 6 (3 ovalization modes)

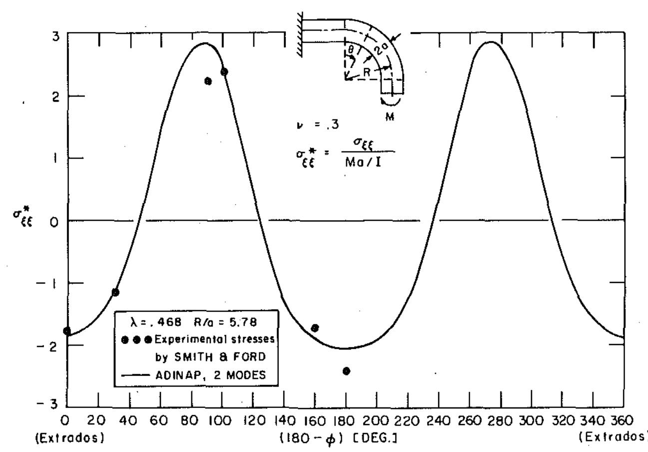

Fig. 13 Hoop stress at outside surface and at $\theta = 45°$ of Smith and Ford bend subjected to an in-plane bending moment

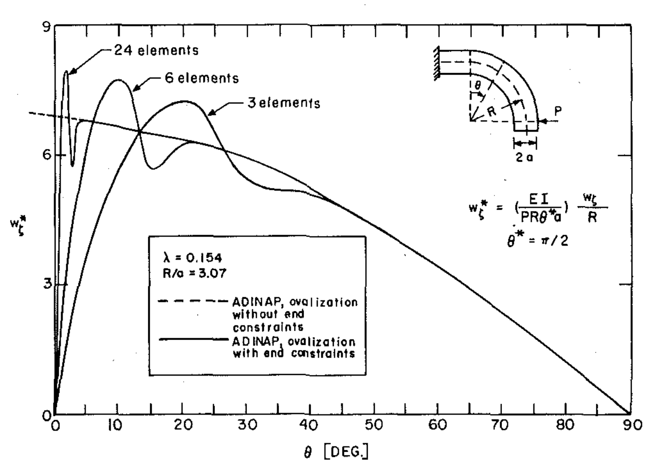

Fig. 11 Radial displacement w_ζ at $\phi = 90°$ of bend in Fig. 6 subjected to a concentrated force (3 ovalization modes)

freedom were set equal to zero at the two ends of the pipe. Fig. 10 shows the variation of ovalization along the pipe bend predicted in this analysis, using 3, 6, and 24 equal elements to model the bend. As expected the finite-element results converge (neglecting the initial overshoot/undershoot) to the analytical solution that is based on the von Karman theory. It should be noted that this theory does not account for elbow end-effects and using this theory there is a stress singularity at $\theta = 0°$ and $90°$; therefore, the present elbow element cannot be used to predict the stresses accurately at the elbow ends.

In the third analysis, the pipe structure was subjected to a concentrated transverse load instead of the concentrated moment. Fig. 11 shows the predicted ovalization again using 3, 6 and 24 equal elements to model the bend. It is seen that the finite-element results converge (again neglecting the initial overshoot/undershoot) to the ovalization predicted by the von Karman theory.

4.3 In-Plane and Out-of-Plane Bending Analysis of a Second Pipe Bend. The second pipe bend shown in Figs. 12–15 was analyzed for in-plane and out-of-plane bending using the same finite-element mesh as was employed in the previous analysis (see Fig. 6(*b*)). Some longitudinal and hoop stress results calculated with ADINAP are shown for the in-plane bending in Figs. 12 and 13, and for the out-of-plane bending in Figs. 14 and 15. The computed results are compared in the figures with experimentally obtained values [22] and good correspondence is noted.

5 Conclusions

The formulation of a simple and versatile pipe elbow element has been presented. The element has been implemented and the solution results of various sample analyses have been presented. Since the element has been formulated using basically beam theory plus an allowance for ovalization of the elbow cross section, the element cannot capture the full three-dimensional shell behavior of elbows,

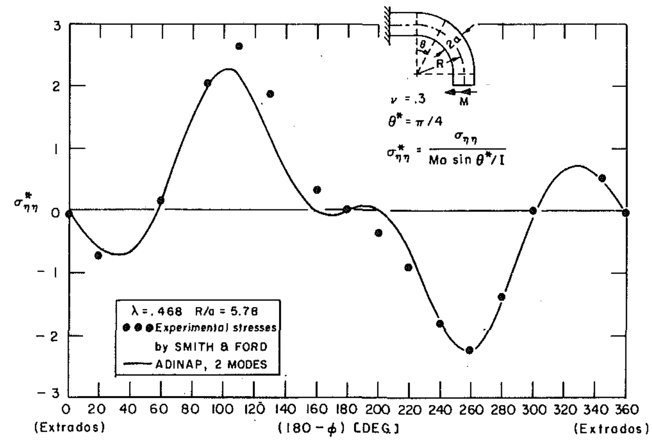

Fig. 14 Longitudinal stress at outside surface and at $\theta = 45°$ of Smith and Ford bend subjected to an out-of-plane bending moment

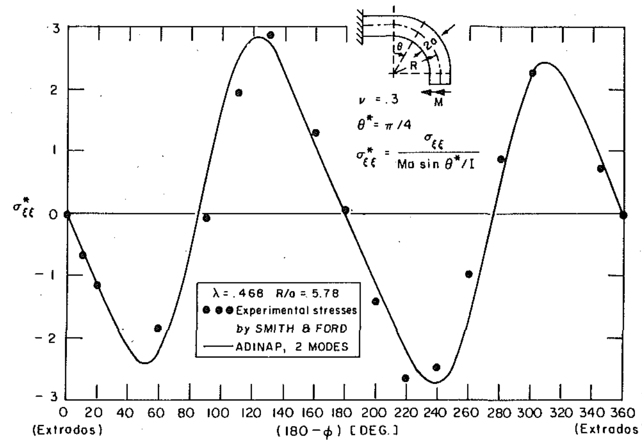

Fig. 15 Hoop stress at outside surface and at $\theta = 45°$ of Smith and Ford bend subjected to an out-of-plane bending moment

if activated. However, the element predicts the significant displacements and stresses accurately for a large range of pipe geometries, and for the same accuracy, the use of the element leads to very much less expensive solutions than other previously published computational tools.

The approach employed in the formulation of the elbow element shows much promise for the development of a simple and effective element that can also model accurately elbow end-effects, internal pressure effects and, in particular, nonlinear material and geometric behavior.

Acknowledgment

We gratefully acknowledge the financial support of A. D. Little, Cambridge, Mass., for the development of the elbow element, and the support of CNEN, Brazil, for C. Almeida's studies.

References

1 Rodabaugh, E. C., and Pickett, A. G., "Survey Report on Structural Design of Piping Systems and Components," EID-25553, Dec. 1970.

2 Vigness, I. "Elastic Properties of Curved Tubes," TRANS. ASME, Vol. 55, 1943, pp. 105–120.

3 Pardue, T. W., and Vigness, I., "Properties of Thin-Walled Curved Tubes of Short-Bend Radius," TRANS. ASME, Vol. 73, 1951, pp. 74–84.

4 Gross, N., and Ford, H., "The Flexibility of Short-Radius Pipe Bends," *Proceedings of the Institution of Mechanical Engineers*, 1952–1953, pp. 480–491.

5 Dodge, W. G., and Moore, S. E., "Stress Indices and Flexibility Factors for Moment Loadings on Elbows and Curved Pipes," *Welding Research Council Bulletin 179*, Dec. 1972.

6 von Karman, T., "Über die Formänderung Dünnwanndiger Rohre, Innsbesondere Federnder Ausgleichrohre," *Zeitschrift des Vereines deutscher Ingenieure*, Vol. 55, 1911, pp. 1889–1895.

7 Turner, C. E., and Ford, H., "Examination of the Theories for Calculating the Stresses in Pipe Bends Subject to In-Plane Bending," *Proceedings of the Institution of Mechanical Engineers*, Vol. 171, 1957, pp. 513–525.

8 Clark, R. A., and Reissner, E., "Bending of Curved Tubes," *Advances in Applied Mechanics*, Vol. 2, 1951, pp. 93–122.

9 Bathe, K. J., and Wilson, E. L., *Numerical Methods in Finite Element Analysis*, Prentice-Hall, Englewood Cliffs, N.J., 1976.

10 MARC—CDC, Nonlinear Finite Element Analysis Program, MARC Analysis Corporation, Palo Alto, Calif., and Control Data Corporation, Minneapolis, Minn., 1974.

11 Shimizu, T., et al., "Some Experiences on Elastic-Plastic Analysis of Shell Structures," *Applications Using ADINA, Proceedings of the ADINA Conference*, Aug. 1977, Bathe, K. J., ed., Report AVL 82448-6, Department of Mechanical Engineering, M.I.T., Aug 1977.

12 Sobel, L. H., "In-Plane Bending of Elbows," *Journal of Computers and Structures*, Vol. 7, 1977, pp. 701–715.

13 Ohtsubo, H., and Watanabe, O., "Stress Analysis of Pipe Bends by Ring Elements," TRANS. ASME, Vol. 100, Feb. 1978, pp. 112–122.

14 Bathe, K. J., Ramm, E., and Wilson, E. L., "Finite Element Formulations for Large Deformation Dynamic Analysis," *International Journal for Numerical Methods in Engineering*, Vol. 9, 1975, pp. 353–386.

15 Bathe, K. J., "Finite Element Formulation, Modeling, and Solution of Nonlinear Dynamic Response," Chapter in *Numerical Methods for Partial Differential Equations*, Parter, S. V., ed., Academic Press, 1979.

16 NONPIPE—ADINAP, Reference [1], Arthur D. Little Report 1979.

17 Zienkiewicz, O. C., *The Finite Element Method*, McGraw-Hill, New York, 1977.

18 Ramm, E., "A Plate/Shell Element for Large Deflections and Rotations," in *Formulations and Computational Algorithms in Finite Element Analysis*, Bathe, K. J., Oden, J. T., and Wunderlich, W., eds., M.I.T. Press, 1977.

19 Kråkeland, B., and Mo, O., "Nonlinear Analysis of Stiffened Shells," *Proceedings of the 7th Structural Analysis S.I.G. Meeting*, Sperry Univac, Nice, France, Oct. 1978.

20 Bathe, K. J., and Bolourchi, S., "A Geometric and Material Nonlinear Plate and Shell Element," *Journal Computers and Structures*, in press.

21 Hughes, T. J. R., Taylor, R. L., and Kanoknukulchai, W., "A Simple and Efficient Finite Element for Plate Bending," *International Journal for Numerical Methods in Engineering*, Vol. 11, 1977, pp. 1529–1543.

22 Smith, R. T., and Ford, H., "Experiments on Pipelines and Pipe Bends Subjected to Three-Dimensional Loading," *Journal of the Mechanical Engineering Sciences*, Vol. 9, 1967, pp. 124–135.

E. Reissner

Department of Applied Mechanics
and Engineering Sciences,
University of California, San Diego,
La Jolla, Calif. 92093
Fellow ASME

On the Transverse Twisting of Shallow Spherical Ring Caps[1]

The problem of transverse twisting of a shallow spherical shell with a small circular hole is solved, in generalization of the corresponding problem of a flat plate. The solution is of interest as a closed-form solution of an unsymmetrical stress concentration problem, with quantitative features depending on its boundary-layer behavior for large values of a relevant parameter. The problem is also of interest as an example of applicability of a previously proposed asymptotic procedure where interior contributions and edge-zone contributions are determined in sequence rather than simultaneously.

Introduction

The original aim of this paper was to formulate a nonrotationally symmetric stress-concentration problem for thin shells which could be solved in closed form, and to obtain the solution of this problem. It appeared in the course of the analysis that this stress-concentration problem was also a particularly fitting example for the application of an asymptotic solution method for unsymmetric shell problems, involving the concepts of interior and edge zone solution contributions and of the concept of contracted boundary conditions for the separate determination of these contributions, which had been proposed sometime earlier [4].

The problem is as follows. We consider an isotropic shallow spherical shell with the edges defined by two pairs of mutually perpendicular planes perpendicular to a base plane, with the corners of the rectangle in the base plane which is determined by the two pairs of mutually perpendicular planes coinciding with the corners of the shell boundary curve. Given this configuration, we assume that the edges of the shell are free of stress, except for the action of equal and opposite concentrated corner forces, as indicated in Fig. 1. Our object is the state of stress in the shell, without or with a *small* concentric circular hole at the apex.

It is evident that a limiting case of the foregoing problem is the corresponding problem of a flat plate, with the solution of the problem without the circular hole being a special case of the problem of Saint Venant torsion of narrow rectangular cross section beams, and with the solution of the circular-hole problem being included in solutions by Goodier for a class of transverse plate flexure problems [2].

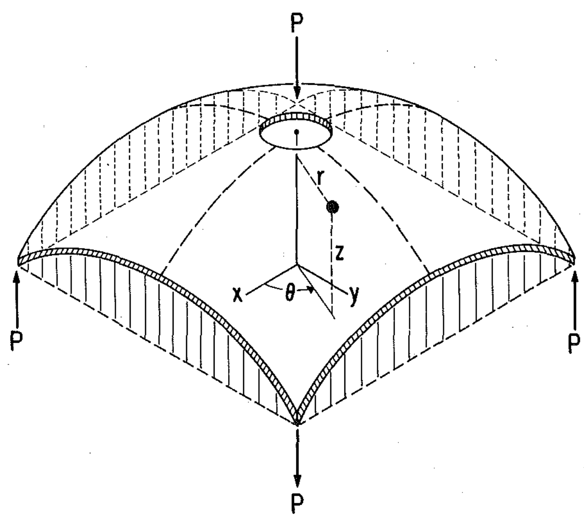

Fig. 1

In the present analysis the plate flexure problem appears upon assuming the value of a certain parameter μ to be zero. At the same time the asymptotic analysis corresponding to the procedure described in [4] is appropriate for values of μ which are large compared to unity. In the interim region of finite values of μ it is necessary to obtain appropriate solutions of the equations of shell theory, which in this instance may be taken from shallow-shell theory.

Regarding the physical aspects of the problem we find, as expected, a dominance of bending stresses over membrane stresses in the interior of the shell region. On the other hand, we also find that for sufficiently large values of μ we have membrane stresses in an edge zone which are of the same order of magnitude as the bending stresses in this zone, in such a way that the value of the stress-concentration factor for this problem of transverse bending involves both bending and membrane stresses in a significant manner.

---

[1] Supported by the Office of Naval Research and dedicated to Professor A. L. Goldenveizer.

Contributed by the Applied Mechanics Division for publication in the JOURNAL OF APPLIED MECHANICS.

Discussion on this paper should be addressed to the Editorial Department, ASME, United Engineering Center, 345 East 47th Street, New York, N. Y. 10017, and will be accepted until June 1, 1980. Readers who need more time to prepare a discussion should request an extension from the Editorial Department. Manuscript received by ASME Applied Mechanics Division, May, 1979.

Equations for Isotropic Homogeneous Shallow Spherical Shells

We consider a shallow spherical shell with middle surface equation $z = H - r^2/2R$, where R is the radius of the shell, H the distance of the apex from the base plane of the shell, and r and θ are polar coordinates in the base plane. We assume that the shell is free of distributed surface forces and have then that tangentional stress resultants N, stress couples M, and transverse stress resultants Q are expressed as follows in terms of a stress function K and a transverse displacement function w, [3],

$$N_{rr} = \frac{K_{,r}}{r} + \frac{K_{,\theta\theta}}{r^2}, \quad N_{\theta\theta} = \nabla^2 K - N_{rr}, \quad N_{r\theta} = -\frac{K_{,\theta r}}{r} + \frac{K_{,\theta}}{r^2}, \quad (1)$$

$$M_{rr} = -D\left[\nabla^2 w - (1-\nu)\left(\frac{w_{,r}}{r} + \frac{w_{,\theta\theta}}{r^2}\right)\right],$$
$$M_{\theta\theta} = -(1+\nu)D\nabla^2 w - M_{rr}, \quad (2)$$
$$M_{r\theta} = -(1-\nu)D\left(\frac{w_{,\theta r}}{r} - \frac{w_{,\theta}}{r^2}\right),$$

$$Q_r = -D(\nabla^2 w)_{,r}, \quad Q_\theta = -D\frac{(\nabla^2 w)_{,\theta}}{r}. \quad (3)$$

Use of appropriate equations of equilibrium and compatibility in conjunction with the foregoing and in conjunction with stress-strain relations of the form $\epsilon_{rr} = B(N_{rr} - \nu N_{\theta\theta})$, etc., leads to differential equations for K and w of the form

$$RB\nabla^2\nabla^2 K - \nabla^2 w = 0, \quad RD\nabla^2\nabla^2 w + \nabla^2 K = 0, \quad (4)$$

where

$$\nabla^2 = (\ \ )_{,rr} + r^{-1}(\ \ )_{,r} + r^{-2}(\ \ )_{,\theta\theta}.$$

It is readily verified that the solution of the system (4) may be expressed in terms of three functions ϕ, ψ, and χ in the form [4],

$$w = \phi + \chi, \quad K = \psi - RD\nabla^2\chi, \quad (5)$$

provided that

$$\nabla^2\phi = 0, \quad \nabla^2\psi = 0, \quad \nabla^2\nabla^2\chi + \lambda^4\chi = 0, \quad (6)$$

where $\lambda^4 = 1/R^2BD$.

We note for what follows as expressions for resultants and couples in terms of ϕ, ψ, and χ

$$N_{rr} = -\psi_{,rr} - RD\left(\frac{(\nabla^2\chi)_{,r}}{r} + \frac{(\nabla^2\chi)_{,\theta\theta}}{r^2}\right), \quad (7)$$

$$N_{\theta\theta} = \psi_{,rr} + RD\left(\frac{(\nabla^2\chi)_{,r}}{r} + \frac{(\nabla^2\chi)_{,\theta\theta}}{r^2} + \lambda^4\chi\right), \quad (8)$$

$$N_{r\theta} = -\frac{\psi_{,r\theta}}{r} + \frac{\psi_{,\theta}}{r^2} + RD\left(\frac{(\nabla^2\chi)_{,r\theta}}{r} - \frac{(\nabla^2\chi)_{,\theta}}{r^2}\right), \quad (9)$$

$$Q_r = -D(\nabla^2\chi)_{,r}, \quad (10)$$

$$M_{rr} = -(1-\nu)D\phi_{,rr} - D\nabla^2\chi + (1-\nu)D\left(\frac{\chi_{,r}}{r} + \frac{\chi_{,\theta\theta}}{r^2}\right) \quad (11)$$

$$M_{\theta\theta} = (1-\nu)D\phi_{,rr} - \nu D\nabla^2\chi - (1-\nu)D\left(\frac{\chi_{,r}}{r} + \frac{\chi_{,\theta\theta}}{r^2}\right), \quad (12)$$

$$M_{r\theta} = (1-\nu)D\left(\frac{\phi_{,\theta}}{r^2} - \frac{\phi_{,r\theta}}{r}\right) + (1-\nu)D\left(\frac{\chi_{,\theta}}{r^2} - \frac{\chi_{,r\theta}}{r}\right), \quad (13)$$

and we also note the designations of ϕ and ψ as *inextensional bending* and *membrane (interior) solution contributions*, respectively, and the designation of χ as *edge zone solution contribution*, with the physical significance of the latter designation depending on an appropriate relation between the length-parameter $1/\lambda$ and an appropriate linear dimension of the shell.

The Boundary-Value Problem

We start out with the observation that the classical solution $w = -Pxy/2(1-\nu)D$ for Saint Venant twisting of a flat rectangular plate as produced by an arrangement of concentrated corner forces P, in conjunction with an assumption of no in-plane stress, that is, in conjunction with the stipulation $K = 0$, also satisfies the differential equations (4) for shallow spherical shells. Furthermore, this solution of (4) satisfies the same corner force conditions for a spherical cap with otherwise free edges, in the event that the projection of these edges onto the base plane of the shell happens to be rectangular.

Having the aforementioned simple solution for transverse twisting of a spherical cap, we ask for the way in which this solution is modified by the presence of a circular hole of radius a, concentric with the apex of the shell, given that a is small compared to the overall dimensions of the cap. Evidently, the boundary conditions for the edge of this hole are of the form

$$r = a; \quad N_{rr} = N_{r\theta} = M_{rr} = Q_r + r^{-1}M_{r\theta,\theta} = 0. \quad (14)$$

As regards the boundary conditions along the outer edges of the cap, we make the stipulation that for large r we will have a homogeneous state of stress with Cartesian couple and resultant components $M_{xy} = -P/2$, $M_{xx} = M_{yy} = 0$, $Q_x = Q_y = N_{xx} = N_{yy} = N_{xy} = 0$. This is transformed, in an elementary manner, into four conditions of the form

$$r \to \infty; \quad M_{rr} = \frac{1}{2}P\sin 2\theta, \quad Q_r + r^{-1}M_{r\theta,\theta} = N_{rr} = N_{r\theta} = 0. \quad (15)$$

Closed-Form Solution

The form of the boundary conditions (14) and (15), in conjunction with the form of the differential equations (4) indicates that suitable expressions for w and K will be product solutions $f(r)\sin 2\theta$. Considering that w and K must be as in (5) and (6), and deleting at the outset terms not compatible with the prescribed boundary conditions at infinity, we have then that w and K will be of the form

$$w = -\frac{Pa^2\sin 2\theta}{2(1-\nu)D}\left(\frac{1}{2}\frac{r^2}{a^2} + c_1\frac{a^2}{r^2} + c_3\operatorname{ker}_2\lambda r + c_4\operatorname{kei}_2\lambda r\right), \quad (16)$$

$$K = \frac{\tfrac{1}{2}Pa^2\sin 2\theta}{(1-\nu)\sqrt{DB}}\left(c_2\frac{a^2}{r^2} - c_3\operatorname{kei}_2\lambda r + c_4\operatorname{ker}_2\lambda r\right), \quad (17)$$

with four arbitrary constants c_n, and with the Kelvin functions ker_2 and kei_2 subject to the two ordinary second-order differential equations

$$\operatorname{ker}_2'' x + x^{-1}\operatorname{ker}_2' x - 4x^{-2}\operatorname{ker}_2 x = -\operatorname{kei}_2 x, \quad (18a)$$

$$\operatorname{kei}_2'' x + x^{-1}\operatorname{kei}_2' x - 4x^{-2}\operatorname{kei}_2 x = \operatorname{ker}_2 x. \quad (18b)$$

In deriving expressions for stress resultants and couples from (16) and (17), it will be convenient to introduce the abbreviations

$$\operatorname{ker}_2 = k_r, \quad \operatorname{kei}_2 = k_i; \quad \lambda r = x, \quad \lambda a = \mu. \quad (19)$$

Therewith, and with (18a,b), we obtain from equations (1) and (3)

$$N_{rr} = \frac{\tfrac{1}{2}P\sin 2\theta}{(1-\nu)\sqrt{DB}}\left\{-6c_2\frac{a^4}{r^4} - \mu^2\left[c_3\left(\frac{k_i'}{x} - \frac{4k_i}{x^2}\right) - c_4\left(\frac{k_r'}{x} - \frac{4k_r}{x^2}\right)\right]\right\}, \quad (20)$$

$$N_{r\theta} = \frac{\tfrac{1}{2}P\cos 2\theta}{(1-\nu)\sqrt{DB}}\left\{-6c_2\frac{a^4}{r^4} - \mu^2\left[2c_3\left(\frac{k_i'}{x} - \frac{k_i}{x^2}\right) - 2c_4\left(\frac{k_r'}{x} - \frac{k_r}{x^2}\right)\right]\right\}, \quad (21)$$

$$M_{rr} = \frac{P\sin 2\theta}{2(1-\nu)}\left\{-\mu^2[c_3k_i - c_4k_r] - (1-\nu)\left(-1 - 6c_1\frac{a^4}{r^4} + \mu^2\left[c_3\left(\frac{k_r'}{x} - \frac{4k_r}{x^2}\right) + c_4\left(\frac{k_i'}{x} - \frac{4k_i}{x^2}\right)\right]\right)\right\}, \quad (22)$$

$$Q_r + \frac{M_{r\theta,\theta}}{r} = -\frac{P\sin 2\theta}{2(1-\nu)a}\{\mu^3[c_3k_i' - c_4k_r']\} - \frac{P\sin 2\theta}{r}\left\{1 - 6c_1\frac{a^4}{r^4} + 2\mu^2\left[c_3\left(\frac{k_r'}{x} - \frac{k_r}{x^2}\right) + c_4\left(\frac{k_i'}{x} - \frac{k_i}{x^2}\right)\right]\right\} \quad (23)$$

Introduction of (20) to (23) into the boundary conditions (14) then leads to the following set of four simultaneous equations for the determination of the four constants of integration c_n,

$$c_3(\mu k_i' - 4k_i) - c_4(\mu k_r' - 4k_r) = -6c_2, \tag{24}$$

$$c_3(\mu k_i' - k_i) - c_4(\mu k_r' - k_r) = -3c_2, \tag{25}$$

$$c_3\left(\frac{\mu^2 k_i}{1-\nu} + \mu k_r' - 4k_r\right) - c_4\left(\frac{\mu^2 k_r}{1-\nu} - \mu k_i' + 4k_i\right) = 6c_1 + 1, \tag{26}$$

$$c_3\left(\frac{\mu^3 k_i'}{1-\nu} + 4\mu k_r' - 4k_r\right) - c_4\left(\frac{\mu^3 k_r'}{1-\nu} - 4\mu k_i' + 4k_i\right) = 12c_1 - 2, \tag{27}$$

where now $k_i \equiv k_i(\mu)$, etc.

Upon suitable transformations, this system of equations can be written in a somewhat simpler form. To begin with, equations (24) and (25) are readily shown to be equivalent to the set[2]

$$-c_2 + c_3 k_i - c_4 k_r = 0, \tag{24'}$$

$$2c_2 + c_3\mu k_i' - c_4\mu k_r' = 0. \tag{25'}$$

Having (24′) and (25′), we may use (26) and (27) so as to obtain in place of these two equations the set

$$-2c_1 - \frac{\mu^2}{1-\nu}c_2 + c_3\mu k_r' + c_4\mu k_i' = -1, \tag{26'}$$

$$c_1 - \frac{1}{2}\frac{\mu^2}{1-\nu}c_2 + c_3 k_r + c_4 k_i = -\frac{1}{2}. \tag{27'}$$

Before evaluating the system (24′) to (27′), it is useful to establish the analytical form of the quantities which are of principal physical interest. These quantities are the edge values of the couple $M_{\theta\theta}$ and of the resultant $N_{\theta\theta}$. We obtain a particularly convenient form of these expressions by making use of equations (1) and (2), in conjunction with two of the boundary conditions in (14), so as to have

$$M_{\theta\theta}(a,\theta) = -(1+\nu)D\nabla^2 w(a,\theta), \quad N_{\theta\theta}(a,\theta) = \nabla^2 K(a,\theta). \tag{28}$$

An introduction of (16) and (17) into (28) gives, with the help of (18a,b),

$$M_{\theta\theta}(a,\theta) = -\frac{P}{2}\frac{1+\nu}{1-\nu}\mu^2(c_3 k_i - c_4 k_r)\sin 2\theta, \tag{29a}$$

$$N_{\theta\theta}(a,\theta) = -\frac{P}{2}\frac{\mu^2}{(1-\nu)\sqrt{DB}}(c_3 k_r + c_4 k_i)\sin 2\theta. \tag{29b}$$

Having (29a,b) we see, with the help of (24′) and (27′), the possibility of the further relations

$$M_{\theta\theta}\left(a,\frac{\pi}{4}\right) = -\frac{P}{2}\frac{1+\nu}{1-\nu}\mu^2 c_2, \tag{30a}$$

$$N_{\theta\theta}\left(a,\frac{\pi}{4}\right) = \frac{P}{2}\frac{\mu^2}{(1-\nu)\sqrt{DB}}\left(\frac{1}{2} + c_1 - \frac{1}{2}\frac{\mu^2}{1-\nu}c_2\right), \tag{30b}$$

and it remains only to determine the coefficients c_1 and c_2 from equations (24′) to (27′). We do this by first expressing c_3 and c_4 in terms of c_2, from (24′) and (25′), in the form

$$c_3 = -\frac{c_2}{\mu}\frac{\mu k_r' + 2k_r}{k_i' k_r - k_r' k_i}, \quad c_4 = -\frac{c_2}{\mu}\frac{\mu k_i' + 2k_i}{k_i' k_r - k_r' k_i}, \tag{31}$$

and by then using (26′) and (27′) in order to obtain the relations

$$c_2 = \frac{1-\nu}{\mu^2}\left[1 + (1-\nu)\frac{(\mu k_r' + 2k_r)^2 + (\mu k_i' + 2k_i)^2}{2\mu^3(k_i' k_r - k_r' k_i)}\right]^{-1}, \tag{32a}$$

$$\frac{1}{2} + c_1 - \frac{c_2}{2}\frac{\mu^2}{1-\nu} = \frac{k_r(\mu k_r' + 2k_r) + k_i(\mu k_i' + 2k_i)}{\mu(k_i' k_r - k_r' k_i)}c_2. \tag{32b}$$

It is possible to simplify the form of (32a,b) somewhat by making use of certain identities involving Kelvin functions of various orders. In this way we obtain,[3] upon introducing (32a,b) into (30a,b), as expressions for the significant edge moment and the significant edge resultant, in terms of *zeroth-order* Kelvin functions,

$$\frac{M_{\theta\theta}(a,\pi/4)}{-P/2} = \frac{1+\nu}{1+(1-\nu)f_1}, \tag{33a}$$

where

$$f_1 = \frac{1}{2\mu}\frac{(\text{ker}'\,\mu)^2 + (\text{kei}'\,\mu)^2}{\text{kei}'\,\mu\,\text{ker}\,\mu - \text{ker}'\,\mu\,\text{kei}\,\mu - 2\mu^{-1}[(\text{ker}'\,\mu)^2 + (\text{kei}'\,\mu)^2]}, \tag{33b}$$

and

$$\frac{N_{\theta\theta}(a,\pi/4)}{P/2} = \frac{1}{\sqrt{DB}}\frac{f_2}{1+(1-\nu)f_1}, \tag{34a}$$

where

$$f_2 = \frac{\text{kei}'\,\mu\,\text{kei}\,\mu + \text{ker}'\,\mu\,\text{ker}\,\mu}{\text{kei}'\,\mu\,\text{ker}\,\mu - \text{ker}'\,\mu\,\text{kei}\,\mu - 2\mu^{-1}[(\text{ker}'\,\mu)^2 + (\text{kei}'\,\mu)^2]} \tag{34b}$$

Stress-Concentration Factors for Bending Stresses and Membrane Stresses. We define a bending stress-concentration factor k_b as the ratio $M_{\theta\theta}(a,\pi/4)/M_0$ where $M_0 = M_{\theta\theta}(\infty,\pi/4) = -P/2$. Therewith k_b is directly given by the right-hand side in (33a).

In order to obtain the corresponding membrane stress-concentration factor k_m, it is necessary to be more specific about the nature of the two-dimensionally isotropic shell medium. We shall assume in what follows that the shell is homogeneous in thickness direction and have then the relation

$$DB = \frac{Eh^3}{12(1-\nu^2)}\frac{1}{Eh} = \frac{h^2}{12(1-\nu^2)}. \tag{35a}$$

We write further

$$\sigma_m = \frac{N_{\theta\theta}(a,\pi/4)}{h}, \quad \sigma_0 = \frac{6M_0}{h^2} = -\frac{3P}{h^2}, \tag{35b}$$

and therewith obtain from (34a)

$$k_m = \frac{\sigma_m}{\sigma_0} = \sqrt{\frac{1-\nu^2}{3}}\frac{f_2}{1+(1-\nu)f_1}. \tag{35c}$$

Stress-Concentration Factors for Small and for Large Values of μ. Given that $\mu = \lambda a = a/\sqrt[4]{R^2BD} = \sqrt[4]{12(1-\nu^2)}a/\sqrt{Rh}$, the limiting case of a flat plate corresponds to the assumption $\mu = 0$. We find, from equations (33b) and (34b), that $f_1(0) = -1/4$ and $f_2(0) = 0$ and therewith from (33a) and (35c),

$$(k_b)_{\mu=0} = \frac{4+4\nu}{3+\nu}, \quad (k_m)_{\mu=0} = 0, \tag{36a,b}$$

with this result coinciding, as it should, with Goodier's result for plates, without consideration of transverse shear deformation [2].

For the case of large μ, corresponding to a shell problem with distinct interior and edge zone solution contributions use may be made of appropriate asymptotic formulas. We find, by making use of certain known cross-product expansion formulas[4] that

$$f_1 \approx -\frac{\sqrt{2}}{2\mu}, \quad f_2 \approx 1 - \frac{3\sqrt{2}}{2\mu}, \tag{37a,b}$$

and therewith,

$$k_b \approx (1+\nu)\left(1 + \frac{1-\nu}{\mu\sqrt{2}}\right), \quad k_m \approx \sqrt{\frac{1-\nu^2}{3}}\left(1 - \frac{2+\nu}{\mu\sqrt{2}}\right). \tag{38a,b}$$

[2] Corresponding to the fact that the conditions $N_{rr} = N_{r\theta} = 0$ for $r = a$ can be shown to be equivalent to conditions $K = K_{,r} = 0$.

[3] See equations (9.9.14) to (9.9.17) in [1].

[4] Equations (9.10.32) to (9.10.34) in [1].

Table 1

μ	f_1	f_2	k_b $\nu = 0$	k_b $\nu = 1/3$	k_b $\nu = 1/2$	k_m $\nu = 0$	k_m $\nu = 1/3$	k_m $\nu = 1/2$
0	−0.250	0	1.333	1.600	1.714	0	0	0
0.1	−0.249	0.012	1.332	1.599	1.713	0.009	0.008	0.007
0.3	−0.243	0.063	1.321	1.591	1.707	0.048	0.041	0.036
0.5	−0.234	0.122	1.305	1.580	1.699	0.092	0.078	0.069
0.8	−0.219	0.206	1.280	1.561	1.684	0.152	0.131	0.116
1	−0.208	0.257	1.263	1.548	1.674	0.187	0.162	0.143
2	−0.165	0.443	1.198	1.498	1.635	0.306	0.271	0.241
3	−0.135	0.557	1.56	1.465	1.609	0.372	0.333	0.299
4	−0.114	0.633	1.128	1.443	1.591	0.413	0.373	0.336
5	−0.098	0.687	1.109	1.427	1.578	0.440	0.400	0.362
∞	0	1.000	1.000	1.333	1.500	0.577	0.544	0.500

Inasmuch as bending and membrane stresses superimpose the relevant stress-concentration factor for the most highly stressed face of the shell comes out to be, for sufficiently large values of μ,

$$k = k_b + k_m \approx 1 + \nu + \sqrt{\frac{1-\nu^2}{3}} - \frac{\sqrt{1-\nu^2}}{\mu\sqrt{2}}\left(\frac{2+\nu}{\sqrt{3}} - \sqrt{1-\nu^2}\right). \tag{39}$$

It may be noted that the numerical values of k for $\mu = 0$ and for $\mu = \infty$ are not greatly different, but that while for $\mu = 0$ the stress concentration is due entirely to bending, a significant fraction of it is, for $1 \ll \mu$, due to membrane rather than due to bending action. Numerical values for f_1, f_2, k_b, and k_m, as a function of μ and ν, may be found in Table 1.

Interior Solution Stresses for Large μ. The form of the expressions (16) and (17) for w and K indicates that for large values of μ the effect of the terms with c_3 and c_4 is significant in a narrow edge zone only and that outside this zone the remaining expression for w is as if bending occurred without stretching and the remaining expression for K is as if the state of stress of the shell was a pure membrane state.

We obtain information on the state of stress outside the narrow edge zone, and in particular on the relative significance of bending and membrane stresses, by determining the values of $M_{\theta\theta}$ and $N_{\theta\theta}$ in accordance with (16) and (17) and the defining relations (1) and (2), by setting $c_3 = c_4 = 0$ in (16) and (17) and by then deriving the relations

$$M_{\theta\theta}^{(i)}\left(a, \frac{\pi}{4}\right) \approx -\frac{P}{2}(1 + 6c_1), \tag{40a}$$

$$N_{\theta\theta}^{(i)}\left(a, \frac{\pi}{4}\right) \approx \frac{P}{2}\frac{6c_2}{(1-\nu)\sqrt{DB}}. \tag{40b}$$

We evaluate (40a) by taking c_1 from equation (26), with c_3 and c_4 as in (31) and (32a). Therewith we obtain, *except for terms small of higher order*

$$\frac{M_{\theta\theta}^{(i)}}{M_0} = \frac{\sigma_b{}^{(i)}}{\sigma_0} \approx c_2\frac{\mu^2}{1-\nu} \approx 1. \tag{41a}$$

A corresponding evaluation of (40b) leads to the relations

$$\frac{hN_{\theta\theta}^{(i)}}{6M_0} = \frac{\sigma_m^{(i)}}{\sigma_0} \approx -c_2\sqrt{12\frac{1+\nu}{1-\nu}} \approx -\frac{\sqrt{12(1-\nu^2)}}{\mu^2}. \tag{41b}$$

A comparison of (41a,b) with (38a,b) shows that the order of magnitude of the *bending* stress in the interior is the same as the order of magnitude of this stress in the edge zone, in such a way that the dimensionless edge zone value $1 + \nu$ decreases to a value 1 in the interior. At the same time the interior *membrane* stress comes out to be small of relative order $1/\mu^2$ so that, effectively, the interior state of the shell is a state of inextensional bending.

Direct Asymptotic Solution for Interior and Edge Zone States

We proceed as in [4] to solve the given boundary-value problem, for values of μ which are sufficiently large compared to unity, through use of equations (5)–(13). Introduction of (7) and (13) into the two sets of boundary conditions (14) and (15) then leaves as conditions for the determination of the two harmonic functions ϕ and ψ and of the "plate on an elastic foundation" function χ, for $r = a$,

$$\psi_{,rr} + RD\left(\frac{(\nabla^2\chi)_{,r}}{r} + \frac{(\nabla^2\chi)_{,\theta\theta}}{r^2}\right) = 0, \tag{42}$$

$$\frac{\psi_{,r\theta}}{r} - \frac{\psi_{,\theta}}{r^2} - RD\left(\frac{(\nabla^2\chi)_{,r\theta}}{r} - \frac{(\nabla^2\chi)_{,\theta}}{r^2}\right) = 0, \tag{43}$$

$$(1-\nu)\phi_{,rr} + \nabla^2\chi - (1-\nu)\left(\frac{\chi_{,r}}{r} + \frac{\chi_{,\theta\theta}}{r^2}\right) = 0, \tag{44}$$

$$\frac{1-\nu}{r}\left(\frac{\phi_{,r\theta}}{r} - \frac{\phi_{,\theta}}{r^2}\right)_{,\theta} + \frac{1-\nu}{r}\left(\frac{\chi_{,r\theta}}{r} - \frac{\chi_{,\theta}}{r}\right)_{,\theta} + (\nabla^2\chi)_{,r} = 0, \tag{45}$$

with equations (42), (43), and (45) also holding for $r = \infty$, and with the right-hand side of (44) being replaced by $-(P/2D)\sin 2\theta$ for $r = \infty$.

We now note that when $1 \ll \mu$ we have the order-of-magnitude relations,

$$\chi = o(a\chi_{,r}), \quad \chi_{,r} = o(a\chi_{,rr}), \tag{46}$$

etc. We use these for an asymptotic solution of the problem, by retaining in (44) and (45) the highest and second highest order-of-magnitude terms in χ, $(\nabla^2\chi)_{,r}$ and $\nabla^2\chi$, only, that is, we replace equations (44) and (45) by the abbreviated equations

$$(1-\nu)\phi_{,rr} + \nabla^2\chi = 0, \tag{47}$$

$$\frac{1-\nu}{r}\left(\frac{\phi_{,r}}{r} - \frac{\phi}{r^2}\right)_{,\theta\theta} + (\nabla^2\chi)_{,r} = 0. \tag{48}$$

An introduction of this into (42) and (43) then leaves as two conditions for the determination of the two harmonic functions ϕ and ψ,[5]

$$\psi_{,rr} - RD\frac{1-\nu}{r^2}\left[\left(\frac{\phi_{,r}}{r} - \frac{\phi}{r^2}\right) + \phi_{,rr}\right]_{,\theta\theta} = 0, \tag{49}$$

$$\frac{\psi_{,r\theta}}{r} - \frac{\psi_{,\theta}}{r^2} + RD\frac{1-\nu}{r^2}\left[\left(\frac{\phi_{,r}}{r} - \frac{\phi}{r^2}\right)_{,\theta\theta} - \phi_{,rr}\right]_{,\theta} = 0. \tag{50}$$

Having determined ϕ and ψ, we *subsequently* determine the associated approximation for the edge zone function χ with the help of

[5] Note that upon writing equations (7)–(13) in the form $N_{rr} = N_{rr}^i + N_{rr}^e$, etc., so as to distinguish between interior and edge zone solution contributions, equations (49) and (50) are equivalent to the previously derived contracted boundary conditions for the determination of the interior state [4], of the form $r^2N_{rr}^i - R(M_{r\theta}^i + M_{rr,\theta}^i)_{,\theta} = r^2N_{r\theta}^i - R(M_{r\theta,\theta}^i - M_{rr}^i)_{,\theta} = 0$.

equations (48),[6] and we use the results obtained in this way in order to obtain from equations (8) and (12) as approximate expressions for the relevant edge values of circumferential stress resultant and stress couple

$$N_{\theta\theta} = \psi_{,rr} + RD\lambda^4\chi, \quad M_{\theta\theta} = -(1-\nu)D\phi_{,rr} - \nu D\nabla^2\chi, \tag{51}$$

for $r = a$.

In order to carry out the remaining simple calculations we write, consistent with (16) and (17), in order to assure satisfaction of all conditions at infinity

$$\phi = w^i = -\frac{Pa^2 \sin 2\theta}{2(1-\nu)D}\left(\frac{1}{2}\frac{r^2}{a^2} + c_1\frac{a^2}{r^2}\right), \tag{52}$$

$$\psi = K^i = \frac{Pa^2 \sin 2\theta}{2(1-\nu)\sqrt{DB}}\left(c_2\frac{a^2}{r^2}\right), \tag{53}$$

and we further write

$$\chi = e^{-\lambda(r-a)/\sqrt{2}}\left(C_3 \cos\lambda\frac{r-a}{\sqrt{2}} + C_4 \sin\lambda\frac{r-a}{\sqrt{2}}\right)\sin 2\theta, \tag{54}$$

and

$$\nabla^2\chi = \lambda^2 e^{-\lambda(r-a)/\sqrt{2}}\left(C_3 \sin\lambda\frac{r-a}{\sqrt{2}} - C_4 \cos\lambda\frac{r-a}{\sqrt{2}}\right)\sin 2\theta. \tag{55}$$

We now introduce (52) and (53) into the boundary conditions (49) and (50) and obtain as two equations for the determination of c_1 and c_2

$$c_2\mu^2 - (1-\nu)(1+6c_1) = 0, \quad c_2\mu^2 - (1-\nu)(1-6c_1) = 0. \tag{56}$$

Equations (56) imply, consistent with (32), that

$$c_2\mu^2 = 1-\nu, \quad c_1 = 0. \tag{57}$$

Having c_2 and c_1 as in (57), we obtain C_3 and C_4 from (47) and (48) in the form

$$C_3 = -P/2D\lambda^2, \quad C_4 = -C_3 - P\sqrt{2}/D\lambda^3 a \approx -C_3, \tag{58}$$

and therewith, from (51),

$$N_{\theta\theta}\left(a, \frac{\pi}{4}\right) = \frac{P}{2\sqrt{DB}}, \quad M_{\theta\theta}\left(a, \frac{\pi}{4}\right) = -(1+\nu)\frac{P}{2}. \tag{59}$$

The above expressions for the edge values of $N_{\theta\theta}$ and $M_{\theta\theta}$ may be compared with the *interior* values of these same two quantities, $N^i_{\theta\theta}(a, \pi/4) = 6P/2\sqrt{DB}\mu^2$ and $M^i_{\theta\theta}(a, \pi/4) = -P/2$, which follow from (52), (53), and (57), consistent with the contents of equation (41).

[6] We note that these equations may be written, equivalently, as $D\nabla^2\chi = M^i_{rr}$ and $D(\nabla^2\chi)_{,r} = r^{-1}M^i_{r\theta,\theta} \approx 0$, for $r = a$.

References

1 Abramowitz, M., and Stegun, J. A., *Handbook of Mathematical Tables*, Dover Publications, Inc., New York, 1965.

2 Goodier, J. N., "The Influence of Circular and Elliptical Holes on the Transverse Flexure of Elastic Plates," *Philosophical Magazine*, Series 7, Vol. 22, 1936, pp. 69–80.

3 Reissner, E., "Stresses and Small Displacements of Shallow Spherical Shells—I," *Journal of Mathematics and Physics*, Vol. 25, 1946, pp. 80–85.

4 Reissner, E., "A Note on Membrane and Bending Stresses in Spherical Shells," *Journal of the Society of Industrial and Applied Mathematics*, Vol. 4, 1956, pp. 230–240.

R. D. Parbery
Lecturer,
Department of Mechanical Engineering.

B. L. Karihaloo
Senior Lecturer,
Department of Civil Engineering.

University of Newcastle,
N.S.W., 2308, Australia

Minimum-Weight Design of Thin-Walled Cylinders Subject to Flexural and Torsional Stiffness Constraints

We consider the problem of determining the cross-sectional shape of a thin-walled cylinder of constant (unknown) wall thickness and given contour length that uses the least possible material to achieve prescribed minimum stiffness in torsion and bending. The corresponding variational problem is shown to belong to a class with nonadditive functionals whose Euler equation is an integrodifferential equation. Cross-sectional shapes are presented for various stiffness ratios and compared with circular and elliptical cylinders.

Introduction

Optimal design problems of mechanical elements usually consist of maximizing or minimizing some mechanical property for given length and volume of the element. Among the mechanical properties are the buckling load [1, 2], frequency of natural vibrations [3], and transverse deflection [4]. The majority of the problems attempted so far involved mechanical elements which were required to perform a single static or dynamic function and these reduced to the solution of an isoperimetric variational problem with a single constraint.

Sometimes, however, the actual working conditions of the designed element are not very clearly defined. In such situations it is advantageous to design versatile mechanical elements that fulfill various requirements at different times during their design life (multipurpose elements). Thus, for example, Banichuk and Karihaloo [5] obtained the minimum-weight design of a solid cylindrical bar that was to act as a shaft or as a beam at different times during its design life and had to have certain minimum torsional and bending stiffness. The shape of a hollow cylindrical bar under the same conditions was found in [6]. These problems differed from those attempted in [1–4] in that, besides an increase in the number of design parameters, they were no longer one-dimensional but were described by partial differential equations, the partial derivatives appearing both in the governing differential equation and the necessary optimality condition (Euler equation).

In the present paper we consider the problem of determining the cross-sectional shape of a thin-walled cylinder of constant (but unknown) wall thickness and given contour length that uses the least amount of material to achieve prescribed minimum stiffness in bending and torsion. This problem might at first appear to be far simpler than that attempted in [6] in the sense that the torsional stiffness of a thin-walled cylinder is defined by a simple algebraic expression and not through a stress function as in the torsion theory of elastic bars [7]. However, as will become clear later, this conceptually simple optimization problem leads to a variational problem belonging to a class with nonadditive functionals whose necessary optimality condition (Euler equation) is an integro-differential equation.

Formulation of Mathematical Problem and Delineation of Special Cases

In order to formulate the optimization problem mathematically it is important to bear in mind that the thin-walled cylinder is required to act as a shaft or as a beam at different times during its design life, but is not expected to withstand twisting and bending moments simultaneously.

Let us consider a thin-walled cylinder the perimeter of whose cross section (center line) is given and equal to L. The wall thickness, t, is constant and is to be determined as a result of minimising the material volume, V. Referring to Fig. 1 and assuming the cross section to be doubly symmetric (this assumption is later confirmed by the transversatility conditions), the optimization problem consists of minimizing the material volume

$$V = 4\int_0^{x_0} t\sqrt{1+{y_x}^2}\,dx = tL \rightarrow \min_y, \tag{1}$$

where y_x denotes dy/dx, and x_0 is a parameter to be determined.

We are looking for the shape of the center line of the cross section $y(x)$ whose torsional stiffness, J, is at least equal to a prescribed value, J_0. For a thin-walled cross section the torsional stiffness is independent of the stress function [7], and therefore, the design requirement in torsion is easily expressed through

$$J = 4A^2t/L \geqslant J_0, \tag{2}$$

where A is the area enclosed by the center line of the contour of un-

Contributed by the Applied Mechanics Division for publication in the JOURNAL OF APPLIED MECHANICS.

Discussion on this paper should be addressed to the Editorial Department, ASME, United Engineering Center, 345 East 47th Street, New York, N. Y. 10017, and will be accepted until June 1, 1980. Readers who need more time to prepare a discussion should request an extension from the Editorial Department. Manuscript received by ASME Applied Mechanics Division, November, 1978; final revision, July, 1979.

known shape defined by

$$A = 4 \int_0^{x_0} y\, dx. \tag{3}$$

Next, consider the action of the thin-walled cylinder as a beam. The primary mechanical property of a beam is its bending stiffness, I. Assuming the bending to take place in the plane yz (z-axis is directed along the length of the beam), the design requirement that I be at least equal to a prescribed value, I_0, is expressed through

$$I = 4t \int_0^{x_0} y^2 \sqrt{1 + y_x^2}\, dx \geqslant I_0. \tag{4}$$

Finally, the requirement of given contour length, L, may be expressed as

$$L = 4 \int_0^{x_0} \sqrt{1 + y_x^2}\, dx. \tag{5}$$

The design constraints (2) and (4) can be rewritten as

$$t \geqslant \frac{1}{F_1^2(y)}, \tag{6}$$

where

$$F_1(y) = \frac{8}{\sqrt{J_0 L}} \int_0^{x_0} y\, dx \tag{7}$$

and

$$t \geqslant \frac{1}{F_2(y)}, \tag{8}$$

where

$$F_2(y) = \frac{4}{I_0} \int_0^{x_0} y^2 \sqrt{1 + y_x^2}\, dx. \tag{9}$$

The optimization problem (1)–(5) therefore reduces to the search of

$$\min_y \max \left\{\frac{1}{F_1^2(y)}, \frac{1}{F_2(y)}\right\},$$

or, in view of the fact that $F_1(y)$ and $F_2(y)$ are positive,

$$\max_y \min\{F_1^2(y), F_2(y)\}, \tag{10}$$

subject to the isoperimetric condition (5), i.e.,

$$F_3(y) \equiv L = 4 \int_0^{x_0} \sqrt{1 + y_x^2}\, dx. \tag{11}$$

Let us analyze the possible solutions to (10). To this end, let us consider the following three cases:

Case 1. $\max_y \min\{F_1^2(y), F_2(y)\}$ is realized on the first functional. In other words, the optimal solution is such that $F_1^2(y) < F_2(y)$. In this case the optimization problem reduces to

$$F_1^2(y) \to \max_y,$$

or, which is the same as

$$F_1(y) \to \max_y, \tag{12}$$

subject to the isoperimetric condition (11). The solution of this isoperimetric problem concerning the maximization of the torsional stiffness is a hollow circular cross section [8] of radius $R = L/2\pi$

$$x^2 + y^2 = (L/2\pi)^2,$$

whose torsional and bending stiffness in terms of prescribed parameters, L, I_0, and J_0 are

$$F_1^2 = L^3/4J_0\pi^2, \quad F_2 = L^3/8I_0\pi^2.$$

From the condition of the validity of the present solution, viz., $F_1^2 < F_2$, we get

$$I_0/J_0 < 1/2. \tag{13}$$

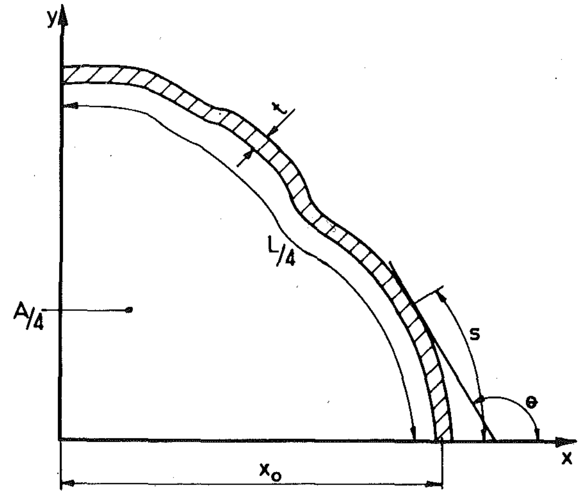

Fig. 1 A quadrant of a thin-walled cross section showing the natural coordinate system (s, θ)

In other words, if the prescribed design constraints on the thin-walled cylinder satisfy the inequality (13), the minimum-weight thin-walled cross section will be circular in shape with wall thickness

$$t = 4J_0\pi^2/L^3. \tag{14}$$

The inequality (13) also follows directly from the fact that for a circular cross section $J = 2I$.

Case 2. Let us consider next the case when $\max_y \min\{F_1^2(y), F_2(y)\}$ is realized on the second functional, i.e., $F_2(y) < F_1^2(y)$. In this case the optimization problem reduces to

$$F_2(y) \to \max_y, \tag{15}$$

subject to the isoperimetric condition (11). The solution of such a problem would result in an indefinite narrowing of the cross section in the x-direction. In other words, $A^2 \to 0$ which is the same as, $J \to 0$. Consequently, $F_1^2(y)$ can become lesser than any positive number, violating the design constraint (2) for all $J_0 \neq 0$. This is easily explained by considering, for example, a thin-walled rectangular cross section of depth, h, wall thickness t, and perimeter L. The area enclosed by such a contour $A = (L - 2h)h/2$. The bending stiffness of the thin-walled section is $I \simeq th^2(3L - 4h)/12$, hence it follows that the bending stiffness is maximized when $h \to L/2$, with the result that $A \to 0$. Hence the possibility that there exists an additional lower bound to I_0/J_0, similar to (13), is clearly excluded for $J_0 \neq 0$.

Case 3. Finally, let us consider the possibility that $\max_y \min\{F_1^2(y), F_2(y)\}$ is simultaneously realized on both functionals. In other words, the optimal design is such that $F_1^2(y) = F_2(y)$. In this case the optimization problem reduces to

$$F_1^2(y) \to \max_y \quad \text{or} \quad F_2(y) \to \max_y, \tag{16}$$

subject to the isoperimetric condition (11) and the requirement that $F_1^2(y) = F_2(y)$.

In the plane of the prescribed design parameters I_0 and J_0, it is clear that Case 3 is possible only if the inequality (13) is violated, i.e., when $I_0/J_0 > 1/2$.

Variational Problem and Optimality Condition

The variational problem corresponding to the optimization problem (16) is obtained by including the constraints through Lagrange multipliers, λ and μ in the functional (16), thereby obtaining the following auxiliary functional:

$$\begin{aligned}\Pi &= F_1^2 - \lambda(F_1^2 - F_2) + \mu(F_3 - L) \\ &= (1 - \lambda)F_1^2 + \lambda F_2 + \mu(F_3 - L).\end{aligned} \tag{17}$$

It should be mentioned that the auxiliary functional could also be formulated as

$$\Pi = (1 - \alpha)F_2 + \alpha F_1{}^2 + \mu(F_3 - L). \quad (18)$$

The latter problem would have the same solution, but the value of Lagrange multipliers would, naturally, be different.

The particular choice of the sign of λ and α is made in order to be in line with their standard range of validity (0, 1) for dual constraints.

Let us rewrite the nonadditive functional Π (17) as

$$\Pi = \psi(F_1{}^2, F_2, F_3), \quad (19)$$

where, from (7), (9), and (11), it follows that

$$F_k = \int_0^{x_0} f_k(x, y, y_x)dx, \quad k = 1, 2, 3.$$

The extremum of the variational problem (19) is sought among a class of continuous functions, $y(x)$, with continuous first derivative. A discontinuous first derivative would require the optimal contour to have sharp corners which are notoriously inefficient in torsion. To derive the necessary stationarity condition, we follow the procedure adopted in [9] and write an expression for the first variation of the functional Π, expand the function ψ in powers of δF_k and retain only terms of the first order of magnitude. By equating $\delta\Pi$ to zero and bearing in mind the arbitrariness of the function $y(x)$, we obtain the following Euler equation:

$$\sum_{k=1}^{3} \frac{\partial\psi}{\partial F_k}\,\delta F_k = 0 \quad (20)$$

where

$$\delta F_k = \frac{\partial f_k}{\partial y} - \frac{d}{dx}\frac{\partial f_k}{\partial y_x}.$$

In deriving the Euler equation (20) account was taken of the natural boundary (transversality) conditions on the function $y(x)$ which require that it be normal to the respective axes at $x = 0$ and $x = x_0$. This confirms the assumption made earlier concerning the doubly symmetric nature of the unknown function $y(x)$.

In the problem under consideration

$$\frac{\partial\psi}{\partial F_1} = 2(1 - \lambda)F_1 = \frac{16(1 - \lambda)}{\sqrt{J_0 L}} \int_0^{x_0} y\,dx,$$
$$\frac{\partial\psi}{\partial F_2} = \lambda, \quad (21)$$
$$\frac{\partial\psi}{\partial F_3} = \mu,$$

and

$$\delta F_1 = \frac{8}{\sqrt{J_0 L}},$$
$$\delta F_2 = \frac{8y}{I_0}\sqrt{1 + y_x{}^2} - \frac{4}{I_0}\left(\frac{y^2 y_x}{\sqrt{1 + y_x{}^2}}\right)_x, \quad (22)$$
$$\delta F_3 = -4\left(\frac{y_x}{\sqrt{1 + y_x{}^2}}\right)_x$$

where, as before, subscript x denotes differentiation with respect to x.

Substituting (21) and (22) into (20) and collecting similar terms, we get the following necessary optimality condition for the optimization problem under consideration:

$$32(1 - \lambda)\frac{I_0}{J_0 L}\int_0^{x_0} y dx + 2\lambda\frac{y}{\sqrt{1 + y_x{}^2}} - \frac{y_{xx}(\lambda y^2 + \nu)}{(1 + y_x{}^2)^{3/2}} = 0, \quad (23)$$

where $\nu = \mu I_0$ is a new Lagrange multiplier.

For a given value of $I_0/J_0 > 1/2$, the optimality condition (23) has to be solved together with the constraint $F_1{}^2 = F_2$ and the isoperimetric condition (11) to determine the unknowns λ, ν, x_0, and the function $y(x)$. Two additional conditions required to determine the four unknowns are the transversality conditions just mentioned.

It should be mentioned that the derivatives $\partial\psi/\partial F_k$ in the Euler equation are to be evaluated at the values of the integrals F_k that correspond to the extremum of the variational problem (19). In this sense the integral term in (23) is a constant at the extremum of $y(x)$.

Note also that the special Cases 1 and 2 delineated in the foregoing correspond to $\lambda = 0$ and 1, respectively. An analysis of the resulting simplified optimality condition would confirm the previously mentioned solutions of these special problems.

Solution Method

In solving the optimality condition (23), together with the constraint $F_1{}^2 = F_2$ and the isoperimetric condition (11) it was found convenient to use natural coordinates s, θ measured from the horizontal axis (Fig. 1) and to normalize the given contour length. Moreover, in view of the doubly symmetric nature of the cross-sectional shape it was only necessary to consider a quadrant, shown in Fig. 1. Note that in this quadrant θ varies from $\pi/2$ to π.

In the natural coordinates the optimality condition (23) and the constraint $F_1{}^2 = F_2$ take the following form:

$$\frac{d\theta}{ds} = \frac{2\lambda y\cos\theta - C}{\lambda y^2 + \nu}, \quad (24)$$

$$16\frac{I_0}{J_0}\left(\int_0^{1/4} y\cos\theta\,ds\right)^2 = \int_0^{1/4} y^2 ds, \quad (25)$$

where

$$C = -32(1 - \lambda)\frac{I_0}{J_0}\int_0^{1/4} y\cos\theta\,ds, \quad (26)$$

$$\frac{dy}{ds} = \sin\theta. \quad (27)$$

Due consideration has been given to the range of θ in the particular quadrant of interest in choosing the sign of the trignometric functions. Note that the result of normalizing the given contour length to unity is manifested in the upper limit of the integrals.

The numerical procedure used consisted in

1 Integrating (24) and (27), using a fourth-order Runge-Kutta scheme, from $s = 0$ to $s = 1/4$ with assumed values of C, λ, and ν subject to the transversality condition $\theta(0) = \pi/2$.

2 Updating the value of λ using the Newton-Raphson (shooting) method and repeating steps (1) and (2) until the transversality condition $\theta(1/4) = \pi$ was satisfied.

3 Calculating a new value of C from (26) and repeating Steps 1–3 until the difference in successive values of C was less than a specified value (2×10^{-6} was found suitable).

4 Updating the value of ν using the Newton-Raphson method and repeating Steps 1–4 until the constraint (25) was satisfied.

In Steps 1 and 4 the necessary derivatives were found numerically requiring two evaluations of the preceding steps.

The results obtained by this procedure are presented and discussed in the next section.

Results and Discussion

The optimal cross-sectional shapes for various values of $I_0/J_0 > 1/2$ are shown in Fig. 2. For $I_0/J_0 \leq 1/2$ the optimal (circular) shape is shown for comparison. It is clear that as I_0/J_0 increases the cross-section narrows in the x-direction. In the limit as $I_0/J_0 \to \infty$, we get the limiting Case 2 mentioned in the foregoing.

The values of the various constants as a function of I_0/J_0 are graphed in Fig. 3, while Fig. 4 shows the thickness ratio t/I_0 of the optimal cylinder for various values of I_0/J_0.

In order to judge the economy made possible by optimization let us compare the optimally designed thin-walled cylinder first with the commonly used circular cylinder and then with an elliptical cylinder.

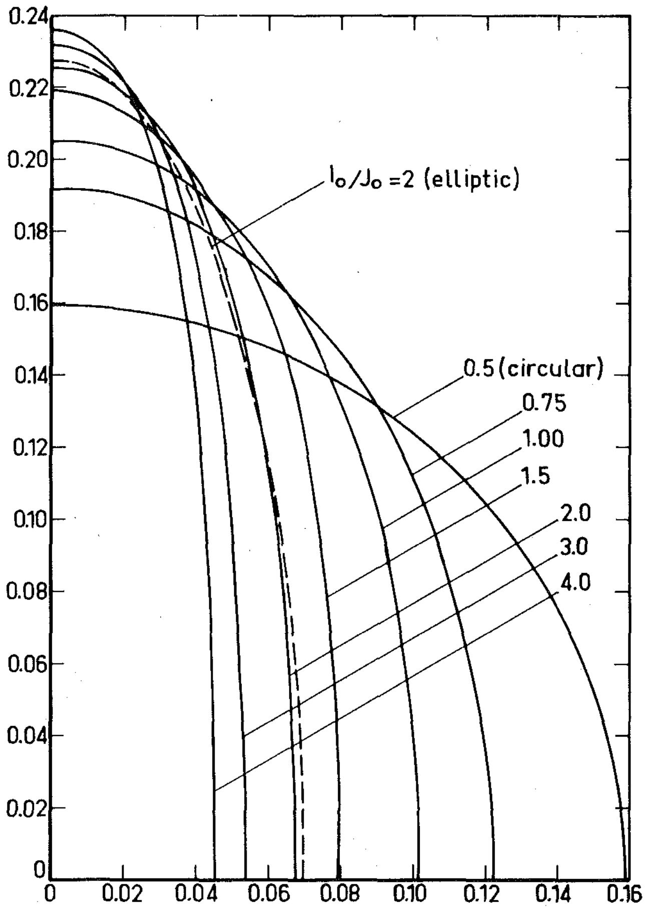

Fig. 2 Cross-sectional shapes for various stiffness ratios I_0/J_0; broken curve represents an elliptic cross section with $I_0/J_0 = 2$

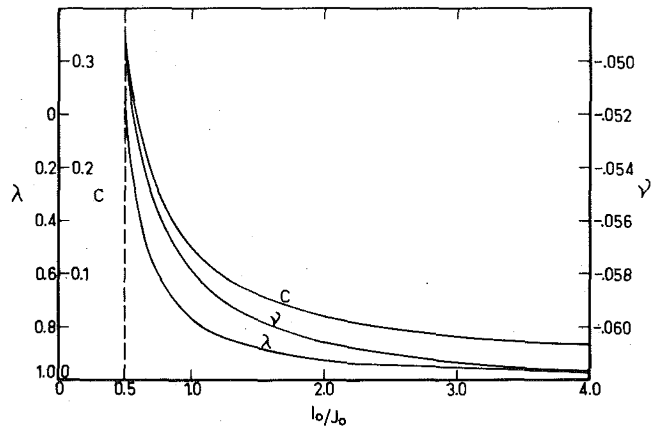

Fig. 3 Variation of constants λ, ν, and C with I_0/J_0; λ = 0 and 1 correspond to special Cases 1 and 3, respectively

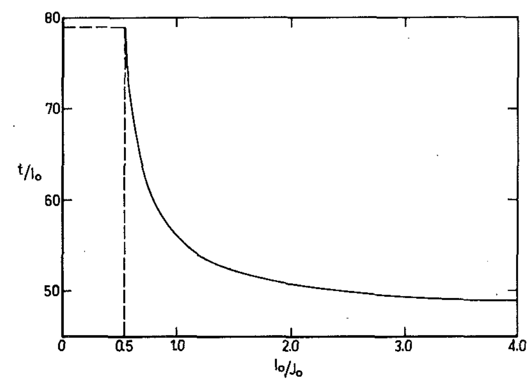

Fig. 4 Variation of thickness ratio t/I_0 with I_0/J_0; the limiting value t/I_0 = 78.957 corresponds to a circular cross section

For a circular cylinder the I/J-value is fixed and equal to one half. Consequently, the value of t/I_0 is also fixed and is equal to 78.957 for unit circumference. Thus, in this case, the design is governed by the prescribed minimum bending stiffness I_0, the torsional stiffness of such a cross section being always greater than the prescribed minimum value J_0. The values of t/I_0 of the optimal thin-walled cylinder are compared in Table 1 with those of a thin-walled circular cylinder having the same value of the bending stiffness I_0. It is clear that a substantial material saving is achieved by optimization, especially for large values of I_0/J_0.

On the other hand, a comparison of the thickness ratios t/I_0 (Table 2) of the optimal thin-walled cylinder and an elliptical cylinder having the same value of I_0/J_0 (expressions for I and J of an elliptic cross section of given length are given in the Appendix) shows that the difference is practically insignificant, although the values of t/I_0 for the optimal cylinder are consistently smaller. Also, the optimal cross-sectional shape is very close to an ellipse except near $x = 0$ and $y = 0$. This is illustrated in Fig. 2 for the case of $I_0/J_0 = 2$. However, it should be emphasized that the optimality condition (23) is not satisfied by an elliptic cross section.

Acknowledgments

The authors are grateful to Dr. N. V. Banichuk for suggesting an alternate formulation of the problem and for his useful comments.

References

1 Keller, J. B., "The Shape of the Strongest Column," *Archive for Rational Mechanics and Analysis*, Vol. 5, 1960, pp. 275–285.

2 Tadjbakhsh, I., and Keller, J. B., "Strongest Columns and Isoperimetric Inequalities for Eigenvalues," ASME JOURNAL OF APPLIED MECHANICS, Vol. 29, 1962, pp. 159–164.

Table 1 Percentage material saving in comparison with a circular cylinder having the same bending stiffness as the optimal cylinder

I_0/J_0	t/I_0	Percent saving
0.5	78.957 (circular cylinder)	0.0
0.75	60.949	22.8
1.00	55.826	29.3
1.50	52.165	33.9
2.00	50.755	35.7
2.50	50.027	36.6
3.00	49.588	37.2
4.00	49.091	37.8

Table 2 Comparison of thickness ratios t/I_0 of the optimal and elliptic cross sections having the same value of I_0/J_0

I_0/J_0	t/I_0 Optimal	t/I_0 Elliptic
0.75	60.949	60.956
1.00	55.826	55.849
1.50	52.165	52.214
2.00	50.755	50.820
2.50	50.027	50.099
3.00	49.588	49.664
4.00	49.091	49.166

3 Niordson, F. I., "On the Optimal Design of a Vibrating Beam," *Quarterly of Applied Mathematics*, Vol. 23, 1965, pp. 47–53.

4 Prager, W., and Taylor, J. E., "Problems of Optimal Structural Design," ASME JOURNAL OF APPLIED MECHANICS, Vol. 35, 1968, pp. 102–106.

5 Banichuk, N. V., and Karihaloo, B. L., "Minimum-Weight Design of Multipurpose Cylindrical Bars," *International Journal of Solids and Structures*, Vol. 12, 1976, pp. 267–273.

6 Parbery, R. D., and Karihaloo, B. L., "Minimum-Weight Design of Hollow Cylinders for Given Lower Bounds on Torsional and Flexural Rigidities," *International Journal of Solids and Structures*, Vol. 13, 1977, pp. 1271–1280.

7 Timoshenko, S., and Goodier, J. N., *Theory of Elasticity*, McGraw-Hill, New York, 1951, p. 299.

8 Polya, G., and Szêgö, G., *Isoperimetric Inequalities in Mathematical Physics*, Princeton University Press, New Jersey, 1951.

9 Banichuk, N. V., and Karihaloo, B. L., "On the Solution of Optimization Problems With Singularities," *International Journal of Solids and Structures*, Vol. 13, 1977, pp. 725–733.

APPENDIX

For a thin-walled elliptic cross section $x = a \cos \phi, y = b \sin \phi (b > a)$. The length of the contour $L = 4bE(k)$ and the area enclosed by the contour center line $A = \pi ab$, hence the torsional stiffness

$$J = \pi^2 a^2 bt/E(k).$$

The bending stiffness I is given by

$$I = 4tb^3 \left\{ \frac{2k^2 - 1}{3k^2} E(k) + \frac{k'^2}{3k^2} K(k) \right\},$$

where

$$k^2 = 1 - (a/b)^2,$$

$$k'^2 = 1 - k^2,$$

and K and E are complete elliptic integrals of the first and second kind, respectively.

Isaac Elishakoff[1]

Associate Professor,
Department of Aerospace Engineering,
Delft University of Technology,
Delft, The Netherlands

Remarks on the Static and Dynamic Imperfection-Sensitivity of Nonsymmetric Structures

The simple static and dynamic buckling model (the three-hinge rigid-rod system, constrained laterally by a nonlinear spring) originally proposed by Budiansky and Hutchinson, is modified so that the force of the spring includes both quadratic and cubic terms. Expressions are given for the buckling load of the imperfect structure as function of the imperfection. These formulas generalize the classical expressions for the static buckling load (due to Koiter), and for the dynamic buckling load (due to Budiansky and Hutchinson) for symmetric or asymmetric structures, to nonsymmetric ones.

Introduction

The general theory of buckling and postbuckling behavior of elastic structures was worked out by Koiter [1, 2]. Further contributions were provided by Budiansky and Hutchinson [3] and other investigators (for an extensive bibliography see, for example, the article by Budiansky [4]). Emphasis in analysis of static imperfection-sensitive structures was shifted to determination of the maximum load λ_s attainable on the prebuckling portion of the load-generalized-displacement curve of an imperfect structure, and to the relationship between λ_s and the initial imperfection. The initial postbuckling analysis employs the following asymptotic expansion of the load parameter λ in terms of the buckling deflection ξ, for small values of the latter

$$\lambda/\lambda_c = 1 + a\xi + b\xi^2 + \dots \tag{1}$$

where coefficients $a, b, \dots$ determine the initial postbuckling behavior and λ_c is the classical buckling load. Distinction is made between symmetric and asymmetric cases, according to "a" does or does not vanish. The symmetric structure is imperfection sensitive (in the sense that an imperfection results in reduced values of the maximum load the structure can support) if $b < 0$ whereas the asymmetric structure is imperfection-sensitive if $a\bar{\xi} < 0$ and reduction of the buckling load with respect to the classical one occurs for one sign or other of $\bar{\xi}$, where $\bar{\xi}$ is the (small) initial imperfection amplitude. For the structures represented by these cases, Koiter's general theory yields the following asymptotic results, respectively:

$$(1 - \lambda_s/\lambda_c)^{3/2} - (3\sqrt{3}/2)|\bar{\xi}|\sqrt{-b}\,\lambda_s/\lambda_c = 0 \tag{2}$$

$$(1 - \lambda_s/\lambda_c)^2 + 4a\bar{\xi}\lambda_s/\lambda_c = 0 \tag{3}$$

These formulas were derived in reference [3] also directly, for the simple model of a three-hinge, rigid-rod column, constrained by a nonlinear spring. A column with a cubic spring represented the symmetric structure with λ_s/λ_c satisfying equation (2) and a column with a quadratic spring—the asymmetric one with λ_s/λ_c satisfying equation (3).

The dynamic counterparts of equations (2) and (3) were derived by Budiansky and Hutchinson [3] for step loading:

$$(1 - \lambda_d/\lambda_c)^{3/2} - (3\sqrt{6}/2)|\bar{\xi}|\sqrt{-b}\,\lambda_d/\lambda_c = 0 \tag{4}$$

$$(1 - \lambda_d/\lambda_c)^2 + (16/3)a\bar{\xi}\lambda_d/\lambda_c = 0 \tag{5}$$

These results were further generalized in reference [5] for buckling under loading characterized by a finite length of time of load application (rectangular and triangular loadings) for both quadratic and cubic structures. In reference [6], Budiansky considered also a quadratic-cubic structure under dynamic loading—in particular the case where a quadratic structure with $a < 0$ and $\bar{\xi} > 0$ is converted into a quadratic-cubic model by incorporation of a cubic term $b\bar{\xi}^3$ with $b > 0$. Numerical analysis showed that with the term $b\bar{\xi}^3$ included, the original results (with $b = 0$) are somewhat on the conservative side, i.e., the term turns out to have a stabilizing effect. In reference [7], Hoff demonstrated the static imperfection-sensitivity of a quadratic-cubic system characterized by $a < 0$ and $b > 0$. Hansen and Roorda [8] considered static and dynamic buckling of an imperfect beam on a quadratic-cubic elastic foundation, assuming that the initial imperfection function is coconfigurational with the buckling mode of the associated linear structure—and solved the problem within the single-mode Galerkin approximation. They obtained relationships between the critical load (both the static and dynamic cases) and the initial imperfection amplitude, valid for rather high-order imperfections but irreducible to those obtained by Budiansky

[1] On sabbatical leave from the Department of Aeronautical Engineering, Technion-Israel Institute of Technology, Haifa, Israel.

Contributed by the Applied Mechanics Division for publication in the JOURNAL OF APPLIED MECHANICS.

Discussion on this paper should be addressed to the Editorial Department, ASME, United Engineering Center, 345 East 47th Street, New York, N. Y. 10017, and will be accepted until June 1, 1980. Readers who need more time to prepare a discussion should request an extension from the Editorial Department. Manuscript received by ASME Applied Mechanics Division, February, 1979; final revision, July, 1979.

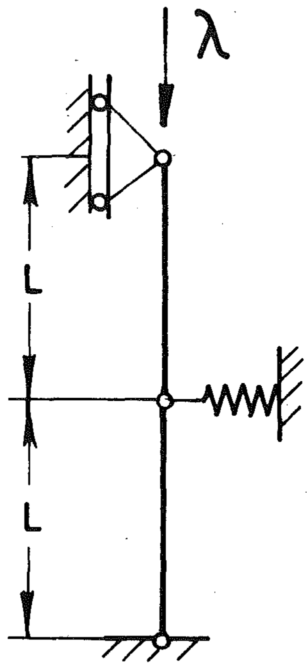

Fig. 1 Idealized column

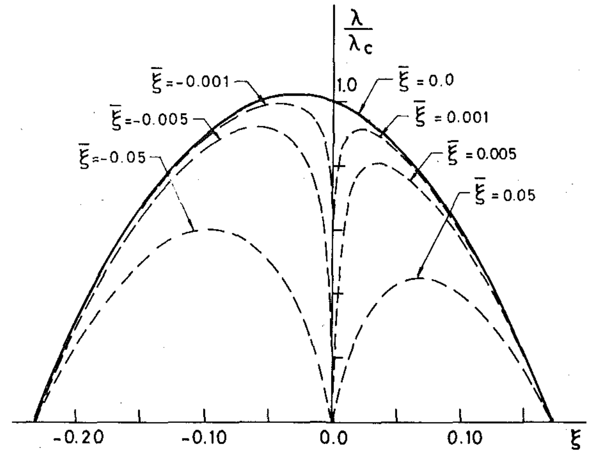

Fig. 2 Nondimensional load-additional displacement curves for nonsymmetric structure ($a = -1.5$, $b = 25$)

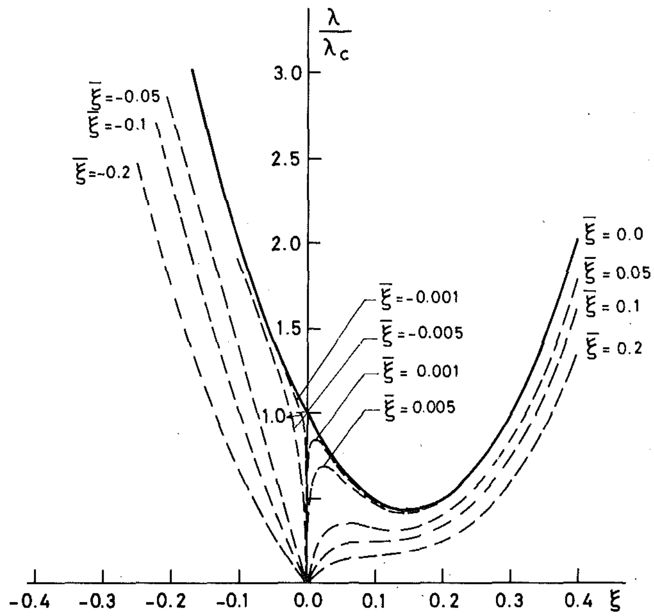

Fig. 3 Nondimensional load-additional displacement curves for nonsymmetric structure ($a = -7.5$, $b = 25$)

and Hutchinson [3], owing to inclusion of nonlinearities in the deformation analysis.

Recently, Tatsa, Tene, and Baruch [9] considered the practicability aspect of formulas (2) and (3). Their main argument was that in complex structures where the initial postbuckling coefficient "a" (and naturally "b") does not lend itself to analytical determination, it would be difficult to establish numerically whether "a" really vanishes—thereby precluding a reliable conclusion as to the behavior of the structure. In these circumstances, possible imperfection-insensitivity may be overlooked in a symmetric structure, which would be designated as symmetric because of a very small value found for "a." The foregoing authors showed that for such structures both initial postbuckling coefficients should be simultaneously taken into consideration. They considered the Budiansky-Hutchinson model with the quadratic-cubic spring; a numerical solution was found by determining λ_s/λ_c, and it was shown that (a) for large values of "a," the "b" values may be neglected, and (b) for $a < 0.01$ and $b < 0$ "a" can be taken as zero.

The present work was motivated by awareness that there are structures nonsymmetric in principle and necessitate a generalization of equations (2)–(5). Although the motivation here differs totally from that of reference [9], the same model, including the quadratic-cubic spring, is considered. Both static and dynamic cases are examined (represented by generalizations of equations (2) and (4), respectively), and conditions for sensitivity to initial imperfections are formulated.

Static Buckling of Nonsymmetric Structures

The simple model (suggested first by Budiansky and Hutchinson [3]) of an idealized column constrained by a nonlinear spring is shown in Fig. 1. The restoring force F is supposed to be related to its shortening (or elongation) x by

$$F = k_1\xi + k_2\xi^2 + k_3\xi^3 \tag{6}$$

where $\xi = x/L$; no restriction is imposed for the moment with regard to the sign of k_2 and k_3 ($k_1 > 0$). Equilibrium of the single member at buckling dictates

$$\lambda = \tfrac{1}{2}F\sqrt{1-\xi^2} = \tfrac{1}{2}(k_1\xi + k_2\xi^2 + k_3\xi^3)\sqrt{1-\xi^2} \tag{7}$$

and for small values of ξ, the following asymptotic result is obtained:

$$\lambda = \lambda_c(\xi + a\xi^2 + b\xi^3 + \ldots), \quad \lambda_c = k_1/2 \tag{8}$$

and "a" and "b" are defined by

$$a = k_2/k_1, \quad b = k_3/k_1 - 0.5 \tag{9}$$

Equation (8) represents the axial load-additional displacement relationship. The diagram $\lambda - \xi$ consists of two branches: the straight line $\xi = 0$ and a parabola which cuts the λ-axis at the value of the classical buckling load λ_c:

$$\lambda/\lambda_c = 1 + a\xi + b\xi^2 \equiv 1 - a^2/4b + b(\xi + a/2b)^2 \tag{10}$$

and its vortex at $(-a/2b; 1 - a^2/4b)$. Consequently

$$(\lambda/\lambda_c)_{\min} = 1 - a^2/4b, \quad \text{for} \quad b > 0;$$
$$(\lambda/\lambda_c)_{\max} = 1 - a^2/4b \quad \text{for} \quad b < 0 \tag{11}$$

In the general case $a \neq 0$, $b \neq 0$ the structure is designated as nonsymmetric; it is said to be symmetric if $a = 0$, $b \neq 0$ and asymmetric

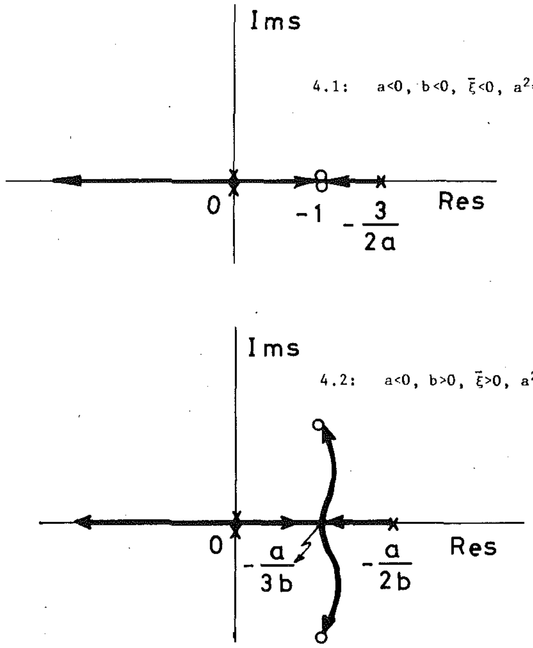

Fig. 4 Root-locus plots

if $a \neq 0$, $b = 0$. In the latter case the parabola (10) degenerates into the straight line $\lambda/\lambda_c = a\xi + 1$. Typical $\lambda - \xi$ curves for nonsymmetric structures are shown in Figs. 2 and 3. Note that the $\lambda - \xi$ curve for $a = -a_1$ and specified "b" represents the mirror image of its counterpart for $a = a_1$ and "b" as before.

We now proceed to the realistic, imperfect, structure. Given that unloaded structures have an initial displacement $\bar{x} = L\bar{\xi}$, then equilibrium dictates instead of equation (7) the following formula:

$$\lambda(\xi + \bar{\xi}) = \tfrac{1}{2}F\sqrt{1 - (\xi + \bar{\xi})^2}$$
$$= \tfrac{1}{2}(k_1\xi + k_2\xi^2 + k_3\xi^3)\sqrt{1 - (\xi + \bar{\xi})^2} \qquad (12)$$

and for small values of ξ, the following asymptotic result is obtained:

$$\lambda(\xi + \bar{\xi}) = \lambda_c(\xi + a\xi^2 + b\xi^3 + \ldots) \qquad (13)$$

Equation (13) indicates that ξ and $\bar{\xi}$ have the same sign (i.e., the additional displacement of the system is such that the total displacement $\xi + \bar{\xi}$ is increased by its absolute value). Otherwise the assumption $\xi\bar{\xi} < 0$ would imply $\lambda < 0$ for $0 < |\xi| < \bar{\xi}$ i.e. the presence of tension which is contrary to our formulation of the problem. Note also that the graph λ/λ_c versus ξ for an imperfect structure issues from the origin of the coordinates. Additional zeros of λ/λ_c coincide with the zero points $(-a \pm \sqrt{a^2 - 4b})/b$ of the parabola (10), representing the behavior of a perfect structure.

We now seek the buckling load λ_s, which is defined as the maximum of λ *on the branch of the solution* $\lambda - \xi$ *originating at zero load,* for specified $\bar{\xi}$.

To be able to conclude whether the structure is sensitive to initial imperfections or not, we have to find whether the first derivative of λ with respect to ξ

$$d\lambda/d\xi = \phi(\xi, \bar{\xi})/(\xi + \bar{\xi})^2;$$
$$\phi(\xi, \bar{\xi}) = \bar{\xi} + 2a\xi\bar{\xi} + (a + 3b\bar{\xi})\xi^2 + 2b\xi^3 \qquad (14)$$

has at least one real root. For our purpose, it suffices to examine the numerator $\phi(\xi, \bar{\xi})$. The structure is imperfection-sensitive if the equation $\phi(\xi, \bar{\xi}) = 0$ has at least one real positive root for $\bar{\xi} > 0$, or at least one real negative root for $\bar{\xi} < 0$.

Using Descartes's rule of sign, it is readily shown that the structure is imperfection-sensitive for $b < 0$ (irrespective of the sign of a and $\bar{\xi}$) and insensitive for $b > 0$ and $a\bar{\xi} > 0$. The case $b > 0$ and $a\bar{\xi} < 0$ can be treated by Evans's root-locus method [10], frequently used in control theory.

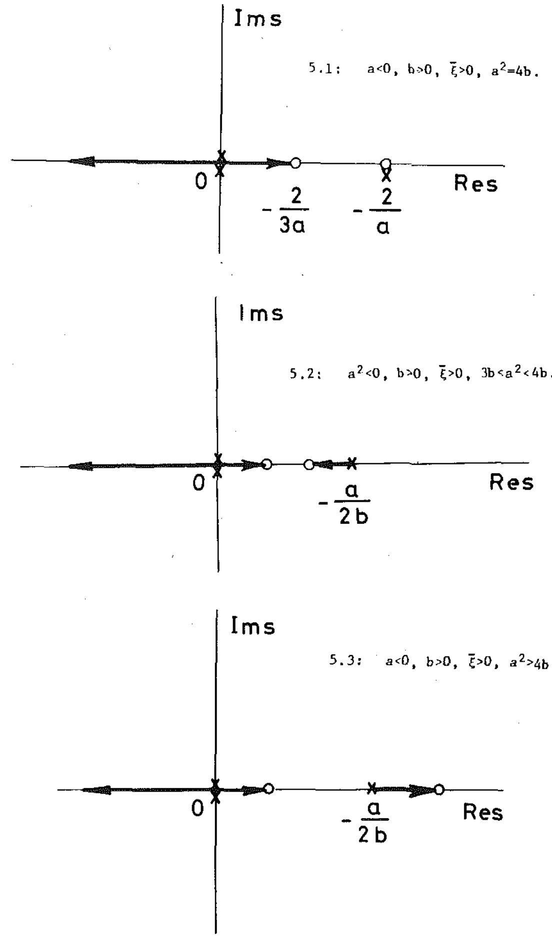

Fig. 5 Root-locus plots

Let us consider first the particular case $b > 0$, $a < 0$, and $\bar{\xi} > 0$. The formal substitution $\bar{\xi} \to s$, where $s = \mathrm{Re}\, s + i\, \mathrm{Im}\, s$ is a complex variable, in equation (12) yields

$$1 + \bar{\xi}\psi(s) = 0, \quad \psi(s) \equiv (3bs^2 + 2as^2 + 1)(a + 2bs)^{-1}s^{-2} \quad (15)$$

We now construct the root-locus plot with $\bar{\xi}$ varying from zero to infinity (obviously, for us only $\bar{\xi} \ll 1$ has physical significance). For $\bar{\xi}$ approaching zero the roots of equation (15) are the poles of $\psi(s)$ marked by "crosses" (X's):

$$s_1 = s_2 = 0, \quad s_3 = -a/2b \qquad (16)$$

The $\bar{\xi} \to \infty$ points of the root loci approach the zeros of $\psi(s)$, marked by "circles" (O's):

$$s_{1,2} = (1/3b)(-a \pm \sqrt{a^2 - 3b}) \qquad (17)$$

$\psi(s)$ *has three poles: one double, at zero, and another at* $(-a/2b) > 0$. A root locus issues from each pole as $\bar{\xi}$ increases above zero; a root locus arrives at each zero of $\psi(s)$ or at infinity, as $\bar{\xi}$ approaches infinity. For the case $a = 3b$ both "circles" coincide. As is seen from Fig. 4.1, equation (15) has two real positive roots, and therefore the structure is imperfection sensitive for any $\bar{\xi} > 0$. For $a^2 < 3b$ both "circles" are complex (Fig. 4.2); for certain values of $\bar{\xi}$ (which is called critical one, $\bar{\xi}_{\mathrm{cr},s}$) a pair of loci break away from the real axis. For $\bar{\xi} > \bar{\xi}_{\mathrm{cr},s}$ equation (15) has no real positive root and, consequently, the structure is imperfection-insensitive. The breakaway point is found as the root of equation

$$dC/ds = 0, \quad C(s) \equiv s^2(a + 2bs)(1 + 2as + 3bs^2)^{-1} \tag{18}$$

The equation has only one real root $s_0 = -a/3b$. Appropriate value of $\bar{\xi}$ equals $-C(s_0)$:

$$\bar{\xi}_{cr,s} = -(a^3/9b)(3b - a^2)^{-1} \tag{19}$$

Static buckling load associated with $\xi = s_0$ and $\bar{\xi} = \bar{\xi}_{cr,s}$ is

$$\lambda_s/\lambda_c = (a/3b)(2a^2/9b - 1)(\bar{\xi}_{cr,s} - a/3b)^{-1} \tag{20}$$

For example, for $b/a^2 = 2/3$, we have $\bar{\xi}_{cr,s} = -(1/6a)$, and $\lambda_s/\lambda_c = 1/2$, and $\bar{\xi} > \bar{\xi}_{cr,s}$ static snap-buckling does not occur; this is in agreement with the result obtained by Budiansky for this particular b/a^2 ratio (reference [6, p. 95]).

For the case $a^2 > 3b$ (see Fig. 5) there always exist two real positive roots to equation $\psi(\xi,\bar{\xi}) = 0$ and the structure is imperfection-sensitive.

Consequently, the structure turns out to be imperfection-sensitive for $a^2 \geqq 3b$; in range $a^2 < 3b$ the structure is imperfection sensitive if $\bar{\xi} \leqq \bar{\xi}_{cr,s}$. We next consider the case $a > 0$, $b < 0$, $\bar{\xi} < 0$. It is readily shown that the inverse root loci for $-\infty < \bar{\xi} \leqq 0$ are the mirror image of the original loci for $0 \leqq \bar{\xi} < \infty$ with respect to the imaginary axis. The system is imperfection-sensitive if $a^2 \geqq 3b$; and also for $a^2 < 3b$ if $\bar{\xi} \geqq \bar{\xi}_{cr,s}$ as per equation (19). For the particular case $a = 0$ the structure is imperfection-sensitive if $b < 0$ (for both $\bar{\xi} > 0$ and $\bar{\xi} < 0$) and insensitive if $b > 0$. For $b = 0$, the structure is imperfection-sensitive if $a\bar{\xi} < 0$ and insensitive in the opposite case.

As for the imperfection-sensitive structure, differentiating equation (13) with respect to ξ and setting

$$d\lambda/d\xi = 0, \quad \lambda = \lambda_s \tag{21}$$

we obtain, after extensive algebraic transformations, the relation between the buckling load λ_s and initial imperfection amplitude $\bar{\xi}$, the relationship

$$\left(1 - \frac{\lambda_s}{\lambda_c} - \frac{a^2}{3b}\right)^3 = -\frac{27}{4}b\left[\frac{a}{3b}\left(1 - \frac{\lambda_s}{\lambda_c}\right) - \frac{2}{27}\frac{a^3}{b^2} + \frac{\lambda_s}{\lambda_c}\bar{\xi}\right]^2 \tag{22}$$

which reduces to the classical equation (2) for $a = 0$ and $b < 0$. Note that the displacement ξ, corresponding to λ_s/λ_c is given by

$$\xi_{1,2} = [-a \pm \sqrt{a^2 - 3b(1 - \lambda_s/\lambda_c)}]/3b \tag{23}$$

where $\xi_{1,2}$ depend on $\bar{\xi}$ via λ_s/λ_c. From equation (22) the static buckling load is obtainable, given the initial imperfection $\bar{\xi}$. The meaningful root λ_s/λ_c of equation (22) is the greatest of those which meet the requirement $\xi\bar{\xi} > 0$. It should be noted that for $\bar{\xi} \to \infty$ we formally have $\lambda_s/\lambda_c \to 0$, and equation (23) reduces to equation (17).

Dynamic Buckling of Nonsymmetric Structures

In the dynamic setting, the central hinge carries a mass M, and the system is subjected to an axial force $\lambda f(t)$. Instead of equation (13) we have

$$\ddot{\xi}/\omega_1^2 + [1 - \lambda f(t)/\lambda_c]\xi + a\xi^2 + b\xi^3 = [\lambda f(t)/\lambda_c]\bar{\xi} \tag{24}$$

where $\omega_1^2 = M/k_1$. As an example, we have the load represented by the Heaviside step function, which vanishes for $t \leq 0$ and equals unity for $t > 0$. The first integral of equation (28) subject to the initial conditions $\xi = 0$, $\dot{\xi} = 0$ at $t = 0$, is readily found to be

$$\dot{\xi}/\omega_1^2 + (1 - \lambda/\lambda_c)\xi^2 + \frac{2}{3}a\xi^3 + \frac{1}{2}b\xi^4 = 2(\lambda/\lambda_c)\bar{\xi}\xi \tag{25}$$

and the corresponding integral curves satisfy

$$\pm \int_0^\xi \left[2(\lambda/\lambda_c)\bar{\xi}\xi - (1 - \lambda/\lambda_c)\xi^2 - \frac{2}{3}a\xi^3 - \frac{1}{2}b\xi^4\right]^{-1/2} d\xi = \omega_1 t \tag{26}$$

where the left-hand side can be evaluated in terms of elliptic integrals [11].

For sufficiently small λ/λ_c the motion is periodic, with its amplitude satisfying

$$(1 - \lambda/\lambda_c)\xi_{\max} + \frac{2}{3}a\xi^2_{\max} + \frac{1}{2}b\xi^3_{\max} = 2(\lambda/\lambda_c)\bar{\xi} \tag{27}$$

This equation is identical with equation (44) in Budiansky's paper [6]. Further, following Budiansky and Hutchinson [3], the dynamic buckling load λ_d is defined by the criterion

$$d\lambda/d\xi_{\max} = 0, \quad \lambda = \lambda_d \tag{28}$$

Note that equation (27) identifies with equation (13) on the following formal substitution:

$$\xi \to \xi_{\max}, \quad \bar{\xi} \to 2\bar{\xi}, \quad a \to \frac{2}{3}a, \quad b \to \frac{1}{2}b \tag{29}$$

Analogically, all conclusions in the static case are readily extended to the dynamic one; namely, the structure under step loading is imperfection sensitive for $b < 0$ (irrespective of the sign of "a" or $\bar{\xi}$), and insensitive for $b > 0$ and $a\bar{\xi} > 0$; for $b > 0$ and $a\bar{\xi} < 0$, it is sensitive for any $\bar{\xi}$, given the following inequality:

$$a^2 \geqq (27/8)b \tag{30}$$

(obtainable from its static counterpart $a^2 \geqq 3b$ by formal substitution (29)), and also when

$$a^2 < (27/8)b \tag{31}$$

for $\bar{\xi} \leqq \bar{\xi}_{cr,d}$ where

$$\bar{\xi}_{cr,d} = -(4/27)(a^3/b)[(27/8)b - a^2]^{-1} \tag{32}$$

The $\xi_{\max}$ value associated with $\xi_{cr,d}$ equals $4a/9b$ and, consequently, the dynamic buckling load is

$$\frac{\lambda_d}{\lambda_c} = \frac{4}{9}\frac{a}{b}\left(\frac{16}{81}\frac{a^2}{b} - 1\right)\left(2\bar{\xi} - \frac{4}{9}\frac{a}{b}\right)^{-1} \tag{33}$$

At $\bar{\xi} = \bar{\xi}_{cr,d}$ the concept of dynamic buckling is preserved by associating λ_d with the point of inflection in the variation of λ with $\xi_{\max}$. Comparison of the latter results with their static counterparts shows that the interval $3b < a^2 < (27/8)b$ is characterized by duality: the structure is statically imperfection-sensitive but dynamically imperfection-insensitive. In the particular case $b/a^2 = 2/3$, considered by Budiansky (reference [6, pp. 95–96]), $\bar{\xi}_{cr,d} = -8/45a$ and $\bar{\xi}_{cr,d} > \bar{\xi}_{cr,s}$ and consequently, the interval $\bar{\xi}_{cr,s} < \bar{\xi} < \bar{\xi}_{cr,d}$ is similarly characterized by duality—the reverse of the preceding case. For $b/a^2 = 1/3$ also considered in reference [6], the structure is statically imperfection sensitive for any $\bar{\xi}$, but dynamically imperfection insensitive, $\bar{\xi}_{cr,d}$ being $(-32/9a)$.

Finally the relation between the buckling load λ_d and the initial imperfection $\bar{\xi}$ is given by

$$\left(1 - \frac{\lambda_d}{\lambda_c} - \frac{8}{27}\frac{a^2}{b}\right)^3 = -\frac{27}{8}b\left[\frac{4}{9}\frac{a}{b}\left(1 - \frac{\lambda_d}{\lambda_c}\right) - \frac{64}{729}\frac{a^3}{b^2} + 2\bar{\xi}\frac{\lambda_d}{\lambda_c}\right]^2 \tag{34}$$

In the case $a < 0$, $b < 0$ with $\bar{\xi}$ such that $\lambda_s/\lambda_c \leqq 1$ and $\lambda_d/\lambda_c \leqq 1$, $\bar{\xi}$ is readily eliminated by correlating equations (22) and (34) for a given structure with a given imperfection. The result relates λ_d to λ_s:

$$\left[-\frac{8}{27b}\left(1 - \frac{\lambda_d}{\lambda_c} - \frac{8}{27}\frac{a^2}{b}\right)^3\right]^{1/2} - \frac{4}{9}\frac{a}{b}\left(1 - \frac{\lambda_d}{\lambda_c}\right) + \frac{64}{729}\frac{a^3}{b^2} = 2\frac{\lambda_d}{\lambda_s}\left\{\left[-\frac{4}{27b}\left(1 - \frac{\lambda_s}{\lambda_c} - \frac{a^2}{3b}\right)^3\right]^{1/2} - \frac{a}{3b}\left(1 - \frac{\lambda_s}{\lambda_c}\right) + \frac{2}{27}\frac{a^3}{b^2}\right\} \tag{35}$$

In this form, λ_d/λ_s is no longer directly dependent on the imperfection, but via λ_s/λ_c. For vanishing "a," the expression readily reduces to that obtained by Budiansky and Hutchinson [3]

$$\lambda_d/\lambda_s = (\sqrt{2}/2)(\lambda_c - \lambda_d)^{3/2}(\lambda_c - \lambda_s)^{-3/2} \tag{36}$$

In the general case, both formulas (22) and (29) have to be applied separately to obtain the λ_d/λ_c versus λ_s/λ_c relationship. Equations (22) and (34) are the respective analogs of equations (20) and (24), in Hansen's and Roorda's study of an imperfect beam [8], obtained by a single-term Galerkin approximation. As already noted, Hansen's and Roorda's formulas do not reduce to equation (36), because of inclusion of nonlinearities in the beam deformation.

Comparison of equations (22) and (34) shows also that as the imperfection tends to zero, $\lambda_s \to \lambda_c$ and $\lambda_d \to \lambda_c$. For very small imperfections, the λ_d/λ_c ratio can be taken as unity and equation (39) reduces to

$$\left[-\frac{8}{27b}\left(1-\frac{\lambda_d}{\lambda_c}-\frac{8}{27}\frac{a^2}{b}\right)^3\right]^{1/2}-\frac{4}{9}\frac{a}{b}\left(1-\frac{\lambda_d}{\lambda_c}\right)+\frac{64}{729}\frac{a^3}{b^2}$$
$$=2\left\{\left[-\frac{4}{27b}\left(1-\frac{\lambda_s}{\lambda_c}-\frac{a^2}{3b}\right)^2\right]^{1/2}-\frac{a}{3b}\left(1-\frac{\lambda_s}{\lambda_c}\right)+\frac{2}{27}\frac{a^3}{b^2}\right\} \quad (37)$$

For vanishing "a," Thompson's [12] expression is obtained

$$(\lambda_c-\lambda_d)^{3/2}=\sqrt{2}(\lambda_c-\lambda_s)^{3/2} \quad (38)$$

Conclusions

The main conclusions of this paper are as follows:

1 Formulas (3) and (5) have to be used for $b = 0$ and $a\,\bar{\xi} < 0$, formulas (2) and (4) for $a = 0$ and $b < 0$.

2 The general nonsymmetric structure under static loading is imperfection-sensitive for $b < 0$, irrespective of the sign of "a" or $\bar{\xi}$; for $b > 0$ and $a\,\bar{\xi} < 0$ it is imperfection-sensitive when $a^2 \geqq 3b$ for any $\bar{\xi}$, and when $a^2 < 3b$ in the interval $\bar{\xi} \leqq \bar{\xi}_{\mathrm{cr},s}$ with the critical imperfection as per (19); it is imperfection-insensitive for $b > 0$ and $a\,\bar{\xi} > 0$.

3 For the nonsymmetric imperfection-sensitive structure formula (22) has to be applied to find λ_s/λ_c as function of the initial imperfection $\bar{\xi}$.

4 The general nonsymmetric structure under step loading is imperfection-sensitive for $b < 0$ irrespective of the sign of "a" or $\bar{\xi}$. For $b > 0$ and $a\,\bar{\xi} < 0$ the structure is imperfection-sensitive when $a^2 \geqq (27/8)b$ for any $\bar{\xi}$, and also when $a^2 < (27/8)b$ in the interval, $\bar{\xi} \leqq \bar{\xi}_{\mathrm{cr},d}$ with the initial imperfection as per (32); it is imperfection-insensitive for $b > 0$ and $a\,\bar{\xi} > 0$. These results similar in nature to the static ones, are readily obtained by formal substitution.

5 For the imperfection-sensitive nonsymmetric structure formula (34) has to be applied to find λ_d/λ_c as function of initial imperfection $\bar{\xi}$.

6 Formula (22) generalizes Koiter's result, given by equation (2) for the symmetric structure, and formula (34) generalized Budiansky's and Hutchinson's result given by equation (4) for the symmetric structure.

Acknowledgments

I wish to thank Professor W. T. Koiter of Delft University of Technology, who encouraged me to study buckling of stochastically imperfect columns on quadratic-cubic foundation, of which this paper forms a part. I am also indebted to Professor M. Baruch of the Technion-I.I.T. for reading the manuscript. The study was supported in part by the Technion Research and Development Foundation.

References

1 Koiter, W. T., "On the Stability of Elastic Equilibrium," (in Dutch), Thesis, Delft University, H. J. Paris, Amsterdam; English translation; (*a*) NASA TT-F-10, 833, 1967; (*b*) AFFDL-TR-70-25, 1970

2 Koiter, W. T., "Elastic Stability and Postbuckling Behavior," in *Nonlinear Problems*, Langer, R. E., ed., University of Wisconsin Press, Madison, Wis., 1963, pp. 257–275.

3 Budiansky, B., and Hutchinson, J. W. "Dynamic Buckling of Imperfection-Sensitive Structures," *Proceedings of the Eleventh International Congress of Applied Mechanics*, Görtler, H., ed., Munich, 1964, pp. 636–651.

4 Budiansky, B., "Theory of Buckling and Postbuckling Behavior of Elastic Structures," *Advances in Applied Mechanics*, Vol. 14, Academic Press, New York, 1974, pp 1–65.

5 Hutchinson, J. W., and Budiansky, B., "Dynamic Buckling Estimates," *AIAA Journal*, Vol. 4, Mar. 1966, pp. 525–530.

6 Budiansky, B., "Dynamic Buckling of Elastic Structures: Criteria and Estimates," in *Dynamic Stability of Structures*, Herrmann, G., ed. Pergamon, 1967, pp. 83–106.

7 Hoff, N. J., "The Perplexing Behavior of Thin Circular Cylindrical Shells in Axial Compression," Second Theodore von Karman Memorial Lecture, Eighth Israel Annual Conference Aviation and Astronautics, Feb. 1966, *Israel Journal of Technology*, Vol. 4, Jan.–Feb. 1966, pp. 1–28.

8 Hansen, J. S., and Roorda, J., "Static and Dynamic Stability of an Imperfect Beam," *Proceedings of the ASCE, Journal of Engineering Mechanics Division*, Vol. 99, No. EM2, Apr. 1973, pp. 271–285.

9 Tatsa, E., Tene, Y., and Baruch, M., "Remarks on the Application of Koiter's General Postbuckling Theory," *Acta Mechanica*, Vol. 22, 1975, pp. 153–162.

10 Ogata, K., *Modern Control Engineering*, Prentice-Hall, Englewood Cliffs, N. J., 1970.

11 Fichtenholz, G. M., *Course of Differential and Integral Calculus*, Vol. II, 5th ed., Fitzmatgis, Moscow, 1962, pp. 86–93.

12 Thompson, J. M. T., "Dynamic Buckling Under Step Loading," in *Dynamic Stability of Structures*, Herrmann, G., ed., Pergamon, 1967, pp. 215–236.

Z. Celep

Associate Professor,
Faculty of Engineering and Architecture,
Technical University,
Istanbul, Turkey

Stability of a Beam on an Elastic Foundation Subjected to a Nonconservative Load

In this investigation, the influence of a Winkler type of elastic foundation on the stability of the cantilever beam subjected to a nonconservative load which consists of a vertical and a follower components is studied. In addition to the common transverse foundation modulus, a rotatory foundation modulus is considered. Approximate solution is obtained by using Galerkin's method. Numerical calculation are reported and displayed for various combinations of the nonconservativeness parameter, transverse and rotatory modulus of the foundation, distance of the point of application of the load and that of the transverse spring. As a result of the numerical study unexpected feature of stability of the cantilever beam in contrast to the behavior of the column is identified.

Introduction

The state of stability of a beam resting on the Winkler elastic foundation subjected to a follower load was investigated by Smith and Hermann [1]. They found an unexpected result that the critical stability load for flutter type of stability loss is completely independent of the modulus of Winkler foundation. The problem from which the foregoing result was drawn is a uniform cantilever column subjected to a concentrated follower load applied at its free end. Sundararajan [2] extended the study and proved the following theorem: "The critical load of an undamped, linearly elastic column subjected to either conservative or nonconservative stationary loads does not decrease due to the introduction of a Winkler-type elastic foundation having a modulus distribution geometrically similar to the mass distribution of the column." The influence of the variable foundation modulus on the stability of the column with constant mass distribution was investigated for the end loading by Hauger and Vetter [3] and for the uniformly distributed loading by the author [4]. It was found that the elastic foundation with variable modulus may have either a stabilizing or a destabilizing effect on the flutter load. The column on an elastic foundation with constant modulus subjected to an end load was investigated by Becker, Hauer, and Winzen [5] by considering the external damping of the elastic foundation, the internal damping of the column and a rotatory foundation modulus. They found that an increasing rotatory foundation modulus increases the stability of the column. In the aforementioned studies it was assumed that the foundation was a Winkler type, i.e., the foundation pressure and moment exerted by the foundation are proportional to the deflection and to the rotation of the foundation at the same point, respectively. The proportionality coefficients which correspond to the foundation modulus were constant or variable along the column.

Menditto [6] investigated the stability behavior of the same cantilever column by assuming it on an elastic foundation with a shear layer, i.e., on a Wieghardt foundation. Anderson [7] studied the stability of the cantilever and the clamped-hinged column subjected to either a uniformly or a linearly distributed tangential load. It was assumed that the column is resting on a Wieghardt-type elastic foundation.

The purpose of this study is to investigate the lateral stability of a narrow rectangular cantilever beam subjected to uniformly distributed vertical and follower loads. The beam is assumed to be on a Winkler-type elastic foundation which responds to the deflection and to the rotation of the beam. Since the stability of the same beam was studied by the author [8] without considering any foundation, in particular, the effect of the constant modulus of the foundation on the divergence and flutter stability loads are investigated here.

Statement of the Problem

Consider a cantilever beam of length l with a narrow rectangular cross section of height h. The beam is resting on two types of elastic foundation with constant modulus K_w and K_θ which exert a foundation pressure and a foundation moment proportional to the deflection and rotation of the beam, respectively. They can be considered as transverse springs with modulus K_w and torsional springs with modulus K_θ. It is assumed the transverse springs are attached to the beam at a distance f measured from the centroid of the cross section. The cases $f = -0.5h$, 0 and $0.5h$ correspond to the springs' attachment to the beam at the bottom, at the centroid and at the top of the cross

Contributed by the Applied Mechanics Division for publication in the JOURNAL OF APPLIED MECHANICS.

Discussion on this paper should be addressed to the Editorial Department, ASME, United Engineering Center, 345 East 47th Street, New York, N. Y. 10017, and will be accepted until June 1, 1980. Readers who need more time to prepare a discussion should request an extension from the Editorial Department. Manuscript received by ASME Applied Mechanics Division, February, 1979; final revision, June, 1979.

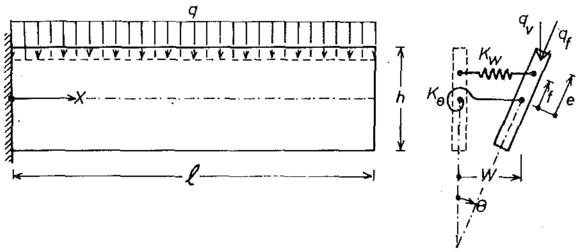

Fig. 1 **Cantilevel beam subjected to uniformly distributed vertical and follower load**

section. Loading of the beam consists of a uniformly distributed vertical load q_v and follower load q_f as shown in Fig. 1. The distance of the point of application of the loads e is measured from the centroid of the cross section. The loading cases where the loads are applied at the bottom, at the centroid and at the top of the cross section correspond to the values of $e = -0.5h$, 0, and $0.5h$.

The stability or instability of the beam is characterized by the behavior of a small disturbance from its equilibrium state. The disturbance of the beam appears as a lateral deflection $W(X, t)$ and as an angle of twist $\Theta(X, t)$ as shown in Fig. 1. The equations of the lateral and torsional motions of the beam about the undisturbed form of equilibrium are obtained combining the equilibrium equations and the relation of the bending and torsional deformations. The functions W and Θ are governed by these equations which can be written in the following form [8]:

$$EI\frac{\partial^4 W}{\partial X^4} + m\frac{\partial^2 W}{\partial t^2} + K_w(W + f\Theta) + q_f\Theta - \frac{ql^2}{2}\frac{\partial^2}{\partial X^2}\left[\left(1 - \frac{X}{l}\right)^2\Theta\right] = 0,$$

$$GJ\frac{\partial^2\Theta}{\partial X^2} - mr^2\frac{\partial^2\Theta}{\partial t^2} - K_w f(W + f\Theta) + (q_v e - K_\theta)\Theta + ql\left(1 - \frac{X}{l}\right)\frac{\partial W}{\partial X} + \frac{ql^2}{2}\frac{\partial}{\partial X}\left[\left(1 - \frac{X}{l}\right)^2\frac{\partial W}{\partial X}\right] = 0, \quad (1)$$

where EI is the small bending rigidity, GJ the torsional rigidity, r the polar radius of inertia, m mass per unit length of the cross section, X the spatial coordinate along the axis of the beam, t the time and $q = q_f + q_v$. Due to the narrowness of the cross section the vertical deflection and the warping rigidity are neglected. It is assumed that the separation of variables is possible, and the governing equations (1) have solutions of the form

$$W(X, t) = lw(x)e^{i\omega t}, \quad \Theta(X, t) = \theta(x)e^{i\omega t},$$

where ω is the frequency of the lateral and torsional vibrations of the beam. Substitution of these solutions into equation (1) gives

$$w^{\mathrm{IV}} + (k_w{}^2 - \omega_b{}^2)w + [\lambda\zeta k_w{}^2 - (1 - \alpha)q_b{}^2]\theta + 2(1 - x)q_b{}^2\theta' - 0.5(1 - x)^2 q_b{}^2\theta'' = 0,$$

$$n\theta'' + [\gamma^2\lambda^2\omega_b{}^2 + (1 - \alpha)\eta\lambda q_b{}^2 - k_\theta{}^2 - \zeta^2\lambda k_w{}^2]\theta + 0.5q_b{}^2(1 - x)^2 w'' - \zeta k_w{}^2 w = 0, \quad (2)$$

where the prime denotes differantion with respect to x and, the additional parameters are defined as follows:

$$x = \frac{X}{l}, \quad \eta = \frac{e}{h}, \quad \zeta = \frac{f}{h}, \quad \alpha = \frac{q_f}{q}, \quad \lambda = \frac{h}{l}, \quad \gamma = \frac{r}{h},$$

$$n = \frac{GJ}{EI}, \quad q_b{}^2 = \frac{ql^3}{EI}, \quad \omega_b{}^2 = \frac{m\omega^2 l^4}{EI},$$

$$k_w{}^2 = \frac{K_w l^4}{EI}, \quad k_\theta{}^2 = \frac{K_\theta l^2}{EI}. \quad (3)$$

The boundary conditions of the problem are written as follows:

$$w(0) = w'(0) = 0, \quad w''(1) = w'''(1) = 0,$$

$$\theta(0) = 0, \qquad \theta'(1) = 0, \quad (4)$$

which imply that the deflection, the slope of the deflection and the rotation of the cross section at the clamped end; and the bending moment, the shearing force, and the torsional moment at the free end have to vanish.

Approximate Solution

To propose an exact solution to the nonself-adjoint eigenvalue problem given by equations (2) and boundary conditions (4) is a difficult task, if not impossible. Therefore, an approximate solution is carried out by using Galerkin's method. To this end, the lateral deflection $w(x)$ and the angle of twist $\theta(x)$ are expanded in a series with undetermined coefficients as follows:

$$w(x) = \sum_j C_{wj}w_j(x), \quad \theta(x) = \sum_j C_{\theta j}\theta_j(x), \quad (5)$$

where C_{wj} and $C_{\theta j}$ are constants and, $w_j(x)$ and $\theta_j(x)$ are the coordinate functions which have to satisfy the boundary conditions (2) identically. These functions are assumed as

$$w_j(x) = \sin a_j x - \sinh a_j x + \frac{\sin a_j + \sinh a_j}{\cos a_j + \cosh a_j}(\cosh a_j x - \cos a_j x),$$

$$\theta_j(x) = \sin\frac{b_j\pi x}{2}, \quad (6)$$

where a_j is the root of the transcendental equation

$$1 + \cos a_j \cdot \cosh a_j = 0$$

and $b_j = 1, 3, 5, \ldots$ The selected coordinate functions (6) correspond to the uncouple lateral bending and torsional-free vibrations of the beam.

By substituting equation (5) into equations (2) two residual functions are obtained. Galerkin's method requires these functions have to be orthogonal with respect to each coordinate function on the definition domain of the problem. After the indicated integrations which appears at the orthogonalization process are performed numerically, a system of homogeneous algebraic equations for the constant C_{wj} and $C_{\theta j}$ is obtained. The trivial solution of the system corresponds to the undisturbed form of the beam. Nontrivial solutions can be obtained if and only if the determinant of this system vanishes. This condition yields a relation between the nondimensional load q_b and frequency ω_b, and illustrates the eigencurve of the beam on the load-frequency plane. This curve characterizes the static and the dynamical behavior of the beam. The free vibration of the beam occurs at the intersection point of the eigencurve with the frequency-axis, and the intersection point with the load-axis corresponds to the divergence instability. Finally, the flutter type of loss of stability occurs at the point of the eigencurve where the two vibration frequencies approach each other and coincide having a double root.

Numerical Results

The numerical calculations were performed on the B3700 Computer at the Computer Center of the Technical University, Istanbul. Remembering that the cross section is a narrow rectangular strip, the shape constants are found to be

$$\gamma = 0.5/\sqrt{3}, \quad n = 2(1 - \mu)$$

where μ is Poisson's ratio. As usual the bending rigidity EI is replaced by $EI/(1 - \mu^2)$ because of the platelike bending behavior of the narrow rectangular cross section. The numerical computations are carried out by putting $\lambda = 0.1$, $\mu = 0.3$. The eigencurve of the beam is drawn for various values of the nondimensional parameter: the nonconservativeness of the loading α, the distance of the point of application of the loads η and that of the transverse spring ζ, the modulus of the transverse springs k_w and that of the rotational springs k_θ. Further, the nondimensional frequency parameter ω_b is assumed to be a complex quantity in general and expressed as

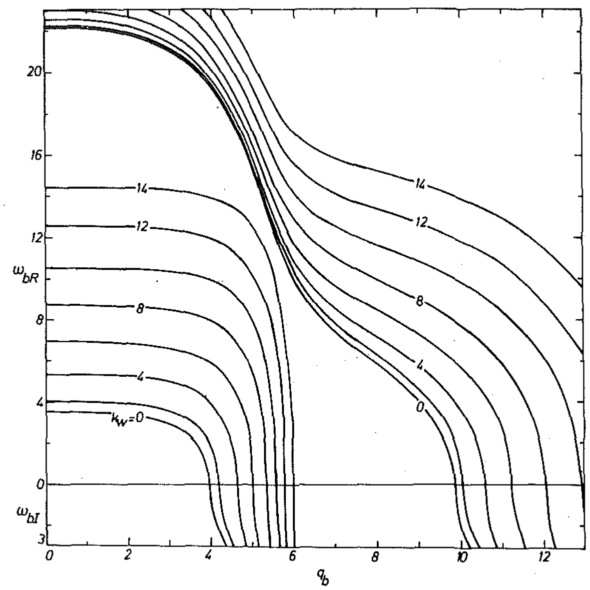

Fig. 2(*a*) Eigencurves of the cantilever beam for the case $\alpha = 0$, $\eta = 0$, $\zeta = 0$ and $k_\theta = 0$

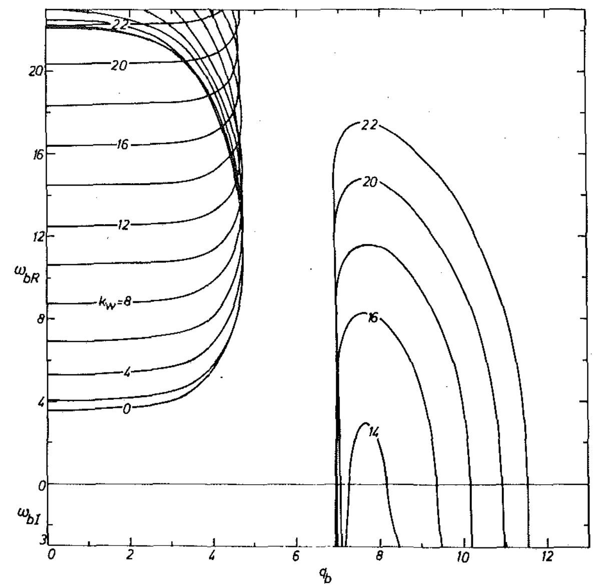

Fig. 3(*a*) Eigencurves of the cantilever beam for the case $\alpha = 1$, $\eta = 0$, $\zeta = 0$ and $k_\theta = 0$

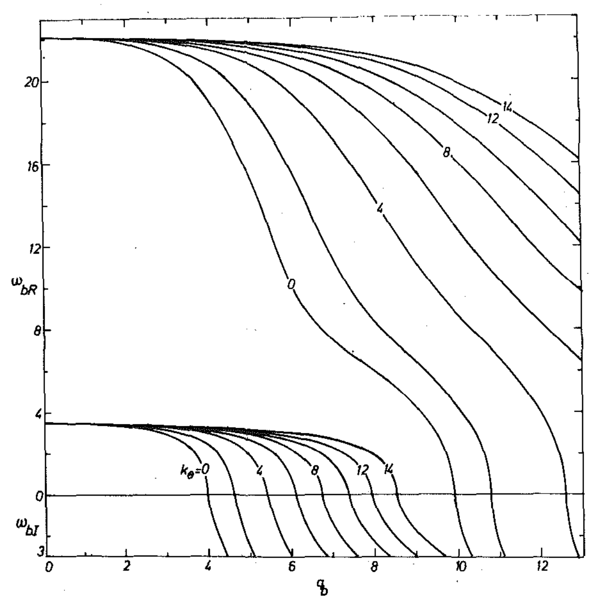

Fig. 2(*b*) Eigencurves of the cantilever beam for the case $\alpha = 0$, $\eta = 0$, $\zeta = 0$ and $k_w = 0$

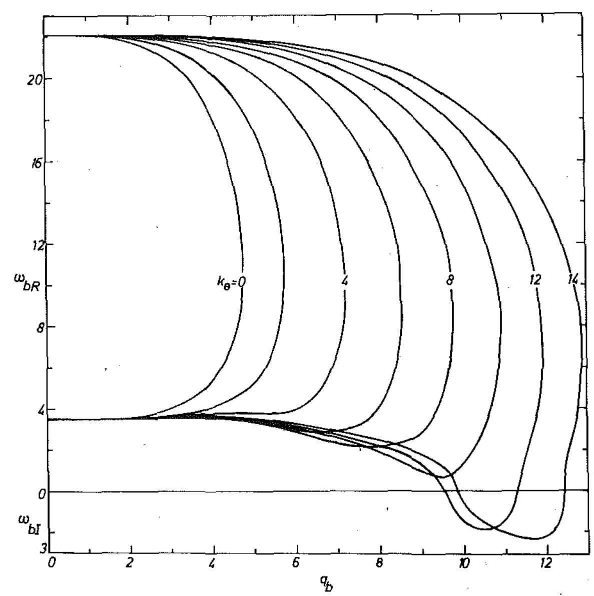

Fig. 3(*b*) Eigencurves of the cantilever beam for the case $\alpha = 1$, $\eta = 0$, $\zeta = 0$ and $k_w = 0$

$$\omega_b = \omega_{bR} + i\omega_{bI}, \quad i = (-1)^{1/2},$$

where ω_{bR} and ω_{bI} are real quantities. The frequency parameter appears as either purely real ($\omega_{bI} = 0$) or purely imaginary quantity ($\omega_{bR} = 0$), which corresponds to the oscillatory motion or to the divergence motion of the cantilever beam, respectively. Because of symmetry of the beam only positive values of the load parameter are considered.

Figs. 2(a, b) illustrates the eigencurve of the beam on elastic foundation subjected to vertical load for various values of the modulus of foundation. It is seen that as the value of the foundation modulus k_w or k_θ increases, the corresponding critical divergence loads increase monotonically. While the first two free-vibration frequencies increase with the foundation modulus k_w, no variation occurs as the modulus k_θ increases, because they correspond to the bending vibration of the beam. Since the free-vibration frequencies of torsional motion are high, they are not seen at the figures.

The eigencurves of the beam subjected to follower load are represented in Figs. 3(a, b). They show that as the value of k_w increases, the eigencurve is shifted further paralel to the frequency-axis on the load-frequency plane. Smith and Hermann [1] and Sundararajan [2] have shown that the shape of the eigencurve does not change during this shifting for the column the disturbance of which is defined by one parameter, i.e., by its deflection only. As it is seen in Fig. 3(a), this is not valid for the cantilever beam which has two freedom functions, i.e., the deflection and the rotation. The flutter load of the beam decreases slightly as the modulus k_w increases. Moreover a second branch of the eigencurve is seen for larger values of k_w. This branch intersect the load-axis at two points, which correspond to the divergence loads of the beam. Because these divergence loads themselves are in the instability region, their importances are lost. This important

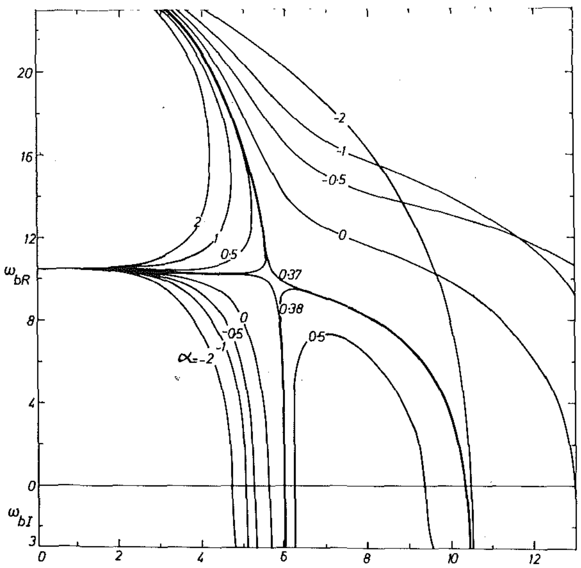

Fig. 4(*a*) Eigencurves of the cantilever beam for the case $\eta = 0$, $\zeta = 0$, $k_w = 10$ and $k_\theta = 0$

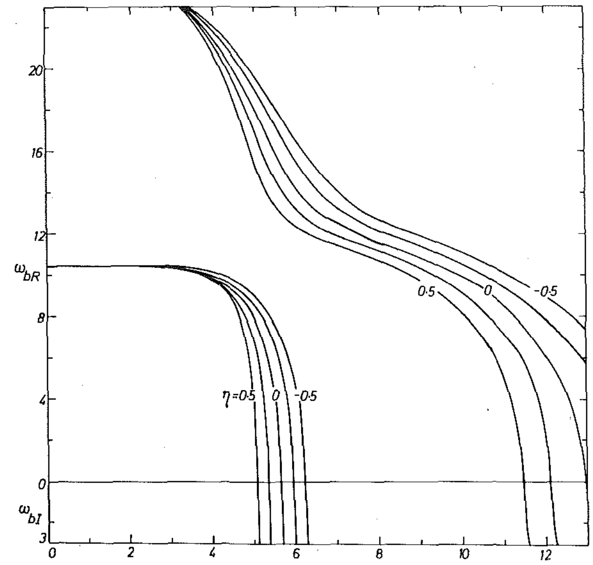

Fig. 5(*a*) Eigencurves of the cantilever beam for the case $\alpha = 0$, $\zeta = 0$, $k_w = 10$ and $k_\theta = 0$

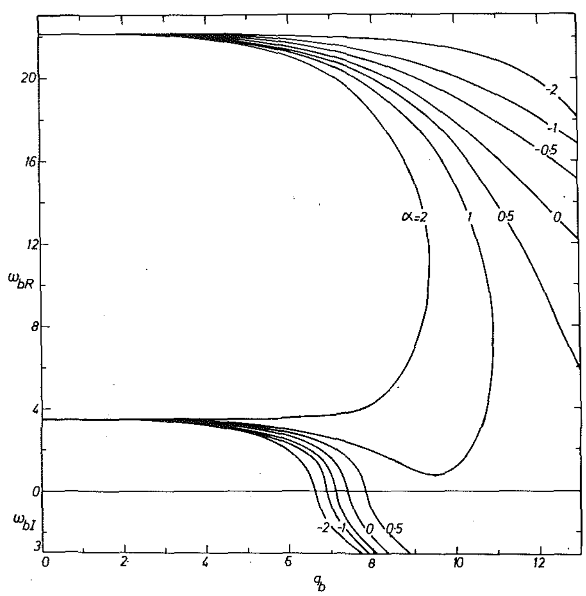

Fig. 4(*b*) Eigencurves of the cantilever beam for the case $\eta = 0$, $\zeta = 0$, $k_w = 0$ and $k_\theta = 10$

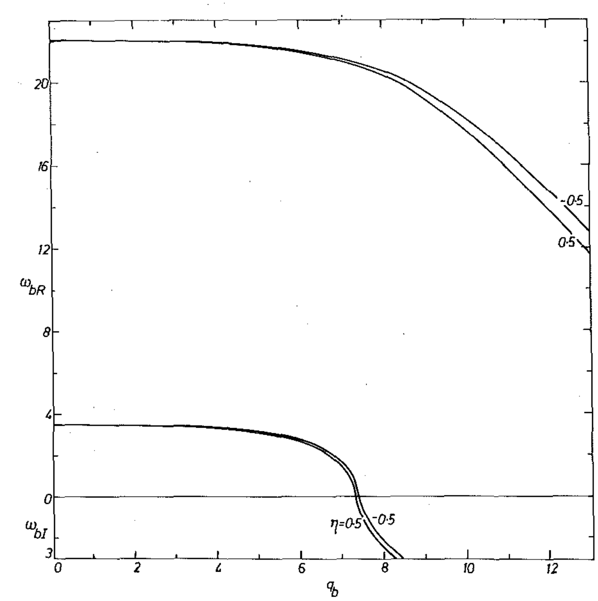

Fig. 5(*b*) Eigencurves of the cantilever beam for the case $\alpha = 0$, $\zeta = 0$, $k_w = 0$ and $k_\theta = 10$

fact indicates that a "critical" load can not always be a critical one, when it is found in a static investigation. Quite different results are displayed in Fig. 3(*b*) where the rotation modulus k_θ is varied. The flutter load increases with the modulus k_θ. The stabilizing effect proceeds until the eigencurve intersects the load-axis where the divergence load comes into being. It is seen from the figures that there may be a jump in the value of the critical load and the type of stability loss will change from the flutter to the divergence. The divergence load will increase with further increase of the modulus k_θ.

Figs. 4(*a, b*) illustrate the variation of the eigencurve with the nonconservativeness parameter α. The two branches of the eigencurves are seen in Fig. 4(*a*), where the modulus k_w has a certain value while k_θ vanishes. Approximately up to $\alpha = 0.37$ the two branches intersect the load-axis at the first two divergence loads. The first divergence load which is the critical one increases with the parameter α. With further increase in α the two branches of the eigencurve coalesce and then appear again approximately for $\alpha > 0.38$. But this time one branch intersects the load-axis two times while the other intersecting the frequency-axis appears above the load-axis, and the flutter type of instability occurs on it. The flutter load which controls the stability domain decreases as the nonconservativeness parameter α increases. Fig. 4(*b*) shows the eigencurve of the beam which rests on an elastic foundation with the modulus k_θ only. As it seen that the flutter instability appears for larger values of α. As the parameter α decreases the flutter load increases, and then the flutter instability gives its place to the divergence instability. The divergence load becomes smaller with the nonconservativeness parameter α.

The influence of the point of application of the loads η is illustrated in Figs. 5(*a, b*) for the conservative loading cases. They show that the type of stability loss does not change and the divergence load becomes greater when the loads move downward. This fact is more evident when the foundation has a modulus k_θ instead of k_w. Finally, Fig. 5(*c*)

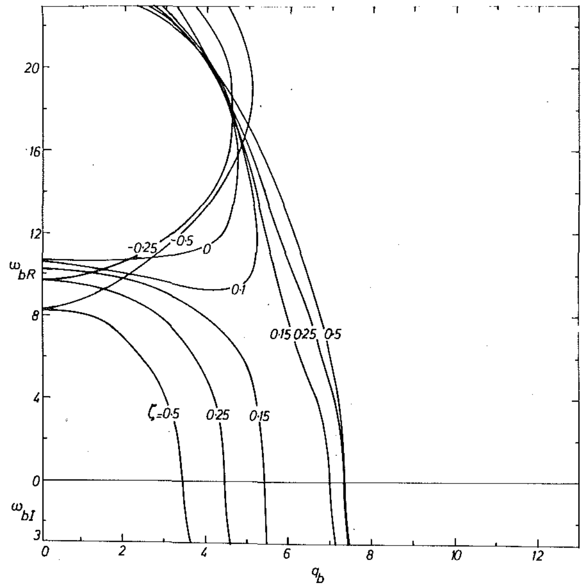

Fig. 5(c) Eigencurves of the cantilever beam for the case $\alpha = 1$, $\eta = 0$, $k_w = 10$ and $k_\theta = 0$

represents the influence of the bounding point of the transverse spring ζ. As it is seen, when the loads move upward the flutter type of stability loss vanishes and the critical load will be a divergence one.

Concluding Remarks

In all the foregoing cases, the critical load of the cantilever beam either increases or decreases with the introduction of the elastic foundation. When the loading is a follower type it decreases with the transverse spring constant and increases with the rotation spring constant which were intuitively unexpected and seemingly unknown behavior of the cantilever beam. Many of these results obtained in this study are in contrast to the before going results which are reported for the column resting on a Winkler foundation without any rotatory modulus.

References

1 Smith, T. E., and Hermann, G., "Stability of a Beam on an Elastic Foundation Subjected to a Follower Force," ASME JOURNAL OF APPLIED MECHANICS, Vol. 39, 1972, pp. 628–629.

2 Sundararajan, C., "Stability of Columns on Elastic Foundations Subjected to Conservative and Nonconservative Forces," *Journal of Sound and Vibration*, Vol. 37, 1974, pp. 79–85.

3 Hauger, W., and Vetter, K., "Influence of an Elastic Foundation on the Stability of a Tangentially Loaded Column," *Journal of Sound and Vibration*, Vol. 47, 1976, pp. 296–299.

4 Celep, Z., "On the Stability of a Column on an Elastic Foundation Subjected to a Nonconservative Load," *Proceedings, Sixth National Science Congress*, The Scientific and Technical Research Council of Turkey, 1977, pp. 301–311.

5 Becker, M., Hauer, W., and Winzen, W., "Influence of Internal and External Damping on the Stability of Beck's Column on an Elastic Foundation," *Journal of Sound and Vibration*, Vol. 54, 1977, pp. 468–472.

6 Menditto, G., "Elastic Stability of a Uniform Cantilever Beam on Elastic Foundation With a Shear Layer Subjected to a Follower Force," *Meccanica*, Vol. 9, 1974, pp. 1–5.

7 Anderson, G. L., "The Influence of a Wieghardt-Type Elastic Foundation on the Stability of Some Beams Subjected to Distributed Tangential Forces," *Journal of Sound and Vibration*, Vol. 44, 1976, pp. 103–118.

8 Celep, Z., "On the Lateral Stability of a Cantilever Beam Subjected to a Nonconservative Load," *Journal of Sound and Vibration*, Vol. 64, 1979, pp. 173–178.

N. G. Stephen[2]

Department of Mechanical Engineering,
Manchester Polytechnic,
Chester Street,
Manchester M15GD, England

Timoshenko's Shear Coefficient From a Beam Subjected to Gravity Loading[1]

The Kennard and Leibowitz method of obtaining the shear coefficient, by equating center-line curvature of a Timoshenko beam to the curvature of a beam subjected to uniform gravity loading, is extended to arbitrary monosymmetric sections. The resulting expression for the coefficient is evaluated for several sections and comparison made with experimental and exact theoretical results.

Introduction

In a recent paper Kaneko [1] reviews the various theoretical methods of determining the shear coefficient in the Timoshenko theory for beam flexural vibration and makes a comparison with the results of several experimental investigations into flexural wave propagation and concludes that the values $K = 6(1 + \nu)^2/(7 + 12\nu + 4\nu^2)$ for the circular section, and $K = 5(1 + \nu)/(6 + 5\nu)$ for the rectangle provide the best agreement. Kaneko also notes that these values may be obtained by equating the Timoshenko phase velocity predictions to the long wavelength approximate solutions of the exact Pochhammer-Chree theory [2] for the circular section and the plane stress solution for a thin rectangular section by Lamb [3], respectively. In a paper by the present author [4] it is shown that the foregoing shear coefficient for a circular section varies but slightly with frequency in order to insure equivalent phase velocity predictions between the Timoshenko theory and the Pochhammer-Chree theory for frequencies up to the cutoff point for the second branch of flexural wave propagation for Poisson's ratio $\nu \geqslant 0.25$.

Since the original definition of the coefficient, as the ratio of average shear stress on a section to shear stress at the centroid has been clearly shown to give unsatisfactory results, the suitability of any other definition must rest on its ability to produce theoretical predictions in agreement with experimental results and the predictions of exact flexural wave propagation theories. Unfortunately exact solutions are available for only one class of section, i.e., the hollow circle, given by Aremenâkas, Gazis, and Herrmann [5] which includes the case of the solid circle. The plane stress solution for the thin rectangle [3] is unlikely to give results valid for a more compact rectangular or square section. The frequency equation for the elliptic section has been given [6] but because of its complexity phase velocity predictions have not been produced.

The suitability of the aforementioned expressions for the circular and thin rectangular sections and the fact that neither expression is given by any well-known theoretical determination of the coefficient, led the author to reconsider previously published theoretical methods of obtaining the coefficient. With few exceptions the methods of previous investigators can be split into two types. The first consists of equating the Timoshenko theory frequency or phase velocity prediction to some special exact solution, such as thickness shear waves or Rayleigh surface waves; the suitability of this method has already been discussed by the present author [4]. The second involves calculating the extra deflection in a beam due to shear deformation, usually employing Saint-Venant flexure shear stress distribution as an approximation to the stress distribution present in a beam performing flexural vibration. One of the most convincing definitions, by Cowper [7], is a byproduct of the derivation of Timoshenko's equations by integration of the equations of equilibrium; again Saint-Venant flexure stress and displacements are assumed.

Now exact, according to the mathematical theory of elasticity, solutions for static bending of beams of arbitrary section are available for four loading conditions:

1 Beam in "pure bending" subjected to terminal bending moments, which is of little importance here as there are no shear effects.

2 Classical Saint-Venant flexure of cantilevered beam subjected to a terminal shearing force.

3 The cantilevered beam subjected to a uniformly distributed load, which has a shear stress distribution identical to condition 2.

4 Beam subjected to uniform body force loading, the solution of which requires the solution to condition 2 and in addition, solution to an associated plane strain problem for the cross section.

Of these exact solutions the gravity loading problem bears greatest resemblance to the loading conditions in a beam performing long wavelength flexural vibration. This discussion led the present author

---

[1] Part of this work was performed while the author was a research student at Exeter University, England.

[2] Formerly, Department of Civil Engineering and Engineering Mechanics, McMaster University, Hamilton, Ontario, Canada, L8S 4L7.

Contributed by the Applied Mechanics Division for publication in the JOURNAL OF APPLIED MECHANICS.

Discussion on this paper should be addressed to the Editorial Department, ASME United Engineering Center, 345 East 47th Street, New York, N.Y. 10017, and will be accepted until June 1, 1980. Readers who need more time to prepare a discussion should request an extension from the Editorial Department. Manuscript received by ASME Applied Mechanics Division, December, 1978.

to employ the Cowper method [7] to evaluate the coefficient for circular and thin rectangular sections using the exact stresses and displacements for the gravity loaded beam, which gave expressions identical to Cowper's for Saint-Venant stresses and displacements; this suggested the Cowper formula to be either insensitive to changes in shear distribution or that a suitable definition must consider more than just the shear stress distribution. Since the stress and displacement distributions in the gravity loaded beam is similar in form to the Saint-Venant flexure case then the latter argument appears closer to the truth.

This led the investigation to consider the Kennard and Leibowitz method [8] of obtaining the coefficient, by equating the center-line curvature of the Timoshenko beam to the curvature of the beam subjected to different loading conditions, in particular a thin rectangle carrying first a uniformly distributed load and second subjected to gravity loading, both loading conditions being considered by Timoshenko [9], giving values $K = 20(1 + \nu)/(24 + 15\nu)$ and $K = 20(1 + \nu)/(24 + 25\nu)$, respectively.

Kennard and Leibowitz do not discuss which loading condition is the better approximation to the dynamically loaded beam and, in consequence, which shear coefficient is the more applicable. Application of the method to a circular section beam subjected to gravity loading gives the value $K = 6(1 + \nu)^2/(7 + 12\nu + 4\nu^2)$, identical to the value obtained from approximation to the exact frequency equation.

A modification to the Kennard and Leibowitz method, equating the Timoshenko curvature to an integrated rather than center-line curvature, for the gravity loaded thin rectangle gave the value $K = 5(1 + \nu)/(6 + 5\nu)$ which is identical to the value from approximation to the plane-stress frequency equation, and did not alter the value for the circle.

In the following, the Kennard and Leibowitz method is modified and extended to beams of arbitrary symmetric section by determining an expression for the integrated curvature for beams subjected to gravity loading; this requires only a knowledge of the Saint-Venant flexure function whereas a complete solution for the gravity loading problem requires solution of the associated plane strain problem. The solution to beams subjected to distributed loadings is discussed in detail by Love [10].

Using the new formula so obtained the coefficient is evaluated for several cross sections and comparison made with exact flexural wave propagation solutions and with published experimental results.

For the sake of simplicity the planes of flexural vibration and gravity loading are taken to be a plane of cross-sectional symmetry.

The Kennard and Leibowitz Method

The basis of this method is the recognition that the elementary moment-curvature relationship

$$M = EI_y \frac{\partial^2 u}{\partial z^2} \tag{1}$$

does not hold for beams subjected to distributed loadings. Here

M = bending moment
E = Young's modulus
I_y = second moment of area about y-axis
u = centroidal displacement in x-direction
z = beam axial coordinate.

In Timoshenko's beam theory, bending moment is related to the centroidal cross-section rotation ψ by

$$M = EI_y \frac{\partial \psi}{\partial z} \tag{2}$$

or noting $\psi = \partial u/\partial z - \gamma$, where γ is the shear angle

$$M = EI_y \left(\frac{\partial^2 u}{\partial z^2} - \frac{\partial \gamma}{\partial z}\right) \tag{3}$$

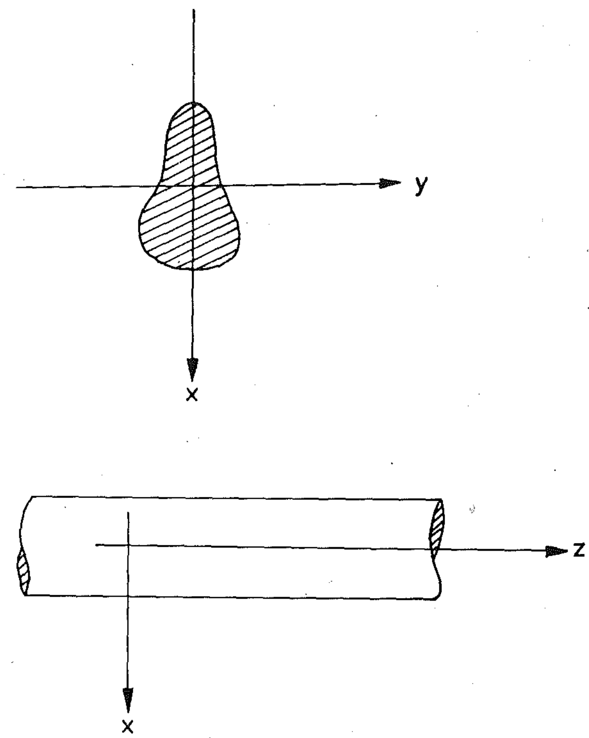

Fig. 1 Uniform isotropic beam of monosymmetric cross section

Thus, if an additional moment due to varying shear force along the beam is denoted by M_s where

$$M_s = EI_y \frac{\partial \gamma}{\partial z} \tag{4}$$

then the elementary relationship may be restored in the form

$$M + M_s = EI_y \frac{\partial^2 u}{\partial z^2} \tag{5}$$

Now the shear angle γ is related to shear force by the expression

$$Q = KAG\, \gamma \tag{6}$$

where

Q = transverse shear force
K = shear coefficient
G = shear modulus
A = cross-sectional area

from which (5) may be written in the form

$$EI_y \frac{\partial^2 u}{\partial z^2} = M + \frac{EI_y}{KAG} \frac{\partial Q}{\partial z} \tag{7}$$

It is immediately obvious that this approach is only applicable to the case of distributed loading when $\partial Q/\partial z \neq 0$

Kennard and Leibowitz proceed by equating the center-line curvature according to (7) to the curvature of a thin rectangle subjected to a uniformly distributed load and to gravity loading and obtain the two coefficients just given.

Curvature of Gravity Loaded Beams

A complete solution to the problem of a beam subjected to uniform body force loading requires a knowledge of the flexure function and solution of an associated plane strain problem; for the present purpose solution of the plane strain problem is not necessary. The notation here is essentially the same as Love [10] where the bending of beams subjected to uniformly distributed loadings is discussed in detail.

We obtain the curvature from the shear strain relationship $\gamma_{xz} = \partial u/\partial z + \partial w/\partial x$. Differentiating with respect to z and rearranging gives

$$\frac{\partial^2 u}{\partial z^2} = \frac{\partial \gamma_{xz}}{\partial z} - \frac{\partial \epsilon_z}{\partial x} \tag{8}$$

where direct strain $\epsilon_z = \partial w/\partial z$.

The strain components γ_{xz} and ϵ_z are given by Love [10] as

$$\epsilon_z = \epsilon_0 - (\kappa_0 + \kappa_1 z + \kappa_2 z^2)x + 2\kappa_2(\chi + xy^2)$$

$$\gamma_{xz} = (\kappa_1 + 2\kappa_2 z)\left\{\frac{\partial \chi}{\partial x} + \frac{\nu x^2}{2} + \left(\frac{2-\nu}{2}\right)y^2\right\} \tag{9}$$

where

$\kappa_0, \kappa_1, \kappa_2$ = constants
ν = Poisson's ratio
χ = flexure function
ϵ_0 = a constant, due to the center-line extension

Substituting into (8) gives

$$\frac{\partial^2 u}{\partial z^2} = (\kappa_0 + \kappa_1 z + \kappa_2 z^2) + \kappa_2 \nu (x^2 - y^2) \tag{10}$$

Thus a knowledge of the constants κ_0, κ_1, κ_2, which depend on the manner of beam support, completely determines the curvature. Kennard and Leibowitz employ the center-line curvature obtained from (10) with $x = y = 0$. In the present modified procedure we employ the integrated rather than center-line transverse displacement given by

$$U = \frac{1}{A}\iint u \, dxdy \tag{11}$$

giving the "integrated" curvature

$$\frac{\partial^2 U}{\partial z^2} = (\kappa_0 + \kappa_1 z + \kappa_2 z^2) + \kappa_2 \nu \frac{(I_y - I_x)}{A} \tag{12}$$

The integrated displacement (11) has been previously used in beam theories by Prescott [14] and Cowper [7] and its effect will be discussed later.

Love [10] shows that the bending moment $M = -\iint x\sigma_z dxdy$ may be expressed in the form

$$M = EI_y(\kappa_0 + \kappa_1 z + \kappa_2 z^2) + \text{constant} \tag{13}$$

where the constant in general is not zero, and is responsible for the failure of the usual moment-curvature relationship for distributed loadings; for bending by terminal couples or terminal shear force the constant is zero.

The constant in question is found by evaluating M at $z = 0$, i.e.,

$$M = EI_y\kappa_0 + \text{constant} = -\iint x\{E\epsilon_z{}^{(0)} + \nu(\sigma_x{}^{(0)} + \sigma_y{}^{(0)})\}dxdy$$

or

$$\text{constant} = -\iint x\{E(\epsilon_z{}^{(0)} + \kappa_0 x) + \nu(\sigma_x{}^{(0)} + \sigma_y{}^{(0)})\}dxdy \tag{14}$$

where the superscript (0) denotes that part of the stress and strain components proportional to z^0. Following Love this may be expressed as

$$M = EI_y(\kappa_0 + \kappa_1 z + \kappa_2 z^2) - \iint Ex(\epsilon_z{}^{(0)} + \kappa_0 x)dxdy$$
$$- \nu \iint \left\{\left(\frac{x^2 - y^2}{2}\right)[\rho g + \tau_{xz}{}^{(1)}] + xy\tau_{yz}{}^{(1)}\right\}dxdy \tag{15}$$

The stress and strain components $\tau_{xz}{}^{(1)}$, $\tau_{yz}{}^{(1)}$, and $\epsilon_z{}^{(0)}$, are given by

$$\tau_{xz}{}^{(1)} = 2G\kappa_2\left(\frac{\partial \chi}{\partial x} + \frac{\nu x^2}{2} + \left(\frac{2-\nu}{2}\right)y^2\right)$$
$$\tau_{yz}{}^{(1)} = 2G\kappa_2\left(\frac{\partial \chi}{\partial y} + (2+\nu)xy\right) \tag{16}$$
$$\epsilon_z{}^{(0)} = \epsilon_0 - \kappa_0 x + 2\kappa_2(\chi + xy^2)$$

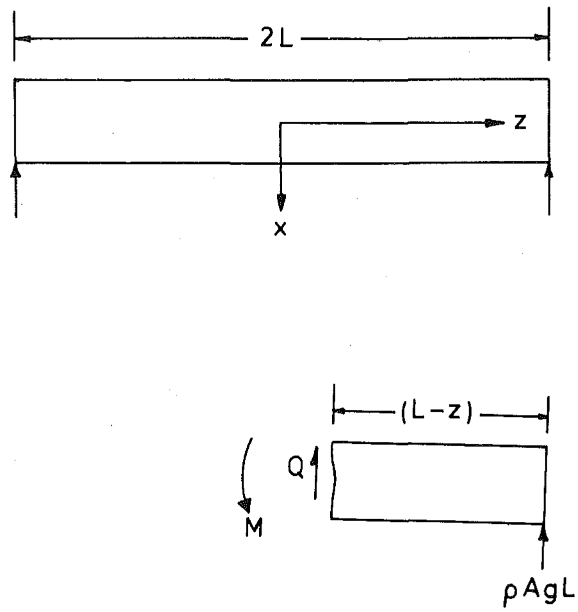

Fig. 2 Simply supported beam—$Q = -\rho Agz$: $M = -\rho Ag/2(L^2 - z^2)$; comparing with $M = EI_y(\kappa_0 + \kappa_1 z + \kappa_2 z^2)$ + constant; $\kappa_2 = \rho Ag/2EI_y$

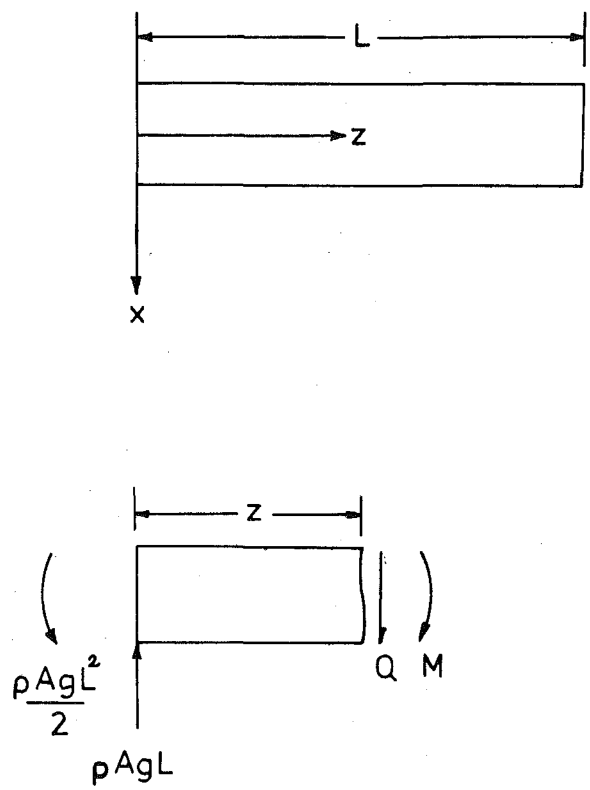

Fig. 3 Cantilevered beam—$Q = -\rho Ag(z - L)$; $M = \rho Ag/2\ (L^2 - 2Lz + z^2)$; comparing with $M = EI_y(\kappa_0 + \kappa_1 z + \kappa_2 z^2)$ + constant; $\kappa_2 = \rho Ag/2EI_y$

Substitution of (16) into (15) gives the moment-curvature relationship

$$M = EI_y(\kappa_0 + \kappa_1 z + \kappa_2 z^2) - 2E\kappa_2 \iint x(\chi + xy^2)dxdy$$
$$- \frac{\nu\rho g}{2}\iint (x^2 - y^2)dxdy - 2G\kappa_2\nu \iint \left(\frac{x^2 - y^2}{2}\right)\left(\frac{\partial \chi}{\partial x}\right. \tag{17}$$

$$+\frac{\nu x^2}{2}+\left(\frac{2-\nu}{2}\right)y^2\Bigg) dxdy - 2G\kappa_2\nu \iint xy\left(\frac{\partial\chi}{\partial y} + (2+\nu)xy\right)dxdy \quad (17)$$

(*Cont.*)

Expression for the Shear Coefficient

Using equation (12) to reexpress (17) in terms of the integrated curvature and requiring equivalence to expression (7) gives

$$\frac{EI_y}{KAG}\frac{\partial Q}{\partial z} = 2E\kappa_2 \iint x(\chi + xy^2)dxdy + \frac{\nu\rho g}{2}\iint (x^2-y^2)dxdy + 2G\kappa_2\nu \iint \left(\frac{x^2-y^2}{2}\right)\left(\frac{\partial\chi}{\partial x} + \frac{\nu x^2}{2} + \left(\frac{2-\nu}{2}\right)y^2\right)dxdy + 2G\kappa_2\nu\iint xy\left(\frac{\partial\chi}{\partial y} + (2+\nu)xy\right)dxdy + \frac{EI_y\kappa_2\nu}{A}(I_y - I_x) \quad (18)$$

and for the simply supported beam, Fig. 2 and the cantilevered beam, Fig. 3, we have

$$\kappa_2 = \frac{\rho A g}{2EI_y}, \frac{\partial Q}{\partial z} = -\rho A g \quad (19)$$

After some manipulation and noting $E/G = 2(1+\nu)$, (18) gives

$$K = \frac{-4(1+\nu)^2 I_y{}^2}{2(1+\nu)A\iint x(\chi + xy^2)dxdy + 2\nu(1+\nu)I_y(I_y - I_x) + \nu A\iint \left\{\left(\frac{x^2-y^2}{2}\right)\left(\frac{\partial\chi}{\partial x} + \frac{\nu x^2}{2} + \left(\frac{2-\nu}{2}\right)y^2\right) + xy\left(\frac{\partial\chi}{\partial y} + (2+\nu)xy\right)\right\}dxdy} \quad (20)$$

and dividing through by $-2(1+\nu)I_y$ gives

$$K = \frac{2(I+\nu)I_y}{\nu(I_x - I_y) - \frac{A}{I_y}\iint x(\chi + xy^2)dxdy - \frac{\nu A}{2(1+\nu)I_y}\iint \left\{\left(\frac{x^2-y^2}{2}\right)\left(\frac{\partial\chi}{\partial x} + \frac{\nu x^2}{2} + \left(\frac{2-\nu}{2}\right)y^2\right) + xy\left(\frac{\partial\chi}{\partial y} + (2+\nu)xy\right)\right\}dxdy} \quad (21)$$

This differs from the expression given by Cowper [7] by the doubling in magnitude of the first term in the denominator, due to employing the integrated rather than center-line curvature thereby including the second-order lateral contraction inertia, and by the last term, which may be further expressed as

$$\frac{\nu A}{W}\iint \left(\frac{x^2-y^2}{2}\right)\tau'_{xz}dxdy + \frac{\nu A}{W}\iint xy\tau'_{yz}dxdy \quad (22)$$

where τ'_{xz} and τ'_{yz} are the shear stress components for a cantilevered beam subjected to a terminal shearing force W, and is due to presence of direct transverse stresses in the gravity loaded beam.

Evaluation of Shear Coefficient for Various Cross Section

(a) Circle. Love [11] gives the stress function as

$$\chi = -\left(\frac{3}{4} + \frac{\nu}{2}\right)a^2 x + \frac{1}{4}(x^3 - 3xy^2) \quad (23)$$

where a is the radius of the circle.

Applying equation (21) the value of K is obtained as

$$K = \frac{6(1+\nu)^2}{7 + 12\nu + 4\nu^2} \quad (24)$$

This is identical to the value obtained by equating phase velocity predictions of Timoshenko beam theory and the exact analysis [2] assuming long wavelengths, and also agrees with the value obtained by Kaneko [1] employing best curve fitting techniques.

(b) Hollow Circle. Love [11] gives the stress function as

$$\chi = -\left(\frac{3}{4} + \frac{\nu}{2}\right)\left((a^2 + b^2)r + \frac{a^2b^2}{r}\right)\cos\theta + \frac{r^3}{4}\cos 3\theta \quad (25)$$

where r, θ are polar coordinates and a and b are the outer and inner radii, respectively.

Equation (21) gives

$$K = \frac{6(1+\nu)^2(1+m^2)^2}{(7 + 34m^2 + 7m^4) + \nu(12 + 48m^2 + 12m^4) + \nu^2(4 + 16m^2 + 4m^4)} \quad (26)$$

where $m = b/a$. For a solid circle $m = 0$, and (26) reduces to (24).

For a thin-walled tube, writing $m = 1 =$ (26) gives

$$K = \frac{1+\nu}{2+\nu} \quad (27)$$

(c) Ellipse. Love [11] gives the stress function as

$$\chi = -a^2\left\{\frac{2(1+\nu)a^2 + b^2}{3a^2 + b^2}\right\}x + \frac{1}{3}\left\{\frac{2a^2 + b^2 + (a^2 - b^2)\nu/2}{3a^2 + b^2}\right\}(x^3 - 3xy^2) \quad (28)$$

for an ellipse $x^2/a^2 + y^2/b^2 = 1$.

Application of (21) gives

$$K = \frac{12(1+\nu)^2(3+\epsilon^2)}{(40 + 74\gamma + 34\nu^2) + \epsilon^2(16 + 20\nu + 4\nu^2) + \epsilon^4(2\nu - 6\nu^2)} \quad (29)$$

where $\epsilon = b/a$.

(d) Rectangle. Love [11] gives the stress function as

$$\chi = \left(\frac{2+\nu}{6}\right)(x^3 - 3xy^2) + \left\{-(1+\nu)a^2 + \frac{1}{3}\nu b^2\right\}x + \frac{4\nu b^3}{\pi^3}\sum_{n=1}^{\infty}\frac{(-1)^n}{n^3}\frac{\sinh\frac{n\pi x}{b}}{\cosh\frac{n\pi a}{b}}\cdot\cos\frac{n\pi y}{b} \quad (30)$$

for the rectangle whose boundary is given by $x = \pm a, y = \pm b$.

Equation (21) gives

$$K = \frac{5(1+\nu)^2}{6 + 11\nu + \nu^2\left(5 - m^4 + \frac{90m^5 S}{\pi^5}\right)} \quad (31)$$

where $m = b/a$, and S is the sum

Table 1

$\frac{a}{b}(=\frac{1}{m})$	$S = \sum_{n=1}^{\infty} \frac{\tanh \frac{n\pi a}{b}}{n^5}$
.05	.16808
.10	.32603
.15	.46738
.20	.58894
.25	.69006
.30	.77185
.35	.83650
.40	.88665
.45	.92499
.50	.95396
.55	.97567
.60	.99183
.65	1.00379
.70	1.01262
.75	1.01912
.80	1.02389
.85	1.02739
.90	1.02995
.95	1.03183
1.00	1.03320
2.00	1.03692

$$S = \sum_{n=1}^{\infty} \frac{\tanh n\pi\, a/b}{n^5} \tag{32}$$

For a thin rectangle, $m \to 0$ and (31) reduces to

$$K = \frac{5(1+\nu)}{6+5\nu} \tag{33}$$

For $m \leqslant 0.5$ the value of (32) differs little from the Riemann zeta function $\zeta(5)$ which has the value 1.03693. For $m \geqslant 0.5$, the sum is shown in Table 1.

(e) Thin-Walled Sections. Cowper [7] outlines the method for determining the value of the first integral in the denominator of (21) by employing the usual thin wall assumption for a cantilevered thin wall section, that shear stress follows the contour of the section and is constant across the thickness; shear stress perpendicular to the contour is assumed zero. By using standard methods for determining the shear stress, the function χ may be obtained. For the sake of completeness the method is given below.

We wish to evaluate the integral

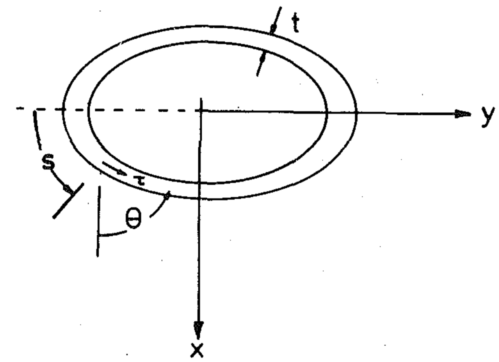

Fig. 4 Arbitrary thin-walled section

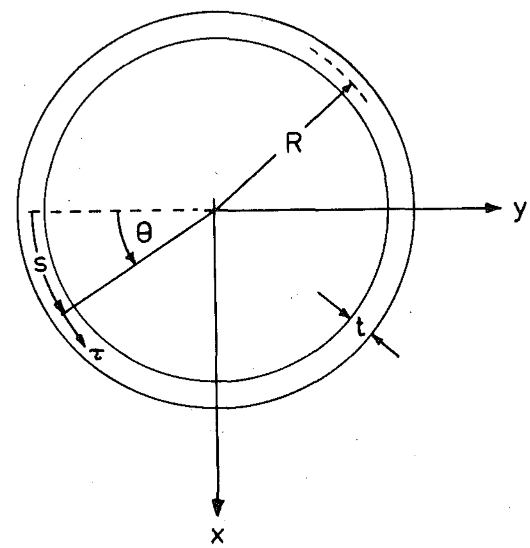

Fig. 5 Thin-walled tube—$I_y = \pi R^3 t$; $A = 2\pi R t$; $x = R \sin\theta$; $y = -R\cos\theta$

$$I = \iint x(\chi + xy^2)\,dx\,dy \tag{34}$$

Writing $\chi = -\psi - xy^2$, (34) becomes

$$I = -\iint x\psi\,dx\,dy \tag{35}$$

For the thin-wall section, Fig. 4, we have

$$\tau = \tau'_{xz}\cos\theta + \tau'_{yz}\sin\theta \tag{36}$$

and noting the expressions for Saint-Venant flexure [11]

$$\tau'_{xz} = -\frac{W}{2(1+\nu)I_y}\left(\frac{\partial\chi}{\partial x} + \frac{\nu x^2}{2} + \frac{(2-\nu)}{2}y^2\right) \tag{37}$$

$$\tau'_{yz} = -\frac{W}{2(1+\nu)I_y}\left(\frac{\partial\chi}{\partial y} + (2+\nu)xy\right)$$

gives

$$\frac{d\psi}{ds} = \frac{2(1+\nu)I_y}{W}\tau + \frac{\nu}{2}(x^2-y^2)\cos\theta + \nu\,xy\sin\theta \tag{38}$$

Integration of (38) enables the evaluation of (34).

The second integral in (21) is best evaluated by noting (22) and again assuming the foregoing distribution for τ.

To illustrate the procedure, and simultaneously validify the suitability of the thin-wall shear stress distribution, we consider the case of the thin-walled tube, Fig. 5.

The shear stress τ is given in [12] as

$$\tau = \frac{R^2 W \cos\theta}{I_y} \tag{39}$$

from which (37) becomes

$$\frac{d\psi}{ds} = 2(1+\nu)R^2\cos\theta - \frac{\nu R^2}{2}(\cos 2\theta\cos\theta + \sin 2\theta\sin\theta) \tag{40}$$

noting $ds = Rd\theta$ and integrating with respect to θ gives

$$\psi = \frac{R^3\sin\theta}{2}(4+3\nu) + \text{constant} \tag{41}$$

and

$$\oint tx\psi ds = \int \frac{tR^5\sin 2\theta}{2}(4+3\nu)\,d\theta = \left(\frac{4+3\nu}{2}\right)R^5\pi t \tag{42}$$

we also have $\tau'_{xz} = \tau\cos\theta$, $\tau'_{yz} = \tau\sin\theta$, from which

$$\frac{\nu A}{W}\iint\left(\frac{x^2-y^2}{2}\right)\tau'_{xz}dxdy = -\frac{\nu AR^5 t}{2I_y}\int(\cos^4\theta - \cos^2\theta\sin^2\theta)d\theta = -\frac{\nu AR^5 t\pi}{4I_y} \tag{43}$$

and

$$\frac{\nu A}{W}\iint xy\tau'_{yz}dxdy = -\frac{\nu AR^5 t}{I_y}\int \sin^2\theta\cos^2\theta d\theta = -\frac{\nu AR^5 t\pi}{4I_y} \tag{44}$$

Substituting into (35) and then into (21) gives $K = (1+\nu)/(2+\nu)$.

This is identical to the value of the coefficient for a hollow tube using the exact stress function when the wall thickness is small.

Comparison With Flexural Wave Propagation Theories and Experimental Results

Long wavelength low phase velocity approximations to the exact frequency equations for solid circular sections and the plane stress thin rectangle can be obtained by expanding in ascending series the Bessel and hyperbolic functions, respectively, and appropriately truncating higher powers of the small quantities. The phase velocity predictions from such a procedure are given in [15] and agreement with the Timoshenko equation is found if the values

$K = 6(1+\nu)^2/(7 + 12\nu + 4\nu^2)$ for the circle

$K = 5(1+\nu)/(6+5\nu)$ for the rectangle

are employed. Since these are the values given by equation (21) it seems reasonable to infer that the assumed similitude of stress distribution for the beam performing long wavelength flexural vibration and the beam subjected to uniform body force loading is justified.

Fig. 6 shows the shear coefficient necessary to insure equivalence of phase velocity between Timoshenko theory and the theoretical predictions [5] for the circular cylindrical shell plotted against a thickness/wavelength parameter (H/L). For the solid circle, corresponding to $H/R = 2$, the required coefficient varies only slightly with wavelength from the long wavelength value given by (21). For the hollow circles $(H/R < 2)$ agreement is good at long wavelength but for the tube with thinner walls the required coefficient displays a marked reduction in value as wavelength decreases before returning to values more comparable with (21) as the ratio of thickness to wavelength approaches unity. This reduction would seem to imply a comparatively large shear deformation for a range of wavelengths, possible caused by modal coupling which the approximate theory would be unlikely to predict.

The task of comparing proposed derived values of the coefficient

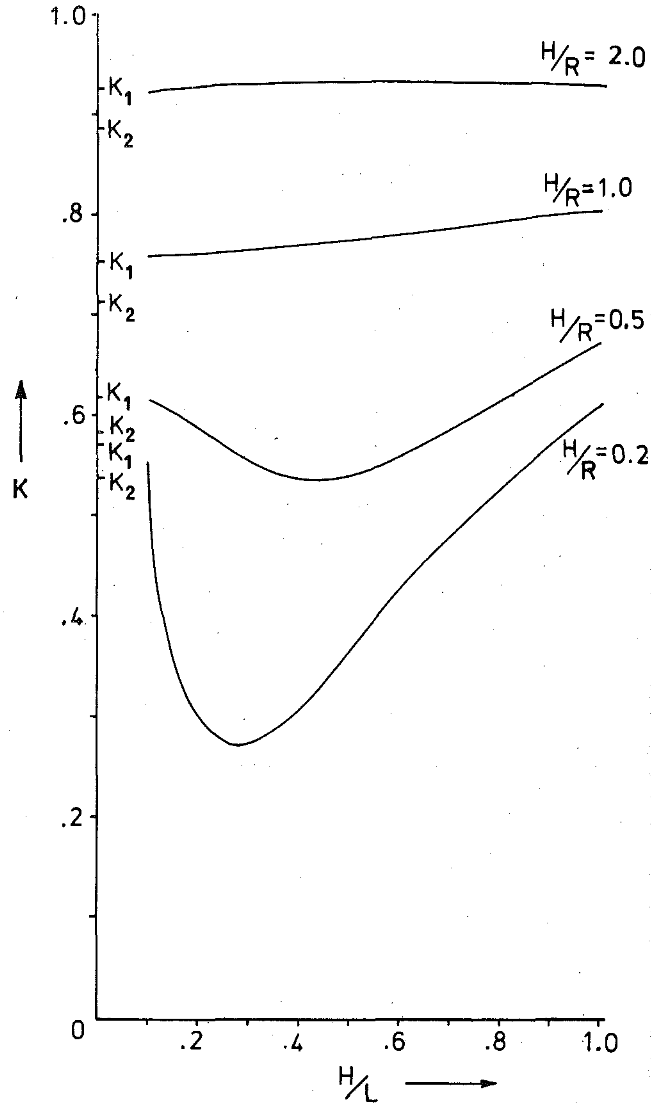

Fig. 6 Necessary shear coefficient to insure equivalence of phase velocities of Timoshenko beam theory and theoretical predictions of Armenàkas, Gazis, and Hermann for hollow circles; Poisson's ratio $\nu = 0.3$

with experimentally obtained values is made difficult by the too frequent lack of complete published data. Thus expression (31) for the rectangle is thought to be the first value of the coefficient to vary with the aspect ratio of the section, while for many of the experimental results published information on sectional dimensions is not given. According to Kaneko [1] the most complete experimental data which allows the best choice of coefficient is that by Spence and Seldin [13] and from this and his own experimental work, Kaneko concludes that the foregoing values for the circle and rectangle provide the best agreement with experimental results. Since agreement or disagreement between theoretical and experimental results is the ultimate test, more reliable data in this field would be desirable.

Discussion and Conclusions

The present method of obtaining the shear coefficient departs from previous derivations in two important ways. First, in place of the more usual Saint-Venant flexure stress distribution as the approximation to the distribution in a beam performing flexural vibration, we have employed the distribution of a beam subjected to uniform body force or gravity loading. Thus, while the cross-sectional distribution of the shear stresses τ_{xz} and τ_{yz} remains unchanged, they now vary linearly with axial coordinate in line with the linearly varying shear force. In addition the two direct transverse stresses σ_x and σ_y and the shear stress τ_{xy} are now nonzero and the longitudinal stress σ_z no longer varies linearly through the depth of the beam but is a function of the sectional coordinates. From equation (14) it may be seen that the moment-curvature relationship for the gravity loaded beam takes into account the direct stresses σ_x and σ_y and the sectional variation of longitudinal strain; the two additional terms (equation (22)) in the denominator of the present coefficient arise from inclusion of the direct transverse stresses.

Second, we have consciously modified the Kennard and Leibowitz method by employing an integrated rather than center-line curvature. The effect of this modification is to include the complete term accounting for the inertia of motion of cross-sectional distortion, or lateral contraction inertia, as may be verified by referring to Love [16] where an equation is obtained accounting for rotatory inertia and the lateral contraction inertia. This latter term is zero for sections possessing "kinetic symmetry," e.g., circular and square sections, since it is based on the difference in the principal second moments of area of the section.

It is notable that comparison of behavior of the Timoshenko beam with the appropriate coefficient in relation to exact solutions has been made solely on the basis of equivalence of phase velocities and since it has been remarked by other authors that such agreement does not guarantee equivalent agreement for stresses and displacement, on the basis of the present work it is reasonable to speculate that pointwise stress and displacement of the vibrating beam may be obtained with some confidence from the gravity loaded beam.

References

1 Kaneko, T., "On Timoshenko's Correction for Shear in Vibrating Beams," *Journal of Physics D: Applied Physics,* Vol. 8, 1975, pp. 1927–1936.

2 Pochhammer, L., "Über die Fortpflanzungsgeswindigkeiten Kleiner Swingungen in Einem Unbergrenzten Isotropen Kreiscylinder," *Journal für die Reine und Angew. Math.* (Crelle), Bd. 81, 1876, pp. 324–336.

3 Lamb, H., "On Waves in an Elastic Plate," *Proceedings of the Royal Society,* London, Series A, Vol. 93, 1917, pp. 114–128.

4 Stephen, N., "On the Variation of Timoshenko's Shear Coefficient With Frequency," ASME JOURNAL OF APPLIED MECHANICS, Vol. 45, 1978, pp. 695–697.

5 Armenàkas, A., Gazis, D., and Herrmann, G., *Free Vibrations of Circular Cylindrical Shells,* Pergamon Press, London, 1969.

6 Wong, P., Miklowitz, J., and Scott, R., "Propagation of Harmonic Flexural Waves in an Infinite Elastic Rod of Elliptical Cross Section," *Journal of the Acoustical Society of America,* Vol. 40, 1960, pp. 393–398.

7 Cowper, G., "The Shear Coefficient in Timoshenko's Beam Theory," ASME JOURNAL OF APPLIED MECHANICS, Vol. 33, 1966, pp. 335–340.

8 Leibowitz, R., and Kennard, E., "Theory of Freely Vibrating Nonuniform Beams, Including Methods of Solution and Applications to Ships," David Taylor Model Basin, Report 1317, 1961.

9 Timoshenko, S., and Goodier, J., *Theory of Elasticity,* 3rd ed., McGraw-Hill, New York, p. 48.

10 Love, A. E. H., *A Treatise on the Mathematical Theory of Elasticity,* Dover Publications, New York, 1944, Chapter 16.

11 Love, A. E. H. *A Treatise on the Mathematical Theory of Elasticity,* Dover Publications, New York, 1944, Chapter 15.

12 Shanley, F., *Mechanics of Materials,* McGraw-Hill, New York, 1967.

13 Spence, G. B., and Seldin, E. J., "Sonic Resonance of a Bar and a Compound Torsion Oscillator," *Journal of Applied Physics,* Vol. 41, No. 8, 1970, pp. 3383–3389.

14 Prescott, J., "Elastic Waves and Vibrations of Thin Rods," *Philosophical Magazine,* Series 7, Vol. 33, 1942, pp. 703–754.

15 Timoshenko, S., "On the Transverse Vibrations of Bars of Uniform Cross Section," *Philosophical Magazine,* Vol. 43, 1922, pp. 125–131.

16 Love, A. E. H., *A Treatise of the Mathematical Theory of Elasticity,* Dover Publications, New York, 1944, Chapter 20.

M. Sathyamoorthy
Research Associate.

C. Y. Chia
Professor.

Department of Civil Engineering,
The University of Calgary,
Calgary, T2N 1N4, Canada

Effect of Transverse Shear and Rotatory Inertia on Large Amplitude Vibration of Anisotropic Skew Plates

Part 1—Theory

A nonlinear vibration theory for anisotropic elastic skew plates is developed with the aid of Hamilton's principle. The effects of transverse shear deformation and rotatory inertia are included in the analysis. The differential equations formulated here readily reduce to the dynamic von Karman-type equations of skew plates when the shear and rotatory inertia effects are neglected. Solutions to these equations are presented for various boundary conditions in the second part of the paper.

Introduction

The dynamic von Karman nonlinear plate theory has been derived by Herrmann [1] and generalized to include the effects of the transverse shear and rotatory inertia in the theories of orthotropic plates by Medwadowski [2] and of anisotropic plates by Ebcioglu [3]. Some other nonlinear plate theories [4–7] also take these effects into account. A solution to these nonlinear equations with these effects, however, cannot be found in the literature. Based on the Berger approach, Wu and Vinson have included the transverse shear deformation and rotatory inertia effects in their analyses of isotropic [8] and specially orthotropic [9] rectangular plates. An improved version of this Berger-type theory has recently been suggested by Sathyamoorthy [10] with numerical results reported for specially orthotropic rectangular plates. The combined effects of the transverse shear deformation and rotatory inertia on the large amplitude vibrations of isotropic skew plates have been also discussed by Sathyamoorthy based on the Berger approach [11] and on a generalization of the classical von Karman plate theory [12]. A review of literature indicates no analysis of anisotropic skew plates is available. The work of Ashton [13] neglecting the transverse shear deformation in the linear static analysis is the only one known to the authors' best knowledge in the elastic behavior of anisotropic skew plates.

In the first part of the paper, Hamilton's principle and the variational calculus are utilized to derive a system of differential equations for the large amplitude flexural vibration of a skew plate in terms of forces and moments, lateral displacement and the two so-called slope functions. Direct stresses normal to the middle surface of the plate are assumed to be of negligible order of magnitude. The plate under consideration is made of orthotropic material whose principal axes of elasticity are inclined arbitrarily with respect to the plate axes as shown in Fig. 1. Airy's stress function and the condition of compatibility are introduced. These equations are reduced to a system of two equations for the lateral displacement and stress function with the terms of transverse shear deformation and rotatory inertia separately grouped together. In addition these two coupled nonlinear differential equations under the present simplifying assumption are solvable. Several examples for illustration of these effects on nonlinear flexural vibrations of anisotropic skew plates are presented in the second part of this paper.

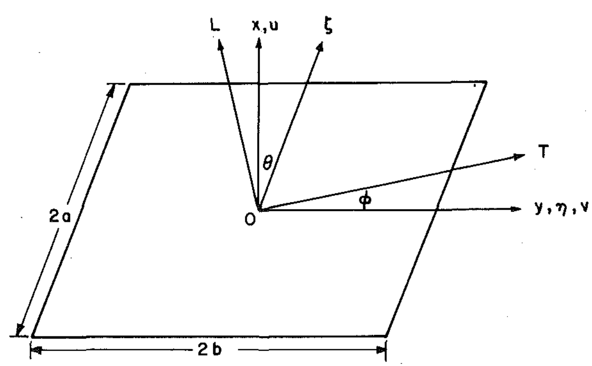

Fig. 1 Geometry and coordinate system of skew plate

Equations of Motion

Consider a skew plate of constant thickness h composed of homo-

Contributed by the Applied Mechanics Division for publication in the JOURNAL OF APPLIED MECHANICS.

Discussion on this paper should be addressed to the Editorial Department, ASME, United Engineering Center, 345 East 47th Street, New York, N. Y. 10017, and will be accepted until June 1, 1980. Readers who need more time to prepare a discussion should request an extension from the Editorial Department. Manuscript received by ASME Applied Mechanics Division, March, 1979; final revision, July, 1979.

geneous anisotropic material whose coordinate system is shown in Fig. 1. The origins of the coordinate systems are located at the center of the midplane of the undeformed plate. The stress-strain relations for the plate may be written as

$$\begin{Bmatrix} \sigma_\zeta \\ \sigma_\eta \\ \sigma_z \\ \sigma_{\eta z} \\ \sigma_{z\zeta} \\ \sigma_{\zeta\eta} \end{Bmatrix} = \begin{bmatrix} a_{11} & a_{12} & a_{13} & 0 & 0 & a_{16} \\ a_{12} & a_{22} & a_{23} & 0 & 0 & a_{26} \\ a_{13} & a_{23} & a_{33} & 0 & 0 & a_{36} \\ 0 & 0 & 0 & a_{44} & a_{45} & 0 \\ 0 & 0 & 0 & a_{45} & a_{55} & 0 \\ a_{16} & a_{26} & a_{36} & 0 & 0 & a_{66} \end{bmatrix} \begin{Bmatrix} \epsilon_\zeta \\ \epsilon_\eta \\ \epsilon_z \\ \epsilon_{\eta z} \\ \epsilon_{z\zeta} \\ \epsilon_{\zeta\eta} \end{Bmatrix} \quad (1)$$

or written in an alternate form as

$$\{\epsilon_{ij}\} = [b_{ij}]\{\sigma_{ij}\} \quad (2)$$

where the coefficients a_{ij} and b_{ij} are such that $a_{ij} = a_{ji}$ and $b_{ij} = b_{ji}$. Since only free vibration is considered here, the normal stress, σ_z, is assumed to be zero. Also, the normal strain is assumed to be zero because of the assumption that w is independent of z [9]. The elastic stiffnesses a_{ij} in equation (1) are defined as follows:

$$\begin{aligned}
& a_{11} = c_{11}/c^3,\ a_{12} = c_{11}s^2/c^3 + c_{12}/c - 2sc_{16}/c^2 \\
& a_{13} = 0,\ a_{16} = c_{16}/c^2 - c_{11}s/c^3 \\
& a_{22} = cc_{22} + c_{12}s^2/c - 2sc_{26} - s^2a_{12} - 2sa_{26},\ a_{23} = 0 \\
& a_{26} = c_{26} - sc_{12}/c - s^2a_{16} - 2sa_{66},\ a_{33} = a_{36} = 0 \\
& a_{44} = cc_{66} - sc_{56}/c - sa_{45},\ a_{45} = cc_{56} - sc_{55}/c \\
& a_{55} = c_{55}/c,\ a_{66} = c_{66}/c - c_{16}s/c^2 - sa_{16},\ c = \cos\theta,\ s = \sin\theta \quad (3)
\end{aligned}$$

The coefficients b_{ij} in equation (2) are defined in Appendix A and coefficients c_{ij} in equation (3) are the material constants of the anisotropic skew plate with reference to the x, y coordinate system. These constants may be expressed in terms of the orthotropic properties along arbitrary principal directions (L, T) by a coordinate transformation as

$$\begin{Bmatrix} c_{11} \\ c_{12} \\ c_{22} \\ c_{16} \\ c_{26} \\ c_{55} \\ c_{56} \\ c_{66} \end{Bmatrix} = \begin{bmatrix} m^4 & 2m^2n^2 & n^4 & 0 & 0 & 4m^2n^2 \\ m^2n^2 & m^4+n^4 & m^2n^2 & 0 & 0 & -4m^2n^2 \\ n^4 & 2m^2n^2 & m^4 & 0 & 0 & 4m^2n^2 \\ nm^3 & mn(n^2-m^2) & -mn^3 & 0 & 0 & 2mn(n^2-m^2) \\ mn^3 & mn(m^2-n^2) & -nm^3 & 0 & 0 & 2mn(m^2-n^2) \\ 0 & 0 & 0 & m^2 & n^2 & 0 \\ 0 & 0 & 0 & -mn & mn & 0 \\ m^2n^2 & -2m^2n^2 & m^2n^2 & 0 & 0 & (m^2-n^2)^2 \end{bmatrix} \begin{Bmatrix} E_L/\mu \\ \nu_{LT}E_T/\mu \\ E_T/\mu \\ G_{LZ} \\ G_{TZ} \\ G_{LT} \end{Bmatrix} \quad (4)$$

in which E_L and E_T are the major and minor Young's moduli, ν_{LT} and ν_{TL} are the Poisson's ratios and G_{LT}, G_{LZ}, G_{TZ} are the shear moduli and in which

$$m = \cos\phi,\ n = \sin\phi,\ \mu = 1 - \nu_{LT}\nu_{TL},\ \text{and}\ \nu_{LT}E_T = \nu_{TL}E_L \quad (5)$$

In order to take into account the effects of the transverse shear deformation and rotatory inertia, the displacement components in the oblique coordinates at a distance z away from the midsurface may be taken in the following form:

$$\begin{aligned}
& u(\zeta,\eta,z,t) = cu^0(\zeta,\eta,t) + sv^0(\zeta,\eta,t) + z\alpha(\zeta,\eta,t) \\
& v(\zeta,\eta,z,t) = v^0(\zeta,\eta,t) + z\,\beta(\zeta,\eta,t) \\
& w(\zeta,\eta,z,t) = w^0(\zeta,\eta,t) = w(\zeta,\eta,t) \quad (6)
\end{aligned}$$

The midsurface strains in terms of the displacement components u^0, v^0, and w may be written as

$$\begin{aligned}
& \epsilon_\zeta^0 = cu^0_{,\zeta} + sv^0_{,\zeta} + (w_{,\zeta})^2/2 \\
& \epsilon_\eta^0 = v^0_{,\eta} + (w_{,\eta})^2/2 \\
& \epsilon_{\zeta\eta}^0 = cu^0_{,\eta} + sv^0_{,\eta} + v^0_{,\zeta} + w_{,\zeta}w_{,\eta} \quad (7)
\end{aligned}$$

The strains at a distance z measured from the midsurface are assumed to be

$$\begin{aligned}
& \epsilon_\zeta = \epsilon_\zeta^0 + z\alpha_{,\zeta} \\
& \epsilon_\eta = \epsilon_\eta^0 + z\beta_{,\eta} \\
& \epsilon_z = 0,\ \epsilon_{\zeta\eta} = \epsilon_{\zeta\eta}^0 + z(\alpha_{,\eta} + \beta_{,\zeta}) \\
& \epsilon_{\zeta z} = \alpha + w_{,\zeta},\ \epsilon_{\eta z} = \beta + w_{,\eta} \quad (8)
\end{aligned}$$

The stress resultants N_{ij} and the stress couples M_{ij} by definition are

$$N_{ij} = \int_{-h/2}^{h/2} \sigma_{ij} d_z,\quad M_{ij} = \int_{-h/2}^{h/2} \sigma_{ij} z dz \quad (9)$$

Equations (1) and (8) are substituted into equation (9) and integrations are performed to obtain

$$\begin{Bmatrix} N_\zeta \\ N_\eta \\ N_{\zeta\eta} \end{Bmatrix} = h \begin{bmatrix} a_{11} & a_{12} & a_{16} \\ a_{12} & a_{22} & a_{26} \\ a_{16} & a_{26} & a_{66} \end{bmatrix} \begin{Bmatrix} \epsilon_\zeta^0 \\ \epsilon_\eta^0 \\ \epsilon_{\zeta\eta}^0 \end{Bmatrix} \quad (10)$$

$$\begin{Bmatrix} M_\zeta \\ M_\eta \\ M_{\zeta\eta} \end{Bmatrix} = \frac{h^3}{12} \begin{bmatrix} a_{11} & a_{12} & a_{16} \\ a_{12} & a_{22} & a_{26} \\ a_{16} & a_{26} & a_{66} \end{bmatrix} \begin{Bmatrix} \alpha_{,\zeta} \\ \beta_{,\eta} \\ \alpha_{,\eta} + \beta_{,\zeta} \end{Bmatrix} \quad (11)$$

The strain energies due to stretching and bending of the plate,

Nomenclature

$2a$, $2b$ = plate dimensions

D = isotropic plate flexural rigidity $Eh^3/[12(1-\nu^2)]$

$E_L, E_T, \nu_{LT}, \nu_{LT}, G_{LT}, G_{LZ}, G_{TZ}$ = elastic orthotropic material constants referred to principal directions (L, T)

h = plate thickness

N_{ij}, M_{ij} = membrane forces and moments per unit width

Q_ζ, Q_η = transverse shear forces per unit width

$q(\zeta, \eta)$ = lateral applied load per unit area of the plate

$R_i = \begin{cases} 1, \text{ when rotatory inertia effect is included} \\ 0, \text{ when rotatory inertia effect is not included} \end{cases}$

$T_s = \begin{cases} 1, \text{ when transverse shear effect is included} \\ 0, \text{ when transverse shear effect is not included} \end{cases}$

u^0, v^0, w = midsurface displacement components along x, y, z-directions, respectively

x, y, z = rectangular Cartesian coordinates

α, β = slope functions defined by equation (6)

ζ, η = oblique coordinates

θ = skew angle

λ = aspect ratio (a/b)

ρ = mass density

ϕ = orientation angle of filaments

denoted by U_s and U_b, respectively, and the kinetic energy of the plate U_k may be expressed in the form

$$U_s = \frac{1}{2} \iint [a_{11}(\epsilon_\zeta^0)^2 + a_{22}(\epsilon_\eta^0)^2 + a_{66}(\epsilon_{\zeta\eta}^0)^2 + 2a_{12}\epsilon_\zeta^0\epsilon_\eta^0 + 2a_{16}\epsilon_\zeta^0\epsilon_{\zeta\eta}^0 + 2a_{26}\epsilon_\eta^0\epsilon_{\zeta\eta}^0] d\zeta d\eta \quad (12)$$

$$U_b = \iint \Big[M_\zeta \alpha_{,\zeta} + M_\eta \beta_{,\eta} + M_{\zeta\eta}(\alpha_{,\eta} + \beta_{,\zeta}) + Q_\zeta(\alpha + w_{,\zeta}) + Q_\eta(\beta + w_{,\eta}) - \frac{6}{h^3}(b_{11}M_\zeta^2 + b_{22}M_\eta^2 + b_{66}M_{\zeta\eta}^2 + 2b_{12}M_\zeta M_\eta + 2b_{16}M_\zeta M_{\zeta\eta} + 2b_{26}M_\eta M_{\zeta\eta}) - \frac{3}{5h}(b_{55}Q_\zeta^2 + b_{66}Q_\eta^2 + 2b_{56}Q_\zeta Q_\eta) \Big] d\zeta d\eta \quad (13)$$

$$U_k = \frac{\rho}{2} \iint \left[h(u_{,t}^2 + v_{,t}^2 + w_{,t}^2) + \frac{h^3}{12}(\alpha_{,t}^2 + \beta_{,t}^2) \right] d\zeta d\eta \quad (14)$$

The equations of motion are now derived from Hamilton's principle by the use of equations (12)–(14). The corresponding Euler's equations constitute a system of 13 equations in terms of membrane forces $N_\zeta, N_\eta, N_{\zeta\eta}$; moments $M_\zeta, M_\eta, M_{\zeta\eta}$; transverse shear forces Q_ζ, Q_η; displacement components u^0, v^0, w and slope functions α and β as given below:

$$M_{\zeta,\zeta} + M_{\zeta\eta,\eta} - Q_\zeta - \frac{\rho h^3}{12} R_i \alpha_{,tt} = 0 \quad (15)$$

$$M_{\eta,\eta} + M_{\zeta\eta,\zeta} - Q_\eta - \frac{\rho h^3}{12} R_i \beta_{,tt} = 0 \quad (16)$$

$$\alpha_{,\zeta} - \frac{12}{h^3}(b_{11}M_\zeta + b_{12}M_\eta + b_{16}M_{\zeta\eta}) = 0 \quad (17)$$

$$\beta_{,\eta} - \frac{12}{h^3}(b_{12}M_\zeta + b_{22}M_\eta + b_{26}M_{\zeta\eta}) = 0 \quad (18)$$

$$\alpha_{,\eta} + \beta_{,\zeta} - \frac{12}{h^3}(b_{16}M_\zeta + b_{26}M_\eta + b_{66}M_{\zeta\eta}) = 0 \quad (19)$$

$$\alpha + w_{,\zeta} - \frac{6T_s}{5h}(b_{55}Q_\zeta + b_{45}Q_\eta) = 0 \quad (20)$$

$$\beta + w_{,\eta} - \frac{6T_s}{5h}(b_{45}Q_\zeta + b_{44}Q_\eta) = 0 \quad (21)$$

$$\epsilon_\zeta^0 - \frac{1}{h}(b_{11}N_\zeta + b_{12}N_\eta + b_{16}N_{\zeta\eta}) = 0 \quad (22)$$

$$\epsilon_\eta^0 - \frac{1}{h}(b_{12}N_\zeta + b_{22}N_\eta + b_{26}N_{\zeta\eta}) = 0 \quad (23)$$

$$\epsilon_{\zeta\eta}^0 - \frac{1}{h}(b_{16}N_\zeta + b_{26}N_\eta + b_{66}N_{\zeta\eta}) = 0 \quad (24)$$

$$N_{\zeta,\zeta} + N_{\zeta\eta,\eta} = \rho h u_{,tt}^0 \quad (25)$$

$$N_{\eta,\eta} + N_{\zeta\eta,\zeta} = \rho h v_{,tt}^0 \quad (26)$$

$$Q_{\zeta,\zeta} + Q_{\eta,\eta} + N_\zeta w_{,\zeta\zeta} + N_\eta w_{,\eta\eta} + 2N_{\zeta\eta} w_{,\zeta\eta} + J_1 = 0 \quad (27)$$

where

$$J_1 = q(\zeta, \eta) - \rho h w_{,tt} \quad (28)$$

In these equations the so-called tracing constants T_s and R_i are introduced to identify the terms which characterize the effects of the transverse shear deformation and rotatory inertia, respectively.

The shearing forces Q_ζ and Q_η are obtained in terms of α and β by solving equations (15)–(19) and then substituted into equations (20) and (21). The resulting two equations are given by

$$\alpha + w_{,\zeta} - T_s(d_1\alpha_{,\zeta\zeta} + d_2\alpha_{,\zeta\eta} + d_3\alpha_{,\eta\eta} + d_4\beta_{,\zeta\zeta} + d_5\beta_{,\zeta\eta} + d_6\beta_{,\eta\eta}) + R_iT_s(d_7\alpha_{,tt} + d_8\beta_{,tt}) = 0 \quad (29)$$

$$\beta + w_{,\eta} - T_s(d_9\alpha_{,\zeta\zeta} + d_{10}\alpha_{,\zeta\eta} + d_{11}\alpha_{,\eta\eta} + d_{12}\beta_{,\zeta\zeta} + d_{13}\beta_{,\zeta\eta} + d_{14}\beta_{,\eta\eta}) + R_iT_s(d_{15}\alpha_{,tt} + d_{16}\beta_{,tt}) = 0 \quad (30)$$

The coefficients d_1 to d_{16} are defined in Appendix B. Assume that the in-plane inertia effects are negligibly small, and introduce a stress function F such that

$$N_\zeta = hF_{,\eta\eta}, \quad N_\eta = hF_{,\zeta\zeta}, \quad N_{\zeta\eta} = -hF_{,\zeta\eta} \quad (31)$$

When $Q_\zeta, Q_\eta, N_\zeta, N_\eta$, and $N_{\zeta\eta}$ are eliminated from equations (15)–(19) and (31), equation (27) can be written as

$$J_1 + J_2(F, w) + J_3(\alpha, \beta) = 0 \quad (32)$$

where

$$J_2 = h(F_{,\eta\eta}w_{,\zeta\zeta} + F_{,\zeta\zeta}w_{,\eta\eta} - 2F_{,\zeta\eta}w_{,\zeta\eta})$$

$$J_3 = e_1\alpha_{,\zeta\zeta\zeta} + e_2\alpha_{,\zeta\zeta\eta} + e_3\alpha_{,\zeta\eta\eta} + e_4\alpha_{,\eta\eta\eta} + e_5\beta_{,\zeta\zeta\zeta} + e_6\beta_{,\zeta\zeta\eta} + e_7\beta_{,\zeta\eta\eta} + e_8\beta_{,\eta\eta\eta} + e_9R_i(\alpha_{,\zeta tt} + \beta_{,\eta tt}) \quad (33)$$

The coefficients e_1–e_9 are defined in Appendix B. The compatibility condition in terms of F may now be obtained by solving equations (22)–(24) and by use of equation (31). The result is

$$b_{22}F_{,\zeta\zeta\zeta\zeta} - 2b_{26}F_{,\zeta\zeta\zeta\eta} + (2b_{12} + b_{66})F_{,\zeta\zeta\eta\eta} - 2b_{16}F_{,\zeta\eta\eta\eta} + b_{11}F_{,\eta\eta\eta\eta} = (w_{,\zeta\eta})^2 - w_{,\zeta\zeta}w_{,\eta\eta} \quad (34)$$

Equations (29), (30), (32), and (34) constitute a system of four equations governing the large amplitude flexural vibrations of anisotropic skew plates. The effects of the transverse shear deformation and rotatory inertia are included in these equations. When a_{ij} are suitably chosen as indicated in Appendix D, these equations can be shown to readily reduce to the corresponding equations applicable for isotropic skew plates [12].

Equations (29) and (30) are solved simultaneously for α and β and substituted in equation (32) thereby eliminating α and β from the governing equations. The equation of motion in the lateral direction of the vibrating plate thus becomes

$$L(J_1 + J_2) + M(w) = 0 \quad (35)$$

where the differential operators L and M are defined as

$$L = r_1\frac{\partial^4}{\partial\zeta^4} + r_2\frac{\partial^4}{\partial\zeta^2\partial\eta^2} + r_3\frac{\partial^4}{\partial\eta^4} + r_4\frac{\partial^4}{\partial\zeta^3\partial\eta} + r_5\frac{\partial^4}{\partial\zeta\partial\eta^3} + r_6\frac{\partial^4}{\partial t^4} + r_7\frac{\partial^4}{\partial\zeta^2\partial t^2} + r_8\frac{\partial^4}{\partial\zeta\partial\eta\partial t^2} + r_9\frac{\partial^4}{\partial\eta^2\partial t^2} + r_{10}\frac{\partial^2}{\partial\zeta^2} + r_{11}\frac{\partial^2}{\partial\eta^2} + r_{12}\frac{\partial^2}{\partial\zeta\partial\eta} - r_{13}\frac{\partial^2}{\partial t^2} - 1 \quad (36)$$

$$M = N + e_9R_i\left(\frac{\partial^4}{\partial\zeta^2\partial t^2} + \frac{\partial^4}{\partial\eta^2\partial t^2}\right) + e_{13}\frac{\partial^6}{\partial\zeta^2\partial\eta^2\partial t^2} + e_{14}\frac{\partial^6}{\partial\zeta^4\partial t^2} + e_{15}\frac{\partial^6}{\partial\zeta^3\partial\eta\partial t^2} + e_9R_id_{15}\frac{\partial^6}{\partial\zeta^2\partial t^4} + e_{16}\frac{\partial^6}{\partial\zeta\partial\eta\partial t^4} + e_{17}\frac{\partial^6}{\partial\zeta\partial\eta^3\partial t^2} + e_{18}\frac{\partial^6}{\partial\eta^4\partial t^2} + e_9R_id_7\frac{\partial^6}{\partial\eta^2\partial t^4} \quad (37)$$

with N being given by

$$N = e_1\frac{\partial^4}{\partial\zeta^4} + e_{10}\frac{\partial^4}{\partial\zeta^2\partial\eta^2} + e_{11}\frac{\partial^4}{\partial\zeta^3\partial\eta} + e_8\frac{\partial^4}{\partial\eta^4} + e_{12}\frac{\partial^4}{\partial\zeta\partial\eta^3} + e_{19}\frac{\partial^6}{\partial\zeta^6} + e_{20}\frac{\partial^6}{\partial\zeta^4\partial\eta^2} + e_{21}\frac{\partial^6}{\partial\zeta^5\partial\eta} + e_{22}\frac{\partial^6}{\partial\zeta^3\partial\eta^3} + e_{23}\frac{\partial^6}{\partial\zeta^2\partial\eta^4} + e_{24}\frac{\partial^6}{\partial\zeta\partial\eta^5} + e_{25}\frac{\partial^6}{\partial\eta^6} \quad (38)$$

The coefficients in equations (36)–(38) are defined in Appendix C. Equations (34) and (35) governing the large amplitude vibrations of anisotropic skew plates include the effects of the transverse shear deformation and rotatory inertia in the analysis. These equations may be specialized for various cases.

(*a*) *No Transverse Shear Effect* ($T_s = 0$, $R_i = 1$).

Let us take $T_s = 0$ in equations (29) and (30). It follows that

$$\alpha = -w_{,\zeta}, \quad \beta = -w_{,\eta} \tag{39}$$

With these expressions for α and β, equation (32) reduces to

$$J_1 + J_2 - J_4 - e_9 R_i (w_{,\zeta\zeta tt} + w_{,\eta\eta tt}) = 0 \tag{40}$$

where

$$J_4 = e_1 w_{,\zeta\zeta\zeta\zeta} + (e_2 + e_5) w_{,\zeta\zeta\zeta\eta} + (e_3 + e_6) w_{,\zeta\zeta\eta\eta} + (e_4 + e_7) w_{,\zeta\eta\eta\eta} + e_8 w_{,\eta\eta\eta\eta} \tag{41}$$

Equations (34) and (40) also govern the large amplitude vibration of anisotropic skew plates but the transverse shear effect has been neglected. These equations, however, include the effect of the rotatory inertia.

(*b*) *No Rotatory Inertia Effect* ($T_s = 1, R_i = 0$)

The governing equations in this case can be obtained by putting $R_i = 0$ in equation (32). It follows that

$$L(J_1 + J_2) + N(w) = 0 \tag{42}$$

Thus equations (34) and (42) constitute a system of two equations governing the large amplitude vibrations of anisotropic skew plates including the effect of the transverse shear deformation only.

(*c*) *Transverse Shear and Rotatory Inertia Effects Both Not Included* ($T_s = R_i = 0$)

When the effects of the transverse shear deformation and rotatory inertia are both neglected in the analysis, equations (29), (30), and (32) reduce to

$$J_1 + J_2 - J_4 = 0 \tag{43}$$

Equations (34) and (43) are the required equations for the large amplitude flexural vibration of anisotropic skew plates in the sense of von Karman. With appropriately simplified coefficients for a_{ij} these equations will reduce to those applicable for isotropic and orthotropic skew plates and are in agreement with the equations available in literature.

From the foregoing derivations it is clear that the system of equations (29), (30), (32), and (34) including the effects of the transverse shear deformation and rotatory inertia can be used as a basic set from which the required set of governing equations for its special cases can be easily obtained such that the individual effect of the transverse shear deformation or the rotatory inertia on the dynamical behavior of isotropic, orthotropic, and anisotropic skew plates can be investigated. In a similar manner, if these effects can be neglected in the analysis, the basic equations can be simplified correspondingly. The present system of equations (29), (30), (32), and (34) and the feasibility of reduction of these equations to those for special cases are considered as improvements compared to the plate theory available in the literature [8, 9].

The system of nonlinear differential equations (34) and (35) is of the tenth order. Therefore, five boundary conditions, as against four in the classical von Karman plate theory, are required in the present theory. The five boundary conditions along each edge consist of three corresponding to the out-of-plane conditions of the linear theory (with the thickness-shear flexibility taken into account) and two corresponding to the in-plane conditions of the nonlinear theory. These conditions which are obtained from the variational technique may be taken as a combination of the out-of-plane and in-plane conditions.

The out-of-plane conditions are

I All Edges Simply Supported (*SS*)

$$\begin{aligned} w &= M_\zeta \cos\theta = M_{\zeta\eta} = 0 \quad \text{at } \zeta = \pm a \\ w &= M_\eta \cos\theta = M_{\zeta\eta} = 0 \quad \text{at } \eta = \pm b \end{aligned} \tag{44}$$

II Two Opposite Edges Simply Supported and the Others Clamped (*SC*)

$$\begin{aligned} w &= M_\zeta \cos\theta = M_{\zeta\eta} = 0 \quad \text{at } \zeta = \pm a \\ w &= \alpha = \beta = 0 \quad \text{at } \eta = \pm b \end{aligned} \tag{45}$$

III All Edges Clamped (*CC*)

$$\begin{aligned} w &= \alpha = \beta = 0 \quad \text{at } \zeta = \pm a \\ w &= \alpha = \beta = 0 \quad \text{at } \eta = \pm b \end{aligned} \tag{46}$$

and the in-plane conditions are

(*a*) All Edges Movable (*M*)

$$\begin{aligned} P_\zeta &= P_{\zeta\eta} = 0 \quad \text{at} \quad \zeta = \pm a \\ P_\eta &= P_{\zeta\eta} = 0 \quad \text{at} \quad \eta = \pm b \end{aligned} \tag{47}$$

where

$$\begin{gathered} P_\zeta = h \int_{-b}^{b} F_{,\eta\eta} d\eta, \quad P_\eta = h \int_{-a}^{a} F_{,\zeta\zeta} d\zeta \\ P_{\zeta\eta} = h \int_{-a}^{a} F_{,\zeta\eta} d\zeta = h \int_{-b}^{b} F_{,\zeta\eta} d\eta \end{gathered} \tag{48}$$

(*b*) All Edges Immovable (*IM*)

$$\begin{aligned} u^0 &= v^0 = 0 \quad \text{at } \zeta = \pm a \\ u^0 &= v^0 = 0 \quad \text{at } \eta = \pm b \end{aligned} \tag{49}$$

Solutions to the system of equations (34) and (35) governing the nonlinear flexural vibration of anisotropic skew plates are presented for six combinations of boundary conditions (44)–(49) in Part 2.

Acknowledgment

The results presented in this paper were obtained in the course of research sponsored by the National Sciences and Engineering Research Council of Canada.

References

1 Herrmann, G., "Influence of Large Amplitudes on Flexural Motions of Elastic Plates," National Advisory Committee for Aeronautics, Technical Note 3578, Washington, D.C., May 1955.

2 Medwadowski, S. J., "A Refined Theory of Elastic, Orthotropic Plates," ASME JOURNAL OF APPLIED MECHANICS, Vol. 25, 1958, pp. 437–443.

3 Ebcioglu, I. K., "A Large Deflection Theory of Anisotropic Plates," *Ingenieur-Archiv,* Vol. 33, 1964, pp. 396–403.

4 Habip, L. M., "Theory of Elastic Plates in the Reference State," *International Journal of Solids and Structures,* Vol. 2, 1966, pp. 157–166.

5 Kaul, R. K., "Finite Thermal Oscillations of Thin Plates," *International Journal of Solids and Structures,* Vol. 2, 1966, pp. 337–350.

6 Chia, C. Y., "Nonlinear Theory of Heterogeneous and Anisotropic Plates," *Proceedings of the 3rd Australasian Conference on the Mechanics of Structures and Materials,* Vol. II, Session B2-Plate Theory, University of Auckland, 1971, pp. 1–25.

7 Schmidt, R., "A Refined Nonlinear Theory of Plates With Transverse Shear Deformation," *Journal of Industrial Mathematics Society,* Vol. 27, 1977, pp. 23–37.

8 Wu, C. I., and Vinson, J. R., "Influences of Large Amplitudes, Transverse Shear Deformation, and Rotatory Inertia on Lateral Vibrations of Transversely Isotropic Plates," ASME JOURNAL OF APPLIED MECHANICS, Vol. 36, 1969, pp. 254–460.

9 Wu, C. I., and Vinson, J. R., "On the Nonlinear Oscillations of Plates Composed of Composite Materials," *Journal of Composite Materials,* Vol. 3, 1969, pp. 548–561.

10 Sathyamoorthy, M., "Vibration of Plates Considering Shear and Rotatory Inertia," *AIAA Journal,* Vol. 16, 1978, pp. 285–286.

11 Sathyamoorthy, M., "Shear and Rotatory Inertia Effects on Large Amplitude Vibration of Skew Plates," *Journal of Sound and Vibration,* Vol. 52, 1977, pp. 155–163.

12 Sathyamoorthy, M., "Vibration of Skew Plates at Large Amplitudes Including Shear and Rotatory Inertia Effects," *International Journal of Solids and Structures,* Vol. 14, 1978, pp. 869–880.

13 Ashton, J. E., "Clamped Skew Plates of Orthotropic Material Under Transverse Load," *Developments in Mechanics,* Vol. 5, 1969, pp. 297–306.

APPENDIX *A*

The elements b_{ij} of the matrix $[b_{ij}]$ in equation (2) which are equal to those of matrix $[a_{ij}]^{-1}$ are

$$b_{11} = (1 - a_{12}b_{12} - a_{16}a_{16})/a_{11}, \; b_{12} = (a_{12} - n_2 b_{16})/n_4$$

$$b_{16} = n_1 a_{12}/(n_1 n_2 - n_3 n_4), \; b_{22} = (1 - a_{12}b_{12} - a_{26}b_{26})/a_{22}$$

$b_{26} = (n_4 b_{12} - a_{12})/n_1,\ b_{44} = a_{55}/n_5, \quad b_{45} = (1 - a_{44}b_{44})/a_{45}$

$b_{55} = (1 - a_{45}b_{45})/a_{55},\ b_{66} = (1 - a_{16}b_{16} - a_{26}b_{26})/a_{66}$

where

$n_1 = a_{16}a_{22} - a_{26}a_{12},\ n_2 = a_{12}a_{16} - a_{11}a_{26},$

$n_3 = a_{26}a_{16} - a_{66}a_{12},\ n_4 = a_{12}^2 - a_{11}a_{22},\ n_5 = a_{44}a_{55} - a_{45}^2$

APPENDIX *B*

The coefficients in equations (29), (30), and (33) are

$d_1 = d(b_{55}p_1 + b_{45}p_2),\ d_2 = d(b_{45}p_3 - b_{55}p_4)$

$d_3 = d(b_{55}p_5 - b_{45}p_6),\ d_4 = d(b_{55}p_7 + b_{45}p_5)$

$d_5 = d(b_{55}p_8 - b_{45}p_9), \quad d_6 = d(b_{55}p_{10} - b_{45}p_{11})$

$d_7 = b_{55}p_{12},\ d_8 = b_{45}p_{12},\ d_9 = d(b_{45}p_1 + b_{44}p_2)$

$d_{10} = d(b_{44}p_3 - b_{45}p_4),\ d_{11} = d(b_{45}p_5 - b_{44}p_6)$

$d_{12} = d(b_{45}p_7 + b_{44}p_5),\ d_{13} = d(b_{45}p_8 - b_{44}p_9)$

$d_{14} = d(b_{45}p_{10} - b_{44}p_{11}),\ d_{15} = b_{44}p_{12},\ d_{16} = d_8$

where

$p_1 = q_5/b_{11},\ p_2 = b_{12}q_4,\ p_3 = q_8,\ p_4 = q_9$

$p_5 = b_{12}q_1,\ p_6 = b_{12}q_3,\ p_7 = q_7/b_{11},\ p_8 = q_6/b_{11} + p_5$

$p_9 = b_4 + b_6,\ p_{10} = p_2 + p_7,\ p_{11} = b_{12}(q_2 - q_1),\ p_{12} = \rho h^2/10$

$q_1 = b_{11}b_{22} - b_{12}^2,\ q_2 = b_{12}b_{66} - b_{16}b_{26}$

$q_3 = b_{11}b_{26} - b_{12}b_{16},\ q_4 = b_{12}b_{26} - b_{16}b_{22}$

$q_5 = e + b_{12}^2 q_2 - b_{12}b_{16}q_4,\ q_6 = b_{16}q_9 - b_{12}q_8$

$q_7 = b_{12}(b_{12}q_3 - b_{16}q_1),\ q_8 = b_{11}q_2 + b_{16}q_3$

$q_9 = b_{11}q_4 + b_{16}q_1,\ e = q_1q_2 - q_3q_4,\ d = h^2/10e$

$e_1 = Hq_5/b_{11},\ e_2 = H(q_7/b_{11} + 2b_{12}q_4)$

$e_3 = Hb_{12}(2q_1 - q_2),\ e_4 = -Hb_{12}q_3,\ e_5 = Hq_7/b_{11}$

$e_6 = H(q_6/b_{11} + 2b_{12}q_1),\ e_7 = -H(2q_9 + b_{12}q_3)$

$e_8 = Hq_8,\ e_9 = -\rho h^3/12 \quad \text{and} \quad H = h^3/12e$

APPENDIX *C*

The coefficients r_i and e_i in equation (36)–(38) are

$r_1 = d_4d_9 - d_1d_{12}$

$r_2 = d_2d_9 + d_4d_{11} + d_5d_{14} - d_1d_{10} - d_3d_{12} - d_6d_{13}$

$r_3 = d_2d_{11} - d_3d_{10},\ r_4 = d_4d_{14} + d_5d_9 - d_1d_{13} - d_6d_{12}$

$r_5 = d_2d_{14} + d_5d_{11} - d_3d_{13} - d_6d_{10},\ r_6 = d_8d_{16} - d_7d_{15}$

$$r_7 = d_1d_{15} + d_7d_{12} - d_8d_9 - d_4d_{16},$$
$$r_8 = d_6d_{15} + d_7d_{13} - d_8d_{14} - d_5d_{16}$$

$r_9 = d_3d_{15} + d_7d_{10} - d_8d_{11} - d_2d_{16},\ r_{10} = d_1 + d_{12}$

$r_{11} = d_3 + d_{10},\ r_{12} = d_6 + d_{13},\ r_{13} = d_7 + d_{15}$

$e_{10} = e_3 + e_6,\ e_{11} = e_2 + e_5,\ e_{12} = e_4 + e_7$

$e_{13} = e_9R_i(d_{14} - d_1 + d_5 - d_{10}) + e_6d_7 - e_2d_8 + e_3d_{15} - e_7d_{16}$

$e_{14} = e_1d_{15} - e_5d_{16} - e_9R_id_{12}$

$e_{15} = e_9R_i(d_4 - d_{13} + d_9) - e_1d_8 - e_6d_{16} + e_2d_{15} + e_5d_7$

$e_{16} = e_9R_i(d_8 + d_{16})$

$e_{17} = e_9R_i(d_2 - d_6 + d_{11}) - e_8d_{16} - e_3d_8 + e_4d_{15} + e_7d_7$

$e_{18} = e_8d_7 - e_9R_id_3 - e_4d_8,\ e_{19} = e_5d_9 - e_1d_{12}$

$$e_{20} = e_1(d_5 - d_{10}) + e_6(d_{14} - d_1) + e_2(d_4 - d_{13}) + e_5(d_{11} - d_6) - e_3d_{12} + e_7d_9$$

$e_{21} = e_1(d_4 - d_{13}) + e_5(d_{14} - d_1) + e_6d_9 - e_2d_{12}$

$$e_{22} = e_1d_2 + e_6(d_{11} - d_6) + e_2(d_5 - d_{10}) - e_5d_3 + e_8d_9 + e_3(d_4 - d_{13}) - e_4d_{12} + e_7(d_{14} - d_1)$$

$$e_{23} = e_2d_2 - e_6d_3 + e_8(d_{14} - d_1) + e_3(d_5 - d_{10}) + e_4(d_4 - d_{13}) + e_7(d_{11} - d_6)$$

$e_{24} = e_8(d_{11} - d_6) + e_3d_2 - e_7d_3 + e_4(d_5 - d_{10})$

$e_{25} = e_4d_2 - e_8d_3$

APPENDIX *D*

Isotropic and specially orthotropic plates: In the case of specially orthotropic plates, $\phi = 0$ and hence $m = 1, n = 0$. The corresponding a_{ij} are obtained from equations (3)–(5).

For isotropic plates $m = 1, n = 0$, and $E_L = E_T = E,\ \nu_{LT} = \nu_{TL} = \nu,\ G_{LT} = G_{LZ} = G_{TZ} = G = E/2(1 + \nu),\ \mu = 1 - \nu^2$.

M. Sathyamoorthy
Research Associate.

C. Y. Chia
Professor.

Department of Civil Engineering,
The University of Calgary,
Calgary, T2N 1N4, Canada

Effect of Transverse Shear and Rotatory Inertia on Large Amplitude Vibration of Anisotropic Skew Plates

Part 2—Numerical Results

Based on the single-mode analysis, solutions to the governing equations developed in Part 1 of this paper are presented for various boundary conditions by use of Galerkin's method and the Runge-Kutta numerical procedure. Excellent agreement is found between the present results and those available for nonlinear bending and large amplitude vibration of skew plates. The present results for moderately thick anisotropic skew plates indicate significant influences of the transverse shear deformation, orientation angle, skew angle, and side ratio on the large amplitude vibration behavior of certain fiber-reinforced composite skew plates.

Introduction

In nonlinear vibration analysis the system of coupled nonlinear differential equations in the sense of von Karman given by Herrmann [1] has been commonly used for isotropic plates and extended to laminated anisotropic plates by Whitney and Leissa [2]. Approximate solutions have been presented by a number of authors for isotropic, orthotropic, anisotropic, and laminated plates. For a compendium see [3, 4]. Among plates of various geometries, skew plates have received much less attention due to the complexities involved in the formulation of solutions. Kennedy and Ng [5] have applied the perturbation technique to analyze the large-deflection problem of isotropic clamped skew plates under uniform pressure. Using the Galerkin procedure, Nowinski [6] has investigated the nonlinear dynamic response of isotropic skew plates. This study has later been extended by Sathyamoorthy and Pandalai [7–9] to include the effects of special orthotropy and various in-plane boundary conditions. When the principal axes of orthotropy are not parallel to the plate edges, the small-deflection analysis of clamped skew plates under uniform pressure [13]* indicates that the angle of orientation of the principal axes of orthotropy has a significant effect on the behavior of plates. In the case of nonlinear bending of anisotropic rectangular plates, similar conclusions have been also reached by Prabhakara and Chia [10, 11]. In all these solutions the effects of the transverse shear deformation and rotatory inertia on the elastic behavior of plates have been neglected.

In this paper, an attempt is made to study the large amplitude flexural vibration of homogeneous anisotropic skew plates with all-simply supported, clamped-simply supported, and all-clamped edges including the effects of the transverse shear deformation and rotatory inertia. The in-plane boundary conditions are regarded as all movable and all immovable. Solutions to the governing equations are formulated on the basis of the single-mode analysis. The resulting time-differential equations are numerically solved to investigate the effects of transverse shear, rotatory inertia, and orientation angle of filaments on the nonlinear vibration behavior of elastic anisotropic skew plates. These time-differential equations can readily reduce to those of isotropic and orthotropic rectangular and skew plates [7–9] when the transverse shear and rotatory inertia effects are neglected. The present results for the static large deflections of isotropic skew plates are in excellent agreement with those of Kennedy and Ng [5].

Method of Solution

The system of equations (34)* and (35)* are coupled and non-linear in nature, so exact solutions to these equations are very difficult. Approximate solutions are attempted here for the six combinations of boundary conditions in equations (44)* to (49)*. In each case a single-mode expression for w is chosen to satisfy the appropriate boundary conditions as well as the geometrical requirements [5]. The assumed mode shapes for the simply supported, simply supported-clamped and clamped-clamped plates, respectively, are

$$SS: \quad w = hf_{ss}(\tau)\cos\frac{\pi\zeta}{2a}\cos\frac{\pi\eta}{2b}$$

$$SC: \quad w = \frac{h}{2}f_{sc}(\tau)\cos\frac{\pi\zeta}{2a}\left(1+\cos\frac{\pi\eta}{b}\right)$$

$$CC: \quad w = \frac{h}{4}f_{cc}(\tau)\left(1+\cos\frac{\pi\zeta}{a}\right)\left(1+\cos\frac{\pi\eta}{b}\right) \qquad (1)$$

Contributed by the Applied Mechanics Division for publication in the JOURNAL OF APPLIED MECHANICS.

Discussion on this paper should be addressed to the Editorial Department, ASME, United Engineering Center, 345 East 47th Street, New York, N. Y. 10017, and will be accepted until June 1, 1980. Readers who need more time to prepare a discussion should request an extension from the Editorial Department. Manuscript received by ASME Applied Mechanics Division, March, 1979; final revision, July, 1979.

in which the mode functions are known to yield reasonably accurate results for the fundamental natural frequencies of isotropic and orthotropic rectangular plates and of skew plates with small skew angles. However, effects of anisotropy and large skew angles may decrease the accuracy of the results thus obtained on the basis of these mode functions. Although a multimode approach would provide better results in such cases, no attempt has been made here to use this approach in view of the tedious nature of the titled problem.

Now expressions (1) are substituted in equation (34)* and solved for F. The result is

$$SS: \quad F = (f_{ss})^2 \left(f_1 \cos\frac{\pi\zeta}{a} + f_2 \cos\frac{\pi\eta}{b} + g_1\zeta^2 + g_2\eta^2 + g_3\zeta\eta \right)$$

$$\begin{aligned} SC: \quad F = (f_{sc})^2 \Big(& h_1 \cos\frac{\pi\zeta}{a} + h_2 \cos\frac{\pi\eta}{b} + h_3 \cos\frac{2\pi\eta}{b} \\ & + h_4 \cos\frac{\pi\zeta}{a}\cos\frac{\pi\eta}{b} + h_5 \sin\frac{\pi\zeta}{a}\sin\frac{\pi\eta}{b} + k_1\zeta^2 \\ & + k_2\eta^2 + k_3\zeta\eta \Big) \end{aligned}$$

$$\begin{aligned} CC: F = (f_{cc})^2 \Big(& l_1 \cos\frac{\pi\zeta}{a} + l_2 \cos\frac{\pi\eta}{b} + l_3 \cos\frac{2\pi\zeta}{a} + l_4 \cos\frac{2\pi\eta}{b} \\ & + l_5 \cos\frac{\pi\zeta}{a}\cos\frac{\pi\eta}{b} + l_6 \cos\frac{\pi\zeta}{a}\cos\frac{2\pi\eta}{b} + l_7 \cos\frac{2\pi\zeta}{a}\cos\frac{\pi\eta}{b} \\ & + l_8 \sin\frac{\pi\zeta}{a}\sin\frac{2\pi\eta}{b} + l_9 \sin\frac{2\pi\zeta}{a}\sin\frac{\pi\eta}{b} + l_{10} \sin\frac{\pi\zeta}{a}\sin\frac{\pi\eta}{b} \\ & + m_1\zeta^2 + m_2\eta^2 + m_3\zeta\eta \Big) \end{aligned} \qquad (2)$$

The coefficients appearing in equation (2) are defined in Appendix A.

Instead of satisfaction of the equation of transverse motion, the Galerkin procedure is used in obtaining the time-differential equation in each case.

If the plate edges are supported in such a way that in-plane displacements are possible [6], it follows from equations (47)*, (48)*, and (2) that $g_1 = g_2 = g_3 = k_1 = k_2 = k_3 = m_1 = m_2 = m_3 = 0$. If the in-plane movements at the boundaries of the plate are fully prevented [7, 8, 9] and given by equations (49)*, the coefficients g_i, k_i, m_i (i = 1, 2, 3) appearing in equations (2) may be evaluated by referring to equations (10)* and using an integration procedure [12]. The coefficients thus obtained are defined in Appendix A. In view of equations (1) and (2), equation (35)* is approximately satisfied by making use of Galerkin's method to obtain a nonlinear ordinary differential equation for the time function in each case for both movable and immovable edges.

$$\begin{aligned} SS: &\quad A_1\frac{d^6 f_{ss}}{d\tau^6} + A_2\frac{d^4 f_{ss1}}{d\tau^4} + \frac{d^2 f_{ss2}}{d\tau^2} + A_3 f_{ss3} = A_7 \\ SC: &\quad B_1\frac{d^6 f_{sc}}{d\tau^6} + B_2\frac{d^4 f_{sc1}}{d\tau^4} + \frac{d^2 f_{sc2}}{d\tau^2} + B_3 f_{sc3} = B_7 \\ CC: &\quad C_1\frac{d^6 f_{cc}}{d\tau^6} + C_2\frac{d^4 f_{cc1}}{d\tau^4} + \frac{d^2 f_{cc2}}{d\tau^2} + C_3 f_{cc3} = C_7 \end{aligned} \qquad (3)$$

where

$$f_{ss1} = f_{ss} + \frac{A_5}{3A_2} f_{ss}{}^3, \quad f_{sc1} = f_{sc} + \frac{B_5}{3B_2} f_{sc}{}^3 \qquad (4)$$

$$\begin{aligned} & f_{cc1} = f_{cc} + \frac{C_5}{3C_2} f_{cc}{}^3, \quad f_{ss2} = f_{ss} + \frac{A_6}{3} f_{ss}{}^3 \\ & f_{sc2} = f_{sc} + \frac{B_6}{3} f_{sc}{}^3, \quad f_{cc2} = f_{cc} + \frac{C_6}{3} f_{cc}{}^3 \\ & f_{ss3} = f_{ss} + \frac{A_4}{A_3} f_{ss}{}^3, \quad f_{sc3} = f_{sc} + \frac{B_4}{B_3} f_{sc}{}^3 \\ & f_{cc3} = f_{cc} + \frac{C_4}{C_3} f_{cc}{}^3 \end{aligned} \qquad \begin{matrix} (4) \\ (Cont.) \end{matrix}$$

The coefficients A_i, B_i, and C_i ($i = 1, 2, \ldots, 7$) in equations (3) and (4) are given in Appendix B. The modal equations (3) have been obtained by solving equations (34)* and (35)* which include the effects of the tranverse shear deformation and rotatory inertia. If either or both of these effects can be neglected, i.e., if $T_s = 1, R_i = 0$; $T_s = 0, R_i = 1$; $T_s = 0$ and $R_i = 0$, then the resulting modal equations reduce to the Duffing-type equations as follows:

$$\begin{aligned} SS: &\quad \frac{d^2 f_{ss}}{d\tau^2} + A_3 f_{ss} + A_4 f_{ss}{}^3 = A_7 \\ SC: &\quad \frac{d^2 f_{sc}}{d\tau^2} + B_3 f_{sc} + B_4 f_{sc}{}^3 = B_7 \\ CC: &\quad \frac{d^2 f_{cc}}{d\tau^2} + C_3 f_{cc} + C_4 f_{cc}{}^3 = C_7 \end{aligned} \qquad (5)$$

The modal equations (3) are nonlinear ordinary differential equations. These equations are solved numerically by the Runge-Kutta method. Solutions to the nonlinear equations (5) are obtained by the elliptic integral method [8]. When the time-dependent terms in equations (3) and (5) are omitted, the load-deflection relationship in the large deflection regime can readily be obtained.

Numerical Results and Discussion

Numerical results are presented for skew and rectangular plates composed of boron-epoxy material. The plate material is treated to be homogenous and its principal axes of elasticity are inclined arbitrarily with respect to the rectangular axes x and y as shown in Fig. 1 of Part 1—Theory. The elastic constants referred to the principal directions (L, T) are assumed to be E_L/E_T = 17.66, ν_{LT} = 0.26, $G_{LT}/E_T = G_{LZ}/E_T$ = 0.35, and G_{TZ}/E_T = 0.20. The ratio of the nonlinear period T of vibration, including effects of transverse shear deformation and rotatory inertia, to the corresponding period T_0 of a classical plate, excluding these effects, was computed for anisotropic skew plates with various skew angles, plate aspect ratios, orientation angles, and thickness-to-span ratios at different nondimensional amplitudes. When the transverse shear and/or rotatory inertia effects are included, the nonlinear period thus obtained depends upon the thickness-to-span ratio r of the plate. For mederately thick plates, values of the linear period T_0 were also calculated in terms of r for comparison with the corresponding nonlinear period T. It is well known that effects of transverse shear deformation and rotatory inertia are not included in the nonlinear classical plate theory. Thus the resulting period ratio is independent of the thickness-to-span ratio. In the numerical integration of equations (3) the nondimensional time interval $\nabla\tau$ was taken as 0.001.

When the effects of transverse shear deformation and rotatory inertia are both neglected, plate equations of transverse motion, and numerical results obtained from the present theory for specially orthotropic and isotropic skew plates are in exact agreement with those presented in [6–9]. In the static case the time-derivative terms

Nomenclature

A = nondimensional amplitude (w_o/h)

q_0 = uniformly distributed lateral load per unit area of the plate

r = thickness-to-span ratio

T = nonlinear period with transverse shear and rotatory inertia effects

T_0 = linear period without transverse shear and rotatory inertia effects

w_0 = maximum deflection

τ = nondimensional time $t(E_L/\rho a^2)^{1/2}$

* = an equation number or reference number with a star refers to the corresponding number in Part 1. The other notations are defined in that part

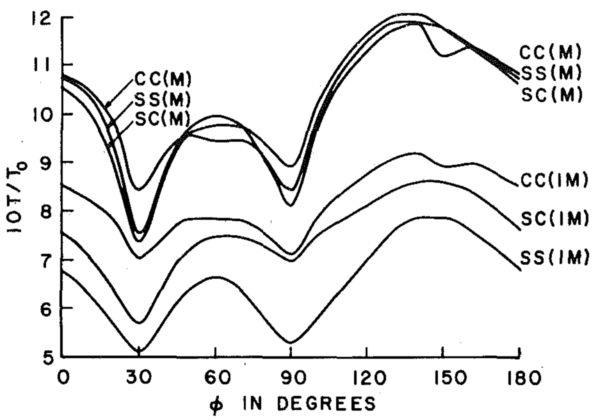

Fig. 1 Relation between period ratio and orientation angle for boron-epoxy plate with $\lambda = 1.0$, $r = 1/20$, $w_0/h = 1.5$, $\theta = 30°$, and different boundary conditions ($T_s = R_i = 1$)

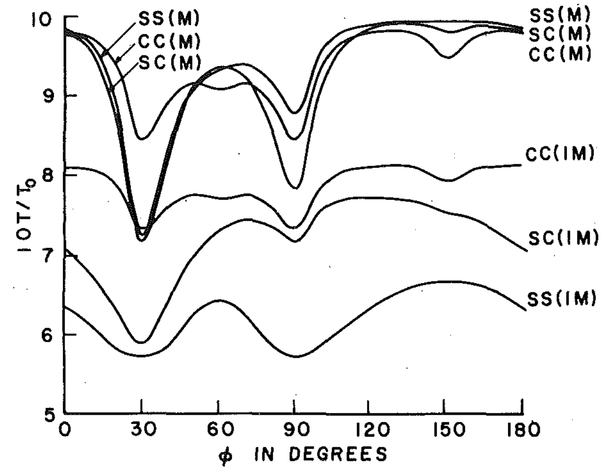

Fig. 2 Variation of period ratio with orientation angle for boron-epoxy plate at $\lambda = 1.0$, $w_0/h = 1.5$, $\theta = 30°$, and different boundary conditions ($T_s = R_i = 0$)

in equations (5) disappear and the resulting nonlinear algebraic equations yield an approximate relation between the nondimensional load q_0b^4/Dh and the nondimensional central deflection w_0/h of isotropic skew plates in the large-deflection regime. The numerical results thus obtained for clamped-clamped isotropic rhombus plate ($\theta = 30°$), skew plate ($\lambda = 1.5$, $\theta = 30°$) and square plate are found to be in very close agreement with those given by Kennedy and Ng [5], but the details are not presented herein. For the vibration problem, the natural (linear) frequencies of vibration for various plate parameters and boundary conditions, which do not include the transverse shear deformation and rotatory inertia effects, can be readily obtained from equations (5) by dropping the nonlinear terms and solving the resulting equations. The numerical results for the natural frequencies thus obtained agree well with those given in [13].

However, the present results, when specialized for rectangular plates with simply supported edges do not agree with those available in [8, 9]* where the effects of transverse shear and rotatory inertia are included in the analysis. A comparison made elsewhere [14] for a similar problem indicates that the results presented in [8, 9]* overestimate the period ratio at large amplitudes of vibration. The discrepancy between present results and those in [8, 9]* may arise mainly from the following reasons. In [8, 9]* the expression for each of slope functions α and β is assumed to be a one-term approximation instead of a general form. As shown in [15] a one-term approximation for in-plane displacements can differ considerably from the true solution for a given w. The result may also apply to the case [8, 9]*. In the present approach α and β are eliminated from the governing equations and, therefore no particular forms for α and β are assumed. It has been shown on several occasions [12, 14] that the Berger approximation overestimates period ratios. The error involved in using this approximation increases with increasing degree of orthotropy of the plate material. In the present analysis the governing equations are a generalizatlion of dynamic von Karman-type plate equations. Furthermore, the effect of rotatory inertia has been neglected in [8, 9]* whereas this effect is accounted for in the present analysis. Neglecting this effect may also introduce a small error in the numerical results.

The period ratio is plotted in Figs. 1 and 2 against the orientation angle ϕ for a 30° skew plate at the nondimensional amplitude and aspect ratio equal to 1.5 and 1.0, respectively. The results presented in Fig. 1 include the effects of transverse shear deformation and rotatory inertia whereas these effects are neglected in the results of Fig. 2. It is clear that the period ratio changes significantly with the orientation angle irrespective of whether these effects are taken into account. A comparison of Figs. 1 and 2 shows that neglecting these effects in the vibration analysis leads to a substantial reduction in the numerical values of the period ratio. It is also observed that for a given

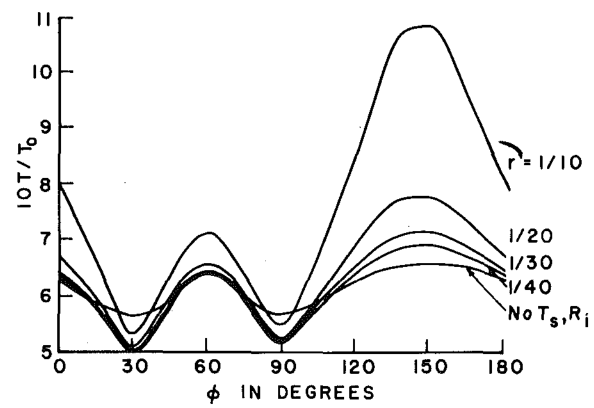

Fig. 3 Relation between period ratio and orientation angle for simply supported immovable boron-epoxy plate with $\lambda = 1.0$, $w_0/h = 1.5$, $\theta = 30°$, and *various values of thickness-to-span ratio ($T_s = R_i = 1$ and $T_s = R_i = 0$)*

value of ϕ the period ratio for a plate with movable edges is greater than that for a corresponding plate with immovable edges. This trend is in agreement with that reported in literature for isotropic and specially orthotropic rectantular and skew plates [8, 9, 16, 17]. For all the combinations of boundary conditions considered here the period ratio is found to be minimum at ϕ equal to 30° for a 30° rhombus plate. A similar phenomenon also occurs for all skew plates with $\lambda = 1$ when the angle of orientation is equal to the skew angle of the plate. These points are of considerable importance for design purposes. In the case of an anisotropic rectangular plate ($\theta = 0$) the curves in Fig. 2 will be symmetric about the line $\phi = 90°$ [18] whereas no such symmetry exists for a skew plate.

The variation of the plate thickness with the period ratio is shown in Fig. 3. The effects of transverse shear and rotatory inertia are included. For comparison the variation of period ratio with ϕ is also shown by neglecting these effects. In general the period ratio decreases as the thickness of the plate decreases. It is seen that the influence of transverse shear deformation and rotatory inertia on the period ratio is very significant for specially orthotropic ($\phi = 0$) and anisotropic ($110° < \phi < 180°$) moderately thick plates. All the curves in Figs. 1–3 are repeated after $\phi = 180$.

In Figs. 4 and 5 the variation of the period ratio with the plate skew angle is shown for an anisotropic plate ($\phi = 30°$) at amplitude equal to 1.0 with six combinations of boundary conditions. In Fig. 4 the transverse shear and rotatory inertia effects are included but in Fig.

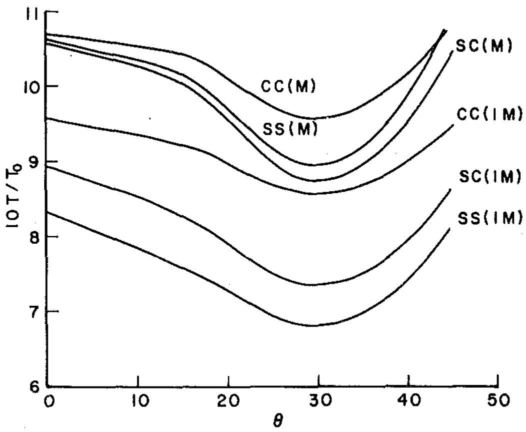

Fig. 4 Variation of period ratio with skew angle for boron-epoxy plate having $\lambda = 1.0$, $w_0/h = 1.0$, $r = 1/20$, $\phi = 30°$, and different boundary conditions ($T_s = R_i = 1$)

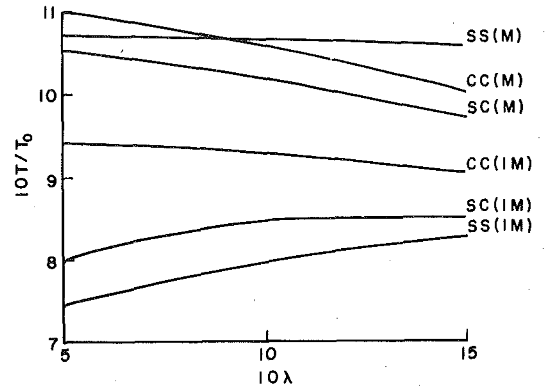

Fig. 6 Variation of period ratio with aspect ratio for boron-epoxy plate at $\theta = 45°$, $\phi = 30°$, $r = 1/20$, $w_0/h = 1.0$, and different boundary conditions ($T_s = R_i = 1$)

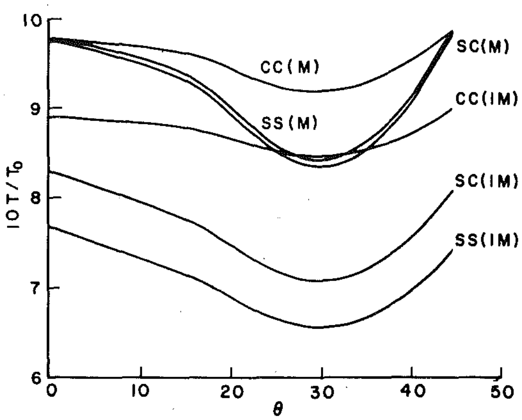

Fig. 5 Relation between period ratio and skew angle for boron-epoxy plate with $\lambda = 1.0$, $w_0/h = 1.0$, $\phi = 30°$, and different boundary conditions ($T_s = R_i = 0$)

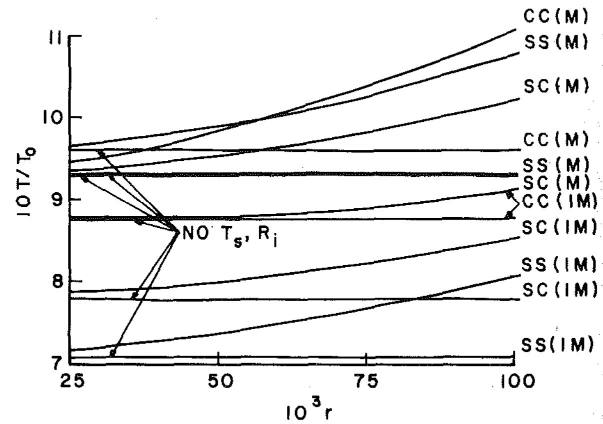

Fig. 7 Relation between period ratio and thickness-to-span ratio for boron-epoxy plate with $\lambda = 1.0$, $\phi = 40°$, $w_0/h = 1.0$, $\theta = 45°$, and different boundary conditions

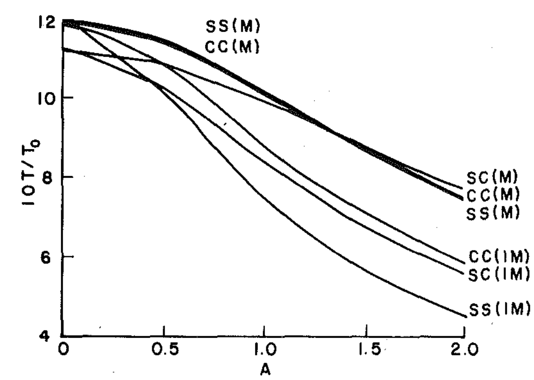

Fig. 8 Amplitude-period response curves for boron-epoxy plate with $\theta = 30°$, $\lambda = 1.5$, $\phi = 30°$, $r = 1/10$, and different boundary conditions ($T_s = R_i = 1$)

5 these effects are neglected. A comparison indicates that the qualitative nature of these two sets of curves is the same although quantitatively the period ratio in Fig. 4 is higher than the corresponding period ratio in Fig. 5. This ratio generally decreases slowly with an increase in the skew angle of the plate and reaches a minimum value at the skew angle $\theta = 30°$ since the orientation angle is also 30 deg. By suitably varying the skew angle of the plate and the orientation angle of the filaments, it is possible to limit the period or frequency ratio to any desired value.

The period ratio is plotted in Fig. 6 against the plate aspect ratio for a 45° skew plate at the amplitude equal to unity and $\phi = 30°$ by taking account of the transverse shear and rotatory inertia effects. It can be seen that the plate aspect ratio has a considerable effect on the vibration behavior of skew plates. While no specific pattern of behavior is found, it is observed that boundary conditions determine the qualitative nature of the variation of the period ratio with the aspect ratio of the plate. A simply supported skew plate with movable boundaries is the one least affected with the variation in the aspect ratio.

The effect of the thickness-to-span ratio on vibration of a rhombus plate with $\theta = 45°$ at unit nondimensional amplitude and orientation angle equal to 40° is illustrated in Fig. 7. The horizontal lines represent the variation of period ratio with r for various boundary conditions when the effects of the transverse shear and rotatory inertia are neglected. They indicate that the period ratios in the case are independent of the thickness-to-span ratio for thin plates. However, those effects are very important for moderately thick plates. As the thickness of the plate decreases, the period ratio decreases due to the decreasing influences of transverse shear and rotatory inertia and reaches asymptotically a value corresponding to the period of a classical thin plate. Thus each horizontal line is an asymptote to the corresponding curve in Fig. 7.

The period-amplitude response curves are shown in Figs. 8 and 9 for a 30° skew plate with $\lambda = 1.5$ and orientation angle at 30°. The effects of the transverse shear and rotatory inertia are included in Fig.

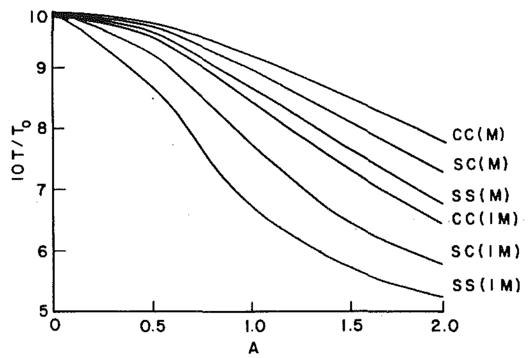

Fig. 9 **Variation of period ratio with amplitude for boron-epoxy plate with $\theta = 30°$, $\lambda = 1.5$, $\phi = 30°$, and different boundary conditions ($T_s = R_i = 0$)**

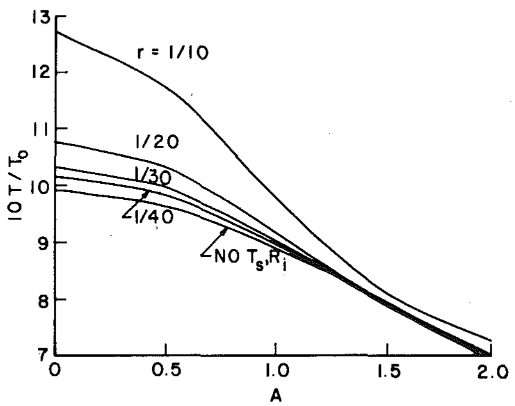

Fig. 10 **Amplitude-period response curves for clamped-clamped immovable boron-epoxy plate with $\theta = 45°$, $\lambda = 1.0$, $\phi = 30°$, and various values of thickness-to-span ratio ($T_s = 1$, $R_i = 0$ and $T_s = R_i = 0$)**

8 but neglected in Fig. 9. For all the boundary conditions considered here, the period decreases with increasing amplitude of vibration thereby exhibiting the hardening type of nonlinearity. The period-amplitude curves in Fig. 8 for six combinations of boundary conditions considered here are seen to cross over one another only when the transverse shear and rotatory inertia effects are included in the analysis. For a plate with any set of the boundary conditions considered here, the period ratio at a given amplitude in Fig. 9 is less than the corresponding value in Fig. 8. This is due to the absence of the effects of transverse shear and rotatory inertia in the curves of Fig. 9.

The curves shown in Fig. 10 take into account only the effect of the transverse shear deformation and those of Fig. 11 include the effect of the rotatory inertia only. It is evident from a comparison of these two sets of curves that the effect of the transverse shear deformation is more significnat than the effect of the rotatory inertia, especially for large values of r (or thick plates). Either of these effects increases the period ratio at any amplitude of vibration. It is also seen that for the thickness-to-span ratio of the plate below a value equal to 1/20, the rotatory inertia has little influence on the vibration behavior of the plate.

Concluding Remarks

The dynamic von Karman nonlinear plate theory is generalized to include the effects of the transverse shear and rotatory inertia in the analysis of anisotropic skew plates. The theory is formulated in a form such that these effects can be investigated individually or totally and that the resulting differential equations are solvable. The present results are in good agreement with several existing solutions for the static and dynamic problems of isotropic and specially orthotropic skew plates in the absence of these effects and can reduce to a recent solution for an isotropic skew plate including these effects. Approximate solutions with numerical results for nonlinear flexural vibrations of anisotropic skew plates of boron-epoxy composites are presented for six sets of boundary conditions.

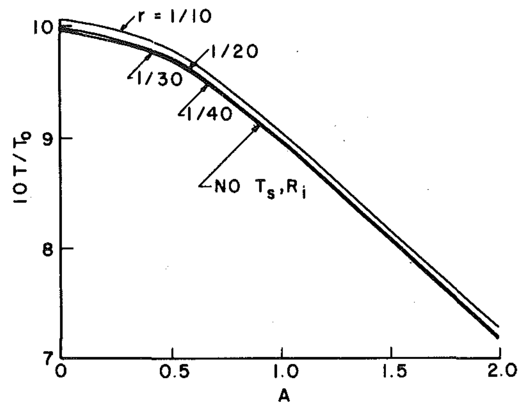

Fig. 11 **Amplitude-period response curves for clamped-clamped immovable boron-epoxy plate with $\theta = 45°$, $\lambda = 1.0$, $\phi = 30°$, and various values of thickness-to-span ratio ($T_s = 0$, $R_i = 1$ and $T_s = R_i = 0$)**

Based on the present results it may be possible to draw some conclusions regarding the dynamic behavior of generally and specially orthotropic skew plates. The effects of the transverse shear and rotatory inertia on the period decrease as the amplitude increases. They generally become less significant at the amplitude twice the plate thickness. These effects also decrease with decreasing the ratio of the thickness to span and, in general, are not significant for thickness-to-span ratios less than 1/30. The effect of the rotatory inertia on the period is much less than that of the transverse shear and can be neglected in the vibration analysis. The period of vibration of the plate generally is considerably influenced by the orientation angle. At certain angles of orientation the period ratio varies more than 30 percent for the numerical results presented in this work. The period ratio also varies significantly with the skew angle. Therefore, the elastic behavior of anisotropic skew plates is not so easily predicted as for the simple shapes of homogeneous plates.

Acknowledgment

The results presented in this paper were obtained in the course of research sponsored by the National Sciences and Engineering Research Council of Canada.

References

1 Herrmann, G., "Influence of Large Amplitudes on Flexural Motions of Elastic Plates," National Advisory Committee for Aeronautics, Technical Note 3578, Washington, D.C., May 1955.

2 Whitney, J. M., and Leissa, A. W., "Analysis of Heterogeneous Anisotropic Plates," ASME JOURNAL OF APPLIED MECHANICS, Vol. 36, 1969, pp. 261–266.

3 Sathyammorthy, M., and Pandalai, K. A. V., "Large Amplitude Vibrations of Certain Deformable Bodies: Part 2–Plates and Shells," *Journal of Aeronautical Society of India*, Vol. 25, 1973, pp. 1–10.

4 Chia, C. Y., *Nonlinear Analysis of Plates*, McGraw-Hill, New York, 1980.

5 Kennedy, J. B., and Ng, S., "Linear and Nonlinear Analyses of Skewed Plates," ASME JOURNAL OF APPLIED MECHANICS, Vol. 34, 1967, pp. 271–277.

6 Nowinski, J. L., "Large Amplitude Oscillations of Oblique Panels With an Initial Curvature," *AIAA Journal*, Vol. 2, 1964, pp. 1025–1031.

7 Sathyamoorthy, M., and Pandalai, K. A. V., "Nonlinear Flexural Vibration of Orthotropic Skew Plates," *Journal of Sound and Vibration*, Vol. 24, 1972, pp. 115–120.

8 Sathyamoorthy, M., and Pandalai, K. A. V., "Nonlinear Vibration of Elastic Skew Plates Exhibiting Rectilinear Orthotropy," *Journal of The Franklin Institute*, Vol. 296, No. 5, 1973, pp. 359–369.

9 Sathyamoorthy, M., and Pandalai, K. A. V., "Large Amplitude Flexural Vibration of Simply Supported Skew Plates," *AIAA Journal*, Vol. 11, 1973, pp. 1279–1282.

10 Prabhakara, M. K., and Chia, C. Y., "Postbuckling of Angle-Ply and Anisotropic Plates," *Ingenieur-Archiv*, Vol. 45, 1976, pp. 131–140.

11 Prabhakara, M. K., and Chia, C. Y., "Nonlinear Bending of Symmetrically Laminated and Homogeneous Anisotropic Plates," *Rozprawy Inzynierskie*, Vol. 24, 1977, pp. 559–570.

12 Sathyamoorthy, M., "Nonlinear Vibration of Rectangular Plates," *Journal of Sound and Vibration*, Vol. 58, 1978, pp. 301–304.
13 Leissa, A. W., "Vibration of Plates," NASA SP-160, 1969.
14 Sathyamoorthy, M., "Effects of Large Amplitude, Shear and Rotatory Inertia on Vibration of Rectangular Plates," *Journal of Sound and Vibration*, Vol. 63, 1979, pp. 161–167.
15 Vendham, C. P., and Das, Y. C., "Application of Rayleigh-Ritz and Galerkin Methods to Nonlinear Vibration of Plates," *Journal of Sound and Vibration*, Vol. 39, 1975, pp. 147–154.
16 Yamaki, N., "Influence of Large Amplitudes on Flexural Vibrations of Elastic Plates," *ZAMM*, Vol. 14, 1961, pp. 501–510.
17 Sathyamoorthy, M., "Nonlinear Vibration of Rectangular Plates," ASME JOURNAL OF APPLIED MECHANICS, Vol. 46, 1979, pp. 215–217.
18 Chia, C. Y., and Sathyamoorthy, M., "Nonlinear Vibration of Anisotropic Skew Plates," *Fiber Science and Technology*, 1979, in press.

APPENDIX *A*

The coefficients in equations (2) are

$$f_1 = A_0D_1/b_{22},\quad f_2 = A_0D_1/b_{11}\lambda^4,\quad g_1 = 4D_2(D_4 - D_3\lambda^2)/3g_4$$

$$g_2 = (4D_2\lambda^2/3 - D_5g_1)/D_4,\quad g_3 = -2(b_{16}g_2 + b_{26}g_1)/b_{66}$$

$$h_1 = f_1,\quad h_2 = f_2,\quad h_3 = h_2/16,\quad h_4 = A_0D_6/g_5$$

$$h_5 = -A_0D_7/g_5,\quad K_1 = (D_4D_2 - D_3d_8\lambda^2)/g_4$$

$$k_2 = (D_8\lambda^2 - K_1D_5)/D_4,\quad K_3 = -2(b_{16}k_2 + b_{26}k_1)/b_{66}$$

$$l_1 = D_9/2,\quad l_2 = l_1/D_{19}\lambda^4,\quad l_3 = l_1/16,\quad l_4 = l_2/16$$

$$l_5 = D_9D_{10}/D_{12},\quad l_6 = D_9D_{16}/2D_{18},\quad l_7 = D_9D_{13}/2D_{15}$$

$$l_8 = D_9D_{17}/2D_{18},\quad l_9 = D_9D_{14}/2D_{15},\quad l_{10} = D_9D_{11}/D_{12}$$

$$m_1 = D_2(D_4 - D_3\lambda^2)/g_4,\quad m_2 = (D_2\lambda^2 - m_1D_5)/D_4$$

$$m_3 = -2(b_{16}m_2 + b_{26}m_1)/b_{66}$$

where

$$A_0 = -h^2\pi^4/32a^2b^2,\quad D_1 = (a/\pi)^4,\quad D_2 = 3h^2\pi^2/128a^2$$

$$D_3 = 2(b_{11} - b_{16}{}^2/b_{66}),\quad D_4 = 2(b_{12} - b_{16}b_{26}/b_{66})$$

$$D_5 = 2(b_{22} - b_{26}{}^2/b_{66}),\quad D_6 = [b_{22} + (2b_{12} + b_{66})\lambda^2 + b_{11}\lambda^4]/D_1$$

$$D_7 = 2\lambda(b_{26} + b_{16}\lambda^2)/D_1,\quad D_8 = 4D_2/3,\quad D_9 = -h^2\lambda^2/16b_{22}$$

$$D_{10} = 1 + D_{20}\lambda^2 + D_{19}\lambda^4, D_{11} = \lambda(D_{21} + D_{22}\lambda^2)$$

$$D_{12} = D_{10}{}^2 - D_{11}{}^2,\quad D_{13} = 16 + 4D_{20}\lambda^2 + D_{19}\lambda^4$$

$$D_{14} = 2\lambda(4D_{21} + D_{22}\lambda^2),\quad D_{15} = D_{13}{}^2 - D_{14}{}^2$$

$$D_{16} = 1 + 4D_{20}\lambda^2 + 16D_{19}\lambda^4,\quad D_{17} = 2\lambda(D_{21} + 4D_{22}\lambda^2)$$

$$D_{18} = D_{16}{}^2 - D_{17}{}^2,\quad D_{19} = b_{11}/b_{22},\quad D_{20} = (2b_{12} + b_{66})/b_{22}$$

$$D_{21} = -2b_{26}/b_{22},\quad D_{22} = -2b_{16}/b_{22},\quad g_4 = D_4{}^2 - D_3D_5$$

$$g_5 = D_6{}^2 - D_7{}^2$$

APPENDIX *B*

The coefficients appearing in equations (3) and (4) are

$$A_1 = 10r^4S_1/S_2,\quad A_2 = 4r^2S_3/S_2,\quad A_3 = S_4/S_2$$

$$A_4 = S_5/S_2,\quad A_5 = 4r^2S_6/S_2,\quad A_6 = S_7/S_2$$

$$A_7 = 4cq_0/\pi^2r^2S_2E_L,\quad B_1 = 64r^6S_9/S_8,\quad B_2 = 16r^4S_{10}/S_8$$

$$B_3 = S_{11}/S_8,\quad B_4 = S_{12}/S_8,\quad B_5 = 48r^4S_{13}/S_8$$

$$B_6 = 12r^2S_{14}/S_8,\quad B_7 = 8cq_0/\pi S_8E_L,\quad C_1 = 64r^6S_{16}/S_{15}$$

$$C_2 = 16r^4S_{17}/S_{15},\quad C_3 = S_{18}/S_{15},\quad C_4 = S_{19}/S_{15}$$

$$C_5 = 48r^4S_{20}/S_{15},\quad C_0 = 12r^2S_{21}/S_{15},\quad C_7 = 4cq_0/S_{15}E_L$$

where

$$S_1 = -cr_6E_L{}^2/\rho^2h^4$$

$$S_2 = -ct_1 + \frac{1}{\rho h}[l^2(e_{14} + e_{13}\lambda^2 + e_{18}\lambda^4) - e_9R_il(1 + \lambda^2)]$$

$$S_3 = E_L[c\rho h(r_7l + r_9l\lambda^2 + r_{13}) - e_9R_il(d_{15} + d_7\lambda^2)]/\rho^2h^3$$

$$S_4 = a^2[l^2(e_1 + e_{10}\lambda^2 + e_8\lambda^4) - l^3(e_{19} + e_{20}\lambda^2 + e_{23}\lambda^4 + e_{25}\lambda^6)]/E_Lh$$

$$S_5 = a^2[t_1t_2 + 2h\lambda g_3t_3l]/E_Lh,\quad S_6 = 3r_6t_2E_L/\rho^2h^3$$

$$S_7 = -3[t_2(r_7l + r_9l\lambda^2 + r_{13}) + 2hlg_3r_8l\lambda^2]/\rho h$$

$$S_8 = 4r^2[c\rho h^2\{3 + l(3r_{10} + 4\lambda^2r_{11}) - l^2(3r_1 + 4\lambda^2r_2] + 16\lambda^4r_3)\}/2 + h\{l^2(3e_{14} + 4\lambda^2e_{13} + 16\lambda^4e_{18}) - e_gR_il(3 + 4\lambda^2)\}/2]/\rho h^2$$

$$S_9 = -3cr_6E_L{}^2/2\rho^2h^4,\quad S_{10} = E_L\left[\frac{c\rho h^2}{2}(3lr_7 + 3r_{13} + 4\lambda^2lr_9) - e_9lhR_i(3d_{15} + 4\lambda^2d_7)/2\right]/\rho^2h^4$$

$$S_{11} = \frac{h}{2}[l^2(3e_1 + 4\lambda^2e_{10} + 16\lambda^4e_8) - l^3(3e_{19} + 4\lambda^2e_{20} + 16\lambda^4e_{23} + 64\lambda^6e_{25})]/E_L.$$

$$S_{12} = 2l^2h^2[l^2(r_1 + 4\lambda l^2r_2 + 16\lambda^4r_3) - (1 + r_{10}l + 4\lambda^2lr_{11})t_3 + 2\lambda l(r_{12} - r_4l - 8\lambda^2lr_5)t_4 + 2(r_1l^2 - r_{10}l - 1)t_5]/E_L$$

$$S_{13} = 2l^2r_6E_L[t_3 + 2t_5]/\rho^2h^2$$

$$S_{14} = 2l^2h[2\lambda lr_8t_4/h - t_3(r_{13} + r_7l + 4\lambda^2r_9l/h)]/\rho$$

$$S_{15} = 4r^2[lh\{4l(3e_{14} + \lambda^2e_{13} + 3\lambda^4e_{18}) - 3e_9R_i(1 + \lambda^2)\} - c\rho h^2\{16l^2(3r_1 + r_2\lambda^2 + 3r_3\lambda^4) - 12l(r_{10} + r_{11}\lambda^2) - 9\}/4]/\rho h^2$$

$$S_{16} = -9cr_6E_L{}^2/4\rho^2h^4$$

$$S_{17} = -E_L[3lhR_ie_9(d_{15} + d_7l^2) - c\rho h^2(9r_{13} + 12lr_7 + 12\lambda^2lr_9)/4]/\rho^2h^4$$

$$S_{18} = lh[4l(3e_1 + \lambda^2e_{10} + 3\lambda^4e_8) - 16l^2(3e_{19} + \lambda^2e_{20} + \lambda^4e_{23} + 3\lambda^6e_{25}]/E_L$$

$$S_{19} = h^4[\{16l^2(r_1 + \lambda^2r_2 + \lambda^4r_4) - 4l(r_{10} + \lambda^2r_{11}) - 1\}t_4 + 4\lambda lt_7(r_{12} - 4r_4l - 4\lambda^2lr_5) + 2t_5(16l^2r_1 - 4lr_{10} - 1) + 2t_6(16\lambda^4l^2r_3 - 4\lambda^2lr_{11} - 1)]/4E_L$$

$$S_{20} = r_6(t_4 + 2t_5 + 2t_6)E_L/4\rho^2$$

$$S_{21} = h^2[-4lr_7(t_4 + 2t_5) + 4\lambda lr_8t_7 - 4\lambda^2lr_9(t_4 + 2t_6) - r_{13}(t_4 + 2t_5 + 2t_6)]/4\rho$$

The t's in the foregoing expressions are given by

$$t_1 + l^2(r_1 + r_2\lambda^2 + r_3\lambda^4) - l(r_{10} + r_{11}\lambda^2) - 1$$

$$t_2 = 2hl[l\lambda^2(f_1 + f_2) - (g_2 + g_1\lambda^2)]$$

$$t_3 = \lambda^2(h_2 + 2h_3 + h_4/2 + 2h_1 - 8k_1a^2/\pi^2) - 2k_2a^2/\pi^2$$

$$t_4 = 16l^2\lambda^2[l_1 + l_2 + l_3 + 2l_4 + (l_6 + l_7)/2]h^2 - 8l(m_2 + m_1\lambda^2)/h^2$$

$$t_5 = 8l^2\lambda^2(l_2 + l_5 + l_7/2)/h^2 - 8lm_2/h^2$$

$$t_6 = 8l^2\lambda^2(l_1 + l_5 + l_6/2)h^2 - 8l\lambda^2m_1/h^2$$

$$t_7 = 8l^2\lambda^2(l_8 + l_9)/h^2 - 8l\lambda m_3/h^2,\quad l = \pi^2/4a^2$$

The coefficients A_i, B_i, C_i ($i = 1, 2 \ldots 7$) for plates with movable boundaries may be readily obtained by taking g_i, k_i, m_i ($i = 1, 2, 3$) to be zero in these expressions.

D. E. Panayotounakos
Dr. Engineer.

P. S. Theocaris
Professor of Mechanics,
Chair of Mechanics A[1] and
Laboratory for Testing Materials. Mem. ASME.

The National Technical University of Athens,
5, K. Zographou Street,
Zographou, Athens 625, Greece

The Dynamically Loaded Circular Beam on an Elastic Foundation

In this investigation an analytical treatment for the determination of the natural frequencies of a circular uniform beam on an elastic foundation, subjected to harmonic loads, is presented. This problem in the most general case of response is reduced to a system of six-coupled linear partial differential equations. The effects of rotatory inertia and transverse shear deformation are also included in the analysis. The problem is treated by considering the beam as a continuous system, as well as a discrete system. The aforementioned solution methodology is successfully demonstrated through several numerical examples.

Introduction

Considerable attention has been given to the linear elastic analysis of beams under dynamic harmonic loads by many investigators. In references [1–8] the dynamic response of beams is examined using mainly Timoshenko's beam theory. In the simple case of straight beams it has been already shown that the effect of rotatory inertia and shear deformation on the natural frequencies is about 1.7 percent. Moreover, in references [3, 10, 11] the influence of damping on the natural frequencies is examined in special cases of beams. Finally, in references [12, 13] an approximate solution for a cantilever beam and a Plexus frame is given, by considering both systems as discrete.

The response of a straight beam on an elastic foundation under harmonic loads is investigated in references [1, 2], in which the effects of rotatory inertia and shear deformation are taken into account. Moreover, the static analysis of a circular beam on an elastic foundation has been studied in references [14–17].

The present investigation refers to the problem of linear dynamic analysis of a circular beam of uniform cross section on an elastic foundation in the most general case of response. The effects of rotatory inertia and transverse shear deformation are included in the analysis. This problem is reduced to a system of six partial differential equations. After an appropriate analytical treatment, the aforegoing system has been uncoupled and a closed-form solution for the determination of natural frequencies is obtained. Finally, using the methodology of references [12, 13, 18], a closed-form solution of the aforementioned problem is given, by assuming that the continuous system is replaced by an equivalent of—n—concentrated masses. The solution developed herein is successfully demonstrated through several numerical examples.

Mathematical Formulation and Solution Technique

Consider a circular beam of uniform cross section lying on an elastic foundation and subjected to a harmonic motion due to a continuous vertical load $q(s,t) = \overline{q}(s)e^{i\omega t}$; s is the arc of the beam and t the time. The acting forces on the elementary arc $ds = Rd\varphi$ are indicated in Fig. 1. If y denotes the transverse deflection and θ the angle of twist of the cross section, the elastic reactions of the soil are $q = ey$ and $m^* = e^*\theta$; where $e = \bar{e}b$ and $e^* = \bar{e}\bar{b}^3/12$. In addition $\bar{e}$ is the coefficient of subgrade reaction and b the width of the cross section of the beam.

The differential equations (in terms of internal force and moments, rotations and deflection) governing the equilibrium of an arc (Fig. 1) are given by

$$\frac{\partial Q}{\partial \varphi} = eRy - \left(q - \overline{m}\frac{\partial^2 y}{\partial t^2}\right)R$$
$$\frac{\partial M}{\partial \varphi} = QR - D - \gamma^*\frac{\partial^2 \psi}{\partial t^2}R \tag{1a}$$
$$\frac{\partial D}{\partial \varphi} = M - e^*R\theta$$

and

$$\frac{\partial \psi}{\partial \varphi} = -kRM - \theta$$
$$\frac{\partial \theta}{\partial \varphi} = -k\mu RD + \psi \tag{1b}$$
$$\frac{\partial y}{\partial \varphi} = R\psi + \gamma RQ$$

where

$$k = \frac{1}{EI}, \quad \mu = \frac{EI}{GI_d}, \quad \gamma^* = \frac{I\epsilon}{g}, \quad \gamma = \frac{\overset{*}{\beta}}{GF} \tag{2}$$

Contributed by the Applied Mechanics Division and presented at the Winter Annual Meeting, New York, N. Y., December 2–7, 1979, of THE AMERICAN SOCIETY OF MECHANICAL ENGINEERS.

Discussion on this paper should be addressed to the Editorial Department, ASME, United Engineering Center, 345 East 47th Street, New York, N. Y. 10017, and will be accepted until June 1, 1980. Readers who need more time to prepare a discussion should request an extension from the Editorial Department. Manuscript received by ASME Applied Mechanics Division, November, 1978; final revision, March, 1979. Paper No. 79-WA/APM-40.

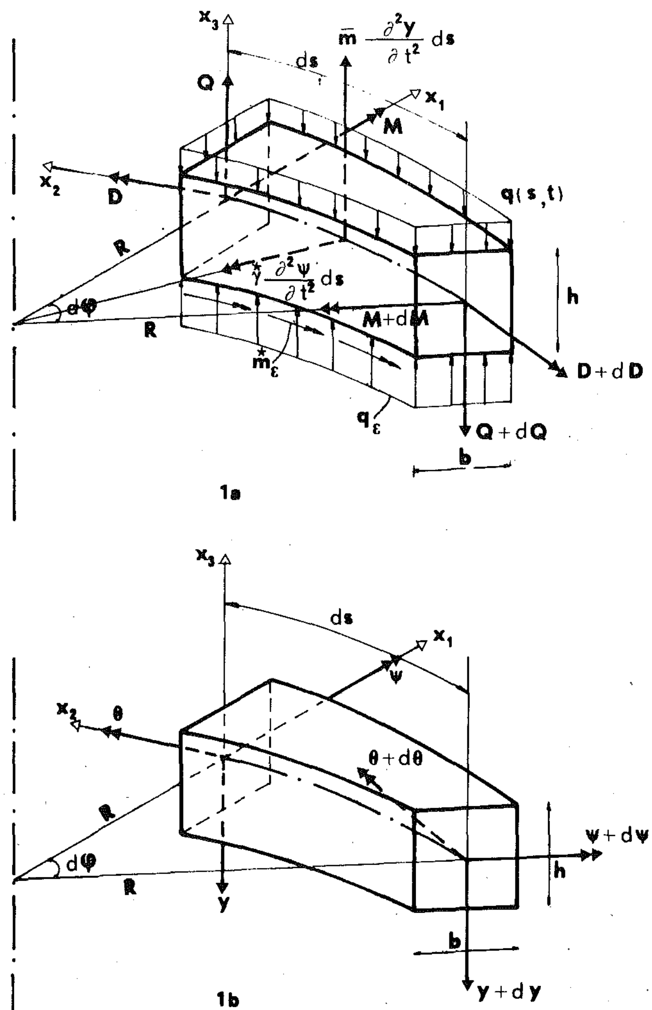

Fig. 1 (a, b) Geometry and sign convention

In the aforementioned relations Q, M, and D denote the shear force, bending moment and twisting moment of the cross section, respectively; ψ is the slope of the deflection curve due only to bending; E and G are the Young's and the shear modulus of elasticity, respectively; F is the cross-section area; I represents the moment of inertia of the cross section with respect to the x_1-axis, while I_d the torsional moment of inertia of the cross section; $\overline{m}$ is the distributed mass per unit length. Finally, ϵ is the specific weight of the material of the beam, g the gravity acceleration, and β a numerical coefficient depending on the shape of the cross section ($\beta = 1.2$ for a rectangular shape and max $\beta \doteq 2.4$ for a I cross section).

It should be noticed that through a simple manipulation of equations (1a) and (1b) the corresponding equations of the static problem can be derived [14–17]. Moreover, by setting $e = e^* = \gamma = 0$ into equations (1a) and (1b) one may obtain the equations (1) and (2) of reference [19].

After a cumbersome manipulation of equations (1a) and (1b), one may decouple these equations and obtain the following partial differential equation for the deflection:

$$\frac{\partial^6 y}{\partial\varphi^6} + A_1\frac{\partial^4 y}{\partial\varphi^4} + A_2\frac{\partial^2 y}{\partial\varphi^2} + A_3 y + A_4\frac{\partial^4 y}{\partial\varphi^2\partial t^2} + A_5\frac{\partial^4 y}{\partial\varphi^2\partial t^2} + A_6\frac{\partial^6 y}{\partial\varphi^2\partial t^4} + A_7\frac{\partial^4 y}{\partial t^4} + A_8\frac{\partial^2 y}{\partial t^2} = A_9 \quad (3)$$

where the constant coefficients A_i ($i = 1, \ldots, 9$) are given in the Appendix.

For a free vibration we may assume a solution for the homogeneous differential equation corresponding to equation (3) of the form:

$$y(s,t) = \overline{Y}(s)e^{i\omega^* t} \quad (4)$$

Introducing relation (4) in the foregoing homogeneous differential equation the following ordinary differential equation of sixth order is obtained:

$$\frac{d^6\overline{Y}}{d\varphi^6} + F^*{}_1\frac{d^4\overline{Y}}{d\varphi^4} + F^*{}_2\frac{d^2\overline{Y}}{d\varphi^2} + F^*{}_3\overline{Y} = 0 \quad (5)$$

where

$$F^*{}_1 = (2 - \mu\nu) + n_1{}^2 + n_2{}^2$$

$$F^*{}_2 = (\nu + \rho + 1 - n^2) - \mu(1+\nu)n_1{}^2 + (2 - \mu\nu)n_2{}^2 + n_1{}^2 \cdot n_2{}^2$$

$$F^*{}_3 = -\{\mu(1+\nu)(\rho - n^2) - (1+\nu)n_2{}^2 + n_1{}^2 n_2{}^2\}$$

$$\rho = keR^4, \quad \nu = keb^2R^2/12 \quad (6)$$

$$n^2 = k\overline{m}R^4\omega^{*2}$$

$$n_1{}^2 = k\gamma^* R^2\omega^{*2}$$

$$n_2{}^2 = \gamma R^2(\overline{m}\omega^{*2} - e) \quad (7)$$

The two last equations include the influences of rotatory inertia and shear deformation.

It is worth noticing that for a rectangular cross section of depth h for which $R \gg 0.45h$ it can be shown that $n^2 \gg n_1{}^2, n_2{}^2$

In effect

$$n^2 = k\overline{m}R^4\omega^{*2} \gg n_1{}^2 = k\gamma^* R^2\omega^{*2} \Rightarrow R^2 \gg I/F \Rightarrow R \gg 0.3h$$

and

$$n^2 = k\overline{m}R^4\omega^{*2} \gg \gamma R^2\overline{m}\omega^{*2} > n_2{}^2 = \gamma R^2|\overline{m}\omega^{*2} - e| \Rightarrow R \gg 0.45h$$

The characteristic equation of the homogeneous differential equation (5)

$$r^6 + F^*{}_1 r^4 + F^*{}_2 r^2 + F^*{}_3 = 0 \quad (8)$$

using the transformation

$$r^2 = z - F^*{}_1/3$$

leads to the following algebraic equation of Cardan's form:

$$z^3 + \Pi z - \upsilon = 0 \quad (9)$$

where

$$\Pi = F^*{}_2 - F^*{}_1{}^2/3$$

$$\upsilon = (-2/27)\, F^*{}_1{}^3 + (1/3)F^*{}_1F^*{}_2 - F^*{}_3 \quad (10)$$

It is known that the nature of the roots of equation (9) depends on the signs of the coefficients Π, υ as well from the sign of the discriminal $\tau = \upsilon^2/4 + \Pi^3/27$.

Clearly the sign of these expressions is dependent on the values of the geometric and elastic characteristics of the beam, as well as on its natural frequencies.

There are, in general, three characteristic cases:

Case *a*: $\Pi < 0, \upsilon < 0, \tau > 0$ which imply one root negative and two roots complex conjugates.

Case *b*: $\Pi > 0, \upsilon > 0, \tau > 0$ which imply one root positive and two roots complex conjugates.

Case *c*: $\tau < 0, \upsilon < 0$ which imply three real roots (one positive and two negatives).

All the roots corresponding to the foregoing cases are given in the Appendix.

The general integral of the homogeneous differential equation of equation (3) can be written under the form

$$y(\varphi,t) = \left\{\sum_{i=1}^{6} c_i\Phi_i\right\}e^{i\omega^* t} \quad (11)$$

where c_i are integration constants which are defined from the boundary conditions and the functions Φ_i have the following expressions:

Case a: $\Phi_1 = \sin r_1\varphi, \Phi_2 = \cos r_1\varphi, \Phi_3 = \sin hu\varphi \cos \lambda\varphi,$
$\Phi_4 = \cosh u\varphi \cos \lambda\varphi, \Phi_5 = \sinh u\varphi \sin \lambda\varphi,$
$$\Phi_6 = \cosh u\varphi \sin \lambda\varphi; \quad (12)$$

where r_1, u, λ are computed from relation (32) given in the Appendix.

Case b:
$$\Phi_1 = \sinh r_1\varphi, \Phi_2 = \cosh r_1\varphi \quad (13)$$

The functions $\Phi_3, \Phi_4, \Phi_5, \Phi_6$ have the same expressions as in *Case a* and r_1, u, λ are computed from relations (32) given in the Appendix.

Case c: $\Phi_1 = \sinh r_1\varphi, \Phi_2 = \cosh r_1\varphi, \Phi_3 = \sin \lambda\varphi,$
$$\Phi_4 = \cos \lambda\varphi, \Phi_5 = \sin u\varphi, \Phi_6 = \cos u\varphi; \quad (14)$$

where r_1, λ, u are computed from relations (33) given in the Appendix.

After the determination of the deflection $y(\varphi,t)$, the internal forces (M,D,Q) and rotations (ψ,θ) can be established through equations (1a) and (1b) as follows:

$$M = \frac{1}{R}\left\{k_1 \frac{d^4y}{d\varphi^4} + k_2 \frac{d^2y}{d\varphi^2} + k_3 y\right\}$$

$$D = \frac{1}{\beta R}\left\{[\alpha(1-k_4) - \beta k_4]k_1 \frac{d^5y}{d\varphi^5} + [(\alpha k_2 - 1)(1-k_4) - \beta k_2 k_4]\frac{d^3y}{d\varphi^3} + [(\alpha k_3 - 1)(1-k_4) - \beta k_3 k_4 + (\mu - 1)n_1{}^2 n_2{}^2 - n_1{}^2]\frac{dy}{d\varphi}\right\}$$

$$Q = -\frac{k_4}{\gamma R}\left\{(\alpha+\beta)k_1 \frac{d^5y}{d\varphi^5} + [(\alpha+\beta)k_2 - 1]\frac{d^3y}{d\varphi^3} + [(\alpha+\beta)k_3 - 1 - n_2{}^2 + \mu n_1{}^2]\frac{dy}{d\varphi}\right\}$$

$$\psi = \frac{k_4}{R}\left\{(\alpha+\beta)k_1 \frac{d^5y}{d\varphi^5} + [(\alpha+\beta)k_2 - 1]\frac{d^3y}{d\varphi^3} + \left[\frac{1}{k_4} + [(\alpha+\beta)k_3 - 1 - n_2{}^2 + \mu n_1{}^2]\right]\frac{dy}{d\varphi}\right\}$$

$$\theta = \frac{1}{R}\left\{\alpha k_1 \frac{d^4y}{d\varphi^4} + (\alpha k_2 - 1)\frac{d^2y}{d\varphi^2} + (\alpha k_3 - n_1{}^2)y\right\} \quad (15)$$

where

$$k_1 = 1/kR(1+\mu)(1+\nu)$$
$$k_2 = k_1\{1 - \nu(1+\mu) + n_2{}^2\}$$
$$k_3 = k_1\{\rho - n^2 + n_1{}^2 n_2{}^2\}$$
$$k_4 = -\gamma/\{\beta R(1 - \gamma\gamma^*\omega^{*2}) - \gamma\}$$
$$\alpha = -kR$$
$$\beta = -k\mu R \quad (16)$$

Relations (15) may be rewritten under the form of two matrix equations as follows:

$$T_1(\varphi,t) = A(\varphi)Ce^{i\omega^* t} \quad (17)$$

$$T_2(\varphi,t) = B(\varphi)Ce^{i\omega^* t} \quad (17a)$$

where

$$T_1 = \{y\ \psi\ \theta\}^T, \quad T_2 = \{M\ D\ Q\}^T$$
$$C = \{C_1, C_2, C_3, C_4, C_5, C_6\}^T$$
$$A = [\alpha_{ij}], \quad B = [\beta_{ij}], \quad (i = 1, 2, 3; j = 1, 2, \ldots, 6) \quad (18)$$

(The superscript "T" indicates the transpose of the matrix).

The elements of matrices A and B have the following expressions for each of the foregoing cases:

Case a: $\alpha_{11} = \sin r_1\varphi, \alpha_{12} = \cos r_1\varphi, \alpha_{13} = \sinh u\varphi \cos \lambda\varphi,$
$\alpha_{14} = \cosh u\varphi \cos \lambda\varphi, \alpha_{15} = \sinh u\varphi \sin \lambda\varphi,$
$\alpha_{16} = \cosh u\varphi \sin \lambda\varphi, \alpha_{21} = a_0\alpha_{12}, \alpha_{22} = -a_0\alpha_{11},$
$\alpha_{23} = d_0\alpha_{14} + f_0\alpha_{15}, \alpha_{24} = d_0\alpha_{13} + f_0\alpha_{16}, \alpha_{25} = d_0\alpha_{16} - f_0\alpha_{13},$
$\alpha_{26} = d_0\alpha_{15} - f_0\alpha_{14}, \alpha_{31} = a_1\alpha_{11}, \alpha_{32} = a_1\alpha_{12},$
$\alpha_{33} = d_1\alpha_{13} + f_1\alpha_{16}, \alpha_{34} = d_1\alpha_{14} + f_1\alpha_{15}, \alpha_{35} = d_1\alpha_{15} - f_1\alpha_{14},$
$\alpha_{36} = d_1\alpha_{16} - f_1\alpha_{13};$
$\beta_{11} = a_2\alpha_{11}, \beta_{12} = a_2\alpha_{12}, \beta_{13} = d_2\alpha_{13} + f_2\alpha_{16},$
$\beta_{14} = d_2\alpha_{14} + f_2\alpha_{15}, \beta_{15} = d_2\alpha_{15} - f_2\alpha_{14},$
$\beta_{16} = d_2\alpha_{16} - f_2\alpha_{13}, \beta_{21} = a_3\alpha_{12}, \beta_{22} = -a_3\alpha_{11},$
$\beta_{23} = d_3\alpha_{14} + f_3\alpha_{15}, \beta_{24} = d_3\alpha_{13} + f_3\alpha_{16}, \beta_{25} = d_3\alpha_{16} - f_3\alpha_{13},$
$\beta_{26} = d_3\alpha_{15} - f_3\alpha_{14}, \beta_{31} = a_4\alpha_{12}, \beta_{32} = -a_4\alpha_{11},$
$\beta_{33} = d_4\alpha_{14} + f_4\alpha_{15}, \beta_{34} = d_4\alpha_{13} + f_4\alpha_{16},$
$$\beta_{35} = d_4\alpha_{16} - f_4\alpha_{13}, \beta_{36} = d_4\alpha_{15} - f_4\alpha_{14}. \quad (19)$$

Case b: $\alpha_{11} = \sinh r_1\varphi, \alpha_{12} = \cosh r_1\varphi, \alpha_{22} = a_0\alpha_{11};$
$$\beta_{22} = a_3\alpha_{11}, \beta_{32} = a_4\alpha_{11}. \quad (20)$$

The remaining elements α_{ij}, β_{ij} have the same expression as in *Case a*.

Case c: $\alpha_{11} = \sinh r_1\varphi, \alpha_{12} = \cosh r_1\varphi, \alpha_{13} = \sin \lambda\varphi, \alpha_{14} = \cos \lambda\varphi,$
$\alpha_{15} = \sin u\varphi, \alpha_{16} = \cos u\varphi, \alpha_{21} = a_0\alpha_{12}, \alpha_{22} = a_0\alpha_{11}, \alpha_{23} = d_0\alpha_{14},$
$\alpha_{24} = -d_0\alpha_{13}, \alpha_{25} = f_0\alpha_{16}, \alpha_{26} = -f_0\alpha_{15}, \alpha_{31} = a_1\alpha_{11}, \alpha_{32} = a_1\alpha_{12},$
$\alpha_{33} = d_1\alpha_{13}, \alpha_{34} = d_1\alpha_{14}, \alpha_{35} = f_1\alpha_{15}, \alpha_{36} = f_1\alpha_{16};$
$\beta_{11} = a_2\alpha_{11}, \beta_{12} = a_2\alpha_{12}, \beta_{13} = d_2\alpha_{13}, \beta_{14} = d_2\alpha_{14}, \beta_{15} = f_2\alpha_{15},$
$\beta_{16} = f_2\alpha_{16}, \beta_{21} = a_3\alpha_{12}, \beta_{22} = a_3\alpha_{11}, \beta_{23} = d_3\alpha_{14}, \beta_{24} = -d_3\alpha_{13},$
$\beta_{25} = f_3\alpha_{16}, \beta_{26} = -f_3\alpha_{15}, \beta_{31} = a_4\alpha_{12}, \beta_{32} = a_4\alpha_{11}, \beta_{33} = d_4\alpha_{14},$
$$\beta_{34} = -d_4\alpha_{13}, \beta_{35} = f_4\alpha_{16}, \beta_{36} = -f_4\alpha_{15}. \quad (21)$$

The coefficients a_i, d_i, f_i $(i = 0, 1, 2, 3, 4)$ corresponding to each of the foregoing cases are given in the Appendix.

The determination of the natural frequencies of the beam will be established by using relations (17), (17a), (18), and the boundary conditions. Thus, considering a circular beam with two free ends, the boundary conditions are

At $\varphi = 0$
$$M(0,t) = D(0,t) = Q(0,t) = 0$$
At $\varphi = \overline{\varphi}$ (total angle of the curved beam)
$$M(\overline{\varphi},t) = D(\overline{\varphi},t) = Q(\overline{\varphi},t) = 0. \quad (22)$$

Using equation (17a) and the boundary conditions given in relations (22), for the nontrivial solution the following determinant must be zero:

$$\begin{vmatrix} \alpha_{11}(0) & \alpha_{12}(0) & \alpha_{13}(0) & \alpha_{14}(0) & \alpha_{15}(0) & \alpha_{16}(0) \\ \alpha_{21}(0) & \alpha_{22}(0) & \alpha_{23}(0) & \alpha_{24}(0) & \alpha_{25}(0) & \alpha_{26}(0) \\ \alpha_{31}(0) & \alpha_{32}(0) & \alpha_{33}(0) & \alpha_{34}(0) & \alpha_{35}(0) & \alpha_{36}(0) \\ \alpha_{11}(\overline{\varphi}) & \alpha_{12}(\overline{\varphi}) & \alpha_{13}(\overline{\varphi}) & \alpha_{14}(\overline{\varphi}) & \alpha_{15}(\overline{\varphi}) & \alpha_{16}(\overline{\varphi}) \\ \alpha_{21}(\overline{\varphi}) & \alpha_{22}(\overline{\varphi}) & \alpha_{23}(\overline{\varphi}) & \alpha_{24}(\overline{\varphi}) & \alpha_{25}(\overline{\varphi}) & \alpha_{26}(\overline{\varphi}) \\ \alpha_{31}(\overline{\varphi}) & \alpha_{32}(\overline{\varphi}) & \alpha_{33}(\overline{\varphi}) & \alpha_{34}(\overline{\varphi}) & \alpha_{35}(\overline{\varphi}) & \alpha_{36}(\overline{\varphi}) \end{vmatrix} = 0 \quad (23)$$

This relation leads to a transcendental equation in ω^{*2} of the form

$$\mathcal{F}(\omega^{*2}; R; \overline{\varphi}; I; I_d; \overline{m}; F; \epsilon; e; \overset{*}{\beta}; g) = 0 \quad (23a)$$

which obviously depends on the values of the parameters $R, \overline{\varphi}, I, I_d, \overline{m}, F, \epsilon, e, \overset{*}{\beta}$, and g.

Moreover the natural frequencies of the aforegoing system are

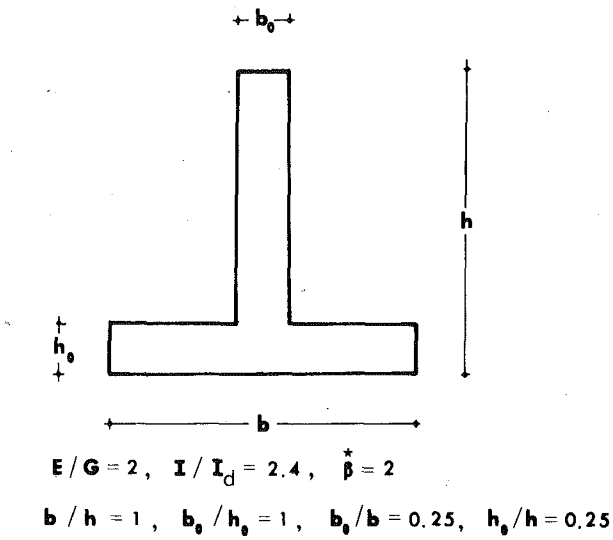

Fig. 2 Cross-section geometry

evaluated by considering that the distributed mass $\overline{m}$ is substituted by n concentrated masses $m_1, \ldots, m_n$ located at n discrete points of the centroidal axis. For harmonic external loads, we may write

$$DY + M\frac{\partial^2 Y}{\partial t^2} = DPe^{i\omega t} \tag{24}$$

where $D = [\delta_{ij}]$ is a $(n \times n)$ symmetrical matrix with elements the influence coefficients of the deflection curve of the beam. The determination of these coefficients for several cases of boundary conditions is given in reference [17]; $P = [P_i]$ is a $(n \times 1)$ matrix of the external concentrated harmonic loads and $M = [m_{ii}]$ is a $(n \times n)$ diagonal matrix of the concentrated masses, (ω is the circular frequency of the existing external loading).

For the determination of the natural frequencies of the aforementioned system an analogous methodology with those given in references [12, 13, 18] is applied. The free motion equation (24) becomes

$$\overline{D}Y + M\frac{\partial^2 Y}{\partial t^2} = [0] \tag{25}$$

where $\overline{D} = D^{-1}$. A solution of this homogeneous equation is sought in the form

$$Y = Xe^{i\omega^* t} \tag{26}$$

where X is a $(n \times 1)$ matrix of the shape functions and ω^* is the natural frequency of the system. Inserting equation (26) to equation (25) for a nontrivial solution yields

$$|\overline{D} - \omega^{*2}M| = 0 \tag{27}$$

Relation (27) leads to an algebraic equation of nth order, from which the n natural frequencies of the system can be determined.

Numerical Results and Discussion

The eigenfrequency equation (23a) is solved numerically on a digital computer for various values of the slenderness ratio $\overline{\lambda} = s^2F/I$ and the ratio R/h for the case of a stubby and a slender beam of $\perp$ cross section (Fig. 2). The respective numerical results are presented in Tables 1 and 2. In all cases considered the length $s(=R\varphi)$ of the beam as well as the parameters shown in Fig. 2 have been kept constant. The results between parentheses correspond to the dimensionless eigenfrequencies in which the influence of the transverse shear effect and rotatory inertia are taken into account.

Table 1 is referred to a stubby beam with $s/h_1 = 13.0$, $\epsilon h/E = 1.83 \times 10^{-6}$ and $\overline{\epsilon}b/E = 0.0015$. From this table the effect of the dimensionless radius of curvature $\overline{R} = R/h_1$ and slenderness ratio $\overline{\lambda}$ upon the dimensionless first and second eigenfrequencies are given. It is clear that as $\overline{R}$ increases (or equivalently the angle φ decreases since $s = R\varphi$ is constant) the first and second eigenfrequencies increase appreciably.

Table 1 Dimensionless eigenfrequencies ($\Omega = \omega^{*2}/EIg/F\epsilon S^4$)

$\overline{R} = R/h_1$ \ $\overline{\lambda}$	40	
3.13	0.77	1.12
	(0.57)	(0.82)
6.25	8.30	9.40
	(7.10)	(7.97)
9.38	32.20	44.37
	(28.02)	(38.60)

Table 2 Dimensionless eigenfrequencies ($\Omega = \omega^{*2}/EIg/F\epsilon S^4$)

$\overline{R} = R/h_2$ \ $\overline{\lambda}$	100	
6.25	2.85	5.58
	(2.76)	(5.40)
12.50	34.89	41.18
	(33.98)	(40.06)
18.76	176.09	190.89
	(175.49)	(185.00)

Table 2 is referred to a slender beam with $s/h_2 = 26.0$, $\epsilon h/E = 0.91 \times 10^{-6}$ and $\overline{\epsilon}b/E = 0.0008$. For s constant it may be derived that $h_2 = h_1/2$ since $s/h_1 = 13.0$, $s/h_2 = 26.0$. From this Table it can be seen that the same influence of $\overline{R}$ on the values of first and second eigenfrequencies is also valid.

Finally, by comparing the results of Tables 1 and 2 the following conclusion may be derived: The effect of the transverse shear deformation upon the eigenfrequencies for large values of the radius of curvature may be neglected even for practical design purposes for stubby beams; however, as the radius of curvature decreases this effect for stubby beams may be appreciable.

Conclusions

In this investigation an analytical treatment for the determination of the natural frequencies of a circular beam on an elastic foundation, in the most general case of response is presented. Among the most important results of this investigation one may list the following;

1 The decoupling of differential equations governing the motion of the aforegoing beam.

2 The closed-form solution of the homogeneous differential equation for the deflection $y(s,t)$ and the determination of the natural frequencies of the circular beam, including the effects of transverse shear deformation and rotatory inertia.

3 The thorough investigation of the nature of the roots of the characteristic equation from which the general integral for deflection is dependent and

4 For stubby beams with small values of the radius of curvature the transverse shear effect upon the eigenfrequencies, may be appreciable.

References

1 Timoshenko, S., Young, D. H., and Weaver, W., *Vibration Problems in Engineering*, 4th ed., Wiley, New York, London, 1974.

2 Gery, P. M., and Calgaro, A., *Les Matrices Transfert dans le Calcul des Structures*, Eyrolles, Paris, 1973.
3 Edmer, A., and Billington, D., "Steady-State Vibration of Damped Timoshenko Beams," *Journal of the Structural Division, Proceedings of the ASCE*, Vol. 94, Mar. 1968, pp. 737–760.
4 Herrmann, G., "Forced Motions of Timoshenko Beams," ASME JOURNAL OF APPLIED MECHANICS, Vol. 22, Mar. 1955, pp. 53–56.
5 Anderson, R. A., "Flexural Vibration of Uniform Beams According to the Timoshenko Theory," ASME JOURNAL OF APPLIED MECHANICS, Vol. 20, Dec. 1953, pp. 504–510.
6 Kounadis, A., "Beam-Columns of Varying Cross Section Under Lateral Harmonic Loads," *Ingenieur-Archiv*, Vol. 44, Springer-Verlag, 1975, pp. 43–51.
7 Cowper, G. R., "On the Accuracy of Timoshenko's Beam Theory," *Proceedings of the ASCE*, EM6, Dec. 1968, pp. 1447–1453.
8 Aalami, B., and Atzori, B., "Flexural Vibrations and Timoshenko's Beam Theory," *AIAA Journal*, Vol. 12, No. 5, 1974.
9 Cowper, G. R., "The Shear Coefficient in Timoshenko's Beam Theory," ASME JOURNAL OF APPLIED MECHANICS, Vol. 33, June 1966, pp. 335–340.
10 Nowacki, W., *Dynamics of Elastic Systems*, Chapman and Hall, London, 1963.
11 Koloušek, V., *Dynamics in Engineering Structures*, Butterworths, London, 1973.
12 Kounadis, A., "Dynamic Response of Cantilevers With Attached Masses," *Journal of the Engineering Mechanics Division, Proceedings of the ASCE*, Vol. 101, Oct. 1975.
13 Panayotounakos, E., "Static and Dynamic Solution of the Plexus Frame by the Matrix Algebra," *Technica Chronica*, Vols. 1–2, Athens, 1966.
14 Volterra, E., "Bending of a Circular Beam Resting on an Elastic Foundation," ASME JOURNAL OF APPLIED MECHANICS, Vol. 19, Mar. 1952, pp. 1–4.
15 Voltera, E., "Deflection of Circular Beams Resting on Elastic Foundation Obtained by the Methods of Harmonic Analysis," ASME JOURNAL OF APPLIED MECHANICS, Vol. 20, June 1953, pp. 227–232.
16 Kameswara, R., N. S. Y., Das, Y. C., and Anandakrishnan, M., "Variational Approach to Beams on Elastic Foundation," *Journal of the Engineering Mechanics Division, Proceedings of the ASCE*, Vol. 97, No. Em. 2, Apr. 1971.
17 Panayotounakos, D., and Theocaris, P., "Circular Beam on Elastic Foundation," *Journal of the Engineering Mechanics Division, Proceedings of the ASCE*, under publication.
18 Chen, J. C., and Wad, B. K., "Criteria for Analysis-Test Correlation of Structural Dynamic Systems," ASME JOURNAL OF APPLIED MECHANICS, Vol. 97, June 1975, pp. 471–477.
19 Culver, G. C., "Natural Frequencies of Horizontally Curved Beams," *Journal of the Structural Division, Proceedings of the ASCE*, Vol. 93, No. ST2, Apr. 1967.

APPENDIX

The coefficients of the partial differential equation (3) are given by

$$A_1 = (2 - \mu\nu) - eR^2\gamma$$

$$A_2 = (\nu + \rho + 1) - eR^2(2 - \mu\nu)\gamma$$

$$A_3 = -\mu\rho(1 + \nu) - eR^2(1 + \nu)\gamma$$

$$A_4 = -R^2(k\gamma^* + \overline{m}\gamma)$$

$$A_5 = kR^2\left[R^2\overline{m} + eR^2\gamma\gamma^* + \mu\,(1 + \nu)\gamma^* - (2 - \mu\nu)\frac{\overline{m}}{k}\gamma\right]$$

$$A_6 = k\overline{m}R^4\gamma\gamma^*$$

$$A_7 = -kR^4\mu(1 + \nu)\overline{m}\gamma\gamma^*$$

$$A_8 = -k\mu R^2\left[R^2(1 + \nu)\overline{m} + (1 + \nu)eR^2\gamma\gamma^* + \frac{(1 + \nu)\overline{m}}{k\mu}\gamma\right]$$

$$A_9 = -R^2\frac{\partial^4 q}{\partial\varphi^4}\gamma + R^2[kR^2 - (2 - \mu\nu)\gamma]\frac{\partial^2 q}{\partial\varphi^2} - R^2[k\mu R^2(1 + \nu) + (1 + \nu)\gamma]q + kR^4\frac{\partial^4 q}{\partial\varphi^2\partial t^2}\gamma\gamma^* - kR^4\mu(1 + \nu)\frac{\partial^2 q}{\partial t^2}\gamma\gamma^* \quad (28)$$

Assuming that $\overline{m} = \gamma^* = 0$ and $q = q(s)$, the resulting new coefficients $A_i (i = 1, \ldots, 9)$ are the same with those of the analogous static system, reference [17].

The roots of equation (9) for the foregoing characteristic cases are

Case *a*: $\Pi < 0, \quad \upsilon < 0, \quad \tau > 0$:

$$z_1 = -[\sqrt[3]{(|\upsilon/2| + \tau^{1/2})} + \sqrt[3]{(|\upsilon/2| - \tau^{1/2})}] < 0$$

$$z_{2,3} = \rho_1 \pm i\rho_2 \quad (29)$$

where

$$\rho_1 = -(1/2)z_1$$

$$\rho_2 = [(3z_1^2 + 4\Pi)/4]^{1/2} \quad (29a)$$

Case *b*: $\Pi > 0, \quad \upsilon > 0, \quad \tau > 0$:

$$z_1 = \sqrt[3]{(\upsilon/2 + \tau^{1/2})} + \sqrt[3]{(\upsilon/2 - \tau^{1/2})} > 0$$

$$z_{2,3} = \rho_1 \pm i\rho_2 \quad (30)$$

where

$$\rho_1 = -(1/2)z_1$$

$$\rho_2 = [(3z_1^2 + 4\Pi)/4]^{1/2} \quad (30a)$$

Case *c*: $\tau < 0, \quad \upsilon < 0$:

$$z_1 = 2\sqrt{-\Pi/3}\cos(x/3) > 0, \quad 0 < x = \arccos[\upsilon/2\sqrt{-27/\Pi^3}] < \pi$$

$$z_2 = -2\sqrt{-\Pi/3}\cos[(\pi - x)/3] < 0$$

$$z_3 = -2\sqrt{-\Pi/3}\cos[(\pi + x)/3] < 0 \quad (31)$$

The expressions of r_1, u, λ for the three characteristic cases are as follows:

Case a: $r_1 = \pm i(|z_1| + F^*{}_1/3)^{1/2}$

$$u = \{[\rho^*{}_1 + (\rho^*{}_1{}^2 + \rho_2{}^2)^{1/2}]/2\}^{1/2}$$

$$\lambda = \rho_2/2\{[\rho^*{}_1 + (\rho^*{}_1{}^2 + \rho_2{}^2)^{1/2}]/2\} \quad (32)$$

where

$$\rho^*{}_1 = \rho_1 - F^*{}_1/3 \quad (32a)$$

Case b: $r_1 = (z_1 - F^*{}_1/3)^{1/2}$
and u, λ have the same expressions as in Case a.

Case c: $r_1 = (z_1 - F^*{}_1/3)^{1/2}$

$$\lambda = i[|z_2| + F^*{}_1/3]^{1/2}$$

$$u = i[|z_3| + F^*{}_1/3]^{1/2} \quad (33)$$

The coefficients a_i, d_i, f_i $(i = 0, \ldots, 4)$ of the matrices A, B given by equations (17), (17a) are defined as follows:

Case a:

$$\begin{aligned}
a_0 &= (r_1 + k_4a_4)/R \\
d_0 &= (u + k_4d_4)/R \\
f_0 &= (\lambda + k_4f_4)/R \\
a_1 &= [\alpha(k_1r_1{}^4 - k_2r_1{}^2 + k_3) + r_1{}^2 - n_1{}^2]/R \\
d_1 &= [\alpha k_1(u^4 - 6u^2\lambda^2 + \lambda^4) + (\alpha k_2 - 1)(u^2 - \lambda^2) \\
&\quad + (\alpha k_3 - n_1{}^2)]/R \\
f_1 &= [-\alpha k_1 4u\lambda(u^2 - \lambda^2) - 2u\lambda(\alpha k_2 - 1)]/R \\
a_2 &= (k_1r_1{}^4 - k_2r_1{}^2 + k_3)/R \\
d_2 &= [k_1(u^4 - 6u^2\lambda^2 + \lambda^4) + k_2(u^2 - \lambda^2) + k_3]/R \\
f_2 &= [-k_14u\lambda(u^2 - \lambda^2) - k_22u\lambda]/R \\
a_3 &= \{(a_1 - 1)r_1 - k_4a_2(\alpha + \beta)r_1 + [k_4(1 - r_1{}^2) \\
&\quad + (\mu - 1)n_1{}^2n_2{}^2]r_1\}/\beta R \\
d_3 &= \{-u + d_1u + f_1\lambda - k_4(\alpha + \beta)u[k_1(u^4 - 10u^2\lambda^2 + 5\lambda^4) \\
&\quad + k_2(u^2 - 3\lambda^2) + k_3]\}/\beta R \\
f_3 &= \{\lambda - d_1\lambda + f_1u - k_4(\alpha + \beta)\lambda[k_1(\lambda^4 + 10u^2\lambda^2 - 5u^4) \\
&\quad + k_2(\lambda^2 - 3u^2) - k_3]\}/\beta R \\
a_4 &= \{a_2\beta r_1 + (a_1 - 1)r_1 + [(\mu + 1)n_1{}^2 - n_2{}^2]r_1\}/ \\
&\quad [\beta R(1 - \gamma\gamma^*\omega^{*2}) - \gamma]R \\
d_4 &= \{(d_2u + f_2\lambda)\beta + (d_1 - 1)u + f_1\lambda \\
&\quad + [(\mu + 1)n_1{}^2 - n_2{}^2]u\}/[\beta R(1 - \gamma\gamma^*\omega^*) - \gamma]R \\
f_4 &= \{(-d_2\lambda + f_2u)\beta - (d_1 - 1)\lambda + f_1u \\
&\quad - [(\mu + 1)n_1{}^2 - n_2{}^2]\lambda\}/[\beta R(1 - \beta\gamma^*\omega^*) - \gamma]R \quad (34)
\end{aligned}$$

Case b:
$$a_1 = [\alpha(k_1 r_1^4 + k_2 r_1^2 + k_3) - r_1^2 - n_1^2]/R$$
$$a_2 = (k_1 r_1^4 + k_2 r_1^2 + k_3)/R \qquad (35)$$

The coefficients $a_0, d_0, f_0; d_1, f_1; d_2, f_2; a_3, d_3, f_3; a_4, d_4, f_4$ have the same expressions as in Case a.

Case c:
$$a_0 = (r_1 + k_4 a_4)/R$$
$$d_0 = (\lambda + k_4 d_4)/R$$
$$f_0 = (u + k_4 f_4)/R$$
$$a_1 = [\alpha(k_1 r_1^4 + k_1 r^2 + k_3) - r_1^2 - n_1^2]/R$$
$$d_1 = [\alpha(k_1 \lambda^4 - k_2 \lambda^2 + k_3) + \lambda^2 - n_1^2]/R$$
$$f_1 = [\alpha(k_1 u^4 - k_2 u^2 + k_3) + u^2 - n_1^2]/R$$
$$a_2 = (k_1 r_1^4 + k_2 r_1^2 + k_3)/R$$
$$d_2 = (k_1 \lambda^4 - k_2 \lambda^2 + k_3)/R$$
$$f_2 = (k_1 u^4 - k_2 u^2 + k_3)/R \qquad (36)$$

$$a_3 = \{(a_1 - 1)r_1 - k_4 a_2(\alpha + \beta)r_1 + [k_4(r_1^2 + 1) + (\mu - 1)n_1^2 n_2^2]r_1\}/\beta R$$
$$d_3 = \{(d_1 - 1)\lambda - k_4 d_2(\alpha + \beta)\lambda + [k_4(1 - \lambda^2) + (\mu - 1)n_1^2 n_2^2]\lambda\}/\beta R$$
$$f_3 = \{(f_1 - 1)u - k_4 f_2(\alpha + \beta)u + [k_4(1 - u^2) + (\mu - 1)n_1^2 n_2^2]u\}/\beta R$$
$$a_4 = \{a_2 \beta r_1 + (a_1 - 1)r_1 + [(\mu + 1)n_1^2 - n_2^2]r_1\}/[\beta R(1 - \gamma\gamma^*\omega^{*2}) - \gamma]R$$
$$d_4 = \{d_2 \beta\lambda + (d_1 - 1)\lambda + [(\mu + 1)n_1^2 - n_2^2]\lambda\}/[\beta R(1 - \gamma\gamma^*\omega^{*2}) - \gamma]R$$
$$f_4 = \{f_2 \beta u + (f_1 - 1)u + [(\mu + 1)n_1^2 - n_2^2]u\}/[\beta R(1 - \gamma\gamma^*\omega^{*2}) - \gamma]R$$
(36)
(*Cont.*)

D. Le Houedec

Dr., Engineering,
Civil Engineering Laboratory, E.N.S.M.,
University of Nantes,
1, rue de la Noé,
44072 Nantes Cedex,
France

Response of a Roadway Lying on an Elastic Foundation to Random Traffic Loads

This paper analyzes the response of a roadway lying on a Westergaard foundation to the pressures of a load moving on a random profile at a constant velocity. The profile power spectrum is based on experimental recordings done on French roads. From the vibrating axle characteristics, we may deduce the power spectrum of the exciting load. Then, we examine random bending vibrations so as to determine the expected mean square displacements of the roadway. We compare the results obtained for random and harmonic profiles. We notice that with the hard rubber foundation, mean values of deflections are comparable. On the other hand, with the soft rubber foundation, the displacement amplitudes for random excitation are much higher than results deduced for harmonic excitation. Consequently, it appears that with various isolation types, the sine profile is not sufficient to predict the roadway behavior. In fact, the actual behavior depends upon the profile power spectrum and vehicle characteristics.

Introduction

Nowadays, road traffic causes various types of nuisances, especially in town centers: air pollution, traffic jams, noise, mechanical vibrations . . . . Obviously more and more traffic is diverted onto peripheral roads and bypasses in order to reduce congestion. However, we must bear in mind that delivery vans and buses will continue in town centers.

During the past years, many papers concerning these traffic vibrations have been published. Thus Abrache [1] has examined the problems of quality of road surfaces and vehicle comfort. Other publications deal with the reduction of traffic vibrations by means of

1 Isolation of buildings [2].

2 Walls cast in the ground [3] or trenches filled with thixotropic mud [4].

3 Isolation of the road (for instance: Farnesina Palace in Roma [5]).

Many papers deal with the response to moving loads of roadway of infinite length [6]. But, in most cases, isolation is a local problem in the neighborhood of a building. According to this notice, in a previous paper [7], we have calculated the response of a roadway of limited length, lying on an elastic foundation and subjected to a harmonic moving load. In this paper, in order to study its true behavior, we propose to determine the bending response of an isolated roadway to random loads moving at constant velocity and deduced from profile spectra.

Contributed by the Applied Mechanics Division for publication in the JOURNAL OF APPLIED MECHANICS.

Discussion on this paper should be addressed to the Editorial Department, ASME, United Engineering Center, 345 East 47th Street, New York, N. Y. 10017, and will be accepted until June 1, 1980. Readers who need more time to prepare a discussion should request an extension from the Editorial Department. Manuscript received by ASME Applied Mechanics Division, November, 1978; final revision, July, 1979.

Motion Equations

Study Hypothesis. We study the bending response of a reinforced concrete roadway lying on various strata: sand, hard or soft rubber. This roadway has a limited length, a rectangular cross section and a random longitudinal profile stated precisely by its power spectrum. For simplicity, we assume that along the roadway the excitation is a stationary random process.

If the roadway consists of concrete, we choose mean values for the mass per unit volume, Young's modulus, and equivalent viscous damping coefficient. We also assume that the isolating rubber is perfectly elastic. Similarly, in the case of a traditional roadway lying on a sand stratum, the Westergaard hypothesis is taken for granted, that is to say that the soil pressure is proportional to the strain. On the other hand, our study excludes the separation problems for soil-roadway contacts.

We compare the roadway behavior with the response of a beam lying on an elastic foundation to a random load moving at a constant velocity. This load is represented by a vibrating axle (Fig. 1) moving on the random profile.

Random Bending Vibrations. We study the bending response of the roadway represented in Fig. 1 and loaded by a force $p(t)$ moving at a constant velocity v_0. We assume that this load is evenly distributed on the width a of a wheelbase. Then, according to the notations mentioned earlier, the motion equation is written

$$EIy_{,xxxx} + m\ddot{y} + \mu\dot{y} + ky = \delta_a(x - v_0t)p(t) \qquad (1)$$

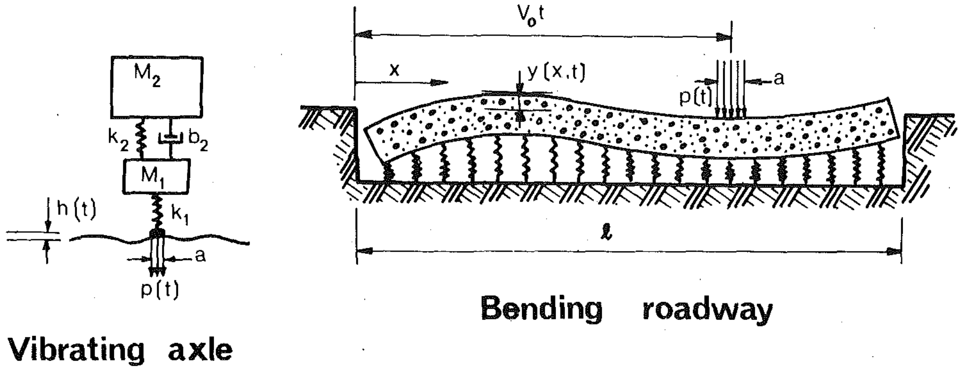

Fig. 1 Problem scheme

where $y(x, t)$ is the roadway displacement and $\delta_a = 1$ for $v_0t - a/2 \leqslant x \leqslant v_0t + a/2$, $\delta_a = 0$ everywhere else.

We notice that the load $p(t)$ has a static component deduced from M_1 and M_2, and a random component, function of the profile. The system response to the static excitation has already been studied [7]. Therefore, we only determine the system response for the random component $u(t)$. Thus we consider the equation

$$EIy_{,xxxx} + m\ddot{y} + \mu\dot{y} + ky = \delta_a(x - v_0t)\, u(t) \qquad (2)$$

For solving equation (2), we apply the generalized Fourier analysis and we try a solution of the type

$$y(x, t) = \frac{1}{2\pi} \int_{-\infty}^{+\infty} Y(x, \omega)\, e^{-i\omega t}\, d\omega$$

where $Y(x, \omega)$ is the Fourier transform of $y(x, t)$.

Similarly, if $U(x, \omega)$ is the Fourier transform of $\delta_a(x - v_0t)\, u(t)$, the equation (2) becomes

$$EIY_{,xxxx}(x, \omega) + (-m\omega^2 - i\mu\omega + m\omega_0^2)\, Y(x, \omega) = U(x, \omega) \qquad (3)$$

We assume that the general solution of this equation is of the form

$$Y(x, \omega) = \sum_{n=1}^{\infty} G_n(x)\, A_n(\omega)$$

where the functions $G_n(x)$ are the natural functions satisfying the differential equation

$$G_{n,xxxx}(x) - \lambda_n{}^4\, G_n(x) = 0 \quad \text{where} \quad \lambda_n{}^4 = m\omega_n{}^2/EI$$

and the four boundary conditions at the free ends of the roadway, that is to say, we have

$$G_n(x) = \text{ch}\lambda_n x + \cos\lambda_n x - \frac{\text{ch}\,\lambda_n l - \cos\lambda_n l}{\text{sh}\lambda_n l - \sin\lambda_n l}(\text{sh}\,\lambda_n x + \sin\lambda_n x)$$

Similarly, if we write that

$$U(x, \omega) = \sum_{n=1}^{\infty} G_n(x)\, B_n(\omega)$$

we obtain

$$A_n(\omega) = \frac{B_n(\omega)}{m(\omega_n{}^2 - \omega^2 + \omega_0{}^2) - i\mu\omega} \qquad (4)$$

We now define the power spectrum $S_y(\omega)$ of the displacement $y(x, t)$ [8]

$$S_y(\omega) = \lim_{T\to\infty} \frac{|Y(x, \omega)|^2}{4\pi T}$$

where T is an arbitrarily long time.

Nomenclature

$A_n(\omega)$ = function of circular frequency ω of order n

b_2 = viscous damping of vehicle system

$B_n(\omega)$ = function of circular frequency ω of order n

C = constant

E = Young's modulus of roadway material

$E(y^2)$ = expected mean square deflection of roadway

f = frequency

$G_n(x)$ = natural mode of vibration of order n

$h(t)$ = roadway profile

i = complex number ($i^2 = -1$)

I = moment of inertia of area about neutral axis

k = linear spring constant of the isolation mattress per unit length

k_1, k_2 = linear spring constants of the vehicle system

l = length of roadway

L = wavelength

m = mass of roadway per unit length

M_1, M_2 = masses of the vehicle system

n = integer

$p(t)$ = moving distributed load on a width a

r = integer

$R_y(\tau)$ = autocorrelation function of displacement

$S_h(\omega), S_u(\omega), S_y(\omega)$ = power spectra of profile, load, and displacement, respectively

$S_{x_1x_2,u(\omega)}$ = cross-correlated spectrum of load

t = time

T = arbitrarily long time

$u(t)$ = random component of load

$U(x, \omega)$ = Fourier's transform of $\delta_a(x - v_0t)\, u(t)$

v_0 = velocity of vehicle

x = coordinate along roadway axis

$y(x, t)$ = roadway deflection

y_{rm}, y_{sm} = mean values of the roadway deflection for random and harmonic excitations, respectively

y_1, y_2, Y_1, Y_2 = displacements of masses for vehicle system

$Y(x, \omega)$ = Fourier's transform of $y(x, t)$

$Z_1(\omega)$ = complex response of the vehicle tire for unit excitation

δ = Kronecker's function

$\lambda_n = (m\omega_n{}^2/EI)^{1/4}$

μ = viscous damping for roadway material

τ = time variation

ω = circular frequency

ω_0 = circular frequency ($\omega_0{}^2 = k/\text{m}$)

ω_n = natural circular frequency

From equation (4), we deduce

$$S_y(\omega) = \sum_{n=1}^{\infty} \sum_{r=1}^{\infty}$$

$$\times \frac{\lim\limits_{T\to\infty} \frac{1}{4\pi T} [B_n(\omega)\, B_r(-\omega)]}{[m(\omega_n{}^2 - \omega^2 + \omega_0{}^2) - i\mu\omega][m(\omega_r{}^2 - \omega^2 + \omega_0{}^2) + i\mu\omega]}$$

$$\times G_n(x)\, G_r(x)$$

The following orthogonality relations

$$\int_0^l G_n(x)\, G_r(x)\, dx = \begin{cases} 0 \text{ for } n \neq r \\ l \text{ for } n = r \end{cases}$$

allows us to write

$$S_y(\omega) = \frac{1}{l^2} \sum_{n=1}^{\infty} \sum_{r=1}^{\infty}$$

$$\times \frac{\lim\limits_{T\to\infty} \frac{1}{4\pi T} \left\{ \int_0^l \int_0^l U(x_1, \omega) U(x_2, -\omega) G_n(x_1) G_r(x_2) dx_1 dx_2 \right\}}{[m(\omega_n{}^2 - \omega^2 + \omega_0{}^2) - i\mu\omega][m(\omega_r{}^2 - \omega^2 + \omega_0{}^2) + i\mu\omega]}$$

$$\times G_n(x)\, G_r(x)$$

For a concentrated load at point $(v_0 t)$, on the hypothesis of a stationary random process, as Erigen [8], we can assume for $\{U(x_1, \omega)\, U(x_2, -\omega)\}$ the following form:

$$\lim_{T\to\infty} \frac{1}{4\pi T} [U(x_1, \omega), U(x_2, -\omega)]$$

$$= S_u(\omega)\, \delta_a(x_1 - v_0 t)\, \delta_a(x_2 - v_0 t) \quad \text{if} \quad x_1 = x_2 \quad \text{or} \quad n = r$$

$$= S_{x_1 x_2, u(\omega)}\, \delta_{a(x_1 - v_0 t)}\, \delta_{a(x_2 - v_0 t)} \quad \text{if} \quad n \neq r$$

where $S_u(\omega)$ is the power spectrum of the random load $u(t)$ and $S_{x_1 x_2, u(\omega)}$ is the cross-correlated spectrum of this same load. But, according to Abrache [1], these cross-correlated spectra are not known for the road traffic; consequently we do not take their effect into account. In fact, we only study the roadway behavior for the power spectrum $S_u(\omega)$. Then, a rough estimate of the power spectrum $S_y(\omega)$ of response is deduced from

$$S_y(\omega) = \frac{a^2}{l^2} \sum_{n=1}^{\infty} \frac{S_u(\omega)}{[m(\omega_n{}^2 - \omega^2 + \omega_0{}^2)]^2 + \mu^2\omega^2} G_n{}^2(V_0 t)\, G_n{}^2(x)$$

The autocorrelation function $R_y(\tau)$ of the deflection $y(x, t)$ is defined by the Wiener-Khintchine equation

$$R_y(\tau) = \int_{-\infty}^{+\infty} S_y(\omega)\, e^{-i\omega\tau}\, d\omega$$

For $\tau = 0$, we obtain the expected mean square displacement $E(y^2)$

$$E(y^2) = R_y(0) = \frac{a^2}{l^2} \sum_{n=1}^{\infty} G_n{}^2(V_0 t) G_n{}^2(x)$$

$$\times \int_{-\infty}^{+\infty} \frac{S_u(\omega)}{m^2(\omega_n{}^2 - \omega^2 + \omega_0{}^2)^2 + \mu^2\, \omega^2} d\omega \qquad (5)$$

The power spectrum of excitation is deduced from roadway profiles and characteristics of moving vehicles.

In our study, the random load is obtained by a vibrating axle moving at constant velocity v_0. Consequently, equation (5) is valid only for $v_0 t \in [0, l]$. For $v_0 t > l$, we assume that the isolated roadway is not loaded: then, of course, the road deflection progressively decreases. But, for a true traffic with jams, the carway is permanently subjected to a random moving load and then the previous data are not valid.

Power Spectrum of Random Exciting Force and Response of the Roadway

Practically, these power spectra are recorded with test apparatus such as profilographs, viagraphs, analyzers of longitudinal profile. Generally, the wavelength of studied roads varies from 1 to 40 m, that is to say, at the usual velocities we obtain excitation frequencies between 0.5 and 20 Hz.

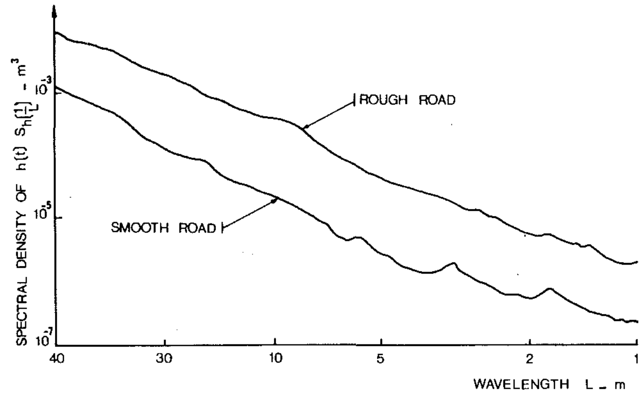

Fig. 2 Profile spectra

As concerns the profile function $h(t)$, the following assumptions are made by Dinca and Sireteanu [9].

1 $h(t)$ is obtained by limiting the spectral band of a δ-correlated random function (traveling over plough-land with a velocity exceeding 15 m/s).

2 $h(t)$ is obtained by limiting the spectral band of a random function with linear exponential correlation (action for paved roads and concrete roads).

3 $h(t)$ is obtained by limiting the spectral band of a random function with damped harmonic correlation (traveling over country roads).

In France, recordings obtained mainly by the "Laboratoire Central des Ponts et Chaussées" (L.C.P.C.) are represented in Fig. 2. These curves are deduced by means of the L.C.P.C. longitudinal profile analyzer. This apparatus is drawn by a vehicle moving at constant velocity. Consequently, we obtain spectra for only one traffic lane.

In a double-logarithmic paper, the obtained curve can be compared with one or two straight lines. In our study, we take a mean straight line of equation

$$S_h(1/L) = C(1/L)^{-2} \quad \text{with} \quad C = 10^{-6}\,\text{m}$$

and

$$L_{\text{II}} = 1\,\text{m} \leqslant L \leqslant L_{\text{I}} = 40\,\text{m}$$

To reach the frequency spectrum, we use the relation

$$S_h(\omega) = S_h(1/L)/2\pi v_0$$

where f notes the frequency. Thus we obtain

$$S_h(\omega) = 2\pi C v_0/\omega^2 \ \text{for} \ \omega_{\text{I}} = 2\pi v_0/L_{\text{I}} \leqslant |\omega| \leqslant \omega_{\text{II}} = 2\pi v_0/L_{\text{II}}$$

$$= 0 \text{ everywhere else} \qquad (6)$$

To determine the spectral density of the exciting force, we use Fig. 1 representing the vibrating axle proposed by Mitschke [10]. Calling the dynamic displacements of solids M_1 and M_2, $y_1(t)$ and $y_2(t)$, the dynamic force transmitted by the tire to the roadway is equal to $k_1[y_1(t) - h(t)] = k_1 Y_1(t)$.

With the given notations and $Y_2(t) = y_2(t) - y_1(t)$, the motion equations of the vibrating axle are written:

$$M_2[\ddot{Y}_1 + \ddot{Y}_2] + b_2\, \dot{Y}_2 + k_2\, Y_2 = -M_2\, \ddot{h} \qquad (7)$$

$$M_1\, \ddot{Y}_1 + k_1\, Y_1 - b_2\, \dot{Y}_2 - k_2\, Y_2 = -M_1\, \ddot{h} \qquad (8)$$

For an unit excitation $h(t) = \exp i\omega t$, the complex frequency response $Z_1(\omega)$ of the displacement $Y_1(t)$ of the vehicle tire is equal to

$$Z_1(\omega) = \frac{\omega^2[(M_1+M_2)k_2 - M_1M_2\omega^2 + ib_2\omega(M_1+M_2)]}{(k_1 - M_1\omega^2)(k_2 - M_2\omega^2) - k_2M_2\omega^2 + ib_2\omega\,[k_1 - (M_1+M_2)\omega^2]}$$

Thus the spectral density of the compression displacement of tire is written

$$S_{Y_1}(\omega) = |Z_1(\omega)|^2 S_h(\omega)$$

$$= 2\pi C v_0 \omega^2 \frac{[(M_1+M_2)k_2 - M_1M_2\omega^2]^2 + b_2{}^2\omega^2(M_1+M_2)^2}{[(k_1 - M_1\omega^2)(k_2 - M_2\omega^2) - k_2M_2\omega^2]^2 + b_2{}^2\omega^2[k_1 - (M_1+M_2)\omega^2]^2}$$

If the load distribution is even on the wheelbase, the power spectrum $S_u(\omega)$ of the distributed random load $u(x, t)$ is deduced from

$$S_u(\omega) = k_1{}^2 S_{Y_1}(\omega)/a^2 \quad \text{for} \quad \omega_{\rm I} \leqslant |\omega| \leqslant \omega_{\rm II}$$

$$= 0 \text{ everywhere else}$$

Consequently, the value of $E(y^2)$ is given by

$$E(y^2) = \frac{4\pi k_1{}^2 C v_0}{l^2} \sum_{n=1}^{\infty} G_n{}^2(v_0 t) G_n{}^2(x) \int_{\omega_{\rm I}}^{\omega_{\rm II}} \frac{[(M_1+M_2)k_2 - M_1M_2\omega^2]^2 + b_2{}^2\omega^2(M_1+M_2)^2}{[(k_1 - M_1\omega^2)(k_2 - M_2\omega^2) - k_2M_2\omega^2]^2 + b_2{}^2\omega^2[k_1 - (M_1+M_2)\omega^2]^2} \times \frac{\omega^2}{m^2(\omega_n{}^2 - \omega^2 + \omega_0{}^2)^2 + \mu^2\omega^2} d\omega$$

Numerical Results and Discussion

In the numerical study, we have chosen the same data as in the case of an alternating force. Thus, we have taken

For the Roadway:

1 Sizes: length: 30 m, width: 3.5 m, thickness: 0.3 m.

2 Material: reinforced concrete.

3 Mean characteristics of material: Young's modulus $E = 4 \times 10^{10}$ Pa, mass per unit volume $= 2.5 \times 10^3$ kg/m^3, equivalent viscous damping coefficient $\mu = 1.8 \times 10^3$ units SI per unit length.

For the Elastic Foundation:

1 Equivalent spring constant of sand layer $k = 3.4 \times 10^7$ N/m per unit length.

2 Equivalent spring constant of Farnesina-type rubber $k = 2.5 \times 10^8$ N/m per unit length.

3 Equivalent spring constant of soft rubber $k = 5 \times 10^6$ N/m per unit length.

For the Moving Load:

1 Constant velocity: $v_0 = 20$ m/s.

2 Characteristics of vibrating axle masses: $M_1 = 10^3$ kg, $M_2 = 11 \times 10^3$ kg; spring constants $k_1 = 5 \times 10^6$ N/m, $k_2 = 5 \times 10^5$ N/m; damping coefficient $b_2 = 1.5 \times 10^4$ units SI.

These values show that for the translation motion of the system roadway-elastic foundation, the natural frequencies are about 18 Hz with a sand foundation, 49 Hz with a hard rubber foundation and 7 Hz with a soft rubber foundation. For the vehicle, the natural frequencies are about 1 Hz (box-resonances) and 12 Hz (wheel-resonances).

The form of the power spectrum $S_u(\omega)$ is given on Fig. 3 as the variations of $|Z_1(\omega)|^2$ and $S_h(\omega)$. These spectra are limited to frequencies between 0.5 and 20 Hz, then the profile wavelengths vary between 1 and 40 m. Consequently, $S_u(\omega) = 0$ for $|\omega| < \pi$ and $|\omega| > 40\,\pi$ rad/s.

For each foundation, we calculate $E(y^2)$ with formula (9). The load moves at a constant velocity equal to 20 m/s and the results give the numerical values of $E(y^2)$ for 20 positions of load, that is to say, every 1.5 m. This computation is effected with an IBM 1130 computer and in order to obtain enough precision, we consider 50 terms in equation (9).

For each position, we compare the results obtained with a random load and with an alternating load deduced from a harmonic profile. This profile has an uneven amplitude equal to 1.8×10^{-3} m and a wavelength equal to 10 m. These values correspond to mean characteristics recorded in France on express roads or motorways.

Thus, for $t = 0.3$ s, that is to say when the vibrating axle is acting at $x = 6$ m, Fig. 4 shows the roadway deflection for the sine profile and the values of $[E(y^2)]^{1/2}$ for the random profile.

We notice that for the random load, the values of $[E[y^2]]^{1/2}$ are almost constant along the roadway. However, these values vary in terms of the load position. These curves represent the roadway behavior at a given moment, but for another load position, the deflection aspect can be different. Thus, for each studied position of the vibrating axle, we calculate for the case of a random load, the mean value of $[E[y^2]]^{1/2}$ which we call y_{rm}. Similarly, for the alternating excitation, we deduce the root mean square value of displacements, called y_{sm}. For each foundation type, Fig. 5 gives variations of y_{rm} and y_{sm} against load position.

The curves show that in the case of isolation with the Farnesina-type rubber, the mean values obtained for random loads are comparable with those calculated for alternating loads. With this hard rubber, the natural frequency is equal to about 49 Hz higher than the excitation frequencies and therefore the amplification factors are reduced.

On the other hand, for the sand foundation and the soft rubber foundation, the calculated displacements are much higher for random loads than for alternating loads. Thus we obtain a mean ratio of deflection equal to 3.4 and 5.7 for sand and soft rubber, respectively. To explain this, we should bear in mind that the natural frequency of the system is about 18 Hz for the sand foundation and 7 Hz for the soft rubber foundation and consequently these frequencies are in the 0.5–20 Hz range of random excitation. Therefore, we have resonance problems with high amplification factors. On the other hand, with the alternating force, the excitation frequency is constant and equal to 2 Hz. Therefore, in this case, we cannot have resonances and the amplification factors are smaller.

Conclusions

In this paper, we have determined the bending dynamic displacements of a roadway lying on elastic solid material (sand or rubber). We have examined both cases: alternating load (sine profile) and random load (true profile of roads). When the resonance frequency of the roadway-foundation system is in the range of load frequencies studies with an alternating load gives results much smaller than those deduced for a random load. This remark is interesting because, if with some foundation types (Farnesina rubber for instance), the alternating load hypothesis is sufficient to find the roadway response, on the other hand, with other foundation types (sand and soft rubber) the results are very different. Consequently, in order to study the actual behavior of the roadway lying on various foundation types, it is preferable to know the characteristics of random traffic loads. Thus we have a more general method for deducing the dynamic displacements of the roadway, and eventually finding the vibration amplitudes acting on building foundations.

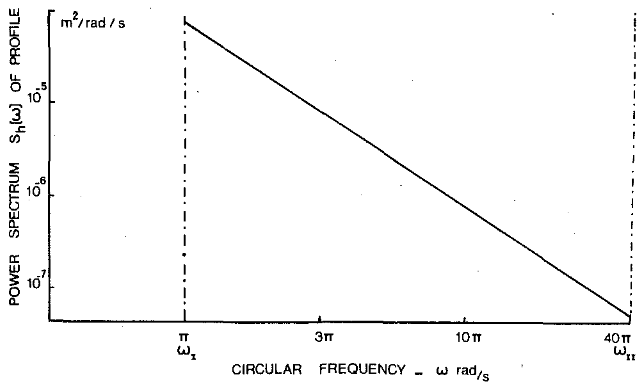

Fig. 3(*a*)

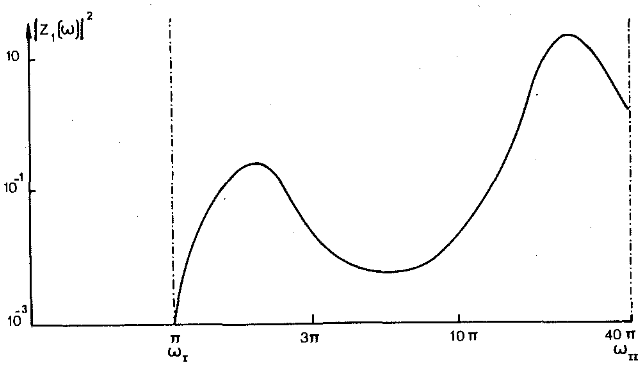

Fig. 3(*b*)

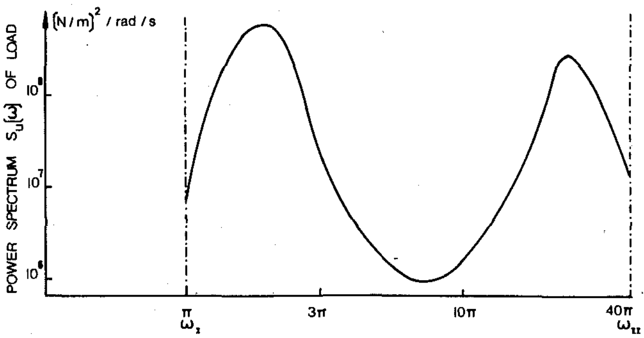

Fig. 3(*c*)

Fig. 3 Variations of $S_h(\omega)$, $|Z(\omega)|^2$, $S_w(\omega)$

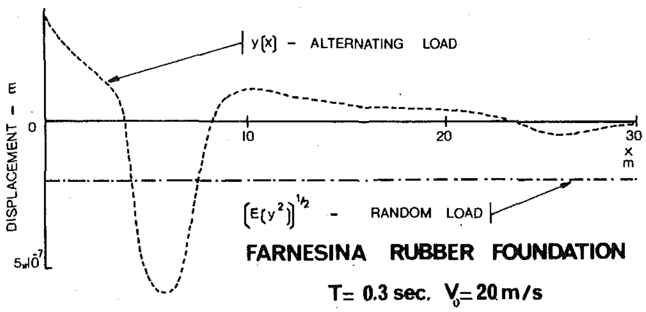

Fig. 4 Variations of $[E[y^2]]^{1/2}$ and $y(x)$ against x

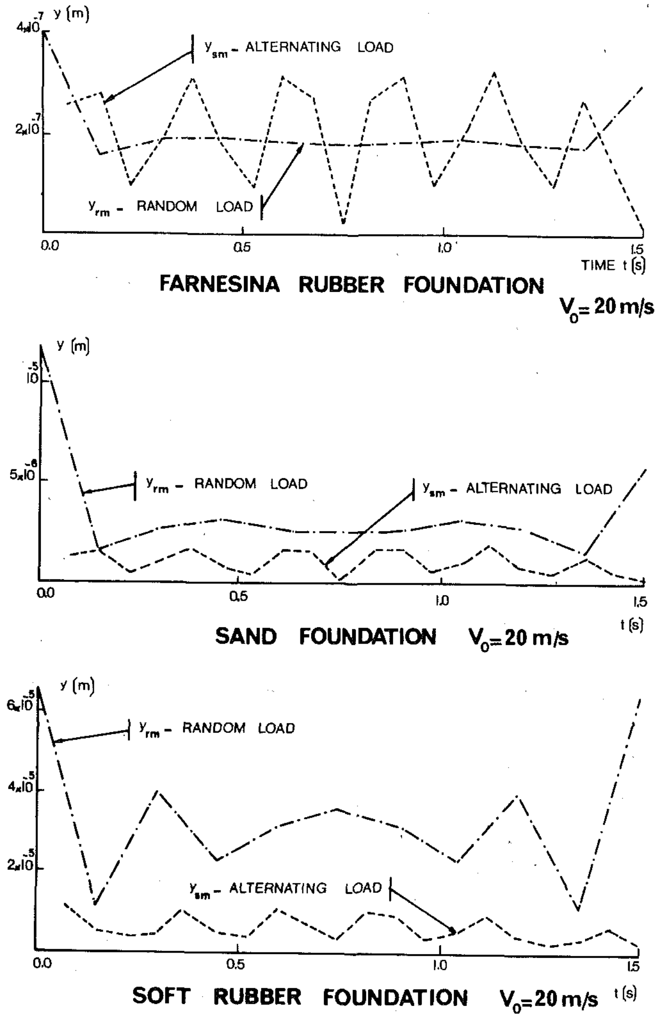

Fig. 5 Mean deflections y_{rm} and y_{sm} for random alternating loads

Acknowledgment

The author wishes to thank Prof. S. H. Crandall for his helpful advice during his stay at the E.N.S.M. Nantes.

References

1 Abrache, M., "Etude sur l'uni des revêtements routiers et le confort du véhicule automobile," *Laboratoire des Ponts et Chaussées,* Paris, Rapport de recherche n° 31, Feb. 1974.

2 Girard, J., "Etude des dispositions à adopter pour la construction des bâtiments dans le voisinage ou au-dessus des voies de circulation ferroviaire ou routière," *Annales de l'ITBTP,* Paris, Série TGC/50, Sept. 1971, pp. 125–140.

3 Haupt, W. A., "Isolation of Vibration by Concrete Core Walls," *Proceedings of the Ninth International Conference on Soil Mechanics and Foundation Engineering,* Vol. 2, Tokyo 1977, pp. 251–256.

4 Dolling, H. I., "Efficiency of Trenches in Isolating Structures Against Vibration," *Vibration in Civil Engineering,* London, Butterwork, 1966, pp. 273–276.

5 Massari, G., "Danno ai monumenti da traffico stradale pesante: il caso della Farnesina di Raffaello," Uria Roma NV VI, estratto della rassegna "Ingegneri architetti," Anno XXXI, 1971.

6 Holder, B. W., and Michalopoulos, C. D., "Response of a Beam on an Inertial Foundation to a Traveling Load," *AIAA Journal,* Vol. 15, n° 8, Aug. 1977, pp. 1111–1115.

7 Bocquenet, D., and Le Houedec, D., "Comportement d'une chaussée reposant sur un matelas antivibratile et soumise à des charges roulantes vibratoires se déplaçant à vitesse constante," *Annales de l'Institut Technique du Bâtiment et des Travaux Publics,* Paris, série: Essais et Mesures, Mar. 1979, pp. 33–56.

8 Eringen, A. C., "Response of Beams and Plates to Random Loads," ASME Journal of Applied Mechanics, Vol. 24, Mar. 1957, pp. 46–52.

9 Dinca, F., and Sireteanu, T., "Random Vibrations in the Dynamics of Motor-Vehicles," *Rev. Roum. Sci. Techn., Mec. Appl.,* Tome 14, n° 4, Bucarest, 1969, pp. 869–894.

10 Mitchke, "Contribution à l'étude des oscillations des vêhicules. Théorie et essais," Institut de l'Université Technique Carola, Wilhelmina Braunschweig, 1962.

Y. K. Wen

Associate Professor,
Department of Civil Engineering,
University of Illinois at Urbana-Champaign,
Urbana, Ill. 61801

Equivalent Linearization for Hysteretic Systems Under Random Excitation

A method of equivalent linearization for smooth hysteretic systems under random excitation is proposed. The hysteretic restoring force is modeled by a nonlinear differential equation and the equation of motion is linearized directly in closed form without recourse to Krylov-Bogoliubov technique. Compared with previously proposed similar methods, the formulation of the present method is versatile and considerably simpler. The accuracy of this method is verified against Monte-Carlo simulation for all response levels. It has a great potential in the analysis of multidegree-of-freedom and degrading systems.

Introduction

Because of the highly nonlinear and hereditary behavior of the restoring force, analytical studies of random response of inelastic structures have been mostly on the development of approximate method [1–6]. In terms of application to practical structures, the method of equivalent linearization (M.E.L.) has the greatest potential; however, there is a very serious limitation that the accuracy is rather poor for elasto-plastic or nearly elasto-plastic systems. The existing M.E.L. relies on a Krylov-Bogoliubov (K-B) technique which is essentially a narrow-band assumption while in reality the response of an inelastic structure could be quite wide band, i.e., it has a tendency to drift and does not undergo as many displacement reversals as in a sinusoidal oscillation implied by the K-B technique. Consequently the K-B method may seriously overestimate the energy dissipation capacity of the system. This may account for the fact that the existing M.E.L. underestimates the RMS response of a nearly elasto-plastic system by up to 50–60 percent in the range $0.5 < \sigma_{x/Y} < 3$ where Y = yielding displacement, σ_x = RMS response [7].

An alternative method based on a direct linearization of the Fokker-Planck equation was used in the study of an offshore structure with bilinear restoring forces [8]. The response statistics were obtained by solving the Liapunov covariance matrix differential equation. The linearized systems coefficients were obtained by a heuristic procedure. RMS responses in the range of 30–80 percent of the yield level were obtained and compared well with simulation results. Recently, a Gaussian closure method was proposed for the study of a hysteretic system with a smooth restoring force [9]. The solution procedure is similar to that in reference [8]. However, the linearized system coefficients are functions of improper integrals involving transcendental functions which can be evaluated only numerically.

The purpose of this paper is to present a method of equivalent linearization for hysteretic systems with smooth restoring forces. No K-B approximation is used and the equation of motion of the systems is linearized directly in closed form, i.e., the coefficients of the linearized system are obtained exactly as simple algebraic functions of the response variable statistics. The solution procedure is the same as in [8, 9]. Both stationary and nonstationary solutions are obtained. The main advantage of the proposed method is the simplicity of the formulation. It can be easily extended to analysis of multidegree-of-freedom (M.D.F.) and degrading systems. The accuracy of this method is verified against Monte-Carlo simulations for all ranges of response levels.

The Hysteretic Restoring Force Model

Following reference [5], the restoring force in a hysteretic system is described by

$$Q(x, \dot{x}) = g(x, \dot{x}) + z(x) \tag{1}$$

in which g = a nonhysteretic component, a function of the instantaneous x and $\dot{x}$. $z = a$ hysteretic component, a function of the time history of x. z is related to x through the following first-order nonlinear differential equation.

$$\dot{z} = -\gamma|\dot{x}|z|z|^{n-1} - \beta\dot{x}|z|^n + A\dot{x} \tag{2}$$

in which γ, β, A, and n are parameters. It has been shown (reference [5]) that a hysteretic relationship exists between z and x and one can construct a variety of restoring forces, such as softening or hardening, narrow or wide-band systems. Parameters γ and β control the shape of the hysteresis loop, A the restoring force amplitude, and n the smoothness of the transition from elastic to plastic response, e.g., a large value of n corresponds to an almost elasto-plastic system.

Without loss of generality, attention will be concentrated on the

Contributed by the Applied Mechanics Division for publication in the JOURNAL OF APPLIED MECHANICS.

Discussion on this paper should be addressed to the Editorial Department, ASME, United Engineering Center, 345 East 47th Street, New York, N. Y. 10017, and will be accepted until June 1, 1980. Readers who need more time to prepare a discussion should request an extension from the Editorial Department. Manuscript received by ASME Applied Mechanics Division, September, 1978; final revision, July, 1979.

response analysis of a S.D.F. system with the following equation of motion (if needed, additional nonlinearity in the damping and stiffness can be easily introduced),

$$\ddot{x} + 2\zeta_0\omega_0\dot{x} + \alpha\omega_0^2 x + (1-\alpha)\omega_0^2 z = f(t)/m \tag{3}$$

For example, for $n = 1, A = 1.0, \gamma = \beta = 0.5$, and $\alpha \ll 1$, equations (2) and (3) represent a nearly elastoplastic oscillator with smooth transition. x = nondimensional (normalized by Y) displacement; ζ_0 = viscous damping ratio; ω_0 = preyielding natural frequency = $\sqrt{Fy/mY}$; α = post to preyielding stiffness ratio.

The Equivalent Linear System

Writing equations (2) and (3) in the form

$$\mathbf{g}(\ddot{\mathbf{x}}, \dot{\mathbf{x}}, \mathbf{x}) = \mathbf{f}(t) \tag{4}$$

in which, the vector $\mathbf{x} = (x, z)$, $\mathbf{g}$ = the left-hand side of equations (2) and (3). If $f(t)/m$ is a zero-mean stationary Gaussian process, it has been shown by Atalik and Utku [10] that under the conditions that $\mathbf{g}$ satisfies some smoothness requirements the mean square error in replacing equation (4) by the equation of motion of a linear system

$$M\ddot{X} + C\dot{X} + KX = f \tag{5}$$

can be minimized if the elements of the matrices are given by

$$M_{ij} = E\left[\frac{\partial g_i}{\partial \ddot{x}_j}\right]$$

$$C_{ij} = E\left[\frac{\partial g_i}{\partial \dot{x}_j}\right]$$

$$K_{ij} = E\left[\frac{\partial g_i}{\partial x_j}\right] \tag{6}$$

in which $E[\ \ ]$ = expected value. It has been shown [11] that equation (6) gives a true (global) minimum if the matrix $E[\bar{x}\bar{x}^T]$ where $\bar{x}$ = vector $(x, \dot{x}, z, \dot{z})^T$ is nonsingular; otherwise, the solution will not be unique but will be as good as any other solution. Therefore the governing equation of motion of the equivalent linear system are

$$\ddot{x} + 2\zeta_0\omega_0\dot{x} + \alpha\omega_0^2 x + (1-\alpha)\omega_0^2 z = f(t)/m \tag{7}$$

$$\dot{z} + C_{21}\dot{x} + K_{22}z = 0 \tag{8}$$

in which, for the case $n = 1$

$$C_{21} = \gamma E\left[z\frac{\partial|\dot{x}|}{\partial \dot{x}}\right] + \beta E[|z|] - A \tag{9}$$

$$K_{22} = \gamma E[|\dot{x}|] + \beta E\left[\dot{x}\frac{\partial|z|}{\partial z}\right] \tag{10}$$

Since $f(t)$ is a Gaussian process, and the system is linear, $\dot{x}$ and z are jointly Gaussian. The two coefficients C_{21} and K_{22} can be evaluated in terms of the second moments of $\dot{x}$ and z.

$$C_{21} = \sqrt{\frac{2}{\pi}}\left[\gamma\frac{E(\dot{x}z)}{\sigma_{\dot{x}}} + \beta\sigma_z\right] - A \tag{11}$$

$$K_{22} = \sqrt{\frac{2}{\pi}}\left[\gamma\sigma_{\dot{x}} + \beta\frac{E(\dot{x}z)}{\sigma_z}\right] \tag{12}$$

Equations (7), (8), (11), and (12) provide a direct closed-form linearization of the equation of motion. Note that no averaging over one cycle of oscillation or narrow-band assumption is made here. C_{21} and K_{22} for the case $n \neq 1$ is given in the Appendix.

For example, for the case $\gamma = \beta = 0.5$, z represents the restoring force of a smooth elasto-plastic system (reference [5]). The dynamic characteristics of the linearized 3rd-order oscillator can be described in terms of the free-vibration solution of the following form:

$$X(t) = C_1 e^{-a_1 t} + C_2 e^{-a_2\omega t}\sin(\omega' t + \phi) \tag{13}$$

in which C_1, C_2, and ϕ are the constants determined by the initial conditions of x, $\dot{x}$, and z. The first term allows some "drift" in the response, an essential feature of inelastic response. When $\alpha = 0$, z is the only restoring force in equation (3). For this case, $a_1 = 0$ and equation (13) gives a damped oscillation around a permanent displacement, the behavior of a elasto-plastic system. Therefore the third-order linear system retains most of the inelastic behaviors of the original system and is easy to handle analytically.

When the excitation is a uncorrelated shot noise (including white noise), the differential equation of the covariance matrix of the response variables x, $\dot{x}$, and z is derived in the following.

Introduce the vector $\mathbf{y}$ ($y_1 = x$, $y_2 = z$, and $y_3 = \dot{x}$); equations (7) and (8) can be rewritten as a system of first-order differential equations

$$\frac{d}{dt}\mathbf{y} = \mathbf{g}\mathbf{y} + \mathbf{F} \tag{14}$$

in which

$$\mathbf{g} = \begin{bmatrix} 0 & 0 & 0 \\ 0 & -K_{22} & -C_{21} \\ -\alpha\omega_0^2 & -(1-\alpha)\omega_0^2 & -2\zeta_0\omega_0 \end{bmatrix}$$

$$\mathbf{F} = \begin{Bmatrix} 0 \\ 0 \\ f(t)/m \end{Bmatrix} \tag{16}$$

Let the covariance matrix of $\mathbf{y}$ be $\mathbf{S}$ with $S_{ij} = E[y_i y_j]$, it can be shown that [12] $\mathbf{S}$ satisfies the following differential equation:

$$\frac{d}{dt}\mathbf{S} = \mathbf{g}\mathbf{S} + \mathbf{S}\mathbf{g}^T + \mathbf{B} \tag{17}$$

in which $\mathbf{g}^T$ = the transpose of $\mathbf{g}$.

$\mathbf{B}$ is a matrix of the expected values of the products of the forcing functions and the response vectors. $B_{ij} = 0$ except that $B_{33} = \mathrm{I}(t)$, the intensity function of the shot noise. If $f(t)/m$ is a white noise, $B_{33} = 2\pi G_0$ where G_0 = power spectral density of the white noise.

If the excitation is stationary, $\mathbf{B}$ is independent of t; the stationary solution can be obtained by solving the Liapunov matrix equation

$$\mathbf{g}\mathbf{S} + \mathbf{S}\mathbf{g}^T + \mathbf{B} = 0 \tag{18}$$

Making use of the fact that $\mathbf{S}$ is symmetric, one can rewrite equation (18) in a standard 6×6 matrix equation. Since K_{22} and C_{21} in $\mathbf{g}$ depend on the response statistics, an iteration solution procedure is generally required. To start the iteration one can use the solution of a linear system with a stiffness equal to the preyielding stiffness of the nonlinear system.

When the excitation is nonstationary, or for the transient solution of the system under stationary excitation, the time-dependent covariance matrix of $\mathbf{y}$ can be obtained by solving equation (17) numerically based on a step-by-step integration method. This method has been used in reference [8].

Solution for Filtered Shot Noise Excitation

When the excitation is correlated, it can be modeled as a filtered-shot noise. For example, in seismic response analysis, one frequently models the excitation by passing the shot noise through a filter with a frequency transfer function of the form of the Kanai spectrum [13]

$$S(\omega) = S_0\left[\frac{\omega_g^4 + 4\omega_g^2\zeta_g^2\omega^2}{(\omega^2 - \omega_g^2)^2 + 4\omega_g^2\zeta_g^2\omega^2}\right] \tag{19}$$

in which ω_g and ζ_g are the natural frequency and damping ratio of the filter representing the spectral characteristics of the ground excitation. For this case, the required equations of motion are

$$\ddot{x} + 2\zeta_0\omega_0\dot{x} + \alpha\omega_0^2 x + (1-\alpha)\omega_0^2 z - \omega_g^2 x_g - 2\zeta_g\omega_g\dot{x}_g = 0 \tag{20}$$

$$\dot{z} + C_{21}\dot{x} + K_{22}z = 0 \tag{21}$$

$$\ddot{x}_g + 2\zeta_g\omega_g\dot{x}_g + \omega_g^2 x_g = f(t) \tag{22}$$

in which $f(t)$ = shot noise with intensity $I(t)$; for the case of stationary excitation $I(t) = 2\pi G_0$. Therefore the solution procedure is identical

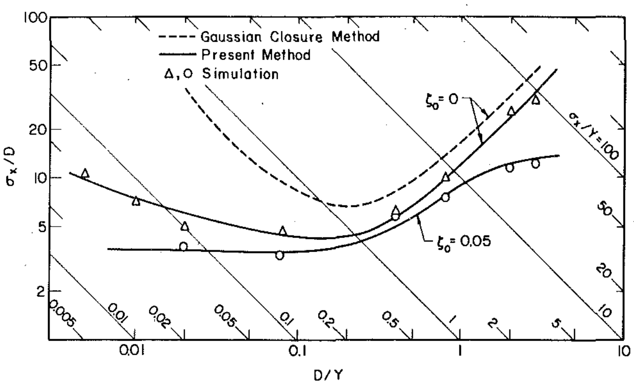

Fig. 1 Nondimensional RMS response and comparison with Monte-Carlo solution

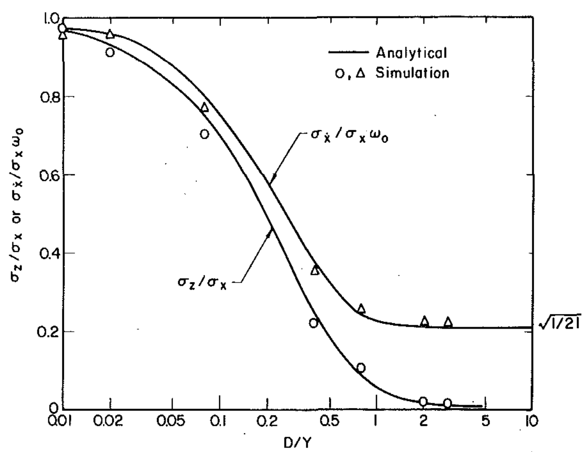

Fig. 2 Comparison of $\sigma_{\dot{x}}/\sigma_x$ (apparent frequency) and σ_z/σ_x with Monte-Carlo solution

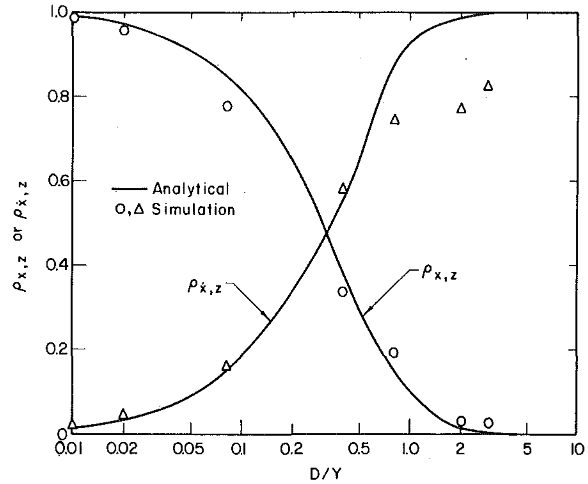

Fig. 3 Comparison of $\rho_{\dot{x},z}$ and $\rho_{x,z}$ with Monte-Carlo solution

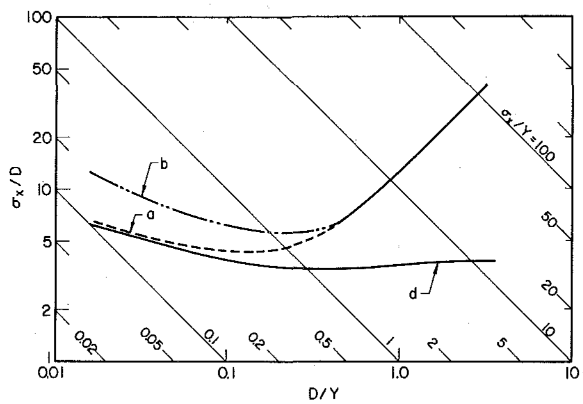

Fig. 4 Nondimensional RMS responses of systems with hysteretic restoring forces type *a*, *b*, and *d* (reference [5])

to the previous case. For example, if $y_1 = x, y_2 = z, y_3 = x_g, y_4 = \dot{x}, y_5 = \dot{x}_g$, **g** in equation (14) is

$$\begin{bmatrix} 0 & 0 & 0 & 1 & 0 \\ 0 & -K_{22} & 0 & -C_{21} & 0 \\ 0 & 0 & 0 & 0 & 1 \\ -\alpha\omega_0{}^2 & -(1-\alpha)\omega_0{}^2 & \omega_g{}^2 & 2\zeta_0\omega_0 & 2\zeta_g\omega_g \\ 0 & 0 & -\omega_g{}^2 & 0 & -2\zeta_g\omega_g \end{bmatrix} \tag{23}$$

$$B_{ij} = 0 \text{ in } \mathbf{B} \text{ except } B_{55} = I(t).$$

Numerical Example and Comparison With Monte-Carlo Solution

A nearly elasto-plastic system ($A = 1.0, \gamma = \beta = 0.5, \alpha = 1/21$, and $N = 1$) under white noise excitation is studied since the existing E.L.M. has given poor result for such systems [7]. $\omega_0 = 1$ rad/sec and $\zeta_0 = 0$ in equation (3). The RMS response σ_x as a function of the excitation level is shown in Fig. 1. σ_x is normalized by $D = \sqrt{2G_0/\omega_0{}^3}$ and the excitation level is indicated by the nondimensional quantity D/Y. Grid lines for the factor $\sigma_{x/Y}$ are also shown in Fig. 1 to indicate the level of yielding that has taken place in the oscillator. It is seen that the results cover a wide range, from $\sigma_{x/Y} = 0.05$ to $\sigma_{x/Y} = 100$. In the Monte-Carlo solutions, white noises are generated digitally and equations (2) and (3) are integrated based on a step-by-step predictor-corrector method. The covariance matrix of the response variables is evaluated by taking the temporal average over a length of 30 cycles of oscillation.

The simulated RMS responses for various excitation levels are compared with the analytical solution in Fig. 1. The agreement is very good for all response levels. The small scatter can be attributed to the sampling fluctuation since 30 cycles of oscillation is not a very long sampling time. The Gaussian closure solution of the same system is also shown in Fig. 1 by the dashed line. The closure method generally gives conservative results which are overly so in the low response range ($\sigma_{x/Y} < 1$).

The apparent frequency $\sigma_{\dot{x}}/\sigma_x$ and the ratio σ_z/σ_x as functions of the nondimensional excitation are compared with the Monte-Carlo results in Fig. 2. Again the agreements are very good. At low excitation level, the oscillator is nearly linear; as a result σ_z/σ_x is almost unity. At high level of excitation, $\sigma_{\dot{x}}/\sigma_x$ approaches the postyielding natural frequency $\sqrt{\alpha}\,\omega_0$ and σ_z/σ_x is almost zero since z is bounded by unity and x increases with the excitation. The correlation coefficients $\rho_{x,z}$ and $\rho_{\dot{x},z}$ (note $\rho_{x,\dot{x}} = 0$) are compared with the Monte-Carlo results in Fig. 3. The agreements are generally very good except that the analytical solution overestimates $\rho_{\dot{x},z}$ by 15–20 percent for $D/Y > 0.8$ (or $\sigma_{x/Y} > 8$).

For a viscous damping ratio of $\zeta_0 = 0.05$, the $\sigma_{x/D}$-values are shown in Fig. 1. The effect of the viscous damping is important at the two tails where the hysteretic energy dissipation is comparatively small. Also, in these regions $\sigma_{x/D}$ approaches a constant value as in the case of a linear system with a constant viscous damping ratio. The comparison with Monte-Carlo result is again very good for all levels of response.

The $\sigma_{x/D}$-values for systems with $\zeta_0 = 0$, $\alpha = 1/21$, $n = 1$ and a hysteretic restoring force z of type b and d described in reference [5] are compared with type a, the nearly elasto-plastic system, in Fig. 4. Type b is a softening system with a "pinched" hysteresis loop while type d is a hardening system. At low level of excitation, the responses

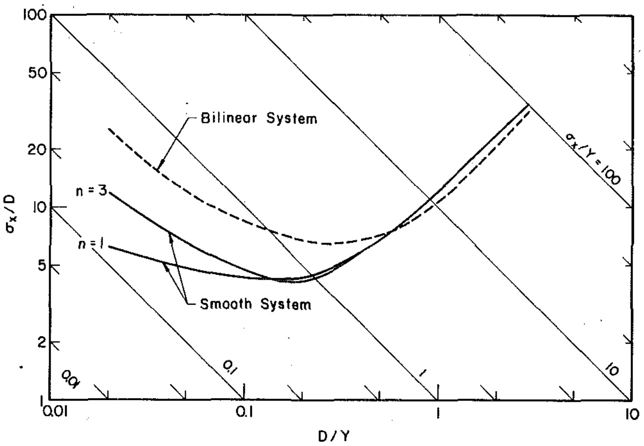

Fig. 5 Comparison of RMS responses of smooth and bilinear systems

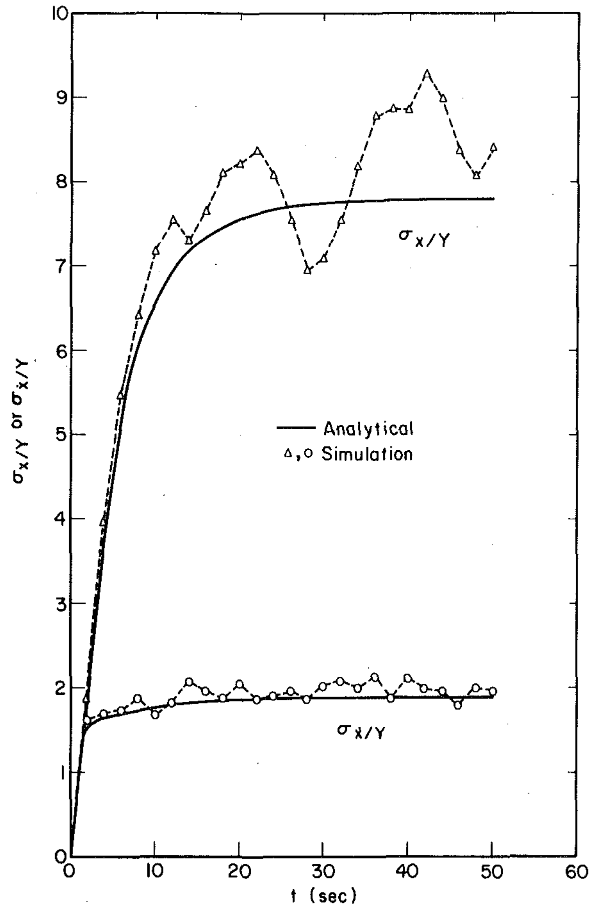

Fig. 6 Comparison of transient response with Monte-Carlo solution

of systems a and d are almost identical while system b is much higher since in this range the hardening or softening effect is not important but damping effect dominates. At high level of excitation the responses of systems a and b are almost identical while that of d is much lower. These of course are what one would expect in view of the restoring force behaviors shown in reference [5]. The $\sigma_{x/D}$-values for the case $n = 1$ and 3 ($\gamma = \beta = 0.5$, $\zeta_0 = 0$ and $\alpha = 1/21$) are compared with those of a similar bilinear system [7] in Fig. 5. There are considerable differences in the low response range, apparently due to the fact that in this range while certain amount of damping exists in the smooth system, particularly the case $n = 1$ (reference [5]), the bilinear system is virtually undamped.

The nonstationary solution of the case $\zeta_0 = 0$, $\gamma = \beta = 0.5$ and $\alpha = 1/21$ is compared with Monte-Carlo solution (ensemble average of 200 responses) in Fig. 6. The agreement is good except that the small oscillation of the mean square responses is not predicted by the analytical method.

Summary and Conclusion

A method of equivalent linearization for smooth hysteretic systems under random excitation is proposed. The hysteretic restoring force is modeled by a nonlinear differential equation and the equation of motion is linearized directly in closed form without recourse to Krylov-Bogliubov approximation. The linearized system is 3rd order and retains most of the inelastic response behavior. Although similar methods of modeling and the solution procedure have been available in the literature, the formulation in the proposed method is versatile and considerably simpler and the accuracy of this method has been verified against Monte-Carlo simulation for all response levels. The method has a great potential in the analysis of multidegree-of-freedom and degrading systems. This is presently under investigation by the author and some preliminary results have already been obtained [14].

Acknowledgment

This research was conducted as part of a research study of Safety Evaluation of Structures to Earthquakes and Other Natural Hazards sponsored by National Science Foundation under Grant No. ENV 77-09090. The author would like to thank Mr. Thomas Baber for carrying out the Monte-Carlo simulation and most of the numerical computations.

Reference

1 Caughey, T. K., "Equivalent Linearization Techniques," *Journal of the Acoustical Society of America*, Vol. 35, No. 11, 1963, pp. 1706–1711.

2 Iwan, W. D., "A Generalization of the Method of Equivalent Linearization," *International Journal of Nonlinear Mechanics*, Vol. 8, 1973, pp. 279–287.

3 Lutes, L. D., and Takemiya, H., "Random Vibration of Yielding Oscillator," *Journal of the Engineering Mechanics Division, Proceedings, ASCE*, Vol. 100, No. EM2, Apr. 1974, pp. 343–358.

4 Vanmarcke, E. H., Yanev, P. I., and DeEstrade, M. B., "Response of Simple Hysteretic System to Random Excitations," M.I.T. Report, Department of Civil Engineering, Massachusetts Institute of Technology, Cambridge, Mass., 1970.

5 Wen, Y. K., "Method for Random Vibration of Hysteretic Systems," *Journal of Engineering Mechanics Division, Proceedings, ASCE*, Vol. 102, No. EM2, Apr. 1976, pp. 249–263.

6 Karnopp D., and Brown, N., "Random Vibration of Multidegree-of-Freedom Hysteretic Structures," *Journal of the Acoustical Society of America*, Vol. 42, No. 1, 1967, pp. 54–59.

7 Iwan, W. D., and Lutes, L. D., "Response of Bilinear Hysteretic System to Stationary Random Excitation," *Journal of the Acoustical Society of America*, Vol. 43, Mar. 1968, pp. 545–552.

8 Kaul, M. K., and Penzien, J., "Stochastic Seismic Analysis of Yielding Offshore Towers," *Proceedings, ASCE*, Vol. 100, No. EM5, Oct. 1974, pp. 1025–1038.

9 Iyengar, R. N., "Study of the Random Vibration of Nonlinear Systems by the Gaussian Closure Technique," ASME JOURNAL OF APPLIED MECHANICS, Vol. 45, June 1978, pp. 393–399.

10 Atalik, T. S., and Utku, S., "Stochastic Linearization of Multidegree-of-Freedom Nonlinear Systems," *Journal of Earthquake Engineering and Structural Dynamics*, Vol. 4, 1976, pp. 411–420.

11 Spanos, P. T., and Iwan, W. D., "On the Existence and Uniqueness of Solutions Generated by Equivalent Linearization," *International Journal of Nonlinear Mechanics*, Vol. 13. No. 2. 1978, pp. 71–78.

12 Lin, Y. K., *Probabilistic Theory of Structural Dynamics*, McGraw-Hill, New York, 1967.

13 Kanai, K., "Semiemprical Formula for the Seismic Characteristics of the Ground Motion," *Bulletin Earth Res. Int.*, University of Tokyo, Vol. 35, 1957, pp. 309–325.

14 Baber, T. T., and Wen, Y. K., "Equivalent Linearization for Hysteretic Structures," *Proceedings of the ASCE*, Specialty Conference on Probabilistic Mechanics and Structural Reliability, Tucson, Ariz., Jan. 1979, pp. 25–29.

APPENDIX

C_{21} and K_{22} for $n \neq 1$

$$C_{21} = \gamma \frac{2^{n/2}}{\pi} \sum_{r=0}^{n-1} \binom{n}{r} \Gamma\left(\frac{r+1}{2}\right) \Gamma\left(\frac{n-r+1}{2}\right) (1 - \rho_{\dot{x}z}{}^2)^{r/2} \times \rho_{\dot{x}z}{}^{n-r} \sigma_z{}^n + \beta \frac{2^{n/2}}{\sqrt{\pi}} \Gamma\left(\frac{n+1}{2}\right) \sigma_z{}^n - A$$

$$K_{22} = \gamma \frac{2^{n/2}}{\pi} \sum_{r=0}^{n-1} \binom{n-1}{r} \Gamma\left(\frac{r+1}{2}\right) \Gamma\left(\frac{n-r+1}{2}\right) (1 - \rho_{\dot{x}z}{}^2)^{r/2} \times \rho_{\dot{x}z}{}^{n-r+1} + \beta n \frac{2^{n/2}}{\sqrt{\pi}} \Gamma\left(\frac{n+1}{2}\right) \rho_{\dot{x}z} \sigma_{\dot{x}} \sigma_z{}^{n-1} \quad r = \text{even}$$

e.g., for $n = 3$

$$C_{21} = \gamma \sqrt{\frac{2}{\pi}} \sigma_z{}^3 \rho (3 - \rho^2) + \beta 2 \sqrt{\frac{2}{\pi}} \sigma_z{}^3 - A$$

$$K_{22} = \gamma\, 3 \sqrt{\frac{2}{\pi}} \sigma_z{}^2 \sigma_{\dot{x}} (1 + \rho^2) + \beta 6 \sqrt{\frac{2}{\pi}} \rho \sigma_{\dot{x}} \sigma_z{}^2$$

$$\rho = E[\dot{x}z] / \sigma_{\dot{x}} \sigma_z$$

T. D. Burton
Department of Mechanical Engineering,
Washington State University,
Pullman, Wash. 99164
Mem. ASME

A. M. Whitman
Department of Mechanical Engineering and
Applied Mechanics,
University of Pennsylvania,
Philadelphia, Pa. 19174
Mem. ASME

Nonlinear Contact Geometry Effects on Wheelset Dynamics

The nonlinear dynamic behavior of a simply restrained railway vehicle wheelset on tangent track is investigated. Nonlinearities due to the kinematics of wheel/rail contact (excluding flange contact) and creep force variation with creepage are considered for mildly noncircular wheel and rail profiles. The general equations of lateral and yawing motion of the wheelset are derived. These are then simplified by considering both normalized amplitude ϵ of the motion and angle of wheel/rail contact in the undisturbed position α_0 as small parameters. Asymptotic solutions describing the influence of the nonlinearities on the stability and frequency of wheelset motion are obtained using the method of multiple time scales. The results are used to derive conditions for which a linear creep force model is valid.

Introduction

The basic motion of a railway vehicle wheelset is a combined lateral translation x and yaw ψ (Fig. 1) which results from the wheel taper. Linear analyses [1, 2] show that influences of axle loading, wheelset inertia, suspension, and creepage forces developed at the wheel/rail interface result in unstable motion above, and stable motion below, a certain forward speed, termed the critical or secondary hunting speed. A knowledge of the factors which influence secondary hunting is important, since wheel/rail wear, passenger/cargo discomfort, and the tendency to derail are increased in the unstable mode.

It is well known [3] that the dynamics of a wheelset are inherently nonlinear. Among the sources of nonlinearity are as follows:

1 The geometry of wheel/rail contact, including flange contact
2 The creep force variation with creepage.
3 The suspension elements which restrain the wheelset motion relative to the truck or bogie.

Most nonlinear analyses conducted to date have dealt with the effects of flange contact, although some have included, in an *ad hoc* way, some of the geometric nonlinearities which occur.

Law [4] and Law and Brand [5] have considered, using the Krylov-Bogolyubov method, the coupled effects of flange contact and nonlinear roll ϕ (Fig. 1), which they assume related to the lateral translation x as $\phi = a_1x + a_2x^3$. Although a significant effect of the nonlinear roll on limit cycle amplitude (with flange contact) was reported, we note that several other nonlinear contact geometry effects are present and, as will be shown, may be as important. Law [6] has used a similar model to study the effect of track irregularity on the response, particularly the "derailment parameter" L/V (ratio of lateral to vertical contact forces). More recently, Cooperrider, et al. [7], have studied the limit cycle oscillations based on a nine-degree-of-freedom wheelset/truck/car body model. In this work the describing function approach [8] was used to model nonlinearities in left and right wheel rolling radii and wheel/rail contact angles.

Cooperrider [9] has also analyzed numerically the nonlinear motion of a truck and two wheelsets. He considered simultaneously flange contact, the hysteretic side bearer friction as modeled by Matsudeira, Arai, and Yokose [10], and a nonlinear lateral and longitudinal creep force model. He found that with flange contact, stable limit cycle motion could occur at speeds below the linear critical speed.

Brann [11] considered a free wheelset with a single geometric nonlinearity in the so-called gravitational restoring force; this restoring force occurs if the wheels are profiled and is due to variation with lateral translation of the lateral components of left and right wheel-rail contact normal forces. Although Brann showed that limit cycle motion could occur, we note that the presence of a profile nonlinearity of the magnitude required will give rise to many other nonlinear effects in the equations of motion.

Hannebrink, et al. [12], have recently used the describing function method to study wheelset limit cycle behavior resulting from flange contact for several wheel and rail profiles, flange clearances, and axle loads. A linear creep force model was used. It was shown that stable limit cycle motions are possible at forward speeds greater than the linear critical speed.

In the aforecited investigations, the equations of wheelset motion have been derived in an *ad hoc* manner, generally by adding specific nonlinear terms to the linearized equations, or by simply replacing certain linear terms with nonlinear ones. These procedures result in the omission of many nonlinear effects of potential importance. In the present investigation, we derive the general equations of motion with no *a priori* assumptions as to the relative magnitudes of the myriad kinematic and dynamic nonlinearities which eventually appear. By considering both normalized lateral translation amplitude ϵ and contact angle α_0 in the undisturbed position ($x = \psi = 0$) as small

Presented at the Eighth U. S. National Congress of Applied Mechanics, University of California at Los Angeles, Los Angeles, Calif., June 26–30, 1978.

Discussion on this paper should be addressed to the Editorial Department, ASME, United Engineering Center, 345 East 47th Street, New York, N. Y. 10017, and will be accepted until June 1, 1980. Readers who need more time to prepare a discussion should request an extension from the Editorial Department. Manuscript received by ASME Applied Mechanics Division, June, 1978; final revision, April, 1979.

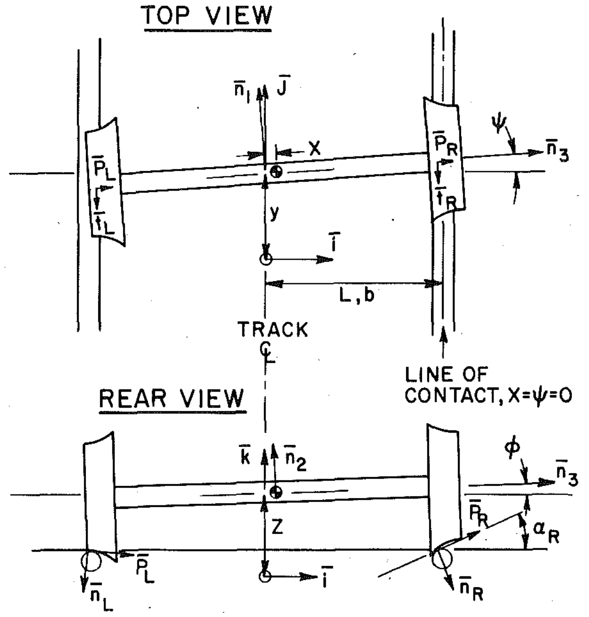

Fig. 1 Definition of wheelset coordinate systems, degrees of freedom

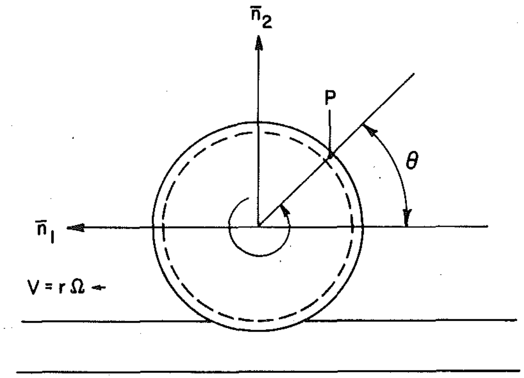

Fig. 2 Spin geometry; right wheel viewed from track center line; at rest $\theta_R = 3\pi/2$

parameters, a systematic assessment of the importance of the individual nonlinearities has been made.

We investigate the influence on wheelset motion of geometric and creep force nonlinearities not associated with flange contact. We consider mildly noncircular wheel and rail profiles and nonlinear creep force variation with creepage. The equations of motion for moderate forward speeds are derived and solved using the method of multiple time scales.

The results show that nonlinearities in the velocities of creep contribute terms to the equations of motion which can be as large as the usual linear terms which describe secondary hunting. However, only the frequency of the motion is thereby affected. The primary effect on system damping is shown to be caused by nonlinear variation of creep force with creepage, which tends to amplify any damping (or undamping) present, but which does not affect the critical speed of secondary hunting. It appears that limit cycle motions cannot occur for the mildly noncircular profiles considered here and without flange contact. Conditions have been derived for the validity of a linear creep model and these show that such a model may be invalid for typical wheelsets in moderate amplitude motion.

Equations of Motion

The six wheelset degrees of freedom are shown in Figs. 1 and 2. The lateral motion is described by lateral translation x, yaw ψ, roll ϕ, and vertical translation z. The forward degrees of freedom are translation y and spin θ. We employ inertial $(\bar{i}, \bar{j}, \bar{k})$, wheelset $(\bar{n}_1, \bar{n}_2, \bar{n}_3)$, and contact zone $(\bar{p}, \bar{t}, \bar{n})$ coordinate systems (Fig. 1). The equations for the forward motion (y, θ) are of second order in x and ψ and can therefore be decoupled from the lateral motion. Furthermore, if both wheels maintain contact with the rails, the vertical displacement z and roll ϕ are uniquely determined in terms of x and ψ, and the motion can be described completely by these two coordinates.

For a simply suspended, mass and configurationally symmetric rigid wheelset driven on tangent track at a constant angular rate $\dot{\theta}$, the equations of motion have been derived in the wheelset coordinate system [13] and are given as follows:

$$m\ddot{x} + k_x x = SF_3 - W\phi \tag{1}$$

$$m(\ddot{y} + 2\dot{x}\dot{\psi} + x\ddot{\psi}) + k_y y = SF_1 \tag{2}$$

$$m(\ddot{z} + 2\dot{x}\dot{\phi} + x\ddot{\phi}) + k_z z = SF_2 - W \tag{3}$$

$$I_T\ddot{\psi} - I_L\dot{\theta}\dot{\phi} + k_\psi\psi = SM_2 + L\Delta F_1 + u_R F_{1_R} + u_L F_{1_L} + R_R \cos\theta_R F_{3_R} + R_L \cos\theta_L F_{3_L} \tag{4}$$

$$-I_T\ddot{\phi} - I_L\dot{\theta}\dot{\psi} - k_\phi\phi = SM_1 + R_R \sin\theta_R F_{3_R} + R_L \sin\theta_L F_{3_L} - L\Delta F_2 - u_R F_{2_R} - u_L F_{2_L} \tag{5}$$

The equation for wheelset spin has not been included, as it serves only to define the driving torque needed to maintain the assumed constant $\dot{\theta}$ condition.

In equations (1)–(5), m is the wheelset mass, W the total load supported by the axle, and I_T and I_L the transverse and longitudinal moments of inertia, respectively (with radii of gyration K_T and K_L). Suspension spring constants are denoted by k_x, k_y, k_z, k_ϕ, and k_ψ. R is the instantaneous rolling radius, u the distance to the contact point along the axle, and θ the location of the contact point around the wheel periphery (Figs. 2 and 3). The subscripts R and L refer to right and left wheel contact values, respectively. In the rest position ($x = \psi = 0$) $R_R = R_L \equiv r$, $\theta_R = \theta_L = 3\pi/2$, and $u_R = u_L = 0$. The distance between the rails is $2L$.

The forces and moments F_1, F_2, F_3, M_1, and M_2 in the $\bar{n}_1$, $\bar{n}_2$, and $\bar{n}_3$-directions are those due to creepage and normal contact, as yet unspecified. We have used the notation $SF_1 = F_{1_R} + F_{1_L}$ and $\Delta F_1 = F_{1_R} - F_{1_L}$, etc. The contact forces and moments will be determined in an axis system fixed in the instantaneous plane of contact (Fig. 1), and then transformed to the wheelset system, using the following transformations [14]:

$$F_{1_R} = -R_R'(1 + R_R'^2)^{-1/2} \cos\theta_R F_{\perp R} + \sin\theta_R F_{\parallel R} - (1 + R_R'^2)^{-1/2} \cos\theta_R N_R \tag{6}$$

$$F_{2_R} = R_R'(1 + R_R'^2)^{-1/2} \sin\theta_R F_{\perp R} + \cos\theta_R F_{\parallel R} + (1 + R_R'^2)^{-1/2} \sin\theta_R N_R \tag{7}$$

$$F_{3_R} = (1 + R_R'^2)^{-1/2} F_{\perp R} \quad -R_R'(1 + R_R'^2)^{-1/2} N_R \tag{8}$$

$F_\perp$ is the lateral creep force, $F_\parallel$ the longitudinal creep force, and N the normal contact force, so that $\overline{F}_R = F_{\perp R}\bar{p}_r + F_{\parallel R}\bar{t}_R + N_R\bar{n}_R$, Fig. 1. The transformations for the left wheel and for the contact moments are the same (note, however, that $M_\perp = M_\parallel = 0$). In equations (6)–(8) R_R' is the rate of change of rolling radius with distance u_R along the right wheel, $R_R' \equiv \partial R_R/\partial u_R$, Fig. 3.

In the sequel the creep forces will be expressed in terms of a product of creep coefficient f and creepage ξ. Defining a normalized creep coefficient $\mu = 2f/W$, we will consider the case of moderate forward speeds, such that $F\epsilon$ is at most order unity and $\mu\epsilon$ is $O(F)$. Therefore, terms of order $\mu\epsilon^3$, $F\epsilon^2$, and ϵ will be retained in the equations of motion. Additional simplification will be made by considering the orderings in rest contact angle α_0.

Equations (1)–(5) are now nondimensionalized using the following nondimensional parameters:

$$F = mV^2/W(Lr)^{1/2} \qquad x = \epsilon\bar{x}(Lr)^{1/2}$$
$$\tau = \alpha_0^{1/2}Vt/(Lr)^{1/2} \qquad \psi = \epsilon\bar{\psi}\alpha_0^{1/2}$$
$$\overline{V} = \dot{y}/V - 1 \qquad S_{x,y,z} = k_{x,y,z}(Lr)^{1/2}/W$$
$$S_{\psi,\phi} = k_{\psi,\phi}/WL$$

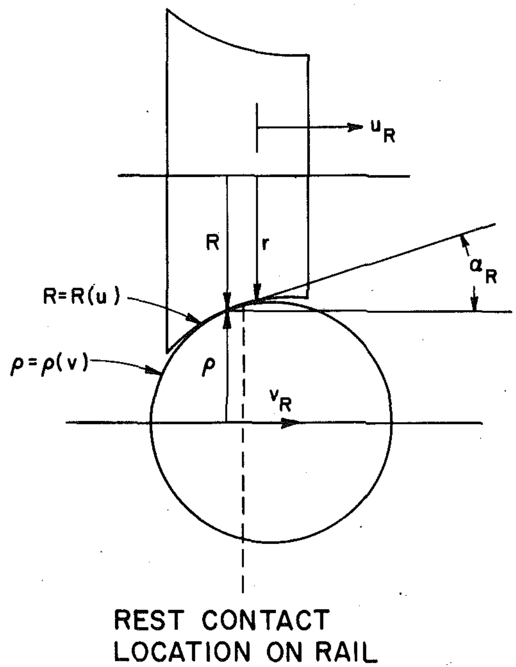

Fig. 3 Definition of contact geometry parameters: u_R, v_R measured from rest contact locations on wheel, rail, respectively; shown is rear view with $x > 0$, $u_R < 0$, $v_R < 0$

where $V \equiv r\dot{\theta}$ and α_0 is the angle between the contact plane and the horizontal when $x = \psi = 0$. The nondimensional equations of motion are

$$\epsilon\alpha_0[F\bar{x}'' + (Lr)^{1/2}\bar{x}/\delta] + \epsilon S_x\bar{x} = SF_3/W \tag{9}$$

$$F\epsilon^2\alpha_0^{1/2}[\bar{V}' + 2\bar{x}'\bar{\psi}'\alpha_0 + \bar{x}\bar{\psi}''\alpha_0] + \epsilon^2 S_y\bar{y}_1 = SF_1/W \tag{10}$$

$$F\epsilon^2\alpha_0[\bar{z}'' + (Lr)^{1/2}\alpha_0(2\bar{x}'^2 + \bar{x}\bar{x}'')/\delta] + \epsilon^2 S_z\bar{z} + 1 = SF_2/W \tag{11}$$

$$\begin{aligned} F\epsilon\alpha_0^{3/2}[(K_T^2/L(Lr)^{1/2})\bar{\psi}'' - (K_L^2\bar{x}'/\delta(Lr)^{1/2})] + \epsilon\alpha_0^{1/2}S_\psi\bar{\psi} \\ = (L + u_A)(\Delta F_1/WL) + u_s(SF_1/WL) + (R\cos\theta)_S(SF_3/WL) \\ + (R\cos\theta)_A(\Delta F_3/WL) + (SM_2/WL) \end{aligned} \tag{12}$$

$$\begin{aligned} -F\epsilon\alpha_0[(K_L^2/Lr)\bar{\psi}' + (\alpha_0 K_T^2/L\delta)\bar{x}''] - \epsilon\alpha_0((Lr)^{1/2}/\delta)S_\phi\bar{x}, \\ = (SM_1/WL) - (L + u_A)(\Delta F_2/WL) - u_S(SF_2/WL) \\ + (R\sin\theta)_S(SF_3/WL) + (R\sin\theta)_A(\Delta F_3/WL) \end{aligned} \tag{13}$$

Primes denote differentiation with respect to the phase angle τ, which is defined in terms of the kinematic frequency for zero wheel curvature. The Froude number F is a ratio of inertial and gravitational influences. The terms S_x, S_ψ, etc., are nondimensional stiffnesses. The barred quantities $\bar{x}$ and $\bar{\psi}$ are nondimensional, and ϵ is a small parameter of the order of the maximum value of $x/(Lr)^{1/2}$, so that $\bar{x}$ and $\bar{\psi}$ are order unity. The kinematic parameter $\delta = L - r\tan\alpha_0$. The S and A subscripts on the kinematic parameters denote symmetric and antisymmetric left and right wheel contributions, i.e., $R_R \sin\theta_R = ½[(R\sin\theta)_S + (R\sin\theta)_A]$, while $R_L\sin\theta_L = 1/2[(R\sin\theta)_S - (R\sin\theta)_A]$.

We now consider the case where both wheel and rail are mildly noncircular and expand the rolling radius R and contact angle α in Taylor expansions about the values r and α_0 at $x = \psi = 0$, e.g.,

$$R_R \cong r + u_R r_R' + (u_R^2 K_w)/2 + (u_R^3 H_w)/3 \tag{14}$$

$$\tan\alpha_R \cong \alpha_{0R} - K_\rho v_R + H_\rho v_R^2 \tag{15}$$

Here K_W and K_ρ are wheel and rail curvatures for $x = \psi = 0$, and H_W and H_ρ are the associated rates of change of curvature. v_R is the horizontal distance along the rail, Fig. 3. The condition of "mild noncircularity" is that H_W and H_ρ be of order unity. Note that, in terms of the present parameters, the "effective conicity" λ [1] is given by $\lambda = \tan\alpha_0/(1-\gamma)$, where γ is the curvature ratio, $\gamma = K_w/K_\rho$.

By combining equations (9), (11)–(13) and (6)–(8), the wheelset response is related directly to the loadings which arise in the contact zones. Equations (14) and (15), along with the kinematic relations derived in [14] for the dependence of u_R, u_L, v_R, v_L, $\cos\theta$, and $\sin\theta$ on x and ψ are then used to express all kinematic parameters in the resulting equations of motion completely in terms of x and ψ. Upon completion of these steps, the equations of motion can be solved for the lateral and longitudinal creep forces and the normal contact forces, as follows:

$$\begin{aligned} \frac{SF_\perp}{W} &= F\epsilon\alpha_0\left[\bar{x}''\frac{\delta}{L} + \frac{\alpha_0 K_L^2}{Lr}\right] + \epsilon\alpha_0\frac{(Lr)^{1/2}}{L}\bar{x} \\ &\quad - \epsilon S_x\frac{\delta}{L}\bar{x} + \frac{\epsilon(Lr)^{1/2}b_0C_0K_w}{L\delta(1-\gamma)}\bar{x} - \frac{\epsilon\alpha_0 b_0 C_0(Lr)^{1/2}}{L\delta(1-\gamma)}\frac{\Delta F_\perp}{W} \end{aligned} \tag{16}$$

$$\begin{aligned} \frac{\Delta F_\parallel}{W} &= -F\epsilon\alpha_0^{3/2}\left[\frac{K_T^2}{L(Lr)^{1/2}}\bar{\psi}'' - \frac{K_L^2}{\delta(Lr)^{1/2}}\bar{x}'\right] - \epsilon\alpha_0^{1/2}S_\psi\bar{\psi} - \frac{SM_n}{WL} \\ &\quad + \frac{\epsilon\alpha_0(Lr)^{1/2}b_0K_w\bar{x}}{\delta(1-\gamma)}\frac{\Delta M_n}{WL} + \epsilon\alpha_0^{3/2}\frac{r}{L}\bar{\psi}\frac{\Delta F_\perp}{W} + \epsilon\frac{\delta}{L}\alpha_0^{3/2}\bar{\psi} \end{aligned} \tag{17}$$

$$\frac{SN}{W} = -1 + \alpha_0\frac{\Delta F_\perp}{W} \tag{18}$$

$$\begin{aligned} \frac{\Delta N}{W} &= F\epsilon\alpha_0\bar{x}''\left[\frac{r}{L} + \alpha_0\left(1 - \frac{K_T^2}{L\delta}\right)\right] \\ &\quad - F\epsilon\alpha_0\frac{K_L^2}{Lr}\bar{\psi}' - \epsilon\alpha_0\frac{(Lr)^{1/2}}{\delta}S_\phi\bar{x} \\ &\quad + \epsilon\left(\alpha_0 + \frac{r}{L}\right)S_x\bar{x} + \epsilon\alpha_0^{3/2}\bar{\psi}\frac{\Delta M_n}{WL} + \frac{\epsilon b_0C_0K_w(Lr)^{1/2}}{L\delta(1-\gamma)}\bar{x}\frac{\Delta F_\perp}{W} \\ &\quad + \epsilon\frac{(Lr)^{1/2}}{\delta}\bar{x}\left[\alpha_0\left(\frac{r}{L}\right)\frac{-b_0}{L(1-\gamma)}\right] \end{aligned} \tag{19}$$

where $b_0 \equiv L + \alpha_0/K_\rho$ and $C_0 \equiv L + \alpha_0/K_w$. $SF_\perp$ is the net lateral creep force on the wheelset, and $\Delta F_\parallel$ is proportional to the yawing moment. Terms of $O(\epsilon\alpha_0^2)$ have been dropped in the equation (16) for lateral translation, as have terms of $O(\epsilon\alpha_0^{5/2})$ in the yaw equation (17).

To describe the creep forces $SF_\perp/W$ *and* $\Delta F_\parallel/W$ *and* the creepage moment M_n, a model similar to that used by Cooperrider [9] has been adopted. Primary lateral and longitudinal creep forces, as well as a contribution from the so-called lateral/spin creep, are included. In addition, a moment about the contact normal is produced in proportion to the component of wheelset angular velocity along this normal. Following Carter [15], the instantaneous rolling velocities $V_R = R_R\dot{\theta}$ and $V_L = R_L\dot{\theta}$ are used to normalize the creep velocities to define the creepages. The normalized creep force model is given as follows:

$$\begin{aligned} \frac{SF_\perp}{W} &= -\mu\xi_{\perp S}\left[1 - \frac{\mu\xi_T}{3\mu_f} + \frac{\mu^2\xi_T^2}{27\mu_f^2}\right] - \mu_{L\theta}\frac{L}{V}(\bar{\omega}\cdot\bar{n})_S \\ \frac{\Delta F_\parallel}{W} &= -\mu\xi_{\parallel A}\left[1 - \frac{\mu\xi_T}{3\mu_f} + \frac{\mu^2\xi_T^2}{27\mu_f^2}\right] \\ \frac{\Delta F_\perp}{W} &= -\mu_{L\theta}\frac{L}{V}(\bar{\omega}\cdot\bar{n})_A - \mu\xi_{\perp A} \\ \frac{SM_n}{WL} &= \mu_{L\theta}\xi_{\perp S} - \mu_\theta\frac{r}{V}(\bar{\omega}\cdot\bar{n})_S \\ \frac{\Delta M_n}{WL} &= \mu_{L\theta}\xi_{\perp A} - \mu_\theta\frac{r}{V}(\bar{\omega}\cdot\bar{n})_A \end{aligned} \tag{20}$$

The symmetric and antisymmetric contributions to lateral and longitudinal creepages $\xi_\perp$ and $\xi_\parallel$, as well as the spin creepage terms $(\bar{\omega}\cdot\bar{n})_S$ and $(\bar{\omega}\cdot\bar{n})_A$, have been given previously [14] for the mildly noncircular profiles considered here. Lateral and longitudinal creep coefficients are assumed equal, and normalized creep coefficients are defined by $\mu_{L\theta} = 2f_{L\theta}/WL$, and $\mu_\theta = 2f_\theta/WLr$. Typically, the lateral/spin creep coefficient $\mu_{L\theta} = O(1)$, while the spin creep coefficient $\mu_\theta = 0(10^{-2})$. The resultant creepage ξ_T appearing in equation (20) is defined by $\xi_T = (\xi_\perp^2 + \xi_\parallel^2)^{1/2}$. The value of sliding friction μ_f defines the lateral or longitudinal contact force $\mu_f N$ at which relative slip occurs over the entire region of contact.

In [13] the influence of variation in the normalized creep coefficient $\mu = 2f/W$ which occurs during wheelset movement (and associated changes in normal contact load and contact geometry) was considered. For cases of practical interest the effect on wheelset stability was found to be quite small; thus creep coefficient variation is not considered in this presentation, and reference should be made to [13] for the details.

Equations (16)–(20), along with the relations given in [14] for the creepage terms, are now combined and yield the equations of motion for lateral translation and yaw of the wheelset, written in the following form:

$$\bar{\psi} + \frac{L}{\delta}\bar{x}' = \epsilon^2\left\{-\eta_1\bar{x}'' - \eta_2\bar{x}\left[S_x + \frac{K_w(Lr)^{1/2}}{(1-\gamma)}\left(1 - \frac{L}{r}\mu_{L\theta}\right)\right] - \frac{LK_w\bar{x}^2(\bar{\psi} + rK_w(\bar{\psi} + \bar{x}'))}{2(1-\gamma)^2} + \frac{\bar{x}^2\bar{x}'(H_w + \gamma^3 H_\rho)}{(1-\gamma)^3}\right\} + \nu\left(\frac{\mu\xi_{\perp S}}{F\epsilon\alpha_0}\right)\left(\frac{\mu\xi_T}{F\epsilon\alpha_0}\right) \quad (21)$$

$$\frac{b_0\bar{x}}{\delta(1-\gamma)} - \bar{\psi}' = \epsilon^2\left\{\frac{\eta_1}{L^2}(K_T{}^2\bar{\psi}'' - K_L{}^2\bar{x}') + \eta_2 S_\psi(r/L)^{1/2}\bar{\psi} + \frac{Lrb_0g_1\bar{x}^3}{2\alpha_0\delta^3(1-\gamma)^2} + \frac{1}{(1-\gamma)^2}\left[LK_w\bar{x}\bar{\psi}^2 + r\frac{(H_w + \gamma^2 H_\rho)\bar{x}^2\bar{\psi}'}{K_\rho(1-\gamma)} - \frac{rg_2\bar{x}^3}{K_\rho(1-\gamma)}\right]\right\} + \nu\left(\frac{S_\psi(r/L)^{1/2}}{F\alpha_0}\right)\left(\frac{\mu\xi_{\parallel A}}{S_\psi\,\epsilon\alpha_0{}^{1/2}}\right)\left(\frac{\mu\xi_T}{F\epsilon\alpha_0}\right) \quad (22)$$

where $\epsilon^2\eta_1 = F\alpha_0{}^{1/2}/\mu$, $\epsilon^2\eta_2 = 1/\mu\alpha_0{}^{1/2}$, and $\nu = F^2\epsilon\alpha_0{}^{3/2}/3\mu\mu_f$, and g_1 and g_2 depend on wheel and rail noncircularity as follows:

$$g_1 = H_w b_0{}^2(2-\gamma) + \gamma^3 C_0{}^2 H_\rho$$

$$g_2 = (H_w + \gamma^2 H_\rho)\left[\frac{2L}{K_\rho(1-\gamma)}(H_w + \gamma H_\rho) - \frac{1}{3}\right]$$

Depending on the geometry, forward speed, and motion amplitude, the terms appearing on the right-hand sides of equations (21) and (22) can all be of comparable magnitude. In forming these equations, terms have been neglected if they were $O(\alpha_0)$ or $O(\epsilon)$ as large as those appearing in equations (21) and (22). A more detailed discussion of magnitude assessments of the many nonlinear terms is given elsewhere [13].

In equations (21) and (22) the homogeneous terms are proportional to the linear lateral and longitudinal velocities of creep and hence describe the wheelset kinematic oscillation. The linear terms in η_1 and η_2 are the inertia, gravitational, suspension, and spin creep terms which describe secondary hunting. Terms in ν result from the nonlinear variation of creep force with creepage. The remaining nonlinear terms arise from nonlinearities in the velocities of creep.

The nonlinear creep velocity terms are due to several sources, including the vertical and rolling motions, deviations from $V = r\dot{\theta}$ in wheelset forward speed, and difference in left and right wheel rolling radii. The largest of these terms is $O(\epsilon^2/\alpha_0)$ and is due to rolling radii difference, equation (22). For moderate speed and yaw restraint, $\mu\epsilon = O(F)$ and $S_\psi = O(1)$, this term may actually be larger than the linear static and inertia terms.

Solution of Equations of Motion

We now solve equations (21) and (22) using the method of multiple time scales. We consider $1/\mu$ and ϵ^2 to be small parameters of comparable magnitude. Hence, the equations of motion are coupled second-order equations with a small parameter multiplying the highest derivative in each (i.e., the equations are of the boundary-layer type). Thus there are two linear modes of motion in addition to the kinematic ones, and these will be of importance in a temporal boundary layer near time zero. Wickens [1, 2] has shown that this boundary layer is of very short duration, i.e., the additional modes are highly damped. We therefore restrict our attention to the effect of the inhomogeneous terms on the kinematic oscillation.

In applying the method of multiple time scales (a detailed description of this method is given by Nayfeh [16]), we assume the nondimensional "time" τ to be a function of several independent time scales, $\tau = \tau(T_0, T_1, T_2, \ldots)$. Both dependent variables $(\bar{x}, \bar{\psi})$ and their derivatives with respect to τ are expanded in series in the small parameters.

We consider three time scales, a "fast" one to describe the kinematic oscillation, and two "slow" ones to characterize the terms on the right-hand sides of equations (21) and (22). The time scales are defined as follows:

$$T_0 = \left(\frac{b_0}{L(1-\gamma)}\right)^{1/2}\tau \equiv \omega\tau$$

$$T_1 = \epsilon^2\tau$$

$$T_2 = \nu\tau$$

Here $\omega\tau/t$ is the kinematic oscillation frequency. In view of the previous discussion, the linear (secondary hunting) terms and the nonlinear creep velocity terms are both described by the same (T_1) time scale.

Expansions for $\bar{x}$ and $\bar{\psi}$ in terms of the small parameters are assumed as follows:

$$\bar{x} = x_0 + \epsilon^2 x_1 + \nu x_2 + \ldots$$

$$\bar{\psi} = \psi_0 + \epsilon^2\psi_1 + \nu\psi_2 + \ldots \quad (23)$$

The derivatives with respect to τ are also expanded,

$$\frac{d}{d\tau} = \omega\frac{\partial}{\partial T_0} + \epsilon^2\frac{\partial}{\partial T_1} + \nu\frac{\partial}{\partial T_2} + \ldots$$

$$\frac{d^2}{d\tau^2} = \omega^2\frac{\partial^2}{\partial T_0{}^2} + 2\omega\epsilon^2\frac{\partial^2}{\partial T_0\partial T_1} + 2\omega\nu\frac{\partial^2}{\partial T_0\partial T_2} + \ldots \quad (24)$$

The magnitudes of the small parameters ϵ^2 and ν are such that the coupling of the two slow time scales produces negligible effect on the response, and such coupling terms have been neglected in equations (23) and (24); thus, the distinction between T_1 and T_2 is really artificial. It has been used to retain the distinction between the nonlinear creep force versus creepage (ν) effects and the effects of nonlinearities in the velocities of creep (ϵ^2).

Equations (23) and (24) are substituted into equations (21) and (22), and terms of orders 1, ϵ^2, and ν are equated, yielding three sets of equations for the three time scales. For the fast time scale T_0 there results

$$\psi_0 + \frac{\omega L}{\delta}\frac{\partial x_0}{\partial T_0} = 0$$

$$\frac{b_0}{\delta(1-\gamma)}x_0 - \omega\frac{\partial\psi_0}{\partial T_0} = 0$$

with the solution expressed in the form

$$x_0 = A(T_1, T_2)e^{iT_0} + \bar{A}(T_1, T_2)e^{-iT_0}$$

$$\psi_0 = -i\omega A(T_1, T_2)e^{iT_0} + i\omega\bar{A}(T_1, T_2)e^{-iT_0} \quad (25)$$

This describes the kinematic oscillation, with complex amplitude A a function of the slow time scales, and $\bar{A}$ the complex conjugate of A.

Using equation (25), the equations for the T_1 time scale can be expressed as the following second-order equation in x_1:

$$\frac{\partial^2 x_1}{\partial T_0{}^2} + x_1 = e^{iT_0}\left\{-\frac{2i}{\omega}\frac{\partial A}{\partial T_1} + i\eta_1\omega\left(1 + \frac{K_T{}^2}{L^2}\right)A - \frac{i\eta_1}{\omega}\frac{K_L{}^2}{L^2}A - \frac{i\eta_2}{\omega}\left[S_\psi\left(\frac{r}{L}\right)^{1/2} + S_x + \frac{K_w(Lr)^{1/2}}{1-\gamma}\left(1 - \frac{L}{r}\mu_{L\theta}\right)\right]A + 3\left[\frac{Lrb_0g_1}{2\alpha_0\delta^3(1-\gamma)} + \frac{r(H_w + \gamma^2 H_\rho - g_2)}{K_\rho(1-\gamma)^3}\right]A^2\bar{A} - \frac{(H_w + \gamma^3 H_\rho)}{(1-\gamma)^3}A^2\bar{A}\right\} + \text{N.S.T.} + \text{cc} \quad (26)$$

where cc denotes the complex conjugate and N.S.T. denotes nonsecular terms (actually, terms in e^{3iT_0}). Equation (26) contains secular terms which, if not eliminated, result in unbounded response for x_1. The secular terms will be eliminated if the coefficient of e^{iT_0} is set equal to zero; this, in turn, dictates the manner in which A must change with T_1 in order that the secular terms be eliminated. Letting $A = (a/2)e^{i\phi}$, where a and ϕ are real functions of the slow time scales T_1 and T_2, secular terms are eliminated if ϕ and a vary with T_1 as follows:

$$\frac{\partial \phi}{\partial T_1} = -\frac{3\omega a^2}{8}\left\{\frac{Lrb_0g_1}{2\alpha_0\delta^3(1-\gamma)} + \frac{r(H_w+\gamma^2H_\rho)\left(\frac{1}{3}+\frac{L(H_w+\gamma H_\rho)}{K_\rho(1-\gamma)}\right)}{K_\rho(1-\gamma)^3} - \frac{(H_w+\gamma^3H_\rho)}{3(1-\gamma)^2}\right\} \quad (27)$$

$$\frac{\partial a}{\partial T_1} = \frac{a}{2\mu\epsilon^2}\left\{\frac{F\alpha_0^{1/2}}{(1-\gamma)}\left[1+\frac{K_T^2}{L^2} - (1-\gamma)\frac{K_L^2}{L^2}\right] - \frac{1}{\alpha_0^{1/2}}\left[S_x + S_\psi\left(\frac{r}{L}\right)^{1/2} + \frac{K_w(Lr)^{1/2}}{(1-\gamma)}\left(1-\frac{L}{r}\mu_{L\theta}\right)\right]\right\} \quad (28)$$

The relation for $\partial\phi/\partial T_1$ indicates that the nonlinear contributions to creep velocity result in a shift in the kinematic frequency, given by

$$\omega_p = \omega\left\{1 - \frac{3}{8}\epsilon^2\left[\frac{Lrb_0g_1}{2\alpha_0\delta^3(1-\gamma)} + \frac{r(H_w+\gamma^2H_\rho)}{K_\rho(1-\gamma)^3}\left[\frac{4}{3} - \frac{2L(H_w+\gamma H_\rho)}{K_\rho(1-\gamma)}\right] - \frac{(H_w+\gamma^3H_\rho)}{3(1-\gamma)^2}\right]\right\}$$

where ω is the linear kinematic frequency, and ω_p the perturbed frequency. This result indicates that the oscillation frequency is altered only if the wheel and/or rail profiles are noncircular. The result is valid for "small" noncircularities ($H_w = O(1)$, $H_\rho = O(1)$) and the magnitude of the perturbation is quite small for this case.

The foregoing relation $\partial a/\partial T_1$ for amplitude variation with T_1 contains the linear terms which characterize secondary hunting. Setting $\partial a/\partial T_1$ to zero and utilizing the definition of Froude number in terms of forward speed V enables the linear critical speed V_c to be calculated,

$$V_c = \left\{\frac{(Lr)^{1/2}(1-\gamma)}{m\alpha_0}\,\frac{\left[S_x + S_\psi\left(\frac{r}{L}\right)^{1/2} + \frac{K_w(Lr)^{1/2}}{1-\gamma}\left(1-\frac{L}{r}\mu_{L\theta}\right)\right]}{\left[1+\frac{K_T^2}{L^2} - \frac{K_L^2(1-\gamma)}{L^2}\right]}\right\} \quad (29)$$

Two effects which are not often contained in this result are the stabilizing influence of longitudinal (spin) inertia and the destabilizing influence of lateral/spin creep. Since $\mu_{L\theta}$ is typically of order unity [13], equation (29) shows that the lateral/spin creep essentially negates the stabilizing influence of gravitational stiffness. Since in practice stability is generally achieved through stiff yaw restraint, the inclusion of the lateral/spin creep effect in equation (29) may not substantially alter the resulting linear critical speed. However, the possibility exists that an unrestrained wheelset would be unstable at all forward speeds.

An important result of equations (27) and (28) is that none of the nonlinear creep velocity terms appear in the relation for $\partial a/\partial T_1$. This indicates that for the mildly noncircular profiles considered here, nonlinearities in the creep velocities affect the frequency, but not the stability, of wheelset motion.

The equations for the second slow time scale (T_2) yield the influence on the motion of nonlinear creep force variation with creepage. The terms which describe this effect in equations (21) and (22) are given in terms of the lateral, longitudinal, and resultant creepages, $\xi_{\perp S}$, $\xi_{\perp A}$, and ξ_T, respectively. These creepages are determined to lowest order using equations (16), (17), (20), and (25), with the following result:

$$\xi_{\perp S} = \left(\frac{\epsilon a}{2\mu}\right) C_\perp (e^{iT_0} + e^{-iT_0})$$

$$c\xi_{\parallel A} = i\left(\frac{\epsilon a}{2\mu}\right) C_\parallel (e^{iT_0} - e^{-iT_0})$$

$$\xi_T = \left(\frac{\epsilon a}{2\mu}\right)[2(C_\perp^2 + C_\parallel^2) + (C_\perp^2 - C_\parallel^2)(e^{2iT_0} + e^{-2iT_0})]^{1/2} \quad (30)$$

where

$$C_\perp = F\alpha_0\omega^2 - S_x - \omega^2K_w(Lr)^{1/2}(1 - \frac{L}{r}\mu_{L\theta})$$

$$C_\parallel = \omega\alpha_0^{1/2}(L/r)^{1/2}\left[\frac{F\alpha_0}{L^2}(\omega^2K_T^2 - K_L^2) - S_\psi(r/L)^{1/2}\right]$$

Utilizing equation (30), the equations for the T_2 time scale can be written as the following second-order equation in x_2.

$$\omega\left(\frac{\partial^2 x_2}{\partial T_0^2} + x_2\right) = -\frac{2\partial^2 x_0}{\partial T_0\partial T_2} + \left(\frac{\mu}{F\epsilon\alpha_0}\right)^2 i\left(\frac{\epsilon a}{2\mu}\right)^2 \cdot \{2C_\perp[e^{iT_0} - e^{-iT_0} + e^{3iT_0} - e^{-3iT_0}] \cdot (C_\perp^2 - C_\parallel^2)[2(C_\perp^2 + C_\parallel^2) + (C_\perp^2 - C_\parallel^2)(e^{2iT_0} + e^{-2iT_0})]^{1/2} + (C_\perp + C_\parallel)(e^{iT_0} - e^{-iT_0})[2(C_\perp^2 + C_\parallel^2) + (C_\perp^2 - C_\parallel^2)(e^{2iT_0} + e^{-2iT_0})]^{1/2}\}$$

In this equation secular terms arise from the average value under the radicals times terms in e^{iT_0}. Now the creepages may be viewed as tracing out an ellipse in the $\xi_\perp - \xi_\parallel$ plane, with semimajor and semiminor axes proportional to $C_\perp$ and $C_\parallel$, the largest being the semimajor axis. The first bracketed terms, which arise from the variation with T_0 of the resultant creepage, are thus proportional to the difference in lateral and longitudinal creep magnitudes ($C_\perp^2 - C_\parallel^2$). We consider the case for which the "creepage ellipse" possesses small eccentricity, i.e., for which $\partial\xi_T/\partial T_0$ is small. For this case the contribution of resultant creepage to secular terms is approximated simply by $\sqrt{2}(C_\perp^2 + C_\parallel^2)^{1/2}$. The perturbation equation of motion is then, with only secular terms retained,

$$\omega\left(\frac{\partial^2 x_2}{\partial T_0^2} + x_2\right) = -\frac{2\partial^2 x_0}{\partial T_2\partial T_0} + \left(\frac{1}{F\epsilon\alpha_0/\mu}\right)^2 i\left(\frac{\epsilon a}{2\mu}\right)^2 (C_\perp + C_\parallel)\sqrt{2}(C_\perp^2 + C_\parallel^2)^{1/2}e^{iT_0} + \text{N.S.T.} + \text{cc}$$

Using equation (25) for x_0, the condition for the elimination of secular terms is as follows:

$$\frac{\partial a}{\partial T_2} = \left(\frac{a}{2\mu\nu}\right)\left\{\frac{F\alpha_0^{1/2}}{1-\gamma}\left[1 + \frac{K_T^2}{L^2} - (1-\gamma)\frac{K_L^2}{L^2}\right] - \frac{1}{\alpha_0^{1/2}}\left[S_x + S_\psi(r/L)^{1/2} + \frac{K_w(Lr)^{1/2}}{(1-\gamma)}\left(1 - \frac{L}{r}\mu_{L\theta}\right)\right]\right\}\frac{\sqrt{2}\epsilon a}{6\mu_f}(C_\perp^2 + C_\parallel^2)^{1/2} \quad (31)$$

The bracketed term in equation (31) is identical to equation (28). Thus the nonlinear creep force variation with creepage serves to amplify the linear damping, whether stabilizing or destabilizing, but without altering the critical speed of secondary hunting. This is expressed quantitatively as

$$\lambda_{NL} = \lambda_L\left\{1 + \frac{\sqrt{2}a}{6\mu_f}(C_\perp^2 + C_\parallel^2)^{1/2}\right\} \quad (32)$$

where λ_L and λ_{NL} are the linear and nonlinear damping factors, respectively. This is interpreted physically as a decrease in the relative dominance of the creep over static and inertia effects, due to the "soft" nature of creep force variation with creepage, i.e., the effective value of μ is reduced in accordance with equation (32). This effect may be fairly large for smooth track ($6\mu_f \approx 1$) and large amplitude motion. For example, with $\epsilon = 0.025$ and using typical wheelset properties and operating conditions, the damping (or undamping) increase can be of the order of 25 percent [13].

The solutions just given are valid for nondimensional times $\tau = 0(1/\nu)$, and this encompasses periods of practical interest. This results from the dominance of creepage, such that inertia, static, and the nonlinear effects influence the motion on very slow time scales.

Validity of Linear Creep Formulation

When the correction factor of equation (32) differs substantially from unity, a linear creep model is no longer valid. We now derive explicit conditions for the validity of a linear creep force/creepage formulation.

Based on the discussion of Hobbs [17], we consider a linear creep model to be valid provided that the spin creep is small and the resultant tangential creep force is less than 25 percent of the limiting value of friction $\mu_f N$. Since $N \approx W/2$, this condition may be written as $\mu\xi_T \leq 0.25\mu_f$. From the relation for ξ_T, equation (30), the maximum resultant creepage occurs when $\partial\xi_T/\partial T_0 = 0$, which leads either to $C_\perp = C_\parallel$ or $e^{2iT_0} = e^{-2iT_0}$, i.e., $e^{2iT_0} = \mp 1$. These two values yield maximum and minimum creepages, depending on the relative magnitudes of $C_\perp$ and $C_\parallel$. To ensure satisfaction of the validity condition, we require simultaneously that

$$\epsilon\left|\frac{F\alpha_0}{1-\gamma} - S_x - \frac{K_w(Lr)^{1/2}}{1-\gamma}\left(1 - \frac{L}{r}\,\mu_{L\theta}\right)\right| \leqslant 0.25\mu_f \qquad (33)$$

$$\epsilon\left|\frac{F\alpha_0}{(1-\gamma)L^2}\,(K_T{}^2 - (1-\gamma)K_L{}^2) - S_\psi(r/L)^{1/2}\right| \leqslant 0.25\mu_f \qquad (34)$$

For large amplitude motion on smooth track and moderate speed and restraint, these conditions are fairly restrictive.

Even if the foregoing conditions are satisfied, a linear creep model may not be valid unless the spin creep is also small. The experimental results summarized by Hobbs [17] and the theoretical results of Kalker [18] indicate that a linear creep model is valid, if in addition to the aforementioned conditions, the following relation for the spin creepage is satisfied:

$$L\mu_{L\theta}\,\frac{(\bar{\omega}\cdot\bar{n}_R)}{V} \leqslant 0.4\mu_f$$

where $\bar{\omega}$ is the wheelset angular velocity. Using the relation given elsewhere [14] for the spin creepage $(\bar{\omega}\cdot\bar{n}_R)/V$, this results in

$$\frac{L}{r}\,\alpha_0 + \frac{\epsilon L K_w(L/r)^{1/2}}{(1-\gamma)} \leqslant 0.4\,\frac{\mu_f}{\mu_{L\theta}} \qquad (35)$$

To illustrate the use of these relations, we consider as an example the following vehicle/rail parameters and operating conditions. Wheelset mass $m = 907$ kg, $W = 133{,}500$ N, $V = 61$ m/sec, $K_T/L = 0.9$, $K_L/L = 0.45$, $S_x = 1$, $S_\psi = 10$, $L = 0.762$ m, $r = 0.533$ m, $K_\rho = 4.92$/m, $\gamma = 0.5$, $\alpha_0 = 0.05$, and $\mu_{L\theta} = 0.45$. Use of these in equations (33)–(35) and selection of the most restrictive condition (equation (34) in this case) results in the requirement that $\epsilon < 0.0067$ (maximum lateral displacement less than 0.43 cm) for a linear creep model to be considered valid.

Concluding Remarks

The influence on the lateral motion of a simply restrained wheelset of nonlinearities arising from the geometry of wheel/rail contact has been investigated analytically for mildly noncircular profile geometries. The equations of motion have been derived and solved using the method of multiple time scales; the main results of this study are summarized qualitatively as follows:

1 Nonlinear velocities of creep produce cubic terms which may be relatively large but which affect only the frequency of wheelset oscillation. The frequency is increased by an amount porportional to the square of the motion amplitude ϵ^2, the profile noncircularity (H_w, H_ρ), and the degree of conformality of contact, $1/(1-\gamma)$.

2 Nonlinear creep force variation with creepage produces second-order terms which cause amplification of the linear damping, whether stabilizing or destabilizing, but with no effect on critical speed. This result arises from a reduction in dominance of creep over static and inertia effects due to the soft nature of creep force variation with creepage and is valid for small spin creepage.

3 Conditions for the validity of a linear creep formulation have been derived. It appears that for large amplitude motion and conformal contact on smooth track, these conditions may not be satisfied.

References

1 Wickens, A. H., "The Dynamic Stability of Railway Vehicle Wheelsets and Bogies Having Profiled Wheels," *International Journal of Solids and Structures*, Vol. I, 1965, pp. 319–341.

2 Wickens, A. H., "The Dynamic Stability of a Simplified Four Wheel Railway Vehicle Having Profiled Wheels," *International Journal of Solids and Structures*, Vol. I, 1965, pp. 319–341.

3 Law, E. H., and Cooperrider, N. K., "A Survey of Railway Vehicle Dynamics Research," ASME *Journal of Dynamic Systems, Measurement, and Control*, Vol. 96, No. 2, June 1974, pp. 132–146.

4 Law, E. H., "Analysis of the Nonlinear Dynamics of a Railway Vehicle Wheelset," PhD Thesis, University of Connecticut, 1971.

5 Law, E. H., and Brand, R. P., "Analysis of the Nonlinear Dynamics of a Railway Vehicle Wheelset," *Journal of Dynamic Systems, Measurement, and Control*, Vol. 95, No. 1, 1973, pp. 28–35.

6 Law, E. H., "Nonlinear Wheelset Dynamic Response to Random Lateral Rail Irregularities," ASME *Journal of Engineering for Industry*, Vol. 96, No. 4, 1974, pp. 1168–1176.

7 Cooperrider, N. K., et al., "The Application of Quasilinearization Techniques to the Prediction of Nonlinear Railway Vehicle Response," *Vehicle System Dynamics*, Vol. 4, No. 2–3, July 1975, pp. 141–148.

8 Gelb, A., and VanderVelde, W., *Multiple-Input Describing Functions and Nonlinear Design*, McGraw-Hill, New York, 1968.

9 Cooperrider, N. K., "The Hunting Behavior of Conventional Railway Trucks," ASME *Journal of Engineering for Industry*, Vol. 94, No. 2, 1972, pp. 752–762.

10 Matsudeira, T., Arai, S., and Yokose, K., "Combined Effect of Frictional and Elastic Moments Against Truck Turning Upon Hunting of Truck," *Quarterly Report RTRI*, Vol. 7, No. 3, 1966, pp. 40–45.

11 Brann, R. P., "Some Aspects of the Hunting of a Railway Axle," *Journal of Sound and Vibration*, Vol. 4, No. 1, 1966, pp. 18–32.

12 Hannebrink, D. N., et al., "Influence of Axle Load, Track Gauge, and Wheel Profile on Rail-Vehicle Hunting," ASME Paper 76-WA/RT-3.

13 Burton, T. D., "Nonlinear Effects of Contact Geometry on Railway Vehicle Wheelset Motions," PhD Thesis, Department of Mechanical Engineering and Applied Mechanics, University of Pennsylvania, 1976.

14 Burton, T. D., and Whitman, A. M., "Nonlinear Kinematics of Wheel-Rail Contact," ASME JOURNAL OF APPLIED MECHANICS Vol. 45, No. 3, 1978, pp. 664–668.

15 Carter, F. W., "On the Stability of Running of Locomotives," *Proceedings of the Royal Society*, London, Series A, Vol. 121, 1928, pp. 585–611.

16 Nayfeh, A. H., *Perturbation Methods*, Wiley, New York, 1973.

17 Hobbs, A. E. W., "A Survey of Creep," TN DYN-52, British Railways Research Department, Derby, Apr. 1967.

18 Kalker, J. J., "On the Rolling Contact of Two Elastic Bodies in the Presence of Dry Friction," Report WTHD-52, Department of Mechanical Engineering, Technical University of Delft, Aug. 1973.

C. H. J. Fox[1]
Research Associate.

J. S. Burdess
Lecturer.

Department of Mechanical Engineering,
University of Newcastle Upon Tyne,
Newcastle Upon Tyne, NE1 7RU,
England

The Dynamical Characteristics of a Gyroscope With a Tuned Elastic Suspension

This study investigates the dynamics of a gyroscope rotor, supported on a "heavy" elastic suspension, using a mathematical model which allows the gyroscope to be treated as a two-degree-of-freedom rigid body on a light suspension. The natural frequencies are functions of spin rate and it is shown that the lower natural frequency can be reduced to zero by appropriate selection of suspension parameters. In this condition the gyroscope is "tuned" and could provide a useful inertial reference. Some problems associated with predicting the tuning speed of a practical gyroscope are highlighted.

Introduction

In recent years a class of gyroscopes known as Dynamically Tuned Gyroscopes has emerged as a low cost replacement for the floated rate integrating gyro which has been the workhorse of inertial guidance systems over the past two decades. Of the tuned gyro family the Oscillogyro [1] and the Hooke's joint suspended gyroscopes [2, 3] have been the most intensively developed and are now capable of matching the performance of floated gyroscopes.

However, alternative designs of dynamically tuned gyro are now evolving with potentially attractive advantages over existing designs. One such gyroscope, in which the rotor is supported by a flexible elastic suspension, was previously studied by Bulman [4] who indicated the possibility of tuning the suspension to give favourable performance characteristics.

In this paper the previous analysis is generalised and extended. A two-degree-of-freedom mathematical model for the gyro is established and the principal dynamical characteristics of the instrument are determined. It is shown that rotation of the instrument as a whole about any axis perpendicular to the drive axis causes the rotor of the gyroscope to deflect relative to the supporting casing in a way which depends upon the relationship between the spin and the natural frequencies of the rotor and suspension assembly. The response of the rotor provides a measure of the applied rotation and is affected to a large degree by the dynamical characteristics of the suspension elements. The free motion of the gyro is studied and the response to steady rates of turn and to harmonic angular inputs is evaluated.

[1] After September 1, 1979, Lecturer, Department of Mechanical Engineering, Nottingham University, University Park, Nottingham, England.

Contributed by the Applied Mechanics Division for publication in the JOURNAL OF APPLIED MECHANICS.

Discussion on this paper should be addressed to the Editorial Department, ASME, United Engineering Center, 345 East 47th Street, New York, N. Y. 10017, and will be accepted until June 1, 1980. Readers who need more time to prepare a discussion should request an extension from the Editorial Department. Manuscript received by ASME Applied Mechanics Division, April, 1979; final revision, August, 1979.

Description of the Instrument

The main elements of the instrument are shown in Fig. 1. A symmetrical rotor is connected to a drive shaft by means of an elastic suspension which consists of four equispaced radial spokes and a circular section axial strut. Built-in connections are provided at the rotor and at the drive shaft.

The masses of the spokes and strut are significant and the suspension cannot be regarded as a massless connection which only provides elastic restraint between the rotor and drive shaft. It is assumed that each element of the suspension may be treated as a uniform beam.

The spokes have a thin rectangular section and are free to deflect in bending and torsion about axes which are perpendicular to the axis of the drive shaft It is assumed that the beams are stiff in bending about the axis of the drive shaft. This constraint provides the drive to the rotor and prevents translation of the rotor perpendicular to the drive shaft axis.

The purpose of the strut is to prevent translation of the rotor along the drive shaft axis. The undeflected strut is aligned with the drive axis but is free to deflect in bending about axes perpendicular to the drive axis.

The center of the suspension, as defined by the intersection of the center lines of the undeflected spokes and strut, lies on the drive axis and is assumed to coincide with the center of mass of the rotor.

The drive shaft spins the rotor and suspension at a constant high angular velocity n relative to the instrument casing.

The effects of damping are neglected, and the rotating assembly is assumed to be dynamically balanced

Analysis

The reference axes used to define the motion of the gyroscope are shown in Fig. 2. $OXYZ$ is a datum set fixed in the casing of the instrument. The origin O is fixed at the center of the suspension and axis OZ is aligned with the axis of the drive shaft. $Oxyz$ are the principal axes of the rotor at O and at time t = zero, they coincide with

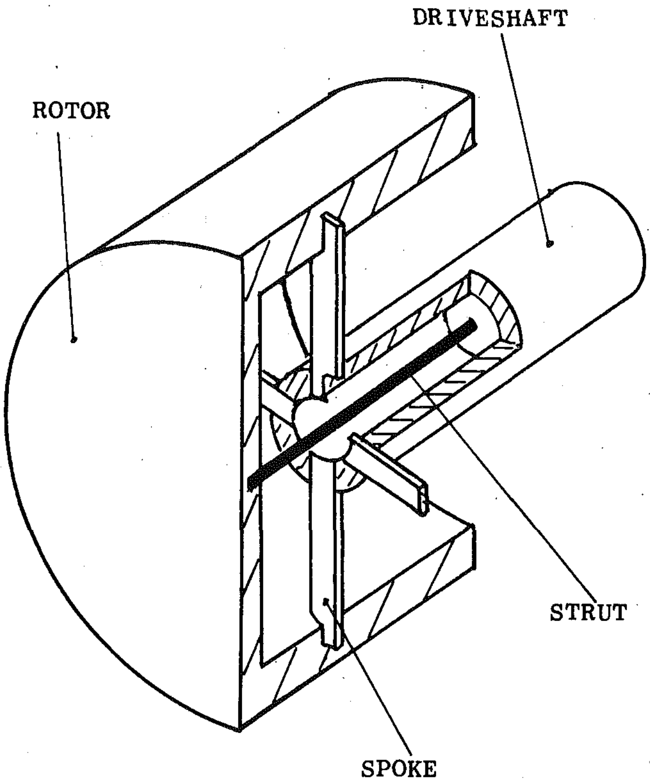

Fig. 1 Schematic of the gyroscope

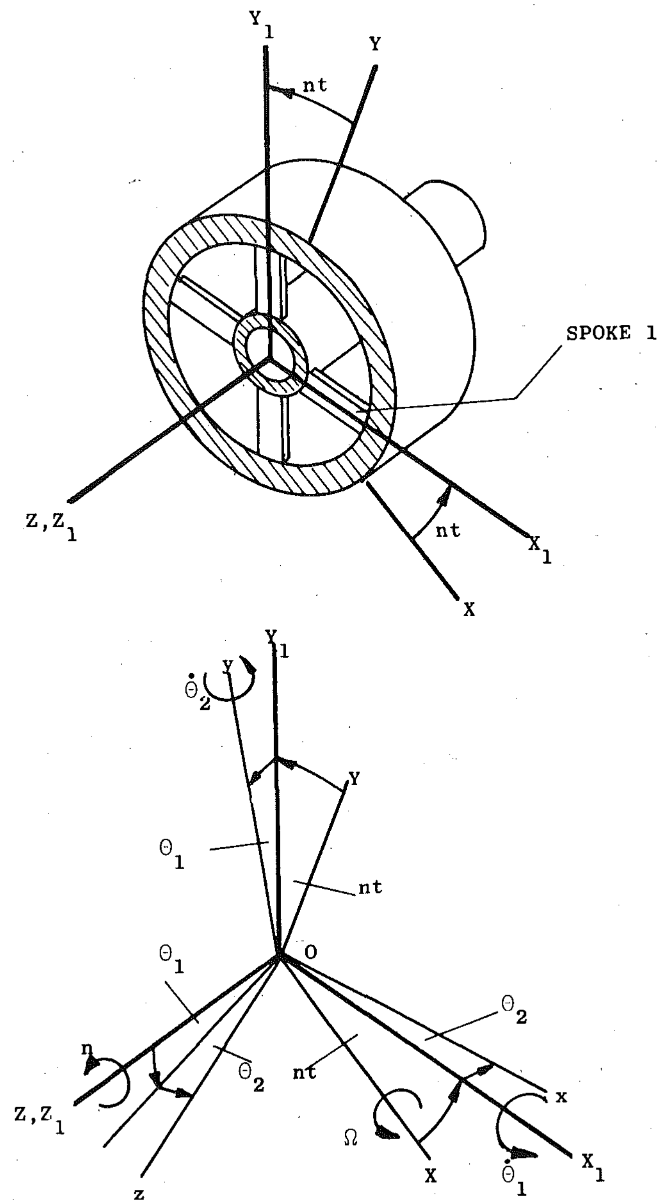

Fig. 2 Reference axes

$OXYZ$. The suspension spokes are fixed to the rotor such that in the undeflected position their radial center lines coincide with Oxy.

The displacment of the rotor relative to the casing is determined by a rotation nt about the drive axis OZ, taking $OXYZ$ to $OX_1Y_1Z_1$ followed by rotations θ_1 and θ_2 about OX_1 and Oy, respectively.

It is assumed that the casing is subjected to a rate of turn $\Omega(\ll n)$ acting about OX and it is the function of the gyroscope to provide a useful measure of this angular input. In a practical instrument Ω and $\dot{\theta}_1$, $\dot{\theta}_2$ are of the same order of magnitude.

Since the gyro consists of a rotor connected to a drive shaft by means of a "heavy" elastic suspension the general motion will be determined by a number of different mode shapes which characterise the way in which the suspension vibrates. As rotor motion is used to estimate the angular input to the casing, only the asymmetric modes of vibration are of interest, the most important of which is the fundamental mode as shown in Fig. 3.

The governing equations of motion will now be established via Lagrange's equations by assuming deflected forms for the spokes and strut which are compatible with the shape of the fundamental mode. This mode shape is defined as follows.

Spoke and Strut Displacements. With reference to Fig. 4 consider the displacement of an element dx, dy of a typical spoke, spoke 1 say, when the rotor is given small constant deflections θ_1 and θ_2. As a result of rotation θ_2 the radial center line of the spoke is assumed to deflect in bending parallel to axis OZ. The constraints imposed at the drive shaft and rotor connections determine the end conditions of the deflection curve. Assuming the spoke to be built in at both ends the end conditions are

$$x = 0, \quad U_z = 0, \quad (dU_z/dx) = 0$$

$$x = L, \quad U_z = -r_0\theta_2, \quad (dU_z/dx) = -\theta_2 \qquad (1)$$

Using (1) the displacement of the beam may be determined from conventional beam theory and is given by

$$U_z = \theta_2\left[(2r_0 - L)\left(\frac{x}{L}\right)^3 + (L - 3r_0)\left(\frac{x}{L}\right)^2\right] = \theta_2 g(x) \qquad (2)$$

In addition, rotation θ_1 is assumed to produce uniform torsion about the center line of the spoke so that line $O'y_e$, situated at radial distance x from the drive shaft connection, rotates about the center line through angle θ_e where

$$\theta_e = \theta_1(x/L) \qquad (3)$$

For small θ_1 and θ_2, elastic coupling between bending and torsion is neglected.

The displacement curve of the axial strut is also of the form expressed by (2). By substituting L_s and r_s for L and r_0 (Fig. 4) the deflections of the strut along OX_1 and OY_1 may be written

$$U_x = -\theta_2 g_1(z); \quad U_y = \theta_1 g_1(z)$$

where

$$g_1(z) = \left[(2r_s - L_s)\left(\frac{z}{L_s}\right)^3 + (L_s - 3r_s)\left(\frac{z}{L_s}\right)^2\right] \qquad (4)$$

To construct the equations of motion using these mode shapes it is necessary to determine the kinetic energy and potential energy of the rotor and suspension assembly.

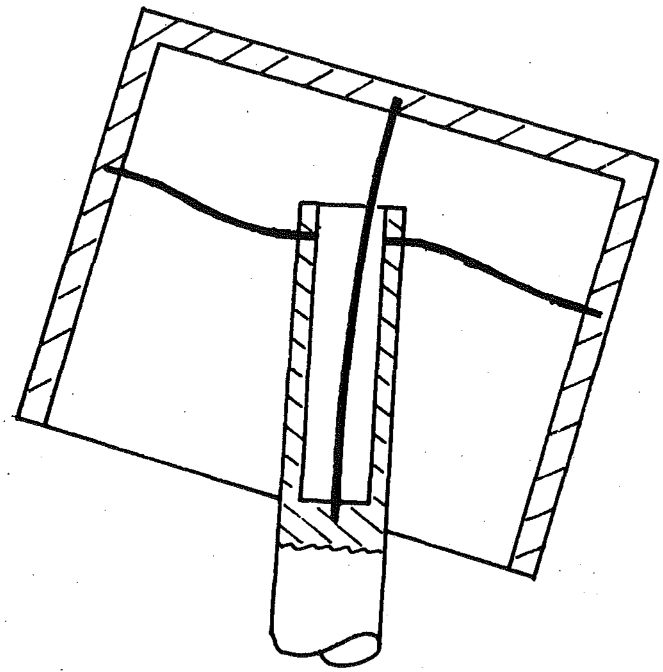

Fig. 3 Schematic to illustrate fundamental mode

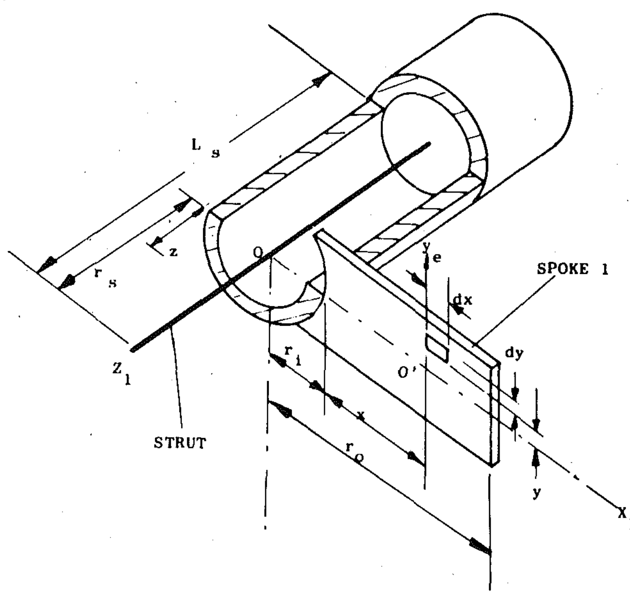

Fig. 4 Detail of spoke and strut

Kinetic Energy. The total kinetic energy of the system comprises the sum of the kinetic energies of the rotor, the spokes and the axial strut.

With the aid of Fig. 2 the angular velocity components of the rotor along $Oxyz$ may be written

$$\omega_x = (\dot{\theta}_1 + \Omega \cos nt) \cos \theta_2 - n \cos \theta_1 \sin \theta_2 - \Omega \sin \theta_2 \sin \theta_1 \sin nt$$

$$\omega_y = \dot{\theta}_2 - \Omega \sin nt \cos \theta_1 + n \sin \theta_1 \quad (5)$$

$$\omega_z = n \cos \theta_1 \cos \theta_2 + \Omega \sin nt \sin \theta_1 \cos \theta_2 + (\dot{\theta}_1 + \Omega \cos nt) \sin \theta_2$$

The kinetic energy of the rotor is

$$T_R = \frac{1}{2} A \omega_x{}^2 + \frac{1}{2} A \omega_y{}^2 + \frac{1}{2} C \omega_z{}^2 \quad (6)$$

where (A, A, C) are the principal moments of inertia of the rotor at O. If we make the small angle approximations $\sin \theta \approx \theta$, $\cos \theta \approx (1 - \theta^2/2)$ equations (5) and (6) may be combined to give the following quadratic expression for the kinetic energy of the rotor:

$$T_R = (A/2)\,[(\dot{\theta}_1 + \Omega \cos nt - n\theta_2)^2 + (\dot{\theta}_2 - \Omega \sin nt + n\theta_1)^2] + (C/2)[n^2(1 - \theta_1{}^2 - \theta_2{}^2) + 2n\theta_1\Omega \sin nt + 2n\theta_2\Omega \cos nt + 2n\dot{\theta}_1\theta_2] \quad (7)$$

Treating the spokes as thin beams the kinetic energy of spoke 1 is given by

$$T_{S1} = \frac{\rho c}{2} \int_0^L \int_{-h/2}^{+h/2} (v_x{}^2 + v_y{}^2 + v_z{}^2) dx dy \quad (8)$$

where c is the thickness of the spoke, ρ is the density of the spoke material, and L and h are, respectively, the length and width of the spoke. The quantities v_x, v_y, v_z are the components of velocity of the beam element with dimensions dx, dy along $OX_1Y_1Z_1$ and are

$$v_x = -ny \cos (\theta_1 x/L) - [U_z + y \sin (\theta_1 x/L)]\, \Omega \sin nt$$

$$v_y = n(x + r_i) - \theta_1(xy/L) \sin (\theta_1 x/L) - [U_z + y \sin (\theta_1 x/L)]\Omega \cos nt \quad (9)$$

$$v_z = (\partial U_z/\partial t) + \Omega(x + r_i) \sin nt + [\dot{\theta}_1 x/L + \Omega \cos nt] y \cos (\theta_1 x/L)$$

Substitution of (9) and (2) in (8) yields an expression for the kinetic energy of spoke 1 which for small θ_1 and θ_2 may be expressed as follows when third and higher-order terms in θ_1, θ_2 are neglected:

$$T_{S1} = \dot{\theta}_1{}^2 I_1 + \dot{\theta}_2{}^2 I_2 - \theta_1{}^2 n^2 I_1 + \Omega(\dot{\theta}_1 \cos nt + n\theta_1 \sin nt) I_3 + \Omega(\dot{\theta}_2 \sin nt - n\theta_2 \cos nt) I_4 + (n^2 + \Omega^2 \cos^2 nt) I_5 + (n^2 + \Omega^2 \sin^2 nt) I_6 \quad (10)$$

Integrals I_1 to I_6 are defined in the Appendix. Similar expressions to (10) define the kinetic energies of spokes 2, 3, and 4.

Following a similar procedure the kinetic energy due to flexural motion of the strut is given by

$$T_S = [\dot{\theta}_1{}^2 + \dot{\theta}_2{}^2 + 2n(\theta_1\dot{\theta}_2 - \theta_2\dot{\theta}_1) + n^2(\theta_1{}^2 + \theta_2{}^2)] I_7 + \Omega[n(\theta_2 \cos nt + \theta_1 \sin nt) - (\dot{\theta}_1 \cos nt - \dot{\theta}_2 \sin nt)] I_9 + \Omega^2 I_8 \quad (11)$$

where I_7, I_8, and I_9 are defined in the Appendix and the contribution due to the polar moment of inertia of the strut has been neglected.

The kinetic energy of the total system is therefore given by

$$T = T_R + T_S + \sum_{i=1}^{4} T_{si} \quad (12)$$

Potential Energy. Potential energy is stored in the suspension as a result of elastic deformation of the spokes and the strut. For small rotor displacements the contribution made by the spokes can be expressed as the sum of the strain energies due to bending and torsion considered separately. For spoke 1 the potential energy due to bending can be written

$$V_{B1} = \frac{EI}{2} \int_0^L \left(\frac{\partial^2 U_z}{\partial x^2}\right)^2 dx + \frac{1}{2} \int_0^L S \left(\frac{\partial U_z}{\partial x}\right)^2 dx \quad (13)$$

where EI is the flexural rigidity and S is the radial load in the spoke. Similarly, the strain energy due to torsion may be written [5]

$$V_{T1} = \frac{1}{2} \int_0^L \frac{hc^3 G}{3} \left(1 + \frac{hS}{4Gc^3}\right) \left(\frac{\partial \Theta}{\partial x}\right)^2 dx \quad (14)$$

where G is the modulus of rigidity of the spoke material, and h and c are as defined for eqution (8).

Equations (13) and (14) show that the strain energy stored in the spokes is a function of the radial load S. For sufficiently large values of S this loading can make a significant contribution to the strain energy. Care is therefore required when interpreting its effect. The value of S is determined by considering the preload, the inertia loading due to centrifugal action and the nature of the shaft and rotor connections to the spoke. If the connections at $x = 0$ and $x = L$ expand by amounts u_1 and u_2 due to centrifugal action, then the radial load S may be written as

$$S = S_0 + Ea(u_2 - u_1)/L + n^2(\rho hc/6)\,[L(L + 3r_i) - 3x^2 - 6r_i x] \quad (15)$$

where S_o is the initial preload in the spoke and a is the cross-sectional area of the spoke.

Substitution from equations (2), (3), and (15) in (13) and (14) yields, for spoke 1

$$V_{B1} = [I_{10} + n^2 I_{11}]\theta_2{}^2 \quad (16)$$

$$V_{T1} = \frac{h}{24L}[4Gc^3 + hS']\theta_1{}^2 = K_T\theta_1{}^2 \quad (17)$$

where $S' = S_0 + Ea(u_2 - u_1)/L$.

Integrals I_{10} and I_{11} are defined in the Appendix, and the potential energies of spokes 2, 3, and 4 are defined by similar expressions to (16) and (17).

The potential energy in the strut due to flexure is given by

$$V_s = \frac{E_s I_s}{2}\int_0^L \left[\left(\frac{\partial^2 U_x}{\partial z^2}\right)^2 + \left(\frac{\partial^2 U_y}{\partial z^2}\right)^2\right] dz$$

$$V_s = I_{12}(\theta_1{}^2 + \theta_2{}^2) \quad (18)$$

where I_{12} is defined in the Appendix.

The total potential energy of the system is therefore

$$V = V_s + \sum_{i=1}^{4} (V_{Bi} + V_{Ti}) \quad (19)$$

Equations of Motion. Although it has been convenient to derive the kinetic and potential energies of the system in terms of coordinates measured relative to rotating frames of reference, visualization of the rotor motion is greatly simplified if the rotor displacements are expressed in terms of the rotations β_1 and β_2 taken along the case fixed directions OXY. This transformation can be achieved, for small θ_1 and θ_2, by resolving θ_1 and θ_2 along OXY so that

$$\beta_1 = \theta_1 \cos nt - \theta_2 \sin nt$$

$$\beta_2 = \theta_1 \sin nt + \theta_2 \cos nt \quad (20)$$

The equations of motion for the gyro now follow on substitution of (12), (19), and (20) into the Lagrange equation in the form

$$\frac{d}{dt}\left(\frac{\partial T}{\partial \dot{\beta}_i}\right) - \frac{\partial T}{\partial \beta_i} + \frac{\partial V}{\partial \beta_i} = 0 \quad i = 1, 2 \quad (21)$$

and may be written

$$A_0\ddot{\beta}_1 + C_0 n\dot{\beta}_2 + [K_0 - n^2K_1]\beta_1 = -F_1\dot{\Omega}$$

$$A_0\ddot{\beta}_2 - C_0 n\dot{\beta}_1 + [K_0 - n^2K_1]\beta_2 = F_2 n\Omega \quad (22)$$

where

$$A_0 = A + 2I_7 + 4I_1 + 4I_2$$
$$C_0 = C + 8I_1 + 8I_2$$
$$K_0 = 4I_{10} + 4K_T + 2I_{12}$$
$$K_1 = 4I_2 - 4I_{11}$$
$$F_1 = A + 2I_3 - 2I_4 - I_9$$
$$F_2 = C + 4I_3 - 4I_4$$

Equations (22) allow the rotor and suspension to be treated as a single rigid body, having two degrees of freedom, connected to the drive shaft by a massless suspension.

The quantities A_0 and C_0 represent the transverse and polar moments of inertia of the equivalent rigid body and $(K_0 - n^2K_1)$ represents the stiffness of the equivalent suspension. K_0 is a function of the bending and torsional stiffnesses of the nonrotating suspension and the radial preload in the spokes. K_1 represents the reduction in stiffness of the suspension due to the dynamical characteristics of the rotating suspension, and includes centrifugal loading effects.

We shall now examine the dynamical characteristics of the gyroscope by considering the free motion of the rotor and the response to steady and harmonic rate inputs.

Free Motion and Tuning. The free motion of the gyroscope is governed by equations (22) with $\Omega = 0$ in which case the rotor displacement takes the form

$$\beta_1 = \sum_{j=1}^{2} \beta_j \sin (p_j t + \delta_j)$$

$$\beta_2 = \sum_{j=1}^{2} \lambda_j\beta_j \cos (p_j t + \delta_j) \quad (23)$$

where

$$\lambda_j = (K_0 - n^2K_1 - p_j{}^2A_0)/(C_0 n p_j)$$

p_j is a natural frequency of free vibration and β_j and δ_j are initial condition constants.

Substitution of (23) in (22) yields the following frequency equation

$$(np_j)^2C_0{}^2 - (K_0 - n^2K_1 - p_j{}^2A_0)^2 = 0 \quad (24)$$

from which

$$p_j = \frac{nC_0}{2A_0} \pm \frac{nC_0}{2A_0}\left[1 + \frac{4A_0(K_0 - n^2K_1)}{n^2C_0{}^2}\right]^{1/2} \quad (25)$$

For a practical gyroscope driven at high speed we may assume that $4\,A_0(K_0 - n^2K_1)/n^2C_0{}^2 \ll 1$. This condition allows the following good approximations to the natural frequencies to be extracted from (25):

$$p_1 \approx (K_0 - n^2K_1)/(C_0 n) \quad (26)$$

$$p_2 \approx (C_0 n/A_0) \gg p_1 \quad (27)$$

The gyro possesses two natural frequencies. At high values of rotor speed that denoted by p_1 has a long period and is determined by the ratio between the equivalent suspension stiffness and the angular momentum of the rotor. The second frequency (p_2) has a very short period and is approximately equal to the nutational frequency of a free disk.

A typical variation of the natural frequencies with spin, n, is illustrated in Fig. 5 for a gyroscope with zero preload in the spokes and having a rigid rotor and drive shaft. When $n = 0$ the two frequencies coincide and have the value $p_1 = p_2 = (K_0/A_0)^{1/2}$. With increasing n the higher natural frequency (p_2) increases steadily and approaches the asymptote $p_2 \approx (C_0 n/A_0)$ as $n \to \infty$.

The lower natural frequency (p_1) decreases steadily with increasing n and is zero when n has the value

$$n_t = (K_0/K_1)^{1/2} \quad (28)$$

at which point the gyroscope is said to be tuned. At this running speed the equations of motion (22) show that the suspension has zero stiffness and that the rotor will behave as a spinning body which is decoupled from the drive shaft. From the definition of K_0 and K_1 it will be seen that the tuning speed is a function of spoke and strut parameters only and is independent of rotor inertia.

The value of K_0, and hence the tuning speed, is however markedly affected by preload in the spokes. Fig. 6 indicates how n_t is affected by a range of preloads which might be introduced into the spokes as a result of thermal stresses and radial expansion of the rotor and drive shaft connection points under centrifugal loading. The tuning speed increases rapidly with preload. As will be shown in the following section, it is advantageous to operate the gyroscope at the tuning speed. The degree of preload in the suspension is therefore a critical factor to consider in the design of the gyroscope.

The mode shapes corresponding to p_1 and p_2 are approximately $\lambda_1 \approx 1$ and $\lambda_2 \approx -1$. The tip of the spin axis thus traces out a circular path. In the case of the lower natural frequency (p_1) the direction of

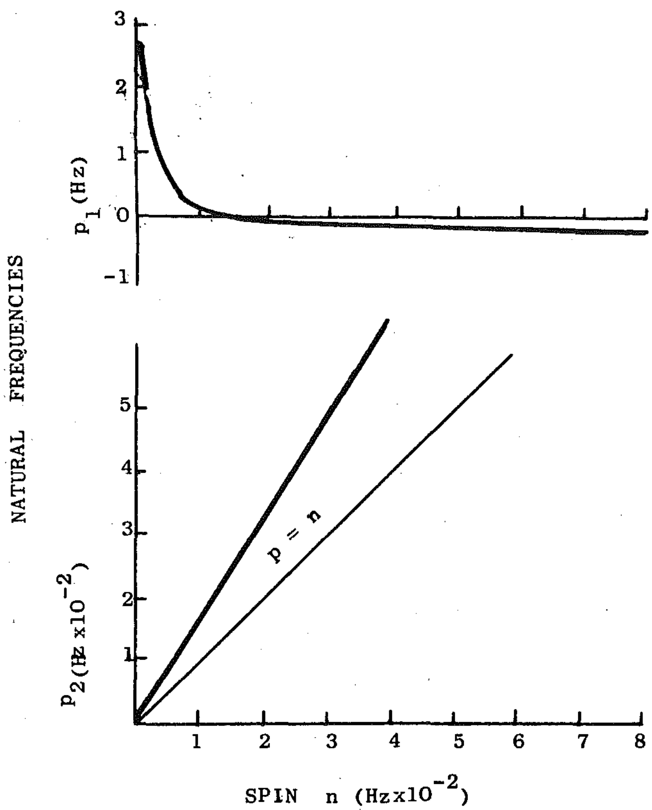

Fig. 5 Typical variation frequencies (p_1 and p_2) with spin frequency (n). Parameter values for gyroscope $A = 8.93 \times 10^{-4}$ kg·m², $C = 1.39 \times 10^{-3}$ kg·m², $h = 19$ mm, $c = 0.1$ mm, $r_0 = 34.9$ mm, $L = 25.4$ mm, $EI = 496$ N/m², $\rho = 8.3$ Mg/m³, $r_s = 12.7$ mm, $L_s = 50.8$ mm, $E_sI_s = 9300$ N/m², $\rho_s = 7.83$ Mg/m³.

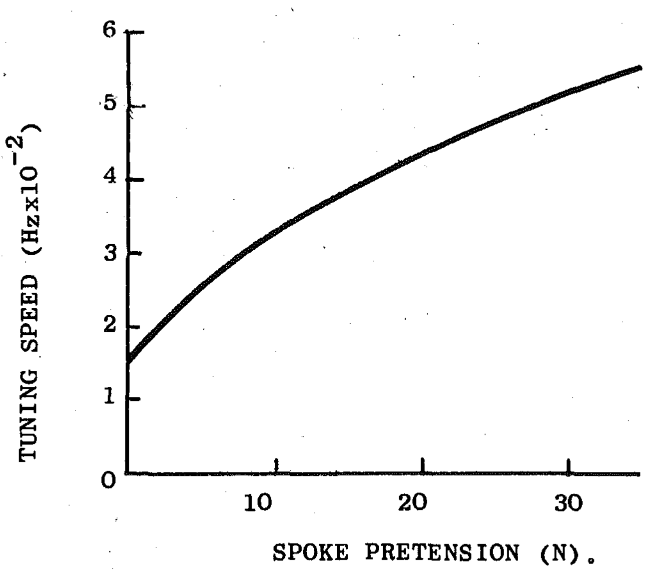

Fig. 6 The effect of spoke pretension on tuning speed; parameter values as for Fig. 5

traverse round the circle depends upon the value of rotor speed. For speeds less than the tuning speed the spin axis moves in the opposite direction to the rotor spin. For values greater than the tuning speed the spin axis moves in the same direction as rotor spin. In the case of the higher natural frequency (p_2) the motion of the spin axis is always in the same direction as the spin.

If the instrument is tuned in accordance with (28) the free motion may be expressed as

$$\beta_1 = \bar{\beta}_{01} + \bar{\beta}_1 \quad \sin \quad (p_2 t + \delta)$$

$$\beta_2 = \bar{\beta}_{02} - \bar{\beta}_1 (p_2 A_0 / n C_0) \quad \cos \quad (p_2 t + \delta) \tag{29}$$

where $\bar{\beta}_1, \bar{\beta}_{01}, \bar{\beta}_{02}$, and δ are initial condition constants.

Solutions (29) indicate that if the rotor spin axis is given a steady offset at time $t = 0$ and released from rest, the rotor will maintain the initial offset, and will thus behave as if it were connected to the drive shaft by a suspension having zero stiffness.

Response to a Steady Rate of Turn Ω. For the untuned instrument ($n \neq n_t$) the steady-state response follows from (22) and shows that the rotor takes up a steady deflection given by

$$\beta_1 = 0$$

$$\beta_2 = F_2 n \Omega / (K_0 - n^2 K_1) \tag{30}$$

Thus, in response to a constant applied rate about OX, the rotor adopts a deflection about OY which is proportional to the applied rate. The deflection therefore provides a measure of the applied rate of turn. An applied rate about OY would produce a similar response about OX. The untuned instrument therefore acts as a two axis rate sensor. The response allows the magnitude and direction of Ω to be estimated by recording the magnitude of the rotor deflection, and the axis about which it occurs.

If the instrument is tuned according to (28) the steady-state motion is proportional to the total turn and is given by

$$\beta_1 = -\left[1 - \frac{4(2I_1 + 2I_2 - I_3 - I_4)}{(C + 8I_1 + 8I_2)}\right] \Omega t$$

$$\beta_2 = 0 \tag{31}$$

Thus, in a tuned gyro, the rotor responds about the same axis as the input rate, but in a direction which tends to maintain the spin axis of the rotor fixed in inertial space. The spin axis does not remain absolutely stationary with respect to an inertial reference but moves at a rate $4\Omega(2I_1 + 2I_2 - I_3 - I_4)/(C + 8I_1 + 8I_2)$ in the same sense as Ω. However, in a practical gyro the polar moment of inertia, C, of the rotor is much greater than the equivalent moments of inertia of the spokes and strut and the response (31) can be written with good approximation as

$$\beta_1 \approx -\Omega t$$

$$\beta_2 = 0 \tag{32}$$

The deflection of the rotor is thus approximately equal to the total applied turn and the gyro provides a usable inertial reference.

Response to Angular Vibration. If the gyro is excited by an angular vibration at frequency s about OX such that $\Omega = \Omega_0 \cos (st + \epsilon)$ where $\Omega_0 \ll n$, the solutions to the equations of motion (22) for the untuned gyro are

$$\beta_1 = \Omega_0 s \frac{[F_1(K_0 - n^2K_1 - s^2A_0) + F_2C_0n^2)]}{[(K_0 - n^2K_1 - s^2A_0)^2 - C_0^2n^2s^2]} \sin (st + \epsilon)$$

$$\beta_2 = \Omega_0 n \frac{[F_1C_0s^2 + F_2(K_0 - n^2K_1 - s^2A_0)]}{[(K_0 - n^2K_1 - s^2A_0)^2 - C_0^2n^2s^2]} \cos (st + \epsilon) \tag{33}$$

The response to angular vibration takes the form of an elliptical whirl of the rotor spin axis at the forcing frequency. Resonance will occur when the forcing frequency (s) is equal to either of the natural frequencies p_1 or p_2.

If the gyro is tuned according to equation (28), the response (33) simplifies and may be written

$$\beta_1 = \left(\frac{\Omega_0}{s}\right) \frac{[F_2C_0n^2 - F_1A_0s^2]}{[A_0^2s^2 - C_0^2n^2]} \sin (st + \epsilon) \tag{34}$$

$$\beta_2 = \Omega_0 n \frac{[F_1C_0 - F_2A_0]}{[A_0^2s^2 - C_0^2n^2]} \cos(st + \epsilon) \qquad (34)\ (Cont.)$$

Equations (34) show that in a tuned instrument resonance only occurs for one nonzero value of forcing frequency. This frequency corresponds to the higher natural frequency, i.e., $s = p_2 = (nC_0/A_0)$. The resonance at zero input frequency corresponds to the response to a constant applied rate of turn.

The response of the tuned gyroscope to angular vibration at twice spin frequency is of particular interest. Other dynamically tuned gyroscopes such as the Oscillogyro [6] and Hooke's joint gyro [7] respond to such angular vibration in a manner which is indistinguishable from the response to a constant applied rate of turn. This phenomenon, known as "2ω-drift," is a source of error which limits the accuracy of tuned gyroscopes as inertial references.

Setting $s = 2n$ in equations (34), the response of the gyroscope considered here is given by

$$\beta_1 = \frac{\Omega_0}{2n} \frac{[F_2C_0 - 4F_1A_0]}{[4A_0^2 - C_0^2]} \sin(2nt + \epsilon)$$

$$\beta_2 = \frac{\Omega_0}{n} \frac{[F_1C_0 - F_2A_0]}{[4A_0^2 - C_0^2]} \cos(2nt + \epsilon) \qquad (35)$$

For a practical gyro in which the rotor inertias are much greater than those of the spokes and strut the response (35) is approximately

$$\beta_1 \approx -\frac{\Omega_0}{2n} \sin(2nt + \epsilon)$$

$$\beta_2 \approx 0 \qquad (36)$$

Comparison of responses (36) and (31) shows that the nature of the response to $2n$ angular vibration is fundamentally different from the response to a constant applied rate. The gyroscope is therefore inherently free from "2ω-drift" errors.

Conclusions

The dynamics of an elastically supported gyroscope consisting of a heavy rotor supported by a radial flexure suspension and an axial strut has been considered. A mathematical model of the gyroscope has been established on the basis of the first mode of vibration of the rotor and suspension assembly. Using this model it has been shown that the dynamics of the suspension members plays an important role in determining the performance characteristics of the gyro.

The two natural frequencies of the gyro, p_1 and p_2, have been determined and are shown to be functions of rotor speed. p_1 decreases with increasing n whereas p_2 increases. By matching the vibrational characteristics of the suspension with the running speed the lower natural frequency, p_1, can be reduced to zero. In this condition the gyroscope is tuned and the rotor behaves approximately as a free spinning body.

In the untuned condition the response of the gyro to an externally applied rate of turn takes the form of a steady deflection of the rotor from which the magnitude and direction of the applied rate of turn can be determined. The gyro acts as a two axis rate sensor. In the tuned condition the displacement of the rotor is a measure of the total turn of the casing and the gyro provides an inertial reference.

The response of the gyroscope to harmonic angular excitation has been considered. For the untuned gyro resonance occurs when the forcing frequency is equal to either of the two natural frequencies. For the tuned gyro resonance only occurs for excitation at the higher natural frequency.

Compared with existing designs of tuned gyro the present device has favorable response characteristics in the presence of angular vibration at twice rotor spin frequency, in that the problem of "2ω-drift" does not occur.

Acknowledgments

The authors acknowledge, with thanks, the finanacial support of the Science Research Council (U.K.).

References

1 Whalley, R., Holgate, M. J., and Maunder, L., "The Oscillogyro," *Journal of Mechanical Engineering Science,* Vol. 9, No. 1, 1967, pp. 55–58.

2 Hill, A. T., "A Theoretical Investigation Into the Tuned Hooke's Gyro," R.A.E. Technical Report 67254, Oct. 1967.

3 Craig, R. J. G., "Theory of Operation of an Elastically Supported Tuned Gyroscope," *IEEE Transactions on Aerospace and Electronic Systems,* Vol. AES-9, No. 3, May 1972, pp. 280–288.

4 Bulman, D. N., "Dynamics of a Gyroscope With an Elastically Supported Rotor," PhD Thesis, University of Newcastle Upon Tyne, Oct. 1972.

5 Timoshenko, S. P., "Longitudinal Normal Stresses in Twisted Bars," *Strength of Materials,* 3rd ed., Vol. 2, Van Nostrand Reinhold, New York, 1958, pp. 288-291.

6 Ormandy, D., and Maunder, L. "Dynamics of the Oscillogyro," *Journal of Mechanical Engineering Science,* Vol. 15, No. 3, 1973, pp. 210–217.

7 Craig, R. J. G., "Theory of Errors of a Multigimbal, Elastically Supported Gyroscope," *IEEE Transactions on Aerospace and Electronic Systems,* Vol. AES-8, No. 3, May 1972, pp. 289–297.

APPENDIX

Definition of Integrals

$$I_1 = \frac{\rho c}{2} \int_0^L \int_{-h/2}^{+h/2} \frac{x^2y^2}{L^2}\, dx\, dy$$

$$I_2 = \frac{\rho c}{2} \int_0^L \int_{-h/2}^{+h/2} [g(x)]^2\, dx\, dy$$

$$I_3 = \rho c \int_0^L \int_{-h/2}^{+h/2} \frac{xy^2}{L}\, dx\, dy$$

$$I_4 = \rho c \int_0^L \int_{-h/2}^{+h/2} g(x)(x + r_i)\, dx\, dy$$

$$I_5 = \frac{\rho c}{2} \int_0^L \int_{-h/2}^{+h/2} y^2\, dx\, dy$$

$$I_6 = \frac{\rho c}{2} \int_0^L \int_{-h/2}^{+h/2} (x + r_i)^2 dx\, dy$$

$$I_7 = \frac{\rho_s a_s}{2} \int_0^{L_s} [g_1(z)]^2\, dz$$

$$I_8 = \frac{\rho_s a_s}{2} \int_0^{L_s} (z + r_s - L_s)^2\, dz$$

$$I_9 = \frac{\rho_s a_s}{2} \int_0^{L_s} (z + r_s - L_s) g_1(z) dz$$

$$I_{10} = \frac{EI}{2} \int_0^L \left[\frac{d^2}{dx^2}[g(x)]\right]^2 dx + \left[S_0 + \frac{Ea}{L}(u_2 - u_1) - Ea\alpha T\right] \int_0^L \left[\frac{d}{dx}[g(x)]\right]^2 dx$$

$$I_{11} = \frac{\rho hc}{2} \int_0^L \left[\frac{L}{6}(L + 3r_i) - \frac{x^2}{2} - r_i x\right] \left[\frac{d}{dx}[g(x)]\right]^2 dx$$

$$I_{12} = \frac{E_s I_s}{2} \int_0^{L_s} \left[\frac{d^2}{dz^2}[g_1(z)]\right]^2 dz$$

J. S. Burdess
Lecturer.

C. H. J. Fox
Research Associate.

Department of Mechanical Engineering,
Newcastle University,
Newcastle Upon Tyne,
England NE1 7RU

The Stabilization of a North-Seeking Platform Using a Dynamically Tuned Hooke's Joint Gyroscope

The paper shows that the ideally tuned Hooke's joint gyroscope is capable of operating as a gyrocompass. The dynamic response of the compass is examined in detail and its accuracy as a north-seeking device is assessed. It it shown that small amounts of mistuning will result in gross errors. The need for precision tuning is eliminated by supporting the gyroscope on a single-degree-of-freedom platform. It is shown that if the platform is driven via feedback of the gyrorotor displacement in azimuth then the response of the combined system is essentially that of the ideal gyroscope. The overall system is insensitive to misturning errors and will automatically align the gyrospin axis with true north irrespective of any initial offset. The effects of damping, mass unbalance, and platform misalignment are assessed.

Introduction

The tuned Hooke's joint gyroscope has recently found application in precision inertial navigation (IN) systems where its function is to detect very small angular displacements. When the suspension is tuned to the running speed it has been shown in [1, 2] that the gyrorotor tends to behave as an inertially free disk. It is this property together with its inherent simplicity and robustness that has enabled it to become a serious competitor to the floated gyro for IN use.

However the free rotor characteristic of the Hooke's joint gyroscope will also enable it to find applications in other areas of work. It will be shown that if a pendulous moment is applied to the rotor the action of the Earth's rotation causes the rotor to move in such a way as to indicate the direction of true north. The ideally tuned Hooke's joint gyroscope has therefore the capacity to function as a north-seeking gyrocompass.

Compass designs based upon a gyrorotor have long been established, for example, the Sperry gyrocompass [3] and the ligament (or spherical air bearing) suspended pendulous compass [4]. Although well established and developed over a number of years the Sperry device is still mechanically complex and remains an expensive instrument. Because of its construction the usefulness of the ligament suspension is restricted to surveying work. Although the ligament simplifies the suspension and eliminates the need for gimbal bearings it lacks robustness and requires an additional system (usually optical) to relate the rotor position to the axis of the theodolite's telescope.

Contributed by the Applied Mechanics Division for publication in the JOURNAL OF APPLIED MECHANICS.

Discussion on this paper should be addressed to the Editorial Department, United Engineering Center, 345 East 47th Street, New York, N. Y. 10017, and will be accepted until June 1, 1980. Readers who need more time to prepare a discussion should request an extension from the Editorial Department. Manuscript received by ASME Applied Mechanics Division, April, 1979; final revision, September, 1979.

Because of the wide separation in cost and performance of these two devices it is anticipated that the simplicity and robustness of the Hooke's joint configuration may offer advantages in this area of application once the performance characteristics have been identified and proven. This paper therefore seeks to evaluate the potential of a system that incorporates a Hooke's joint gyroscope operating as a north-seeking device.

Description of Instrument and Equations of Motion

To form an appreciation of the dynamic chracteristics of a north-seeking system based upon a tuned Hooke's joint gyroscope it is instructive to first assess the ability of the ideally tuned gyroscope to function as a north-seeking device. The basic sensing element of the proposed gyrocompass takes the form shown in Fig. 1. The arrangement consists of an axisymmetric rotor supported by a Hooke's joint suspension comprising of two identical parallel gimbals phased at 90°. Torsional pivots of equal stiffness k are fixed along principal axes in the gimbals and provide the means of connecting the rotor to the drive shaft. The rotor is therefore free to deflect relative to the drive shaft along the axes of these pivots. When the rotor axis is in alignment with the drive axis it is assumed that the hinge axes are coplanar and coincide with the principal axes of the rotor.

A drive motor spins the rotor and gimbal suspension at a high angular velocity relative to the casing.

To apply control over the displacement of the rotor it is usual practice to provide two sets of torquer coils fixed in the casing. These coil sets are mounted along orthogonal axes perpendicular to the drive axis and link with a permanent (axisymmetric) magnetic field fixed in the rotor. The application of a controlled current through these coils provides the means of generating the appropriate rotor torques.

Fig. 2 shows the gyrocasing axes $OXYZ$ on the surface of the Earth at latitude λ with OX vertical and the drive axis OZ in the horizontal

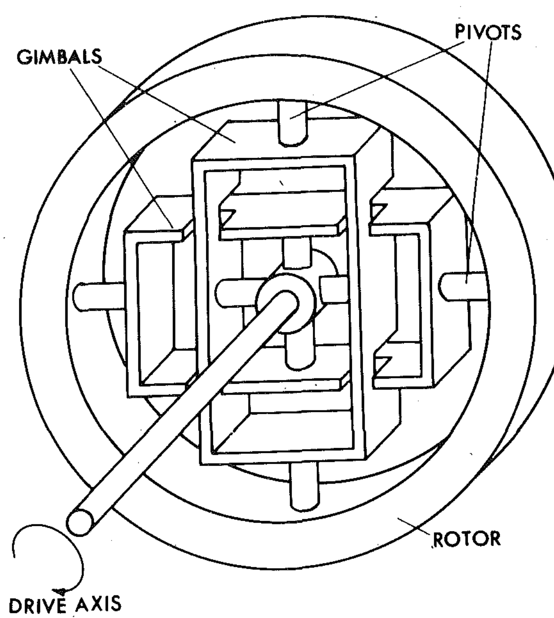

Fig. 1 Two gimbal Hooke's joint gyroscope

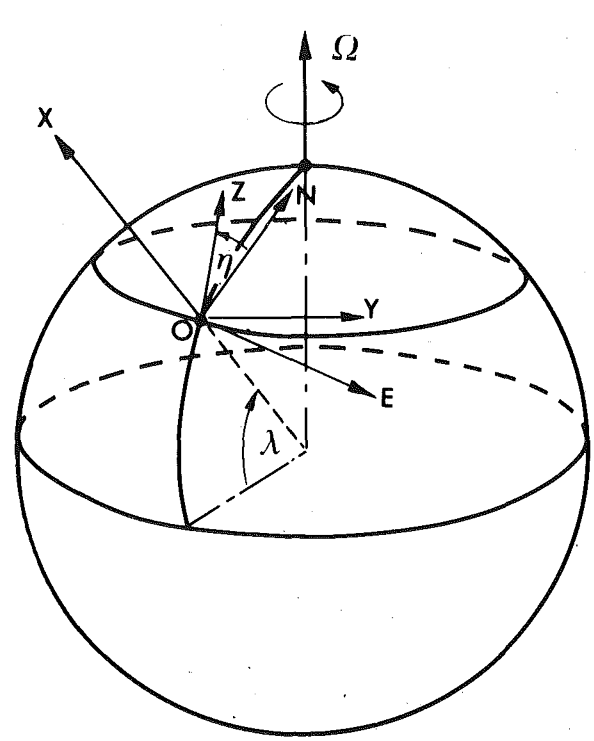

Fig. 2 Casing axes

plane at an angle η west of north ON. Due to the motion of the Earth about its polar axis these axes rotate with angular velocities

$$\dot{\Phi}_1 = \Omega \sin \lambda$$

$$\dot{\Phi}_2 = \Omega \cos \lambda \sin \eta$$

$$\dot{\Phi}_3 = \Omega \cos \lambda \cos \eta \qquad (1)$$

about OX, OY, and OZ, respectively. These angular velocities provide the input to the gyro and are central to its function as a gyrocompass.

The displacement of the gyrorotor with respect to $OXYZ$ is derived as shown in Fig. 3. Rotor motion is given by a rotation β_1 about OX to take $OXYZ$ to $Ox_1y_1z_1$ followed by a rotation β_2 about Oy_1 to $Oxyz$. Axes $Oxyz$ are fixed along the principal axes of the rotor. Since all axes in the plane of the rotor can be regarded as principal axes (axisymmetric rotor) the spin (nt) about the rotor axis Oz can occur without rotating $Oxyz$ with the rotor spin. If β_1 and β_2 are assumed small they may be regarded as the transverse deflections of the rotor with respect to axes fixed in the casing.

Using this coordinate system to describe the displacement of the gyrorotor the equations of motion for the compass may be deduced from the general theory of the Hooke's joint gyroscope as presented in [1, 2].

$$\begin{aligned}(A + a_1)\ddot{\beta}_1 + [n(C + 2a_1) - J\dot{\Phi}_3]\dot{\beta}_2 \\ + [(2k - n^2J_1) + n\dot{\Phi}_3(C + 2(c_1 - a_1))]\beta_1 \\ = -(A + a_1)\ddot{\Phi}_1 - n(C + c_1)\dot{\Phi}_2 + T_1\end{aligned}$$

$$\begin{aligned}(A + a_1)\ddot{\beta}_2 - [n(C + 2a_1) - J\dot{\Phi}_3]\dot{\beta}_1 \\ + [(2k - n^2J_1) + n\dot{\Phi}_3(C + 2(c_1 - a_1))]\beta_2 \\ = -(A + a_1)\ddot{\Phi}_2 + n(C + c_1)\dot{\Phi}_1 + T_2 \qquad (2)\end{aligned}$$

where T_1 and T_2 are the control torques, $J = 2A - C$ and $J_1 = 2a_1 - c_1$.

In other forms of pendulous north-seeking gyroscopes the pendulosity has usually been provided by a physical pendulum built into the device, e.g., the mercury ballistic in the Sperry compass. For the Hooke's joint configuration however pendulosity is provided by the torquing coils by arranging

$$T_1 = 0$$

$$T_2 = -K\beta_2 \qquad (3)$$

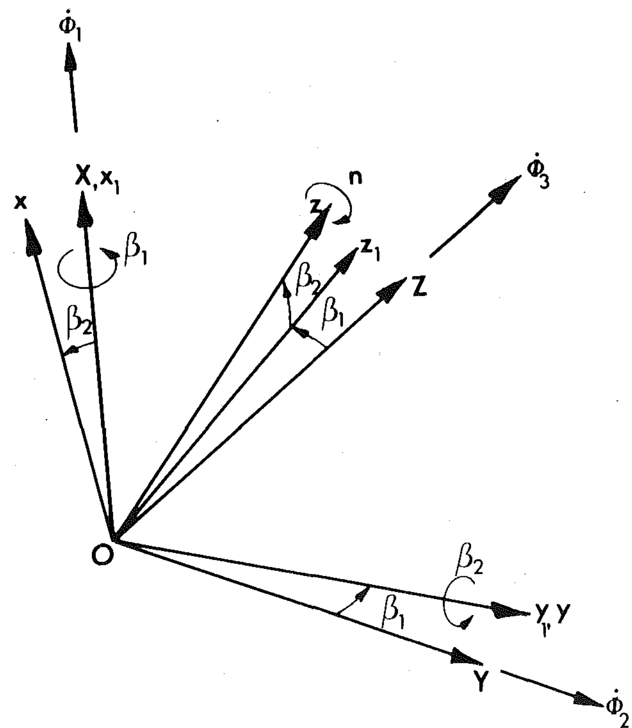

Fig. 3 Rotor axes

Ideal North-Seeking Gyroscope

For the Hooke's joint gyroscope to act as a north-seeking device it is first necessary to eliminate the spring and inertia torques transmitted to the rotor by the suspension. This condition may be achieved if the gyroscope is operated at its tuning speed [1]. From the equations of motion (2) the tuning condition is readily identified and can be seen to be given by

$$2k - n^2 J_1 = 0 \tag{4}$$

If equations (1), (3), and (4) are now substituted into (2) the performance of the gyro as a compass can be assessed. We now assume $Cn \gg J\Omega$, $K \gg Cn\Omega$, and $A, C \gg a_1, c_1$. These conditions can readily be realized in practice and allow equation (2) to be written to a good approximation as

$$\begin{aligned} A\ddot{\beta}_1 + Cn\dot{\beta}_2 + Cn\Omega \cos\lambda \cos\eta \beta_1 &= -Cn\Omega \cos\lambda \sin\eta \\ A\ddot{\beta}_2 - Cn\dot{\beta}_1 + K\beta_2 &= Cn\Omega \sin\lambda \end{aligned} \tag{5}$$

from which

$$\begin{aligned} \beta_1 &\approx -\tan\eta + \sum_{j=1}^{2} \phi_j \sin(p_j t + \delta_j) \\ \beta_2 &\approx \frac{Cn\Omega \sin\lambda}{K} + \sum_{j=1}^{2} R_j \phi_j \cos(p_j t + \delta_j); \quad R_j = \frac{Cn\, p_j}{K - p_j^2 A} \end{aligned} \tag{6}$$

Where ϕ_j and δ_j are arbitrary constants and p_j are the natural frequencies of free vibration that have approximate values

$$p_1 \approx \sqrt{\frac{K\Omega \cos\lambda \cos\eta}{Cn}} \quad \text{and} \quad p_2 \approx \frac{Cn}{A} \tag{7}$$

The results presented in equations (5)–(7) bear a very close relationship to those derived for alternative compass configurations [3, 4], and show that the rotor motion is composed of a steady offset superimposed upon which is a slow compassing mode at frequency p_1 and a high frequency nutational mode at p_2.

Since the pendulosity $K \gg Cn\Omega$ it follows from (6) that the mean value of β_2 is small and that the steady rotor motion occurs chiefly in the horizontal plane. As a result of offsetting the drive axis, an amount η from the north, it is shown that the rotor moves away from its null position and tends to realign its spin axis with true north. Thus, provided the initial misalignment is small, $\tan\eta \approx \eta$, the rotor will provide an accurate indication of north. The alignment is maintained by the small pendulous torque $K\beta_2$, which is sufficient to precess the rotor about its vertical axis as the Earth rotates.

The shape of the low frequency "compassing" motion about this mean position is determined by the factor

$$R_1 \approx \sqrt{\frac{Cn\Omega \cos\lambda \cos\eta}{K}}.$$

Since $0 < R_1 \ll 1$ the tip of the rotor spin axis will be seen to trace out an elongated ellipse (major axis horizontal) in a direction opposite to rotor spin. Nutation is characterized by $R_2 \approx -1$ and causes the spin axis to move in a circular orbit in the same sense as rotor spin. This latter motion has very little influence on the workings of the instrument. It can only be initiated by an impulsive moment and in practice would be quickly damped out.

The instrument therefore essentially oscillates at the compassing frequency p_1 and in the absence of damping north would have to be determined by finding the mean values of successive turning points in β_1.

Damping. For one-off north finding applications, such as in surveying, the continuous oscillation of the rotor spin axis about north is not a limiting factor. However for navigational purposes the oscillation is unacceptable and it is necessary to introduce some form of damping. This may be achieved by introducing either damping at the gimbal pivots as described in [5], or by following a similar procedure to that adopted in the original Sperry compass; that is, the damping mechanism is provided by a small torque about OX proportional to the rotor tilt β_2, i.e., $T_1 = -K_d\beta_2$.

If we regard the slow compassing mode as dominant and neglect the terms $A\ddot{\beta}_1$ and $A\ddot{\beta}_2$ in (5) the equation describing the damped motion in azimuth may be shown to reduce to

$$\ddot{\beta}_1 + \frac{K_d}{Cn}\dot{\beta}_1 + p_1^2\beta_1 = -p_1^2\eta - \frac{K_d}{K} p_1^2 \tan\lambda \tag{8}$$

This equation represents a damped vibration

$$\beta_1 = \beta_0 e^{-\xi p_1 t} \sin(p_{1d} t + \delta_1) - \eta - \frac{K_d}{K} \tan\lambda \tag{9}$$

where $\xi = K_d/2Cnp_1$ is the damping factor and $p_{1d} = p_1\sqrt{1 - \xi^2}$ is the damped natural frequency. Once the transient has decayed (9) shows that the rotor adopts a steady offset.

$$\beta_1 \approx -\eta - \frac{K_d}{K} \tan\lambda \tag{10}$$

The introduction of the damping torque therefore introduces an error in indicated north which varies with latitude and is proportional to the ratio between the damping torque and the pendulous control torque. For example, if we consider the case of the critically damped instrument, i.e., $\xi = 1$, the magnitude of this error is

$$\beta_e \approx 2\sqrt{\frac{Cn\Omega}{K} \tan\lambda \sin\lambda}$$

and, since $Cn\Omega/K \ll 1$, can be seen to be small at all but extremely high latitudes. In practice however it is usual to calculate this error at each latitude and numerically compensate the compass reading.

Mistuning and Alternative Configuration

The foregoing shows that the *tuned* Hooke's joint gyroscope has the capacity to function as a gyrocompass provided the spin axis is reasonably aligned with true north. However before proceeding to develop the instrument further it is worthwhile to consider the limitations of the ideal system. In the practical instrument small amounts of mistuning, windage friction and mass unbalance will occur and these will tend to modify the response (10) of the compass. By applying the results presented in [5] to this problem it is straightforward to show that mistuning and gimbal windage can give rise to serious errors. To demonstrate this we shall consider the effects of mistuning. If mistuning is present such that $2k - n^2J_1 = \Delta K \neq 0$ the governing equation (8) can be rewritten

$$\ddot{\beta}_1 + \frac{K_d}{Cn}\dot{\beta}_1 + p_1^2(1 + \sigma)\beta_1 = -p_1^2\eta - \frac{K_d}{K} p_1^2 \tan\lambda \tag{11}$$

where $\sigma = \Delta K/Cn\Omega \cos\lambda$.

The steady response in azimuth corresponding to the rotation of the Earth is

$$\beta_1 \approx -\frac{1}{(1 + \sigma)}\left(\eta + \frac{K_d}{K} \tan\lambda\right) \tag{12}$$

which shows that the rotor offset from true north is dependent on the mistuning.

For accurate alignment it is necessary to insure $\sigma \ll 1$, and for a typical gyroscope with $\sigma = 0.01$ say, this would require the tuning speed to be set to within 10^{-7} percent. This requirement is well beyond the tuning requirements of the corresponding inertial instrument and cannot be achieved with the speed control systems available to date. Thus, at first sight, it would appear that the nonideal device will be incapable of operating as a north-seeking compass. Fortunately this is not the case and it will be shown how the nonideal instrument can be used to control the alignment of a north-seeking platform. The response of the combined system is similar to that of the ideal Hooke's joint instrument.

A North-Seeking Platform. It would be advantageous if the compass could be developed in such a way as to eliminate the mistuning type of error and to seek north irrespective of the magnitude of the initial offset. We shall show how this may be achieved by mounting the gyroscope on a servo-controlled platform.

Fig. 4 shows a Hooke's joint gyroscope of the type just described, mounted on a horizontal platform which is free to rotate in bearings about a vertical axis. It will be assumed that the vertical axis of the platform is not precisely aligned with the true vertical. This offset is shown in Fig. 5 and is derived from $OXYZ$ by small fixed rotations, ϵ about OY and δ about OZ'. The displacement α of the platform (and the rotor drive axis) about its vertical axis OX' represents its motion

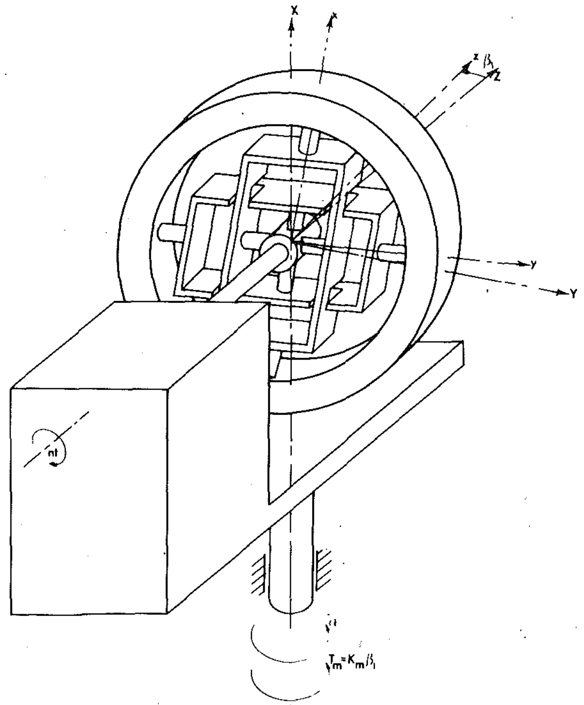

Fig. 4 Platform

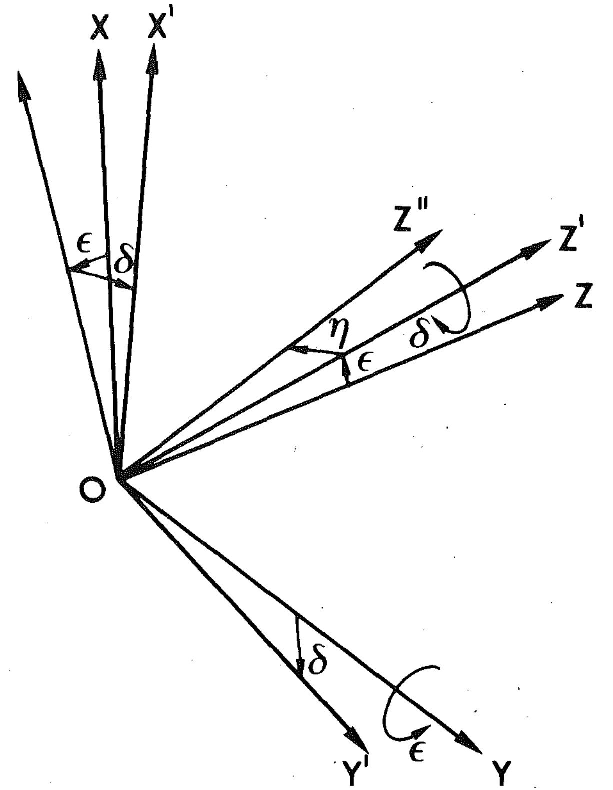

Fig. 5 Platform axes

with respect to the Earth and is measured from an arbitrary datum OZ'' displaced an amount η from OZ'. Clearly if $\epsilon = \delta = 0$ then η would represent the initial offset of the rotor spin axis from true north.

The angular velocities of the gyrocasing and platform are therefore

$$\dot{\Phi}_1 = \dot{\alpha} + \Omega \sin \lambda - \epsilon\Omega \cos \lambda$$

$$\dot{\Phi}_2 = (\Omega \cos \lambda + \epsilon\Omega \sin \lambda) \sin (\eta + \alpha) - \delta\Omega \sin \lambda \cos (\eta + \alpha)$$

$$\dot{\Phi}_3 = (\Omega \cos \lambda + \epsilon\Omega \sin \lambda) \cos (\eta + \alpha) + \delta\Omega \sin \lambda \sin (\eta + \alpha) \quad (13)$$

about OX', OY', and OZ', respectively.

A torque motor provides the drive and it is assumed that the motion of the platform is resisted by viscous friction μ.

Damping within the gyro arises because of windage and flexure hysteresis and will be assumed to be viscous. By following the analysis presented in [5] it has been shown that the damping torque applied to the rotor may be divided into components due to rotor windage and suspension windage and hysteresis and for the case of a gyro with identical gimbals phased at 90° takes the special form

$$T_{f1} = -(D + d)\dot{\beta}_1 - nd\beta_2$$

$$T_{f2} = -(D + d)\dot{\beta}_2 + nd\beta_1 \quad (14)$$

where D and d represent the damping coefficients associated with the rotor and the suspension, respectively.

Mass unbalance can clearly occur in both the rotor and the gimbals in a general way, however for the special application considered in this paper the results given in [6, 7] show that its significance can be assessed by considering only the axial component of rotor unbalance. If the center of mass of the rotor is offset from the center of the suspension by a small amount h then gravity will give rise to a rotor torque about OY' which is given by

$$T_b = -Mgh \quad (15)$$

where M is the mass of the rotor.

If torques (14) and (15) are now combined with the rotor control torques and the input rates (13) substituted into (2) the equations of motion of the rotor are written, for large rotor inertias and small angles as

$$A\ddot{\beta}_1 + (D + d)\dot{\beta}_1 + Cn\dot{\beta}_2 + [\Delta K + Cn\Omega \cos \lambda]\beta_1 + (K_d + nd)\beta_2 \approx -A\ddot{\alpha} - Cn\Omega \cos \lambda\,(\eta + \alpha) + \delta Cn\Omega \sin \lambda$$

$$A\ddot{\beta}_2 + (D + d)\dot{\beta}_2 - Cn\dot{\beta}_1 + K\beta_2 - nd\beta_1 \approx Cn(\Omega \sin \lambda + \dot{\alpha}) - \epsilon Cn\Omega \cos \lambda - Mgh. \quad (16)$$

A third equation is required before the dynamics of the total system is completely defined and this follows from consideration of the platform torques and the angular momentum of the platform and gyroscope assembly. If gimbal inertias are neglected the equation of motion of the combined system about OX' follows from Euler's equations and may be shown to be given by

$$(A + I)\ddot{\alpha} + A\ddot{\beta}_1 + Cn\dot{\beta}_2 + Cn\Omega \cos \lambda\beta_1 + Cn\Omega \cos \lambda(\eta + \alpha) \approx T_m - \mu\dot{\alpha} + \delta Cn\Omega \sin \lambda \quad (17)$$

To illustrate the essential north-seeking capacity of the system we have assumed that the initial offset, η, is small so that linear theory can apply. For large values of η the system can be shown to retain its north-seeking action.

We now arrange the motor torque T_m to act on the platform in such a way as to allow the platform to follow the motion of the spin axis in azimuth. This strategy will attempt to maintain the alignment between the drive axis and the rotor spin axis and is achieved by setting $T_m = K_m\beta_1$. It will be assumed that the motor gain parameter K_m is large and comparable with the pendulosity K, and therefore $K_m \gg \Delta K$, $Cn\Omega$. Also since the rotor operates in an evacuated environment and the pivots manufactured from low hysteresis material the damping will be small and we can further assume that $K, K_m \gg nd$. Furthermore since only the low frequency motion of the compass is significant it is legitimate to ignore the terms involving $\ddot{\beta}_1$, $\ddot{\beta}_2$ and $\ddot{\alpha}$ in much of the analysis. Thus equations (16) and (17) may be reduced correspondingly, from which it can be shown that the motion of the platform can be expressed in the form

$$\alpha \approx \alpha_0 e^{-K_m t/\mu} + \alpha_1 e^{-\xi p_1 t} \sin(p_{1d}t + \delta_1) - \eta - \frac{(Cn\Omega \sin\lambda - Mgh - \epsilon Cn\Omega \cos\lambda)(K_d + nd)(K_m - Cn\Omega\cos\lambda)}{Cn\Omega\cos\lambda[K(K_m + \Delta K) + nd(K_d + nd)]} + \delta \tan\lambda. \quad (18)$$

where the damping factor ξ is now given by $\xi = (K_d + nd)/2Cnp_1$.

Since it is likely that $K_m/\mu \gg \xi p_1$ equation (18) shows that the transient response of the platform is determined by the compassing mode of the ideal compass. We should note that the damping factor is increased by an amount proportional to the suspension damping and that rotor windage does not have a first-order effect on the decay of the vibration. In the steady state the platform approaches true north but is offset, as shown in (19) by amounts determined by the damping, the rotor unbalance and the vertical misalignment of the platform; i.e.,

$$\alpha_e \approx -\frac{(K_d + nd)}{K}\tan\lambda + \frac{gMh}{Cn\Omega\cos\lambda} \times \frac{(K_d + nd)}{K} + \frac{\epsilon(K_d + nd)}{K} + \delta\tan\lambda \quad (19)$$

The form of the damping error is virtually unaffected by the introduction of the platform and the restrictions described in the section, "Damping," would apply in this case. The error introduced by mistuning has been totally eliminated and, since $K_m \gg \Delta K$ allows for considerable mistuning, precise tuning of the gyro is not necessary. The error corresponding to axial mass unbalance is a function of latitude but is principally determined by the factor $Mgh/Cn\Omega$. By careful balancing this factor can be made very small, for example in the tuned gyro used for inertial navigation purposes it is possible [8] to achieve a level of balance which insures that $gMh/Cn\Omega < 0.01$. This result together with the fact that $(K_d + nd)/K \ll 1$ insures that the error due to axial mass unbalance will be small at all but extremely high latitudes. Similar reasoning shows that small vertical misalignments of the platform axis due to a rotation ϵ about the $E - W$ axis causes a small error in indicated north. However a significant error could be introduced as a result of a platform displacement δ about the $N - S$ axis. This error is directly proportional to δ and increases with latitude. In this situation careful alignment is necessary.

Conclusions

It has been shown that the basic Hooke's joint gyroscope can be made to perform as a north-seeking device provided the suspension is *precisely tuned* and if appropriate pendulous control torques are applied to the rotor. The response characteristics are similar to those exhibited by alternative designs of gyrocompass and the rotor is shown to align its spin axis along the direction of true north provided any initial offset is small.

However, the performance of the basic configuration is shown to be so sensitive to tuning errors that the required control over spin frequency would be beyond the capabilities of present day speed control systems.

A more practical design was then proposed, based on a Hooke's joint gyroscope mounted on a stabilized platform. The dynamical performance of this system has been evaluated, taking account of damping and mass unbalance in the gyro, and misalignment of the platform. By driving the platform about a vertical axis using control torques generated by the azimuth displacement of the gyrorotor it has been shown that the gyro driveshaft can be automatically aligned with north, irrespective of its initial offset. The platform therefore, after the decay of the compassing mode, provides a stabilized direction which indicates true north. The arrangement is shown to be insensitive to mistuning provided the platform gain $K_m \gg \Delta K$. Since this requirement is easily achieved the need for precision tuning to an order $\Delta K \ll Cn\Omega$ is not necessary. Errors associated with damping, mass unbalance, and misalignment of the platform axis from the vertical are identified and quantified. These errors, in general, will be small, with the exception of the error due to vertical axis misalignment which could be minimized by appropriate operating procedures.

Acknowledgments

The authors acknowledge with thanks the help of Prof. L. Maunder for reading and commenting on the manuscript. The authors also acknowledge the support of the Science Research Council.

References

1 Craig, R. J. G., "Theory of Operation of an Elastically Supported Tuned Gyroscope," *IEEE Trans. Aerospace and Electronic Systems,* Vol. AES, No. 3, May 1972.

2 Burdess, J. S., and Fox, C. H. J., "The Dynamics of a Multigimbal Hooke's Joint Gyroscope," *Journal of the Mechanical Engineering Science,* Vol. 20, No. 5, 1978, pp. 255–262.

3 Arnold, R. N., and Maunder, L., *Gyrodynamics and Its Engineering Application,* Academic Press, New York, 1962.

4 Fox, C. H. J., and Maunder, L., "The Dynamics of a Ligament Suspended North-Seeking Gyroscope," *Journal of the Mechanical Engineering Science,* Vol. 21, No. 2, 1979.

5 Burdess, J. S., and Fox, C. H. J., "The Dynamics of an Imperfect Hooke's Joint Gyroscope," *Journal of the Mechanical Engineering Science,* Vol. 20, No. 5, 1978, pp. 263–269.

6 Craig, R. J. G., "Theory of Errors of a Multigimbal, Elastically Supported Tuned Gyroscope," *IEEE Trans. Aerospace and Electronic Systems,* Vol. AES, No. 3, May 1972.

7 Burdess, J. S., and Maunder, L., "The Dynamics of a Hooke's Joint Gyroscope With Mass Unbalance," Conference on Vibrations in Rotating Machinery (Inst. of Mechanical Engineers), Churchill College, University of Cambridge, Sept. 1976.

8 AGARD—Lecture Series—LS-95. Strap-Down Inertial Systems.

E. H. Dowell
Professor,
Department of Mechanical
and Aerospace Engineering,
Princeton University,
Princeton, N. J. 08540
Mem. ASME

Component Mode Analysis of Nonlinear and Nonconservative Systems

Introduction

In a series of publications [1–21], the present author and others have exploited the power of Lagrange's equations and the use of Lagrange multipliers to study the dynamics of interconnected systems in terms of their several components. Studies to date have emphasized *linear, conservative* systems although Klein and Dowell [13] and Hallquist and Snyder [14] have shown how, from a knowledge of modal damping of individual components, one may calculate modal damping of the total system of interconnected components. Here the method is extended to *nonlinear and nonconservative* systems. No attempt is made to develop a general formal theory, but rather the method is used in rather specific contexts to suggest the potential of the method for dealing with nonlinear and nonconservative systems. The next logical step would be the development of such a theory, which would appear within reach based upon the present approach and results.

There is a very substantial literature on variational methods for nonlinear and/or nonconservative systems, e.g., see references [22–31]. However none of this literature addresses the question of component mode synthesis or even constraints (with or without Lagrange multipliers). Nevertheless the reader will find this literature of intrinsic interest as well as helpful in placing the present work in context.

Nonlinear Systems

As a concrete example, consider a beam connected to a spring-mass system (Fig. 1). The spring is taken as a nonlinear element.

The kinetic and potential energies are

$$T = \frac{1}{2}\sum_{i=1}^{I} M_i \dot{a}_i^2 + \frac{1}{2} M\dot{z}^2 \tag{1}$$

$$V = \frac{1}{2}\sum_{i=1}^{I} M_i \omega_i^2 a_i^2 + \frac{1}{2} M\omega_z^2 z^2 + \epsilon\frac{z^4}{4} \tag{2}$$

where z is the spring-mass deflection and w, the beam deflection, is expressed in modal form as

$$w(x,t) = \sum_i a_i(t)\phi_i(x) \tag{3}$$

Contributed by the Applied Mechanics Division for publication in the JOURNAL OF APPLIED MECHANICS.

Discussion on this paper should be addressed to the Editorial Department, ASME, United Engineering Center, 345 East 47th Street, New York, N. Y. 10017, and will be accepted until June 1, 1980. Readers who need more time to prepare a discussion should request an extension from the Editorial Department. Manuscript received by ASME Applied Mechanics Division, December, 1978; final revision, July, 1979.

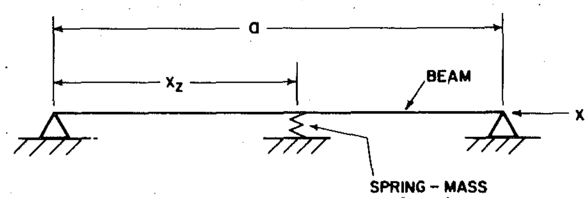

Fig. 1 A simple combined dynamical system

ω_i are the natural frequencies of the beam alone, ω_z the natural frequency of the spring mass alone, and ϵ the nonlinear stiffness coefficient. The constraint equation which states the beam and spring-mass are connected is

$$f \equiv \sum_i a_i\phi_i(x = x_z) - z = 0 \tag{4}$$

The Lagrangian is

$$L \equiv T - V + \beta f$$

where β is the Lagrange Multiplier.

Lagrange's equations provide

$$M_i[\ddot{a}_i + \omega_i^2 a_i] - \beta\phi_i(x = x_z) = 0 \tag{5}$$

$$M[\ddot{z} + \omega_z^2 z] + \epsilon z^3 + \beta = 0 \tag{6}$$

The method of harmonic balance [32] will be applied to equations (4)–(6). Assuming simple harmonic motion (only the fundamental harmonic is retained in this simplest version of the theory), let

$$z = \text{Real Part }\{\bar{z}e^{i\omega t}\}$$
$$a_i = \bar{a}_i e^{i\omega t}$$
$$\beta = \bar{\beta}e^{i\omega t} \tag{7}$$

Substitute (7) into (4)–(6) and

$$\int_0^{2\pi/\omega} [(4), (5), (6)]\cos\omega t\, dt = 0$$

The results are

$$\sum_i \bar{a}_i\phi_i(x_z) - \bar{z} = 0 \tag{8}$$

$$M_i[-\omega^2 + \omega_i{}^2]\bar{a}_i - \bar{\beta}\phi_i(x_z) = 0 \tag{9}$$

$$M[-\omega^2 + \omega_z{}^2]\bar{z} + \epsilon\bar{z}^3\frac{3}{4} + \bar{\beta} = 0 \tag{10}$$

Solve for β in terms of $\bar{z}$ from (10)

$$\bar{\beta} = -M[-\omega^2 + \omega_z{}^2]\bar{z} - \epsilon\bar{z}^3\frac{3}{4} \tag{11}$$

Using (9) and (11),

$$\bar{a}_i = \frac{\bar{\beta}\phi_i(x_z)}{M_i[-\omega^2 + \omega_i{}^2]} = \phi_i\left\{\frac{-M[-\omega^2 + \omega_z{}^2]\bar{z} - \epsilon\bar{z}^3\frac{3}{4}}{M_i[-\omega^2 + \omega_i{}^2]}\right\} \tag{12}$$

(12) in (8) gives

$$\left\{-M[-\omega^2 + \omega_z{}^2]\bar{z} - \epsilon\bar{z}^3\frac{3}{4}\right\}\left\{\sum_i \frac{\phi_i{}^2(x_z)}{M_i[-\omega^2 + \omega_i{}^2]}\right\} - \bar{z} = 0 \tag{13}$$ [1]

Define

$$\epsilon \equiv \frac{M\omega_z{}^2}{z_0{}^2}\alpha, \quad \tilde{z} \equiv \bar{z}/z_0, \quad \mu_i \equiv M_i/M$$

where α is nondimensional and z_0 is a scaling of the oscillation amplitude. Then (13) becomes

$$D \equiv \left\{-[-\omega^2 + \omega_z{}^2]\tilde{z} - \omega_z{}^2\tilde{z}^3\alpha\frac{3}{4}\right\} \times \left\{\sum_i \frac{\phi_i{}^2(x_z)}{\mu_i[-\omega^2 + \omega_i{}^2]}\right\} - \tilde{z} = 0 \tag{14}$$

To determine the natural frequencies from (14), the computational procedure is as follows:

Specify μ_i, ω_i, ω_z, α, and $\tilde{z}$. Plot D versus ω to find the nonlinear eigenvalues, ω, which make $D = 0$. Note that one may select $\alpha = 1$ without loss of generality for a hardening spring. For a softening spring one may choose $\alpha = -1$. Also it is convenient to scale all frequencies by the fundamental frequency of beam alone, ω_1. Finally, note that for $\tilde{z} \ll 1$, the known linear theory result is retrieved from (14) [20].

Numerical Examples. Consider a simply supported beam for which

$$\omega_i/\omega_1 = i^2$$

$$\phi_i(x_z) = \sin\frac{i\pi x_z}{a}$$

$$\mu_i = \frac{M_i}{M} = \frac{ma}{M}\int_0^a \phi_i{}^2\frac{dx}{a} = \frac{ma}{2M}; \quad \text{for all } i$$

In the numerical examples below, μ_i is set equal to unity.

In Fig. 2, the fundamental mode natural frequency of the total system is plotted versus the spring-mass oscillation amplitude for a ratio of spring-mass component natural frequency/beam component fundamental natural frequency, ω_z/ω_1, of 2 and various positions of the spring-mass, x_z/a. As can be seen the strongest effect of the spring-mass nonlinearity is when the spring-mass is placed at beam midspan. Of course, there is no effect when the spring-mass is placed at the end of the beam.

In Fig. 3, similar results are shown for several ω_z/ω_1 and one position of the spring-mass, $x_z/a = 0.5$. As expected the total system

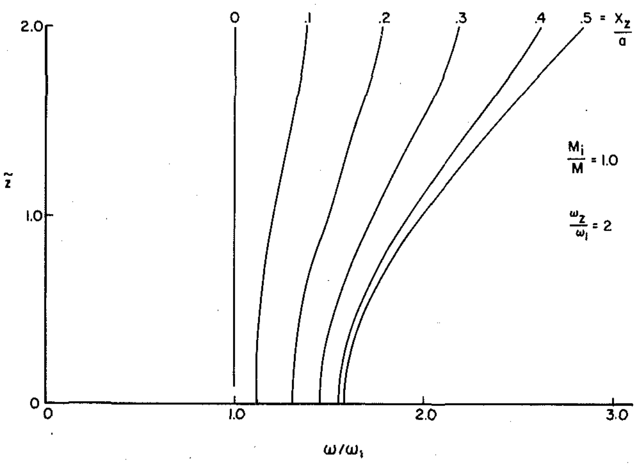

Fig. 2 **Fundamental frequency versus motion amplitude**

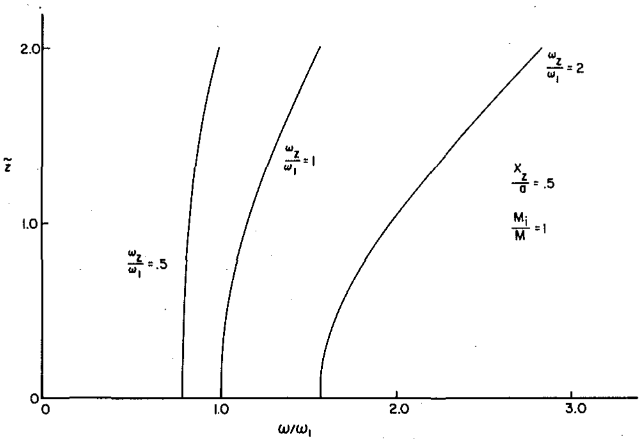

Fig. 3 **Fundamental frequency versus motion amplitude**

fundamental mode frequency is less than or greater than unity as ω_z/ω_1 is less than or greater than one for small oscillation amplitudes [20]. However, due to nonlinearities the total system frequency which is less than unity for small amplitudes may exceed unity for larger ones.

Discussion. The attentive reader will have noted that equations (13) and (14) include *all* of the beam modes. That is, the combined system of the beam plus spring-mass has an infinity of degrees of freedom. The power of the component mode synthesis procedure using the Lagrange multiplier technique as employed here (and previously [1, 11–13, 15–20] for linear, conservative systems) is that an infinite-degree-of-freedom system can be described by a much smaller number of equations. In the example treated above the nonlinear component is a single degree of freedom, i.e., the spring-mass. Hence it has been possible to reduce the infinite system of equations (8)–(10) to a single (nonlinear) equation, (13) or (14), while still retaining all of the (infinite) beam degrees of freedom. This can be generalized as follows. For a number, say N, single-degree-of-freedom *nonlinear* elements or for a *nonlinear* element of N degrees of freedom which is equivalent to N single-degree-of-freedom elements, a reduction to N nonlinear equations is possible. For a system with a *continuous, nonlinear* element with an *infinity* of degrees of freedom, such a reduction cannot occur. However, another idea has proven attractive as one way to resolve this dilemma. Often only the lower modes of a continuous, nonlinear element will exhibit significant nonlinear behavior. Of course one may use this to approximate such an element by a finite number of modes, say N. However in fact one can do better than this. All of the modes above N may be retained with nonlinear

[1] A result for arbitrary time-dependence (which does not *require* the harmonic balance method) may be obtained by solving (6) for β in terms of z and (5) for a_i in terms of β. Substituting the results into (4) gives a nonlinear integrodifferential equation for z. This equation *per se* is exact and may be attacked by standard methods including the method of harmonic balance. Using the latter on this integrodifferential equation and retaining only the lowest harmonic would produce (13).

terms in these modal coordinates neglected. Using component mode synthesis techniques the *linear* modal coordinates may be eliminated in terms of the *nonlinear* modal coordinates, and thus a reduction achieved.

A few words concerning the choice of the ϕ_i in equation (3) may be helpful. The natural modes of the unconstrained beam have been used. These have several advantages.

1 For a *linear* (but unfortunately not for a nonlinear) system, convergence is assured as the number of ϕ_i retained is increased. In practice numerical convergence studies will be desirable for any application even when a formal convergence theorem exists.

2 The orthogonality of the ϕ_i allows each of the beam modal coordinates, a_i, to be solved readily in terms of the Lagrange multiplier, β, and hence the nonlinear element modal coordinate, z; see equations (5) and (6). This is because these ϕ_i uncouple the a_i *per se* and the a_i are thus only coupled indirectly through their common dependence on β and subsequently z. This is a major computational advantage and is essential to the subsequent reduction of the infinite system of equations, (4)–(6) to a single equation (14). Because, fundamentally, the method is a Rayleigh-Ritz approach with constraint conditions, the ϕ_i only need be complete and satisfy geometric and not natural boundary conditions. However the use of natural, unconstrained modes is superior for the reasons just cited.

3 Once the reduction to a single equation in one unknown has been achieved, equation (14), the retention of any reasonable number of unconstrained beam modes, ϕ_i, is feasible. Very little computational cost is associated with retaining additional ϕ_i in the present method because additional ϕ_i only increase the number of terms in (14). In the present calculations ten ϕ_i were retained even though preliminary calculations suggested that half this number would provide results indistinguishable from those shown in Figs. 2 and 3.

4 The present method, using the suggested ϕ_i, has reproduced known solutions for linear problems where independent, exact results are available; for example, see references [1 and 11]. Unfortunately nonlinear examples solved by other methods have not been found which provide a true test of the present method. Clearly the finite-element method, for example, could provide such an independent check. Of course, as discussed in reference [12], the present method from a fundamental point of view may be said to include the finite-element method (or vice versa, if one prefers).

The aforementioned ideas can be embedded in a formal theory and this will be done in subsequent work. However the essence of the matter is as described here.

Nonconservative Systems

For definiteness, consider the physical problem of an elastic plate embedded in an otherwise rigid surface; see Fig. 4. Over the top of the plate there is a uniform, high supersonic fluid flow. The equation of motion is [33]

$$D\frac{\partial^4 w}{\partial x^4} + m\frac{\partial^2 w}{\partial t^2} + \rho\frac{U^2}{M}\left[\frac{\partial w}{\partial x} + \frac{1}{U}\frac{\partial w}{\partial t}\right] = 0 \tag{15}$$

where w is the plate deflection, x is the spatial coordinate, t is time, D is the plate stiffness, m is the plate mass/length, ρ is the flow density, U is the flow velocity, and M is the Mach number. Assuming an eigensolution of the form

$$w = \phi_i(x)e^{i\omega_i t} \tag{16}$$

(15) becomes in nondimensional form

$$\phi_i'''' + \lambda\phi_i' + k_i\phi_i = 0 \tag{17}$$

where

$$\lambda \equiv \rho U^2 a^3/MD, \quad ' \equiv \frac{d}{dx/a}$$

and the eigenvalue is

$$k_i \equiv -\frac{m\omega_i^2 a^4}{D} + i\left(\frac{m\omega_i^2 a^4}{D}\right)^{1/2}(\mu/\lambda M)^{1/2}$$

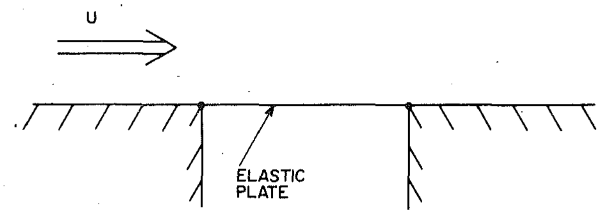

Fig. 4 Elastic plate and flow geometry

where

$$\mu \equiv \rho a/m$$

and a is the plate length.

The adjoint to equation (17) is

$$\phi_i^{*''''} - \lambda\phi_i^{*'} + k_i\phi_i^* = 0 \tag{18}$$

and satisfies the same boundary conditions. Equations (17) and (18) have common eigenvalues, k_i, but different eigenfunctions, ϕ_i and ϕ_i^*, which nevertheless satisfy an orthogonality relationship of the form

$$\int_0^a \phi_i^*\phi_j dx = 0 \quad \text{for} \quad i \neq j \tag{19}$$

Consider now, for example, a constraint of zero displacement such that

$$w(x_z, t) = 0 \tag{20}$$

From (20) and an expansion of w in terms of eigenmodes,

$$w(t, x_z) = \sum_{i=1}^{I} q_i\phi_i(x_z) = 0 \tag{21}$$

and

$$w(t, x_z) = \sum_{i=1}^{I} q_i^*\phi_i^*(x_z) = 0 \tag{22}$$

Now let us invoke Hamilton's principle, including the constraint relation and variation of w expressed in terms of adjoint eigenmodes. First, Hamilton's principle reads

$$\int_{t_1}^{t_2} [(\delta T - \delta V) + \delta W]dt = 0 \tag{23}$$

where

$$T \equiv \frac{1}{2}\int_0^a m\left(\frac{\partial w}{\partial t}\right)^2 dx$$

$$V \equiv \frac{1}{2}\int_0^a D\left(\frac{\partial^2 w}{\partial x^2}\right)^2 dx$$

$$\delta W \equiv -\int p\delta w \, dx \tag{24}$$

and the aerodynamic pressure loading, p, is given by

$$p \equiv \frac{\rho U^2}{M}\left[\frac{\partial w}{\partial x} + \frac{1}{U}\frac{\partial w}{\partial t}\right] \tag{25}$$

The Euler-Lagrange equation obtained from the foregoing is, of course, equation (15). The natural boundary conditions also are obtained from Hamilton's principle in the usual way.

Now add to Hamilton's principle the constraint relation

$$\int_{t_1}^{t_2} [(\delta T - \delta V) + \delta W + \beta\delta w(x_z, t)]dt = 0 \tag{26}$$

Inserting (24) and (25) into (26) and also using

$$w = \sum_i q_i\phi_i \tag{27}$$

and

$$\delta w = \sum_i \delta q_i{}^* \phi_i{}^* \quad (28)$$

one obtains after integrations by parts, invoking the geometric and natural boundary conditions, assuming simple harmonic motion, and nondimensionalizing, the following equation

$$\int_0^a \left\{ \sum_i q_i [\phi_i'''' + \lambda \phi_i' + k\phi_i] \right\} \left(\sum_j \delta q_j{}^* \phi_j{}^* \right) dx + \beta \sum_j \delta q_j{}^* \phi_j{}^*(x_z) = 0 \quad (29)$$

where k is as k_i with ω_i replaced by ω.

Equation (29) may be simplified using equation (17) to

$$\sum_i \sum_j (-k_i + k) \left[\int_0^a \phi_i \phi_j{}^* dx \right] q_i \delta q_j{}^* + \beta \sum_j \phi_j{}^*(x_z) \delta q_j{}^* = 0 \quad (30)$$

Employing the usual arguments [34] about independence of $I - 1$ of the $q_j{}^*$ and employing the freedom to choose the Lagrange multiplier, β, *each* coefficient of each $\delta q_i{}^*$ can be equated to zero. Thus

$$\sum_{i=1}^{I} q_i(-k_i + k) \int_0^a \phi_i \phi_j{}^* dx + \beta \phi_j{}^*(x_z) = 0 \quad (31)$$

for each $j = 1, \ldots, I$.

However, invoking orthogonality as given by equation (19), equation (31) may be simplified to

$$q_j(-k_j + k)M_j + \beta \phi_j{}^*(x_z) = 0 \quad (32)$$

for each $j = 1, \ldots, I$ where

$$M_i \equiv \int_0^a \phi_i \phi_i{}^* dx$$

Equation (32) combined with equation (21) gives $I + 1$ equations for $I + 1$ unknowns, $q_1, q_2, \ldots, q_I$, and β.

Solving (32) for q_i in terms of β and substituting the result into (21), gives

$$\beta \sum_{I=1}^{I} \frac{\phi_i{}^*(x_z)\phi_i(x_z)}{M_i[k_i - k]} = 0 \quad (33)$$

For nontrivial solutions, $\beta \neq 0$, we require that

$$\sum_{i=1}^{I} \frac{\phi_i{}^*(x_z)\phi_i(x_z)}{M_i[k_i - k]} = 0 \quad (34)$$

For the present case, the eigenmodes are complex conjugate and thus (34) has some further simplifying properties, but these are not pursued here. Rather it is emphasized that the final result holds for any eigenvalue problem governed by a linear differential and/or integral operator. With respect to the latter, the discussion of Courant and Hilbert [35], Vol. 2, pp. 234–237, is helpful background reading. The more recent literature of Leipholz and others [22–31] is most relevant here. The result of (34) is formally analogous to that obtained for self-adjoint systems [20], except, of course, both the eigenmode and its adjoint appear in (34). Also here the k_i are, in general, complex numbers and the M_i need not be positive real numbers.

Whether (34) will be of practical computational value, as is its self-adjoint counterpart, remains to be seen. Its primary value may be conceptual rather than computational. That is, it demonstrates that the method of component mode synthesis is not limited to conservative, self-adjoint systems, but may be extended to nonconservative, nonself-adjoint systems as well. Implicitly in the foregoing the completeness of the ϕ_i and $\phi_i{}^*$ has been assumed as has the convergence of the method. These matters deserve attention, but in practice the choice of ϕ_i as natural modes of the unconstrained system is the obvious one and a numerical study of convergence will always be desirable even if there is a formal mathematical assurance of (eventual) convergence.

Concluding Remarks

The extension of the present analysis for nonlinear systems to consider multiple nonlinear elements is straightforward. However, the numerical computation will then involve the determination of the eigenvalues from several simultaneous nonlinear algebraic equations. It also would clearly be of interest to consider higher harmonics in the motion even for a system with a single nonlinear element.

For nonconservative, but linear systems, the central question is whether there is some computational advantage to the present formulation. If there should prove to be such, then it would be of interest to consider systems which are both nonlinear and nonconservative.

Acknowledgments

The author would like to thank Prof. L. Meirovitch who suggested the consideration of nonself-adjoint (nonconservative) systems.

References

1 Dowell, E. H., "Free Vibrations of an Arbitrary Structure in Terms of Component Modes," ASME JOURNAL OF APPLIED MECHANICS, Vol. 39, 1972, pp. 727–732.

2 Saczalski, K. J., and Huang, T. C., "Coupled Response of Spatial Vibratory Structures Mounted to Isotropic Plate Elements," ASME *Journal of Engineering for Industry,* Vol. 94, 1972, pp. 15–22.

3 Yang, W. H., "Vibrations of a Plate With Internal Constraints," ASME JOURNAL OF APPLIED MECHANICS, Vol. 41, 1974, pp. 1072–1074.

4 Danĕk, O., "Application de la resolvante de Green dans les problémes dynamiques," *Roum. Sci. Techn.-Mech. Appl.,* Bucharest, Vol. 16, 1971, pp. 499–506.

5 Bishop, R. E. D., and Johnson, D. C., *The Mechanics of Vibration,* Cambridge University Press, 1960.

6 Simpson, A., and Taborrok, B., "On Kron's Eigenvalue Procedure and Related Methods of Frequency Analysis," *Quarterly Journal of Mechanics and Applied Mathematics,* Vol. 21, 1968, pp. 1–39.

7 Simpson, A., "Eigenvalue and Vector Sensitivities in Kron's Method," *Journal of Sound Vibration,* Vol. 31, 1973, pp. 73–87.

8 Simpson, A., "Scanning Kron's Determinant," *Quarterly Journal of Mechanics and Applied Mathematics,* Vol. 27, 1974, pp. 27–43.

9 Jacquot, R. G., and Soedel, W., "Vibrations of Elastic Surface Systems Carrying Dynamic Elements," *Journal of the Acoustical Society of America,* Vol. 47, 1970, pp. 1354–1358.

10 Wittrick, W. H., and Williams, F. W., "A General Algorithm for Computing Natural Frequencies of Elastic Structures," *Quarterly Journal of Mechanics and Applied Mathematics,* Vol. 24, 1972, pp. 263–284.

11 Dowell, E. H., "Free Vibrations of a Linear Structure With Arbitrary Support Conditions," ASME JOURNAL OF APPLIED MECHANICS, Vol. 38, 1971, pp. 595–600.

12 Klein, L., "Transverse Vibrations of Nonuniform Beams," *Journal of Sound Vibrations,* Vol. 37, 1974, pp. 491–505.

13 Klein, L., and Dowell, E. H., "Analysis of Modal Damping by Component Modes Method Using Lagrange Multipliers," ASME JOURNAL OF APPLIED MECHANICS, Vol. 41, 1974, pp. 527–528.

14 Hallquist, J., and Snyder, V. W., "Linear Damped Vibrating Structures With Arbitrary Support Conditions," ASME JOURNAL OF APPLIED MECHANICS, Vol. 40, 1973, pp. 312–313.

15 Klein, L., "Vibrations of Constrained Plates by a Rayleigh-Ritz Method Using Lagrange Multipliers," *Quarterly Journal of Mechanics and Applied Mathematics,* Vol. 30, 1977, pp. 51–70.

16 Grief, R., and Chung, H., "Constrained Shell Vibrations," *AIAA Journal,* Vol. 11, 1973, pp. 1049–1051.

17 Grief, R., and Chung, H., "Vibrations of Constrained Cylindrical Shells," *AIAA Journal,* Vol. 13, 1975, pp. 1190–1198.

18 Grief, R., and Mittendorf, S. C., "Structural Vibrations and Fourier Series," *Journal of Sound Vibration,* Vol. 48, 1976, pp. 113–122.

19 Mittendorf, S. C., and Grief, R., "Vibrations of Segmented Beams by a Fourier Series Component Mode Method," *Journal of Sound Vibration,* Vol. 55, 1977, pp. 431–441.

20 Dowell, E. H., "On Some General Properties of Combined Dynamical Systems," ASME JOURNAL OF APPLIED MECHANICS, Vol. 46, 1979, pp. 206–209.

21 Weissenburger, J. T., "Effect of Local Modifications on the Vibration Characteristics of Linear Systems," ASME JOURNAL OF APPLIED MECHANICS, Vol. 35, 1968, pp. 327–341.

22 Levinson, M., "Application of the Galerkin and Ritz Methods to Nonconservative Problems of Elastic Stability," *ZAMP,* Vol. 17, 1966, pp. 431–442.

23 Leipholz, H., *Stability Theory,* Academic Press, New York, N. Y., 1970, QA 871.L47313.

24 Leipholz, H., "On the Application of the Energy Method to the Stability Problems of Nonconservative Systems, Development in Theoretical and Applied Mechanics," *Proceedings of the Ninth Sectrm,* Nashville, 1978, pp. 427–437, 8230.309.

25 Prasad, S. N., and Herrmann, G., "The Usefulness of Adjoint Systems,

etc.," *International Journal of Solids and Structures,* Vol. 5, 1969, pp. 727–735.

26 Leipholz, H., "On the Generalization of Hamilton's Principle for Linear Nonconservative Problems," *Ingenieur-Archiv,* Vol. 40, 1971, pp. 55–67, in German.

27 Leipholz, H., "On a Stability Theory of Nonselfadjoint Mechanical Systems," *Acta Mechanica,* Vol. 14, 1972, pp. 283–295.

28 Leipholz, H., "On a Hybrid Type of Galerkin's equations," *Proceedings of the International Conference on Variational Methods in Engineering,* Sept. 1972, Southampton University, England, Section 6, pp. 17–27, TA 347.C3V37.

29 Leipholz, H., "On the Calculation of Buckling Loads by Means of Hybrid Ritz Equations," *Archives of Mechanics,* Vol. 25, 1973, pp. 895–901.

30 Leipholz, H., "On Conservative Systems of the First and Second Kind," *Ingenieur-Archiv,* Vol. 43, 1974, pp. 255–266.

31 Leipholz, H., *Direct Variational Methods and Eigenvalue Problems in Engineering,* Noordhoff Int. Publ., Leyden, 1977; see specifically Chapter 5 (The Method of Adjoint Systems).

32 Bolotin, V. V., *Nonconservative Problems of the Elastic Theory of Stability,* Pergamon Press, 1963.

33 Dowell, E. H., *Aeroelasticity of Plates and Shells,* Noordhoff International Publishing, 1975.

34 Goldstein, H., *Classical Mechanics,* Addison-Wesley Publishing Company, Inc., 1950.

35 Courant, R., and Hilbert, D., *Methods of Mathematical Physics,* Interscience Publishers, 1962.

P. C. Hughes[1]

Visiting Professor,
School of Aeronautics and Astronautics,
Purdue University,
West Lafayette, Ind. 47907

Modal Identities for Elastic Bodies, With Application to Vehicle Dynamics and Control

It is a standard procedure to analyze a flexible vehicle in terms of its vibration frequencies and mode shapes. However, the entire mode shape is not needed per se, but two integrals of the mode shape, p_i and h_i, which correspond to the momentum and angular momentum in Mode i. Together with the natural frequencies ω_i, these modal parameters satisfy several important identities, 25 of which are derived in this paper. Expansions in terms of both "constrained" and "unconstrained" modes are considered. A simple illustrative example is included. The paper concludes with some remarks on the theoretical and practical utility of these results, and several potential extensions to the theory are suggested.

1 Introduction

It is well known that great strides have been made in the last two decades in structural dynamics calculations. This increase in sophistication has made possible the accurate modeling of structures whose distributions of inertia and stiffness are quite general. Of the many applications for this capability, the one of principal interest in this paper is the dynamics and control of flexible vehicles. As a class, vehicles have a number of characteristics that distinguish them from more conventional ground-based structures, the most obvious one being the existence of "rigid-body" modes. Rigid-body modes (or "rigid" modes, for short) consist of uniform translation, or rotation, of all, or part, of the vehicle. The generalized stiffness associated with these modes is zero because no elastic deformation occurs. A rigid mode therefore has a "natural frequency" equal to zero.

Virtually all vehicles are intended to be as rigid as possible, and only cost and weight considerations dictate some degree of structural flexibility. Therefore the rigid modes can be identified with the normal, desirable functioning of the vehicle, and excitation of the elastic modes (modes of vibration) represents an undesirable disturbing effect. In practice, these effects can range from quite negligible oscillations superimposed on normal (rigid) motion, to catastrophic instability. Many of the most interesting examples occur with spacecraft [1], whose diversity of configurations and typically lightweight structures have led to major advances in the dynamics and control of flexible vehicles [2, 3]. In parallel, and apparently independently, the dynamics of deformable aircraft has continued to develop [4], with the prediction and control of aeroelastic phenomena as the main goals. Elastic deformations of ships—both surface vessels and submarines—can also be important under certain circumstances.

In all cases, the dynamical interest centers on the interaction between the translational and rotational motions of the vehicle (rigid modes) and the structural dynamics (elastic modes). In general, some of the energy, momentum, and angular momentum of the system will reside in the deformational degrees of freedom. This suggests the definition of a modal momentum coefficient p_i which, when multiplied by $\dot{q}_i(t)$ (where q_i is the generalized coordinate associated with the ith elastic mode), produces the momentum contributed by the ith mode: $p_i\dot{q}_i(t)$. The modal parameter p_i can be calculated once the ith mode shape is known. A flexible-vehicle dynamicist therefore requires, in addition to the natural frequencies $\{\omega_i\}$, appropriate modal momentum coefficients $\{p_i\}$. This paper is concerned with identifying these modal momentum coefficients, showing how they arise quite naturally in the dynamics of flexible bodies, and, most importantly, with establishing many identities among the modal parameters, including the $\{p_i\}$.

Two general approaches will be employed. In one, the elastic deformations are expanded in terms of the natural modes of individual elastic parts of the vehicles. These are termed constrained modes [5] because the point of attachment to the remainder of the vehicle is constrained not to move during the calculation of these modes. In the literature on flexible spacecraft dynamics, constrained modes are the most frequently used. The other modal expansion, in terms of unconstrained modes [5], is directly in terms of the natural modes for the vehicle as a whole. This is the normal practice in the analysis of flexible aircraft [4]. Many of the identities derived below relate unconstrained modal parameters to constrained modal parameters.

[1] Professor, Institute for Aerospace Studies, University of Toronto, Toronto, Ontario, Canada M3H 576.

Contributed by the Applied Mechanics Division and presented at the Winter Annual Meeting, New York, N. Y. December 2–7, 1979, of THE AMERICAN SOCIETY OF MECHANICAL ENGINEERS.

Discussion on this paper should be addressed to the Editorial Department, ASME, United Engineering Center, 345 East 47th Street, New York, N. Y. 10017, and will be accepted until June 1, 1980. Readers who need more time to prepare a discussion should request an extension from the Editorial Department. Manuscript received by ASME Applied Mechanics Division, March, 1979; final revision, May, 1979. Paper No. 79-WA/APM-34.

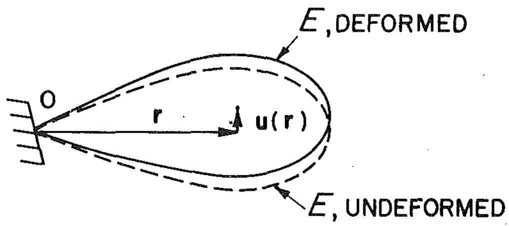

Fig. 1 A single cantilevered elastic body

To lend more prominence to the principle results of this paper, identities are labeled alphabetically as they are derived. Most of these occur in Sections 4, 6, and 7. Section 8 illustrates some of the identities with a simple numerical example, and Section 9 discusses several of their applications, both analytical and numerical.

2 Constrained Elastic Body, $\mathcal{E}$

Consider the elastic body $\mathcal{E}$ shown in Fig. 1. We will presently take $\mathcal{E}$ to be all, or part, of a flexible vehicle. It is fixed rigidly at point O so that neither translation nor rotation is possible at O. We assume that in response to a distributed static force/volume $\mathbf{f}(\mathbf{r})$, the structure experiences static deformations $\mathbf{u}(\mathbf{r})$. Thus a volume element of material found at $\mathbf{r}$ in the absence of any force is found at $\mathbf{r} + \mathbf{u}(\mathbf{r})$ when $\mathbf{f}(\mathbf{r})$ is applied. Under the assumptions of linear elasticity and small deformations, $\mathbf{f}(\mathbf{r})$ and $\mathbf{u}(\mathbf{r})$ are related by a linear *stiffness operator* $\mathcal{S}$ as follows:

$$\mathcal{S}[\mathbf{u}(\mathbf{r})] = \mathbf{f}(\mathbf{r}) \tag{1}$$

It is well known (see, for example, Meirovitch [6]) that $\mathcal{S}$ is, under present assumptions, a self-adjoint operator. Because $\mathcal{E}$ is constrained, $\mathcal{S}$ is also positive-definite. It therefore has an inverse operation $\mathcal{F} \triangleq \mathcal{S}^{-1}$, called the *flexibility operator,* which is also self-adjoint and positive-definite.

$\mathcal{S}$ is typically a differential operator, while $\mathcal{F}$ is an integral operator. We include the boundary conditions as part of the symbol $\mathcal{S}$. In fact, $\mathcal{F}$ can be represented as follows [6]:

$$\mathbf{u}(\mathbf{r}) = \mathcal{F}[\mathbf{f}(\mathbf{r})] = \int_{\mathcal{E}} \mathbf{F}(\mathbf{r}, \boldsymbol{\xi})\mathbf{f}(\boldsymbol{\xi})d\xi \tag{2}$$

where $\mathbf{F}$ is, in turn, symmetric and positive-definite. Thus

$$\int_{\mathcal{E}}\int_{\mathcal{E}} \mathbf{f}^T(\mathbf{r})\mathbf{F}(\mathbf{r}, \boldsymbol{\xi})\mathbf{f}(\boldsymbol{\xi})d\mathbf{r}d\xi > 0 \tag{3}$$

for all $\mathbf{f}(\mathbf{r})$ except $\mathbf{f} \equiv \mathbf{0}$, and

$$\mathbf{F}^T(\boldsymbol{\xi}, \mathbf{r}) \equiv \mathbf{F}(\mathbf{r}, \boldsymbol{\xi}) \tag{4}$$

The function $\mathbf{F}$ is called by many names, including *Green's function, induction function,* and *flexibility influence function.* We shall refer to it as the *flexibility kernel.*

It is noted for completeness that the strain energy stored in $\mathcal{E}$ is given by

$$V = \tfrac{1}{2} \int_{\mathcal{E}} \mathbf{u}^T\mathcal{S}[\mathbf{u}]d\mathbf{r} \tag{5}$$

which leads to the physical interpretation of self-adjointness and positive-definiteness.

3 Natural (Constrained) Modes of Vibration for $\mathcal{E}$

We turn now from statics to dynamics. The new information needed is the mass distribution, which is denoted by $\sigma(\mathbf{r})$, the volume mass density of $\mathbf{r}$. In accordance with the philosophy of d'Alembert, we write the total force at $\mathbf{r}$ as a superposition of the inertial "force" and real external forces, $\mathbf{f}_e$:

$$\mathbf{f}(\mathbf{r}, t) = -\sigma(\mathbf{r})\ddot{\mathbf{u}}(\mathbf{r}, t) + \mathbf{f}_e(\mathbf{r}, t) \tag{6}$$

Generalizing a standard development to three dimensions, the elastic body $\mathcal{E}$ has a motion that can be written as a superposition of natural modes of vibration. These constrained modes preclude translation and rotation at O. Thus

$$\mathbf{u}(\mathbf{r}, t) = \sum_{j=1}^{\infty} \mathbf{U}_j(\mathbf{r})Q_j(t) \tag{7}$$

where $\mathbf{U}_j(\mathbf{r})$ is the shape of the ith constrained vibration mode, and the modal coordinates Q_j satisfy

$$\ddot{Q}_j + \Omega_j{}^2Q_j = \Upsilon_j(t) \tag{8}$$

where $\{\Omega_j\}$ are the (constrained) natural frequencies, and $\{\Upsilon_j\}$ are the modal forces defined by

$$\Upsilon_j(t) \triangleq \int_{\mathcal{E}} \mathbf{U}_j{}^T(\mathbf{r})\mathbf{f}_e(\mathbf{r}, t)d\mathbf{r} \tag{9}$$

The constrained-mode eigenvalue problem is expressible in either the differential or the integral form:

$$\mathcal{S}[\mathbf{U}_j(\mathbf{r})] = \Omega_j{}^2\sigma(\mathbf{r})\mathbf{U}_j(r) \tag{10}$$

$$\mathbf{U}_j(\mathbf{r}) = \Omega_j{}^2 \int_{\mathcal{E}} \mathbf{F}(\mathbf{r}, \boldsymbol{\xi})\mathbf{U}_j(\boldsymbol{\xi})\sigma(\boldsymbol{\xi})d\boldsymbol{\xi} \tag{11}$$

and the corresponding orthonormality conditions are, in three dimensions,

$$\int_{\mathcal{E}} \mathbf{U}_i{}^T(\mathbf{r})\mathbf{U}_j(\mathbf{r})\sigma(\mathbf{r})d\mathbf{r} = \delta_{ij} \quad \text{(Kronecker } \delta) \tag{12}$$

$$\int_{\mathcal{E}} \mathbf{U}_i{}^T(\mathbf{r})\mathcal{S}[\mathbf{U}_j(\mathbf{r})]d\mathbf{r} = \Omega_i{}^2\delta_{ij} \tag{13}$$

The motion of $\mathcal{E}$ must be resisted by a reaction force $\mathbf{F}_R$ and torque $\mathbf{G}_R$ on $\mathcal{E}$ at O in order to maintain the constraint that there be no translation or rotation at O:

$$\mathbf{u}(\mathbf{0}, t) \equiv \mathbf{0}; \quad \tilde{\nabla}\mathbf{u}(0, t) \equiv \mathbf{0} \tag{14}$$

(The rotation at a point $\mathbf{r}$ in $\mathcal{E}$ is defined to be $1/2\tilde{\nabla}\mathbf{u}(\mathbf{r}, t)$, where $\tilde{(\cdot)}$ is the skew-symmetric 3×3 matrix associated with the vector cross product.) It follows that $\mathbf{F}(\mathbf{0}, \boldsymbol{\xi}) \equiv \mathbf{0}$ and $\tilde{\nabla}\mathbf{F}(\mathbf{0}, \boldsymbol{\xi}) \equiv \mathbf{0}$, and similarly for the modes: $\mathbf{U}_j(\mathbf{0}) = \mathbf{0}$, $\tilde{\nabla}\mathbf{U}_j(\mathbf{0}) = \mathbf{0}$. From (6), the reaction force and torque at O are

$$-\mathbf{F}_R(t) \triangleq \int_{\mathcal{E}} \mathbf{f}(\mathbf{r}, t)d\mathbf{r} = \mathbf{F} - \sum_{j=1}^{\infty} \mathbf{P}_j\ddot{Q}_j \tag{15}$$

$$-\mathbf{G}_R(t) \triangleq \int_{\mathcal{E}} \tilde{\mathbf{r}}\mathbf{f}(\mathbf{r}, t)d\mathbf{r} = \mathbf{G} - \sum_{j=1}^{\infty} \mathbf{H}_j\ddot{Q}_j \tag{16}$$

where

$$\mathbf{F}(t) \triangleq \int_{\mathcal{E}} \mathbf{f}_e(\mathbf{r}, t)d\mathbf{r}; \quad \mathbf{G}(t) \triangleq \int_{\mathcal{E}} \tilde{\mathbf{r}}\mathbf{f}_e(\mathbf{r}, t)d\mathbf{r} \tag{17}$$

$$\mathbf{P}_j \triangleq \int_{\mathcal{E}} \mathbf{U}_j(r)\sigma(\mathbf{r})d\mathbf{r}; \quad \mathbf{H}_j \triangleq \int_{\mathcal{E}} \tilde{\mathbf{r}}\mathbf{U}_j(r)\sigma(\mathbf{r})d\mathbf{r} \tag{18}$$

The constants $\{\mathbf{P}_j\}$ and $\{\mathbf{H}_j\}$ will be called, respectively, the *modal momentum coefficients* and the *modal angular-momentum coefficients.* This name is derived from the fact that the momentum and angular momentum of $\mathcal{E}$ are, respectively, $\Sigma\mathbf{P}_j\dot{Q}_j$ and $\Sigma\mathbf{H}_j\dot{Q}_j$.

The kinetic energy of the motion is

$$T = \tfrac{1}{2} \int_{\mathcal{E}} \mathbf{v}^T\mathbf{v}\sigma(\mathbf{r})d\mathbf{r} = \tfrac{1}{2} \sum_{j=1}^{\infty} \dot{Q}_j{}^2 \tag{19}$$

where $\mathbf{v}(\mathbf{r}, t) \triangleq \dot{\mathbf{u}}(\mathbf{r}, t)$, and the stored strained energy is, from (5),

$$V = \tfrac{1}{2} \sum_{j=1}^{\infty} \Omega_j{}^2Q_j{}^2 \tag{20}$$

where the orthonormality conditions (12) and (13) have been imposed.

4 Identities Involving Constrained Modal Parameters

Attention is now drawn to a series of identities involving the mode shapes $\{\mathbf{U}_j\}$, the frequencies $\{\Omega_j\}$, and the modal momentum coefficients, $\{\mathbf{P}_j\}$ and $\{\mathbf{H}_j\}$. The usefulness of these identities will be illustrated in Section 8. To cite the first identity, we note that the flexibility kernel can be expressed in terms of the mode shapes

$$\mathbf{F}(\mathbf{r}, \boldsymbol{\xi}) = \sum_{j=1}^{\infty} \frac{\mathbf{U}_j(\mathbf{r})\mathbf{U}_j^T(\boldsymbol{\xi})}{\Omega_j^2} \tag{A}$$

This is a generalization to three dimensions of a standard result [7].

Identities for $\{\Omega_j\}$. A second group of identities relate the natural frequencies $\{\Omega_j\}$ to the distributions of inertia and flexibility, $\sigma(\mathbf{r})$ and $\mathbf{F}(\mathbf{r}, \boldsymbol{\xi})$. The simplest member of this group is the following identity:

$$\sum_{j=1}^{\infty} \frac{1}{\Omega_j^2} = \text{trace} \int_{\mathcal{E}} \mathbf{F}(\mathbf{r}, \mathbf{r})\sigma(\mathbf{r})d\mathbf{r} \tag{B}$$

To prove this result, one has only to substitute (A) into (B), and invoke (12). It is furthermore true that

$$\sum_{j=1}^{\infty} \frac{1}{\Omega_j^4} = \text{trace} \int_{\mathcal{E}} \int_{\mathcal{E}} \mathbf{F}(\boldsymbol{\xi}, \mathbf{r})\mathbf{F}(\mathbf{r}, \boldsymbol{\xi})\sigma(\mathbf{r})\sigma(\boldsymbol{\xi})d\mathbf{r}d\boldsymbol{\xi} \tag{C}$$

To demonstrate this identity, it is necessary to substitute (A) into (C) and contract twice using (12). Further identities in this sequence can be developed, including $\Sigma\Omega_j^{-6}$, $\Sigma\Omega_j^{-8}$, and so on, but these become unattractive from a practical point of view owing to the multiple integrations required to evaluate the right side.

Identities for $\{\mathbf{P}_j\}$ and $\{\mathbf{H}_j\}$. Another family of identities involves only the modal momentum coefficients, $\{\mathbf{P}_j\}$ and $\{\mathbf{H}_j\}$:

$$\sum_{j=1}^{\infty} \mathbf{P}_j\mathbf{P}_j^T = m\mathbf{1} \tag{D}$$

$$\sum_{j=1}^{\infty} \mathbf{H}_j\mathbf{P}_j^T = \tilde{\mathbf{c}} \tag{E}$$

$$\sum_{j=1}^{\infty} \mathbf{H}_j\mathbf{H}_j^T = \mathbf{J} \tag{F}$$

where m, $\mathbf{c}$, and $\mathbf{J}$ are the zeroth, first, and second moments of inertia of $\mathcal{E}$ about O. In other words, m is the mass of $\mathcal{E}$, $\mathbf{c}/m$ is the position of the mass center of $\mathcal{E}$ with respect to O, and $\mathbf{J}$ is the moment-of-inertia matrix for $\mathcal{E}$ about O.

The proofs of (D)–(F) rest on Parseval's theorem and on the assumption that the mode shapes $\mathbf{U}_j$ satisfy the *completeness* property. According to a theorem quoted by Higgins [8], "a non-null symmetric L^2 kernel is positive-definite only if all its eigenvalues are positive and in addition the totality of eigenfunctions is complete in $L^2(a, b)$." This theorem (extended to three variables) affirms in effect that if the structure $\mathcal{E}$ has its eigenvalues $\{\Omega_j^2\}$ positive, and if $\mathbf{F}$ is positive-definite (as we have already assumed), then the eigenfunctions $\mathbf{U}_j(\mathbf{r})$ are complete. This paves the way for applying Parseval's theorem to prove (D)–(F). (For other relevant information on completeness of functions, see Mikhlin [9].) If $\mathbf{g}(\mathbf{r})$ is any 3×1 matrix function defined for $\mathbf{r} \in \mathcal{E}$ and satisfying $\int \mathbf{g}^T\mathbf{g}d\mathbf{r} < \infty$ then we define the Fourier coefficients of $\mathbf{g}$ with respect to the basis $\{\mathbf{U}_j\}$ by

$$a_j \triangleq \int_{\mathcal{E}} \mathbf{U}_j^T(r)\mathbf{g}(\mathbf{r})\sigma(\mathbf{r})d\mathbf{r} \tag{21}$$

Parseval's theorem, generalized to three independent variables, and to include the weighting function $\sigma(\mathbf{r}) > 0$, states that because of the completeness and orthonormality of the $\{\mathbf{U}_j\}$, it follows that

$$\sum_{j=1}^{\infty} a_j^2 = \int_{\mathcal{E}} \mathbf{g}^T\mathbf{g}\sigma(\mathbf{r})d\mathbf{r} \tag{22}$$

More generally (e.g., [8, p. 17]), if a_{1j} and a_{2j} are the Fourier coefficients of $\mathbf{g}_1(\mathbf{r})$ and $\mathbf{g}_2(\mathbf{r})$ with respect to $\{\mathbf{U}_j\}$,

$$\sum_{j=1}^{\infty} a_{1j}a_{2j} = \int_{\mathcal{E}} \mathbf{g}^T\mathbf{g}_2\sigma(\mathbf{r})d\mathbf{r} \tag{23}$$

These observations can be used to prove the identities (D)–(F). For, let

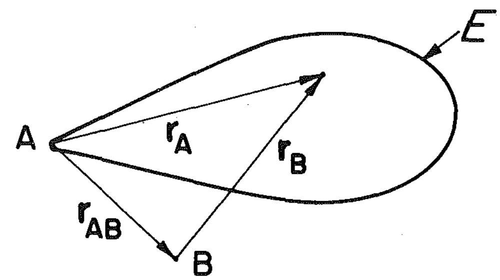

Fig. 2 Geometry of parallel-axis theorem for momentum coefficients

$$\mathbf{g}_1(\mathbf{r}) \equiv \begin{bmatrix} 1 \\ 0 \\ 0 \end{bmatrix}; \quad \mathbf{g}_2(\mathbf{r}) \equiv \begin{bmatrix} 0 \\ 1 \\ 0 \end{bmatrix}; \quad \mathbf{g}_3(\mathbf{r}) \equiv \begin{bmatrix} 0 \\ 0 \\ 1 \end{bmatrix} \tag{24}$$

Then

$$a_{1j} = \int_{\mathcal{E}} \mathbf{U}_j^T\mathbf{g}_1\sigma d\mathbf{r} = P_{1j}$$

that is, a_{1j} equals the first element in the 3×1 matrix $\mathbf{P}_j$. We conclude from (22) that

$$\sum_{j=1}^{\infty} P_{1j}^2 = \int_{\mathcal{E}} 1\sigma d\mathbf{r} = m \tag{25}$$

Similarly, it may be shown that $\Sigma P_{2j}^2 = \Sigma P_{3j}^2 = m$. Furthermore, using (23) it follows immediately that $\Sigma P_{1j}P_{2j} = \Sigma P_{2j}P_{3j} = \Sigma P_{3j}P_{1j} = 0$. These results are collected in the single matrix equation (D). The identities (E) and (F) are demonstrated in an analogous fashion.

In spite of their usefulness (see Section 9), these identities have not generally appeared in the literature. The equivalent of the identity for modal angular-momentum coefficients (F) was realized by Likins ([10, p. 69]); he arrived at it via a physical argument involving a limiting case. The same identity was mentioned in [5], where a different proof was used (equating coefficients of a certain null equation to zero). It is believed that the proof given in the foregoing is the most rigorous; it forces an explicit consideration of the assumptions under which the identity is valid. As for the other two identities, (D) and (E), they have not been reported before (as far as the author is aware).

Parallel-Axis Theorem for $\{\mathbf{P}_j\}$ and $\{\mathbf{H}_j\}$. A "parallel-axis theorem" for the momentum coefficients is now presented. As in Fig. 2, consider two reference points, namely, A and B. As shown, locations with respect to A and B are denoted $\mathbf{r}_A$ and $\mathbf{r}_B$, and

$$\mathbf{r}_A = \mathbf{r}_B + \mathbf{r}_{AB} \tag{26}$$

where $\mathbf{r}_{AB}$ is the (constant) location of B with respect to A. Also, $d\mathbf{r}_A = d\mathbf{r}_B \equiv d\mathbf{r}$. The first and second moments of inertia with respect to A and B are

$$\mathbf{c}_A \triangleq \int_{\mathcal{E}} \mathbf{r}_A\sigma d\mathbf{r}; \quad \mathbf{c}_B \triangleq \int_{\mathcal{E}} \mathbf{r}_B\sigma d\mathbf{r} \tag{27}$$

$$\mathbf{J}_A \triangleq -\int_{\mathcal{E}} \tilde{\mathbf{r}}_A\tilde{\mathbf{r}}_A\sigma d\mathbf{r}; \quad \mathbf{J}_B \triangleq -\int_{\mathcal{E}} \tilde{\mathbf{r}}_B\tilde{\mathbf{r}}_B\sigma d\mathbf{r} \tag{28}$$

The parallel-axis theorems for $\mathbf{c}$ and $\mathbf{J}$ are well known and easily demonstrated from the aforementioned definitions

$$\mathbf{c}_A = \mathbf{c}_B + m\mathbf{r}_{AB} \tag{29}$$

$$\mathbf{J}_A = \mathbf{J}_B - m\tilde{\mathbf{r}}_{AB}\tilde{\mathbf{r}}_{AB} - \tilde{\mathbf{c}}_B\tilde{\mathbf{r}}_{AB} - \tilde{\mathbf{r}}_{AB}\tilde{\mathbf{c}}_B \tag{30}$$

Of more novel interest are the momentum coefficients. The $\{\mathbf{P}_j\}$ are independent of the reference point, while, for the $\{\mathbf{H}_j\}$,

$$\mathbf{H}_{Aj} \triangleq \int_{\mathcal{E}} \tilde{\mathbf{r}}_A\mathbf{U}_j\sigma d\mathbf{r}; \quad \mathbf{H}_{Bj} \triangleq \int_{\mathcal{E}} \tilde{\mathbf{r}}_B\mathbf{U}_j\sigma d\mathbf{r} \tag{31}$$

which implies the result sought

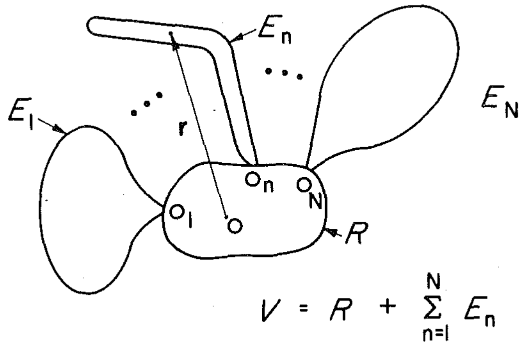

Fig. 3 Vehicle: one rigid body and N elastic bodies

$$\mathbf{H}_{Aj} = \mathbf{H}_{Bj} + \tilde{\mathbf{r}}_{AB}\mathbf{P}_j \qquad (G)$$

As a check, if one starts from the identities (D)–(F) with A as a reference point, and substitutes (G), then the parallel-axis theorems (29), (30) can be employed to show that the identities (D)–(F) also hold with B as a reference point. Identity (G) is particularly useful when adding a flexible body of known characteristics to a vehicle.

Identities for $\{\mathbf{P}_j\}$, $\{\mathbf{H}_j\}$, and $\{\Omega_j\}$ Together. To complete this section, a trio of identities is presented that involves both the natural frequencies $\{\Omega_j\}$ and the momentum coefficients $\{\mathbf{P}_j, \mathbf{H}_j\}$:

$$\sum_{j=1}^{\infty} \frac{\mathbf{P}_j\mathbf{P}_j{}^T}{\Omega_j{}^2} = \int_{\mathcal{E}}\int_{\mathcal{E}} \mathbf{F}(\mathbf{r}, \boldsymbol{\xi})\sigma(\mathbf{r})\sigma(\boldsymbol{\xi})d\mathbf{r}d\boldsymbol{\xi} \qquad (H)$$

$$\sum_{j=1}^{\infty} \frac{\mathbf{H}_j\mathbf{P}_j{}^T}{\Omega_j{}^2} = \int_{\mathcal{E}}\int_{\mathcal{E}} \tilde{\mathbf{r}}\mathbf{F}(\mathbf{r}, \boldsymbol{\xi})\sigma(\mathbf{r})\sigma(\boldsymbol{\xi})d\mathbf{r}d\boldsymbol{\xi} \qquad (I)$$

$$\sum_{j=1}^{\infty} \frac{\mathbf{H}_j\mathbf{H}_j{}^T}{\Omega_j{}^2} = -\int_{\mathcal{E}}\int_{\mathcal{E}} \tilde{\mathbf{r}}\mathbf{F}(\mathbf{r}, \boldsymbol{\xi})\tilde{\boldsymbol{\xi}}\sigma(\mathbf{r})\sigma(\boldsymbol{\xi})d\mathbf{r}d\boldsymbol{\xi} \qquad (J)$$

The proofs consist of inserting (A) for $\mathbf{F}(\mathbf{r}, \boldsymbol{\xi})$ on the right side, and using the definitions (18) for $\{\mathbf{P}_i, \mathbf{H}_i\}$.

5 Rigid Body With N Flexible Appendages

Consider now a vehicle consisting of a rigid body $\mathcal{R}$, to which are cantilevered N elastic bodies $\{\mathcal{E}_1, \ldots, \mathcal{E}_N\}$. This implies that at O_n, the attachment point of $\mathcal{E}_n$ to $\mathcal{R}$, there is neither translation nor rotation of $\mathcal{E}_n$ with respect to $\mathcal{R}$. Some flexible vehicles, especially spacecraft, are particular cases of the abstract model shown in Fig. 3. Other types of vehicle (aircraft, for example) may be more naturally modeled as a single large elastic body (Section 6).

No constraints are placed on the motion of $\mathcal{R}$, except that its translation and rotation be "small" to correspond to the small elastic deflections. Therefore, having picked a point of reference, O, in $\mathcal{R}$, the total displacement of a mass element in the vehicle is the sum of three terms: a translation $\mathbf{w}_0$, due to the translation of O; a rotation $\boldsymbol{\theta}$, due to the rotation of $\mathcal{R}$ about O; and an elastic displacement $\mathbf{u}$. In symbols,

$$\mathbf{w}(\mathbf{r}, t) = \mathbf{w}_0(t) - \tilde{\mathbf{r}}\boldsymbol{\theta} + \begin{cases} \mathbf{0}, & \mathbf{r} \in \mathcal{R} \\ \mathbf{u}(\mathbf{r}, t), & \mathbf{r} \in \Sigma\mathcal{E}_n \end{cases} \qquad (32)$$

The motion equations for the vehicle may be arrived at by observing that the momentum and angular momentum (the latter about O) are given by

$$\mathbf{p}(t) = \int_{\mathcal{V}} \mathbf{v}dm; \quad \mathbf{h}_0(t) = \int_{\mathcal{V}} \tilde{\mathbf{r}}\mathbf{v}dm \qquad (33)$$

where $\mathbf{v}(\mathbf{r}, t) \triangleq \dot{\mathbf{w}}(\mathbf{r}, t)$, $dm \triangleq \sigma(\mathbf{r})d\mathbf{r}$, and $\mathcal{V} = \mathcal{R} + \Sigma\mathcal{E}_n$ is the whole vehicle. The motion equations corresponding to $\mathbf{w}_0$ and $\boldsymbol{\theta}$ are then $\dot{\mathbf{p}} = \mathbf{F}$ and $\dot{\mathbf{h}}_0 = \mathbf{G}$ under the assumption of small $\dot{\mathbf{w}}_0$, $\boldsymbol{\theta}$ and $\mathbf{u}$, where $\mathbf{F}$ and $\mathbf{G}$ are the total external force and torque (about O) on $\mathcal{V}$. The motion equations corresponding to $\mathbf{u}(\mathbf{r}, t)$, $\mathbf{r} \in \mathcal{E}_n$, $(n = 1, \ldots, N)$, are all of the form (8), except for additional terms due to the extra inertial "force" field in (6):

$$\mathbf{f}(\mathbf{r}, t) = -\sigma(\mathbf{r})\ddot{\mathbf{w}}(\mathbf{r}, t) + \mathbf{f}_e(\mathbf{r}, t) \qquad (34)$$

and $\ddot{\mathbf{w}}(\mathbf{r}, t)$ is inferred from (32). Collecting the motion equations together, and recognizing that all second-order terms in $\dot{\mathbf{w}}_0$, $\boldsymbol{\theta}$ and $\mathbf{u}$ are to be dropped, we have

$$\left.\begin{aligned} m\ddot{\mathbf{w}}_0 - \tilde{\mathbf{c}}\ddot{\boldsymbol{\theta}} + \sum_{n=1}^{N}\sum_{j=1}^{\infty} \mathbf{P}_{jn}\ddot{Q}_{jn} &= \mathbf{F} \\ \tilde{\mathbf{c}}\ddot{\mathbf{w}}_0 + \mathbf{J}\ddot{\boldsymbol{\theta}} + \sum_{n=1}^{N}\sum_{j=1}^{\infty} \mathbf{H}_{jn}\ddot{Q}_{jn} &= \mathbf{G} \\ \mathbf{P}_{jn}{}^T\ddot{\mathbf{w}}_0 + \mathbf{H}_{jn}{}^T\ddot{\boldsymbol{\theta}} + (\ddot{Q}_{jn} + \Omega_{jn}{}^2Q_{jn}) &= \Upsilon_{jn} \\ (j = 1, \ldots, \infty; n = 1, \ldots, N) \end{aligned}\right\} \qquad (35)$$

where

$$\left.\begin{aligned} m &= m_r + \sum_{n=1}^{N} m_n \triangleq m_r + m_e \\ \mathbf{c} &= \mathbf{c}_r + \sum_{n=1}^{N} \mathbf{c}_n \triangleq \mathbf{c}_r + \mathbf{c}_e \\ \mathbf{J} &= \mathbf{J}_r + \sum_{n=1}^{N} \mathbf{J}_n \triangleq \mathbf{J}_r + \mathbf{J}_e \end{aligned}\right. \qquad (36)$$

The subscript "r" denotes "rigid body"; $\mathbf{c}_n$ and $\mathbf{J}_n$ are defined in (37). Note that (35) can be simplified slightly by choosing the reference point O to be the vehicle mass center, whence $\mathbf{c} = \mathbf{0}$. $\mathbf{P}_{in}$ is the modal momentum coefficient associated with the ith mode in the nth elastic appendage; similarly, the $\{\mathbf{H}_{in}\}$ are modal angular-momentum coefficients. However, in the case of the $\{\mathbf{H}_{in}\}$, note that the moment arm is with respect to O, not O_n, and the identities for $\mathbf{H}_{in}$ reflect this fact. Thus, referring to (D)–(F),

$$\sum_{j=1}^{\infty} \mathbf{P}_{jn}\mathbf{P}_{jn}{}^T = m_n\mathbf{1}, \quad \sum_{j=1}^{\infty} \mathbf{H}_{jn}\mathbf{P}_{jn}{}^T = \tilde{\mathbf{c}}_n,$$

$$\sum_{j=1}^{\infty} \mathbf{H}_{jn}\mathbf{H}_{jn}{}^T = \mathbf{J}_n \qquad (D, E, F)'$$

where the first and second moments of inertia are evaluated with respect to O:

$$\mathbf{c}_n \triangleq \int_{\mathcal{E}_n} \mathbf{r}dm; \quad \mathbf{J}_n \triangleq -\int_{\mathcal{E}_n} \tilde{\mathbf{r}}\tilde{\mathbf{r}}dm = \int_{\mathcal{E}_n} (r^2\mathbf{1} - \mathbf{r}\mathbf{r}^T)dm \qquad (37)$$

This same point is noteworthy in connection with the identities (I) and (J).

Compact Form for Motion Equations. The motion equations (35) are now written in a more compact form with the aid of the definition

$$\mathbf{P}^{nT} \triangleq [\mathbf{P}_{1n}\mathbf{P}_{2n}\ldots]; \quad \mathbf{H}^{nT} \triangleq [\mathbf{H}_{1n}\mathbf{H}_{2n}\ldots] \qquad (38)$$

$$\mathbf{Q}^{nT} \triangleq [Q_{1n}Q_{2n}\ldots]; \quad \boldsymbol{\Omega}^n \triangleq \mathrm{diag}\,\{\Omega_{1n}, \Omega_{2n}, \ldots\} \qquad (39)$$

$$\boldsymbol{\Upsilon}^{nT} \triangleq [\Upsilon_{1n}\Upsilon_{2n}\ldots] \qquad (40)$$

(all for $n = 1, \ldots, N$). The next stage results from defining

$$\mathbf{P} \triangleq \begin{bmatrix} \mathbf{P}^1 \\ \vdots \\ \mathbf{P}^N \end{bmatrix}; \quad \mathbf{H} \triangleq \begin{bmatrix} \mathbf{H}^1 \\ \vdots \\ \mathbf{H}^N \end{bmatrix}; \quad \mathbf{u}_e \triangleq \begin{bmatrix} \boldsymbol{\Upsilon}^1 \\ \vdots \\ \boldsymbol{\Upsilon}^N \end{bmatrix}; \quad \mathbf{Q}(t) \triangleq \begin{bmatrix} \mathbf{Q}^1 \\ \vdots \\ \mathbf{Q}^N \end{bmatrix} \qquad (41)$$

$$\boldsymbol{\Omega} \triangleq \mathrm{diag}\,\{\boldsymbol{\Omega}^1, \ldots, \boldsymbol{\Omega}^N\} \qquad (42)$$

whereupon they become

$$\begin{aligned} m\ddot{\mathbf{w}}_0 - \tilde{\mathbf{c}}\ddot{\boldsymbol{\theta}} + \mathbf{P}^T\ddot{\mathbf{Q}} &= \mathbf{F} \\ \tilde{\mathbf{c}}\ddot{\mathbf{w}}_0 + \mathbf{J}\ddot{\boldsymbol{\theta}} + \mathbf{H}^T\ddot{\mathbf{Q}} &= \mathbf{G} \\ \mathbf{P}\ddot{\mathbf{w}}_0 + \mathbf{H}\ddot{\boldsymbol{\theta}} + \ddot{\mathbf{Q}} + \boldsymbol{\Omega}^2\mathbf{Q} &= \mathbf{u}_e \end{aligned} \qquad (43)$$

From the identities $(D, E, F)'$ it is learned that

$$\mathbf{P}^T\mathbf{P} = m_e\mathbf{1}; \quad \mathbf{H}^T\mathbf{P} = \tilde{\mathbf{c}}_e; \quad \mathbf{H}^T\mathbf{H} = \mathbf{J}_e \qquad (D, E, F)''$$

where m_e, $\mathbf{c}_e$, and $\mathbf{J}_e$ are the zeroth, first, and second moments of inertia of $\Sigma\mathcal{E}_n$ about O, and were defined in (36).

We can without loss of generality assume that the reference point O is selected to coincide with the mass center of the (undeformed) vehicle; we also denote the moment-of-inertia matrix with respect to the mass center by $\mathbf{I}$:

$$\mathbf{c} \rightarrow \mathbf{0}; \quad \mathbf{J} \rightarrow \mathbf{I} \tag{44}$$

To distinguish between the rigid and elastic terms in (43), we further define

$$\mathbf{M}_r \triangleq \begin{bmatrix} m\mathbf{1} & \mathbf{0} \\ \mathbf{0} & \mathbf{I} \end{bmatrix}; \quad \mathbf{M}_e \triangleq [\mathbf{P}\ \mathbf{H}]; \quad \mathbf{q}_r \triangleq \begin{bmatrix} \mathbf{w}_0 \\ \boldsymbol{\theta} \end{bmatrix}; \quad \mathbf{u}_r \triangleq \begin{bmatrix} \mathbf{F} \\ \mathbf{G} \end{bmatrix} \tag{45}$$

whereupon (43) becomes

$$\mathbf{M}\ddot{\mathbf{q}} + \mathbf{K}\mathbf{q} = \mathbf{u}(t) \tag{46}$$

where

$$\mathbf{M} \triangleq \begin{bmatrix} \mathbf{M}_r & \mathbf{M}_e{}^T \\ \mathbf{M}_e & \mathbf{1} \end{bmatrix}; \quad \mathbf{K} \triangleq \begin{bmatrix} \mathbf{O} & \mathbf{O} \\ \mathbf{O} & \boldsymbol{\Omega}^2 \end{bmatrix}; \quad \mathbf{q} \triangleq \begin{bmatrix} \mathbf{q}_r \\ \mathbf{Q} \end{bmatrix}; \quad \mathbf{u} \triangleq \begin{bmatrix} \mathbf{u}_r \\ \mathbf{u}_e \end{bmatrix} \tag{47}$$

The total kinetic and potential energies of the system are, respectively,

$$T = \frac{1}{2}\dot{\mathbf{q}}^T\mathbf{M}\dot{\mathbf{q}}; \quad V = \frac{1}{2}\mathbf{q}^T\mathbf{K}\mathbf{q} \tag{48, 49}$$

Note also that $\mathbf{M}$, the *system inertia matrix,* is symmetric and positive-definite ($\mathbf{M}^T = \mathbf{M} > 0$), and that $\mathbf{K}$, the *system stiffness matrix,* is symmetric and positive-semidefinite ($\mathbf{K}^T = \mathbf{K} \geq 0$).

6 Natural (Unconstrained) Modes of Vibration for $\mathcal{V}$

In the absence of external influences ($\mathbf{f}_e \equiv \mathbf{0}$), the motion of $\mathcal{V}$ consists of a superposition of natural modes of vibration. To emphasize that there are no constraints on this motion, we will refer to these modes as unconstrained modes. It is possible to derive these modes in several ways and by comparing the results of two or more derivations several identities can be established. In this section, the unconstrained modes are developed without reference to the constrained modes of earlier sections, that is, without reference to (43). We shall subsequently return to (43) in order to deduce certain identities.

Consider a (static) stiffness operator for $\mathcal{V}$ in the same spirit as the stiffness operator for $\mathcal{E}_n$, given by (1):

$$\mathcal{S}[\mathbf{w}(\mathbf{r})] = \mathbf{f}(\mathbf{r}) \quad \mathbf{r} \in \mathcal{V} \tag{50}$$

A solution to (50) does not generally exist because $\mathcal{S}$ is only positive-semidefinite due to the lack of constraints. Indeed, the following eigenfunctions correspond to zero eigenvalues for $\mathcal{S}$:

$$\mathbf{w}(\mathbf{r}) = \begin{bmatrix} 1 \\ 0 \\ 0 \end{bmatrix}, \quad \begin{bmatrix} 0 \\ 1 \\ 0 \end{bmatrix}, \quad \begin{bmatrix} 0 \\ 0 \\ 1 \end{bmatrix}, \quad \begin{bmatrix} 0 \\ -r_3 \\ r_2 \end{bmatrix}, \quad \begin{bmatrix} r_3 \\ 0 \\ -r_1 \end{bmatrix}, \quad \begin{bmatrix} -r_2 \\ r_1 \\ 0 \end{bmatrix} \tag{51}$$

These correspond to "rigid" translations and rotations of $\mathcal{V}$. Solutions for (50) exist only for right-hand sides $\mathbf{f}(\mathbf{r})$ that are orthogonal to the eigenfunctions (51). These restrictions may be summarized thus

$$\int_{\mathcal{V}} \mathbf{f}(\mathbf{r})d\mathbf{r} = \mathbf{0}; \quad \int_{\mathcal{V}} \tilde{\mathbf{r}}\mathbf{f}(\mathbf{r})d\mathbf{r} = \mathbf{0} \tag{52}$$

The evident physical interpretation is that the net force and torque on $\mathcal{V}$ must be zero. Furthermore, since $\mathbf{w}(\mathbf{r}) = \mathbf{w}_0 - \tilde{\mathbf{r}}\boldsymbol{\theta} + \mathbf{u}(\mathbf{r})$ (the last term present only on $\Sigma\mathcal{E}_n$), (50) becomes

$$\mathcal{S}_\Sigma[\mathbf{u}(\mathbf{r})] = \mathbf{f}(\mathbf{r}) \quad \mathbf{r} \in \sum\mathcal{E}_n \tag{53}$$

since we already know that $\mathbf{u}(\mathbf{r}) \equiv \mathbf{0}$ for $\mathbf{r} \in \mathcal{R}$. The subscript Σ on $\mathcal{S}$ is a reminder of the restriction $\mathbf{r} \in \Sigma\mathcal{E}_n$ in (53). In fact, under the conditions (52), the operator inverse to $\mathcal{S}_\Sigma$, $\mathcal{F}_\Sigma$, can be expressed in terms of the flexibility kernels for $\mathcal{E}_1, \ldots, \mathcal{E}_N$:

$$\mathbf{u}(r) = \mathcal{F}_\Sigma[\mathbf{f}(\mathbf{r})] = \sum_{n=1}^{N} \int_{\mathcal{E}_n} \mathbf{F}_n(\mathbf{r}, \boldsymbol{\xi})\mathbf{f}(\boldsymbol{\xi})d\boldsymbol{\xi} \tag{54}$$

which should be compared with (2).

Generalizing from statics to dynamics via d'Alembert's principle, and noting that

$$\mathbf{f}(\mathbf{r}, t) = -\sigma(\mathbf{r})\ddot{\mathbf{w}}(\mathbf{r}, t) + \mathbf{f}_e(\mathbf{r}, t) \tag{55}$$

(52) and (53) become

$$\int_{\mathcal{V}} \ddot{\mathbf{w}}dm = \mathbf{F}; \quad \int_{\mathcal{V}} \tilde{\mathbf{r}}\ddot{\mathbf{w}}dm = \mathbf{G} \tag{56}$$

$$\mathcal{S}_\Sigma[\mathbf{u}(\mathbf{r}, t)] = -\sigma(\mathbf{r})\ddot{\mathbf{w}}(\mathbf{r}, t) + \mathbf{f}_e(\mathbf{r}, t) \tag{57}$$

where, as before, $\mathbf{F}$ and $\mathbf{G}$ are the total external force and torque on $\mathcal{V}$.

The unconstrained modes for $\mathcal{V}$, namely,

$$\mathbf{w}_\alpha(\mathbf{r}) = \mathbf{w}_{0\alpha} - \tilde{\mathbf{r}}\boldsymbol{\theta}_\alpha + \begin{cases} \mathbf{0}, & \mathbf{r} \in \mathcal{R} \\ \mathbf{u}_\alpha(\mathbf{r}), & \mathbf{r} \in \sum\mathcal{E}_n \end{cases} \tag{58}$$

are found by setting $\mathbf{f}_e \equiv \mathbf{0}$. From (56) we learn that

$$\omega_\alpha{}^2(\mathbf{p}_\alpha + m\mathbf{w}_{0\alpha}) = \mathbf{0}; \quad \omega_\alpha{}^2(\mathbf{h}_\alpha + \mathbf{I}\boldsymbol{\theta}_\alpha) = \mathbf{0} \tag{59}$$

where

$$\mathbf{p}_\alpha \triangleq \sum_{n=1}^{N} \int_{\mathcal{E}_n} \mathbf{u}_\alpha dm; \quad \mathbf{h}_\alpha \triangleq \sum_{n=1}^{N} \int_{\mathcal{E}_n} \tilde{\mathbf{r}}\mathbf{u}_\alpha dm \tag{60}$$

while, from (57),

$$\mathcal{S}_\Sigma[\mathbf{u}_\alpha(\mathbf{r})] = \sigma(\mathbf{r})\omega^2{}_\alpha\mathbf{w}_\alpha(\mathbf{r}) \tag{61}$$

After dividing out the anticipated $\omega^2 = 0$ cases (corresponding to rigid modes), (59) states that the total momentum and angular momentum associated with the elastic modes are zero. Note that $\mathbf{p}_\alpha$ and $\mathbf{h}_\alpha$ are associated with the momentum and angular momentum of the αth mode due to elastic deformations in $\Sigma\mathcal{E}_n$. In numbering the ω_α, ω_1 will correspond to the first *elastic* mode of $\mathcal{V}$ (the rigid modes will not be numbered). The following orthonormality conditions can be demonstrated from (59)–(61):

$$\left.\begin{aligned} \int_{\mathcal{V}} \mathbf{w}_\alpha{}^T\mathbf{w}_\beta\sigma(\mathbf{r})d\mathbf{r} &= \delta_{\alpha\beta} \\ \sum_{n=1}^{N} \int_{\mathcal{E}_n} \mathbf{u}_\alpha{}^T\mathbf{w}_\beta\sigma(\mathbf{r})d\mathbf{r} &= \delta_{\alpha\beta} \\ \sum_{n=1}^{N} \int_{\mathcal{E}_n} \mathbf{u}_\alpha{}^T\mathcal{S}_\Sigma[\mathbf{u}_\beta]d\mathbf{r} &= \omega_\alpha{}^2\delta_{\alpha\beta} \\ \sum_{n=1}^{N} \int_{\mathcal{E}_n} \mathbf{u}_\alpha{}^T\mathbf{u}_\beta\sigma(\mathbf{r})d\mathbf{r} - \boldsymbol{\theta}_\alpha{}^T\mathbf{I}\boldsymbol{\theta}_\beta &= \delta_{\alpha\beta} \end{aligned}\right\} \tag{62}$$

It is instructive to compare (62) with the orthonormality conditions for constrained modes, (12) and (13).

We now give two identities that follow immediately. Since, from (54),

$$\mathbf{u}_\alpha(\mathbf{r}) = \omega_\alpha{}^2 \sum_{n=1}^{N} \int_{\mathcal{E}_n} \mathbf{F}_n(\mathbf{r}, \boldsymbol{\xi})\mathbf{w}_\alpha(\boldsymbol{\xi})\sigma(\boldsymbol{\xi})d\boldsymbol{\xi} \tag{63}$$

it can be demonstrated that

$$\mathbf{F}_n(\mathbf{r}, \boldsymbol{\xi}) = \sum_{\alpha=1}^{\infty} \frac{\mathbf{u}_\alpha(\mathbf{r})\mathbf{u}_\alpha{}^T(\boldsymbol{\xi})}{\omega_\alpha{}^2} \quad \mathbf{r} \in \mathcal{E}_n; \quad \boldsymbol{\xi} \in \mathcal{E}_n \tag{K}$$

which should be compared to (*A*). In like manner to (*B*), we also have

$$\text{trace} \sum_{n=1}^{N} \int_{\mathcal{E}_n} \mathbf{F}_n(\mathbf{r}, \mathbf{r})\sigma(\mathbf{r})d\mathbf{r} = \sum_{\alpha=1}^{\infty} \frac{1 + m\mathbf{w}_\alpha{}^T\mathbf{w}_{0\alpha} + \boldsymbol{\theta}_\alpha{}^T\mathbf{I}\boldsymbol{\theta}_\alpha}{\omega_\alpha{}^2} \tag{L}$$

To solve for the general motion ($\mathbf{f}_e \not\equiv 0$), let

$$\mathbf{w}(\mathbf{r}, t) = \mathbf{W}(t) - \tilde{\mathbf{r}}\boldsymbol{\Theta}(t) + \sum_{\alpha=1}^{\infty} \mathbf{w}_\alpha(\mathbf{r})\eta_\alpha(t) \tag{64}$$

where the translation $\mathbf{W}(t)$ and the rotation $\mathbf{\Theta}(t)$ are included to accommodate the rigid modes. Upon substitution of (63) into the motion equations (55) and (57) (remembering that O is the mass center of $\mathcal{V}$), and taking advantage of the orthonormality conditions (62), we find

$$m\ddot{\mathbf{W}} = \mathbf{F}; \quad \mathbf{I}\ddot{\mathbf{\Theta}} = \mathbf{G}$$

$$\mathbf{p}_\alpha{}^T\ddot{\mathbf{W}} + \mathbf{h}_\alpha{}^T\ddot{\mathbf{\Theta}} + \ddot{\eta}_\alpha + \omega_\alpha{}^2\eta_\alpha = f_\alpha(t) \quad (\alpha = 1, 2, \ldots) \tag{65}$$

where the (unconstrained) modal input is

$$f_\alpha(t) \triangleq \sum_{n=1}^{N} \int_{\mathcal{E}_n} \mathbf{u}_\alpha{}^T\mathbf{f}_e(\mathbf{r}, t)d\mathbf{r} \tag{66}$$

With generous use of the orthonormality conditions (62), the kinetic and potential energies of $\mathcal{V}$ reduce to the following relatively simple forms

$$T = \frac{1}{2}\int_{\mathcal{V}} \mathbf{v}^T\mathbf{v}dm = \frac{1}{2}m\dot{\mathbf{W}}^T\dot{\mathbf{W}} + \frac{1}{2}\dot{\mathbf{\Theta}}^T\mathbf{I}\dot{\mathbf{\Theta}} + \frac{1}{2}\sum_{\alpha=1}^{\infty}\dot{\eta}_\alpha{}^2 \tag{67}$$

$$V = \frac{1}{2}\sum_{n=1}^{N}\int_{\mathcal{E}_n} \mathbf{u}^T\mathcal{S}_\Sigma[\mathbf{u}]d\mathbf{r} = \frac{1}{2}\sum_{\alpha=1}^{\infty}\omega_\alpha{}^2\eta_\alpha{}^2 \tag{68}$$

It is worthwhile comparing these with (19), (20), and (49).

The motion equations (65) must be equivalent to the set (44), an equivalence which requires the observation that

$$\mathbf{w}_0 = \mathbf{W} + \sum_{\alpha=1}^{\infty}\mathbf{w}_{0\alpha}\eta_\alpha; \quad \boldsymbol{\theta} = \mathbf{\Theta} + \sum_{\alpha=1}^{\infty}\boldsymbol{\theta}_\alpha\eta_\alpha \tag{69}$$

It is through this equivalence that several identities can now be derived.

7 Identities Between Constrained and Unconstrained Modal Parameters

To facilitate a comparison of the two equivalent systems (43) and (65), Laplace transforms are beneficial. We are especially interested in the response of $\mathbf{w}_0$ and $\boldsymbol{\theta}$ to $\mathbf{f}_e$. To deal first with (43), Laplace transforms are taken (zero initial conditions will be assumed) forming a system of equations for $\overline{\mathbf{w}}_0$, $\overline{\boldsymbol{\theta}}$, $\overline{\mathbf{Q}}$. Laplace-transformed variables are designated by overbars and the Laplace variable is s. After substitution for $\overline{\mathbf{Q}}$, the result can be expressed in the form

$$\overline{\mathbf{M}}(s)s^2\overline{\mathbf{q}}_r = \overline{\mathbf{u}}_T(s) \tag{70}$$

where (the symbols of (45) are used)

$$\overline{\mathbf{M}}(s) \triangleq \mathbf{M}_r - s^2\mathbf{M}_e{}^T(s^2\mathbf{1} + \mathbf{\Omega}^2)^{-1}\mathbf{M}_e \tag{71}$$

$$\overline{\mathbf{u}}_T(s) \triangleq \overline{\mathbf{u}}_r(s) - s^2\mathbf{M}_e{}^T(s^2\mathbf{1} + \mathbf{\Omega}^2)^{-1}\overline{\mathbf{u}}_e(s) \tag{72}$$

More explicitly, the *system inertance*, $\overline{\mathbf{M}}(s)$, is given by

$$\overline{\mathbf{M}}(s) = \mathbf{M}_r - \sum_{n=1}^{N}\sum_{j=1}^{\infty}\frac{s^2\begin{bmatrix}\mathbf{P}_{jn}\\ \mathbf{H}_{jn}\end{bmatrix}\begin{bmatrix}\mathbf{P}_{jn}\\ \mathbf{H}_{jn}\end{bmatrix}^T}{s^2 + \Omega_{jn}{}^2} \tag{73}$$

and the total input (the right-hand side of (70)) is

$$\overline{\mathbf{u}}_T(s) = \overline{\mathbf{u}}_r(s) - \sum_{n=1}^{N}\sum_{j=1}^{\infty}\frac{s^2\begin{bmatrix}\mathbf{P}_{jn}\\ \mathbf{H}_{jn}\end{bmatrix}}{s^2 + \Omega_{jn}{}^2}\overline{\Upsilon}_{jn} \tag{74}$$

Note that even though we have arranged to have $\mathbf{c} = \mathbf{0}$, the translational and rotational motions are coupled via elastic vibrations, as represented by the products $\mathbf{P}_{jn}\mathbf{H}_{jn}{}^T$, which are not generally zero. Under certain symmetry conditions, however, their combined effect vanishes and the translational and rotational motions are uncoupled

$$\overline{\mathbf{m}}(s)s^2\overline{\mathbf{w}}_0 = \mathbf{u}_{Tw}(s); \quad \overline{\mathbf{i}}(s)s^2\overline{\boldsymbol{\theta}} = \mathbf{u}_{T\theta}(s) \tag{75}$$

where $\overline{\mathbf{m}}(s)$ and $\overline{\mathbf{i}}(s)$, respectively, called the *translational* and *rotational inertance*, are given by

$$\overline{\mathbf{m}}(s) = m\mathbf{1} - \sum_{n=1}^{N}\sum_{j=1}^{\infty}\frac{s^2\mathbf{P}_{jn}\mathbf{P}_{jn}{}^T}{s^2 + \Omega_{jn}{}^2} \tag{76}$$

$$\overline{\mathbf{i}}(s) = \mathbf{I} - \sum_{n=1}^{N}\sum_{j=1}^{\infty}\frac{s^2\mathbf{H}_{jn}\mathbf{H}_{jn}{}^T}{s^2 + \Omega_{jn}{}^2} \tag{77}$$

and the inputs are

$$\overline{\mathbf{u}}_{Tw}(s) = \overline{\mathbf{F}} - \sum_{n=1}^{N}\sum_{j=1}^{\infty}\frac{s^2\mathbf{P}_{jn}}{s^2 + \Omega_{jn}{}^2}\overline{\Upsilon}_{jn} \tag{78}$$

$$\overline{\mathbf{u}}_{T\theta}(s) = \overline{\mathbf{G}} - \sum_{n=1}^{N}\sum_{j=1}^{\infty}\frac{s^2\mathbf{H}_{jn}}{s^2 + \Omega_{jn}{}^2}\overline{\Upsilon}_{jn} \tag{79}$$

Identities for ω_α in Terms of $\{\Omega_{jn}, \mathbf{P}_{jn}, \mathbf{H}_{jn}\}$. The first identity comes from the realization that the unconstrained frequencies ω_α satisfy

$$\det \overline{\mathbf{M}}(i\omega_\alpha) = 0 \tag{M}$$

In particular, with symmetry, this characteristic equation devolves into two parts

$$\det \overline{\mathbf{m}}(i\omega_\beta) \equiv \det\left[m\mathbf{1} + \omega_\beta{}^2\sum_{n=1}^{N}\sum_{j=1}^{\infty}\frac{\mathbf{P}_{jn}\mathbf{P}_{jn}{}^T}{\Omega_{jn}{}^2 - \omega_\beta{}^2}\right] = 0 \quad (\beta = 1, 2, \ldots) \tag{$(M)_w$}$$

$$\det \overline{\mathbf{i}}(i\omega_\gamma) \equiv \det\left[\mathbf{I} + \omega_\gamma{}^2\sum_{n=1}^{N}\sum_{j=1}^{\infty}\frac{\mathbf{H}_{jn}\mathbf{H}_{jn}{}^T}{\Omega_{jn}{}^2 - \omega_\gamma{}^2}\right] = 0 \quad (\tau = 1, 2, \ldots) \tag{$(M)_\theta$}$$

Note that the subscripts β and γ are used to distinguish the "translational" modes from the "rotational" modes; then $\{\omega_\alpha\} = \{\omega_\beta\} \cup \{\omega_\gamma\}$.

With the aid of the simple device $\omega_\alpha{}^2 \equiv (\omega_\alpha{}^2 - \Omega_{jn}{}^2) + \Omega_{jn}{}^2$, and observing the identities $(D)'$, $(E)'$, and $(F)'$, an alternate form for identity (M) can be deduced. Illustrated for the symmetric case, $(M)_w$ and $(M)_\theta$ become

$$\det \overline{\mathbf{m}}(i\omega_\beta) = \det\left[m_r\mathbf{1} + \sum_{n=1}^{N}\sum_{j=1}^{\infty}\frac{\Omega_{jn}{}^2\mathbf{P}_{jn}\mathbf{P}_{jn}{}^T}{\omega_\beta{}^2 - \Omega_{jn}{}^2}\right] = 0 \quad (\beta = 1, 2, \ldots) \tag{$(N)_w$}$$

and similarly for $\det \mathbf{I}(i\omega_\gamma)$.

The Laplace transform of the equivalent system, (65) and (69), is taken next. After substitution for $\overline{\eta}_\alpha$, the result is

$$s^2\overline{\mathbf{q}}_r = \overline{\mathbf{M}}^{-1}(s)\overline{\mathbf{u}}_r + \overline{\mathbf{u}}_{ee} \tag{80}$$

where, using (59) also, we find

$$\mathbf{M}^{-1}(s) = \mathbf{M}_r{}^{-1} + \sum_{\alpha=1}^{\infty}\frac{s^2\begin{bmatrix}\mathbf{w}_{0\alpha}\\ \boldsymbol{\theta}_\alpha\end{bmatrix}\begin{bmatrix}\mathbf{w}_{0\alpha}\\ \boldsymbol{\theta}_\alpha\end{bmatrix}^T}{s^2 + \omega_\alpha{}^2} \tag{81}$$

$$\overline{\mathbf{u}}_{ee}(s) \triangleq \sum_{\alpha=1}^{\infty}\frac{s^2\begin{bmatrix}\mathbf{w}_{0\alpha}\\ \boldsymbol{\theta}_\alpha\end{bmatrix}}{s^2 + \omega_\alpha{}^2}\overline{f}_\alpha \tag{82}$$

The notation $\overline{\mathbf{M}}^{-1}(s)$ is used for the coefficient matrix in (80) because a comparison with (70), (72) indicates that the coefficient matrix must indeed be $\overline{\mathbf{M}}^{-1}$.

Identities Between $\{\omega_\alpha, \mathbf{p}_\alpha, \mathbf{h}_\alpha\}$ and $\{\Omega_{jn}, \mathbf{P}_{jn}, \mathbf{H}_{jn}\}$. By a direct comparison of (73) and (81), several identities are deduced. The two expressions evidently agree for $s = 0$. By setting $s = i\Omega_{jn}$, for any j ($j = 1, 2, \ldots$) and any n ($n = 1, \ldots, N$), we note from (73) that $\det \overline{\mathbf{M}}^{-1}(i\Omega_{jn}) = \mathbf{0}$. With symmetry, this is equivalent to

$$\Omega_{jn}{}^2\sum_{\beta=1}^{\infty}\frac{\mathbf{p}_\beta\mathbf{p}_\beta{}^T}{\omega_\beta{}^2 - \Omega_{jn}{}^2} = m\mathbf{1} \tag{O}$$

$$\sum_{\alpha=1}^{\infty}\frac{\mathbf{p}_\alpha\mathbf{h}_\alpha{}^T}{\omega_\alpha{}^2 - \Omega_{jn}{}^2} = \mathbf{0} \tag{P}$$

$$\Omega_{jn}{}^2\sum_{\gamma=1}^{\infty}\frac{\mathbf{h}_\gamma\mathbf{h}_\gamma{}^T}{\omega_\gamma{}^2 - \Omega_{jn}{}^2} = \mathbf{I} \tag{Q}$$

where the choice of j and n is restricted to appendage modes that contribute to $\mathbf{w}_0$ (in (O)) or $\boldsymbol{\theta}$ (in (Q)).

Identities for $\{\mathbf{p}_\alpha\}$ and $\{\mathbf{h}_\alpha\}$. The next set of identities is obtained by examining the limit as $s \to \infty$. From (73),

$$\lim_{s\to\infty} \overline{\mathbf{M}}(s) = \begin{bmatrix} m_r 1 & -\tilde{\mathbf{c}}_r \\ \tilde{\mathbf{c}}_r & \mathbf{J}_r \end{bmatrix} \tag{83}$$

To arrive at this conclusion, identities of the type $(D)'$–$(F)'$ have been inserted for each $\mathcal{E}_n$, and the definitions (36) used. We shall need the inverse of this matrix. After some algebra,

$$\lim_{s\to\infty} \overline{\mathbf{M}}(s)^{-1} = \begin{bmatrix} m_r^{-1}1 - \tilde{\mathbf{r}}_{cr}\mathbf{I}_r^{-1}\tilde{\mathbf{r}}_{cr} & \tilde{\mathbf{r}}_{cr}\mathbf{I}_r^{-1} \\ -\mathbf{I}_r^{-1}\tilde{\mathbf{r}}_{cr} & \mathbf{I}_r^{-1} \end{bmatrix} \tag{84}$$

where $\mathbf{I}_r$ is the moment-of-inertia matrix for $\mathcal{R}$ about the mass center of $\mathcal{R}$, given by

$$\mathbf{I}_r = \mathbf{J}_r + m_r\tilde{\mathbf{r}}_{cr}\tilde{\mathbf{r}}_{cr} \tag{85}$$

and $\mathbf{r}_{cr}$ is the position of the mass center of $\mathcal{R}$ with respect to O (the latter having been chosen as the mass center of $\mathcal{V}$).

Applying the same reasoning to (81), and applying (59), we conclude that

$$\sum_{\alpha=1}^{\infty} \mathbf{p}_\alpha\mathbf{p}_\alpha{}^T = (mm_e/m_r)1 - m^2\tilde{\mathbf{r}}_{cr}\mathbf{I}_r{}^{-1}\tilde{\mathbf{r}}_{cr} \tag{R}$$

$$\sum_{\alpha=1}^{\infty} \mathbf{p}_\alpha\mathbf{h}_\alpha{}^T = m\tilde{\mathbf{r}}_{cr}\mathbf{I}_r{}^{-1}\mathbf{I} \tag{S}$$

$$\sum_{\alpha=1}^{\infty} \mathbf{h}_\alpha\mathbf{h}_\alpha{}^T = \mathbf{I}\mathbf{I}_r{}^{-1}\mathbf{I} - \mathbf{I} \tag{T}$$

When symmetry prevails ($\boldsymbol{\theta}_\beta = \mathbf{0}$, $\mathbf{w}_{0\gamma} = \mathbf{0}$, and $\mathbf{r}_{cr} = \mathbf{0}$), more simple forms can be written. It is interesting to compare these identities for the unconstrained modal momentum coefficients with the earlier identities, (D)–(F), for their constrained counterparts. Another variation on this theme can be created by employing the artifice $\Omega_{jn}{}^2 \equiv (\Omega_{jn}{}^2 - \omega_\alpha{}^2) + \omega_\alpha{}^2$ in (O)–(Q), and reducing the result with (R)–(T).

Value of the Sum $\boldsymbol{\Sigma\omega_\alpha{}^{-2}}$. The next identity to be presented is the following:

$$\sum_{\alpha=1}^{\infty}\frac{1}{\omega_\alpha{}^2} = \sum_{n=1}^{N}\sum_{j=1}^{\infty}\frac{1}{\Omega_{jn}{}^2} - \frac{1}{m}\sum_{n=1}^{N}\sum_{j=1}^{\infty} \times\frac{\mathbf{P}_{jn}{}^T\mathbf{P}_{jn}}{\Omega_{jn}{}^2} - \sum_{n=1}^{N}\sum_{j=1}^{\infty}\frac{\mathbf{H}_{jn}{}^T\mathbf{I}^{-1}\mathbf{H}_{jn}}{\Omega_{jn}{}^2} \tag{U}$$

To prove this result, it is noted from (46), (47) that the characteristic equation for ω^2 can be written

$$\det\begin{bmatrix} \omega^2\mathbf{M}_r & \omega^2\mathbf{M}_e{}^T \\ \omega^2\mathbf{M}_e & \omega^2 1 - \boldsymbol{\Omega}^2 \end{bmatrix} = 0 \tag{86}$$

We may factor out ω from each of the first six rows and also from each of the first six columns of the matrix in (86) to eliminate the rigid modes. To avoid the apparent problem of elements becoming unbounded, we may pre- and postmultiply this matrix by the nonsingular matrix diag $(\mathbf{1}, \boldsymbol{\Omega}^{-1})$ whence the characteristic equation for $\omega^2 \neq 0$ is

$$\phi(\omega^2) \triangleq \det\begin{bmatrix} \mathbf{M}_r & \omega\mathbf{M}_e{}^T\boldsymbol{\Omega}^{-1} \\ \omega\boldsymbol{\Omega}^{-1}\mathbf{M}_e & \omega^2\boldsymbol{\Omega}^{-2} - 1 \end{bmatrix} = 0 \tag{87}$$

Noting that ϕ is a polynomial in ω^2, we conclude that

$$\sum_{\alpha=1}^{\infty}\frac{1}{\omega_\alpha{}^2} = -\left.\frac{\phi(\omega^2)}{d\phi/d\omega^2}\right|_{\omega^2=0} \tag{88}$$

After considerable algebra, and using mathematical induction, it can be shown that

$$\sum_{\alpha=1}^{\infty}\frac{1}{\omega_\alpha{}^2} = \sum_{n=1}^{N}\sum_{j=1}^{\infty}\frac{1}{\Omega_{jn}{}^2} - \sum_{n=1}^{N}\sum_{j=1}^{\infty}\frac{\begin{bmatrix}\mathbf{P}_{jn}\\ \mathbf{H}_{jn}\end{bmatrix}^T \mathbf{M}_r{}^{-1}\begin{bmatrix}\mathbf{P}_{jn}\\ \mathbf{H}_{jn}\end{bmatrix}}{\Omega_{jn}{}^2} \tag{89}$$

Upon substitution of $(45a)$ into (89), the identity (U) is proven.

Yet another identity can be obtained by differentiating (81) with respect to s^2, and evaluating the result at $s = 0$. Note that

$$\frac{d}{ds^2}\overline{\mathbf{M}}(s)^{-1} = -\overline{\mathbf{M}}(s)^{-1}\left(\frac{d}{ds^2}\overline{\mathbf{M}}(s)\right)\overline{\mathbf{M}}(s)^{-1} \tag{90}$$

Evaluating (90) at $s = 0$ with the aid of (73), we arrive at the desired results (see (59) also):

$$\sum_{\alpha=1}^{\infty}\frac{\mathbf{p}_\alpha\mathbf{p}_\alpha{}^T}{\omega_\alpha{}^2} = \sum_{n=1}^{N}\sum_{j=1}^{\infty}\frac{\mathbf{P}_{jn}\mathbf{P}_{jn}{}^T}{\Omega_{jn}{}^2} \tag{V}$$

$$\sum_{\alpha=1}^{\infty}\frac{\mathbf{p}_\alpha\mathbf{h}_\alpha{}^T}{\omega_\alpha{}^2} = \sum_{n=1}^{N}\sum_{j=1}^{\infty}\frac{\mathbf{P}_{jn}\mathbf{H}_{jn}{}^T}{\Omega_{jn}{}^2} \tag{W}$$

$$\sum_{\alpha=1}^{\infty}\frac{\mathbf{h}_\alpha\mathbf{h}_\alpha{}^T}{\omega_\alpha{}^2} = \sum_{n=1}^{N}\sum_{j=1}^{\infty}\frac{\mathbf{H}_{jn}\mathbf{H}_{jn}{}^T}{\Omega_{jn}{}^2} \tag{X}$$

As usual, simplifications are possible when $\mathcal{V}$ is symmetric.

As a final result, we note that $\overline{\mathbf{M}}(s)$ may also be expressed as

$$\overline{\mathbf{M}}(s) = \mathbf{M}_r\frac{\prod_{\alpha=1}^{\infty}\left(1 + \dfrac{s^2}{\omega_\alpha{}^2}\right)}{\sum_{n=1}^{N}\prod_{j=1}^{\infty}\left(1 + \dfrac{s^2}{\Omega_{jn}{}^2}\right)} \tag{Y}$$

The proof consists of noting that (i) both sides of (Y) have the same poles and zeros, and (ii) they agree for $s = 0$.

8 Numerical Example

As a simple example of some of the preceding results, consider the long slender cantilevered rod shown in Fig. 4, and for which the flexibility kernel is given by

$$F(x, \xi) = \begin{cases} x^2(3\xi - x)/6B, & 0 \le x \le \xi \le l \\ \xi^2(3x - \xi)/6B, & 0 \le \xi \le x \le l \end{cases} \tag{91}$$

The identities of Section 4 can be illustrated; since

$$\rho\int_0^l F(x, x)dx = \frac{\rho l^4}{12B} \tag{92}$$

$$\rho^2\int_0^l\int_0^l F(x, \xi)dxd\xi = \frac{\rho^2 l^5}{10B} \tag{93}$$

$$\rho^2\int_0^l\int_0^l x\xi F(x, \xi)dxd\xi = \frac{11\rho^2 l^7}{210B} \tag{94}$$

simple closed-form sums are available for the series in Identities (B),

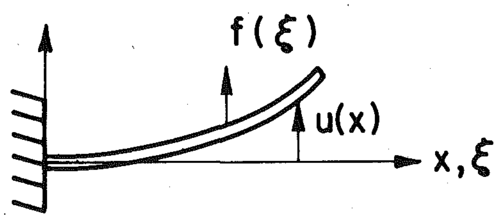

Fig. 4 Long slender cantilevered rod

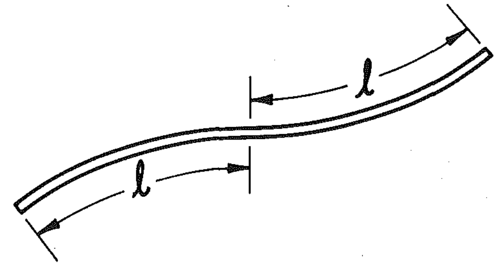

Fig. 5 Vehicle with two appendages

(H), and (J). For example, it is known that the first two natural frequencies of a cantilevered rod approximately satisfy $\Omega_1^{-2} + \Omega_2^{-2} \cong (12.08B)^{-1}\rho l^4$ which concurs with (B). Identities (H) and (J) can be compared in a similar fashion.

This example can be extended to illustrate many of the unconstrained modal identities as well. In Fig. 5 is shown a "vehicle" with two flexible "appendages," each a long slender rod of length l. According to Identity (U) and the sums (92)–(93), we should have

$$\sum_{\alpha=1}^{\infty} \frac{1}{\omega_\alpha^2} = \frac{4\rho l^4}{105B} \cong 0.0381\, \rho l^4/B \tag{95}$$

(The mass, $m = 2\rho l$, and the moment of inertia about O, $2\rho l^3/3$, have also been substituted.) The standard results for the free-free vibrations of a rod (e.g., [6, p. 165]) give $\omega_1^{-2} + \omega_2^{-2} + \omega_3^{-2} + \omega_4^{-2} \cong 0.0376\, \rho l^4/B$. The first and third modes are skew-symmetric and the second and fourth are symmetric.

Although this example illustrates the meaning of the identities, and verifies them for a simple case, the results in this paper attain their full usefulness when applied to more complex structures.

9 Usefulness of the Results

Many uses for the identities derived above can be cited, and it is likely that more will be found in the future. Some of these are theoretical, while others are practical or numerical. On the theoretical side, several of the earlier identities were used as intermediate results in the proof of later identities, and it is certain that many further results in the same vein can be found. Also of interest from a theoretical standpoint, virtually all the identities involve the sum of an infinite series. By finding the value of the sum, it has been demonstrated *a fortiori* that the series converges. As a final instance of theoretical utility, consider the system of coupled equations (43) for the motion of $\mathcal{V}$ and, for simplicity, assume $\mathbf{c} = \mathbf{0}$ and that mass-center motions and attitude motions are uncoupled

$$\left.\begin{aligned} \mathbf{I}\ddot{\boldsymbol{\theta}} + \mathbf{H}^T\ddot{\mathbf{Q}} &= \mathbf{G}(t) \\ \mathbf{H}\ddot{\boldsymbol{\theta}} + \ddot{\mathbf{Q}} + \boldsymbol{\Omega}^2\mathbf{Q} &= \mathbf{u}_e(t) \end{aligned}\right\} \tag{96}$$

These are well-known equations in the attitude dynamics of flexible vehicles (e.g., equation (288) in [10]). For any of several reasons (numerical integration, for example), it may be desirable to solve for $\ddot{\boldsymbol{\theta}}$ and $\ddot{\mathbf{Q}}$. Using Identity $(F)''$, and noting that $\mathbf{I} = \mathbf{J}_r + \mathbf{J}_e$, it is straightforward to show that

$$\begin{bmatrix} \mathbf{I} & \mathbf{H}^T \\ \mathbf{H} & \mathbf{1} \end{bmatrix}^{-1} = \begin{bmatrix} \mathbf{J}_r^{-1} & -\mathbf{J}_r^{-1}\mathbf{H}^T \\ -\mathbf{H}\mathbf{J}_r^{-1} & \mathbf{1} + \mathbf{H}\mathbf{J}_r^{-1}\mathbf{H}^T \end{bmatrix} \tag{97}$$

whence

$$\left.\begin{aligned} \ddot{\boldsymbol{\theta}} &= \mathbf{J}_r^{-1}[\mathbf{G}_0 - \mathbf{H}^T(\mathbf{u}_e - \boldsymbol{\Omega}^2\mathbf{Q})] \\ \ddot{\mathbf{Q}} &= -\mathbf{H}\mathbf{J}_r^{-1}\mathbf{G}_0 + (\mathbf{1} + \mathbf{H}\mathbf{J}_r^{-1}\mathbf{H}^T)(\mathbf{u}_e - \boldsymbol{\Omega}^2\mathbf{Q}) \end{aligned}\right\} \tag{98}$$

The motion equations are now ready to integrate.

Many of the identities are also eminently practical. Most importantly, they provide a sound basis for modal truncation. If, for example, the retained modes satisfy $\Sigma\Sigma H_{jn}^2 = 0.99J_e$ or $\Sigma h_\alpha^2 = 0.99II_e/I_r$, there is a clear indication that the modes omitted do not contribute materially to the motion (other things being equal). The identities for the unconstrained modal parameters in terms of constrained modal parameters also permit an assessment of the influence of each constituent elastic body on the vehicle as a whole. If the parameters of $\mathcal{E}_n$ change, it is not necessary to reanalyze the whole vehicle. The new vehicle frequencies and momentum coefficients $\{\omega_\alpha, \mathbf{p}_\alpha, \mathbf{h}_\alpha\}$ can in principle be calculated from (M) and (O), (P), (Q), respectively.

10 Concluding Remarks

Throughout this paper, only the "exact" modes have been discussed and no truncation of modes has been made. Theoretical results are sought, and there is neither need nor motivation for making either type of approximation. Indeed, it is one of the chief aims of the paper to provide quantitative criteria for the error introduced when such approximations are necessary (numerical work). Vehicle modes can also be synthesized [12, 13] from (discrete) "component modes."

Structural dissipation of energy has not been considered although an analogous set of identities can be derived which relate the unconstrained modal damping factors for the vehicle to the constrained modal damping factors for individual appendages, provided these factors are small (as they usually are) and can therefore be treated as first-order quantities. There are also many other generalizations of these identities; in fact, this paper is really just a beginning. Modal parameter identities can also be found [11] if $\mathcal{V}$ is spinning, or, if not spinning, contains spinning wheels or rotors. Moreover, if the elastic bodies $\mathcal{E}_n$ are not cantilevered to $\mathcal{R}$ but are instead hinged (introducing new rigid modes for $\mathcal{V}$), similar identities can be derived. Even for general topological trees of rigid and elastic bodies, identities of the form derived herein can be shown to exist.

Acknowledgments

This work was supported, in part, by the Natural Science and Engineering Research Council of Canada under Grant No. A4183 and, in part, by the Jet Propulsion Laboratory under Contract No. 955369.

References

1 Likins, P. W., and Bouvier, H. K., "Attitude Control of Nonrigid Spacecraft," *Aeronautics and Astronautics*, Vol. 9, No. 5, 1971.

2 Meirovitch, L., ed., "Dynamics and Control of Large Flexible Spacecraft," *Proceedings of Symposium*, Blacksburg, Va., June 13–15, 1977.

3 Modi, V. J., "Attitude Dynamics of Satellites With Flexible Appendages—A Brief Review," *Journal of Spacecraft and Rockets*, Vol. 11, No. 11, 1974.

4 Taylor, A. S., and Woodcock, D. L., "Mathematical Approaches to the Dynamics of Deformable Aircraft," Aeronautical Research Council (British), R.&.M., No. 3776, 1976.

5 Hughes, P. C., "Dynamics of Flexible Space Vehicles With Active Attitude Control," *Celestial Mechanics Journal*, Vol. 9, 1974, pp. 21–39.

6 Meirovitch, L., *Analytical Methods in Vibrations*, Macmillan, 1967.

7 Courant, R., and Hilbert, D., *Methods of Mathematical Physics*, Interscience, 1955.

8 Higgins, J. R., *Completeness and Basis Properties of Sets of Special Functions*, Cambridge University Press, 1977.

9 Mikhlin, S. G., *Variational Methods in Mathematical Physics*, Pergamon, 1964.

10 Likins, P. W., "Dynamics and Control of Flexible Space Vehicles," Jet Propulsion Laboratory Technical Report 32-1329, Rev. 1, 1970.

11 Poelaert, D. H. L., "Dynamic Analysis of a Non-Rigid Spacecraft," *Proceedings of First VPI & SU/AIAA Conference on the Dynamics and Control of Large Flexible Spacecraft*, Meirovitch, L., ed., Blacksburg, Va., June, 1977.

12 Hurty, W. C., "Dynamic Analysis of Structural Systems Using Component Modes," *AIAA Journal*, Vol. 3, No. 4, 1965, pp. 678–685.

13 Benfield, W. A., and Hruda, R. F., "Vibration Analysis of Structures by Component Modes Substitution," *AIAA Journal*, Vol. 9, No. 7, 1971, pp. 1255–1261.

C. S. Hsu

Professor of Applied Mechanics,
Department of Mechanical Engineering,
University of California,
Berkeley, Calif. 94720
Fellow ASME

A Theory of Index for Point Mapping Dynamical Systems

Dynamical systems governed by discrete time-difference equations are referred to as point mapping dynamical systems in this paper. Based upon the Poincaré theory of index for vector fields, a theory of index is established for point mapping dynamical systems. Besides its intrinsic theoretic value, the theory can be used to help search and locate periodic solutions of strongly nonlinear systems.

1 Introduction

In recent years the method of point-to-point mapping has been receiving increasing attention for treating nonlinear dynamical systems. The general method dated back to Poincaré [1] and Birkhoff [2], and in the past 20 years or so it has received a great deal of mathematical development, mainly by people working in the field of differentiable dynamics; see, for instance, the work by Arnol'd [3], Smale [4], Markus [5], Takens [6], and Marsden and McCracken [7].

Consider a nonlinear dynamical system

$$\dot{\mathbf{x}}(t) = \mathbf{f}(\mathbf{x}(t),t) \tag{1}$$

If the system is periodic so that $\mathbf{f}$ is explicitly periodic in t, then the point mapping approach is particularly attractive. The existence of a period allows one to view the dynamical system as a mapping which relates the state of the system at the end of one period to the state at the end of the next period. Viewed in this manner, the governing equation for the system takes on the form

$$\mathbf{x}(n+1) = \mathbf{G}(\mathbf{x}(n)) \tag{2}$$

This approach has been used in [8–13] to study certain strongly nonlinear mechanical systems under periodic parametric excitations. By this approach various interesting bifurcation phenomena and special features of global responses can be studied in a very effective manner. It is also strongly believed that since the point-to-point mapping method is extremely well suited for computer adaptation, there will be a much greater development of the method in the coming years, particularly for the purpose of studying the global behavior of strongly nonlinear systems. In this paper we offer a development which might be said to provide point mapping dynamical systems a *theory of index,* analogous to Poincaré's theory for two-dimensional autonomous differential equations which is well known to be one of the most elegant theories in the field of nonlinear oscillations. In this connection we mention here an early work by Levinson [14] which contains results directly related to the present development.

Beside giving the theory, some examples of application will be discussed in Section 8. Through these examples, it will be seen that in addition to its intrinsic theoretic value this theory of index can be used to advantage to help search periodic solutions of strongly nonlinear systems and to verify the existence and the number of these solutions within a given region of the phase plane.

Although we have introduced (2) here as the point-to-point mapping equation resulting from conceptually integrating (1) over one period, it is, of course, not necessary to take such a narrow view. Equation (2) can in fact arise as the basic governing equation for certain dynamical systems in many fields of science and engineering. For this reason in the following development of the theory of index we shall consider (2) in its own right, namely; a class of dynamical systems governed by a system of diffference equations.

A few words about the terminology might be in order here. In [8], for convenience, dynamical systems governed by (1) or (2) are, respectively, referred to as *differential dynamical systems* or *difference dynamical systems.* These names are quite adequate and in a sense very precise. In this paper we elect, however, to use the more descriptive name *point mapping dynamical systems* for systems governed by (2). We also refer to (2) as a *point mapping*, or sometimes simply a *map*.

2 Theory of Index for Two-Dimensional Vector Fields

The theory of Poincaré's is basically a theory of index for two-dimensional vector fields. Let $\mathbf{F} = (F_1, F_2)$ be a continuous real-valued vector function defined on a bounded open set B_0 in the (x_1, x_2) phase plane. A point at which $\mathbf{F} = 0$ is called a *singular point* of $\mathbf{F}$. We assume that all the singular points of $\mathbf{F}$ are isolated. Let J be a Jordan curve in B_0 passing through no singular points of $\mathbf{F}$. At every point on J, $\mathbf{F}$ is defined. Let φ be the angle the vector $\mathbf{F}$ makes with some fixed direction. Let Φ be the total change of φ as (x_1, x_2) moves along J once in the positive direction. The classical theory of Poincaré's is embodied in the following definitions and theorems:

Definition 1. The index of J with respect to $\mathbf{F}$, to be denoted by $I(J, \mathbf{F})$, is defined to be $\Phi/2\pi$.

Contributed by the Applied Mechanics Division for publication in the JOURNAL OF APPLIED MECHANICS.

Discussion on this paper should be addressed to the Editorial Department, ASME, United Engineering Center, 345 East 47th Street, New York, N.Y. 10017, and will be accepted until June 1, 1980. Readers who need more time to prepare a discussion should request an extension from the Editorial Department. Manuscript received by ASME Applied Mechanics Division, August, 1979; final revision, October 1979.

Theorem 1. If J is a Jordan curve which contains no singular points of $\mathbf{F}$ on it or in its interior, then $I(J, \mathbf{F}) = 0$.

Corollary 1.1. If J_1 is a Jordan curve which is contained in the interior of another Jordan curve J_2 and if no singular points of $\mathbf{F}$ lie between J_1 and J_2, then $I(J_1, \mathbf{F}) = I(J_2, \mathbf{F})$.

Definition 2. The index of an isolated singular point $\mathbf{P}$ with respect to a vector field $\mathbf{F}$ is defined as the index of any Jordan curve which contains only $\mathbf{P}$ and no other singular points of $\mathbf{F}$ in its interior, and is to be denoted by $I(\mathbf{P}, \mathbf{F})$.

Theorem 2. If J is a Jordon curve containing a finite number $\mathbf{P}_1, \mathbf{P}_2, \cdots, \mathbf{P}_N$ of singular points of $\mathbf{F}$ in its interior, then

$$I(J, \mathbf{F}) = \sum_{i=1}^{N} I(\mathbf{P}_i, \mathbf{F}).$$

Next, we present the dependence of the index of a singular point of $\mathbf{F}$ on the local property of $\mathbf{F}$ near the singular point. Without loss of generality, let the singular point be located at the origin $\mathbf{O} = (0, 0)$ and let $\mathbf{F}$ admit the form

$$\mathbf{F}(\mathbf{x}) = \mathbf{L}\mathbf{x} + \mathbf{P}(\mathbf{x}) \tag{3}$$

where $\mathbf{L}$ is a 2×2 constant matrix and $\mathbf{P}$ represents the nonlinear part of $\mathbf{F}$ and is assumed to satisfy

$$\lim \frac{\|\mathbf{P}(\mathbf{x})\|}{\|\mathbf{x}\|} = 0 \quad \text{as} \quad \|\mathbf{x}\| \to 0. \tag{4}$$

Here we take the norm of a vector to be its Euclidean norm. We also assume

$$\det \mathbf{L} \neq 0 \tag{5}$$

The origin is now an isolated nondegenerate singular point of $\mathbf{F}$. Its index with respect to $\mathbf{F}$ is entirely determined by the linear part $\mathbf{L}\mathbf{x}$ of $\mathbf{F}$, as embodied in the following two theorems:

Theorem 3. $I(\mathbf{O}, \mathbf{F}) = I(\mathbf{O}, \mathbf{L})$.

Theorem 4. Given a nondegenerate singular point of $\mathbf{F}$ at the origin, its index with respect to $\mathbf{F}$ of (3) is $+1$ or -1, according as ($\det \mathbf{L}$) > 0 or < 0.

These results are classic. We record them here in order to set up the notation and also for the purpose of easy reference as we proceed to present a theory of index for point mapping dynamical systems in the next few sections.

3 Periodic Solutions of Point Mappings

Consider now point mappings $\mathbf{G}$ of (2). Let us denote by $\mathbf{G}^k$ the mapping $\mathbf{G}$ applied k times, with $\mathbf{G}^0$ understood to be an identity mapping. A *periodic solution* of period K of a mapping $\mathbf{G}$ is a set of K distinct points $\mathbf{x}^*(j)$, $j = 1,2,\ldots,K$, such that

$$\mathbf{x}^*(m+1) = \mathbf{G}^m(\mathbf{x}^*(1)), \quad m = 1,2,\cdots,K-1, \tag{6}$$
$$\mathbf{x}^*(1) = \mathbf{G}^K(\mathbf{x}^*(1)).$$

Since we will refer to periodic solutions of this kind time and again, it is convenient to adopt an abbreviated name. We shall call a periodic solution of period K as a *P-K solution* and any of its elements $\mathbf{x}^*(j)$, $j = 1, 2, \ldots, K$, a periodic point of period K, or, in abbreviation, a *P-K point*.

The P-1 points can of course be interpreted as the equilibrium states of the point mapping dynamical systems. As such, they occupy a unique position and perhaps deserve a special name other than just "P-1 points." However, if the point mapping is in fact obtained from a system of differential equations by integrating over one period, then a P-1 point could very well correspond to a periodic solution of period 1 for the differential dynamical system and the P-K points correspond to subharmonic solutions of period K. Because of this possible interpretation we elect here not to use a special name for the P-1 points.

4 The Index of a P-1 Point of a Point Mapping

Having defined the periodic points, we consider in this section the index of a P-1 point.

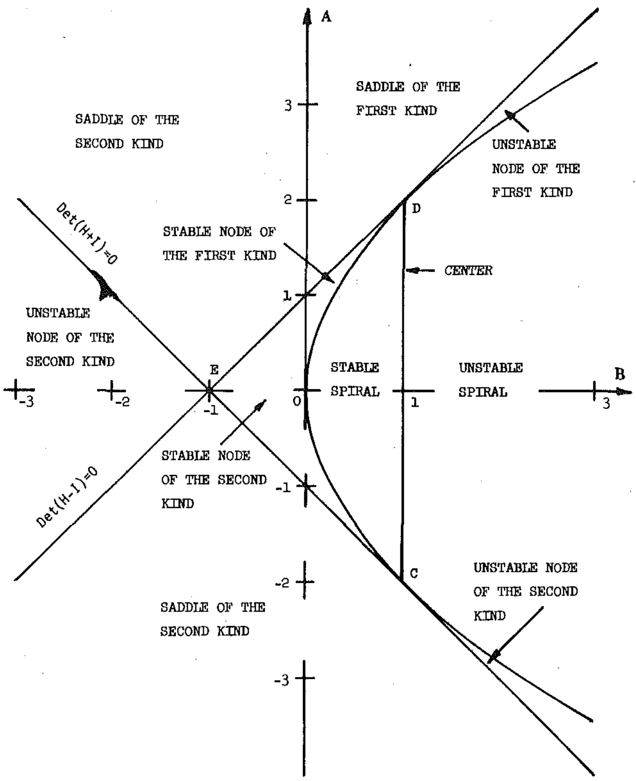

Fig. 1 Dependence of the character of a periodic point on A and B.

4.1 The Index of a P-1 Point With Respect To $\mathbf{G} - \mathbf{I}$. First, we identify the vector field $\mathbf{F}$ of Section 2 with $(\mathbf{G} - \mathbf{I})(\mathbf{x})$ where $\mathbf{I}$ is the identity mapping.

$$\mathbf{F}(\mathbf{x}) = (\mathbf{G} - \mathbf{I})(\mathbf{x}) = \mathbf{G}(\mathbf{x}) - \mathbf{x} \tag{7}$$

It is obvious that all the P-1 points of $\mathbf{G}$ are the singular points of $\mathbf{F}$ as defined by (7) and all the singular points of $\mathbf{F}$ are the P-1 points of $\mathbf{G}$. Consider now one of the P-1 points, say $\mathbf{x}^*$. Near $\mathbf{x}^*$, $\mathbf{F}$ may be put in the form

$$\mathbf{F}(\mathbf{x}) = (\mathbf{H}(\mathbf{x}^*) - \mathbf{I})\boldsymbol{\xi} + \mathbf{P}(\boldsymbol{\xi}) \tag{8}$$

where

$$\boldsymbol{\xi} = \mathbf{x} - \mathbf{x}^*, \tag{9}$$

$\mathbf{H}(\mathbf{x}^*)$ is the Jacobian matrix of $\mathbf{G}$ with respect to $\mathbf{x}$ evaluated at $\mathbf{x} = \mathbf{x}^*$ and is also to be written as

$$\mathbf{H}(\mathbf{x}^*) = \mathbf{D}\mathbf{G}(\mathbf{x}^*), \tag{10}$$

and $\mathbf{P}(\boldsymbol{\xi})$ symbolically represents the nonlinear part of the mapping $\mathbf{G}$ and it is also the nonlinear part of the vector field $\mathbf{F}$ near $\mathbf{x}^*$.

If we let

$$A(\mathbf{x}^*) = \operatorname{trace} \mathbf{H}(\mathbf{x}^*), \qquad B(\mathbf{x}^*) = \det \mathbf{H}(\mathbf{x}^*), \tag{11}$$

then one easily finds that

$$\det(\mathbf{H}(\mathbf{x}^*) - \mathbf{I}) = 1 - A(\mathbf{x}^*) + B(\mathbf{x}^*) = 1 - A + B. \qquad (12)^1$$

Let us assume that $\det(\mathbf{H}(\mathbf{x}^*) - \mathbf{I}) \neq 0$. Such a singular point will be called a nondegenerate singular point of $\mathbf{F}$ of (7), or a P-1 point of $\mathbf{G}$ nondegenerate with respect to $(\mathbf{G} - \mathbf{I})$. $(\mathbf{H} - \mathbf{I})$ being the linear part of $\mathbf{F}$ near $\mathbf{x}^*$, it can be identified with $\mathbf{L}$ of **Theorem 4.** This leads to the following result which can also be found in [14].

[1] When it is desirable to indicate $\mathbf{H}$, A, and B to be those associated with a particular point $\mathbf{P}$, we shall use the notation $\mathbf{H}(\mathbf{P})$, $A(\mathbf{P})$, and $B(\mathbf{P})$. But when no ambiguity is likely to occur we will drop the label $\mathbf{P}$ and simply use $\mathbf{H}$, A, and B.

Theorem 5. If $\mathbf{x}^*$ is a P-1 point of $\mathbf{G}$ nondegenerate with respect to $(\mathbf{G}-\mathbf{I})$, then its index with respect to $(\mathbf{G}-\mathbf{I})$, to be denoted by $I(\mathbf{x}^*, \mathbf{G}-\mathbf{I})$, is equal to $+1$ or -1, according as det $(\mathbf{H}-\mathbf{I}) > 0$ or < 0.

Next, we will relate the index of a P-1 point to its geometric character. At this stage it is necessary to recall the dependence of the geometric character of a P-1 point on the linear map $\mathbf{H}$. A P-1 point may be a center, a stable or unstable spiral point, a stable or unstable node of the first or the second kind, or a saddle point of the first or the second kind, depending upon the relative magnitudes of trace $\mathbf{H}$ and det $\mathbf{H}$. For a detailed discussion the reader is referred to [11], but for the sake of easy reference this dependence is shown graphically here by Fig. 1. One notes here that according to Theorem 5, all the points above the line det $(\mathbf{H}-\mathbf{I}) = 0$ will have an index -1 while all the points below the line have an index $+1$.

Here one notes the first drastic departure of the theory of index for point mapping dynamical systems from the theory of Poincaré for two-dimensional autonomous differential equations. For that classical theory [15, 16] the index is -1 if the singular point is a saddle point and is $+1$ if it is of any other kind. For the point mapping systems we find that included in the case of -1 index are certain unstable nodes of the second kind and included in the case of $+1$ index are certain saddle points of the second kind. More differences between the two theories of index will be seen later.

Combining Theorems 2 and 5, we have the following global result:

Theorem 6. Given a point mapping $\mathbf{G}$, if a Jordan curve J contains a finite number $\mathbf{P}_1, \mathbf{P}_2, \cdots, \mathbf{P}_N$ of P-1 points of $\mathbf{G}$ in its interior, and if p_1 is the number of points having positive det $(\mathbf{H}(\mathbf{P}_i)-\mathbf{I})$ and q_1 is the number of points having negative det $(\mathbf{H}(\mathbf{P}_i)-\mathbf{I})$, with $p_1 + q_1 = N$, then the index of J with respect to $(\mathbf{G}-\mathbf{I})$, to be denoted by $I(J, \mathbf{G}-\mathbf{I})$, is $p_1 - q_1$.

4.2 The Index of a *P*-1 Point With Respect To $\mathbf{G}^2 - \mathbf{I}$. Again consider a P-1 point $\mathbf{x}^*$ but let us now consider a vector field $\mathbf{F}$ defined as

$$\mathbf{F}(\mathbf{x}) = \mathbf{G}^2(\mathbf{x}) - \mathbf{x} = (\mathbf{G}^2 - \mathbf{I})(\mathbf{x}) \tag{13}$$

This vector is obtained as the difference between the image of a point after point-mapped twice and the point itself. The P-1 point $\mathbf{x}^*$ is again a singular point of $\mathbf{F}$. Near $\mathbf{x}^*$ one has

$$\mathbf{F}(\mathbf{x}) = (\mathbf{H}^2(\mathbf{x}^*) - \mathbf{I})\boldsymbol{\xi} + \mathbf{P}(\boldsymbol{\xi}) \tag{14}$$

where $\mathbf{H}$, $\boldsymbol{\xi}$, and $\mathbf{P}$ have the same meanings as before. Let us further assume that the P-1 point $\mathbf{x}^*$ of $\mathbf{G}$ is nondegenerate with respect to $(\mathbf{G}^2 - \mathbf{I})$ so that det $(\mathbf{H}^2(\mathbf{x}^*) - \mathbf{I}) \neq 0$. Using $\mathbf{F}$ as given by (13) and applying Theorem 4, we have the following result:

Theorem 7. If $\mathbf{x}^*$ is a P-1 point of $\mathbf{G}$ nondegenerate with respect to $(\mathbf{G}^2-\mathbf{I})$, then its index with respect to $(\mathbf{G}^2-\mathbf{I})$, to be denoted by $I(\mathbf{x}^*, \mathbf{G}^2-\mathbf{I})$, is $+1$ or -1, according as det $(\mathbf{H}^2(\mathbf{x}^*)-\mathbf{I}) > 0$ or < 0.

It is easily shown that

$$\begin{aligned}\det(\mathbf{H}^2 - \mathbf{I}) &= [\det(\mathbf{H}-\mathbf{I})][\det(\mathbf{H}+\mathbf{I})]\\ &= (1 - A + B)(1 + A + B)\end{aligned} \tag{15}$$

With this result the last expression in Theorem 7 may be replaced by

$$[\det(\mathbf{H}-\mathbf{I})][\det(\mathbf{H}+\mathbf{I})] \gtrless 0 \tag{16}$$

or

$$(1 - A + B)(1 + A + B) \gtrless 0. \tag{17}$$

We may again refer to Fig. 1 to relate the index to the geometric character of the P-1 point. Now one finds that the condition for the index $I(\mathbf{x}^*, \mathbf{G}^2 - \mathbf{I})$ to be -1 is represented precisely by the two 90° sectors occupied by saddle points and the condition for the index to be $+1$ is represented by the other two 90° sectors occupied by points of the other kinds. It is most interesting that when the index of the P-1 point is evaluated with respect to the vector field $(\mathbf{G}^2 - \mathbf{I})(\mathbf{x})$ we recover the same geometrical result as in the classical theory of Poincaré for differential dynamical systems. This is, however, not surprising. The difference between the two theories as described in Section 4.1 concerns certain nodes and saddle points of the second kind. By going to $(\mathbf{G}^2 - \mathbf{I})$ and, therefore, applying the mapping twice, one removes the complication of the behavior associated with singular points of the second kind and consequently leads to a simpler geometrical result. On this point it might be instructive for the reader to see the portraits of the possible discrete trajectories around the various kinds of singular points; see, for instance, Fig. 1.1 of [13].[2]

While the geometrical meaning of the index $I(\mathbf{x}^*, \mathbf{G}^2 - \mathbf{I})$ is much simpler, for a reason to be discussed shortly, we cannot immediately establish a global result analogous to Theorem 6. That will have to await until later.

4.3 The Index of a *P*-1 Point With Respect to $\mathbf{G}^k - \mathbf{I}$. Next, let us take the vector field to be

$$\mathbf{F}(\mathbf{x}) = \mathbf{G}^k(\mathbf{x}) - \mathbf{x} = (\mathbf{G}^k - \mathbf{I})(\mathbf{x}) \tag{18}$$

A P-1 point $\mathbf{x}^*$ of $\mathbf{G}$ is again a singular point of this $\mathbf{F}$. Near $\mathbf{x}^*$, F has the form

$$\mathbf{F}(\mathbf{x}) = (\mathbf{H}^k(\mathbf{x}^*) - \mathbf{I})\boldsymbol{\xi} + \mathbf{P}(\boldsymbol{\xi}) \tag{19}$$

Assume now that $\mathbf{x}^*$ is nondegenerate with respect to $(\mathbf{G}^k - \mathbf{I})$ in the sense that det $(\mathbf{H}^k(\mathbf{x}^*) - \mathbf{I}) \neq 0$. Then by Theorem 4 the index $I(\mathbf{x}^*, \mathbf{G}^k - \mathbf{I})$ is $+1$ or -1 depending upon whether det $(\mathbf{H}^k(\mathbf{x}^*) - \mathbf{I}) > 0$ or <0. Here it is necessary to examine det $(\mathbf{H}^k(\mathbf{x}^*) - \mathbf{I})$ in a greater detail. When k is odd it can be expressed in the form

$$\det(\mathbf{H}^k - \mathbf{I}) = [\det(\mathbf{H} - \mathbf{I})] \cdot D_1 \tag{20}$$

where

$$D_1 = \det(\mathbf{H}^{k-1} + \mathbf{H}^{k-2} + \cdots + \mathbf{H} + \mathbf{I}) \tag{21}$$

In (20) and (21) and in the remainder of this section we drop the argument $\mathbf{x}^*$ of $\mathbf{H}$. D_1 may be further expressed as

$$\begin{aligned}D_1 = (\lambda_1{}^{2p} + \lambda_1{}^{2p-1} + \cdots + \lambda_1 + 1)&\\ \times(\lambda_2{}^{2p} + \lambda_2{}^{2p-1} + \cdots + \lambda_2 + 1)&\end{aligned} \tag{22}$$

where λ_1 and λ_2 denote the eigenvalues of $\mathbf{H}$ and where we have replaced $k - 1$ by $2p$ to indicate the even degree of the polynomials.

D_1 can be shown to be non-negative. In fact, if λ_1 and λ_2 are real, then each of the two factors on the right-hand side of (22) is positive and hence D_1 is positive. If λ_1 and λ_2 are complex (then necessarily complex conjugate), D_1 is again in general positive and it becomes zero only when

$$\begin{matrix}\lambda_1\\ \lambda_2\end{matrix} = \exp\left\{\pm \frac{2\pi j}{2p+1} i\right\}, \quad j = 1,2,\cdots,2p. \tag{23}$$

Thus, when k is odd, det $(\mathbf{H}^k - \mathbf{I}) = 0$ only when $1 - A + B = 0$ or when (23) is satisfied. Apart from these special cases which are ruled out by nondegeneracy, the sign of det $(\mathbf{H}^k - \mathbf{I})$ coincides with the sign of det $(\mathbf{H} - \mathbf{I})$ because D_1 is positive. This leads to the following result:

Theorem 8. If k is odd and if $\mathbf{x}^*$ is a P-1 point of $\mathbf{G}$ nondegenerate with respect to $(\mathbf{G}^k - \mathbf{I})$, then the index of $\mathbf{x}^*$ with respect to $(\mathbf{G}^k - \mathbf{I})$ is equal to its index with respect to $(\mathbf{G} - \mathbf{I})$.

Next, consider the case when k is even. In that case one has

$$\det(\mathbf{H}^k - \mathbf{I}) = [\det(\mathbf{H}^2 - \mathbf{I})] \cdot D_2 \tag{24}$$

where

$$D_2 = \det(\mathbf{H}^{k-2} + \mathbf{H}^{k-4} + \cdots \mathbf{H}^2 + \mathbf{I}) \tag{25}$$

$$\begin{aligned}&= (\lambda_1{}^{k-2} + \lambda_1{}^{k-4} + \cdots \lambda_1{}^2 + 1)(\lambda_2{}^{k-2}\\ &\quad + \lambda_2{}^{k-4} + \cdots + \lambda_2{}^2 + 1).\end{aligned} \tag{26}$$

Again one finds D_2 to be non-negative. It is always positive if λ_1 and

[2] Unfortunately, there is not a uniform terminology for the various singular points. The singular points of the second kind discussed in [8,11] and referred to in this paper are called singular points of type 2 and type 3 in [13]. The names used in [14] also differ from those used in this paper.

λ_2 are real. If λ_1 and λ_2 are complex, D_2 is in general positive except that it vanishes when

$$\frac{\lambda_1}{\lambda_2} = \exp\left\{\pm \frac{2\pi j}{k} i\right\}, \quad j = 1,2,\cdot\cdot,\frac{k}{2}-1,\frac{k}{2}+1,\cdot\cdot,k-1. \quad (27)$$

Thus, for k even det $(\mathbf{H}^k - \mathbf{I}) = 0$ only when $1 - A + B = 0, 1 + A + B = 0$, or (27) is satisfied. Apart from these cases the sign of det $(\mathbf{H}^k - \mathbf{I})$ coincides with the sign of det $(\mathbf{H}^2 - \mathbf{I})$.

Theorem 9. If k is even and if $\mathbf{x}^*$ is a P-1 point of $\mathbf{G}$ nondegenerate with respect to $(\mathbf{G}^k - \mathbf{I})$, then the index of $\mathbf{x}^*$ with respect to $(\mathbf{G}^k - \mathbf{I})$ is equal to its index with respect to $(\mathbf{G}^2 - \mathbf{I})$.

A remark about the conditions $1 - A + B = 0, 1 + A + B = 0$, (23) and (27) might be in order here. When one of these conditions is met, det $(\mathbf{H}^k - \mathbf{I}) = 0$ for some k and the corresponding index cannot be determined. Analytically, it is of interest to note that as discussed in [11] these condition are precisely the conditions for bifurcation from P-1 to P-1, from P-1 to P-2, or from P-1 to P-k. The inapplicability of the simple method of index determination of singular points at the critical points of bifurcation is perhaps to be expected. For more information on the general topic of bifurcation phenomena of maps the reader is referred to [6,7].

5 The Index of a P-K Point

Consider now a P-K solution of $\mathbf{G}$. Such a solution satisfies (6) and consists of K elements: $\mathbf{x}^*(j), j = 1,2,\cdots,K$. Let us take $\mathbf{x}^*(j)$ as a typical P-K point. Moreover, let us take $(\mathbf{G}^K - \mathbf{I})(\mathbf{x})$ to be the vector field $\mathbf{F}$. Evidently, $\mathbf{x}^*(j)$ is a singular point of $\mathbf{F}$. Near $\mathbf{x}^*(j)$,

$$\mathbf{F}(\mathbf{x}) = (\mathbf{H}^{(K)}(\mathbf{x}^*(j)) - \mathbf{I})\boldsymbol{\xi} + \mathbf{P}(\boldsymbol{\xi}) \quad (28)$$

where

$$\boldsymbol{\xi} = \mathbf{x} - \mathbf{x}^*(j) \quad (29)$$

and $\mathbf{P}$ again represents the nonlinear part of $\mathbf{F}$. Here, $\mathbf{H}^{(K)}(\mathbf{x}(j))$ is however the Jacobian matrix of $\mathbf{G}^K$ with respect to $\mathbf{x}$ evaluated at $\mathbf{x} = \mathbf{x}^*(j)$

$$\mathbf{H}^{(K)}(\mathbf{x}^*(j)) = [\mathbf{D}\mathbf{G}^K]_{\mathbf{x}=\mathbf{x}^*(j)} \quad (30)$$

which may also be put in the form

$$\mathbf{H}^{(K)}(\mathbf{x}^*(j)) = [\mathbf{DG}(\mathbf{x}^*(j-1))]\cdots[\mathbf{DG}(\mathbf{x}^*(1))] \times[\mathbf{DG}(\mathbf{x}^*(K))]\cdots[\mathbf{DG}(\mathbf{x}^*(j))]. \quad (31)$$

In this notation the previous $\mathbf{H}(\mathbf{x}^*)$ associated with a P-1 point may be written as $\mathbf{H}^{(1)}(\mathbf{x}^*(1))$.

If, instead of $(\mathbf{G}^+G - \mathbf{I})$, we take F to be $(\mathbf{G}^{kK} - \mathbf{I})$ where k is a positive integer, we have near $^*(j)$

$$\mathbf{F}(\mathbf{x}) = [(\mathbf{H}^{(K)}(\mathbf{x}^*(j)))^k - \mathbf{I}]\boldsymbol{\xi} + \mathbf{P}(\boldsymbol{\xi})$$

Assume now that $\mathbf{x}^*(j)$ is nondegenerate with respect to $(\mathbf{G}^{kK} - \mathbf{I})$ so that det $[(\mathbf{H}^{(K)}(\mathbf{x}^*(j)))^k - \mathbf{I}] \neq 0$. Then by Theorem 4 we have the following results:

Theorem 10. If k is odd and if $\mathbf{x}^*(j)$ is a $P - K$ point of $\mathbf{G}$ nondegenerate with respect to $(\mathbf{G}^{kK} - \mathbf{I})$, then the index of $\mathbf{x}^*(j)$ with respect to $(\mathbf{G}^{kK} - \mathbf{I})$ is $+1$ or -1, according to whether det $[(\mathbf{H}^{(K)}(\mathbf{x}^*(j))) - \mathbf{I}] > 0$ or < 0.

Theorem 11. If k is even and if $\mathbf{x}^*(j)$ is a $P - K$ point of $\mathbf{G}$ nondegenerate with respect to $(\mathbf{G}^{kK} - \mathbf{I})$, then the index of $\mathbf{x}^*(j)$ with respect to $(\mathbf{G}^{kK} - \mathbf{I})$ is $+1$ or -1, according to whether det $[(\mathbf{H}^{(K)}(\mathbf{x}^*(j)))^2 - \mathbf{I}] > 0$ or < 0.

The geometric character of a $P - K$ point $\mathbf{x}^*(j)$ is determined by $\mathbf{H}^{(K)}(\mathbf{x}^*(j))$ according to Fig. 1 with $\mathbf{H}$ replaced by $\mathbf{H}^{(K)}(\mathbf{x}^*)(j))$. The relation between the geometric character and the index can therefore be established in a way similar to that discussed in Sections 4.1 and 4.2.

6 The Index of a Jordan Curve With Respect to $\mathbf{G}^L - \mathbf{I}$.

With all the developments of Sections 4 and 5 at hand, we can now examine some general global results of the index theory for point mapping dynamical systems. Consider a Jordan curve J and consider $\mathbf{F}(\mathbf{x}) = \mathbf{G}^L(\mathbf{x}) - \mathbf{x} = (\mathbf{G}^L - \mathbf{I})(\mathbf{x})$ where L is a positive integer. Let $f_1 = 1, f_2, f_3, \cdots, f_Q = L$ be the complete set of positive integer factors of L. Then it is obvious that all P-1, P-f_2, P-$f_3, \cdots$, P-L points of $\mathbf{G}$ are singular points of $\mathbf{F}(\mathbf{x})$, and vice versa. Let N of these points be contained in the interior of J and let them be labeled as $\mathbf{P}_i(K_i)$, $i = 1,2, \cdots, N$ where K_i equal to one of the factors f_q, $q = 1,2,\cdots,Q$, is used to indicate the periodicity of the point. To each point $\mathbf{P}_i(K_i)$ is associated a number $k_i = L/K_i$. We assume that all the $\mathbf{P}_i(K_i)$ points are nondegenerate in the sense that det $[(\mathbf{H}^{(K_i)}(\mathbf{P}_i))^{k_i} - \mathbf{I}] \neq 0$. The index $I(\mathbf{P}_i(K_i), \mathbf{G}^{k_iK_i} - \mathbf{I})$ of each point $\mathbf{P}_i(K_i)$ with respect to $(\mathbf{G}^L - \mathbf{I})$ can then be determined by Theorem 10 if k_i is odd or by Theorem 11 if k_i is even. These considerations permit us to give the following global result which is nothing but a restatement of Theorem 2:

Theorem 12. The index of J with respect to $(\mathbf{G}^L - \mathbf{I})$ is

$$I(J, \mathbf{G}^L - \mathbf{I}) = \sum_{i=1}^{N} I(\mathbf{P}_i(K_i), \mathbf{G}^{k_iK_i} - \mathbf{I}).$$

7 The Index of a Singular Point or a Jordan Curve With Respect to a General $F(\mathbf{x})$

In this section we digress from our main development to discuss a point which could lead to further developments of this theory of index and thus enhance the usefulness of the theory in the direction of application.

It is seen in Sections 4–6 that the index theory for point mapping dynamical systems is much more complex than that for differential dynamical systems. The theory is also richer in another direction which we shall explore very briefly here. In terms of a given point mapping $\mathbf{G}$ the vector field $\mathbf{F}$ may be selected in a very general way, not just those possibilities discussed in Sections 4–6. Some of the more general ones may yield additional useful information while others may not. It is not easy to pursue this discussion in a general way. Let us simply take some specific vector fields and see what are the implications.

7.1 The Index of a Singular Point. Consider the index of a P-1 point $\mathbf{x}^*$ of $\mathbf{G}$. Let us take $\mathbf{F} = \mathbf{G} - \mathbf{I}$, take a very small circle around $\mathbf{x}^*$ as J, and calculate the change of the angle of the vector $\mathbf{F}$ along J in order to determine the index of $\mathbf{x}^*$. If it is -1 then the character of the P-1 point is as in the region above the line det $(\mathbf{H} - \mathbf{I}) = 0$ in Fig. 1. If $+1$, it is as in the region below the line. Next, we can choose $\mathbf{F} = \mathbf{G}^2 - \mathbf{I}$ and repeat the calculation. The new index will narrow further the region in Fig. 1 to which the P-1 point belongs. For example, if in both cases the index turns out to be $+1$ the character of the P-1 point is necessarily represented by a point located in the 90° sector to the right of point E. We can do yet a third calculation by taking $\mathbf{F} = \mathbf{G}^2 - \mathbf{G}$. One can readily show that the index of $\mathbf{x}^*$ with respect to $(\mathbf{G}^2 - \mathbf{G})$ is given by

$$I(\mathbf{x}^*, \mathbf{G}^2 - \mathbf{G}) = \begin{matrix} +1 \\ -1 \end{matrix} \quad \text{if} \quad B(1 - A + B) \gtrless 0. \quad (33)$$

This will give additional information on the character of the P-1 point. For example, if for the same P-1 point discussed in the foregoing the index from the third calculation is -1, then the P-1 point has to be represented by a point located in the triangular region with E, $(0, -1)$ and $(0, +1)$ as the vertices.

On course, it is not suggested here that the theory of index be used to determine the local geometric character of a P-1 point, because if $\mathbf{x}^*$ is known its geometric character can be easily ascertained by directly computing the matrix $\mathbf{H}(\mathbf{x}^*)$. The aforementioned discussion does, however, show the richness of the index theory on account of the freedom in selecting the vector field $\mathbf{F}$.

7.2 The Index of a Jordan Curve. The same freedom in selecting $\mathbf{F}$ is of course also available in establishing the global relations between a Jordan curve and the singular points contained in its interior. However, here one must take into account the possibility that a generalized vector field may introduce new kinds of singular points. For example, take $\mathbf{F} = \mathbf{G}^2 - \mathbf{G}$. Assuming $\mathbf{G}(\mathbf{O}) = \mathbf{O}$, the singular points of $\mathbf{F}$ now include two kinds: (i) all the P-1 points of $\mathbf{G}$, and (ii) all the points which **G** will map into one of the P-1 points. The index of the Jordan curve J will depend upon not only P-1 points but also points of the (ii) kind which are contained in its interior. Unless one is also interested in the points of the latter kind, the index of J will not have much meaning. On the other hand, if it is known that singular points of the (ii) kind do not exist either because the mapping is a diffeomorphism (one-to-one) or because of other reasons, then the use of this **F** might be advantageous because the singular points in the interior of J will still consist of only P-1 points and a different relation between the index and the P-1 points contained in the curve is now available.

The foregoing discussion indicates the vast possibilities by which one can apply the index theory to the global analysis. In this paper we shall not pursue this aspect further.

8 An Example of Application

It has been well recognized that a nonlinear point mapping dynamical system can have very complex global responses. To a large extent the global behavior of a system is controlled by the distribution of its periodic stable as well as unstable solutions in the state space. For strongly nonlinear systems the determination of these periodic solutions, which could be quite numerous in number, is however not a simple task even with the aid of a computer. Often it requires a very time-consuming systematic search throughout the state space. This task of search can be made considerably easier by utilizing the theory of index presented in this paper. The basic idea comes from the observation that if the Jordan curve J is varied in a systematic way, its index with respect to a vector field changes by +1 or −1 whenever J moves across a singular point of the field.

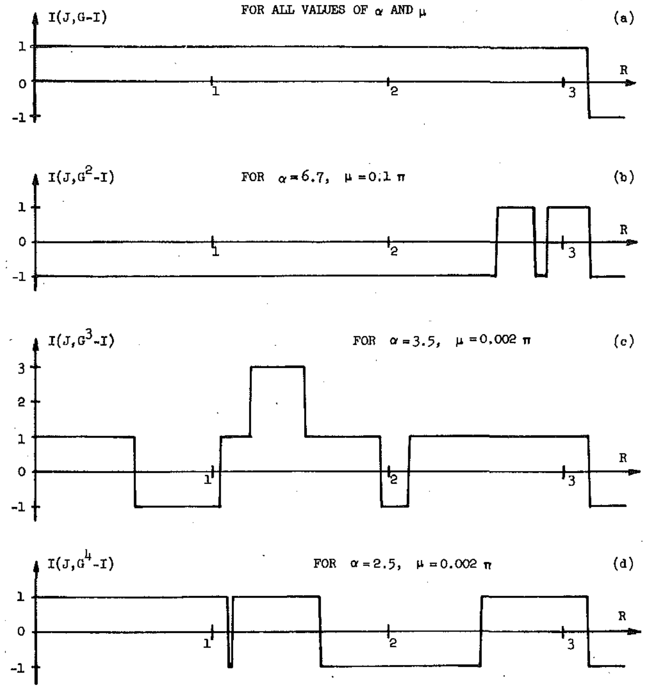

Fig. 2 Variation of I(J, F) with radius R for various values of α and μ

To illustrate such an application consider the nonlinear mechanical problem treated in [9]; namely, the vibration of a hinged bar subjected to a periodic impact load at the free end. The impact load is assumed to have a fixed direction. This problem, although nonlinear, permits integration of the equation over one period in a simple analytic form. This leads to an exact point mapping governing the dynamic behavior of the system. For a detailed discussion of this class of problems the reader is referred to [9]. Here let us just consider the case where the bar is elastically unrestrained but damping may be present. The mapping **G** is found to be

$$x_1(n+1) = x_1(n) - \frac{1-e^{-2\mu}}{2\mu}\alpha\sin x_1(n) + \frac{1-e^{-2\mu}}{2\mu}x_2(n)$$
$$x_2(n+1) = -e^{-2\mu}\alpha\sin x_1(n) + e^{-2\mu}x_2(n) \qquad (34)$$

where $x_1(n)$ is the angular displacement of the bar and $x_2(n)$ is essentially the angular velocity of the bar, both at the instant just before the application of each impact load, α is a parameter representing the magnitude of the load, and μ the damping magnitude.

This system in general has a large number of periodic solutions of various periods. To help locate the periodic points of **G** let us take J to be a circle centered at the origin of the (x_1, x_2) plane and of radius R. One can then easily compute the index of J with respect to any selected vector field **F** *according to Definition 1.*

To locate the P-1 points of **G** we take **F** = **G** − **I**. A straightforward computation shows that as R varies from 0.01 to 3.14 (in steps of 0.1 or 0.01 in actual computation) the index remains unchanged as shown in Fig. 2(a). This is true for all values of α and all values of μ. It confirms the analytic result that there is only one P-1 point at (0, 0) within the circle of radius $R < \pi$ around the origin. When R changes from 3.14 to 3.15 we find that the index is changed to −1. Hence, there must be new P-1 points in the annular region $3.14 < R < 3.15$ with a total sum of their indices equal to −2. Analytically one can easily confirm that there are one unstable P-1 point at $(\pi, 0)$ and one unstable P-1 point at $(-\pi, 0)$. Both have $\det(H - I) < 0$ and, therefore, have −1 as their indices. This picture of a jump by −2 units at $R = \pi$ is again true for all values of α and μ.

Consider an example of P-2 points. We take **F** = $\mathbf{G}^2$ − **I**. Again, take various R for the Jordan curve J. For $\alpha = 6.7$ and $\mu = 0.1\pi$ one finds the variation of $I(J, \mathbf{G}^2 - \mathbf{I})$ with R as shown in Fig. 2(b). Here the change of the index from +1 to −1 from $R = 3.14$ to $R = 3.15$ is again due to the presence of the P-1 points discussed in the last paragraph. Other changes of the index are however caused by P-2 points. According to the index theory, there are at least two P-2 points in each of the annular regions $2.61 < R < 2.62$, $2.83 < R < 2.84$, and $2.90 < R < 2.91$.

An example for P-3 points is taken for the case $\alpha = 3.5$ and $\mu = 0.002\pi$ and is shown in Fig. 2(c). Again, the index change from $R = 3.14$ to $R = 3.15$ is due to P-1 points. All other changes at six places are caused by the P-3 points. According to the index theory, there are at least two P-3 points in each of the following annular regions: $0.55 < R < 0.56$, $1.04 < R < 1.05$, $1.21 < R < 1.22$, $1.52 < R < 1.53$, $1.95 < R < 1.96$, $2.11 < R < 2.12$.

The last example shown in Fig. 2(d) is for P-4 points and is for the case $\alpha = 2.5$ and $\mu = 0.002\pi$. Besides the index change at $R = \pi$ due to P-1 points, there are changes at four other places. For this case a computation with respect to $\mathbf{G}^2$ − **I** shows that there are no P-2 points in the range of R shown. Therefore, the four index changes are all caused by P-4 points. According to the index theory, there are at least two P-4 points in each of the following annular regions: $1.09 < R < 1.10$, $1.11 < R < 1.12$, $1.61 < R < 1.62$, $2.52 < R < 2.53$.

These examples show searching by expanding a circle. It is a one-dimensional radial search. One can, of course, also search in the x_1 and/or x_2-directions. No general purpose is served with additional examples. The potential use of the theory of index in this direction is clear.

Acknowledgments

The results presented here were obtained in the course of research supported by a grant from the National Science Foundation.

References

1 Poincaré, H., "Sur les courbes définies par les équations différentielles," *J. Math. Pure Appl.*, Series (3), Vol. 7, 1881, pp. 375–422.

2 Birkhoff, G. D., "Surface Transformations and Their Dynamical Applications," *Acta Mathematics*, Vol. 43, 1920, pp. 1–119.

3 Arnol'd, V. I., "Small Denominators and Problems of Stability of Motion in Classical and Celestial Mechanics," *Russian Mathematical Surveys*, Vol. 18, 1963, pp. 85–191.

4 Smale, S., "Differentiable Dynamical Systems," *Bulletins of the American Mathematical Society*, Vol. 73, 1967, pp. 747–817.

5 Markus, L., *Lectures on Differentiable Dynamics*, Regional Conference

Series in Mathematics, No. 3, American Mathematical Society, Providence, R.I., 1971.
6 Takens, F., *Introduction to Global Analysis,* Communications of the Mathematical Institute, Rijksuniversiteit Utrecht, 1973.
7 Marsden, J. E., and McCracken, M., *The Hopf Bifurcation and Its Applications,* Springer-Verlag, New York, 1976.
8 Hsu, C. S., Yee, H. C., and Cheng, W. H., "Determination of Global Regions of Asymptotic Stability for Difference Dynamical Systems," ASME JOURNAL OF APPLIED MECHANICS, Vol. 44, 1977, pp. 147–153.
9 Hsu, C. S., Yee, H. C., and Cheng, W. H., "Steady-State Response of a Nonlinear System Under Impulsive Periodic Parametric Excitation," *Journal of Sound and Vibration,* Vol. 50, 1977, pp. 95–116.
10 Hsu, C. S., "Bifurcation in the Theory of Nonlinear Difference Dynamical Systems," *Melanges,* a volume in honor of Dr. Th. Vogel, Ed., Rybak, B., Janssens, P., and Jessel, M., 1978, pp. 195–206.
11 Hsu, C. S., "On Nonlinear Parametric Excitation Problems," *Advances in Applied Mechanics,* Vol. 17, 1977, pp. 245–301.
12 Hsu, C. S., "Nonlinear Behavior of Multibody Systems Under Impulsive Parametric Excitation," *Dynamics of Multibody Systems,* Ed. Magnus, K., Springer-Verlag, *Proceedings of the IUTAM Symposium on Dynamics of Multibody Systems,* held in Munich, Germany, August 29–September 3, 1977, pp. 63–74.
13 Bernussou, J., *Point Mapping Stability,* Pergamon Press, 1977.
14 Levinson, N., "Transformation Theory of Nonlinear Differential Equations of the Second Order," *Annals of Mathematics,* Vol. 45, 1944, pp. 723–737; also, a Correction, *Annals of Mathematics,* Vol. 49, 1948, p. 738.
15 Coddington, E. A., and Levinson, N., *Theory of Ordinary Differential Equations,* McGraw-Hill, New York, 1955.
16 Minorsky, N., *Nonlinear Oscillations,* D. Van Nostrand Company, Princeton, N.J., 1962.

Journal of Applied Mechanics

Brief Notes

A Brief Note is a short paper which presents a specific solution of technical interest in mechanics but which does not necessarily contain new general methods or results. A Brief Note should not exceed 1500 words *or equivalent* (a typical one-column figure or table is equivalent to 250 words; a one line equation to 30 words). Brief Notes will be subject to the usual review procedures prior to publication. After approval such Notes will be published as soon as possible. The Notes should be submitted to the Technical Editor of the JOURNAL OF APPLIED MECHANICS. Discussions on the Brief Notes should be addressed to the Editorial Department, ASME, United Engineering Center, 345 East 47th Street, New York, N. Y. 10017, or to the Technical Editor of the JOURNAL OF APPLIED MECHANICS. *Discussions on Brief Notes appearing in this issue will be accepted* until two months after publication. Readers who need more time to prepare a Discussion should request an extension of the deadline from the Editorial Department.

A Note on the Behavior of Plates on an Elastic Foundation

R. Jones[1] and J. Mazumdar[2]

Introduction

Numerous attempts have been made in the past to describe the behavior of plates on an elastic or viscoelastic foundation. A survey of available literature has recently been given in an excellent paper by Kerr [1] where various models currently used in the literature are discussed in detail. However, all these models correspond to a frictionless plate foundation interface.

In the present Note, a variational approach is used to examine the behavior of plates on an elastic foundation allowing for friction at the plate-foundation interface. The approach is a generalization of Vlasov's technique and reduces to the Vlasov and Pasternak foundation models in the case of a frictionless plate-foundation interface.

Analysis

Consider an elastic foundation of thickness H, Young's modulus E_s, and Poisson's ratio ν_s, resting on a rigid base. A plate of flexural rigidity D, Young's modulus E_p, Poisson's ratio ν_p and thickness h, lies on the upper surface of this foundation, and is subject to a vertical load $q(x,y)$ as shown in Fig. 1. Taking the oxy plane at the upper surface with the z-axis directed positively downward, we assume that the interface conditions can be written as

$$\left.\begin{aligned} u &= \frac{\beta h}{2}\frac{\partial w}{\partial x} \\ v &= \frac{\beta h}{2}\frac{\partial w}{\partial y} \end{aligned}\right\} \text{ on } z = 0 \qquad (1)$$

where β is a constant whose value lies between 0 and 1 and in fact, depends on the coefficient of friction at the interface. Here u, v, and w are the displacement components in the x, y, and z-directions, respectively. In the case of a frictionless boundary we have $\beta = 0$. We further assume that the horizontal and vertical deformations may be expressed in the form

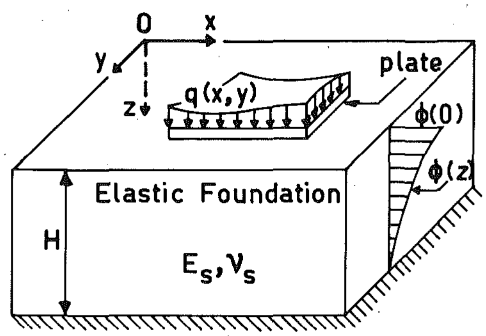

Fig. 1 Plate resting on an elastic foundation

$$\begin{aligned} u(x,y,z) &= U(x,y)\psi(z) \\ v(x,y,z) &= V(x,y)\psi(z) \\ w(x,y,z) &= W(x,y)\varphi(z) \end{aligned} \qquad (2)$$

where $U(x,y)$, $V(x,y)$, $W(x,y)$ represent the movements at the foundations upper surface and $\varphi(z)$, $\psi(z)$ are functions of the vertical distribution of the displacements, chosen in accordance with the nature of the problem. Clearly both $\psi(z)$ and $\varphi(z)$ have the value unity on the surface $z = 0$. Based upon experimental evidence, the function $\varphi(z)$ was chosen by Vlasov [2] in the form

$$\varphi(z) = \sin h[\gamma(H - z)]/\sin h\gamma H \qquad (3)$$

where γ is an experimental constant determining the variation, with depth, of the vertical displacements. This form for φ has subsequently been theoretically justified [3]. In Vlasov's original work, because there was no horizontal loading, the horizontal displacements $U(x,y)$, $V(x,y)$ were considered negligible in comparison with the vertical displacement and did not enter into the subsequent analysis. This will not be the case in the present analysis as the horizontal displacements are no longer negligible. Indeed substituting for U or V, as given by equation (1), into equation (2), we obtain

$$\begin{aligned} u(x,y,z) &= \frac{\beta h}{2}\frac{\partial w}{\partial x}\psi(z) \\ v(x,y,z) &= \frac{\beta h}{2}\frac{\partial w}{\partial y}\psi(z) \end{aligned} \qquad (4)$$

and $u = v = 0$ outside the region vertically below the slab. Under these assumptions the strain energy of the foundation is given by

[1] Department of Structure, Aeronautical Research Laboratory, Melbourne, Australia; formerly, Department of Applied Mathematics, The University of Adelaide, Adelaide, South Australia 5001.

[2] Department of Applied Mathematics, The University of Adelaide, Adelaide, South Australia 5001.

Manuscript received by ASME Applied Mechanics Division, January, 1979; final revision, July, 1979.

$$\forall = ½\iiint \left[\frac{E}{1-\nu^2}\left\{W^2\left(\frac{d\varphi}{dz}\right)^2 + \nu h\beta\frac{d\varphi}{dz}\varphi W\nabla^2 W + \frac{h^2\beta^2\psi^2}{4}\left(\nabla^2 W)^2 - 2(1-\nu)\left[\frac{\partial^2 W}{\partial x^2}\frac{\partial^2 W}{\partial y^2} - \left(\frac{\partial^2 W}{\partial x\partial y}\right)^2\right]\right)\right\} + \frac{E}{2(1+\nu)}\left[\varphi + \frac{h\beta}{2}\frac{d\psi}{dz}\right]^2\left(\left(\frac{\partial W}{\partial x}\right)^2 + \left(\frac{\partial W}{\partial y}\right)^2\right)\right] dxdydz \quad (5)$$

where E and ν are related to the Young's modulus E_s and the Poisson's ratio ν_s of the foundation by

$$E = \frac{E_s}{1-\nu_s{}^2}, \quad \nu = \frac{\nu_s}{1-\nu}. \quad (6)$$

Here the volume integration is over the entire volume of the foundation. Of course, β vanishes outside the region of the plate. The requirement that the total potential energy π is minimized, now yields

$$\delta\pi = \delta(\forall - \iint Wq dxdy) = 0, \quad (7)$$

which leads to the following partial differential equation:

$$D^*\nabla^4 W + kW - 2t^*\nabla^2 W = q(x,y), \quad (8)$$

where

$$D^* = \frac{Eh^2\beta^2}{4(1-\nu^2)}\int_0^H \psi^2 dz, \quad k = \frac{E}{1-\nu^2}\int_0^H \left(\frac{d\varphi}{dz}\right)^2 dz,$$

$$t^* = \frac{E}{4(1+\nu)}\int_0^H \left[\varphi + \frac{\beta h}{2}\frac{d\psi}{dz}\right]^2 dz + \frac{\nu h E\beta}{2(1-\nu^2)}\int_0^H \psi\frac{d\varphi}{dz}dz \quad (9)$$

Clearly, for $\beta = 0$ (the case of frictionless plate-foundation interface), we obtain the usual two parameter foundation model [4]

$$kW - 2t\nabla^2 W = q(x,y) \quad (10)$$

where

$$t = \frac{E}{4(1+\nu)}\int_0^H \varphi^2 dz \quad (11)$$

Both models, as given by equations (8) and (10) have the same value for k, which characterizes the compressive strain in the foundation and is equivalent to a Winkler spring constant (or modulus of subgrade reaction). However, the shear strain parameters t and t^* are different in those two models. Clearly, for $\beta \neq 0$ the rigidity coefficient D^* is a nonzero quantity. In the case of a relatively thin foundation, we may proceed, as in [2], by assuming a linear form for the vertical distribution of the displacements in the foundation, given by

$$\psi = \varphi = \frac{H-z}{H} \quad (12)$$

so that we obtain

$$D^* = \frac{Eh^2\beta^2 H}{12(1-\nu^2)},$$

$$t^* = \frac{EH}{12(1+\nu)}\left[\left(1-\frac{\beta h}{H}\right)^3 + \frac{\beta^3 h^3}{H} - \frac{3\nu\beta h}{H(1+\nu)}\right] \quad (13)$$

$$k = \frac{E}{H(1-\nu^2)},$$

$$t = \frac{EH}{12(1+\nu)}$$

Clearly, when the ratio $h/H \ll 1$ which is the case in most engineering situations even for thin foundations we have from the foregoing relationship

$$t^* \approx t \quad (14)$$

Thus the foundation modulus t^* and k remain effectively unaltered for $\beta \neq 0$.

Let us now consider the other extreme case—an infinitely deep foundation. In this case, we take the depth profile functions ψ and φ in accordance with [2] as

$$\psi = e^{-\gamma_1/az}$$
$$\varphi = e^{-\gamma_2/az} \quad (15)$$

where a is a dimensional parameter of the plate and γ_1,γ_2 are experimental constants. In this case

$$D^* = \frac{Eh^2\beta^2 a}{8(1-\nu^2)\gamma_2}$$

$$t^* = \frac{Ea}{8(1+\nu)\gamma_2}\left[1 - \frac{\gamma_1{}^2\beta}{(\gamma_1+\gamma_2)}\frac{h}{a} + \frac{\beta^2\gamma_1{}^2}{4}\frac{h^2}{a^2} - \frac{4\nu\gamma_1\gamma_2\beta}{(1-\nu)}\frac{h}{a}\right],$$

$$k = \frac{E\gamma_2}{(1-\nu^2)2a},$$

$$t = \frac{Ea}{8(1+\nu)\gamma_2} \quad (16)$$

For a thin plate, this again yields $t^* \approx t$ so that as in the case of a thin foundation the modulii t^* and k are relatively unaffected. We thus see that in the case of both a thin and an infinitely deep foundation the major effect of $\beta \neq 0$ is only on the rigidity of the plate. Other parameters remain approximately the same.

We thus see that the response of a plate on an elastic foundation, with an arbitrary plate-foundation boundary condition, may be modeled using existing computer programs and analysis by simply modifying the rigidity of the plate, i.e., altering it from D to $(D + D^*)$. The only additional experimental quantity required is the parameter β at the interface.

Acknowledgments

The authors wish to acknowledge the financial support of the Australian Research Grant Committee to carry out this investigation at the University of Adelaide. The technical assistance of the Metallurgy, Mechanics and Materials Science Department of Michigan State University during the preparation of the manuscript while the second author is on study leave is also gratefully acknowledged.

References

1 Kerr, A. D., "Elastic and Viscoelastic Foundation Models," ASME JOURNAL OF APPLIED MECHANICS, Vol. 31, 1964, pp. 491–498.

2 Vlasov, V. Z., and Leontev, N. N., "Beams, Plates, Shells on Elastic Foundations," (translated from Russian), Israel Program for Scientific Translations; available from the Clearinghouse of U.S. Department of Commerce, 1966.

3 Jones, R., and Xenophontas, J., "The Vlasov Foundation Model," *International Journal of Mechanical Sciences*, Vol. 19, 1977, pp. 317–323.

4 Pasternak, P. L., "Fundamentals of a New Method of Analysis of an Elastic Foundation by Means of Two Foundation Constants," (in Russian), *Gosuedarstvennoe Izdatelstvo Literaturi po Stroitelstvu i Arkhitekture*, Moscow, 1954.

Effects of Strain-Hardening on Dynamic Responses of Elastic/Viscoplastic Frames

R. C. Shieh[1]

In a recent study by the author [1], analytical techniques (computerized) applicable to the dynamic analysis of elastic/perfectly viscoplastic plane frames were developed and an experimental verification study was made. The latter revealed some discrepancies between the analytical and experimental results primarily due to neglect

[1] Transportation Branch, U.S. Nuclear Regulatory Commission, Washington, D.C. 20555.

Manuscript received by ASME Applied Mechanics Division, March, 1979; final revision, July, 1979.

$$\forall = \tfrac{1}{2}\int\int\int\left[\frac{E}{1-\nu^2}\left\{W^2\left(\frac{d\varphi}{dz}\right)^2 + \nu h\beta\frac{d\varphi}{dz}\varphi W\nabla^2 W + \frac{h^2\beta^2\psi^2}{4}\left((\nabla^2 W)^2 - 2(1-\nu)\left[\frac{\partial^2 W}{\partial x^2}\frac{\partial^2 W}{\partial y^2} - \left(\frac{\partial^2 W}{\partial x\partial y}\right)^2\right]\right)\right\} + \frac{E}{2(1+\nu)}\left[\varphi + \frac{h\beta}{2}\frac{d\psi}{dz}\right]^2\left(\left(\frac{\partial W}{\partial x}\right)^2 + \left(\frac{\partial W}{\partial y}\right)^2\right)\right] dxdydz \quad (5)$$

where E and ν are related to the Young's modulus E_s and the Poisson's ratio ν_s of the foundation by

$$E = \frac{E_s}{1-\nu_s{}^2}, \quad \nu = \frac{\nu_s}{1-\nu}. \quad (6)$$

Here the volume integration is over the entire volume of the foundation. Of course, β vanishes outside the region of the plate. The requirement that the total potential energy π is minimized, now yields

$$\delta\pi = \delta(\forall - \int\int Wq dxdy) = 0, \quad (7)$$

which leads to the following partial differential equation:

$$D^*\nabla^4 W + kW - 2t^*\nabla^2 W = q(x,y), \quad (8)$$

where

$$D^* = \frac{Eh^2\beta^2}{4(1-\nu^2)}\int_0^H \psi^2 dz, \quad k = \frac{E}{1-\nu^2}\int_0^H \left(\frac{d\varphi}{dz}\right)^2 dz,$$

$$t^* = \frac{E}{4(1+\nu)}\int_0^H\left[\varphi + \frac{\beta h}{2}\frac{d\psi}{dz}\right]^2 dz + \frac{\nu h E\beta}{2(1-\nu^2)}\int_0^H \psi\frac{d\varphi}{dz}dz \quad (9)$$

Clearly, for $\beta = 0$ (the case of frictionless plate-foundation interface), we obtain the usual two parameter foundation model [4]

$$kW - 2t\nabla^2 W = q(x,y) \quad (10)$$

where

$$t = \frac{E}{4(1+\nu)}\int_0^H \varphi^2 dz \quad (11)$$

Both models, as given by equations (8) and (10) have the same value for k, which characterizes the compressive strain in the foundation and is equivalent to a Winkler spring constant (or modulus of subgrade reaction). However, the shear strain parameters t and t^* are different in those two models. Clearly, for $\beta \neq 0$ the rigidity coefficient D^* is a nonzero quantity. In the case of a relatively thin foundation, we may proceed, as in [2], by assuming a linear form for the vertical distribution of the displacements in the foundation, given by

$$\psi = \varphi = \frac{H-z}{H} \quad (12)$$

so that we obtain

$$D^* = \frac{Eh^2\beta^2 H}{12(1-\nu^2)},$$

$$t^* = \frac{EH}{12(1+\nu)}\left[\left(1 - \frac{\beta h}{H}\right)^3 + \frac{\beta^3 h^3}{H} - \frac{3\nu\beta h}{H(1+\nu)}\right] \quad (13)$$

$$k = \frac{E}{H(1-\nu^2)},$$

$$t = \frac{EH}{12(1+\nu)}$$

Clearly, when the ratio $h/H \ll 1$ which is the case in most engineering situations even for thin foundations we have from the foregoing relationship

$$t^* \approx t \quad (14)$$

Thus the foundation modulus t^* and k remain effectively unaltered for $\beta \neq 0$.

Let us now consider the other extreme case—an infinitely deep foundation. In this case, we take the depth profile functions ψ and φ in accordance with [2] as

$$\psi = e^{-\gamma_1/az}$$
$$\varphi = e^{-\gamma_2/az} \quad (15)$$

where a is a dimensional parameter of the plate and γ_1, γ_2 are experimental constants. In this case

$$D^* = \frac{Eh^2\beta^2 a}{8(1-\nu^2)\gamma_2}$$

$$t^* = \frac{Ea}{8(1+\nu)\gamma_2}\left[1 - \frac{\gamma_1{}^2\beta}{(\gamma_1+\gamma_2)}\frac{h}{a} + \frac{\beta^2\gamma_1{}^2}{4}\frac{h^2}{a^2} - \frac{4\nu\gamma_1\gamma_2\beta}{(1-\nu)}\frac{h}{a}\right],$$

$$k = \frac{E\gamma_2}{(1-\nu^2)2a},$$

$$t = \frac{Ea}{8(1+\nu)\gamma_2} \quad (16)$$

For a thin plate, this again yields $t^* \approx t$ so that as in the case of a thin foundation the modulii t^* and k are relatively unaffected. We thus see that in the case of both a thin and an infinitely deep foundation the major effect of $\beta \neq 0$ is only on the rigidity of the plate. Other parameters remain approximately the same.

We thus see that the response of a plate on an elastic foundation, with an arbitrary plate-foundation boundary condition, may be modeled using existing computer programs and analysis by simply modifying the rigidity of the plate, i.e., altering it from D to $(D + D^*)$. The only additional experimental quantity required is the parameter β at the interface.

Acknowledgments

The authors wish to acknowledge the financial support of the Australian Research Grant Committee to carry out this investigation at the University of Adelaide. The technical assistance of the Metallurgy, Mechanics and Materials Science Department of Michigan State University during the preparation of the manuscript while the second author is on study leave is also gratefully acknowledged.

References

1 Kerr, A. D., "Elastic and Viscoelastic Foundation Models," ASME JOURNAL OF APPLIED MECHANICS, Vol. 31, 1964, pp. 491–498.

2 Vlasov, V. Z., and Leontev, N. N., "Beams, Plates, Shells on Elastic Foundations," (translated from Russian), Israel Program for Scientific Translations; available from the Clearinghouse of U.S. Department of Commerce, 1966.

3 Jones, R., and Xenophontas, J., "The Vlasov Foundation Model," *International Journal of Mechanical Sciences*, Vol. 19, 1977, pp. 317–323.

4 Pasternak, P. L., "Fundamentals of a New Method of Analysis of an Elastic Foundation by Means of Two Foundation Constants," (in Russian), *Gosuedarstvennoe Izdatelstvo Literaturi po Stroitelstvu i Arkhitekture*, Moscow, 1954.

Effects of Strain-Hardening on Dynamic Responses of Elastic/Viscoplastic Frames

R. C. Shieh[1]

In a recent study by the author [1], analytical techniques (computerized) applicable to the dynamic analysis of elastic/perfectly viscoplastic plane frames were developed and an experimental verification study was made. The latter revealed some discrepancies between the analytical and experimental results primarily due to neglect

[1] Transportation Branch, U.S. Nuclear Regulatory Commission, Washington, D.C. 20555.

Manuscript received by ASME Applied Mechanics Division, March, 1979; final revision, July, 1979.

of material strain-hardening effects in the analysis. The present study extends the previous study to include such effects in the analysis and obtains excellent analytical/experimental correlation results.

Consider a mass-less beam element of length l, cross-sectional area A, and second moment of inertia I. In terms of stress resultants (bending moment M and axial force N) and strain resultants (curvature K and centroidal axial strain ϵ), the constitutive equation similar to that of Malvern's [2] can be written as

$$\dot{K} = \frac{\dot{M}}{EI} + \left(\frac{M - M_s}{DI^*}\right)^n; M_s = M_0 + EI\eta\left(K - \frac{M_0}{EI}\right)$$
$$\dot{\epsilon} = \frac{\dot{N}}{EA} + \left(\frac{N - N_s}{DA}\right)^n; N_s = N_0 + EA\eta\left(\epsilon - \frac{N_0}{EA}\right) \qquad (1)$$

in which the effect of bending moment/axial force interaction on inelastic deformation has been neglected. In equation (1), $\hat{M} \equiv M - M_s = 0$ if $|\hat{M}| \leq |M_s|$ and $\hat{N} \equiv N - N_s = 0$ if $|N| \leq |N_s|$; M_0 and N_0, the static yield moment and axial force, respectively, E the Young's modulus, and n and D are the material strain-rate-sensitivity constants, η the strain-hardening parameter, the dots indicate material time derivatives, and

$$I^* = \int_A y^{(n+1)/n} dA \qquad (2)$$

Within the context of elementary beam theory, the beam element end force-deformation ($\{S\} - \{e\}$) relationships for the elastic/perfectly viscoplastic case ($\eta = 0$) have been obtained in [1] as

$$\{\dot{S}\} + [H][\beta]\{\dot{\chi}_p\} = [G]\{\dot{e}\} \qquad (3)$$

Here, the components S_i, e_i are the bending ($i = 1, 2$) and axial ($i = 3$) components of the vectors $\{S\}$ and $\{e\}$, respectively, (with clockwise and tensile components regarded positive) and $\{\chi_p\}$ the corresponding plastic parts of the end strain resultant vector $\{\chi\}$, the matrices $[G]$, $[\beta]$, and $[H]$ are given by

$$[G] = \begin{bmatrix} [G_M] & \{0\} \\ [0] & \alpha_N/l \end{bmatrix}, \quad [H] = \begin{bmatrix} [H_M] & \{0\} \\ [0] & \mu_N \end{bmatrix},$$

$$[G_M] = \frac{2\alpha_M}{l}\begin{bmatrix} 2 & 1 \\ 1 & 2 \end{bmatrix}, \qquad [\beta] = \begin{bmatrix} \beta_M & 0 & 0 \\ 0 & \beta_M & 0 \\ 0 & 0 & \beta_N \end{bmatrix}$$

$$[H_M] = \frac{2\mu_M}{n+1}\begin{bmatrix} \xi_1[2 - 3\xi_1/(n+2)], & \xi_2[1 - 3\xi_2/(n+2)] \\ \xi_1[1 - 3\xi_1/(n+2)], & \xi_2[2 - 3\xi_2/(n+2)] \end{bmatrix} \quad \text{if} \quad S_1 + S_2 \neq 0$$
$$= \mu_M \begin{bmatrix} 1 & 0 \\ 0 & 1 \end{bmatrix} \quad \text{if} \quad S_1 + S_2 = 0 \qquad (4)$$

Here, $\mu_i = \alpha_i/\beta_i$ ($i = M, N$), $\alpha_M = EI$, $\alpha_N = EA$, $\beta_M = (DI^*)^n$, and $\beta_N = (DA)^n$, and $\xi_i l$ for $0 \leq \xi_i \leq 1$ ($i = 1, 2$) are the ith end inelastic zone spreading lengths.

In the presence of strain-hardening ($\eta \neq 0$), the force-deformation equations are approximately given by equation (3) with $\{\dot{\chi}_p\}$ given by (cf., equation (1)):

$$\{\dot{\chi}_p\} = [\beta]^{-1}\{\hat{S}^n\}(\{\hat{S}^n\} = \{\hat{S}_1{}^n, \hat{S}_2{}^n, \hat{S}_3{}^n\}) \qquad (5a)$$

$$\{\dot{\chi}\} = [\alpha]^{-1}\{\dot{S}\} + [\beta]^{-1}\{\hat{S}^n\} \qquad (5b)$$

that is,

$$\{\dot{S}\} + [H]\{\hat{S}^n\} = [G]\{\dot{e}\}(\eta \neq 0) \qquad (6)$$

where $[\alpha]$ is a (3×3) diagonal matrix whose diagonal elements are EI, EI, EA, and $\hat{S}_i = S_i - S_i{}^s$ ($S_i{}^s$ = static parts of S_i). In view of equation (1),

$$\{\hat{S}\} = \{S\} - \{S^s\}, \quad \{S^s\} = \eta[\alpha]\{\chi\} + (1 - \eta)\{S_0\}$$

where $\{S_0\}$ is the static yield stress resultant vector. The parameters ξ_i for the case of entire beam element being in inelastic state now are given by

$$\xi_i = \hat{S}_i/(\hat{S}_1 + \hat{S}_2) \quad (i = 1, 2) \qquad (7)$$

and for the other cases (partially elastic and partially inelastic) determined from

$$M(z_i, t) = [S_i - (S_1 + S_2)z_i/l](-1)^{i+1} = M_s(z_i, t) \quad (i = 1, 2) \qquad (8a)$$

where $z_1 = \xi_1 l$ and $z_2 = (1 - \xi_2)l$. Under the assumption of linear distribution of $M_s(x, t)$, it can be shown that

$$\dot{\xi}_i(t) = (1 - \eta)[\dot{S}_i - (\dot{S}_1 + \dot{S}_2)\xi_i]\xi_i/\hat{S}_i \qquad (8b)$$

if the ith end, inelastic zone is contracting.

In the case that the ith end elastic-plastic zone is expanding, ξ_i can be approximately determined from equation (8a) by approximating $M_s(x, t)$ at any instant t with a piecewise linear function of x; the corner points of the piecewise linear function are located at both ends of beam element and the maximum plastic zone penetration fronts experienced by the beam element up to current time, t.

It is interesting to note that the bending parts of the end, force-deformation equations, equation (6), can also be obtained from the assumption of linear variation of M_s in x within an end inelastic zone, relationship $M = S_1 - (S_1 + S_2)x/l$ and the complementary energy-type variational equation

$$\dot{e}_1\delta S_1 + \dot{e}_2\delta S_2 = \int_0^l \frac{\dot{M}}{EI}\delta M dx + \int_0^{\xi_1 l}(\hat{M}/DI^*)^n \delta M dx + \int_{(1-\xi_2)l}^l (\hat{M}/DI^*)^n \delta M dx$$

in M, i.e., $\delta M = \delta S_1 - (\delta S_1 + \delta S_2)x/l$.

It should be noted that the end, force-deformation equations just derived can be apparently used in a general plane frame analysis in which axial force/bending moment interaction effects are negligible. This is because as the number of beam elements used in discretizing the frame increases, the M_s function of x would approach to a linear one and inelastic zone status within each beam element would approach closer to the one with two or fewer end inelastic zones.

The equations of motion for a plane frame undergoing arbitrarily large joint displacements $\{u\}$ and composed of n_B-beam elements can be written as [1]

$$[\rho]\{\ddot{u}\} + \sum_{j=1}^{n_B} [B]_j{}^T\{S\}_j = \{P(t)\} \qquad (9)$$

where subscript "j" stands for jth beam element, $[\rho]$ is the diagonal mass matrix, $\{P(t)\}$ (which may also be a function of $\{u\}$), the prescribed joint force vector, $[B(\{u\})]_j$ the jth beam element compatibility matrix associated with the joint displacements,

$$\{\dot{e}\}_j = [B]_j\{\dot{u}\} \qquad (10)$$

Equations (5)–(10), together with the following initial conditions, can be used to solve $\{u\}$, $\{S\}_i$, and $\{\chi\}_i$ simultaneously

$$\{u\} = \{u(t_r - 0)\}, \quad \{\dot{u}\} = \{\dot{u}(t_r - 0)\}, \quad \{S\}_i = \{S(t_r - 0)\}_i, \quad \{S^s\}_i = \{S^s(t_r - 0)\}_i,$$
$$\{\xi\}_i = \{\xi(t_r - 0)\}_i, \quad \{\chi\}_i = \{\chi(t_r - 0)\}_i \quad \text{at} \quad t = t_r + 0 \; (i = 1, 2, \ldots, n_B) \qquad (11)$$

where $\{u(t_r - 0)\}$, $\{S(t_r - 0)\}_i, \ldots$ were computed from the preceding time step of integration (from $t = t_{r-1}$ to $t = t_r$) if subscript $r \geq 1$ and prescribed if $r = 0$.

The foregoing solution procedure has been implemented in the previously developed general purpose computer code "RATE" [1], which is designated as RATE 2. Numerical verifications of the computer program and analytical predictive techniques have been made by comparing the RATE 2 results with the existing solution results

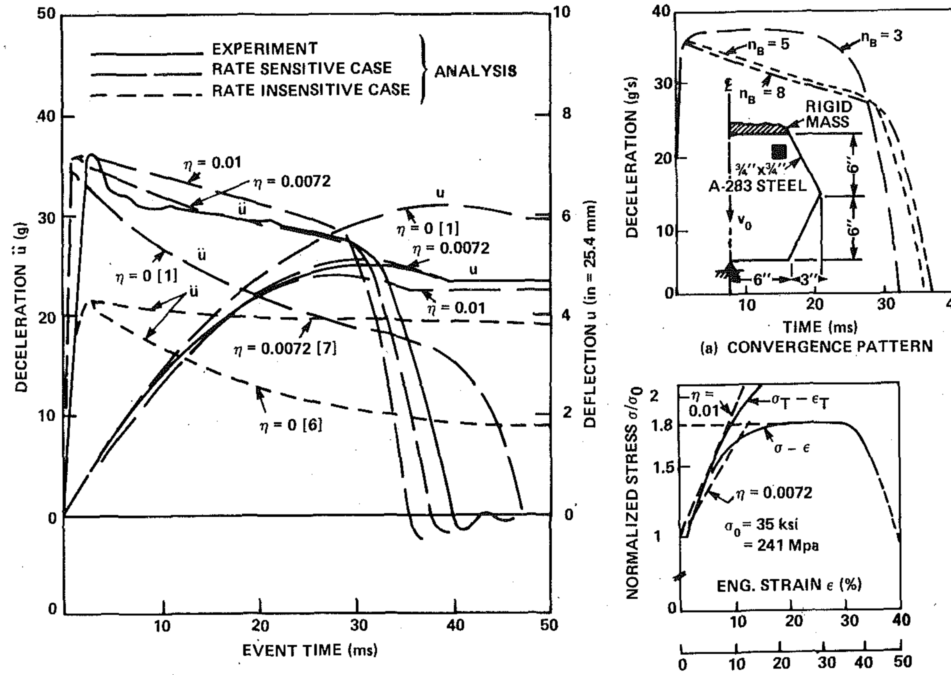

(b) ANALYTICAL/EXPERIMENTAL GUIDING MASS ACCELERATION ü AND DEFLECTION RESULTS u

(c) STATIC STRESS-STRAIN RELATIONS

Fig. 1 Drop impact responses of a mild steel frame at V_0 = 20 mph (32.18 Km/hr)

(for linear power law case) [5] and experimental frame drop impact response results (reported below) with satisfactory results.

In a laboratory test, a hexagonal plane frame carrying a heavy rear mass with total weight $W = 116.5$ lb (52.955 Kg) was drop-impacted onto a narrow stiff pole obstacle at $v_0 = 20$ mph (32 km/hr) in a nearly symmetrical manner.

Fig. 1(a) shows the numerical convergence pattern of mass deceleration/time history versus number of beam elements (n_B) used in discretizing the frame structure. A similar numerical convergence study was made to determine appropriate integration step size Δt = 0.1 ms. The material constants used in the analysis were: $E = 30 \times 10^3$ ksi (206.85 Gpa), σ_0 = static yield stress = 35 ksi (241.325 Mpa), η = 0.0072, $D^* = (\sigma_0/D)^n = 40.4\ \mathrm{s}^{-1}$, and $n = 5$ [3]. Rapid convergence of the numerical solution is seen.

The analytical and experimental results for mass acceleration and displacement using the foregoing material constants are shown in Fig. 1(b) for η = 0.01 and 0.0072 cases. Comparison of the analytical/experimental results shows that use of strain-hardening parameter value of $\eta = 0.01$ gives somewhat (less than 10 percent) stiffer dynamic acceleration and displacement responses than the actually measured ones, while use of $\eta = 0.0072$ gives a better (excellent) correlation result. This is because, for mild steel, coupon test results show that the degree of strain-hardening decreases with increase in strain rate [4] and $\eta = 0.01$ represents the absolute maximum value of η (based on the true stress/true strain curve in Fig. 1(c)) even for the static case. Also shown in Fig. 1(b) for comparison purposes are the corresponding dynamic response results for various special cases in which either strain-hardening or strain rate or both effects are absent [1, 6, 7]. Strain rate effects are seen to be very important under the impact loading, while strain-hardening effects are seen to become increasingly important as deformation becomes larger and larger.

Finally, it should be noted that the computerized study developed herein can also be used to predict buckling or parametric resonance behavior (through use of the exact nonlinear compatibility matrices $[B]_j$ in equations (9) and (10) to the extent that the assumption of negligibly small axial force/bending moment interaction effects on inelastic deformation as well as the other assumptions of the study is valid.

References

1 Shieh, R. C., "Large Displacement Matrix Analysis of Elastic/Viscoplastic Plane Frame Structures," ASME *Journal of Engineering for Industry*, Vol. 79, Nov. 1975, pp. 1238–1244.

2 Malvern, L., "The Propagation of Longitudinal Waves of Plastic Deformation in a Bar of Material Exhibiting a Strain-Rate Effect," ASME JOURNAL OF APPLIED MECHANICS, Vol. 18, 1951, pp. 203–208.

3 Cowper, G., and Symonds, P., "Strain-Hardening and Strain-Rate Effects in the Impact Loading of Cantilever Beams," Technical Report No. 28, Brown University, Providence, R.I., Sept. 1957.

4 Manjoine, M., "Influence of Rate of Strain and Temperature on Yield Stresses of Mild Steel," ASME JOURNAL OF APPLIED MECHANICS, Vol. 11, 1944, p. A-211.

5 Weiss, R., and Neubert, V., "Theoretical Dynamic Response of an Elastic-Viscoplastic Cantilever Beam," Progress Report No. 5, N00014-67-A-0385-0010, Department of Engineering Mechanics, Pennsylvania State University, College Park, Pa., June 1974.

6 Shieh, R. C., "Basic Research in Crashworthiness II—Experimental Validation Study of the Analytical Predictive Techniques for the Large Deflection Dynamic Analysis of Plane Elasto-Plastic Frame Structures," Calspan Report No. YB-2987-V, May 1973.

7 Shieh, R. C., "Exploratory Study of the Dynamic Response of Building Structures Subjected to Strong Earthquake Loadings," Calspan Report No. HH-5384-V-1, June 1975.

Analytic Approximations for the Elastic Contact of Rough Spheres

B. D. Hughes[1] and L. R. White[2]

The basic equations of a model of Greenwood and Tripp for contact

[1] Research Student, Department of Applied Mathematics, Research School of Physical Sciences, Australian National University, Canberra, Australia 2600.

[2] Post-Doctoral Fellow, Department of Applied Mathematics, Research School of Physical Sciences, Australian National University, Canberra, Australia 2600.

Manuscript received by ASME Applied Mechanics Division, April, 1979; final revision, August, 1979.

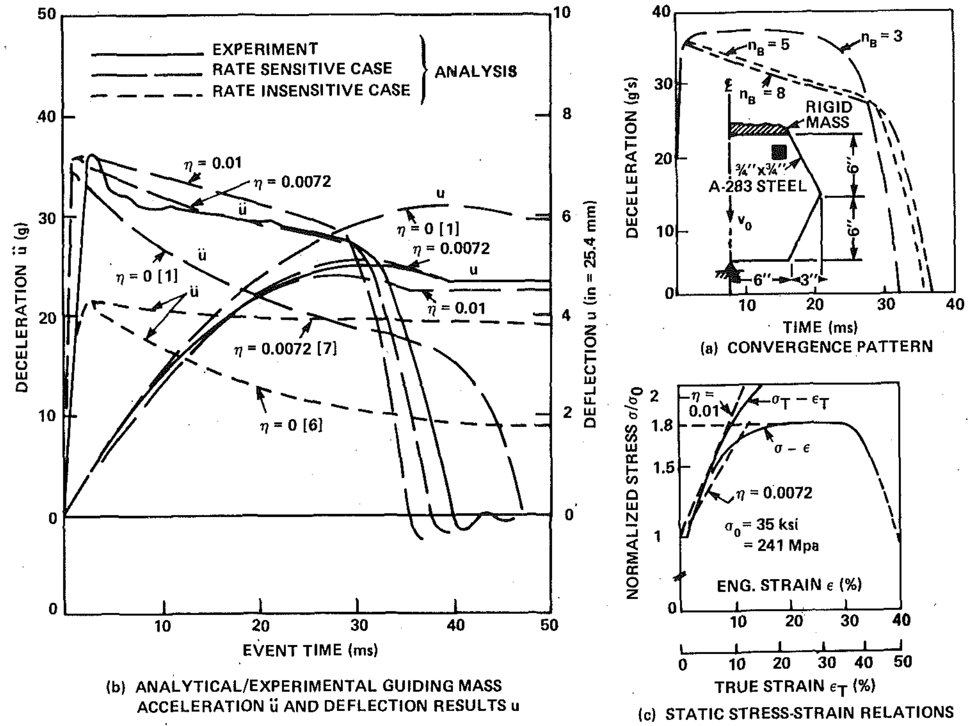

Fig. 1 Drop impact responses of a mild steel frame at V_0 = 20 mph (32.18 Km/hr)

(for linear power law case) [5] and experimental frame drop impact response results (reported below) with satisfactory results.

In a laboratory test, a hexagonal plane frame carrying a heavy rear mass with total weight W = 116.5 lb (52.955 Kg) was drop-impacted onto a narrow stiff pole obstacle at v_0 = 20 mph (32 km/hr) in a nearly symmetrical manner.

Fig. 1(a) shows the numerical convergence pattern of mass deceleration/time history versus number of beam elements (n_B) used in discretizing the frame structure. A similar numerical convergence study was made to determine appropriate integration step size Δt = 0.1 ms. The material constants used in the analysis were: $E = 30 \times 10^3$ ksi (206.85 Gpa), σ_0 = static yield stress = 35 ksi (241.325 Mpa), η = 0.0072, $D^* = (\sigma_0/D)^n = 40.4\ \mathrm{s}^{-1}$, and n = 5 [3]. Rapid convergence of the numerical solution is seen.

The analytical and experimental results for mass acceleration and displacement using the foregoing material constants are shown in Fig. 1(b) for η = 0.01 and 0.0072 cases. Comparison of the analytical/experimental results shows that use of strain-hardening parameter value of η = 0.01 gives somewhat (less than 10 percent) stiffer dynamic acceleration and displacement responses than the actually measured ones, while use of η = 0.0072 gives a better (excellent) correlation result. This is because, for mild steel, coupon test results show that the degree of strain-hardening decreases with increase in strain rate [4] and η = 0.01 represents the absolute maximum value of η (based on the true stress/true strain curve in Fig. 1(c)) even for the static case. Also shown in Fig. 1(b) for comparison purposes are the corresponding dynamic response results for various special cases in which either strain-hardening or strain rate or both effects are absent [1, 6, 7]. Strain rate effects are seen to be very important under the impact loading, while strain-hardening effects are seen to become increasingly important as deformation becomes larger and larger.

Finally, it should be noted that the computerized study developed herein can also be used to predict buckling or parametric resonance behavior (through use of the exact nonlinear compatibility matrices $[B]_j$ in equations (9) and (10) to the extent that the assumption of negligibly small axial force/bending moment interaction effects on inelastic deformation as well as the other assumptions of the study is valid.

References

1 Shieh, R. C., "Large Displacement Matrix Analysis of Elastic/Viscoplastic Plane Frame Structures," ASME *Journal of Engineering for Industry*, Vol. 79, Nov. 1975, pp. 1238–1244.

2 Malvern, L., "The Propagation of Longitudinal Waves of Plastic Deformation in a Bar of Material Exhibiting a Strain-Rate Effect," ASME JOURNAL OF APPLIED MECHANICS, Vol. 18, 1951, pp. 203–208.

3 Cowper, G., and Symonds, P., "Strain-Hardening and Strain-Rate Effects in the Impact Loading of Cantilever Beams," Technical Report No. 28, Brown University, Providence, R.I., Sept. 1957.

4 Manjoine, M., "Influence of Rate of Strain and Temperature on Yield Stresses of Mild Steel," ASME JOURNAL OF APPLIED MECHANICS, Vol. 11, 1944, p. A-211.

5 Weiss, R., and Neubert, V., "Theoretical Dynamic Response of an Elastic-Viscoplastic Cantilever Beam," Progress Report No. 5, N00014-67-A-0385-0010, Department of Engineering Mechanics, Pennsylvania State University, College Park, Pa., June 1974.

6 Shieh, R. C., "Basic Research in Crashworthiness II—Experimental Validation Study of the Analytical Predictive Techniques for the Large Deflection Dynamic Analysis of Plane Elasto-Plastic Frame Structures," Calspan Report No. YB-2987-V, May 1973.

7 Shieh, R. C., "Exploratory Study of the Dynamic Response of Building Structures Subjected to Strong Earthquake Loadings," Calspan Report No. HH-5384-V-1, June 1975.

Analytic Approximations for the Elastic Contact of Rough Spheres

B. D. Hughes[1] and L. R. White[2]

The basic equations of a model of Greenwood and Tripp for contact

[1] Research Student, Department of Applied Mathematics, Research School of Physical Sciences, Australian National University, Canberra, Australia 2600.

[2] Post-Doctoral Fellow, Department of Applied Mathematics, Research School of Physical Sciences, Australian National University, Canberra, Australia 2600.

Manuscript received by ASME Applied Mechanics Division, April, 1979; final revision, August, 1979.

of rough elastic spheres are discussed using analytic approximation techniques.

Introduction

Greenwood and Tripp [1] have proposed a model for the elastic contact of rough spheres and obtained numerical solutions of their fundamental equations, which they have compared with the results of the classical Hertz theory. In this Note we show how analytic approximate solutions of their equations may be constructed for all values of the appropriate dimensionless parameters. The mathematical techniques outlined here are applicable to a general class of nonclassical elastic contact problems [2, 3].

Basic Equations

Consider the case of contact of a smooth sphere of radius B with a rough plane, whose asperities have area density η and radius of curvature β at their tips. Denoting the standard deviation of the asperity heights by σ and letting $\phi^*(s)$ denote the distribution of asperity heights (standardized to unit variance), the Greenwood-Tripp equations may be written

$$p^*(\rho) = \mu F_{3/2}(d^* + \rho^2 + w^*(\rho) - w^*(0)), \tag{1}$$

$$w^*(\rho) = \tfrac{1}{2} \int_0^\infty p^*(\xi) I(\xi/\rho) d\xi, \tag{2}$$

$$w^*(0) = \int_0^\infty p^*(\xi) d\xi, \tag{3}$$

$$F_{3/2}(h) = \int_h^\infty (s-h)^{3/2} \phi^*(s) ds, \tag{4}$$

where $I(z) = (4/\pi) z K(z)$ for $z < 1$ and $I(z) = (4/\pi) K(1/z)$ for $z > 1$, $K(z)$ denoting the usual complete elliptic integral of modulus z. The quantities d^* and w^* represent the minimum separation and displacement of the nominal surfaces, scaled with σ. Also $\mu \equiv \tfrac{8}{3}\eta\sigma\sqrt{2B\beta}$, while ρ denotes the radial coordinate scaled against $\sqrt{2B\sigma}$ and p^* denotes the dimensionless pressure.

Greenwood and Tripp obtained iterative numerical solutions to their equations for various values of d^* and $w^*(0)$, deducing the results for given values of μ and the dimensionless total load

$$T = \int_0^\infty 2\pi\rho p^*(\rho) d\rho \tag{5}$$

after finding suitable values of d^* and $w^*(0)$ by trial and error. We note that it is in fact possible to work directly with μ and d^* (inferring $w^*(0)$ later if it is needed) by defining

$$v^*(\rho) = w^*(0) - w^*(\rho) \geqslant 0 \tag{6}$$

and solving the equation

$$v^*(\rho) = \tfrac{1}{2}\mu \int_0^\infty \{2 - I(\xi/\rho)\} F_{3/2}(d^* + \xi^2 - v^*(\xi)) d\xi, \tag{7}$$

the solution of which vanishes at the origin.

Technique of Analytic Approximate Solution

We construct analytic approximate solutions to equation (7) by a "self-consistent" technique. A trial solution involving a small number of adjustable parameters is inserted into the right-hand side of (7) and the parameters are chosen to insure that, when both sides of (7) are expanded in a Taylor series about $\rho = 0$, the first few coefficients are equal. The trial solution selected must embody the basic physics of the problem. We consider two different trial solutions, with overlapping regions of validity, which allow a complete discussion of the problem for all values of μ and d^*.

Solution in the Light Load Regime. One may in principle solve (7) by making the substitution $v^*(\rho) = \sum_{n=1}^\infty \gamma_n \rho^{2n}$ in both sides, expanding the right-hand side as a power series in ρ and equating coefficients, leading to an infinite set of coupled nonlinear equations for the γ_n. In practice, if $F_{3/2}(h)$ is sufficiently rapidly decaying as $h \to \infty$, it is necessary to take enough terms (N, say) in the series to represent $v^*(\rho)$ near $\rho = 0$ and to select the N coefficients so that the first N terms on both sides of (7) agree. We illustrate this procedure here with the simplest case, viz., $v^*(\rho) \sim \gamma\rho^2$.

Replace $2 - I(\xi/\rho)$ in (7) by the Mellin integral representation [2], valid for $-2 < b = \operatorname{Re} s < 0$,

$$2 - I(\xi/\rho) = -\frac{1}{2\pi i} \int_{b-i\infty}^{b+i\infty} \frac{2\pi^2(\xi/\rho)^s ds}{\sin(\pi s)\Gamma(1 - \tfrac{1}{2}s)^2 \Gamma(\tfrac{1}{2} + \tfrac{1}{2}s)^2}. \tag{8}$$

Initially restricting b to the range $-1 < b < 0$, we may interchange orders of integration in (7) and deduce that

$$v^*(\rho) = -\frac{\mu\pi^2}{2\pi i} \int_{b-i\infty}^{b+i\infty} \frac{ds \rho^{-s}}{\sin(\pi s)\Gamma(1 - \tfrac{1}{2}s)^2 \Gamma(\tfrac{1}{2} + \tfrac{1}{2}s)^2} \times \int_0^\infty \xi^s F_{3/2}(d^* + \xi^2 - v(\xi)) d\xi. \tag{9}$$

Inserting the trial solution $v(\xi) \sim \gamma\xi^2$, setting $\tau = [1 - \gamma]\xi^2$ and interchanging the order of integration,

$$\int_0^\infty \xi^s F_{3/2}(d^* + \xi^2 - v(\xi)) d\xi \simeq \tfrac{1}{2}[1 - \gamma]^{-1/2(s+1)} \times \frac{\Gamma(\tfrac{1}{2}s + \tfrac{1}{2})\Gamma(\tfrac{5}{2})}{\Gamma(\tfrac{1}{2}s + 3)} \int_0^\infty x^{1/2s+2} \phi^*(d^* + x) dx. \tag{10}$$

If $\phi^*(t) = O(t^{-3})$ as $t \to \infty$, combining (9) and (10) yields an inverse Mellin transform, the integrand of which is holomorphic for $-6 < \operatorname{Re} s < 0$, save for simple poles at $s = -2$ and $s = -4$. Hence, translating the integration contour to $-4 < \operatorname{Re} s < -2$,

$$v^*(\rho) \simeq \left\{\frac{3\pi}{16} \int_0^\infty x \phi^*(d^* + x) dx\right\} \mu [1 - \gamma]^{1/2} \rho^2 + O(\rho^4). \tag{11}$$

Denoting the term in curly brackets by θ, the self-consistency condition is $\gamma = \mu\theta[1 - \gamma]^{1/2}$, hence for $\theta > 0$

$$\gamma = \tfrac{1}{2}\{\sqrt{\mu^4\theta^4 + 4\mu^2\theta^2} - \mu^2\theta^2\}. \tag{12}$$

The large $\mu\theta$ asymptotic form, $\gamma = 1 - O([\mu\theta]^{-2})$, reflects the onset [2] of a Hertz limit (macroscopic flattening).

Inserting $v^*(\xi) \sim \gamma\xi^2$ into (7), with γ given by (12), will give an approximation for $v^*(\rho)$ for all values of ρ, provided that $\mu\theta$ is not so large that $\mu\theta \simeq 1$. Also, inserting $v^*(\xi) \simeq \gamma\xi^2$ into (3) and (5),

$$w^*(0) \simeq \frac{3\pi\mu}{16(1 - \gamma)^{1/2}} \int_0^\infty x^2 \phi^*(d^* + x) dx, \tag{13}$$

$$T \simeq \frac{2\pi\mu}{5(1 - \gamma)} \int_0^\infty x^{5/2} \phi^*(d^* + x) dx. \tag{14}$$

Equations (12) and (14) may be used to deduce a single equation involving T, μ, and d^*, so that plots of any two of these quantities with the third held constant are easily constructed for any given asperity height distribution ϕ^*. The relation between $w^*(0)$, μ, and d^* may be analyzed similarly.

Solution in the Heavily Loaded (Near-Hertzian) Regime. Although the range of validity of the foregoing approximation may be extended by taking a higher-order polynomial trial solution, we choose instead to exploit the apparent onset of a "Hertz limit" under heavily loaded conditions [2, 4]. Where k and c are to be determined, we set

$$p^*(\rho)/p^*(0) \equiv F_{3/2}(d^* + \rho^2 - v^*(\rho))/F_{3/2}(d^*) \simeq \begin{cases} (1 - \rho^2/c^2)^k, & \rho \leqslant c \\ 0 & \rho > c \end{cases} \tag{15}$$

in the right-hand side of (7) and extract a series for $v^*(\rho)$ valid for small ρ (using the Mellin transform technique just employed)

$$v^*(\rho) \simeq \{\tfrac{1}{4}\mu c F_{3/2}(d^*) \pi^{1/2} \Gamma(k+1)/\Gamma(k + \tfrac{1}{2})\} \times \{(\rho/c)^2 - \tfrac{3}{8}(k - \tfrac{1}{2})(\rho/c)^4 + \ldots\}. \tag{16}$$

Noting from (15) that

$$1 + \{F'_{3/2}(d^*)/F_{3/2}(d^*)\}[\rho^2 - v^*(\rho)] + \tfrac{1}{2}\{F''_{3/2}(d^*)/F_{3/2}(d^*)\}[\rho^2 - v^*(\rho)]^2 \simeq 1 - k\rho^2/c^2 + \tfrac{1}{2}k(k-1)\rho^4/c^4, \quad (17)$$

we easily obtain [4] equations for k and c by requiring "self-consistency" up to and including terms in ρ^4. Also, with the approximation (15),

$$T \simeq \pi c^2 \mu F_{3/2}(d^*)/(1+k) \quad (18)$$

and

$$w^*(0) = \tfrac{1}{2}c\mu F_{3/2}(d^*)\pi^{1/2}\Gamma(k+1)/\Gamma(k+\tfrac{3}{2}). \quad (19)$$

A trial solution of the form (15) with $k = 2$ (and only the parameter c to be adjusted) has been employed by Lo [5] in a study of the two-dimensional analog of the Greenwood-Tripp problem. Lo determines c by requiring the two representations of $p^*(\rho)/p^*(0)$ in (15) to agree at one point (not close to either end) in the interval $0 < \rho < c$. The scheme outlined here is a distinct improvement over that of Lo for two reasons. Firstly, by matching terms in ρ^2 and ρ^4, we obtain over an *interval* containing the origin a good representation of the pressure and its low-order derivatives, while Lo matches up the pressure at one point only. Secondly (and more importantly), the class of trial solutions chosen includes the Hertz solution $p^*(\rho)/p^*(0) = (1 - \rho^2/c^2)^{1/2}$. Indeed we find [4] that $k \to \tfrac{1}{2}$ from the foregoing as $\mu \to \infty$ at constant d^*, so that the approximate solution approaches the Hertz solution under heavily loaded conditions.

We furnish below numerical evidence, for a particular asperity distribution function, that the regimes of validity of the two approximation schemes overlap. A similar result may be predicted for a general distribution function from an examination of the asymptotic forms of quantities derived from integrals over the pressure distribution, e.g., T, $w^*(0)$ and the Greenwood-Tripp "effective radius of contact" $\alpha^* = 0.375T/w^*(0)$. For each of these quantities, in either of the limiting cases $\mu \to 0$ or $\mu \to \infty$ (at constant d^*), the asymptotic forms derived from both schemes are in qualitative agreement. For example, as $\mu \to \infty$ both schemes predict $T \propto \mu^3$, but only the heavy load scheme furnishes the proportionality constant required to extract Hertz's theory. Similarly as $\mu \to 0$, $T \propto \mu$ for both schemes, with different proportionality constants, but in this regime the light load scheme gives correct results [2, 4]. The proportionality constants depend both on the functional form of ϕ^* and on d^*.

The Gaussian Asperity Height Distribution

In [1] only the Gaussian distribution $\phi^*(s) = (2\pi)^{-1/2}\exp(-\tfrac{1}{2}s^2)$ was considered in detail. This case is easily discussed here. All the integrals over $\phi^*(s)$ arising may be evaluated in terms of parabolic cylinder functions [6], since for Re $s > 0$,

$$\int_0^\infty x^{s-1}\exp(-\tfrac{1}{2}x^2 - d^*x)dx = \Gamma(s)\exp(\tfrac{1}{4}d^{*2})D_{-s}(d^*).$$

We have constructed curves showing the relationship between T, μ, and d^* predicted by our approximation. These are shown in Fig. 1, together with the iterative solutions of [1] for comparison. The two approximate solution techniques evidently have overlapping domains of validity and thus enable the relation between T and μ at constant d^* to be found for $0 < \mu < \infty$. All other relations of interest in the Greenwood-Tripp theory may be discussed similarly without recourse to iterative numerical solution of (7), e.g., $\alpha^* \sim c$ as $\mu \to \infty$. In the heavy load regime, where iterative numerical solution of (7) is extremely difficult, the approximate solution technique yields all relevant information at the cost of solving a single nonlinear equation (for k). A more detailed discussion of a general class of nonclassical elastic contact problems in the light and large load regimes has been given elsewhere [2, 4].

Acknowledgments

We thank Prof. D. Tabor and the referees for supplying useful references and helpful suggestions.

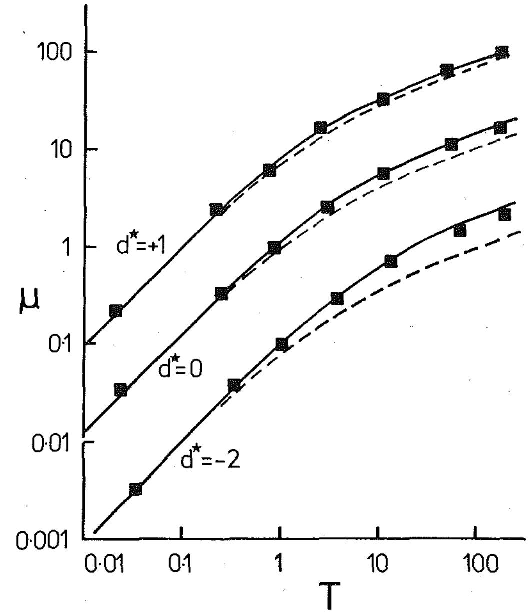

Fig. 1 The relationship between T (dimensionless total load) and μ (dimensionless parameter proportional to the density of asperities and the standard deviation of asperity heights) for three values of d^* (the dimensionless minimum separation of the nominal surfaces): ■ iterative solution drawn from [1]; —— "self-consistent" approximation for light load ($v^*(\rho) \sim \gamma\rho^2$); — "self-consistent" approximation for heavy load (equation (15))

References

1 Greenwood, J. A., and Tripp, J. H., "The Elastic Contact of Rough Spheres," ASME JOURNAL OF APPLIED MECHANICS, Vol. 34, 1967, pp. 153–159.
2 Hughes, B. D., and White, L. R., "'Soft' Contact Problems in Linear Elasticity," *Quarterly Journal of Mechanics and Applied Mathematics*, Vol. 32, 1979, in press.
3 Hughes, B. D., and White, L. R., "The Implications of Elastic Deformation on the Direct Measurement of Surface Forces," *Journal of the Chemical Society, Faraday Transactions I*, in press.
4 Hughes, B. D., and White, L. R., "Approximate Solutions of 'Soft' Contact Problems in Linear Elasticity Under Large Load," to appear.
5 Lo, C. C., "Elastic Contact of Rough Cylinders," *International Journal of Mechanical Sciences*, Vol. 11, 1969, pp. 105–115.
6 Abramowitz, M., and Stegun, I. A., eds., *Handbook of Mathematical Functions*, Dover, New York, 1965, Chapter 19.

Oscillating Flow of a Conducting Fluid With a Suspension of Spherical Particles

L. M. Srivastava[1] and R. P. Agarwal[1]

Introduction

Fluid-dynamics of a particulate suspension (the suspended matter may consist of solid particles, liquid droplets, gas bubbles, etc.) has, from historic times, been the object of scientific and engineering research. The theoretical study of this system of fluid is very useful in understanding various engineering problems concerned with powder technology, rain erosion of guided missiles, sedimentation, atmo-

[1] Department of Applied Mathematics, Motilal Nehru Regional Engineering College, Allahabad, India.
Manuscript recieved by ASME Applied Mechanics Division, March, 1979; final revision, July, 1979.

$$1 + \{F'_{3/2}(d^*)/F_{3/2}(d^*)\}[\rho^2 - \upsilon^*(\rho)] + \tfrac{1}{2}\{F''_{3/2}(d^*)/F_{3/2}(d^*)\}[\rho^2 - \upsilon^*(\rho)]^2 \simeq 1 - k\rho^2/c^2 + \tfrac{1}{2}k(k-1)\rho^4/c^4, \quad (17)$$

we easily obtain [4] equations for k and c by requiring "self-consistency" up to and including terms in ρ^4. Also, with the approximation (15),

$$T \simeq \pi c^2 \mu F_{3/2}(d^*)/(1+k) \quad (18)$$

and

$$w^*(0) = \tfrac{1}{2}c\mu F_{3/2}(d^*)\pi^{1/2}\Gamma(k+1)/\Gamma(k+\tfrac{3}{2}). \quad (19)$$

A trial solution of the form (15) with $k = 2$ (and only the parameter c to be adjusted) has been employed by Lo [5] in a study of the two-dimensional analog of the Greenwood-Tripp problem. Lo determines c by requiring the two representations of $p^*(\rho)/p^*(0)$ in (15) to agree at one point (not close to either end) in the interval $0 < \rho < c$. The scheme outlined here is a distinct improvement over that of Lo for two reasons. Firstly, by matching terms in ρ^2 and ρ^4, we obtain over an *interval* containing the origin a good representation of the pressure and its low-order derivatives, while Lo matches up the pressure at one point only. Secondly (and more importantly), the class of trial solutions chosen includes the Hertz solution $p^*(\rho)/p^*(0) = (1 - \rho^2/c^2)^{1/2}$. Indeed we find [4] that $k \rightarrow \tfrac{1}{2}$ from the foregoing as $\mu \rightarrow \infty$ at constant d^*, so that the approximate solution approaches the Hertz solution under heavily loaded conditions.

We furnish below numerical evidence, for a particular asperity distribution function, that the regimes of validity of the two approximation schemes overlap. A similar result may be predicted for a general distribution function from an examination of the asymptotic forms of quantities derived from integrals over the pressure distribution, e.g., T, $w^*(0)$ and the Greenwood-Tripp "effective radius of contact" $\alpha^* = 0.375T/w^*(0)$. For each of these quantities, in either of the limiting cases $\mu \rightarrow 0$ or $\mu \rightarrow \infty$ (at constant d^*), the asymptotic forms derived from both schemes are in qualitative agreement. For example, as $\mu \rightarrow \infty$ both schemes predict $T \propto \mu^3$, but only the heavy load scheme furnishes the proportionality constant required to extract Hertz's theory. Similarly as $\mu \rightarrow 0$, $T \propto \mu$ for both schemes, with different proportionality constants, but in this regime the light load scheme gives correct results [2, 4]. The proportionality constants depend both on the functional form of ϕ^* and on d^*.

The Gaussian Asperity Height Distribution

In [1] only the Gaussian distribution $\phi^*(s) = (2\pi)^{-1/2}\exp(-\tfrac{1}{2}s^2)$ was considered in detail. This case is easily discussed here. All the integrals over $\phi^*(s)$ arising may be evaluated in terms of parabolic cylinder functions [6], since for Re $s > 0$,

$$\int_0^\infty x^{s-1}\exp(-\tfrac{1}{2}x^2 - d^*x)dx = \Gamma(s)\exp(\tfrac{1}{4}d^{*2})D_{-s}(d^*).$$

We have constructed curves showing the relationship between T, μ, and d^* predicted by our approximation. These are shown in Fig. 1, together with the iterative solutions of [1] for comparison. The two approximate solution techniques evidently have overlapping domains of validity and thus enable the relation between T and μ at constant d^* to be found for $0 < \mu < \infty$. All other relations of interest in the Greenwood-Tripp theory may be discussed similarly without recourse to iterative numerical solution of (7), e.g., $\alpha^* \sim c$ as $\mu \rightarrow \infty$. In the heavy load regime, where iterative numerical solution of (7) is extremely difficult, the approximate solution technique yields all relevant information at the cost of solving a single nonlinear equation (for k). A more detailed discussion of a general class of nonclassical elastic contact problems in the light and large load regimes has been given elsewhere [2, 4].

Acknowledgments

We thank Prof. D. Tabor and the referees for supplying useful references and helpful suggestions.

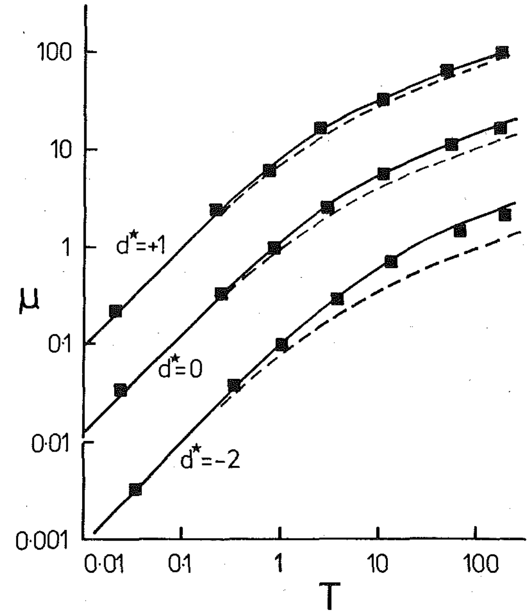

Fig. 1 The relationship between T (dimensionless total load) and μ (dimensionless parameter proportional to the density of asperities and the standard deviation of asperity heights) for three values of d^* (the dimensionless minimum separation of the nominal surfaces): ■ iterative solution drawn from [1]; —— "self-consistent" approximation for light load ($v^*(\rho) \sim \gamma\rho^2$); — "self-consistent" approximation for heavy load (equation (15))

References

1 Greenwood, J. A., and Tripp, J. H., "The Elastic Contact of Rough Spheres," ASME Journal of Applied Mechanics, Vol. 34, 1967, pp. 153–159.

2 Hughes, B. D., and White, L. R., "'Soft' Contact Problems in Linear Elasticity," *Quarterly Journal of Mechanics and Applied Mathematics*, Vol. 32, 1979, in press.

3 Hughes, B. D., and White, L. R., "The Implications of Elastic Deformation on the Direct Measurement of Surface Forces," *Journal of the Chemical Society, Faraday Transactions I*, in press.

4 Hughes, B. D., and White, L. R., "Approximate Solutions of 'Soft' Contact Problems in Linear Elasticity Under Large Load," to appear.

5 Lo, C. C., "Elastic Contact of Rough Cylinders," *International Journal of Mechanical Sciences*, Vol. 11, 1969, pp. 105–115.

6 Abramowitz, M., and Stegun, I. A., eds., *Handbook of Mathematical Functions*, Dover, New York, 1965, Chapter 19.

Oscillating Flow of a Conducting Fluid With a Suspension of Spherical Particles

L. M. Srivastava[1] and R. P. Agarwal[1]

Introduction

Fluid-dynamics of a particulate suspension (the suspended matter may consist of solid particles, liquid droplets, gas bubbles, etc.) has, from historic times, been the object of scientific and engineering research. The theoretical study of this system of fluid is very useful in understanding various engineering problems concerned with powder technology, rain erosion of guided missiles, sedimentation, atmo-

[1] Department of Applied Mathematics, Motilal Nehru Regional Engineering College, Allahabad, India.

Manuscript recieved by ASME Applied Mechanics Division, March, 1979; final revision, July, 1979.

spheric fallout, combustion, fluidization, electrostatic precipitation of dust, nuclear reactor cooling, acoustics batch settling, aerosol and paint spraying, aircraft icing, flows in rocket tube where small carbon or metallic particles are used, lunar ash flows, environmental pollution and many others. More recently, the oscillating flow of fluid embedded with solid spherical particles is an important prelude to understand blood flow in mammalian capillaries in which one attempts to account for the presence of red cells in blood. Blood is a suspension of various cells (red cells, white cells, platelets) in an aqueous solution called plasma having the properties of a Newtonian fluid. There are about 5×10^9 cells in a milliliter of human blood. The cells occupy about 40–50 percent of the whole blood by volume. Most of the cells in blood are "red cells" (about 94 percent). The red cells make up about 45 percent of the blood by volume in the average human. Therefore for realistic description of blood flow, it is perhaps more appropriate to treat the blood as a two-phase fluid that is a suspension of red cells in plasma. Also certain observed phenomena in blood flow including the Fahraeus-Linquist effect, non-Newtonian behavior cannot be explained fully by considering the blood as a single-phase homogeneous fluid. In order to include some of these properties of blood, it seems to be important and necessary to consider the whole blood as a fluid-particle system. It is also important to have an estimate of the damping that might result from the relative motion of the blood cells and plasma in the pulsatile flow. Perhaps the change in the shape of a pressure pulse wave as it moves down the artery may be attributed to blood cells plasma interaction which in turn is likely to have some effect on the impedance (pressure-flow relationship). Nayfeh [1], Chow [2], and Kamail [3] studied some problems of blood flow by assuming whole blood as a fluid-particle system. It is observed that for a long operation, present mechanical pumping systems for blood is not suitable as it cause several undesirable effects including mechanical trauma, hemolysis, and thrombus formation. Keeping this in view, recently Sud and Mishra [4] presented a new analysis of pumping of blood by means of a noninvasive circulatory assist device using the principle of magnetohydrodynamics (since blood is an electrically conducting fluid). Their studies indicated that such a blood pump would require the application of a slowly moving axial magnetic field of strength of about 10^6 oersted. In view of the foregoing discussion it is therefore of some interest to investigate the effect of magnetic field on blood flow assuming that the blood constitutes a suspension of cells in plasma instead of a simple homogeneous fluid. In the following, we analyze the oscillating flow of incompressible, viscous conducting fluid which contains suspended inert rigid spherical particles between two infinite plates, in the presence of transverse magnetic field. Blood cells are actually irregularly shaped deformable particles. But for the simplicity one may consider blood cells as rigid spherical particles. This limits our study in large arteries and veins. In small arteries and veins and capillaries, it is necessary to take into account the deformation of cells since the size of the vessel is the same or less order of magnitude as the red cells [Allen, De Silva, and Kline [5]]. Moreover Bugliarello and Sevilla [6] has already pointed out that such deformability is not significant at low shear rates. One prime incentive for this work was its possible utility in understanding of blood flow in mammalian capillaries in which one attempts to treat the blood as two-phase fluid that is a suspension of red cells plasma.

The Formulation of the Problem

We consider the flow of fluid-particle system infinite in extent in the vicinity of two infinite flat plates executive simple harmonic oscillation with a frequency "ω" in their own planes $y = \pm h$. The x and y-axes are taken along and transverse to parallel plates and uniform magnetic field acting along y-axis. The appropriate equations in nondimensionalized form from Nayfeh [1] are

$$\frac{\partial u}{\partial t} = \frac{1}{R}\frac{\partial^2 u}{\partial y^2} + \frac{f}{\tau}(v - u) - Mu, \quad \tau\frac{\partial v}{\partial t} = (u - v), \qquad (1)$$

where u and v are velocities of fluid and particles, respectively. R is the Reynold's number, f is the mass concentration of the particles, $M = \sigma B^2/\rho\omega$ is magnetic parameter, y and t are the nondimensionalized distance and time, with respect to h and $1/\omega$, respectively, and τ is the relaxation time of the particles nondimensionalized with respect to $1/\omega$. Initial and boundary conditions are $u = v = 0$ at $t = 0$ for all y, $u = u_0 \sin t$ at $y = 1$ and $\partial u/\partial y = 0$ at $y = 0$, for the flow is symmetrical about the plan $y = 0$, only the flow in the region $0 \leq y \leq 1$ is considered.

Solution of the Problem

The solution of equation (1) subject to the foregoing boundary conditions is carried out using the standard techniques and yields the following expressions for the fluid and particle velocities:

$$\begin{aligned} u = {} & (u_0/(E^2 + F^2))[E_y(\sin t - F\cos t) \\ & + F_y(E\cos t + F\sin t)] + (u_0\pi/R)\sum_{n=0}^{\infty}[(-1)^n \\ & \times (2n+1)\cos(0.5(2n+1)\pi y)[\{(\exp(p_1 t))(1 + p_1\tau)^2/ \\ & ((1 + p_1{}^2)((1 + p_1\tau)^2 + f))\} + \{(\exp(p_2 t))(1 + p_2\tau)^2/ \\ & ((1 + p_2)^2((1 + p_2\tau)^2 + f))\}]] \quad \text{for} \quad 0 \leq y < 1 \end{aligned} \qquad (2)$$

$$\begin{aligned} v = {} & (u_0/(1 + \tau^2)(E^2 + F^2))[E_y(E - F\tau)\sin t - (F + E\tau)\cos t \\ & + F_y(F + E\tau)\sin t + (E - F\tau)\cos t] \\ & + (u_0\pi/R)\sum_{n=0}^{\infty}[(-1)^n \cdot (2n+1) \cdot \cos(0.5(2n+1)\pi y)[\{(\exp(p_1 t)) \\ & \times (1 + p_1\tau)/((1 + p_1{}^2)((1 + p_1\tau)^2 + f))\} \\ & + \{(\exp(p_2 t))(1 + p_2\tau)/((1 + p_2{}^2)((1 + p_2\tau)^2 + f))\}]] \\ & + u_0\tau(\exp(-t/\tau))/(1 + \tau^2) \quad \text{for} \quad 0 \leq y < 1 \end{aligned} \qquad (3)$$

$$v = u_0/(1 + \tau^2)[\sin t - \tau\cos t + \tau\exp(-t/\tau)], \quad \text{at} \quad y = 1 \qquad (4)$$

where

$$\begin{aligned} & E = \cosh(\sqrt{X}).\cos(\sqrt{Y}); \quad F = \sinh(\sqrt{X}).\sin(\sqrt{Y}); \\ & E_y = \cosh(y\sqrt{X})\cos(y\sqrt{Y}); \quad F_y = \sinh(y\sqrt{X})\sin(y\sqrt{Y}) \\ & X = \tfrac{1}{2}\{x \pm (x^2 + z^2)^{1/2}\}; \quad Y = z^2/(2(x \pm (x^2 + z^2)^{1/2})), \\ & x = MR + f\tau R/(1 + \tau^2); \quad z = R(1 + f + \tau^2)/(1 + \tau^2); \\ & p_1 = A + B; \quad p_2 = A - B; \quad A = -[((1 + f)/(2\tau)) \\ & + ((2n+1)^2\pi^2/(8R)) + M/2]; \quad B = (1/8R\tau)[16R^2(1 + f)^2 \\ & + \tau^2\pi^4(2n+1)^4 + 16R^2\tau M(\tau M + 2f - 2) \\ & + 8R\tau\pi^2(2n+1)^2(\tau M + f - 1)]^{1/2} \end{aligned}$$

Large-Time Solution. In the limiting case $t \to \infty$, (2)–(4) reduce to

$$\begin{aligned} u = {} & (u_0/(E^2 + F^2))[E_y(E\sin t - F\cos t) \\ & + F_y(E\cos t + F\sin t)] \quad \text{for} \quad 0 \leq y < 1 \end{aligned} \qquad (5)$$

$$\begin{aligned} v = {} & (u_0/(1 + \tau^2)(E^2 + F^2))[E_y((E - F\tau)\sin t - (F + E\tau)\cos t) \\ & + F_y((F + E\tau)\sin t + (E - F\tau)\cos t)] \quad \text{for} \quad 0 \leq y < 1 \end{aligned} \qquad (6)$$

$$v = u_0[\sin t - \tau\cos t]/(1 + \tau^2) \quad \text{at} \quad y = 1 \qquad (7)$$

Some Limiting Cases. Solutions for the several limiting cases of the problem may be obtained from (2)–(4) in the following manners:

Case 1. Solution for clean (particle-free) magnetohydrodynamic flow → this is the limiting case of vanishing particle density $f \to 0$.

Case 2. Solution for two-phase hydrodynamic flow → the magnetic field now vanishing, i.e., $M \to 0$.

Case 3. Solution for clean hydrodynamic flow → this is the limiting case of vanishing particle density and magnetic field, i.e., $f \to 0$; $M \to 0$.

Case 4. Solution for two-phase hydrodynamic flow for large time → this is the limiting case $t \to \infty$ and $M \to 0$.

Wall Shear Stress. The dimensionless values of the shear stress at the wall $y = 1$ is obtained from (2) as

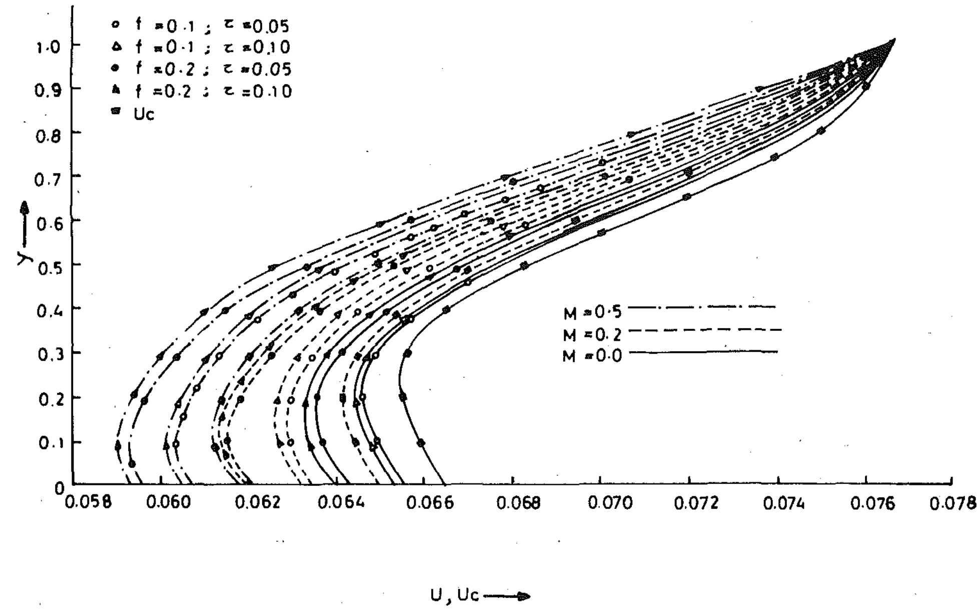

Fig. 1 Velocity profiles for fluid containing particles (U) and fluid-free from particles (Uc) at $t = 50$

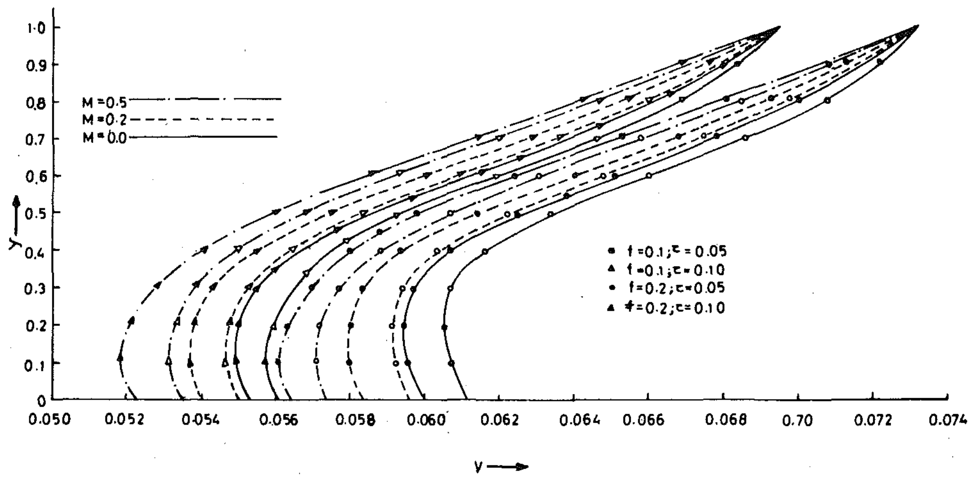

Fig. 2 Velocity profiles for particles (V) at $t = 50$

$$
\begin{aligned}
(\partial u/\partial y)_{y=1} = {} & (u_0/(E^2+F^2))[(E\sin t - F\cos t) \\
& \times(\sqrt{X}\sinh\sqrt{X}\cos\sqrt{Y} - \sqrt{Y}\sin\sqrt{Y}\cosh\sqrt{X}) \\
& + (E\cos t + F\sin t)(\sqrt{X}\cosh\sqrt{X}\sin\sqrt{Y} \\
& + \sqrt{Y}\cos\sqrt{Y}\sinh\sqrt{X})] - (u_0\pi^2/(2R))\sum_{n=0}^{\infty}[(2n+1)^2 \\
& \times\{\exp(p_1 t)(1+p_1\tau)^2/(1+p_1{}^2)[(1+p_1\tau)^2+f]\} \\
& + (\exp(p_2 t)(1+p_2\tau)^2/(1+p_2{}^2)[(1+p_2\tau)^2+f]\}] \quad (8)
\end{aligned}
$$

The wall shear stress for the classical case (clean fluid), $(\partial u_c/\partial y)_{y=1}$ may be obtained from (8) by taking $f \to 0$.

Discussion and Conclusions

To gain an insight into the patterns of flow, the velocities of fluid containing particles (u), particles (v), and fluid-free from particles (u_c) have been plotted, for different values of the magnetic parameter M, mass concentration of the particle f and relaxation time of the particle τ at times $t = 50$ and $t = 500$. The value of Reynolds number $R = 10^3$ and $u_0 = 0.1$ have been taken. Figs. 1–4 represent the variations of u, u_c, and v with y at $t = 50$ and $t = 500$. It is clear that the presence of the magnetic field at any instant decreases the velocities of fluid containing particles, and fluid-free from particles at any fixed point between the plates. It can be seen from the Figs. 1–2 that, as we move away from the plate, the effect of increasing the particle-density is to reduce both the fluid and particle velocities while there is no effect of particle-density on fluid and particle velocities at the plate. Also, as we move away from the plate, the effect of increasing the relaxation time τ of the particle is to reduce both the fluid and particle velocities while at the plate fluid velocity is unaffected by τ but particle velocity reduces considerably. Graphs further reveal that, as we move away from the plate, the change in particle-density f has considerable effect on fluid velocity compared to the very small effect due to a change in relaxation time τ of the particle, whereas change in relaxation time of the particle has much more influence on particle velocity than a change in particle-density f has. On the other hand, very near the plate, the fluid velocity is unaffected by the presence of particles while the particle velocity is the same for all particle-density but depends on relaxation time τ of the particle. Therefore it may be concluded that the fluid velocity depends more on the mass

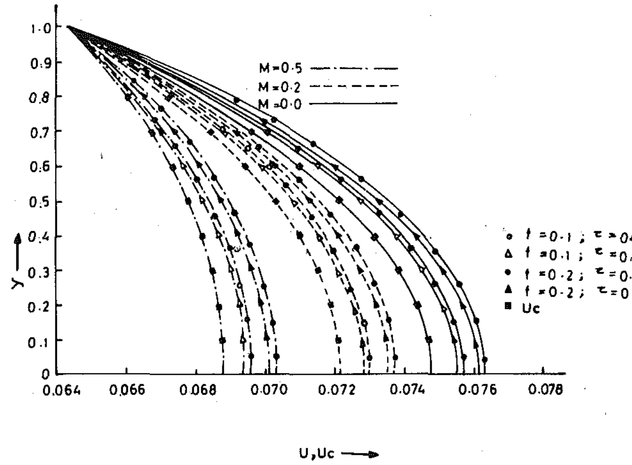

Fig. 3 Velocity profiles for fluid containing particles (U) and fluid-free from particles (Uc) at t = 500

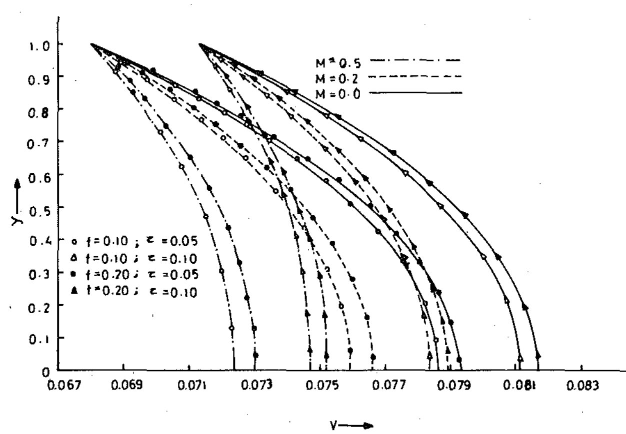

Fig. 4 Velocity profiles for particles (V) at t = 500

concentration of the particles than on their size. On the contrary, the size of the particles has more influence on the velocity of the particles than their concentration itself has. Further, the velocity profile for fluid containing particles are similar to that of the fluid-free from particles, showing that the presence of particulate phase does not have any effect on the manner in which u varies with y. Also, the particle velocity v varies in the same manner as u does. Figs. 1–2 further reveal that the presence of magnetic field has more effect on fluid velocity compared to particle velocity. But after a long time (Figs. 3–4) magnetic field influences particle velocity more compared to fluid velocity.

After a long time, the velocities u, u_c, and v become periodic but are still dependent on the size and concentration of particles suspended in the fluid and on the applied magnetic field. Comparison between the patterns of flow at short and long time can be made from Figs. 1–4. At t = 50, an increase in particle density and in the size of the particle leads to a decrease in fluid velocity for the same magnetic field M while at t = 500, an increase in particle density leads to an increase in fluid velocity but an increase in the size of the particle leads to a decrease in fluid velocity for the same magnetic field M. On the other hand at t = 50, particle velocity decreases as particle density and size of the particle decrease while at t = 500, particle velocity increases as particle density and size of the particles increases for the same M. Also the effect of magnetic field on y and v increases as time increases for every combination of f and τ. Furthermore the difference between the two values of u, v, and u_c at the plate and at the center is very large at t = 50, compared to corresponding difference at t = 500 for M = 1. Also the effect of increasing the magnetic field from M = 0 to M = 1 is to increase the difference between the two values of u, v, and u_c at t = 50 but to decrease these diferences at t = 500. Shear stress of fluid containing particles and fluid-free from the particles have been plotted in Fig. 5. It is clear that increase in the magnetic field increase the shear stress both of fluid containing particles and fluid-free from particles. Fig. 5 further reveals that shear stress increases with an increase in mass concentration and relaxation time of the particles. Also it can be seen in graph that shear stress depends more on the mass concentration of the particles than on their size. The effect of increasing the time is to reduce the shear stress of fluid containing particles but to increase the shear stress of fluid free from particles. Furthermore, the difference between shear stresses of fluid and fluid free from particles for fixed f, τ, and M, decreases with increase in time in the beginning. At one time these two stresses come very close but after attending this stage, the difference between shear-stresses increases rapidly with increase in time. It is interesting to note that at t = 40, shear stress of fluid containing particle is almost unaffected by the presence of particles for the values of magnetic parameter M = 0.1, mass concentration of the particle f = 0.2, and relaxation time of the particle τ = 0.1.

Acknowledgments

The authors are indebted to Prof. Jagdish Lal for stimulating his interest and for many enlightening discussions. The work was supported by a Project-grant from the Ministry of Education and Social Welfare, Government of India.

References

1 Nayfeh, A. H., "Oscillating Two-Phase Flow Through a Rigid Pipe," *AIAA Journal*, Vol. 4, 1966, pp. 1868–1870.

2 Chow, J. C. F., "Blood Flow; Theory, Effective Viscosity and Effects of Particle Distribution," *Bulletin Math. Biology*, Vol. 37, 1975, pp 472–488.

3 Kamil, M. R., "Peristaltic Pumping of a Newtonian Fluid With Particle Suspended in it at a Low Reynolds Number Under Long Wavelength Ap-

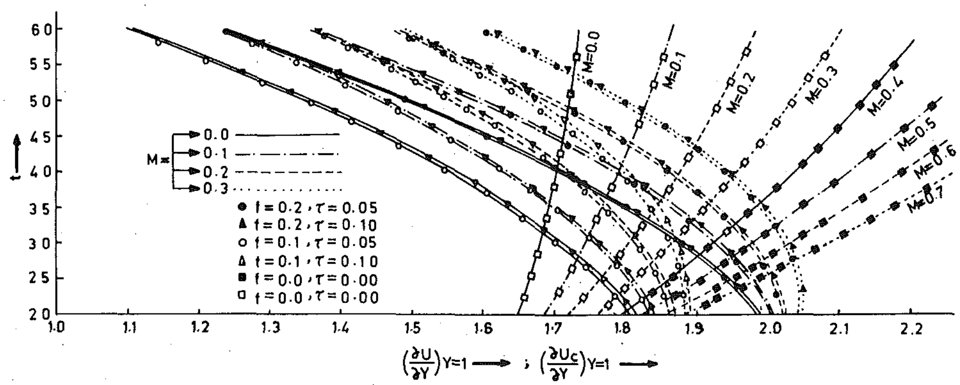

Fig. 5 Wall shear stress for fluid containing particles and fluid-free from particles

proximation," ASME JOURNAL OF APPLIED MECHANICS, Vol. 45, 1978, pp. 32–36.

4 Sud, V. K., Sephon, G. S., and Mishra, R. K., "Pumping Action on Blood Flow by a Magnetic Field," *Bulletin Math. Biology*, Vol. 39, 1977, pp. 385–390.

5 Allen, S. J., DeSilva, C. N., and Kline, K. A., "A Theory of Simple Deformable Directed Fluids," *Physics of Fluids*, Vol. 10, 1967, pp. 2551–2555.

6 Bugliarello, G., and Sevilla, J., "Velocity Distribution and Other Characteristics of Steady and Pulsatile Blood Flow in Fine Glass," *Biorheology*, Vol. 7, 1970, pp. 85.

An Iterative Numerical Solution for the Elastica With Causally Mixed Inputs

M. Hubbard[1]

An iterative numerical solution is given for the case of a thin elastic rod whose inputs are simultaneously the positions of the two ends and an applied moment at one end. The development begins by considering the real rod as an end section of a longer fictitious rod loaded with end forces only. Newton's method is then used to obtain both the shape of the real rod and its vector restoring force. The results show that both the magnitude and the direction of the restoring force are changed considerably from the zero-moment case, especially when the percent deflection of the elastica is small. Such a model is a useful alternative to a pure force-deflection one because it accounts not only for the direct effect of the applied moment on the reaction rigid body but the indirect contribution to the reaction force as well.

Nomenclature

A = coefficient matrix
B = stiffness of rod
E = elliptic integral of second kind
f = unknown functional relationship
k = modulus of elliptic integrals
K = elliptic integral of first kind
l = compressed chord length of rod
L = total rod length
M, N = applied end moment
$\overline{R}$ = rod restoring force
s = arc length measured from origin along rod
u = dimensionless arc length
α = slope of rod at origin relative to chord direction
γ = slope of rod at origin relative to $\overline{R}$-direction
δ = percent deflection $(L - l)/L$
ϕ = amplitude of the elliptic integral
x, y = position coordinates of points on rod

Subscripts

i = iteration index

Superscripts

$'$ denotes coordinate system with x-axis parallel to $\overline{R}$

Introduction

The calculation of the shape of the plane curve assumed by a thin rod (elastica) loaded by arbitrary forces at its ends, one of the first problems in the theory of elasticity, was solved by Euler in 1729 [1]. As is well known, the coordinates of the center line of the rod are given by elliptic functions which result from the integration of the exact nonlinear rod differential equation.

[1] Assistant Professor, Department of Mechanical Engineering, University of California, Davis, Calif., 95616

Manuscript received by ASME Applied Mechanics Division, February, 1979; final revision, September, 1979.

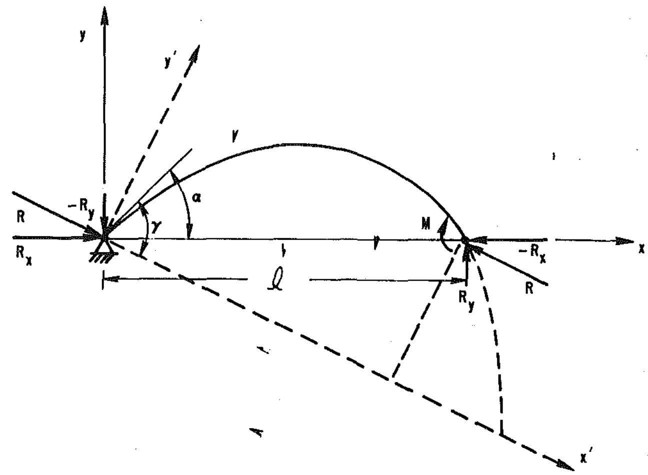

Fig. 1 A schematic diagram of an elastica of fixed chord length *l* loaded with a moment *M* and its relation to a longer fictitious elastica loaded with *R* only

Most textbooks [2–5] consider only the loading by concentrated forces at the ends, which may be termed a "compliance" viewpoint since they calculate the resulting deflections. Frequently, when such a rod appears as a structural member component of a dynamical system, a "stiffness" viewpoint becomes more natural. The rod is taken to be a force generator (a nonlinear spring) whose force-displacement function characterizes it and the energy storage element is said to be in "integral causality" [6, 7].

In the case where the ends of the rod are not torque-free, the inputs (the positions of the ends and the applied torque) are of a *mixed causal form* and the outputs (the shape of the rod and the restoring force) are mixed causally as well. In this Note a solution technique is discussed for the calculation of the restoring force and shape of the elastica as a function of simultaneous end position and torque inputs. The equivalent linear stiffness of the rod is shown to be greatly affected by the applied moment. Quantitative results are given.

Mathematical Model of Elastica: Zero Applied Moment

A schematic diagram of the elastica of total length L is shown in Fig. 1. We here consider one end to be pinned at the origin of the xy coordinate system while the other end is located at the point $(l, 0)$, $l < L$, and has an applied moment M. Since the rod is in force as well as moment equilibrium the reaction forces at either end are equal and opposite and in a direction which defines the x'-axis of a $x'y'$ coordinate system to be used in what follows.

Before treating the more general situation we first summarize the theory for the simpler case where the applied moment is zero. Here the x and x'-axes coincide and the "compliance" solution is well known [2, 4, 8]. The reaction force has an x component only and the left end is an inflection point of the rod.

Following [2], we introduce a dimensionless arc length

$$u = s\sqrt{R/B} \tag{1}$$

and a modulus k related to the slope at the pinned end by

$$k = \sin\frac{\alpha}{2}. \tag{2}$$

Using these variables the nonlinear rod differential equation can be integrated twice to yield expressions for the x and y coordinates of the rod (see [4 and 2]),

$$x\sqrt{\frac{R}{B}} = [2\{E(u + K, k) - E(K, k)\} - u] \tag{3}$$

proximation," ASME JOURNAL OF APPLIED MECHANICS, Vol. 45, 1978, pp. 32–36.

4 Sud, V. K., Sephon, G. S., and Mishra, R. K., "Pumping Action on Blood Flow by a Magnetic Field," *Bulletin Math. Biology*, Vol. 39, 1977, pp. 385–390.

5 Allen, S. J., DeSilva, C. N., and Kline, K. A., "A Theory of Simple Deformable Directed Fluids," *Physics of Fluids*, Vol. 10, 1967, pp. 2551–2555.

6 Bugliarello, G., and Sevilla, J., "Velocity Distribution and Other Characteristics of Steady and Pulsatile Blood Flow in Fine Glass," *Biorheology*, Vol. 7, 1970, pp. 85.

An Iterative Numerical Solution for the Elastica With Causally Mixed Inputs

M. Hubbard[1]

An iterative numerical solution is given for the case of a thin elastic rod whose inputs are simultaneously the positions of the two ends and an applied moment at one end. The development begins by considering the real rod as an end section of a longer fictitious rod loaded with end forces only. Newton's method is then used to obtain both the shape of the real rod and its vector restoring force. The results show that both the magnitude and the direction of the restoring force are changed considerably from the zero-moment case, especially when the percent deflection of the elastica is small. Such a model is a useful alternative to a pure force-deflection one because it accounts not only for the direct effect of the applied moment on the reaction rigid body but the indirect contribution to the reaction force as well.

Nomenclature

A = coefficient matrix
B = stiffness of rod
E = elliptic integral of second kind
f = unknown functional relationship
k = modulus of elliptic integrals
K = elliptic integral of first kind
l = compressed chord length of rod
L = total rod length
M, N = applied end moment
$\overline{R}$ = rod restoring force
s = arc length measured from origin along rod
u = dimensionless arc length
α = slope of rod at origin relative to chord direction
γ = slope of rod at origin relative to $\overline{R}$-direction
δ = percent deflection $(L - l)/L$
ϕ = amplitude of the elliptic integral
x, y = position coordinates of points on rod

Subscripts

i = iteration index

Superscripts

$'$ denotes coordinate system with x-axis parallel to $\overline{R}$

Introduction

The calculation of the shape of the plane curve assumed by a thin rod (elastica) loaded by arbitrary forces at its ends, one of the first problems in the theory of elasticity, was solved by Euler in 1729 [1]. As is well known, the coordinates of the center line of the rod are given by elliptic functions which result from the integration of the exact nonlinear rod differential equation.

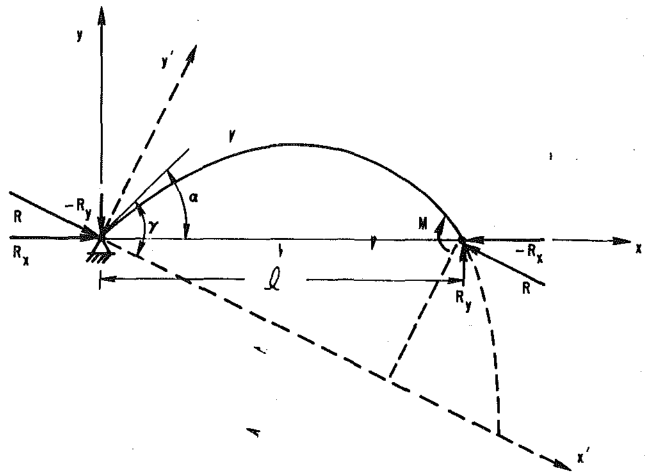

Fig. 1 A schematic diagram of an elastica of fixed chord length l loaded with a moment M and its relation to a longer fictitious elastica loaded with R only

Most textbooks [2–5] consider only the loading by concentrated forces at the ends, which may be termed a "compliance" viewpoint since they calculate the resulting deflections. Frequently, when such a rod appears as a structural member component of a dynamical system, a "stiffness" viewpoint becomes more natural. The rod is taken to be a force generator (a nonlinear spring) whose force-displacement function characterizes it and the energy storage element is said to be in "integral causality" [6, 7].

In the case where the ends of the rod are not torque-free, the inputs (the positions of the ends and the applied torque) are of a *mixed causal form* and the outputs (the shape of the rod and the restoring force) are mixed causally as well. In this Note a solution technique is discussed for the calculation of the restoring force and shape of the elastica as a function of simultaneous end position and torque inputs. The equivalent linear stiffness of the rod is shown to be greatly affected by the applied moment. Quantitative results are given.

Mathematical Model of Elastica: Zero Applied Moment

A schematic diagram of the elastica of total length L is shown in Fig. 1. We here consider one end to be pinned at the origin of the xy coordinate system while the other end is located at the point $(l, 0)$, $l < L$, and has an applied moment M. Since the rod is in force as well as moment equilibrium the reaction forces at either end are equal and opposite and in a direction which defines the x'-axis of a $x'y'$ coordinate system to be used in what follows.

Before treating the more general situation we first summarize the theory for the simpler case where the applied moment is zero. Here the x and x'-axes coincide and the "compliance" solution is well known [2, 4, 8]. The reaction force has an x component only and the left end is an inflection point of the rod.

Following [2], we introduce a dimensionless arc length

$$u = s\sqrt{R/B} \tag{1}$$

and a modulus k related to the slope at the pinned end by

$$k = \sin\frac{\alpha}{2}. \tag{2}$$

Using these variables the nonlinear rod differential equation can be integrated twice to yield expressions for the x and y coordinates of the rod (see [4 and 2]),

$$x\sqrt{\frac{R}{B}} = [2\{E(u + K, k) - E(K, k)\} - u] \tag{3}$$

[1] Assistant Professor, Department of Mechanical Engineering, University of California, Davis, Calif., 95616

Manuscript received by ASME Applied Mechanics Division, February, 1979; final revision, September, 1979.

$$y\sqrt{\frac{R}{B}} = -2k \text{ cn } (u + K) \tag{4}$$

where

$$K = K(k) = \int_0^{\pi/2} \frac{d\xi}{\sqrt{1 - k^2 \sin^2 \xi}} \tag{5}$$

denotes the complete elliptic integral of the first kind which is also the real quarter period of the Jacobian elliptic functions cn (u) and dn (u) [9] and where

$$E(u, k) = \int_0^u \text{dn}^2 (u) du = \int_0^\phi (1 - k^2 \sin^2 \xi)^{1/2} d\xi \tag{6}$$

denotes the incomplete elliptic integral of the second kind and

$$\cos \phi = \text{cn } (u). \tag{7}$$

Similarly, it can be shown [4] that the arc length is given by

$$u = s\sqrt{\frac{R}{B}} = \int_\phi^{\pi/2} \frac{d\xi}{\sqrt{1 - k^2 \sin^2 \xi}}. \tag{8}$$

If (8) is evaluated at the half length of the rod, $s = L/2$ ($\phi = 0$), it becomes

$$L\sqrt{R/B} = 2K(k). \tag{9}$$

In addition, the distance l between two successive inflection points can be calculated [2] to be

$$l\sqrt{R/B} = 4\,E(k) - 2K(k) \tag{10}$$

where $E(k)$ is (6) evaluated when $\phi = \pi/2$, the complete elliptic integral of the second kind. Equations (9) and (10) can be combined to yield an expression for the percent deflection of the rod

$$\frac{\delta}{L} = \frac{L - l}{L} = 2\left[1 - \frac{E(k)}{K(k)}\right]. \tag{11}$$

Now given a rod of length L loaded by a force R, k can be determined from (9) and the percent deflection of the rod from (11), thus yielding the compliance function of the rod. Alternately, if the compressed length l is given rather than the applied force R, (11) can be used to find k since $E(k)/K(k)$ is single-valued; then (9) yields R as the stiffness solution. When the load is nondimensionalized by the Euler critical buckling load and plotted versus the percent deflection the results are as shown in the middle curve of Fig. 2.

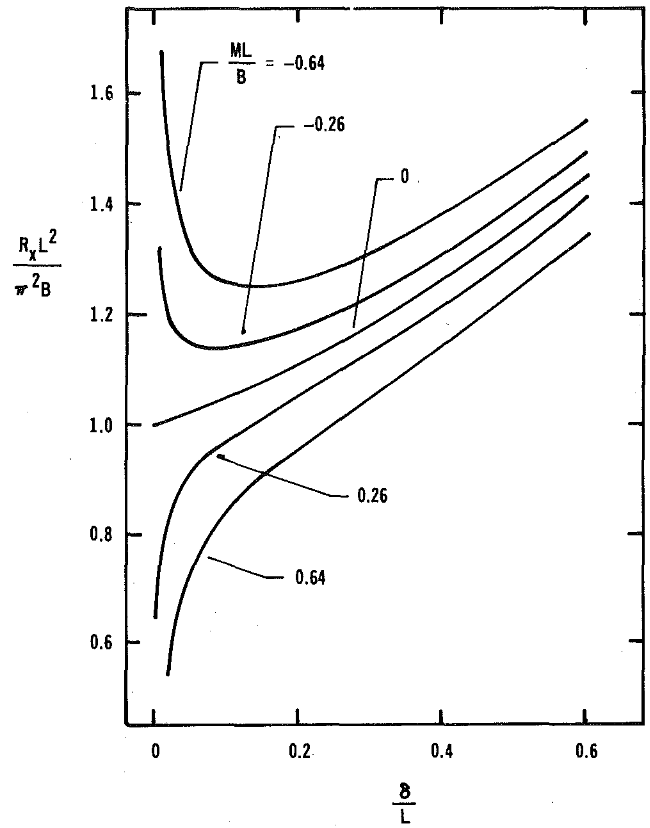

Fig. 2 Elastica along-chord restoring force versus percent shortening for various values of the applied moment including the zero moment case

Solution for Arbitrary *M* and *l*

We now turn our attention to a more complicated situation than that just summarized. Specifically we desire the solution for the elastica when an applied moment M is given in addition to the compressed length l, the most general case depicted by Fig. 1. Since no known analytical solution exists we seek an iterative solution based on the following heuristic reasoning.

When a moment M (positive as shown in Fig. 1) is applied to the rod, a y component of the reaction force $\overline{R}$ is induced at the free end

$$R_y = -M/l. \tag{12}$$

It is not hard to see that there exists a fictitious rod with length $L' > L$, stiffness B, and loaded *only with end forces* equal vectorially to $\overline{R}$, which coincides exactly with the real rod over its left-hand end segment of length L. At each point in this segment the real and fictitious rods have the same displacements, reaction forces, and interior moments. Hence, we solve the problem of the fictitious rod instead, and note that equations (1)–(10) apply to it when suitably interpreted.

Suppose we have initial guesses R_0 and γ_0 for the magnitude of the force and the slope of the pinned end relative to the x'-axis, respectively. Evaluating (2) and (1) for $\alpha = \gamma_0$, $R = R_0$ and $s = L$ gives the corresponding values of the nondimensional arc length u and the modulus k for the fictitious rod. Then using (5) and subsequently (3) and (4) allows calculation of the coordinates (x', y') of the interior point located at an arc length L from the left-hand end. The interior moment (which is equal to the required applied moment for the same R_0 and γ_0) and the chord length can then be determined from

$$M_0 = R_0 y' \tag{13}$$

and

$$l_0 = (x'^2 + y'^2)^{1/2} \tag{14}$$

Almost certainly these determined values of M_0 and l_0 will not equal the given applied moment M and compressed length l. But since $y' = y'(\gamma, R)$ and $x' = x'(\gamma, R)$, then for small changes $d\gamma$ and dR from the initial guesses the corresponding perturbations in the coordinates are given by

$$dy' = \frac{\partial y'}{\partial \gamma} d\gamma + \frac{\partial y'}{\partial R} dR \tag{15a}$$

$$dx' = \frac{\partial x'}{\partial \gamma} d\gamma + \frac{\partial x'}{\partial R} dR \tag{15b}$$

and the perturbations in the interior moment and chord length are

$$\begin{bmatrix} dl \\ dM \end{bmatrix} = \begin{bmatrix} \frac{x'}{l}\frac{\partial x'}{\partial \gamma} + \frac{y'}{l}\frac{\partial y'}{\partial \gamma} & \frac{x}{l}\frac{\partial x'}{\partial R} + \frac{y'}{l}\frac{\partial y'}{\partial R} \\ R\frac{\partial y'}{\partial \gamma} & y' + R\frac{\partial y'}{\partial R} \end{bmatrix} \begin{bmatrix} d\gamma \\ dR \end{bmatrix} = A \begin{bmatrix} d\gamma \\ dR \end{bmatrix}. \tag{16}$$

This allows corrections to the initial guesses to be calculated using Newton's method

$$\begin{bmatrix} d\gamma \\ dR \end{bmatrix} = A^{-1} \begin{bmatrix} dl \\ dM \end{bmatrix} \tag{17}$$

where

$$\begin{bmatrix} dl \\ dM \end{bmatrix} = \begin{bmatrix} l - l_0 \\ M - M_0 \end{bmatrix}. \tag{18}$$

This procedure can be repeated as many times (i) as required to make the guess (γ_i, R_i) yield (M_i, l_i) arbitrarily close to the pair (M, l). Although the partial derivatives in (16) could in principle be determined either analytically or numerically, the latter would probably be preferred since the whole scheme is fundamentally a numerical one.

Results

Using the principles of dimensional analysis [10] it is possible to deduce the general form of dependence of the parameters of the problem in the most general case. If we apply the Buckingham π theorem, three dimensionless groups emerge; RL^2/B, ML/B, and δ/L. Hence the first is related functionally to the second two and we may write

$$R = B/L^2 f(ML/B, \delta/L). \tag{19}$$

Numerical solution of the procedure was accomplished on a computer for a given rod (B, L) and for a range of values of the input variables M and δ. In light of (18), however, such a specific solution can be generalized to an elastica of arbitrary length and stiffness. These general results are also shown in Fig. 2. Since the y component of $\overline{R}$ is always given by (12) only the component R_x parallel to the chord is plotted.

It is clear from the figure that the deviation of the along-chord force component R_x is strongly dependent on the percent deflection δ/L with an apparent singularity at $\delta/L = 0$ when $M \neq 0$. This singularity disappears for a real beam since the deflections due to axial strain (neglected in the analysis above) eventually become (as $\delta/L \rightarrow 0$) large compared to those due to bending. For $\delta/L < 0.1$, a rather nominal applied moment M produces large changes in the force R_x. As an example for a rod of length 5 m, stiffness 1955 Nt-m^2 and chord length 4.75 m, an applied moment of 250 Nt-m gives a 32 percent increase or a 28 percent decrease, depending on its sign, from the zero-moment restoring force of 770 Nt.

We here note that a somewhat more complicated solution similar to that developed previously could be given for the case where parallel moments are applied at *both* ends of a rod whose compressed length is fixed. In this case the restoring force $\overline{R}$ will be a function of a third dimensionless group NL/B involving the second applied moment N, and the shape and interior moment will be identical to those of an unknown *interior* section of a longer fictitious rod loaded with $\overline{R}$ only. This interior section could then be found using an iterative method similar to that described previously.

General applications of the model have been mentioned in the introductory section; a further specific application is the modeling of the pole vault [8]. In all cases, the additional complexity of the model accounting for the effects of end applied moments yields two advantages. First, the applied moment can now enter directly into the rotational dynamic equations for the object connected to the rod. But in addition (and more subtly), the indirect effect of the applied moment, on the translational equations through the rod restoring force, is accounted for.

Conclusions

An iterative solution for the shape and restoring force of a thin elastic rod with end positions given and loaded with an applied moment at one end has been formulated. Numerical studies were carried out which indicate that the applied moment can significantly magnify or attenuate the rod restoring force and also change its direction relative to the chord, especially when the percent deflection of the rod is small ($\delta/L < 0.1$). The additional complexity of such a model would be desirable when the rod connects rigid bodies which can exert such a torque, because the complete effects of the torque are then detailed, including contributions to both translational and rotational equations.

References

1 Truesdell, C., "The Rational Mechanics of Flexible or Elastic Bodies, 1638-1788," *Introduction to Leonhardi Euleri Opera Omnia*, Vol. X et XI, seriei secundae, O. Füssli, Turici, 1960.

2 Love, A. E. H., *A Treatise on the Mathematical Theory of Elasticity*, 4th ed., Dover Publications, New York, 1944, pp. 401–405.

3 Timoshenko, S. P., and Gere, J. M., *Theory of Elastic Stability*, McGraw-Hill, New York, 1961, pp. 76–82.

4 Southwell, R. V., *An Introduction to the Theory of Elasticity*, 2nd ed., Oxford University Press, 1941, pp. 429–436.

5 Prescott, J., *Applied Elasticity*, Dover Publications, New York, 1961, pp. 99–105.

6 Karnopp, D. C., and Rosenberg, R. C., *System Dynamics: A Unified Approach*, Wiley, New York, 1975.

7 Karnopp, D. C., and Rosenberg, R. C., "Analysis and Simulation of Multiport Systems," M.I.T. Press, 1968.

8 Walker, H. S., and Kirmser, P. G., "Computer Modeling of Pole Vaulting," *Mechanics and Sport*, AMD—Vol. 4, ASME, 1973.

9 Abramowitz, M., and Stegun, I. A., (eds.), *Handbook of Mathematical Functions*, National Bureau of Standards, U. S. Government Printing Office, 1972.

10 Bridgman, P. W., *Dimensional Analysis*, Yale University Press, 1931.

On Stress Boundary Conditions in Shell Theory

J. Lyell Sanders, Jr.[1]

Boundary conditions on the stress-functions of shell theory in terms of given boundary data are derived. The results are shown to be fully equivalent to the Kirchhoff boundary conditions and have the same form for all first-approximation theories of thin shells.

In his book Goldenveizer [1] derives the stress-stress function relations in shell theory by a process which involves a preliminary construction of two vector fields obtained by integration of edge forces and couples along arbitrary curves on the middle surface. The same ideas appear in the works of Chernykh [2] and Pietraszkiewicz [3, 4] and are used for a variety of purposes. The expression of an integrated form of the stress boundary conditions in terms of stress functions follows from the results of these authors but does not seem to have been explicitly stated. The results in question are produced in the present Note and are shown to be equivalent to the Kirchhoff boundary conditions and to have exactly the same form in all acceptable first-approximation theories of thin shells. Special results for shallow shells and for the semi-infinite circular cylinder have been given previously [5, 6].

The present derivation begins with a restatement of some of the fundamental formulas of the statics of thin shells. Associated with an arbitrary smooth curve Γ on the middle surface there is defined a vector of forces per unit length T^i expressible in terms of surface components as follows:

$$T^i = T^\alpha x^i_{,\alpha} + Qn^i \tag{1}$$

In terms of the membrane stress measure $N^{\alpha\beta}$ (unsymmetric and unmodified) and the transverse shear stress measure Q^α one has

$$T^\beta = N^{\alpha\beta} n_\alpha, \quad Q = Q^\alpha n_\alpha \tag{2}$$

The notation and the formulas from differential geometry used herein occur frequently and will be assumed to be familiar. There is likewise defined on Γ a vector of couples per unit length S^i tangent to the middle surface expressible in terms of surface components by

[1] Gordon McKay Professor of Structural Mechanics, Division of Applied Sciences, Harvard University, Cambridge, Mass. 02138.

Manuscript received by ASME Applied Mechanics Division, July, 1979.

$$\begin{bmatrix} dl \\ dM \end{bmatrix} = \begin{bmatrix} l - l_0 \\ M - M_0 \end{bmatrix}. \quad (18)$$

This procedure can be repeated as many times (i) as required to make the guess (γ_i, R_i) yield (M_i, l_i) arbitrarily close to the pair (M, l). Although the partial derivatives in (16) could in principle be determined either analytically or numerically, the latter would probably be preferred since the whole scheme is fundamentally a numerical one.

Results

Using the principles of dimensional analysis [10] it is possible to deduce the general form of dependence of the parameters of the problem in the most general case. If we apply the Buckingham π theorem, three dimensionless groups emerge; RL^2/B, ML/B, and δ/L. Hence the first is related functionally to the second two and we may write

$$R = B/L^2 f(ML/B,\ \delta/L). \quad (19)$$

Numerical solution of the procedure was accomplished on a computer for a given rod (B, L) and for a range of values of the input variables M and δ. In light of (18), however, such a specific solution can be generalized to an elastica of arbitrary length and stiffness. These general results are also shown in Fig. 2. Since the y component of $\overline{R}$ is always given by (12) only the component R_x parallel to the chord is plotted.

It is clear from the figure that the deviation of the along-chord force component R_x is strongly dependent on the percent deflection δ/L with an apparent singularity at $\delta/L = 0$ when $M \neq 0$. This singularity disappears for a real beam since the deflections due to axial strain (neglected in the analysis above) eventually become (as $\delta/L \to 0$) large compared to those due to bending. For $\delta/L < 0.1$, a rather nominal applied moment M produces large changes in the force R_x. As an example for a rod of length 5 m, stiffness 1955 Nt-m^2 and chord length 4.75 m, an applied moment of 250 Nt-m gives a 32 percent increase or a 28 percent decrease, depending on its sign, from the zero-moment restoring force of 770 Nt.

We here note that a somewhat more complicated solution similar to that developed previously could be given for the case where parallel moments are applied at *both* ends of a rod whose compressed length is fixed. In this case the restoring force $\overline{R}$ will be a function of a third dimensionless group NL/B involving the second applied moment N, and the shape and interior moment will be identical to those of an unknown *interior* section of a longer fictitious rod loaded with $\overline{R}$ only. This interior section could then be found using an iterative method similar to that described previously.

General applications of the model have been mentioned in the introductory section; a further specific application is the modeling of the pole vault [8]. In all cases, the additional complexity of the model accounting for the effects of end applied moments yields two advantages. First, the applied moment can now enter directly into the rotational dynamic equations for the object connected to the rod. But in addition (and more subtly), the indirect effect of the applied moment, on the translational equations through the rod restoring force, is accounted for.

Conclusions

An iterative solution for the shape and restoring force of a thin elastic rod with end positions given and loaded with an applied moment at one end has been formulated. Numerical studies were carried out which indicate that the applied moment can significantly magnify or attenuate the rod restoring force and also change its direction relative to the chord, especially when the percent deflection of the rod is small ($\delta/L < 0.1$). The additional complexity of such a model would be desirable when the rod connects rigid bodies which can exert such a torque, because the complete effects of the torque are then detailed, including contributions to both translational and rotational equations.

References

1 Truesdell, C., "The Rational Mechanics of Flexible or Elastic Bodies, 1638-1788," *Introduction to Leonhardi Euleri Opera Omnia*, Vol. X et XI, seriei secundae, O. Füssli, Turici, 1960.

2 Love, A. E. H., *A Treatise on the Mathematical Theory of Elasticity*, 4th ed., Dover Publications, New York, 1944, pp. 401–405.

3 Timoshenko, S. P., and Gere, J. M., *Theory of Elastic Stability*, McGraw-Hill, New York, 1961, pp. 76–82.

4 Southwell, R. V., *An Introduction to the Theory of Elasticity*, 2nd ed., Oxford University Press, 1941, pp. 429–436.

5 Prescott, J., *Applied Elasticity*, Dover Publications, New York, 1961, pp. 99–105.

6 Karnopp, D. C., and Rosenberg, R. C., *System Dynamics: A Unified Approach*, Wiley, New York, 1975.

7 Karnopp, D. C., and Rosenberg, R. C., "Analysis and Simulation of Multiport Systems," M.I.T. Press, 1968.

8 Walker, H. S., and Kirmser, P. G., "Computer Modeling of Pole Vaulting," *Mechanics and Sport*, AMD—Vol. 4, ASME, 1973.

9 Abramowitz, M., and Stegun, I. A., (eds.), *Handbook of Mathematical Functions*, National Bureau of Standards, U. S. Government Printing Office, 1972.

10 Bridgman, P. W., *Dimensional Analysis*, Yale University Press, 1931.

On Stress Boundary Conditions in Shell Theory

J. Lyell Sanders, Jr.[1]

Boundary conditions on the stress-functions of shell theory in terms of given boundary data are derived. The results are shown to be fully equivalent to the Kirchhoff boundary conditions and have the same form for all first-approximation theories of thin shells.

In his book Goldenveizer [1] derives the stress-stress function relations in shell theory by a process which involves a preliminary construction of two vector fields obtained by integration of edge forces and couples along arbitrary curves on the middle surface. The same ideas appear in the works of Chernykh [2] and Pietraszkiewicz [3, 4] and are used for a variety of purposes. The expression of an integrated form of the stress boundary conditions in terms of stress functions follows from the results of these authors but does not seem to have been explicitly stated. The results in question are produced in the present Note and are shown to be equivalent to the Kirchhoff boundary conditions and to have exactly the same form in all acceptable first-approximation theories of thin shells. Special results for shallow shells and for the semi-infinite circular cylinder have been given previously [5, 6].

The present derivation begins with a restatement of some of the fundamental formulas of the statics of thin shells. Associated with an arbitrary smooth curve Γ on the middle surface there is defined a vector of forces per unit length T^i expressible in terms of surface components as follows:

$$T^i = T^\alpha x^i_{,\alpha} + Qn^i \quad (1)$$

In terms of the membrane stress measure $N^{\alpha\beta}$ (unsymmetric and unmodified) and the transverse shear stress measure Q^α one has

$$T^\beta = N^{\alpha\beta} n_\alpha, \quad Q = Q^\alpha n_\alpha \quad (2)$$

The notation and the formulas from differential geometry used herein occur frequently and will be assumed to be familiar. There is likewise defined on Γ a vector of couples per unit length S^i tangent to the middle surface expressible in terms of surface components by

[1] Gordon McKay Professor of Structural Mechanics, Division of Applied Sciences, Harvard University, Cambridge, Mass. 02138.

Manuscript received by ASME Applied Mechanics Division, July, 1979.

$$S^i = S^\alpha x^i_{,\alpha} \tag{3}$$

Bending moment and twisting moment scalars M_n and M_t associated with Γ

$$M_n = M^{\alpha\beta} n_\alpha n_\beta, \quad M_t = M^{\alpha\beta} n_\alpha t_\beta \tag{4}$$

can be used to express S^α in the form

$$S^\alpha = M_n t^\alpha - M_t n^\alpha \tag{5}$$

The combined moment about the origin of forces and couples associated with Γ is given by the vector

$$C^i = S^i + \epsilon_{ijk} x^j T^k \tag{6}$$

The Goldenveizer vectors are constructed in terms of integrals of T^i and C^i. Choose any reference point x^i_0 on the middle surface, let s be arc length measured away from x^i_0 along a curve Γ, and let t^α and n^α point ahead and to the right as usual. Define F^i, M^i, and H^i associated with Γ by the equations

$$F^i = \int_0^s T^i ds, \quad M^i = \int_0^s C^i ds, \quad H^i = M^i - \epsilon_{ijk} x^j F^k \tag{7}$$

If the shell is in equilibrium in the absence of surface loads then, by the laws of statics, F^i and M^i must vanish when the integrals are calculated over any closed path. Equivalently stated: F^i, M^i, and thus H^i, defined in (7), are independent of the path Γ and hence constitute vector fields on the middle surface provided the shell is in equilibrium without surface loads.

The surface components χ^α and ψ of H^i, defined by

$$H^i = \chi^\alpha x^i_{,\alpha} + \psi n^i \tag{8}$$

and the normal component $F^i n^i$ of F^i are Goldenveizer's stress functions. As a consequence of $S^i n^i = 0$ for arbitrary Γ the following relation holds between the tangential components of F^i and the surface gradient of H^i,

$$F^i x^i_{,\alpha} = g_{\alpha\beta} \epsilon^{\beta\gamma} H^i_{,\gamma} n^i \tag{9}$$

The normal component of F^i is an independent stress function. However, as has been shown [7–9], the equilibrium equations and stress boundary conditions of shell theory can be written exactly (in various ways) in terms of "combined" or "reduced" stress measures and in all cases the reduced stress measures are expressible in terms of the components of H^i alone.

Now consider Γ to be the edge of a shell on which T^i and S^i, or equivalently the five variables T^α, Q, M_n, and M_t, are given. These five physical boundary conditions collapse into the four Kirchhoff boundary conditions for the four "effective" edge loads given by M_n and

$$\overline{T}^\alpha = T^\alpha + M_t b^\alpha_\beta t^\beta$$

$$V = Q + \frac{dM_t}{ds} \tag{10}$$

Let a vector $\overline{T}^i$ be defined by

$$\overline{T}^i = \overline{T}^\alpha x^i_{,\alpha} + V n^i \tag{11}$$

The vectors T^i and $\overline{T}^i$ are simply related to each other

$$T^i = \overline{T}^i - \frac{d}{ds}(M_t n^i) \tag{12}$$

Likewise define $\overline{S}^i$ (see equations (3) and (5)) by

$$\overline{S}^i = \overline{S}^\alpha x^i_{,\alpha}, \quad \overline{S}^\alpha = M_n t^\alpha \tag{13}$$

and define $\overline{C}^i$ as in (6) but with $\overline{S}^i$ and $\overline{T}^i$ on the right. The following relation, similar to (12) holds:

$$C^i = \overline{C}^i - \epsilon_{ijk} \frac{d}{ds}(M_t x^j n^k) \tag{14}$$

In a similar fashion define $\overline{F}^i$, $\overline{M}^i$, and $\overline{H}^i$ by formulas analogous to (7). By means of (12) and (14) there follows from (7) and these definitions

$$F^i = \overline{F}^i - M_t n^i + M_{t,0} n^i_0 \tag{15}$$

$$H^i = \overline{H}^i - \epsilon_{ijk} M_{t,0}(x^j - x^j_0) n^k_0 \tag{16}$$

For the final result it is important to note that H^i and the scalar $F^i t^i$ differ from $\overline{H}^i$ and $\overline{F}^i t^i$ only by terms with the constant factor $M_{t,0}$, and that $\overline{F}^i$ and $\overline{H}^i$ are expressible in terms of effective edge loads only. The vector t^i referred to here is the Cartesian form of the unit vector t^α tangent to Γ.

That the terms with the constant factor $M_{t,0}$ are inconsequential to the result can be argued as follows. The vector H^i is the static-geometric analog of the displacement vector U^i, and F^i is the analog of the rotation vector Ω^i. These facts are more or less obvious and are simply borrowed here from the general theory for reasons of brevity. Interpreted in terms of displacements and rotations the expressions

$$U^i = -\epsilon_{ijk} M_{t,0}(x^j - x^j_0) n^k_0$$

and (17)

$$\Omega^i = M_{t,0} n^i_0$$

correspond to a rigid-body motion and have no effect upon strains. Therefore, by analogy, the terms with $M_{t,0}$ in $F^i t^i$ and H^i can be deleted with no effect upon stresses or the statement of stress boundary conditions. The point is perhaps reinforced a bit by the fact that the effective variables M_n and $\overline{T}^i$ can be expressed in terms of H^i and $F^i t^i$ by the following formulas (not involving $M_{t,0}$) which are not difficult to derive.

$$M_n = \frac{dH^i}{ds} t^i \tag{18}$$

$$\overline{T}^i = \frac{d}{ds}\left[F^j t^j n^i + \frac{dH^j}{ds}(n^j \nu^i - n^i \nu^j)\right]$$

where ν^i is the Cartesian form of n^α.

One more relation is needed before stating the final result. From (9) there follows:

$$F^i t^i = -\frac{dH^i}{dn} n^i \tag{19}$$

The final result is this: the stress boundary conditions in terms of stress functions, fully equivalent to the Kirchhoff boundary conditions, are given by

$$\left.\begin{array}{ll} \chi_\alpha = H^i x^i_{,\alpha}, & \psi = H^i n^i \\ (\psi_{,\alpha} - b_{\alpha\beta}\chi^\beta) n^\alpha = -F^i t^i & \end{array}\right\} \text{on } \Gamma \tag{20}$$

where F^i and H^i on Γ are constructed in terms of the boundary data according to equations (6) and (7). Since H^i is the fundamental stress function vector common to all first-approximation shell theories, the statement of stress boundary conditions in the form (20) holds in all cases (as does the analogous form of the statement for displacement boundary conditions). Of course, the expressions for the stress measures in terms of the stress functions χ^α and ψ depend upon how the stress measures are defined. Given in the form (20), the boundary conditions require no additional statements for the case in which Γ has corners.

Acknowledgment

This work was supported in part by the National Science Foundation under Grant MCS78-07598, and by the Division of Applied Sciences, Harvard University.

References

1 Goldenveizer, A. L., *Theory of Elastic Thin Shells* (English translation), Pergamon Press, 1961.

2 Chernykh, K. F., *Linear Theory of Shells*, NASA Translation TT F-441, 1968.

3 Pietraszkiewicz, W., "On the Multivaluedness of Stress Functions in the

Linear Theory of Shells," *Bull. de L'Academie Polonaise des Sciences,* Vol. XV, 1967, pp. 619–624.
4 Pietraszkiewicz, W., "Multivalued Stress Functions in the Linear Theory of Shells," *Archiwum Mechaniki Stosowanej,* Vol. 20, 1968, pp. 37–45.
5 Sanders, J. L., "Cutouts in Shallow Shells," ASME JOURNAL OF APPLIED MECHANICS, Vol. 37, 1970, pp. 374–383.
6 Sanders, J. L., "Closed-Form Solution to the Semi-Infinite Cylindrical Shell Problem," *Contributions to the Theory of Aircraft Structures,* The van der Neut Volume, Delft University Press, Rotterdam, 1972, pp. 229–237.
7 Lurie, A. I., "On the Equations of the General Theory of Elastic Shells," *Prikladnaya Matematika und Mechanika,* Vol. 12, 1950, p. 558.
8 Novozhilov, V. V., *The Theory of Thin Shells* (English translation), P. Noordhoff, Groningen, 1959.
9 Budiansky, B., and Sanders, J. L., "On the 'Best' First-Order Linear Shell Theory," *Progress in Applied Mechanics,* The Prager Anniversary Volume, Macmillan Co., 1963, pp. 129–140.

An Unusual Closed-Form Solution for a Variable-Thickness Plate on an Elastic Foundation

H. D. Conway[1]

Introduction

This short Note is concerned with the unsymmetrical bending of a particular circular plate of variable thickness which is supported by a Winkler-type elastic foundation. What is remarkable about this solution is that it is in a closed form which is far simpler than the constant-thickness disk solution which involves Kelvin functions. Moreover the quartic characteristic equation which is involved in the present solution possesses particularly simple roots. Aside from its academic interest and possible design applications, this solution is exact and could possibly be used for assessing the accuracy of various approximate methods of solutions.

Analysis

The governing differential equation for the disk is readily obtained from the three equations of equilibrium in polar coordinates and the three moment-curvature relationships [1]. For a flexural rigidity $D = D(r)$ the governing differential equation for the nonsymmetrical bending of the plate is the very complicated

$$D\nabla^4 w + \frac{dD}{dr}\left[2\frac{\partial^3 w}{\partial r^3} + \frac{2+\nu}{r}\frac{\partial^2 w}{\partial r^2} - \frac{1}{r^2}\frac{\partial w}{\partial r} + \frac{2}{r^2}\frac{\partial^3 w}{\partial r \partial\theta^2} - \frac{3}{r^3}\frac{\partial^2 w}{\partial\theta^2}\right] + \frac{d^2D}{dr^2}\left[\frac{\partial^2 w}{\partial r^2} + \frac{\nu}{r}\frac{\partial w}{\partial r} + \frac{\nu}{r^2}\frac{\partial^2 w}{\partial\theta^2}\right] = q - kw \quad (1)$$

with the usual plate notation and where k is the elastic foundation modulus. Writing $D = D_0 r^4$ and $w = F(r)\cos n\theta$, where n is an integer for a complete disk, we find for the complementary solution that

$$\left(\frac{d^2}{dr^2} + \frac{1}{r}\frac{d}{dr} - \frac{n^2}{r^2}\right)\left(\frac{d^2F}{dr^2} + \frac{1}{r}\frac{dF}{dr} - \frac{n^2}{r^2}F\right) + \frac{8}{r}\frac{d^3F}{dr^3} + \frac{4(5+\nu)}{r^2}\frac{d^2F}{dr^2} - \frac{4(1-3\nu+2n^2)}{r^3}\frac{dF}{dr} + \frac{[12n^2(1-\nu) + k/D_0]}{r^4}F = 0 \quad (2)$$

This is a homogeneous linear equation. If we write $F = Ar^\lambda$, the characteristic equation is then

$$\lambda^4 + 4\lambda^3 + 2(2\nu - n^2)\lambda^2 - 4(2 - 2\nu + n^2)\lambda + n^4 + 6n^2 - 12\nu^2 + \frac{k}{D_0}F = 0 \quad (3)$$

A most remarkable thing about this quartic equation is that it readily factors in the form

$$(\lambda + 1 + \beta_1)(\lambda + 1 - \beta_1)(\lambda + 1 + \beta_2)(\lambda + 1 - \beta_2) = 0 \quad (4)$$

since comparing respective coefficients of λ^2 and λ leads to the same equation! Multiplication of the terms in equation (4) and comparison with equation (3) leads to

$$\beta_1^2 + \beta_2^2 = 6 - 4\nu + 2n^2$$
$$\beta_1^2\beta_2^2 = n^4 + 8n^2 + 5 - 4\nu - 12\nu n^2 + \frac{k}{D_0} \quad (5)$$

from which β_1 and β_2 are readily obtained, and the solution is

$$w = [A_1 r^{-1-\beta_1} + A_2 r^{-1+\beta_1} + A_3 r^{-1-\beta_2} + A_4 r^{-1+\beta_2}]\cos n\theta. \quad (6)$$

This exact closed-form solution is valid for any boundary conditions on the inner and outer edges of the disk. Of particular interest is the fact that the solution is in terms of elementary functions, and not the Kelvin functions ber_n, bei_n, ker_n, kei_n for a constant-thickness plate. Finally it should be mentioned that a similar simple closed-form solution has been found[2] for the free nonsymmetrical vibrations of a disk having $D = D_0 r^6$.

References

1 Leissa, A. W., "Vibration of Plates," NASA SP-160, 1969, p. 285.
2 Lenox, T. A., and Conway, H. D., "An Exact, Closed-Form Solution for the Flexural Vibration of a Thin Annular Plate Having a Parabolic Thickness Variation," *Journal of Sound and Vibration* Vol. 67, No. 4, Dec. 1979.

[1] Professor, Department of Theoretical and Applied Mechanics, Cornell University, Ithaca, N.Y. 14853.

Manuscript received by ASME Applied Mechanics Division, September, 1979.

Buckling of a Column With Nonlinear Restraints and Random Initial Displacement[1]

W. B. Day[2]

The nondimensional form of the equation for lateral displacement w of a column under load λ and initial random displacement $\epsilon w_0''$ is given by $w^{\mathrm{iv}} + 2\lambda w'' + w - w^3 = -2\lambda\epsilon w_0''$. This paper derives an expression for the average value of λ for which buckling occurs.

The nondimensional form of the equation for the lateral displacement w of a column with load λ, a nonlinear restoring force, and initial random displacement $\epsilon w_0''$ is given by

$$w^{\mathrm{iv}} + 2\lambda w'' + w - w^3 = -2\lambda\,\epsilon\,w_0'' \quad (1)$$

and is derived in [1, 2]. The discussion that follows applies to any homogeneous boundary conditions. For simplicity we use $w(\pm\pi) =$

[1] This paper was written while on sabbatical leave at the Courant Institute of Mathematical Sciences, New York University, New York, 10012.

[2] Department of Mathematics, Auburn University, Auburn, Ala. 36830.

Manuscript received by ASME Applied Mechanics Division, May, 1979; final revision, September, 1979.

Linear Theory of Shells," *Bull. de L'Academie Polonaise des Sciences,* Vol. XV, 1967, pp. 619–624.
4 Pietraszkiewicz, W., "Multivalued Stress Functions in the Linear Theory of Shells," *Archiwum Mechaniki Stosowanej,* Vol. 20, 1968, pp. 37–45.
5 Sanders, J. L., "Cutouts in Shallow Shells," ASME JOURNAL OF APPLIED MECHANICS, Vol. 37, 1970, pp. 374–383.
6 Sanders, J. L., "Closed-Form Solution to the Semi-Infinite Cylindrical Shell Problem," *Contributions to the Theory of Aircraft Structures,* The van der Neut Volume, Delft University Press, Rotterdam, 1972, pp. 229–237.
7 Lurie, A. I., "On the Equations of the General Theory of Elastic Shells," *Prikladnaya Matematika und Mechanika,* Vol. 12, 1950, p. 558.
8 Novozhilov, V. V., *The Theory of Thin Shells* (English translation), P. Noordhoff, Groningen, 1959.
9 Budiansky, B., and Sanders, J. L., "On the 'Best' First-Order Linear Shell Theory," *Progress in Applied Mechanics,* The Prager Anniversary Volume, Macmillan Co., 1963, pp. 129–140.

An Unusual Closed-Form Solution for a Variable-Thickness Plate on an Elastic Foundation

H. D. Conway[1]

Introduction

This short Note is concerned with the unsymmetrical bending of a particular circular plate of variable thickness which is supported by a Winkler-type elastic foundation. What is remarkable about this solution is that it is in a closed form which is far simpler than the constant-thickness disk solution which involves Kelvin functions. Moreover the quartic characteristic equation which is involved in the present solution possesses particularly simple roots. Aside from its academic interest and possible design applications, this solution is exact and could possibly be used for assessing the accuracy of various approximate methods of solutions.

Analysis

The governing differential equation for the disk is readily obtained from the three equations of equilibrium in polar coordinates and the three moment-curvature relationships [1]. For a flexural rigidity $D = D(r)$ the governing differential equation for the nonsymmetrical bending of the plate is the very complicated

$$D\nabla^4 w + \frac{dD}{dr}\left[2\frac{\partial^3 w}{\partial r^3} + \frac{2+\nu}{r}\frac{\partial^2 w}{\partial r^2} - \frac{1}{r^2}\frac{\partial w}{\partial r} + \frac{2}{r^2}\frac{\partial^3 w}{\partial r\partial\theta^2} - \frac{3}{r^3}\frac{\partial^2 w}{\partial\theta^2}\right] + \frac{d^2D}{dr^2}\left[\frac{\partial^2 w}{\partial r^2} + \frac{\nu}{r}\frac{\partial w}{\partial r} + \frac{\nu}{r^2}\frac{\partial^2 w}{\partial\theta^2}\right] = q - kw \quad (1)$$

with the usual plate notation and where k is the elastic foundation modulus. Writing $D = D_0 r^4$ and $w = F(r)\cos n\theta$, where n is an integer for a complete disk, we find for the complementary solution that

$$\left(\frac{d^2}{dr^2} + \frac{1}{r}\frac{d}{dr} - \frac{n^2}{r^2}\right)\left(\frac{d^2F}{dr^2} + \frac{1}{r}\frac{dF}{dr} - \frac{n^2}{r^2}F\right) + \frac{8}{r}\frac{d^3F}{dr^3} + \frac{4(5+\nu)}{r^2}\frac{d^2F}{dr^2} - \frac{4(1-3\nu+2n^2)}{r^3}\frac{dF}{dr} + \frac{[12n^2(1-\nu)+k/D_0]}{r^4}F = 0 \quad (2)$$

This is a homogeneous linear equation. If we write $F = Ar^\lambda$, the characteristic equation is then

$$\lambda^4 + 4\lambda^3 + 2(2\nu - n^2)\lambda^2 - 4(2 - 2\nu + n^2)\lambda + n^4 + 6n^2 - 12\nu^2 + \frac{k}{D_0}F = 0 \quad (3)$$

A most remarkable thing about this quartic equation is that it readily factors in the form

$$(\lambda + 1 + \beta_1)(\lambda + 1 - \beta_1)(\lambda + 1 + \beta_2)(\lambda + 1 - \beta_2) = 0 \quad (4)$$

since comparing respective coefficients of λ^2 and λ leads to the same equation! Multiplication of the terms in equation (4) and comparison with equation (3) leads to

$$\beta_1^2 + \beta_2^2 = 6 - 4\nu + 2n^2$$
$$\beta_1^2\beta_2^2 = n^4 + 8n^2 + 5 - 4\nu - 12\nu n^2 + \frac{k}{D_0} \quad (5)$$

from which β_1 and β_2 are readily obtained, and the solution is

$$w = [A_1 r^{-1-\beta_1} + A_2 r^{-1+\beta_1} + A_3 r^{-1-\beta_2} + A_4 r^{-1+\beta_2}]\cos n\theta. \quad (6)$$

This exact closed-form solution is valid for any boundary conditions on the inner and outer edges of the disk. Of particular interest is the fact that the solution is in terms of elementary functions, and not the Kelvin functions ber_n, bei_n, ker_n, kei_n for a constant-thickness plate. Finally it should be mentioned that a similar simple closed-form solution has been found[2] for the free nonsymmetrical vibrations of a disk having $D = D_0 r^6$.

References

1 Leissa, A. W., "Vibration of Plates," NASA SP-160, 1969, p. 285.
2 Lenox, T. A., and Conway, H. D., "An Exact, Closed-Form Solution for the Flexural Vibration of a Thin Annular Plate Having a Parabolic Thickness Variation," *Journal of Sound and Vibration* Vol. 67, No. 4, Dec. 1979.

[1] Professor, Department of Theoretical and Applied Mechanics, Cornell University, Ithaca, N.Y. 14853.
Manuscript received by ASME Applied Mechanics Division, September, 1979.

Buckling of a Column With Nonlinear Restraints and Random Initial Displacement[1]

W. B. Day[2]

The nondimensional form of the equation for lateral displacement w of a column under load λ and initial random displacement $\epsilon w_0''$ is given by $w^{\mathrm{iv}} + 2\lambda w'' + w - w^3 = -2\lambda\epsilon w_0''$. This paper derives an expression for the average value of λ for which buckling occurs.

The nondimensional form of the equation for the lateral displacement w of a column with load λ, a nonlinear restoring force, and initial random displacement $\epsilon w_0''$ is given by

$$w^{\mathrm{iv}} + 2\lambda w'' + w - w^3 = -2\lambda\,\epsilon\, w_0'' \quad (1)$$

and is derived in [1, 2]. The discussion that follows applies to any homogeneous boundary conditions. For simplicity we use $w(\pm\pi) =$

[1] This paper was written while on sabbatical leave at the Courant Institute of Mathematical Sciences, New York University, New York, 10012.
[2] Department of Mathematics, Auburn University, Auburn, Ala. 36830.
Manuscript received by ASME Applied Mechanics Division, May, 1979; final revision, September, 1979.

On Dispersion of Periodically Layered Composites in Plane Strain

A. A. Golebiewska[1]

Introduction

In recent years, considerable attention was paid to wave propagation in periodically layered elastic composites, cf. references [1–5], the analysis being based on the theory of Floquet waves. While the behavior of SH-waves (horizontally polarized shear waves) in such systems is reasonably well understood, [4], wave propagation in plane strain has been only incompletely explored. This is due to the fact that such waves involve a complicated coupling between P-waves (compressional waves) and SV-waves (vertically polarized shear waves). The dispersion equation is given by an 8×8 functional determinant which in the past has been evaluated numerically.

It is the purpose of this Note to show that the dispersion equation for plane strain can be expanded in closed form. This should facilitate considerably a later systematic analysis. It is shown further, that if the ratio of the two thicknesses of the composite is small, the dispersion relation uncouples into two independent equations, representing two separate surfaces in the frequency-wave number space. This uncoupling is rigorously valid for any ratio of elastic constants and mass densities of the two constituents of the composite. The system corresponds to the case of matrix being reinforced by thin, periodically distributed layers.

The General Dispersion Relation

The composite under consideration consists of periodically alternating layers of two different isotropic and homogeneous elastic materials, perfectly bonded along their plane interfaces. The properties of the two materials are described by the Lamé constants λ, μ (or Poisson's ratio, ν) and λ', μ' (or ν'), as well as the mass density ρ and ρ'. The thicknesses of the two layers are $2h$ and $2h'$, respectively. The Cartesian system of reference is chosen in such a way that the bonding planes are normal to the y-axis.

For plane strain the components of the displacement fields $\mathbf{u}$ and $\mathbf{u}'$ in the composite are

$$u = u(x, y_N, t), \quad v = v(x, y_N, t), \quad \mathrm{w} = 0 \tag{1}$$

where y_N is a local coordinate of the Nth layer normal to the interface, chosen in such a way that $-h < y_N < h$. The same holds for $\mathbf{u}'$.

The fields $\mathbf{u}$ and $\mathbf{u}'$ can be represented by the Lamé potentials, e.g., for $\mathbf{u}$

$$u = \frac{\partial \Phi}{\partial x} + \frac{\partial \psi}{\partial y_N}, \quad v = \frac{\partial \Phi}{\partial x} - \frac{\partial \psi}{\partial y_N} \tag{2}$$

and substitution into the equation of motion leads to two wave equations for the potentials ϕ and ψ with velocities c_1 and c_2

$$c_1 = [(\lambda + 2\mu)/\rho]^{1/2}, \quad c_2 = [\mu/\zeta^{-r0}]^{1/2} \tag{3}$$

which denote longitudinal and transversal wave velocities in the unprimed solid. The same holds true for the primed solid. By solving the equations of motion in terms of potentials and making use of (2), we obtain $\mathbf{u}$ and $\mathbf{u}'$. The expression for each vector involves four coefficients C_1, C_2, C_3, C_4 and C_1', C_2', C_3', C_4', respectively. Continuity and periodicity conditions for displacements and tractions across the interfaces supply 8 equations: these form a system of 8 homogeneous linear equations for the 8 unknown coefficients C_i and C_i' ($i = 1, \ldots, 4$). For nontrivial solutions the vanishing of the determinant

$$\begin{vmatrix}
\zeta B_- & \zeta B_+ & \alpha A_- & -\alpha A_+ & -\zeta B_+' & -\zeta B_-' & -\alpha' A_+' & \alpha' A_-' \\
\beta B_- & -\beta B_+ & -\zeta A_- & -\zeta A_+ & -\beta' B_+' & \beta' B_-' & \zeta A_+' & \zeta A_-' \\
2\gamma\beta\zeta B_- & -2\gamma\beta\zeta B_+ & \gamma\phi A_- & \gamma\phi A_+ & -2\beta'\zeta B_+' & 2\beta'\zeta B_-' & -\phi' A_+' & -\phi' A_-' \\
\gamma\phi B_- & \gamma\phi B_+ & -2\gamma\alpha\zeta A_- & 2\gamma\alpha\zeta A_+ & -\phi' B_+' & -\phi' B_-' & 2\alpha'\zeta A_+' & -2\alpha'\zeta A_-' \\
\zeta B_+ & \zeta B_- & \alpha A_+ & -\alpha A_- & -\zeta B_-'\tau & -\zeta B_+'\tau & -\alpha' A_-'\tau & \alpha' A_+'\tau \\
\beta B_+ & -\beta B_- & -\zeta A_+ & -\zeta A_- & -\beta' B_-'\tau & \beta' B_+'\tau & \zeta A_-'\tau & \zeta A_+'\tau \\
2\gamma\beta\zeta B_+ & -2\gamma\beta\zeta B_- & \gamma\phi A_+ & \gamma\phi A_- & -2\beta'\zeta B_-'\tau & 2\beta'\zeta B_+'\tau & -\phi' A_-'\tau & -\phi' A_+'\tau \\
\gamma\phi B_+ & \gamma\phi B_- & -2\gamma\alpha\zeta A_+ & 2\gamma\alpha\zeta A_- & -\phi' B_+'\tau & -\phi' B_+'\tau & 2\alpha'\zeta A_-'\tau & -2\alpha'\zeta A_+'\tau
\end{vmatrix} = 0 \tag{4}$$

is required, where

$$A_\pm = \exp[\pm i\pi\alpha/2], \quad B_\pm = \exp[\pm i\pi\beta/2],$$
$$\phi = \alpha^2 - \zeta^2, \quad \tau = \exp[ip\eta]$$
$$A_\pm' = \exp[\pm i\pi\epsilon\alpha'/2], \quad B_\pm' = \exp[\pm i\pi\epsilon\beta'/2], \quad \phi' = \alpha'^2 - \zeta^2 \tag{5}$$
$$\epsilon = h'/h, \quad \gamma = \mu/\mu', \quad \sigma^2 = \frac{\mu\rho'}{\mu'\rho} = \frac{c_2^2}{c_2'^2},$$
$$l = \frac{1 - 2\nu}{2(1 - \nu)}, \quad l' = \frac{1 - 2\nu'}{2(1 - \nu')}$$
$$\Omega = \frac{2h}{\pi}\frac{\omega}{c_2}, \quad \zeta = \frac{2h}{\pi}k_x, \quad \eta = \frac{2h}{\pi}k_y, \quad p = \pi(1 + \epsilon)$$
$$\alpha = \sqrt{\Omega^2 - \zeta^2} = \frac{2h}{\pi}\sqrt{(\omega/c_2)^2 - k_2^2},$$
$$\alpha' = \sqrt{\sigma^2\Omega^2 - \zeta^2} = \frac{2h}{\pi}\sqrt{(\omega/c_2')^2 - k_x^2}$$
$$\beta = \sqrt{\Omega^2 l - \zeta^2} = \frac{2h}{\pi}\sqrt{(\omega/c_1)^2 - k_x^2},$$
$$\beta' = \sqrt{\sigma^2\Omega^2 l' - \zeta^2} = \frac{2h}{\pi}\sqrt{(\omega/c_1')^2 - k_x^2} \tag{6}$$

Here ω is the circular frequency, k_x and k_y are the wave numbers in the x and y-direction, respectively. After cumbersome and lengthy algebraic manipulations, it is possible to expand the determinant (4) and represent the dispersion equation in the form

$$\begin{aligned}
&2\tau^2[-L_1(c_\alpha c_\beta + c_{\alpha'}c_{\beta'}) + L_2 s_\alpha s_\beta(1 - c_{\alpha'}c_{\beta'}) + L_3 s_{\alpha'}s_{\beta'}(1 - c_\alpha c_\beta) \\
&\quad - L_5 c_\alpha s_\beta c_{\alpha'} s_{\beta'} - L_6 s_\alpha c_\beta s_{\alpha'} c_{\beta'} - L_8 c_\alpha s_\beta s_{\alpha'} c_{\beta'} - L_9 s_\alpha c_\beta c_{\alpha'} s_{\beta'} \\
&\quad + (L_{11} + L_{12}) c_\alpha c_\beta c_{\alpha'} c_{\beta'} + \tfrac{1}{2} L_{10} s_\alpha s_\beta s_{\alpha'} s_{\beta'}] + \tau(\tau^2 + 1) \\
&\times [-L_4(c_\alpha c_{\alpha'} + c_\beta c_{\beta'}) + L_5 s_\beta s_{\beta'} + L_6 s_\alpha s_{\alpha'} + L_7(c_\alpha c_{\beta'} + c_\beta c_{\alpha'}) \\
&\quad + L_8 s_\beta s_{\alpha'} + L_9 s_\alpha s_{\beta'}] + 2\tau^2 L_{11} + (\tau^4 + 1) L_{12} = 0
\end{aligned} \tag{7}$$

where

$$\begin{aligned}
L_1 &= 2\alpha\beta\alpha'\beta' P_1 P_2 P_4 P_5, \\
L_2 &= \alpha'\beta'[(\alpha\beta P_1 P_2)^2 + (P_4 P_5)^2], \\
L_3 &= \alpha\beta[(P_1 P_4)^2 + (\alpha'\beta' P_2 P_5)^2], \\
L_4 &= 2\alpha\beta\alpha'\beta' P_1 P_5 P_3 P_6, \\
L_5 &= \alpha\alpha' P_3 P_6[(P_1\beta)^2 + (P_5\beta')^2], \\
L_6 &= \beta\beta' P_3 P_6[(P_1\alpha)^2 + (P_5\alpha')^2], \\
L_7 &= 2\alpha\beta\alpha'\beta' P_3 P_6 P_2 P_4
\end{aligned} \tag{8}$$

[1]Division of Applied Mechanics, Stanford University, Stanford, Calif. 94305.

Manuscript received by ASME Applied Mechanics, July, 1978; final revision, October, 1979.

$$
\begin{aligned}
L_8 &= \alpha\beta' P_3 P_6[(P_2\beta\alpha')^2 + P_4{}^2] \\
L_9 &= \beta\alpha' P_3 P_6[(P_2\alpha\beta')^2 + P_4{}^2] \\
L_{10} &= (\alpha\beta)^2 P_1{}^4 + (\alpha\beta\alpha'\beta')^2 P_2{}^4 + P_4{}^4 \\
&\quad + (\alpha'\beta')^2 P_5{}^4 + (P_3P_6)^2[(\alpha\beta')^2 + (\alpha'\beta)^2] \\
L_{11} &= \alpha\beta\alpha'\beta'[(P_1P_5)^2 + (P_2P_4)^2] \\
L_{12} &= \alpha\beta\alpha'\beta'(P_3P_6)^2
\end{aligned}
\qquad (8)\ (Cont.)
$$

$$
\begin{aligned}
c_\alpha &= \cos \pi\alpha, \quad c_\beta = \cos \pi\beta, \quad c_{\alpha'} = \cos \pi\alpha'\epsilon, \quad c_{\alpha'} = \cos \pi\beta'\epsilon \\
s_\alpha &= \sin \pi\alpha, \quad s_\beta = \sin \pi\beta, \quad s_{\alpha'} = \sin \pi\alpha'\epsilon, \quad s_{\beta'} = \sin \pi\beta'\epsilon
\end{aligned}
\qquad (9)
$$

and

$$
\begin{aligned}
P_1 &= \sigma^2\Omega^2 + 2\zeta^2(\gamma - 1), \quad P_2 = -2\zeta(\gamma - 1), \quad P_3 = \gamma\Omega^2, \quad P_6 = \sigma^2\Omega^2 \\
P_4 &= \zeta[2\zeta^2(\gamma - 1) + \Omega^2(\sigma^2 - \gamma)], \quad P_5 = \gamma\Omega^2 - 2\zeta^2(\gamma - 1)
\end{aligned}
\qquad (10)
$$

It is to be noted that the dispersion relation (7) is still a complex function even for real values of k_x and k_y (or ζ and η) because $\tau = \exp(ip\eta)$.

Simplification for Small h'/h

The dispersion relation (7) is very complicated due to coupling between P and SV-waves in the same layer as well as between two diferent layers. It can be shown, however, that a significant simplification, i.e., uncoupling, can be achieved if the ratio $\epsilon = h'/h$ of the thicknesses of the two layers is assumed to be much smaller than unity. Indeed, in this case the dispersion relation (7) separates into two independent relations

$$2\alpha\gamma\Omega^2(c_\alpha - c_\eta) + \pi\epsilon(2\alpha\gamma\Omega^2\eta s_\eta - J_2 s_\alpha) = 0 \qquad (11)$$

$$2\beta\gamma\Omega^2(c_\beta - c_\eta) + \pi\epsilon(2\beta\gamma\Omega^2\eta s_\eta - J_1 s_\beta) = 0 \qquad (12)$$

where

$$
\begin{aligned}
J_1 &= \Omega^2 l[\sigma^2\Omega^2 + 4\zeta^2\gamma(\gamma - 1)] \\
&\quad + l'[\gamma\Omega^2 - 2\zeta^2(\gamma - 1)]^2 - 2\zeta^2[2\zeta^2(\gamma - 1)^2 + \gamma\Omega^2] \qquad (13)
\end{aligned}
$$

$$
\begin{aligned}
J_2 &= \omega^2[\sigma^2\Omega^2 + 4\zeta^2(\gamma - 1)(1 + l'(\gamma - 1))] \\
&\quad + [\gamma\Omega^2 - 2\zeta^2(\gamma - 1)]^2 - 2\zeta^2[2\zeta^2 l'(\gamma - 1)^2 + \gamma\Omega^2] \qquad (14)
\end{aligned}
$$

It is to be emphasized that the uncoupled dispersion relations (12) and (13) are valid for small ratios of the thicknesses of the two layers, but for arbitrary values of the elastic constants and the densities in the two constituent materials.

Acknowledgment

This work was supported in part by ONR Contract N00014-76-C-0054 to Stanford University.

References

1 Sve, C., "Time Harmonic Waves Traveling Obliquely in a Periodically Laminated Medium," ASME JOURNAL OF APPLIED MECHANICS, Vol. 38, 1971, pp. 477–482.

2 Lee, E. H., and Yang, W. J., "On Waves in Composite Materials With Periodic Structure," *SIAM Journal of Applied Mathematics*, Vol. 25, 1973, pp. 492–499.

3 Sun, C.-T., Achenbach, J. D. and Herrmann, G., "Time-Harmonic Waves in a Stratified Medium Propagating in the Direction of the Layering," ASME JOURNAL OF APPLIED MECHANICS, Vol. 35, 1968, pp. 408–411.

4 Delph, T. J., Herrmann, G., and Kaul, R. K., "Harmonic Wave Propagation in a Periodically Layered, Infinite Elastic Body: Antiplane Strain," ASME JOURNAL OF APPLIED MECHANICS, Vol. 45, 1978, pp. 343–349.

5 Delph, T. J., Herrmann, G., and Kaul, R. K., "Harmonic Wave Propagation in a Periodically Layered, Infinite Elastic Body: Plane Strain, Analytical Results," ASME JOURNAL OF APPLIED MECHANICS, Vol. 46, 1979, pp. 113–119.

Discontinuity and Moment Dipole Along a V-Butt Weld in Plates

R. H. Bryant[1] and C. H. Wu[2]

Problem

One of the commonly used practices in welding steel plates is the so-called V-butt weld, Fig. 1. The shrinking of the weld after cooling gives rise to a discontinuity in slope across the weld line. The magnitude of this angular distortion is, of course, governed by many factors [1]. If, however, we make the assumption that the discontinuity in slope is purely a function of the weld, then this angular distortion becomes a given condition for the welded structure to satisfy. We show in the following that such a discontinuity is directly related to a moment dipole so that the deformation of the welded structure may be determined by direct integration via the introduction of an appropriate Green's function.

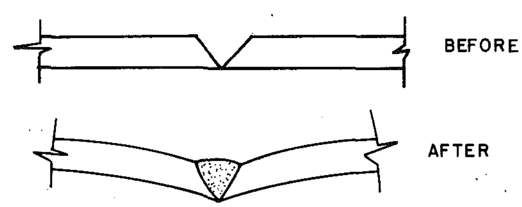

Fig. 1 ***V*-butt weld**

Solution

Let (Z_1,Z_2) be rectangular Cartesian coordinates and let D be the domain of the (Z_1,Z_2)-plane characterizing the shape of a plate. Certain boundary conditions are specified along ∂D, the boundary of D. The deflection of the plate at $\mathbf{z} = \mathbf{x}$ due to a unit load applied at $\mathbf{z} = \mathbf{y}$ may be written as

$$G(\mathbf{x};\mathbf{y}) = r^2 \ln r + R(\mathbf{x};\mathbf{y}), \qquad (1)^3$$

where

$$r = |\mathbf{x} - \mathbf{y}|, \qquad (2)$$

and R is a regular function for all $\mathbf{x}$ and $\mathbf{y}$ in D. Moreover, G satisfies the boundary conditions specified on ∂D.

Let C be a simple curve in D defined by

$$C: Z_\alpha = z_\alpha(s) \qquad s \in I\,\{l_1 \le s \le l_2\} \qquad (3)$$

where s measures the arc length along C. The unit tangent and normal vectors $\mathbf{t}$ and $\mathbf{n}$ of C are

$$\mathbf{t} = z'_\alpha(s)\mathbf{e}_\alpha, \quad \mathbf{n} = \epsilon_{\alpha\beta} z'_\beta(s)\mathbf{e}_\alpha, \qquad (4)$$

where $\epsilon_{\alpha\beta}$ are the components of the two-dimensional alternator, and

[1] Associate Professor of Structural Mechanics, Department of Materials Engineering, University of Illinois at Chicago Circle, Chicago, Ill. 60680.

[2] Professor, Department of Materials Engineering, University of Illinois at Chicago Circle, Chicago, Ill. 60680. Mem. ASME.

Manuscript received by ASME Applied Mechanics Division, May, 1979; final revision, October, 1979.

[3] All quantities in this Note are written in dimensionless form. Thus, if L is the length scale, then the force scale is $8\pi[Eh^3/12(1 - \nu^2)L]$ where E, ν, h are, respectively, Young's modulus, Poisson's ratio, and thickness.

$$
\begin{aligned}
L_8 &= \alpha\beta' P_3 P_6[(P_2\beta\alpha')^2 + P_4{}^2]\\
L_9 &= \beta\alpha' P_3 P_6[(P_2\alpha\beta')^2 + P_4{}^2]\\
L_{10} &= (\alpha\beta)^2 P_1{}^4 + (\alpha\beta\alpha'\beta')^2 P_2{}^4 + P_4{}^4\\
&\quad + (\alpha'\beta')^2 P_5{}^4 + (P_3P_6)^2[(\alpha\beta')^2 + (\alpha'\beta)^2]\\
L_{11} &= \alpha\beta\alpha'\beta'[(P_1P_5)^2 + (P_2P_4)^2]\\
L_{12} &= \alpha\beta\alpha'\beta'(P_3P_6)^2
\end{aligned}
\qquad (8)\ (Cont.)
$$

$$
\begin{aligned}
&c_\alpha = \cos\pi\alpha, \quad c_\beta = \cos\pi\beta, \quad c_{\alpha'} = \cos\pi\alpha'\epsilon, \quad c_{\alpha'} = \cos\pi\beta'\epsilon\\
&s_\alpha = \sin\pi\alpha, \quad s_\beta = \sin\pi\beta, \quad s_{\alpha'} = \sin\pi\alpha'\epsilon, \quad s_{\beta'} = \sin\pi\beta'\epsilon
\end{aligned}
\qquad (9)
$$

and

$$
\begin{aligned}
&P_1 = \sigma^2\Omega^2 + 2\zeta^2(\gamma - 1), \quad P_2 = -2\zeta(\gamma - 1), \quad P_3 = \gamma\Omega^2, \quad P_6 = \sigma^2\Omega^2\\
&P_4 = \zeta[2\zeta^2(\gamma - 1) + \Omega^2(\sigma^2 - \gamma)], \quad P_5 = \gamma\Omega^2 - 2\zeta^2(\gamma - 1)
\end{aligned}
\qquad (10)
$$

It is to be noted that the dispersion relation (7) is still a complex function even for real values of k_x and k_y (or ζ and η) because $\tau = \exp(ip\eta)$.

Simplification for Small h'/h

The dispersion relation (7) is very complicated due to coupling between P and SV-waves in the same layer as well as between two diferent layers. It can be shown, however, that a significant simplification, i.e., uncoupling, can be achieved if the ratio $\epsilon = h'/h$ of the thicknesses of the two layers is assumed to be much smaller than unity. Indeed, in this case the dispersion relation (7) separates into two independent relations

$$
2\alpha\gamma\Omega^2(c_\alpha - c_\eta) + \pi\epsilon(2\alpha\gamma\Omega^2\eta s_\eta - J_2 s_\alpha) = 0 \qquad (11)
$$

$$
2\beta\gamma\Omega^2(c_\beta - c_\eta) + \pi\epsilon(2\beta\gamma\Omega^2\eta s_\eta - J_1 s_\beta) = 0 \qquad (12)
$$

where

$$
\begin{aligned}
J_1 &= \Omega^2 l[\sigma^2\Omega^2 + 4\zeta^2\gamma(\gamma - 1)]\\
&\quad + l'[\gamma\Omega^2 - 2\zeta^2(\gamma - 1)]^2 - 2\zeta^2[2\zeta^2(\gamma - 1)^2 + \gamma\Omega^2]
\end{aligned}
\qquad (13)
$$

$$
\begin{aligned}
J_2 &= \omega^2[\sigma^2\Omega^2 + 4\zeta^2(\gamma - 1)(1 + l'(\gamma - 1))]\\
&\quad + [\gamma\Omega^2 - 2\zeta^2(\gamma - 1)]^2 - 2\zeta^2[2\zeta^2 l'(\gamma - 1)^2 + \gamma\Omega^2]
\end{aligned}
\qquad (14)
$$

It is to be emphasized that the uncoupled dispersion relations (12) and (13) are valid for small ratios of the thicknesses of the two layers, but for arbitrary values of the elastic constants and the densities in the two constituent materials.

Acknowledgment

This work was supported in part by ONR Contract N00014-76-C-0054 to Stanford University.

References

1 Sve, C., "Time Harmonic Waves Traveling Obliquely in a Periodically Laminated Medium," ASME JOURNAL OF APPLIED MECHANICS, Vol. 38, 1971, pp. 477–482.

2 Lee, E. H., and Yang, W. J., "On Waves in Composite Materials With Periodic Structure," *SIAM Journal of Applied Mathematics*, Vol. 25, 1973, pp. 492–499.

3 Sun, C.-T., Achenbach, J. D. and Herrmann, G., "Time-Harmonic Waves in a Stratified Medium Propagating in the Direction of the Layering," ASME JOURNAL OF APPLIED MECHANICS, Vol. 35, 1968, pp. 408–411.

4 Delph, T. J., Herrmann, G., and Kaul, R. K., "Harmonic Wave Propagation in a Periodically Layered, Infinite Elastic Body: Antiplane Strain," ASME JOURNAL OF APPLIED MECHANICS, Vol. 45, 1978, pp. 343–349.

5 Delph, T. J., Herrmann, G., and Kaul, R. K., "Harmonic Wave Propagation in a Periodically Layered, Infinite Elastic Body: Plane Strain, Analytical Results," ASME JOURNAL OF APPLIED MECHANICS, Vol. 46, 1979, pp. 113–119.

Discontinuity and Moment Dipole Along a *V*-Butt Weld in Plates

R. H. Bryant[1] and C. H. Wu[2]

Problem

One of the commonly used practices in welding steel plates is the so-called V-butt weld, Fig. 1. The shrinking of the weld after cooling gives rise to a discontinuity in slope across the weld line. The magnitude of this angular distortion is, of course, governed by many factors [1]. If, however, we make the assumption that the discontinuity in slope is purely a function of the weld, then this angular distortion becomes a given condition for the welded structure to satisfy. We show in the following that such a discontinuity is directly related to a moment dipole so that the deformation of the welded structure may be determined by direct integration via the introduction of an appropriate Green's function.

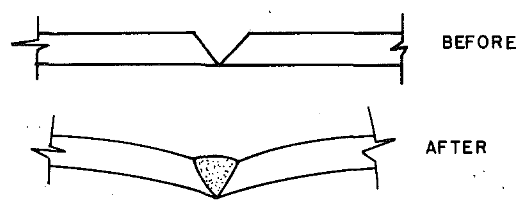

Fig. 1 *V*-**butt weld**

Solution

Let (Z_1, Z_2) be rectangular Cartesian coordinates and let D be the domain of the (Z_1, Z_2)-plane characterizing the shape of a plate. Certain boundary conditions are specified along ∂D, the boundary of D. The deflection of the plate at $\mathbf{z} = \mathbf{x}$ due to a unit load applied at $\mathbf{z} = \mathbf{y}$ may be written as

$$
G(\mathbf{x};\mathbf{y}) = r^2 \ln r + R(\mathbf{x};\mathbf{y}), \qquad (1)^3
$$

where

$$
r = |\mathbf{x} - \mathbf{y}|, \qquad (2)
$$

and R is a regular function for all $\mathbf{x}$ and $\mathbf{y}$ in D. Moreover, G satisfies the boundary conditions specified on ∂D.

Let C be a simple curve in D defined by

$$
C: Z_\alpha = z_\alpha(s) \qquad s \in I\{l_1 \le s \le l_2\} \qquad (3)
$$

where s measures the arc length along C. The unit tangent and normal vectors $\mathbf{t}$ and $\mathbf{n}$ of C are

$$
\mathbf{t} = z'_\alpha(s)\mathbf{e}_\alpha, \quad \mathbf{n} = \epsilon_{\alpha\beta} z'_\beta(s)\mathbf{e}_\alpha, \qquad (4)
$$

where $\epsilon_{\alpha\beta}$ are the components of the two-dimensional alternator, and

[1] Associate Professor of Structural Mechanics, Department of Materials Engineering, University of Illinois at Chicago Circle, Chicago, Ill. 60680.

[2] Professor, Department of Materials Engineering, University of Illinois at Chicago Circle, Chicago, Ill. 60680. Mem. ASME.

Manuscript received by ASME Applied Mechanics Division, May, 1979; final revision, October, 1979.

[3] All quantities in this Note are written in dimensionless form. Thus, if L is the length scale, then the force scale is $8\pi[Eh^3/12(1 - \nu^2)L]$ where E, ν, h are, respectively, Young's modulus, Poisson's ratio, and thickness.

$\mathbf{e}_\alpha$ the unit vectors associated with Z_α. The radius of curvature $\rho(s)$ of C is defined by

$$\frac{d\mathbf{t}}{ds} = -\frac{1}{\rho(s)}\mathbf{n}(s). \tag{5}$$

For convenience, we introduce an orthogonal coordinate θ such that θ_1 measures the distance from $\mathbf{z}(s)$ along $\mathbf{n}(s)$ and $\theta_2 = s$. It follows that the transformation between θ_α and Z_α is just

$$Z_\alpha = f_\alpha(\theta_1, \theta_2) = z_\alpha(\theta_2) + \theta_1 n_\alpha(\theta_2). \tag{6}$$

Our objective is to determine the deflection $w(\mathbf{x})$ of the plate satisfying the boundary conditions implied by (1) and the jump condition

$$\lim_{\epsilon\to 0}\left[\frac{\partial}{\partial\theta_1} w\,(\mathbf{f}(\theta_1,s))\right]_{\theta_1=-\epsilon}^{\theta_1=+\epsilon} = \phi(s), \quad (s \in I). \tag{7}$$

We shall show that the solution is just

$$w(\mathbf{x}) = -\frac{1}{4\pi}\int_{l_1}^{l_2} G_D(\mathbf{x};s)\phi(s)\,ds, \tag{8}$$

where G_D is Green's function for a moment dipole (see, e.g., [2])

$$G_D(\mathbf{x};s) = \left[\frac{\partial^2}{\partial\theta_1^2} G(\mathbf{x};\mathbf{f}(\theta_1,s))\right]_{\theta_1=0}. \tag{9}$$

Let $H(s)$ be the unknown moment dipole at s associated with the pair of couples

$$\begin{cases} \dfrac{H(s)}{\epsilon}\mathbf{t}(s) \quad \text{at} \quad \theta_1 = +\dfrac{\epsilon}{2}, \quad \theta_2 = s \\ -\dfrac{H(s)}{\epsilon}\mathbf{t}(s) \quad \text{at} \quad \theta_1 = -\dfrac{\epsilon}{2}, \quad \theta_2 = s. \end{cases} \tag{10}$$

Then

$$w(\mathbf{x}) = \int_{l_1}^{l_2} H(s) G_D(\mathbf{x};s)\,ds \tag{11}$$

The function G_D defined by (9) and (1) may be written as

$$G_D(\mathbf{x};s) = 2\ln r_c + R_D(\mathbf{x};s) \tag{12}$$

where

$$r_c = |\mathbf{x} - \mathbf{z}(s)| \tag{13}$$

$$R_D(\mathbf{x};s) = 1 + 2\left\{\frac{[\mathbf{x}-\mathbf{z}(s)]\cdot\mathbf{n}(s)}{r_c}\right\}^2 + \left[\frac{\partial^2}{\partial\theta_1^2} R(\mathbf{x};\mathbf{f}(\theta_1,s))\right]_{\theta_1=0} \tag{14}$$

It is clear that R_D is regular for all $\mathbf{x}$ in D and all $s \in I$. The solution (11) may now be written as

$$w(\mathbf{x}) = w_1(\mathbf{x}) + w_2(\mathbf{x}), \tag{15}$$

where

$$w_1(\mathbf{x}) = 2\int_{l_1}^{l_2} H(s)\ln r_c(\mathbf{x};s)\,ds, \tag{16}$$

$$w_2(\mathbf{x}) = \int_{l_1}^{l_2} R_D(\mathbf{x};s) H(s)\,ds. \tag{17}$$

The function $H(s)$ must be determined in such a way that (7) is satisfied. Since w_2 is regular, w_1 must satisfy the jump condition (7).

The function $w_1(\mathbf{x})$ is just the deflection of an "infinite membrane" subjected to a "line load" $H(s)$. It follows that

$$\lim_{\epsilon\to 0}\left[\frac{\partial}{\partial\theta_1} w_1(\mathbf{f}(\theta_1,s))\right]_{\theta_1=-\epsilon}^{\theta_1=+\epsilon} = -4\pi H(s) = \phi(s) \tag{18}$$

This establishes the validity of (8).

Example

Consider the semi-infinite plate ($x_1 > 0$) with a built-in support along $x_1 = 0$. The function G defined by (1) is [2]

$$G(\mathbf{x};\mathbf{y}) = 2x_1y_1 - r^2\ln r_1/r, \tag{19}$$

$$r^2 = (x_1-y_1)^2 + (x_2-y_2)^2, \quad r_1^2 = (x_1+y_1)^2 + (x_2-y_2)^2. \tag{20}$$

Let a weld be located along the straight line C defined by (c.f. (3))

$$C: \quad z_1 = s\cos\alpha, \quad z_2 = b + s\sin\alpha, \quad l_1 < s < l_2, \tag{21}$$

where b and α are constants. Then $\mathbf{t}$ and $\mathbf{n}$ defined by (4) are just

$$\mathbf{t} = \cos\alpha\,\mathbf{e}_1 + \sin\alpha\,\mathbf{e}_2, \quad \mathbf{n} = \sin\alpha\,\mathbf{e}_1 - \cos\alpha\,\mathbf{e}_2. \tag{22}$$

The orthogonal coordinates θ_α defined by (6) are just

$$\theta_1 = n, \quad \theta_2 = s \tag{23}$$

where n measures the distance from C along $\mathbf{n}$.

Substituting the aforementioned relations into (9), we obtain

$$G_D(\mathbf{x};\mathbf{s}) = \left[\frac{\partial^2 G}{\partial y_1^2}\sin^2\alpha + \frac{\partial^2 G}{\partial y_2^2}\cos^2\alpha - 2\frac{\partial^2 G}{\partial y_1\partial y_2}\sin\alpha\cos\alpha\right]_{\mathbf{y}=\mathbf{z}(s)}. \tag{24}$$

The following identities are useful for the purpose of integrating (8)

$$\frac{\partial^2 G}{\partial y_1^2} = \frac{\partial G_1}{\partial y_1} = \frac{\partial F_1}{\partial y_2}, \tag{25}$$

$$\frac{\partial^2 G}{\partial y_2^2} = \frac{\partial F_2}{\partial y_1} = \frac{\partial G_2}{\partial y_2}, \tag{26}$$

$$\frac{\partial^2 G}{\partial y_1\partial y_2} = \frac{\partial G_2}{\partial y_1} = \frac{\partial G_1}{\partial y_2}, \tag{27}$$

where

$$G_1(\mathbf{x};\mathbf{y}) = 2x_1 - (x_1-y_1)\left(1 + \ln\frac{r^2}{r_1^2}\right) - (x_1+y_1)\frac{r^2}{r_1^2}, \tag{28}$$

$$G_2(\mathbf{x};\mathbf{y}) = -(x_2-y_2)\left(1+\ln\frac{r^2}{r_1^2}\right) + (x_2-y_2)\frac{r^2}{r_1^2}, \tag{29}$$

$$F_1(\mathbf{x};\mathbf{y}) = (x_2-y_2)\ln\frac{r_1^2}{r^2} - x_2\frac{r^2}{r_1^2} + y_2\left(\frac{r^2}{r_1^2}-1\right) - 4(x_1-y_1)\left[\tan^{-1}\frac{x_2-y_2}{x_1-y_1} + \tan^{-1}\frac{x_2-y_2}{x_1+y_1}\right], \tag{30}$$

$$F_2(\mathbf{x};\mathbf{y}) = (x_1-y_1)\ln\frac{r_1^2}{r^2} + x_1\frac{r^2}{r_1^2} + y_1\left(\frac{r^2}{r_1^2}-1\right) - 4(x_2-y_2)\left[\tan^{-1}\frac{x_1-y_1}{x_2-y_2} + \tan^{-1}\frac{x_1+y_1}{x_2-y_2}\right]. \tag{31}$$

If we now assume that the property of the weld along C is independent of s, then $\phi(s)$ is a constant and (8) becomes

$$w(\mathbf{x}) = -\frac{\phi}{4\pi}\int_{l_1}^{l_2} G_D(\mathbf{x};s)\,ds. \tag{32}$$

Substituting (24) into (32) we get

$$w(\mathbf{x}) = -\frac{\phi}{4\pi}\Big[F_2(\mathbf{x};\mathbf{z}(s))\cos\alpha + F_1(\mathbf{x};\mathbf{z}(s))\sin\alpha\Big]_{s=l_1}^{s=l_2} - (l_2-l_1)4\pi\sin\alpha\cos\alpha + 4\sin 2\alpha\int_{l_1}^{l_2}\left[\frac{(x_1-z_1(s))(x_2-z_2(s))}{r^2} + \frac{(x_2-z_2(s))z_1(s)}{r_1^2}\right]ds. \tag{33}$$

For welds parallel to the coordinate axes, the explicit results are

Horizontal Weld: ($z_2 = b$, $l_1 < z_1 < l_2$)

$$w(\mathbf{x}) = -\frac{\phi}{4\pi}[F_2(\mathbf{x};l_2,b) - F_2(\mathbf{x};l_1,b)], \tag{34}$$

Vertical Weld: ($z_1 = a$, $l_1 < z_2 < l_2$)

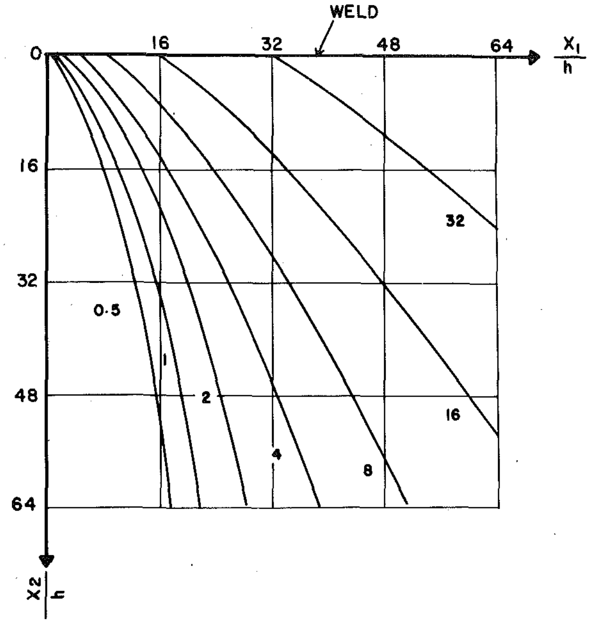

Fig. 2 Surface for $8\pi W/\phi$

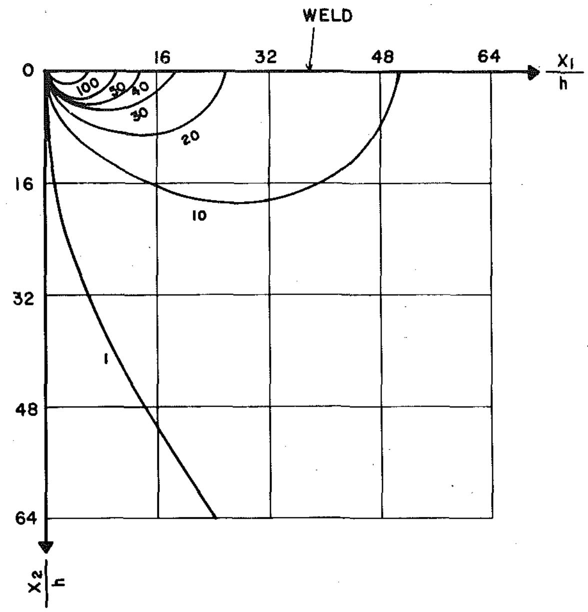

Fig. 3 Surface for $-16\varphi\, M_{x_2x_2}/\phi$

$$w(\mathbf{x}) = -\frac{\phi}{4\pi}\,[F_1(\mathbf{x};a,l_2) - F_1(\mathbf{x};a,l_2)]. \tag{35}$$

Finally, for a single semi-infinite weld along the x_1-axis, the solution is

$$w(x_i,x_2) = \frac{2\phi}{\pi}\left(x_1 - x_2\tan^{-1}\frac{x_1}{x_2}\right) \tag{36}$$

Using h, the plate thickness, as the length scale L the contours of constant $8w\pi/\phi$ are given in Fig. 2. The dimensionless bending moment $M_{x_2x_2}$ is

$$M_{x_2x_2} = -\frac{2\phi}{\pi}\,\frac{x_1(x_1^2 + \nu x_2^2)}{(x_1^2 + x_2^2)^2} \tag{37}$$

For $\nu = 0.3$, the contours of constant $-16\pi M_{x_2x_2}/\phi$ are plotted in Fig. 3.

References

1 Masubuchi, K., "Analytical Investigation of Residual Stresses and Distortions," *Journal of the American Welding Society*, Vol. 39, No. 12, Dec. 1960, pp. 525s–537s.

2 Timoshenko, S., and Woinowsky-Krieger, S., *Theory of Plates and Shells*, McGraw-Hill, New York, 1959, p. 327.

Formulation of Stochastic Linearization for Symmetric or Asymmetric M.D.O.F. Nonlinear Systems

P-T. D. Spanos[1]

A formulation of the method of stochastic linearization so that it is applicable for symmetric or asymmetric nonlinear systems is presented. Formulas for the generation of the equivalent linear system are given. The solution procedure for determining nonstationary or stationary system response statistics is outlined.

Introduction

The method of stochastic or equivalent linearization has been studied and used extensively. Typical examples of pertinent research effort may be found in references [1–6]. In this Brief Note a formulation of the method is given so that it is applicable for both symmetric or asymmetric nonlinear systems and for the approximate determination of both stationary and nonstationary system response statistics to Gaussian random excitations. It is clarified, however, that several of the concepts introduced in the present formulation could have been developed by a careful examination of pertinent references. Furthermore, it is emphasized that the intent of the present Note is to extend, generalize, and systematize existing linearization procedures.

[1] Assistant Professor of Engineering Mechanics, The University of Texas at Austin, Assoc. Mem. ASME.

Manuscript received by ASME Applied Mechanics Division, August, 1978; final revision, September, 1979.

Equation for the Response Offset

Consider the stochastic vector differential equation

$$M\ddot{\mathbf{x}} + C\dot{\mathbf{x}} + K\mathbf{x} + \mathbf{f}(\mathbf{x}, \dot{\mathbf{x}}) = w(t)\mathbf{g}(t), \tag{1}$$

where a dot above a variable denotes differentiation with respect to the independent variable t; M, C, K are constant $n \times n$ matrices; $\mathbf{f}(\mathbf{x}, \dot{\mathbf{x}})$ is an n-vector function of the dependent variable $\mathbf{x}(t)$ and its derivative $\dot{\mathbf{x}}(t)$; $\mathbf{g}(t)$ is time-dependent deterministic vector and $w(t)$ is a stationary delta-correlated and zero-mean stationary Gaussian process; that is $\langle w(t)w(t+\tau)\rangle = \delta(\tau)$, where the symbols $\langle\cdot\rangle$ and δ stands for the operator of mathematical expectation and the Dirac delta function, respectively.

In general the nonlinear function $\mathbf{f}(\mathbf{x}, \dot{\mathbf{x}})$ can be asymmetric with respect to $(\mathbf{x}, \dot{\mathbf{x}})$; that is,

$$\mathbf{f}(\mathbf{x}, \dot{\mathbf{x}}) \neq -\mathbf{f}(-\mathbf{x}, -\dot{\mathbf{x}}) \tag{2}$$

Due to the asymmetry, the solution of equation (1) may not have a zero mean value. Therefore, it is assumed that

$$\mathbf{x}(t) = \mathbf{x}_m(t) + \hat{\mathbf{x}}(t), \tag{3}$$

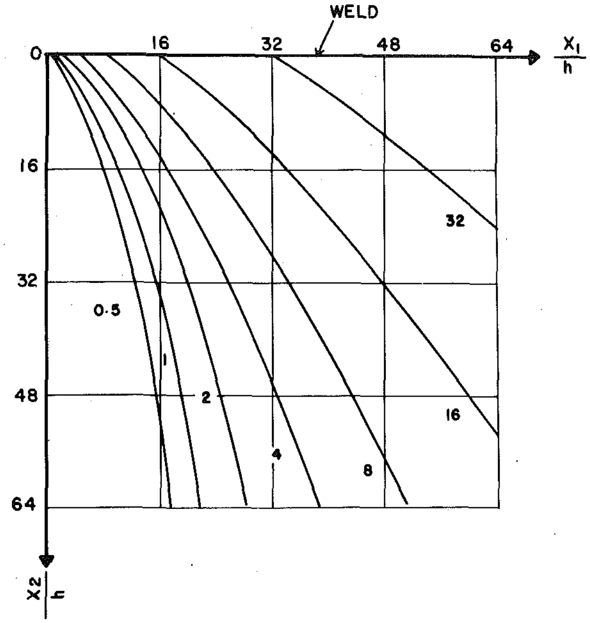

Fig. 2 Surface for $8\pi W/\phi$

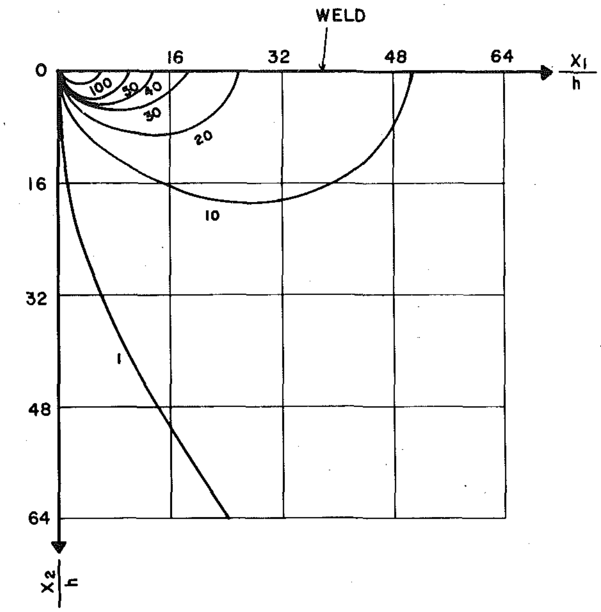

Fig. 3 Surface for $-16\varphi\, M_{x_2x_2}/\phi$

$$w(\mathbf{x}) = -\frac{\phi}{4\pi}\,[F_1(\mathbf{x};a,l_2) - F_1(\mathbf{x};a,l_2)]. \tag{35}$$

Finally, for a single semi-infinite weld along the x_1-axis, the solution is

$$w(x_i,x_2) = \frac{2\phi}{\pi}\left(x_1 - x_2\tan^{-1}\frac{x_1}{x_2}\right) \tag{36}$$

Using h, the plate thickness, as the length scale L the contours of constant $8w\pi/\phi$ are given in Fig. 2. The dimensionless bending moment $M_{x_2x_2}$ is

$$M_{x_2x_2} = -\frac{2\phi}{\pi}\,\frac{x_1(x_1^2 + \nu x_2^2)}{(x_1^2 + x_2^2)^2} \tag{37}$$

For $\nu = 0.3$, the contours of constant $-16\pi M_{x_2x_2}/\phi$ are plotted in Fig. 3.

References

1 Masubuchi, K., "Analytical Investigation of Residual Stresses and Distortions," *Journal of the American Welding Society*, Vol. 39, No. 12, Dec. 1960, pp. 525s–537s.

2 Timoshenko, S., and Woinowsky-Krieger, S., *Theory of Plates and Shells*, McGraw-Hill, New York, 1959, p. 327.

Formulation of Stochastic Linearization for Symmetric or Asymmetric M.D.O.F. Nonlinear Systems

P-T. D. Spanos[1]

A formulation of the method of stochastic linearization so that it is applicable for symmetric or asymmetric nonlinear systems is presented. Formulas for the generation of the equivalent linear system are given. The solution procedure for determining nonstationary or stationary system response statistics is outlined.

Introduction

The method of stochastic or equivalent linearization has been studied and used extensively. Typical examples of pertinent research effort may be found in references [1–6]. In this Brief Note a formulation of the method is given so that it is applicable for both symmetric or asymmetric nonlinear systems and for the approximate determination of both stationary and nonstationary system response statistics to Gaussian random excitations. It is clarified, however, that several of the concepts introduced in the present formulation could have been developed by a careful examination of pertinent references. Furthermore, it is emphasized that the intent of the present Note is to extend, generalize, and systematize existing linearization procedures.

Equation for the Response Offset

Consider the stochastic vector differential equation

$$M\ddot{\mathbf{x}} + C\dot{\mathbf{x}} + K\mathbf{x} + \mathbf{f}(\mathbf{x},\dot{\mathbf{x}}) = w(t)\mathbf{g}(t), \tag{1}$$

where a dot above a variable denotes differentiation with respect to the independent variable t; M, C, K are constant $n \times n$ matrices; $\mathbf{f}(\mathbf{x}, \dot{\mathbf{x}})$ is an n-vector function of the dependent variable $\mathbf{x}(t)$ and its derivative $\dot{\mathbf{x}}(t)$; $\mathbf{g}(t)$ is time-dependent deterministic vector and $w(t)$ is a stationary delta-correlated and zero-mean stationary Gaussian process; that is $\langle w(t)w(t+\tau)\rangle = \delta(\tau)$, where the symbols $\langle\cdot\rangle$ and δ stands for the operator of mathematical expectation and the Dirac delta function, respectively.

In general the nonlinear function $\mathbf{f}(\mathbf{x}, \dot{\mathbf{x}})$ can be asymmetric with respect to $(\mathbf{x}, \dot{\mathbf{x}})$; that is,

$$\mathbf{f}(\mathbf{x},\dot{\mathbf{x}}) \neq -\mathbf{f}(-\mathbf{x},-\dot{\mathbf{x}}) \tag{2}$$

Due to the asymmetry, the solution of equation (1) may not have a zero mean value. Therefore, it is assumed that

$$\mathbf{x}(t) = \mathbf{x}_m(t) + \hat{\mathbf{x}}(t), \tag{3}$$

[1] Assistant Professor of Engineering Mechanics, The University of Texas at Austin, Assoc. Mem. ASME.

Manuscript received by ASME Applied Mechanics Division, August, 1978; final revision, September, 1979.

where $\mathbf{x}_m$ is a deterministic offset vector and $\hat{\mathbf{x}}(t)$ is a zero-mean random vector.

Substituting equation (3) into equation (1) gives

$$M\ddot{\mathbf{x}} + C\dot{\mathbf{x}} + K\hat{\mathbf{x}} + M\ddot{\mathbf{x}}_m + C\dot{\mathbf{x}}_m + K\mathbf{x}_m + \mathbf{f}(\hat{\mathbf{x}} + \mathbf{x}_m, \dot{\hat{\mathbf{x}}} + \dot{\mathbf{x}}_m) = w(t)\mathbf{g}(t). \quad (4)$$

Ensemble averaging equation (4) yields

$$M\ddot{\mathbf{x}}_m + C\dot{\mathbf{x}}_m + K\mathbf{x}_m + \langle \mathbf{f}(\hat{\mathbf{x}} + \mathbf{x}_m, \dot{\hat{\mathbf{x}}} + \dot{\mathbf{x}}_m)\rangle = 0 \quad (5)$$

Equation (5) can be put in the form

$$\dot{\overset{*}{\mathbf{x}}}_m = P_m\mathbf{x}_m + \mathbf{R}_m, \quad (6)$$

where

$$\overset{*}{\mathbf{x}}{}_m^T = (\mathbf{x}_m^T, \dot{\mathbf{x}}_m^T), \quad (7)$$

$$P_m = \begin{bmatrix} 0 & I \\ -M^{-1}K & -M^{-1}C \end{bmatrix} \quad (8)$$

and

$$\mathbf{R}_m = \begin{bmatrix} \mathbf{0} \\ -M^{-1}\langle \mathbf{f}(\hat{x} + x_m, \dot{\hat{\mathbf{x}}} + \dot{\mathbf{x}}_m)\rangle \end{bmatrix}. \quad (9)$$

The symbol T as a superscript denotes the operation of transposing.

Generation of an Equivalent Linear System

In order to obtain an approximate solution for the system described by equation (4), an equivalent linear system is constructed in the form

$$M\ddot{\hat{\mathbf{x}}} + [C + \hat{C}]\dot{\hat{\mathbf{x}}} + [K + \hat{K}]\hat{\mathbf{x}} = w(t)\mathbf{g}(t), \quad (10)$$

where matrices C and K are such that

$$\langle \boldsymbol{\epsilon}^T\boldsymbol{\epsilon}\rangle \equiv \text{minimum}. \quad (11)$$

The error vector $\boldsymbol{\epsilon}$ is defined by the equation

$$\boldsymbol{\epsilon} \equiv \hat{C}\dot{\mathbf{x}}_m + \hat{K}\mathbf{x}_m + \mathbf{f}(\hat{\mathbf{x}} + \mathbf{x}_m, \dot{\hat{\mathbf{x}}} + \dot{\mathbf{x}}_m) - \hat{C}\dot{\hat{\mathbf{x}}} - \hat{K}\hat{\mathbf{x}}. \quad (12)$$

The criterion expressed by equation (11) must be satisfied for every member of the class of solutions of equation (11).

Due to the fact that the excitation $w(t)$ is Gaussian, the response of the linear system described by equation (10) will be Gaussian. Therefore, the minimization criterion, equation (11), should be satisfied for every Gaussian vector $\mathbf{x}(t)$. Applying the theory developed in references [4–6] it can be shown that a necessary condition for the minimization criterion to be satisfied is

$$\langle \overset{*}{\mathbf{x}}\mathbf{F}^T\rangle = X[\hat{K}, \hat{C}]^T, \quad (13)$$

where

$$\overset{*}{\mathbf{x}}{}^T = (\hat{\mathbf{x}}^T, \dot{\hat{\mathbf{x}}}^T) \quad (14)$$

$$X = \langle \overset{**}{\mathbf{x}\mathbf{x}}{}^T\rangle, \quad (15)$$

and

$$\mathbf{F} = M\ddot{\mathbf{x}}_m + C\dot{\mathbf{x}}_m + K\mathbf{x}_m + \mathbf{f}(\hat{\mathbf{x}} + \mathbf{x}_m, \dot{\hat{\mathbf{x}}} + \dot{\mathbf{x}}_m). \quad (16)$$

For every zero-mean Gaussian vector it can be proved under quite general restrictions that [5]

$$\overset{*}{\mathbf{x}}\mathbf{F}^T = XJ\left(\frac{\mathbf{F}}{\overset{*}{\mathbf{x}}}\right)^T \quad (17)$$

where $J(\mathbf{F}/\overset{*}{\mathbf{x}})$ denotes the Jacobian of the components of the vector $\mathbf{F}$ with respect to the components of the vector $\overset{*}{\mathbf{x}}$.

The requirement of zero mean for the vector $\overset{*}{\mathbf{x}}$ for the validity of the general equation (17), makes evident the usefulness of the form of the solution $\mathbf{x}$ assumed in equation (3).

Combining equations (13) and (17) leads to the equation

$$X\left\{\left\langle J\left(\frac{\mathbf{F}}{\overset{*}{\mathbf{x}}}\right)^T\right\rangle - [\hat{K}, \hat{C}]^T\right\} = 0. \quad (18)$$

Equation (18) is satisfied when

$$[\hat{K}, \hat{C}] = \left\langle J\left(\frac{\mathbf{F}}{\overset{*}{\mathbf{x}}}\right)\right\rangle. \quad (19)$$

Componentwise, equation (19) may be rewritten as

$$k_{ij} = \left\langle\frac{\partial F_i}{\partial \hat{x}_j}\right\rangle, \quad j = 1, \ldots m \quad (20)$$

and

$$c_{ij} = \left\langle\frac{\partial F_j}{\partial \dot{\hat{x}}_j}\right\rangle. \quad (21)$$

If the matrix X is nonsingular, equation (19) will be the unique solution of equation (18). Furthermore, it can be shown by using a theorem of reference [6], that in this case the matrices $\hat{K}$ and $\hat{C}$ yield an absolute minimum for $\langle \boldsymbol{\epsilon}^T\boldsymbol{\epsilon}\rangle$. If the matrix X is singular, equation (18) will not possess a unique solution. However, it can be proved, by using again the theorem of reference [6], that in this case the linear system constructed by means of equation (19) will be no worse than any other linear substitute system in terms of the value of $\langle \boldsymbol{\epsilon}^T\boldsymbol{\epsilon}\rangle$.

Solution Procedure

Equation (10) can be rewritten as

$$\dot{\overset{*}{\mathbf{x}}} = P\overset{*}{\mathbf{x}} + w(t)\mathbf{R}, \quad (22)$$

where

$$P = \begin{bmatrix} 0 & I \\ -M^{-1}(K + \hat{K}) & -M^{-1}(C + \hat{C}) \end{bmatrix} \quad (23)$$

and

$$\mathbf{R} = \begin{bmatrix} 0 \\ M^{-1}g(t) \end{bmatrix}. \quad (24)$$

The symbols I and 0 represent, respectively, then the $n \times n$ identity and zero matrices.

Applying standard methods of analysis of linear systems, equation (22) leads to the following ordinary differential equation for the covariance matrix X:

$$\dot{X} = PX + XP^T + RR^T \quad (25)$$

Equations (6) and (25) are nonlinear ordinary differential equations which can be solved numerically for specified initial conditions. For stationary response, $\dot{X} = 0$, $\dot{\mathbf{x}}_m = 0$, they become

$$P_m\overset{*}{\mathbf{x}}_{m,s} + \mathbf{R}_{m,s} = \mathbf{0}, \quad (26)$$

and

$$PX_s + X_sP^T + \mathbf{R}_s\mathbf{R}_s^T = 0, \quad (27)$$

where the subscripts designate stationary values.

Equations (26) and (27) are nonlinear algebraic equations which again can be solved numerically.

It is noted that if the initial displacement and velocity of the system are equal to zero, and the nonlinear force is symmetric, that is

$$\mathbf{f}(\mathbf{x}, \dot{\mathbf{x}}) = -\mathbf{f}(-\mathbf{x}, -\dot{\mathbf{x}}), \quad (28)$$

equations (6) and (26) are satisfied for $\mathbf{x}_m \equiv \mathbf{0}$. Therefore, only equation (25) or equation (27) must be solved in order to determine the nonstationary or stationary, respectively, form of the matrix X.

Reliability and Efficiency of the Linearization Scheme

The discussed linearization procedure has been used for the system

$$\ddot{x} + \beta\dot{x} + x[1 + 3\epsilon + 3\epsilon x + \epsilon x^2] = \sqrt{2\beta}w(t)g(t), \quad x(0) = \dot{x}(0) = 0$$
$$\beta = 0.10, \quad \epsilon = 0.2, \quad g(t) = \exp(-0.025t) - \exp(-0.25t) \quad (29)$$

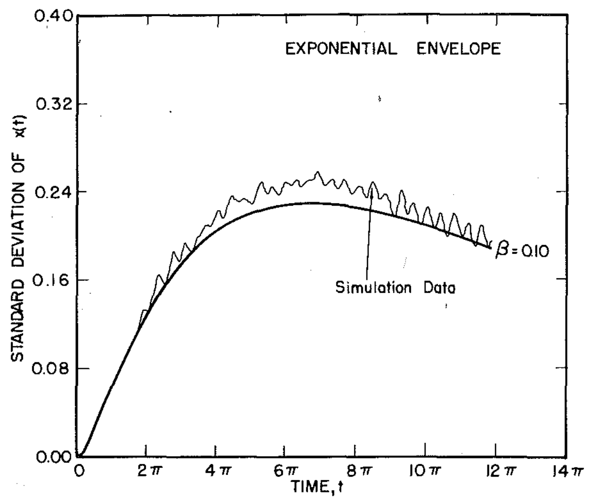

Fig. 1 Standard deviation of $x(t)$ versus time, $\epsilon = 0.2$

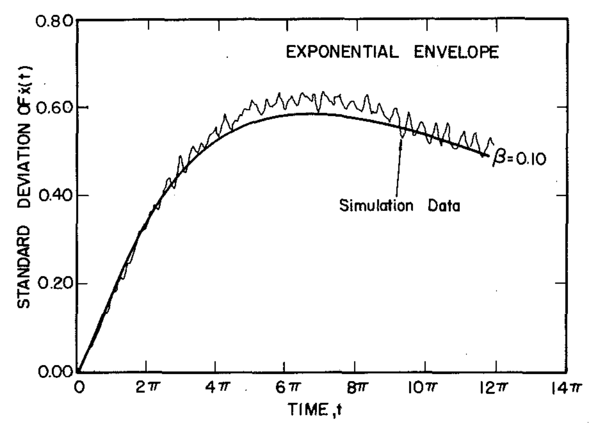

Fig. 2 Standard deviation of $\dot{x}(t)$ versus time, $\epsilon = 0.2$

Figs. 1 and 2 show results for the mean and the standard deviation of the response. In these figures data obtained by Monte Carlo simulations with ensemble size equal to 300 are shown as well. It can be seen that the solutions for the offset (mean) and the standard deviation of $x(t)$ obtained by the two methods compare quite well. Not only the proper trends are observed but the actual numerical values are in close agreement. It is interesting to note that the reported studies have indicated that the linearization scheme is approximately 500 times more efficient computationally than the Monte Carlo simulation in determining the response statistics.

Summary and Conclusions

A formulation of the technique of equivalent linearization has been presented so that it is applicable for the determination of nonstationary and stationary response statistics of symmetric or asymmetric nonlinear dynamic systems. On the basis of the preceding analytical developments and the reported numerical studies it may be concluded that the discussed method is reliable and computationally efficient.

References

1 Sawaragi, Y., Sugai, N., and Sunahara, Y., *Statistical Studies on Non-Linear Control Systems*, Nippon, Osaka, Japan, 1962.

2 Van del Velde, W. E., and Gelb, A., *Multiple-Input Describing Functions and Nonlinear System Design*, McGraw-Hill, New York, 1968.

3 Caughey, T. K., "Nonlinear Theory of Random Vibrations," *Advances in Applied Mechanics*, Vol. 11, 1971, pp. 209–253.

4 Iwan, W. D., "A Generalization of the Method of Equivalent Linearization," *International Journal of Nonlinear Mechanics*, Vol, 8, 1973, p. 279–287.

5 Atalik, T. S., and Utku, S., "Stochastic Linearization of Multidegree-of-Freedom Nonlinear Systems," *Earthquake Engineering and Structural Dynamics*, Vol. 4, 1976, pp. 411–420.

6 Spanos, P-T., D., and Iwan, W. D., "On the Existence and Uniqueness of Solutions Generated by Equivalent Linearization," *International Journal of Nonlinear Mechanics*, Vol. 13, 1978, pp. 71–78.

Bounds on Modal Damping by a Component Modes Method Using Lagrange Multipliers

E. H. Dowell[1]

The author has deduced recently some general properties for the natural frequencies of dynamical systems which are composed of several components [1]. The question has arisen as to whether analogous results may be obtained for damping characteristics of such systems.[2] Earlier Klein and the author [2] and, also, Hallquist and Snyder [3] had studied modal damping by component mode methods using Lagrange multipliers. It is shown that for two component systems a simple explicit formula for modal damping is available *once* the total system natural frequencies are calculated. From this result it is also shown that in a special, but important, case an explicit analytical bound is obtainable for damping *without* the necessity of computing first the system natural frequencies. In the general case a simple numerical procedure is suggested for obtaining bounds.

Most of the foregoing results are obtained by assuming lightly damped components as are typical of structural systems. While this approximation could be eliminated in a formal theory, in practice it is often useful and of sufficient accuracy particularly for lightly damped systems. The advantage of this assumption is that it avoids the necessity of dealing with the adjoints of the system components and the consequent complex eigenfunctions.

General Analysis

The results of reference [2] are set out first. Conceptually disassemble the total structure into N-components [4] for which one knows for each mode the following information, the generalized masses, $M_j^{(n)}$, the damping coefficients, $\zeta_j^{(n)}$, the natural undamped frequencies, $\omega_j^{(n)}$, for $j = 1, 2, \ldots, \infty$; $n = 1, \ldots, N$. For the total system, one has kinetic energy, potential energy, and the damping dissipation function as given in (1)–(3).

$$T = \tfrac{1}{2} \sum_{n=1}^{N} \sum_{j=1}^{\infty} M_j^{(n)} \dot{q}_j^{2(n)} \tag{1}$$

$$U = \tfrac{1}{2} \sum_{n=1}^{N} \sum_{j=1}^{\infty} M_j^{(n)} \omega_j^{2(n)} q_j^{2(n)} \tag{2}$$

$$D = \tfrac{1}{2} \sum_{n=1}^{N} \sum_{j=1}^{\infty} 2\zeta_j^{(n)} \omega_j^{(n)} M_j^{(n)} \dot{q}_j^{2(n)} \tag{3}$$

One also has interconnecting (constraint) conditions between the components,

$$f_r \equiv \sum_{n=1}^{N} \sum_{j=1}^{\infty} \beta_{rj}^{(n)} q_j^{(n)} = 0; \quad r = 1, \ldots, R \tag{4}$$

where the $\beta_{rj}^{(n)}$ are determined by the geometry of the connections

[1] Professor, Department of Mechanical and Aerospace Engineering, Princeton University, Princeton, N.J. 08544. Mem. ASME.

[2] The author would like to thank Prof. Hold Ashley who asked this question and thus motivated the present study.

Manuscript received by ASME Applied Mechanics Division, January, 1979; final revision, August, 1979.

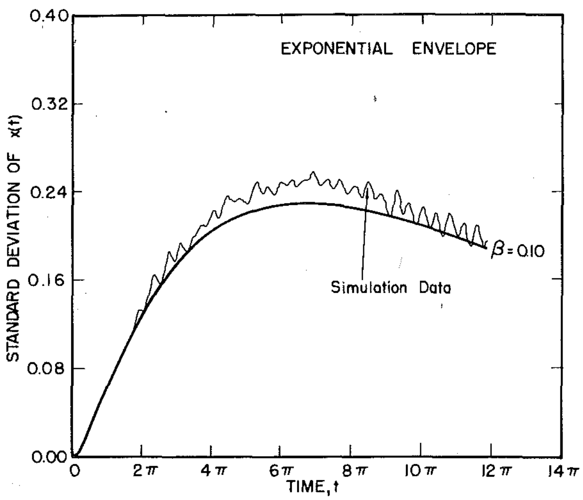

Fig. 1 Standard deviation of $x(t)$ versus time, $\epsilon = 0.2$

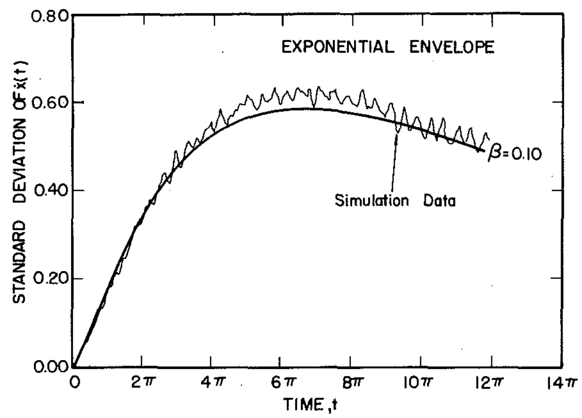

Fig. 2 Standard deviation of $\dot{x}(t)$ versus time, $\epsilon = 0.2$

Figs. 1 and 2 show results for the mean and the standard deviation of the response. In these figures data obtained by Monte Carlo simulations with ensemble size equal to 300 are shown as well. It can be seen that the solutions for the offset (mean) and the standard deviation of $x(t)$ obtained by the two methods compare quite well. Not only the proper trends are observed but the actual numerical values are in close agreement. It is interesting to note that the reported studies have indicated that the linearization scheme is approximately 500 times more efficient computationally than the Monte Carlo simulation in determining the response statistics.

Summary and Conclusions

A formulation of the technique of equivalent linearization has been presented so that it is applicable for the determination of nonstationary and stationary response statistics of symmetric or asymmetric nonlinear dynamic systems. On the basis of the preceding analytical developments and the reported numerical studies it may be concluded that the discussed method is reliable and computationally efficient.

References

1 Sawaragi, Y., Sugai, N., and Sunahara, Y., *Statistical Studies on Non-Linear Control Systems*, Nippon, Osaka, Japan, 1962.

2 Van del Velde, W. E., and Gelb, A., *Multiple-Input Describing Functions and Nonlinear System Design*, McGraw-Hill, New York, 1968.

3 Caughey, T. K., "Nonlinear Theory of Random Vibrations," *Advances in Applied Mechanics*, Vol. 11, 1971, pp. 209–253.

4 Iwan, W. D., "A Generalization of the Method of Equivalent Linearization," *International Journal of Nonlinear Mechanics*, Vol, 8, 1973, p. 279–287.

5 Atalik, T. S., and Utku, S., "Stochastic Linearization of Multidegree-of-Freedom Nonlinear Systems," *Earthquake Engineering and Structural Dynamics*, Vol. 4, 1976, pp. 411–420.

6 Spanos, P-T., D., and Iwan, W. D., "On the Existence and Uniqueness of Solutions Generated by Equivalent Linearization," *International Journal of Nonlinear Mechanics*, Vol. 13, 1978, pp. 71–78.

Bounds on Modal Damping by a Component Modes Method Using Lagrange Multipliers

E. H. Dowell[1]

The author has deduced recently some general properties for the natural frequencies of dynamical systems which are composed of several components [1]. The question has arisen as to whether analogous results may be obtained for damping characteristics of such systems.[2] Earlier Klein and the author [2] and, also, Hallquist and Snyder [3] had studied modal damping by component mode methods using Lagrange multipliers. It is shown that for two component systems a simple explicit formula for modal damping is available *once* the total system natural frequencies are calculated. From this result it is also shown that in a special, but important, case an explicit analytical bound is obtainable for damping *without* the necessity of computing first the system natural frequencies. In the general case a simple numerical procedure is suggested for obtaining bounds.

Most of the foregoing results are obtained by assuming lightly damped components as are typical of structural systems. While this approximation could be eliminated in a formal theory, in practice it is often useful and of sufficient accuracy particularly for lightly damped systems. The advantage of this assumption is that it avoids the necessity of dealing with the adjoints of the system components and the consequent complex eigenfunctions.

General Analysis

The results of reference [2] are set out first. Conceptually disassemble the total structure into N-components [4] for which one knows for each mode the following information, the generalized masses, $M_j^{(n)}$, the damping coefficients, $\zeta_j^{(n)}$, the natural undamped frequencies, $\omega_j^{(n)}$, for $j = 1, 2, \ldots, \infty$; $n = 1, \ldots, N$. For the total system, one has kinetic energy, potential energy, and the damping dissipation function as given in (1)–(3).

$$T = \tfrac{1}{2} \sum_{n=1}^{N} \sum_{j=1}^{\infty} M_j^{(n)} \dot{q}_j^{2(n)} \tag{1}$$

$$U = \tfrac{1}{2} \sum_{n=1}^{N} \sum_{j=1}^{\infty} M_j^{(n)} \omega_j^{2(n)} q_j^{2(n)} \tag{2}$$

$$D = \tfrac{1}{2} \sum_{n=1}^{N} \sum_{j=1}^{\infty} 2\zeta_j^{(n)} \omega_j^{(n)} M_j^{(n)} \dot{q}_j^{2(n)} \tag{3}$$

One also has interconnecting (constraint) conditions between the components,

$$f_r \equiv \sum_{n=1}^{N} \sum_{j=1}^{\infty} \beta_{rj}^{(n)} q_j^{(n)} = 0; \quad r = 1, \ldots, R \tag{4}$$

where the $\beta_{rj}^{(n)}$ are determined by the geometry of the connections

[1] Professor, Department of Mechanical and Aerospace Engineering, Princeton University, Princeton, N.J. 08544. Mem. ASME.

[2] The author would like to thank Prof. Hold Ashley who asked this question and thus motivated the present study.

Manuscript received by ASME Applied Mechanics Division, January, 1979; final revision, August, 1979.

between components and the $q_j^{(n)}$ are modal generalized coordinates. The Lagrangian is

$$L \equiv T - U + \sum_{r=1}^{R} \lambda_r f_r$$

where the Lagrange multipliers, λ_r, are as yet unknown forces of constraint. After Goldstein [5], Lagrange's equations are

$$\frac{d}{dt}\left(\frac{\partial L}{\partial \dot{q}_j}\right) - \frac{\partial L}{\partial q_j} + \frac{\partial D}{\partial \dot{q}_j} = 0$$

Using (1), (2), (4) to evaluate L and substituting the result along with (3) into the foregoing gives

$$M_j^{(n)}[\ddot{q}_j^{(n)} + 2\zeta_j^{(n)}\omega_j^{(n)}\dot{q}_j^{(n)} + \omega_j^{2(n)} q_j^{(n)}] - \sum_{r=1}^{R} \lambda_r \beta_{rj}^{(n)} = 0 \quad (5)$$

Assume time-dependent motion of the form,

$$q_j^{(n)}(t) = \bar{q}_j^{(n)} e^{(-\beta\Omega + i\Omega\sqrt{1-\beta^2})t}$$

$$\lambda_r(t) = \bar{\lambda}_r e^{(-\beta\Omega + i\Omega\sqrt{1-\beta^2})t}$$

This form is selected so that Ω is the undamped natural frequency and β is a true damping ratio; β and Ω are both real numbers.

An eigenvalue equation for β, Ω is obtained by substituting the foregoing forms for $q_j^{(n)}$ and λ_r into (4) and (5). Then from (5) one may solve for $\bar{q}_j^{(n)}$ in terms of $\bar{\lambda}_r$ and substitute the result into (4). Requiring nontrivial solutions for the $\bar{\lambda}_r$ gives the following determinantal equation:

$$|\Delta_{pq}| = 0 \quad p, q = 1, \ldots, R$$

where the determinant elements are

$$\Delta_{pq} = \sum_{n=1}^{N}\sum_{j=1}^{\infty}\left[\frac{\beta_{pj}^{(n)}\beta_{qj}^{(n)}}{M_j^{(n)}\{[\Omega^2(2\beta^2-1) - 2\zeta_j^{(n)}\omega_j^{(n)}\Omega\beta + \omega_j^{2(n)}] + 2i\Omega\sqrt{1-\beta^2}\,\zeta_j^{(n)}\omega_j^{(n)} - \Omega\beta)\}}\right] \quad (6)$$

For the case where the damping coefficients are small for each mode, one may neglect terms of order β^2 and $\zeta_j^{(n)}\beta$ compared to one. Then (6) becomes

$$\Delta_{pq} = \sum_{n=1}^{N}\sum_{j=1}^{\infty} \times \left[\frac{\beta_{pj}^{(n)}\beta_{qj}^{(n)}[(\omega_j^{(n)2} - \Omega^2) - 2i\Omega(\zeta_j^{(n)}\omega_j^{(n)} - \Omega\beta)]}{M_j^{(n)}(\omega_j^{(n)2} - \Omega^2)^2}\right] \quad (7)$$

Further note that for small damping, the natural frequencies, Ω_J, $J = 1, 2, \ldots$, are the same as for the undamped system. Using (7), the determinantal equation *for determining the system natural frequencies*, $|\Delta_{pq}| = 0$, becomes (to consistent order in β and $\zeta_j^{(n)}$)

$$|\Delta_{pq}^R| = 0 \quad (7a)$$

where Δ_{pq}^R is the real part of Δ_{pq}, see equation (7). The imaginary part of $|\Delta_{pq}| = 0$ then is a polynomial in β which determines the system model, dampings, $\beta_1, \beta_2, \ldots$, once the natural frequencies, $\Omega = \Omega_1, \Omega_2, \ldots$ have been determined from equation (7a).

Two Components With a Single Constraint

For this special, but fundamental, case the determinantal equation consists of but a single element. It should be emphasized that any number of components and constraints can be treated sequentially by using two components and a single constraint as the basic building block.

For a single element determinant, the complex determinantal equation, (6) or (7), may be written as two separate real equations of particularly simple forms. Using (7), one has

$$\sum_{n=1}^{2}\sum_{j=1}^{\infty}\left[\frac{\beta_{1j}^{(n)}\beta_{1j}(n)}{M_j^{(n)}(\omega_j^{(n)2} - \Omega_J^2)}\right] = 0 \quad (8)$$

and

$$\sum_{n=1}^{2}\sum_{j=1}^{\infty}\left[\frac{\beta_{1j}^{(n)}\beta_{1j}^{(n)}(\zeta_j^{(n)}\omega_j^{(n)} - \Omega_J\beta_J)}{M_j^{(n)}(\omega_j^{(n)2} - \Omega_J^2)^2}\right] = 0 \quad (9)$$

where $J = 1, 2, \ldots$ orders the total system frequencies by increasing magnitude along with their associated damping ratios.

Equation (8) is the usual result for determining the undamped natural frequencies, Ω_J. Equation (9) then allows a simple computation of the corresponding damping ratios, β_J. Solving (9) for the β_J, one has

$$\beta_J = \frac{\sum_{n=1}^{2}\sum_{j=1}^{\infty}\left[\frac{\beta_{1j}^{(n)}\beta_{1j}^{(n)}\zeta_j^{(n)}\omega_j^{(n)}/\Omega_J}{M_j^{(n)}(\omega_j^{(n)2} - \Omega_J^2)^2}\right]}{\sum_{n=1}^{2}\sum_{j=1}^{\infty}\left[\frac{\beta_{1j}^{(n)}\beta_{1j}^{(n)}}{M_j^{(n)}(\omega_j^{(n)2} - \Omega_J^2)^2}\right]} \quad (10)$$

The entire right-hand side of (10) is known once the Ω_J have been determined from (8). Hence (10) is the promised explicit formula for β_J.

Bounds on β_J: First consider the *special case* $\zeta_j^{(n)}\omega_j^{(n)}$ = constant, which is a reasonable approximation for some simple structural elements. (10) reduces to

$$\beta_J = \zeta_j^{(n)}\omega_j^{(n)}/\Omega_J \quad (10a)$$

In reference (1) it is shown that one may order the frequencies so that $\omega_j^{(n)}/\Omega_J < 1$ for each associated pair of $\omega_j^{(n)}$ and Ω_J. Hence from (10a) $\beta_J < \zeta_j^{(n)}$. Thus, in this *special case*, the total system modal damping is less than the damping in the corresponding component mode. Moreover, upper and lower bounds on the β_J are known immediately from the previously obtained bounds on Ω_J; see reference [1].

It is worth emphasizing that in the *general case* by using the explicit formula for β_J for a known Ω_J, i.e., equations (10) or (10b), one can always obtain *bounds* on β_J without first determining Ω_J by *numerically* computing the right-hand side of (10) or (10b) for *all* values of Ω between any two ω_j and ω_{j+1}. This procedure can also be applied to the even more general case for any number of components and connections, c.f. (6), (7), and (7a).

It is possible that an analytical formula for bounds can be obtained, but the obvious method for determining minima and maxima of β_J leads to a complicated numerical calculation. That is, if one uses (10) to determine the Ω for which $d\beta_J/d\Omega = 0$ then the calculation of such Ω is no simpler than determining the natural frequencies, Ω_J, from (8). Substitution of Ω_J into (10) gives the exact β_J, of course, and bounds become of little interest. On the whole the author is pessimistic about obtaining explicit analytical bounds for the β_J.

A Numerical Example

Consider two identical, simply supported beams which are crossed and pinned at their centers; see Fig. 1. For simplicity only doubly symmetric modes are considered. From symmetry, the doubly symmetric modes correspond to the clamping of each beam at its center.

The constraint condition for the problem is

$$\sum_j q_j^{(1)}\phi_j^{(1)}(x = 0) - \sum_j q_j^{(2)}\phi_j^{(2)}(x = 0) = 0 \quad (4a)$$

where $x = 0$ denotes the coordinate of the beam center. Comparing (4a) to (4), it is seen that

$$\beta_{1j}^{(1)} = \phi_j^{(1)}(x = 0), \quad \beta_{1j}^{(2)} = -\phi_j^{(2)}(x = 0) \quad (11)$$

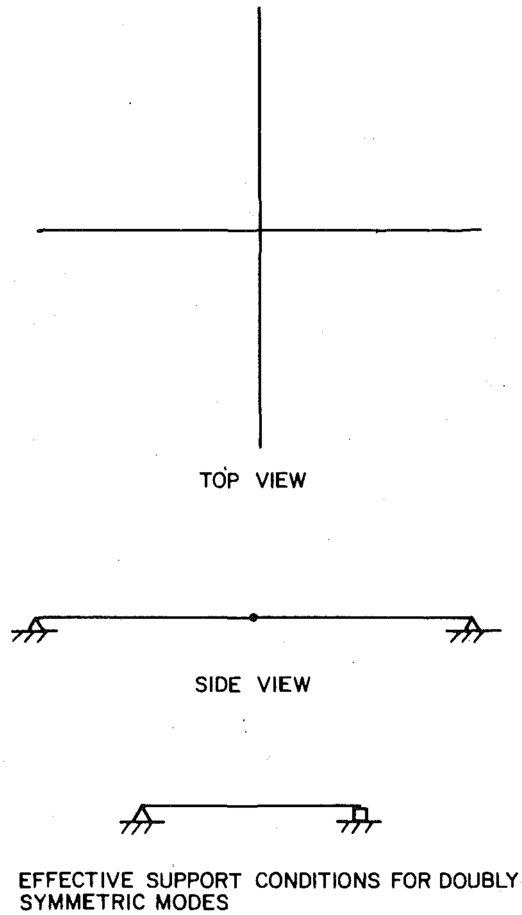

EXAMPLE GEOMETRY
Fig. 1

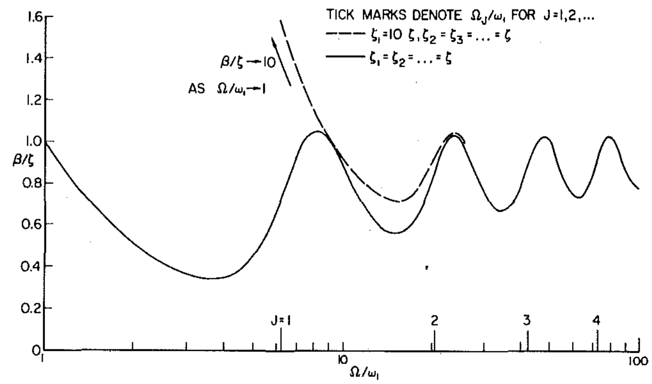

Fig. 2

Using (11) in (8) and (10) and recalling that for this example the two beams are identical, one has

$$\sum_{j=1}^{\infty}\left[\frac{\phi_j{}^2\,(x=0)}{M_j\,(\omega_j{}^2-\Omega_J{}^2)}\right]=0 \tag{8b}$$

and

$$\beta_J=\frac{\displaystyle\sum_{j=1}^{\infty}\left[\frac{\phi_j{}^2\,(x=0)\;\zeta_j\;\omega_j/\Omega_J}{M_j\,(\omega_j{}^2-\Omega_J{}^2)^2}\right]}{\displaystyle\sum_{j=1}^{\infty}\left[\frac{\phi_j{}^2\,(x=0)}{M_j\,(\omega_j{}^2-\omega_J{}^2)^2}\right]} \tag{10b}$$

Numerics have been carried out for two specific choices of component damping factors, ζ_j. Case I corresponds to $\zeta_j = \zeta$, a constant, for all j. Case II corresponds to $\zeta_1 = 10\,\zeta$ and $\zeta_j = \zeta$ for all $j \geqslant 2$. Ω_J is computed from (8b) then β_J is computed for (10b). The results for β_J/ζ are shown in Table 1 for $J = 1, \ldots, 10$. As may be seen $\beta_J/\zeta_j <$ 1 for each pair, $J = j = 1, 2, 3$, etc. Note that as $J \rightarrow \infty$, $\beta_J/\zeta \rightarrow 1$. This is to be expected on physical grounds.

In Fig. 2, the right-hand side of equation (10b) is plotted versus Ω. The maxima and minima give bounds on the β_J shown in Table 1. Determining these bounds, of course, does not require first determining the Ω_J. Note that the results for Cases I and II approach each other as $\Omega/\omega_1 \rightarrow \infty$ as one would expect.

Table 1 Beam clamped at center—symmetric modes only; $\Omega_J/\omega_1 \cong 4\,(J + 1/4)^2 = (2J + 1/2)^2$ [6]

J	Ω_J/ω_1	$\zeta_1 = \zeta_2 = \zeta$, etc. β_J/ζ	$\zeta_1 = 10\,\zeta$, $\zeta_2 = \zeta$, etc. β_J/ζ
1	6.25	0.7470	1.535
2	20.25	0.8585	0.9300
3	42.25	0.9021	0.9184
4	72.25	0.9251	0.9307
5	110.25	0.9344	0.9418
6	156.25	0.9491	0.9503
7	210.25	0.9561	0.9568
8	272.25	0.9614	0.9618
9	343.25	0.9656	0.9658
10	420.25	0.9689	0.9691

References

1 Dowell, E. H., "On Some General Properties of Combined Dynamical Systems," ASME JOURNAL OF APPLIED MECHANICS, Vol. 46, No. 1, Mar. 1979, pp. 206–209.

2 Klein, L. R., and Dowell, E. H., "Analysis of Modal Damping by Component Modes Method Using Lagrange Multiplier," ASME JOURNAL OF APPLIED MECHANICS, Vol. 41, No. 2, June 1974, pp. 527–528.

3 Hallquist, J., and Snyder, V. W., "Linear Damped Vibrating Structures With Arbitrary Support Conditions," ASME JOURNAL OF APPLIED MECHANICS, Vol. 40, No. 1, Mar. 1973, pp. 312–313.

4 Dowell, E. H., "Free Vibrations of an Arbitrary Structure in Terms of Component Modes," ASME JOURNAL OF APPLIED MECHANICS, Vol. 39, Sept. 1972, pp. 727–731.

5 Goldstein, H., *Classical Mechanics,* Addison-Wesley Publishing Company, Inc., Reading, Mass. 1965.

6 Young, D., and Felgar, R. P., Jr., "Tables of Characteristic Functions Representing Normal Modes of Vibrations of a Beam," The University of Texas Publication No. 4913, July 1, 1949, p. 25.

On the Invariance Group of the Plane Squeezing Flow of a Viscous Fluid

N. Phan-Thien[1]

A plane flow of a viscous incompressible fluid can be adequately described by the following stream-function equation:

$$\nabla^2\psi_t + \psi_y\nabla^2\psi_x - \psi_x\nabla^2\psi_y = \nu\nabla\psi, \tag{1}$$

where the stream-function ψ is defined by $u = \partial\psi/\partial y \equiv \psi_y$, $v =$

[1] Lecturer, Department of Mechanical Engineering, University of Newcastle, New South Wales, 2308, Australia.
Manuscript received by ASME Applied Mechanics Division, July, 1979.

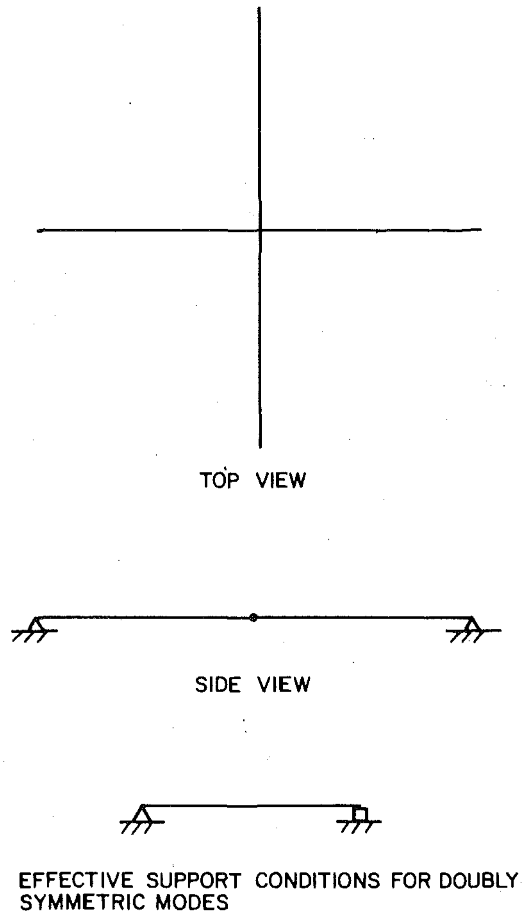

EXAMPLE GEOMETRY

Fig. 1

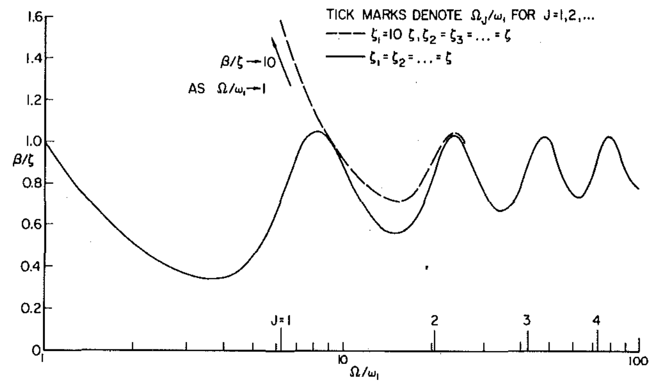

Fig. 2

Table 1 Beam clamped at center—symmetric modes only; $\Omega_J/\omega_1 \cong 4\,(J + 1/4)^2 = (2J + 1/2)^2$ [6]

J	Ω_J/ω_1	$\zeta_1 = \zeta_2 = \zeta$, etc. β_J/ζ	$\zeta_1 = 10\,\zeta$, $\zeta_2 = \zeta$, etc. β_J/ζ
1	6.25	0.7470	1.535
2	20.25	0.8585	0.9300
3	42.25	0.9021	0.9184
4	72.25	0.9251	0.9307
5	110.25	0.9344	0.9418
6	156.25	0.9491	0.9503
7	210.25	0.9561	0.9568
8	272.25	0.9614	0.9618
9	343.25	0.9656	0.9658
10	420.25	0.9689	0.9691

Using (11) in (8) and (10) and recalling that for this example the two beams are identical, one has

$$\sum_{j=1}^{\infty} \left[\frac{\phi_j^2\,(x=0)}{M_j\,(\omega_j^2 - \Omega_J^2)}\right] = 0 \tag{8b}$$

and

$$\beta_J = \frac{\displaystyle\sum_{j=1}^{\infty} \left[\frac{\phi_j^2\,(x=0)\,\zeta_j\,\omega_j/\Omega_J}{M_j\,(\omega_j^2 - \Omega_J^2)^2}\right]}{\displaystyle\sum_{j=1}^{\infty} \left[\frac{\phi_j^2\,(x=0)}{M_j\,(\omega_j^2 - \omega_J^2)^2}\right]} \tag{10b}$$

Numerics have been carried out for two specific choices of component damping factors, ζ_j. Case I corresponds to $\zeta_j = \zeta$, a constant, for all j. Case II corresponds to $\zeta_1 = 10\,\zeta$ and $\zeta_j = \zeta$ for all $j \geqslant 2$. Ω_J is computed from (8b) then β_J is computed for (10b). The results for β_J/ζ are shown in Table 1 for $J = 1, \ldots, 10$. As may be seen $\beta_J/\zeta_j < 1$ for each pair, $J = j = 1, 2, 3$, etc. Note that as $J \to \infty$, $\beta_J/\zeta \to 1$. This is to be expected on physical grounds.

In Fig. 2, the right-hand side of equation (10b) is plotted versus Ω. The maxima and minima give bounds on the β_J shown in Table 1. Determining these bounds, of course, does not require first determining the Ω_J. Note that the results for Cases I and II approach each other as $\Omega/\omega_1 \to \infty$ as one would expect.

References

1 Dowell, E. H., "On Some General Properties of Combined Dynamical Systems," ASME Journal of Applied Mechanics, Vol. 46, No. 1, Mar. 1979, pp. 206–209.

2 Klein, L. R., and Dowell, E. H., "Analysis of Modal Damping by Component Modes Method Using Lagrange Multiplier," ASME Journal of Applied Mechanics, Vol. 41, No. 2, June 1974, pp. 527–528.

3 Hallquist, J., and Snyder, V. W., "Linear Damped Vibrating Structures With Arbitrary Support Conditions," ASME Journal of Applied Mechanics, Vol. 40, No. 1, Mar. 1973, pp. 312–313.

4 Dowell, E. H., "Free Vibrations of an Arbitrary Structure in Terms of Component Modes," ASME Journal of Applied Mechanics, Vol. 39, Sept. 1972, pp. 727–731.

5 Goldstein, H., *Classical Mechanics,* Addison-Wesley Publishing Company, Inc., Reading, Mass. 1965.

6 Young, D., and Felgar, R. P., Jr., "Tables of Characteristic Functions Representing Normal Modes of Vibrations of a Beam," The University of Texas Publication No. 4913, July 1, 1949, p. 25.

On the Invariance Group of the Plane Squeezing Flow of a Viscous Fluid

N. Phan-Thien[1]

A plane flow of a viscous incompressible fluid can be adequately described by the following stream-function equation:

$$\nabla^2\psi_t + \psi_y\nabla^2\psi_x - \psi_x\nabla^2\psi_y = \nu\nabla\psi, \tag{1}$$

where the stream-function ψ is defined by $u = \partial\psi/\partial y \equiv \psi_y$, $v =$

[1] Lecturer, Department of Mechanical Engineering, University of Newcastle, New South Wales, 2308, Australia.

Manuscript received by ASME Applied Mechanics Division, July, 1979.

$-\partial\psi/\partial x \equiv -\psi_x$, ν is the kinematic viscosity of the liquid and ∇ is the two-dimensional gradient operator.

Cantwell [1] has reported a 10-parameter Lie group of space-time coordinates transformations that leaves (1) invariant. Infinitesimally, this 10-parameter Lie group is described by

$$\begin{cases} \tilde{x} = x + \epsilon\xi + O(\epsilon^2), \\ \tilde{y} = y + \epsilon\rho + O(\epsilon^2), \\ \tilde{t} = t + \epsilon\tau + O(\epsilon^2), \\ \tilde{\psi} = \psi + \epsilon\eta + O(\epsilon^2), \end{cases} \tag{2}$$

where

$$\begin{cases} \xi = ax + by + cty + f_1(t) + d \\ \rho = -bx + ay - ctx + f_2(t) + e \\ \tau = 2at + h \\ \eta = 1/2c(x^2+y^2) - \dot{f}_2(t)x + \dot{f}_1(t)y + s(t) + p. \end{cases} \tag{3}$$

a, b, c, d, e, h, p are constants and $f_1(t)$, $f_2(t)$, and $s(t)$ are arbitrary functions of t. In (3), the dot denotes derivative with respect to time.

It is the purpose of this communication to show that the plane squeeze film flow of a viscous fluid admits a similarity solution if the velocity of approach of the plates is proportional to $(2at+h)^{-1/2}$.

To do that, we need to find a particular subgroup of (3) that leaves the boundary conditions of the plane squeezing flow invariant. Now the velocity field at the upper plate ($y = H(t)$) must satisfy

$$u(x, y = H(t)) = \psi_y\,(x, y = H(t)) = 0 \tag{4}$$

$$v(x, y = H(t)) = -\psi_x\,(x, y = H(t)) = -\dot{H}(t) \tag{5}$$

Invariance of the boundary curve $y = H(t)$ implies

$$\tilde{y} = H(\tilde{t})$$

that is,

$$\rho(x, y = H(t)) = \dot{H}(t)\,\tau(x, y = H(t))$$

which requires that

$$-bx + aH(t) - ctx + f_2(t) + e = \dot{H}(t)(2at+h).$$

For this to be satisfied identically we need $b = 0 = c$ and

$$f_2(t) = \dot{H}(t)(2at+h) - aH(t) - e. \tag{6}$$

Next, invariance of (4) implies

$$\tilde{\psi}_{\tilde{y}}\,(x, y = H(t)) = 0,$$

which requires that

$$\frac{D\eta}{Dy} - \frac{D\xi}{Dy}\psi_x - \frac{D\rho}{Dy}\psi_y - \frac{D_\tau}{Dy}\psi_t = 0 \tag{7}$$

at $y = H(t)$. D/Dx_i is the total derivative (Bluman and Cole [2]) defined in the four-dimensional space (x, y, t, ψ) by

$$\frac{D}{Dx_i} \equiv \frac{\partial}{\partial x_i} + \psi_i \frac{\partial}{\partial \psi}, \quad x_i \equiv x, y, \text{ or } t.$$

Condition (7) requires that $\dot{f}_1 = 0$ or $f_1(t) =$ constant.

Invariance of the second boundary condition (5) requires that

$$\tilde{\psi}_{\tilde{x}}\,(x, y = H(t)) = \dot{H}(\tilde{t})$$

which implies

$$\frac{D\eta}{Dx} - \frac{D\xi}{DX}\psi_x - \frac{D\rho}{Dx}\psi_y - \frac{D\tau}{Dx}\psi_t = \dot{H}(t)\tau \quad \text{at} \quad y = H(t),$$

that is,

$$\dot{f}_2(t) = -\ddot{H}(t)(2at+h) - a\dot{H}(t). \tag{8}$$

Compatibility between (8) and (5) dictates that the normal velocity of approach of the plates must satisfy

$$\ddot{H} + \frac{a}{2at+h}\dot{H} = 0,$$

that is,

$$\dot{H}(t) = q(2at+h)^{-1/2}, \quad H(t) = \frac{q}{a}(2at+h)^{1/2} \tag{9}$$

that is, if $\dot{H}(t)$ is given by (9), then the plane squeezing flow admits similarity solutions described by the following 6-parameter Lie group of transformations

$$\begin{cases} \xi = ax + \beta \\ \rho = ay \\ \tau = 2at + h \\ \eta = s(t) + p \end{cases} \tag{10}$$

For example, the case where $\beta = p = 0 \equiv s(t)$ admits the following similarity solution:

$$\frac{dx}{ax} = \frac{dy}{ay} = \frac{dt}{2at+h} = \frac{d\psi}{0} \tag{11}$$

that is,

$$\psi = F(\xi_1, \xi_2), \tag{12}$$

where

$$\xi_1 = \frac{x}{\sqrt{2at+h}} \quad \text{and} \quad \xi_2 = \frac{y}{\sqrt{2at+h}} \tag{13}$$

are two invariants of (11).

Substitution of (12) into (1) results in a reduction in the order of the p.d.e. Alternatively, the velocities can be scaled appropriately according to (12) and their substitution into the Navier-Stokes equations results in an ordinary differential equation. This equation has been studied extensively by Wang [3] who found that when H is proportional to $\sqrt{1-\alpha t}$ a similarity solution for the plane (and circular) squeezing flow is possible. The flow is then described by a single parameter $S = \alpha R^2/\nu$, where R is a length scale. Among many other things reported in this paper, Wang has shown numerically that the squeezing force may not necessarily follow the direction of approach for certain values of S.

References

1 Cantwell, B. J., "Similarity Transformations for the Two-Dimensional, Unsteady, Stream-Function Equation," *Journal of Fluid Mechanics*, Vol. 85, 1978, pp. 257–271.

2 Bluman, G. W., and Cole, J. D., *Similarity Methods for Differential Equations*, Springer-Verlag, 1974.

3 Wang, C. Y., "The Squeezing of a Fluid Between Two Plates," ASME JOURNAL OF APPLIED MECHANICS, Vol. 43, 1976, pp. 579–583.

Torsional Vibrations of Poroelastic Cylinders

M. Tajuddin[1] and K. S. Sarma[2]

Introduction

The study of torsional vibrations is of importance, both from theoretical and practical considerations. Such vibrations, for example,

[1] Presently, Kothagudem School of Mines, Osmania University, KOTHAGUDEM—507 101, India; formerly, Department of Mathematics, Regional Engineering College, Warangal 506 004, India.

[2] Department of Mathematics, Regional Engineering College, Warangal 506 004, India.

Manuscript received by ASME Applied Mechanics Division, June, 1978; final revision, June, 1979.

$-\partial\psi/\partial x \equiv -\psi_x$, ν is the kinematic viscosity of the liquid and ∇ is the two-dimensional gradient operator.

Cantwell [1] has reported a 10-parameter Lie group of space-time coordinates transformations that leaves (1) invariant. Infinitesimally, this 10-parameter Lie group is described by

$$\begin{cases} \tilde{x} = x + \epsilon\xi + O(\epsilon^2), \\ \tilde{y} = y + \epsilon\rho + O(\epsilon^2), \\ \tilde{t} = t + \epsilon\tau + O(\epsilon^2), \\ \tilde{\psi} = \psi + \epsilon\eta + O(\epsilon^2), \end{cases} \tag{2}$$

where

$$\begin{cases} \xi = ax + by + cty + f_1(t) + d \\ \rho = -bx + ay - ctx + f_2(t) + e \\ \tau = 2at + h \\ \eta = 1/2c(x^2+y^2) - \dot{f}_2(t)x + \dot{f}_1(t)y + s(t) + p. \end{cases} \tag{3}$$

a, b, c, d, e, h, p are constants and $f_1(t)$, $f_2(t)$, and $s(t)$ are arbitrary functions of t. In (3), the dot denotes derivative with respect to time.

It is the purpose of this communication to show that the plane squeeze film flow of a viscous fluid admits a similarity solution if the velocity of approach of the plates is proportional to $(2at + h)^{-1/2}$.

To do that, we need to find a particular subgroup of (3) that leaves the boundary conditions of the plane squeezing flow invariant. Now the velocity field at the upper plate ($y = H(t)$) must satisfy

$$u(x, y = H(t)) = \psi_y\,(x, y = H(t)) = 0 \tag{4}$$

$$v(x, y = H(t)) = -\psi_x\,(x, y = H(t)) = -\dot{H}(t) \tag{5}$$

Invariance of the boundary curve $y = H(t)$ implies

$$\tilde{y} = H(\tilde{t})$$

that is,

$$\rho(x, y = H(t)) = \dot{H}(t)\,\tau(x, y = H(t))$$

which requires that

$$-bx + aH(t) - ctx + f_2(t) + e = \dot{H}(t)(2at + h).$$

For this to be satisfied identically we need $b = 0 = c$ and

$$f_2(t) = \dot{H}(t)(2at + h) - aH(t) - e. \tag{6}$$

Next, invariance of (4) implies

$$\tilde{\psi}_{\tilde{y}}\,(x, y = H(t)) = 0,$$

which requires that

$$\frac{D\eta}{Dy} - \frac{D\xi}{Dy}\psi_x - \frac{D\rho}{Dy}\psi_y - \frac{D_\tau}{Dy}\psi_t = 0 \tag{7}$$

at $y = H(t)$. D/Dx_i is the total derivative (Bluman and Cole [2]) defined in the four-dimensional space (x, y, t, ψ) by

$$\frac{D}{Dx_i} \equiv \frac{\partial}{\partial x_i} + \psi_i \frac{\partial}{\partial \psi}, \quad x_i \equiv x, y, \text{ or } t.$$

Condition (7) requires that $\dot{f}_1 = 0$ or $f_1(t) =$ constant.

Invariance of the second boundary condition (5) requires that

$$\tilde{\psi}_{\tilde{x}}\,(x, y = H(t)) = \dot{H}(\tilde{t})$$

which implies

$$\frac{D\eta}{Dx} - \frac{D\xi}{DX}\psi_x - \frac{D\rho}{Dx}\psi_y - \frac{D\tau}{Dx}\psi_t = \ddot{H}(t)\tau \quad \text{at} \quad y = H(t),$$

that is,

$$\dot{f}_2(t) = -\ddot{H}(t)(2at + h) - a\dot{H}(t). \tag{8}$$

Compatibility between (8) and (5) dictates that the normal velocity of approach of the plates must satisfy

$$\ddot{H} + \frac{a}{2at + h}\dot{H} = 0,$$

that is,

$$\dot{H}(t) = q(2at + h)^{-1/2}, \quad H(t) = \frac{q}{a}(2at + h)^{1/2} \tag{9}$$

that is, if $\dot{H}(t)$ is given by (9), then the plane squeezing flow admits similarity solutions described by the following 6-parameter Lie group of transformations

$$\begin{cases} \xi = ax + \beta \\ \rho = ay \\ \tau = 2at + h \\ \eta = s(t) + p \end{cases} \tag{10}$$

For example, the case where $\beta = p = 0 \equiv s(t)$ admits the following similarity solution:

$$\frac{dx}{ax} = \frac{dy}{ay} = \frac{dt}{2at + h} = \frac{d\psi}{0} \tag{11}$$

that is,

$$\psi = F(\xi_1, \xi_2), \tag{12}$$

where

$$\xi_1 = \frac{x}{\sqrt{2at + h}} \quad \text{and} \quad \xi_2 = \frac{y}{\sqrt{2at + h}} \tag{13}$$

are two invariants of (11).

Substitution of (12) into (1) results in a reduction in the order of the p.d.e. Alternatively, the velocities can be scaled appropriately according to (12) and their substitution into the Navier-Stokes equations results in an ordinary differential equation. This equation has been studied extensively by Wang [3] who found that when H is proportional to $\sqrt{1 - \alpha t}$ a similarity solution for the plane (and circular) squeezing flow is possible. The flow is then described by a single parameter $S = \alpha R^2/\nu$, where R is a length scale. Among many other things reported in this paper, Wang has shown numerically that the squeezing force may not necessarily follow the direction of approach for certain values of S.

References

1 Cantwell, B. J., "Similarity Transformations for the Two-Dimensional, Unsteady, Stream-Function Equation," *Journal of Fluid Mechanics*, Vol. 85, 1978, pp. 257–271.

2 Bluman, G. W., and Cole, J. D., *Similarity Methods for Differential Equations*, Springer-Verlag, 1974.

3 Wang, C. Y., "The Squeezing of a Fluid Between Two Plates," ASME JOURNAL OF APPLIED MECHANICS, Vol. 43, 1976, pp. 579–583.

Torsional Vibrations of Poroelastic Cylinders

M. Tajuddin[1] and K. S. Sarma[2]

Introduction

The study of torsional vibrations is of importance, both from theoretical and practical considerations. Such vibrations, for example,

[1] Presently, Kothagudem School of Mines, Osmania University, KOTHAGUDEM—507 101, India; formerly, Department of Mathematics, Regional Engineering College, Warangal 506 004, India.

[2] Department of Mathematics, Regional Engineering College, Warangal 506 004, India.

Manuscript received by ASME Applied Mechanics Division, June, 1978; final revision, June, 1979.

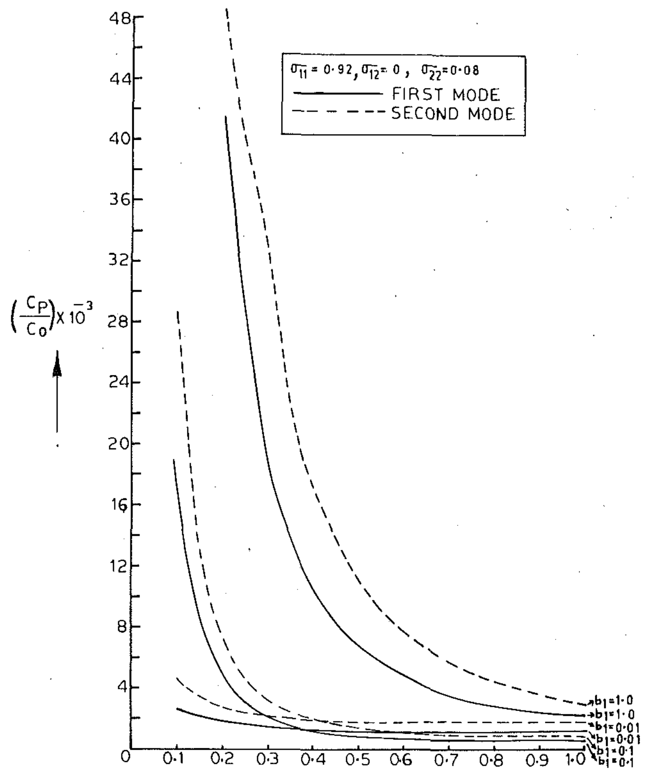

Fig. 1

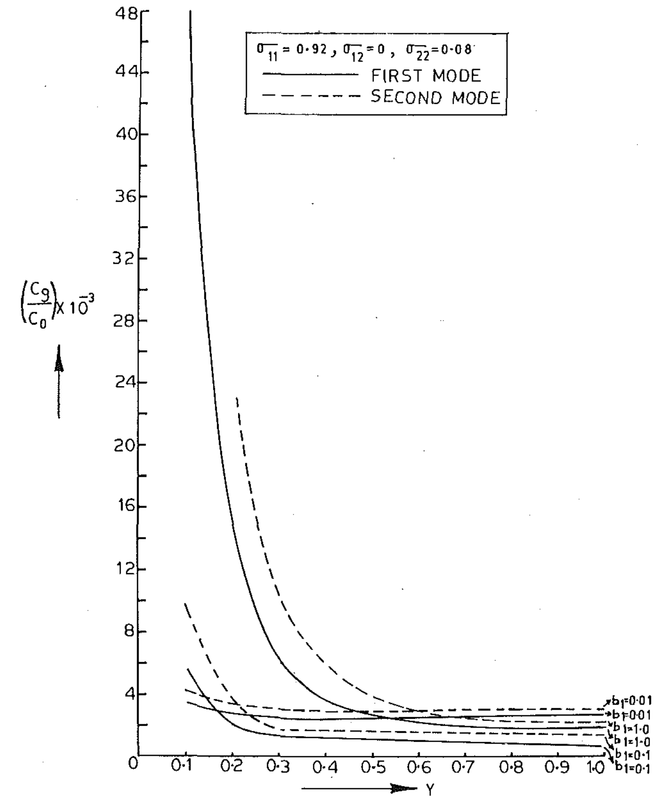

Fig. 2

are used in delay lines. Further, based on the reflections and refractions during the propagation of a pulse, imperfections can be identified. Still another use of torsional vibrations is the measurement of the shear modulus of a crystal.

In this Note, torsional vibrations of an infinite, isotropic, homogeneous poroelastic cylinder are studied. Plots of nondimensional phase velocity, group velocity, and wavelength as a function of nondimensional frequency are presented.

Solution of the Problem

Let r, θ, z be cylindrical polar coordinates with z-axis along the axis of the cylinder. The nonzero displacement component of solid u_θ and liquid U_θ are to be determined from

$$N(\nabla^2 - r^{-2})u_\theta = \frac{\partial^2}{\partial t^2}(\rho_{11}u_\theta + \rho_{12}U_\theta) + b\frac{\partial}{\partial t}(u_\theta - U_\theta)$$

$$0 = \frac{\partial^2}{\partial t^2}(\rho_{12}u_\theta + \rho_{22}U_\theta) - b\frac{\partial}{\partial t}(u_\theta - U_\theta). \qquad (1)$$

Here ρ_{11}, ρ_{12}, and ρ_{22} are mass densities as introduced in [1], N is a shear modulus, b is a dissipation coefficient, and ∇^2 is the Laplacian operator. From the conditions of stress-free curved surface, the frequency equation of torsional vibrations of a circular poroelastic cylinder of radius a is

$$J_2(R) = 0, \qquad (2)$$

where J_2 is the Bessel function of first kind and of order two.

The propagation mode shapes are given by

$$u_\theta = \begin{cases} C_1 J_1(k_n r)\exp[i(\alpha z + pt)] & \text{when} \quad k_n \neq 0 \\ C_1 r \exp[i(\alpha z + pt)] & \text{when} \quad k_n = 0, \end{cases} \qquad (3)$$

where α is the wave number, p is the frequency, and J_1 is the Bessel function of first kind and of order one. In these equations, R_n is the nth nonzero root of equation (2) and

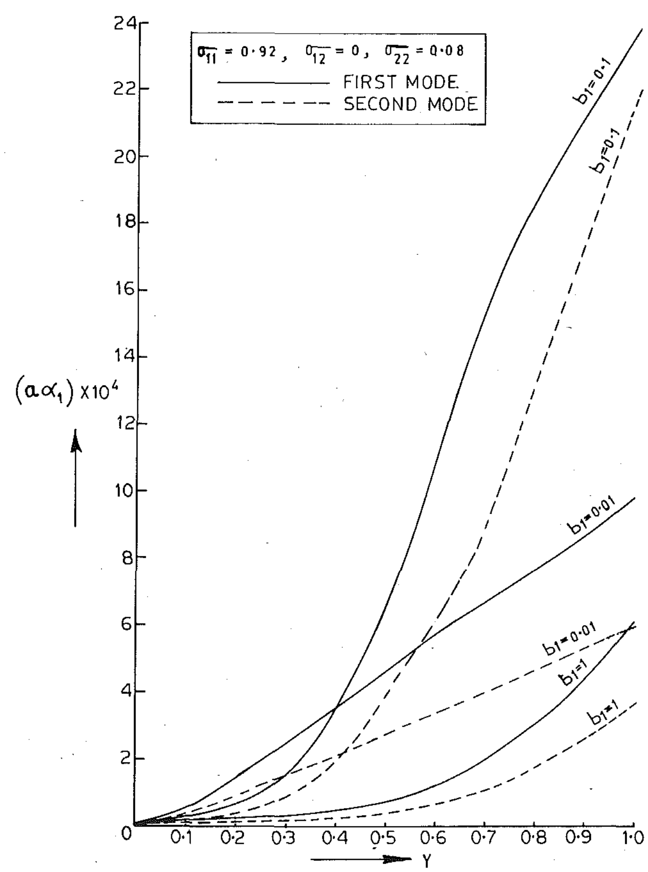

Fig. 3

$$R_n{}^2 = k_n{}^2a^2, \quad k_n{}^2 = \frac{p^2(\tau_{11}\tau_{22} - \tau_{12}{}^2)}{N\tau_{22}} - \alpha^2, \tag{4}$$

where

$$\tau_{11} = \rho_{11} - \frac{ib}{p}, \quad \tau_{12} = \rho_{12} + \frac{ib}{p}, \quad \tau_{22} = \rho_{22} - \frac{ib}{p}.$$

The roots of equation (2) are well known.

On combining and rearranging equations (4), we can write

$$\frac{N(R_n{}^2 + a^2\alpha^2)}{a^2p^2\rho} = E_r - iE_i,$$

where

$$E_r = \frac{y^2\sigma_{22}(\sigma_{11}\sigma_{22} - \sigma_{12}{}^2) + b_1{}^2}{y^2\sigma_{22}{}^2 + b_1{}^2},$$

$$E_i = \frac{yb_1(\sigma_{12} + \sigma_{22})^2}{y^2\sigma_{22}{}^2 + b_1{}^2}. \tag{5}$$

b_1, y, σ_{ij} are nondimensional dissipation coefficient, frequency, and mass densities, respectively, defined by

$$b_1 = \frac{ab}{\rho c_0}, \quad y_1 = \frac{ap}{c_0}, \quad \sigma_{ij} = \frac{\rho_{ij}}{\rho}, \quad \rho = \rho_{11} + 2\rho_2 + \rho_{22}, \quad c_0{}^2 = \frac{N}{\rho}.$$

Because of the dissipative nature of the medium, in general, the wave number α is complex [1]. Letting

$$\alpha = \alpha_r + i\alpha_i,$$

then phase velocity $c_p(= p/|\alpha_r|)$ is given by

$$c_p/c_0 = 2^{1/2}y(B_1 + B_2)^{-1/2}. \tag{6}$$

The group velocity is

$$c_g/c_0 = 2^{3/2}B_3{}^{-1}(B_1 + B_2)^{1/2}. \tag{7}$$

The attenuation x_a $(= 1/|\alpha_i|)$ is

$$x_a/a = 2^{1/2}(B_1 - B_2)^{-1/2}, \tag{8}$$

where

$$B_1 = \{y^4(E_r{}^2 + E_i{}^2) - 2y^2E_rR_n{}^2 + R_n{}^4\}^{1/2}, \quad B_2 = y^2E_r - R_n{}^2,$$

$$B_3 = y^2G_1(1 + y^2E_rB_1{}^{-1} - R_n{}^2B_1{}^{-1}) + 2yE_r(1 - R_n{}^2B_1{}^{-1}) + y^3B_1{}^{-1}(yE_iG_2 + 2E_r{}^2 + 2E_i{}^2),$$

$$G_1 = \frac{2b_1{}^2(E_r - 1)}{y(y^2\sigma_{22}{}^2 + b_1{}^2)}, \quad G_2 = \frac{(b_1{}^2 - y^2\sigma_{22}{}^2)E_i}{y(y^2\sigma_{22}{}^2 + b_1{}^2)}. \tag{9}$$

It is observed that the square of the wave number is the average of B_1 and B_2.

Discussions

In the general case, even the least mode is observed to be dispersive where as it is nondispersive in the absence of dissipation. Consequently, the least mode can be used in delay lines [2]. In higher modes vibrations are dispersive. Phase velocity, group velocity, wavelength are calculated for different values of frequency for a cylindrical bone whose parameters are given in [3] and are presented graphically. From Fig. 1, it is observed that when dissipative coefficient increases from 0.01 to 0.10, the phase velocity curves of first and second modes intersect around the wavelength (= y) is equal to 0.4. For wavelength greater than 0.4 phase velocity is decreasing in both the modes and when dissipative force is equal to 1, the wave velocity is higher than in all other cases. The group velocity and wavelength are given in Figs. 2 and 3. When the values of dissipative force are small, the graphs for wavelength are straight lines and their slope increases with increasing b_1.

In absence of dissipative force vibrations are not attenuated and the same conclusions as that of classical theory are valid.

References

1 Biot, M. A., "Theory of Propagation of Elastic Waves in Fluid-Saturated Porous Solid," *Journal of the Acoustical Society of America*, Vol. 28, 1956, pp. 168–178.

2 Redwood, M., *Mechanical Wave Guides*, Pergamon Press, New York, 1960, pp. 146–148.

3 Nowinski, J. L., and Davis, C. F., "Propagation of Longitudinal Waves in a Circularly Cylindrical Bone Element," ASME Journal of Applied Mechanics, Vol. 38, 1971, pp. 578–584.

A Condition of Bending-Free Torsion to Define the Center of Twist

N. G. Stephen[1]

Introduction

A beam subjected to terminal tractions and displacement restraints will in general experience direct and shearing stresses dependent on the magnitude and distribution of the stresses over the end surface rather than the types of forces and couples producing these terminal stresses. However, it is convenient for the engineer to be able to identify the stress resultants in terms of the applied loads. Thus a cantilevered beam subjected to a terminal shearing force [1] will experience direct and shearing stresses and it is convenient to differentiate between direct stresses due to bending and warping restraints, and shearing stresses due to shear and torsion. Toward this end the center of flexure is defined as that point through which the terminal shearing force must pass in order to produce "torsion-free bending," a state usually defined [2] by zero overall local rotation of the section which is mathematically equivalent to zero rotation of the centroid of the section, vanishing of shearing stresses due to torsion and hence zero torsional stress resultant.

The center of twist is usually defined [3] according to a minimum potential energy of warping, which can easily be shown to correspond mathematically to rotation about an axis such that the warping integral will be a minimum. The relationship between the two centers as defined previously is shown in [4]. The exact solution for torsion with restrained warping is not known, but since restraint gives rise to axial direct stresses it seems natural to investigate the condition under which these stresses do not constitute a resultant bending moment, equivalent to "bending-free torsion," and it is shown that this leads to coordinates of the center of twist agreeing with those obtained on the basis of minimum warping energy.

Theory

If x and y are the principal axes and z coincides with the axis of centroids then for a uniform isotropic rod the most general form of the displacements during twist are [3]

$$u = \frac{d\theta}{dz}(-zy + a + qz - ry) \tag{1a}$$

$$v = \frac{d\theta}{dz}(zx + b + rx - pz) \tag{1b}$$

$$w = \frac{d\theta}{dz}(\phi(x,y) + c + py - qx) \tag{1c}$$

[1] Lecturer, Department of Mechanical, Production and Chemical Engineering, Manchester Polytechnic, John Dalton Faculty of Technology, Chester Street, Manchester M1 5GD, England.

Manuscript received by ASME Applied Mechanics Division, May, 1979; final revision, October, 1979.

$$R_n^2 = k_n^2 a^2, \quad k_n^2 = \frac{p^2(\tau_{11}\tau_{22} - \tau_{12}^2)}{N\tau_{22}} - \alpha^2, \tag{4}$$

where

$$\tau_{11} = \rho_{11} - \frac{ib}{p}, \quad \tau_{12} = \rho_{12} + \frac{ib}{p}, \quad \tau_{22} = \rho_{22} - \frac{ib}{p}.$$

The roots of equation (2) are well known.

On combining and rearranging equations (4), we can write

$$\frac{N(R_n^2 + a^2\alpha^2)}{a^2p^2\rho} = E_r - iE_i,$$

where

$$E_r = \frac{y^2\sigma_{22}(\sigma_{11}\sigma_{22} - \sigma_{12}^2) + b_1^2}{y^2\sigma_{22}^2 + b_1^2},$$

$$E_i = \frac{yb_1(\sigma_{12} + \sigma_{22})^2}{y^2\sigma_{22}^2 + b_1^2}. \tag{5}$$

b_1, y, σ_{ij} are nondimensional dissipation coefficient, frequency, and mass densities, respectively, defined by

$$b_1 = \frac{ab}{\rho c_0}, \quad y_1 = \frac{ap}{c_0}, \quad \sigma_{ij} = \frac{\rho_{ij}}{\rho}, \quad \rho = \rho_{11} + 2\rho_2 + \rho_{22}, \quad c_0^2 = \frac{N}{\rho}.$$

Because of the dissipative nature of the medium, in general, the wave number α is complex [1]. Letting

$$\alpha = \alpha_r + i\alpha_i,$$

then phase velocity $c_p (= p/|\alpha_r|)$ is given by

$$c_p/c_0 = 2^{1/2}y(B_1 + B_2)^{-1/2}. \tag{6}$$

The group velocity is

$$c_g/c_0 = 2^{3/2}B_3^{-1}(B_1 + B_2)^{1/2}. \tag{7}$$

The attenuation x_a $(= 1/|\alpha_i|)$ is

$$x_a/a = 2^{1/2}(B_1 - B_2)^{-1/2}, \tag{8}$$

where

$$B_1 = \{y^4(E_r^2 + E_i^2) - 2y^2E_rR_n^2 + R_n^4\}^{1/2}, \quad B_2 = y^2E_r - R_n^2,$$

$$B_3 = y^2G_1(1 + y^2E_rB_1^{-1} - R_n^2B_1^{-1}) + 2yE_r(1 - R_n^2B_1^{-1}) + y^3B_1^{-1}(yE_iG_2 + 2E_r^2 + 2E_i^2),$$

$$G_1 = \frac{2b_1^2(E_r - 1)}{y(y^2\sigma_{22}^2 + b_1^2)}, \quad G_2 = \frac{(b_1^2 - y^2\sigma_{22}^2)E_i}{y(y^2\sigma_{22}^2 + b_1^2)}. \tag{9}$$

It is observed that the square of the wave number is the average of B_1 and B_2.

Discussions

In the general case, even the least mode is observed to be dispersive where as it is nondispersive in the absence of dissipation. Consequently, the least mode can be used in delay lines [2]. In higher modes vibrations are dispersive. Phase velocity, group velocity, wavelength are calculated for different values of frequency for a cylindrical bone whose parameters are given in [3] and are presented graphically. From Fig. 1, it is observed that when dissipative coefficient increases from 0.01 to 0.10, the phase velocity curves of first and second modes intersect around the wavelength (= y) is equal to 0.4. For wavelength greater than 0.4 phase velocity is decreasing in both the modes and when dissipative force is equal to 1, the wave velocity is higher than in all other cases. The group velocity and wavelength are given in Figs. 2 and 3. When the values of dissipative force are small, the graphs for wavelength are straight lines and their slope increases with increasing b_1.

In absence of dissipative force vibrations are not attenuated and the same conclusions as that of classical theory are valid.

References

1 Biot, M. A., "Theory of Propagation of Elastic Waves in Fluid-Saturated Porous Solid," *Journal of the Acoustical Society of America*, Vol. 28, 1956, pp. 168–178.

2 Redwood, M., *Mechanical Wave Guides*, Pergamon Press, New York, 1960, pp. 146–148.

3 Nowinski, J. L., and Davis, C. F., "Propagation of Longitudinal Waves in a Circularly Cylindrical Bone Element," ASME JOURNAL OF APPLIED MECHANICS, Vol. 38, 1971, pp. 578–584.

A Condition of Bending-Free Torsion to Define the Center of Twist

N. G. Stephen[1]

Introduction

A beam subjected to terminal tractions and displacement restraints will in general experience direct and shearing stresses dependent on the magnitude and distribution of the stresses over the end surface rather than the types of forces and couples producing these terminal stresses. However, it is convenient for the engineer to be able to identify the stress resultants in terms of the applied loads. Thus a cantilevered beam subjected to a terminal shearing force [1] will experience direct and shearing stresses and it is convenient to differentiate between direct stresses due to bending and warping restraints, and shearing stresses due to shear and torsion. Toward this end the center of flexure is defined as that point through which the terminal shearing force must pass in order to produce "torsion-free bending," a state usually defined [2] by zero overall local rotation of the section which is mathematically equivalent to zero rotation of the centroid of the section, vanishing of shearing stresses due to torsion and hence zero torsional stress resultant.

The center of twist is usually defined [3] according to a minimum potential energy of warping, which can easily be shown to correspond mathematically to rotation about an axis such that the warping integral will be a minimum. The relationship between the two centers as defined previously is shown in [4]. The exact solution for torsion with restrained warping is not known, but since restraint gives rise to axial direct stresses it seems natural to investigate the condition under which these stresses do not constitute a resultant bending moment, equivalent to "bending-free torsion," and it is shown that this leads to coordinates of the center of twist agreeing with those obtained on the basis of minimum warping energy.

Theory

If x and y are the principal axes and z coincides with the axis of centroids then for a uniform isotropic rod the most general form of the displacements during twist are [3]

$$u = \frac{d\theta}{dz}(-zy + a + qz - ry) \tag{1a}$$

$$v = \frac{d\theta}{dz}(zx + b + rx - pz) \tag{1b}$$

$$w = \frac{d\theta}{dz}(\phi(x,y) + c + py - qx) \tag{1c}$$

[1] Lecturer, Department of Mechanical, Production and Chemical Engineering, Manchester Polytechnic, John Dalton Faculty of Technology, Chester Street, Manchester M1 5GD, England.

Manuscript received by ASME Applied Mechanics Division, May, 1979; final revision, October, 1979.

where $d\theta/dz$ is the twist rate assumed constant for unrestrained warping, $\phi(x,y)$ is the Saint-Venant warping function and the last three terms in each expression are rigid-body translations and rotations.

Considering the rod to be composed of a collection of initially straight longitudinal filaments, real within the section and imaginary without, the axis of twist is now defined as that filament which does not distort into a helix during twist but remains straight when the rod is in a state of bending-free torsion. The center of twist (x_T, y_T) is then the position of this axis in any cross section and is given by

$$\frac{\partial u}{\partial z} = \frac{\partial v}{\partial z} = 0 \tag{2}$$

If the twist rate is assumed constant, from equations (1) we find

$$x_T = p, \quad y_T = q \tag{3}$$

The state of bending-free torsion is obtained from the usual stress-strain relationship

$$E\,\epsilon_z = \sigma_z - \nu(\sigma_x + \sigma_y) \tag{4}$$

Multiplication of (4) by x and y in turn and integration over the cross section yields

$$E\frac{\partial}{\partial z}\iint_A xw\,dxdy = \iint_A x\sigma_z\,dxdy - \nu\iint_A x(\sigma_x + \sigma_y)dxdy \tag{5a}$$

$$E\frac{\partial}{\partial z}\iint_A yw\,dxdy = \iint_A y\sigma_z\,dxdy - \nu\iint_A y(\sigma_x + \sigma_y)dxdy \tag{5b}$$

From Love [5] it is known that for a uniform isotropic beam subjected to terminal loadings only, the stress distributions of Saint-Venant flexure and torsion where stress components are either independent or linear functions of the axial coordinate z requires that $\sigma_x = \sigma_y = 0$, and requiring the bending moments

$$M_y = \iint_A x\sigma_z\,dxdy \tag{6a}$$

$$M_x = \iint_A y\sigma_z\,dxdy \tag{6b}$$

to be zero the condition of bending-free torsion becomes

$$\frac{\partial}{\partial z}\iint_A xw\,dxdy = 0 \tag{7a}$$

$$\frac{\partial}{\partial z}\iint_A yw\,dxdy = 0 \tag{7b}$$

For nonuniform torsion the twist rate is not constant and equations (7) with (1) and (3) yield the center of twist coordinates in the familiar form

$$x_T = -\frac{1}{I_x}\iint_A y\phi(x,y)dxdy \tag{8a}$$

$$y_T = \frac{1}{I_y}\iint_A x\phi(x,y)dxdy \tag{8b}$$

This coincides with the center of twist as in [3] and as used by Tsai [6].

Concluding Remarks

The approximate nature of the center of twist within the mathematical theory of elasticity is clearly illustrated by the inconsistency contained in the above theory, which is also intrinsic to the alternative approach based upon minimum potential energy of warping [3]. We see that the theory up to and including equations (7) assumes Saint-Venant torsion displacements which require a constant twist rate; however the results in (8) depend on a nonzero value of the derivative of the twist rate, i.e.,

$$\frac{d^2\theta}{dz^2} \neq 0.$$

This dilemma arises from the lack of an exact theory for torsion with restrained warping, when an appropriate theory is constructed by assuming Saint-Venant displacements except with a variable twist rate.

References

1 Sokolnikoff, I. S., *Mathematical Theory of Elasticity*, 2nd edition, McGraw-Hill, New York, 1956, Chapter 4.

2 Goodier, J. N., "A Theorem on the Shearing Stress in Beams With Application to Multicellular Sections," *Journal of the Aeronautical Sciences*, Vol. 11, 1944, pp. 272–280.

3 Weinstein, A. S., "The Centers of Shear and Twist," *Quarterly of Applied Mathematics*, Vol. 5, No. 1, 1947, pp. 97–99.

4 Stephen, N. G., and Maltbaek, J. C., "The Relationship Between the Centers of Flexure and Twist," *International Journal of Mechanical Sciences*, Vol. 21, No. 6, 1979, pp. 373–377.

5 Love, A. E. H., *A Treatise on the Mathematical Theory of Elasticity*, Dover Publications, New York, 1944, Chapter 16.

6 Tsai, W. T., "Note on the Center of Twist," ASME JOURNAL OF APPLIED MECHANICS, Vol. 39, 1972, pp. 297–298.

ERRATUM

Erratum on "On Laminar Dispersion for Flow Through Round Tubes," by J. S. Yu, and published in the December, 1979, issue of the ASME JOURNAL OF APPLIED MECHANICS, Vol. 46, No. 4, pp. 750–756.

Because of a misinterpretation of the results obtained by the method of Fast Fourier Transform, the presently calculated concentration profiles shown in Figs. 1–3 are in error. Concentrations at the positive and negative values of $2\zeta/\tau$ having the same magnitude should be interchanged or the correct results can be obtained by rigidly rotating the entire profiles 180 deg about the axis at $2\zeta/\tau = 0$ in the existing coordinate plane. The location of the peak of the concentration profiles appears therefore downstream of the mean flow position and approaches $2\zeta/\tau = 0$ asymptotically at large times. The author apologizes for inadvertently making such a serious mistake in reporting the numerical results.

Journal of Applied Mechanics

Book Reviews

The Dynamics of Explosion and Its Use. By Josef Henrych. Elsevier, New York. 1979. Pages 558. Price $107.25.

REVIEWED BY G. R. ABRAHAMSON[1]

This book is an extensive work covering an unusually broad range of topics:

1 Characteristics of explosions (chemical and nuclear).
2 Loads generated by explosions in extended media (air, water, rock, soil) and on structures.
3 Cratering, quarrying, and subsurface rubblization.
4 Response of structures to surface loads.
5 Response of structures to seismic loads.

The book is mainly a review: a total of 246 references are cited. The references are in two lists; the main list (140 references) contains about 70 percent Russian and Czechoslovakian articles, the supplementary list (106 references) contains mostly Western articles. Overall, the treatment tends to be mathematical, as indicated by the 13 pages of symbols used; however, for the first three topics there is considerable qualitative description, and when coming to applications empirical relations are often given.

The material on characteristics of explosions concerns mainly chemical explosions. The treatment of detonation phenomena and the initial shock pressure transmitted to adjacent materials is conventional and straightforward. As an example of an application, the impulse produced at a point by a contact charge is calculated from the initial shock pressure and the time required for a rarefaction wave to reach the point. This is later used in an oversimplified analysis to calculate the explosive needed to perforate a plate by multiple spalls from the back surface. In another application, the theory of lined-cavity charges (called cumulative charges) is reviewed.

The basic processes involved in nuclear explosions are described in eight pages, starting from the fundamentals of quantum mechanics and ending with a qualitative description of the development of the blast wave.

Spherical shock waves in air are described using Brodes' theory and empirical relations obtained by the author of the book. Shock reflections and loads on structures projecting above the ground are discussed. Inflow and propagation of shock waves in straight and jointed tunnels is treated.

Shock wave propagation in soils and rock is discussed extensively, for both buried charges and above-ground charges. The main applications considered are cratering and quarrying, and to a lesser extent demolition of structures.

The last third of the book concerns the response of structures to idealized surface loads and seismic loads. For surface loads, elastic and elastoplastic structures of single and multiple degrees of freedom are considered (frames, beams, plates, arches). Surface loads include the ideal impulse with various distributions and finite duration loads of various idealized distributions and time variations. Some results are given in terms of dynamic load factor, others include formulas for critical moments, deflections, etc. This part of the book is the most extensive compilation of theoretical results on the response of structures to pulse-type surface loads that this reviewer has seen. No experimental results are given. Seismic loads are in the form of oscillatory imputs to foundations of structures of single and multiple degrees of freedom.

The shortcomings of the book are few, but significant. The introduction appears somewhat overoptimistic concerning the use of explosives, particularly nuclear explosives. It also contains some confusing statements; for example, an excessive energy transient in a nuclear reactor is confused with a nuclear explosion. In the discussion of detonation and stress waves, some derivations are made from a mathematical viewpoint when a physical viewpoint might be more useful for practicing civil engineers. The translation suffers from some unconventional word usage and awkward sentences that would make the book difficult for beginners to follow. Occasional oversimplified explanations and assumptions appear. For example, the section on stress waves ends with a short commentary on failure caused by stress waves that is greatly oversimplified.

In spite of the shortcomings, the overall impact of the book is that it is an extensive and useful compilation of information on theory and applications of explosives. The type setting and printing are nearly perfect.

Numerical Solution of Differential Equations. By Isaac Fried. Academic Press, New York. 1979. Pages xii-261. Price $23.50.

REVIEWED BY T. BELYTSCHKO[2]

This book provides an introduction to the numerical solution of partial differential equations by both finite-difference and finite-element methods. Included are chapters on finite differences, variational formulations, finite elements, discretization accuracy, eigenproblems, two point boundary-value problems, and the equations of heat transfer, motion, and wave propagation.

The emphasis is on the fundamental concepts of numerical procedures, which are carefully illustrated through examples. Although the book introduces many mathematical concepts such as L_∞ error estimates, it is written in a lucid style that should be clear to a non-mathematician; the only exception is the assumption of the reader's familiarity with linear algebra, but this assumption is only invoked sparingly. Because of the wide range of topics covered, the examples are confined to one dimension, which again conforms with the author's intent that this be a "concept" book rather than an applications text.

I would recommend this book both to graduate students and researchers who would like an introduction to numerical methods or to improve their understanding of its mathematical aspects. I found reading the book to be enjoyable and profitable.

[1] Director, Poulter Laboratory, Stanford Research Institute International, Menlo Park, Calif 94025.

[2] Professor, Department of Civil Engineering, Northwestern University, Evanston, Ill. 60201.

Vibrations in Technology. (Vibratsii v Tekhnike). Handbook in six volumes. Volume I. Vibrations in Linear Systems (Kolebaniya Lineinykh Sistem) Moskva, "Mashinostroenie." 1978. (In Russian.) Academician V. V. Bolotin, Editor. Pages 352.

REVIEWED BY R. M. EVAN-IWANOWSKI[3]

The objective of this handbook is to present in depth an exhaustive and comprehensive treatment of major parts of physics, mechanics, and technology related to vibrations. This objective is excellently met: the book is well organized, well written, supplemented by numerous tables and graphs.

It is prepared for a wide range of readers, with main emphasis on practicing engineers working in the areas of creating new techniques and a new technology. Volume I deals with linear systems, and contains the following chapters:

PART I
Vibrations of Linear Systems With Finite Degrees of Freedom

Chapter I Basic Notions
Chapter II Mathematical Descriptions of Vibratory Systems With Finite Degrees of Freedom
Chapter III Free Vibrations in Conservative Systems
Chapter IV The Methods of Calculation of the Natural Frequencies and the Normal Modes for the Systems With Multiple Degrees of Freedom
Chapter V Nonconservative Autonomous Systems With Lumped Parameters, Stability of Linear Systems
Chapter VI Forced Vibrations
Chapter VII Parametric Vibrations

PART II
Vibrations of Linear Continuous Systems

Chapter VIII Mathematical Description of Continuous Systems
Chapter IX General Properties of Natural Frequencies and Normal Modes
Chapter X Determination of the Natural Frequencies and Normal Modes of Elastic Systems
Chapter XI Natural Frequencies and Normal Modes of Elastic Beams and Beamlike Structures
Chapter XII The Natural Frequencies and the Normal Modes of Elastic Plates
Chapter XIII The Natural Frequencies and the Normal Modes of Elastic Shells
Chapter XIV Forced Vibrations of Elastic Systems
Chapter XV Dynamic Stability of Continuous Systems
Chapter XVI Wave Propagation and Impact Processes in Elastic Systems

PART III
Random Vibrations of Linear Systems

Chapter XVII Information on the Theory of Random Processes and Fields
Chapter XVIII Random Vibrations of a System With Finite Degrees of Freedom
Chapter XIX Parametric Vibrations in Random Excitations
Chapter XX Random Vibrations in Continuous Systems
Chapter XXI Foundations of the Theory of Vibratory Reliability

The contents of the chapters are self-explanatory from their titles. Chapter XIX "Parametric Vibrations in Random Excitations" and Chapter XXI "Foundations of the Theory of Vibration Reliability," contain recent contributions developed in the U.S.S.R., in particular, by the Editor, Academician V. V. Bolotin.

The handbook is highly recommended as an indispensible addendum to the references on vibrations, even for the persons with a rudementary knowledge of Russian, since the material is presented in a nondimensional form, and the specific system configurations are shown in clear diagrams.

[3]Professor, Department of Mechanical and Aerospace Engineering, Syracuse University, Syracuse, N.Y. 13210.

Elastic Analysis of Soil-Foundation Interaction. By A. P. S. Selvadurai. Elsevier Scientific Publishing Co., Amsterdam, N.Y. 1979. Pages xii–546. Price $107.50.

REVIEWED BY G. M. L. GLADWELL[4]

This is the kind of book that one can use to hand to a graduate student starting to work on the subject of beams and plates on elastic foundations. It has a wealth of information, well organized, and not having too much detail. In addition, and most importantly, it has an extensive list of references, about 800 in all, covering the literature both in the Soviet Union and in the West.

The book is written for engineers, not mathematicians, so that the emphasis is on methods of analysis which lead to numerical, and particularly graphical, results for quantities of engineering interest—contact stresses, deflections, etc. Little emphasis is placed on topics such as integral transforms, dual integral equations, etc. Where such topics are introduced they are treated merely as tools which may be used to obtain solutions to problems.

The main body of the book is devoted to a study of the wide variety of problems relating to an elastic structure lying on a foundation, which again is almost always assumed to be elastic. The variety of problems arises because the structure may be taken to be rigid or elastic, and may be a beam, thin or thick, finite or infinite; a plate, circular or rectangular, thin or thick, finite or infinite. The foundation also may take various forms; it may be a simple Winkler foundation made up of independent linear springs, it may be some more complicated, Vlasov-Leont'ev or two-parameter model, or it may be a continuum, isotropic or anisotropic, homogeneous or nonhomogeneous. Virtually all the important combinations are studied and compared with each other. Most of the work is quasi-analytical, but purely numerical methods such as the finite-difference and finite-element methods are introduced and used.

A final chapter deals with the determination of soil parameters, particularly by experimental methods, and a series of appendices give the details of the mathematical analysis of some of the basic plate-foundation problems.

This book performs the valuable task of bringing the reader up to date, organizing the research which has been done, and pointing out some areas which still remain to be studied. I value its addition to my library.

[4] Professor, Department of Civil Engineering, University of Waterloo, Waterloo, Ontario, Canada N2L 3G1.

Numerical Simulation of Fluid Motion. Edited by J. Noye. North Holland. 1978. Pages ix-580. Price $66.75.

REVIEWED BY M. HOLT[5]

In this volume, the papers presented at an International Conference on Numerical Methods applied to Problems in Fluid Dynamics, held at Monash University, Melbourne, Australia, in 1976, are published. The volume reveals clearly that Australia is rapidly becoming a leading center in Computational Methods and ranks well among the longer established centers in U.S., U.S.S.R., and Western Europe. The major contributions in the volume are from Australia itself, but there are also two papers from New Zealand, one from New Guinea, and one from the U.S.

The volume begins with a long and thorough account, by B. J. Noye, of finite-difference methods as applied to the Linear Heat Conduction Equation in one or more dimensions. This updates the existing monographs on this topic, such as the classical book by Richtmyer and Morton, and could serve as the basis for a graduate text. The second work, by Clive Fletcher, consists of an exhaustive but very readable description of Galerkin methods. This is certainly more complete than other works on this topic known to the reviewer and covers Fletcher's own contributions to Galerkin techniques as well as recent work on combining Galerkin methods with finite-element and spectral methods. Two shorter survey articles follow, the first, by G. P. Steven, deals with the applications of finite-element methods to fluid flow problems and the second, by Fix, discusses hybrid finite-element methods. The remaining survey papers concern Marker and Cell techniques (Browne), a critical comparison of numerical techniques for solving fluid flow problems (Pearson), and a relativistic approach to numerical solutions of dynamic systems problems (Barnett).

The second part of the volume, dealing with applications, begins with a long paper on the simulation of tides and currents in gulfs by Noye and Tronson, followed by three other papers on oceanographical problems. Morrison and Smith apply network techniques to open channel flows in estuaries, while a further paper by Noye concerns the effect of wind on circulation in lakes and other large bodies of water. Interspersed with three other papers on hydraulic problems are two papers on cavity flows by Gupta and Patterson, respectively, a paper on Supersonic Cone Flow by Fletcher, one introducing thermal and buoyancy effects into fluid flow problems (Stevens), the application of Galerkin techniques to sound propagation in nonuniform ducts (Eversman) and a discussion of sea breezes by Pearson and Williams. The volume ends with a paper by Wallington on the numerical analysis of geophysical field data.

The editor and organizers of the conference are to be commended on assembling this collection of important new contributions in Numerical Fluid Dynamics.

Elastic-Plastic Fracture. Edited by J. D. Landes, J. A. Begley, and G. A. Clarke. ASTM Special Technical Publication 668. American Society for Testing and Materials. 1979. Pages 1–771. Price $58.75.

REVIEWED BY A. S. KOBAYASHI[6]

A symposium on Elastic-Plastic Fracture sponsored by ASTM Committee E-24 Committee was held in Atlanta, Ga., in November, 1977, to provide a forum for discussing the state of science in elastic-plastic fracture. The 33 papers contained in this symposium proceedings are grouped into the following three parts: Elastic-Plastic Fracture Criteria and Analysis; Experimental Test Techniques and Fracture Toughness Data; and Application of Elastic-Plastic Methodology. Of particular interest to JAM readers are the first and third parts of this book which will be briefly reviewed in the following.

The analysis papers in the first part dealt with new as well as assessment of existing criteria for stable crack growth and ductile instability. The first paper by Paris, et al., presented a forceful justification for a new nondimensional material parameter, the "tearing modulus" as a material's resistance to tearing stability. The next paper by Hutchison, et al., provided the theoretical basis for use of J-integral for crack growth analysis in the previous paper. Shih, et al., and Kanninen, et al., followed with experimental and numerical justifications for the use of crack opening angle in addition to the tearing modulus as a resistance to crack growth. Two-dimensional elastic-plastic finite-element analysis was used by Sorensen, McMeeking, et al., Nakagaki, et al., Miller, et al., and D'Escatha, et al., to determine J-integral changes with stable crack growth and/or in the presence of finite strains, the crack surface energy release rate, G^{Δ}, for stable crack growth and a ductile damage function based on void nucleation, growth, and coalescence.

The application papers were directed toward elastic-plastic fracture of pressure vessels, pipelines, and fracture specimens. Chell used an equivalent J-integral analysis to interpret the failure assessment curve by Harrison while Harrison, et al., discussed the application of COD approach for material selection, defect assessment, and failure investigation of actual structures. Elastic-plastic fracture mechanics was used by McHenry, et al., to study the maximum surface flaw size in pipeline girthwelds and Simpson, et al., used COD and elastic-plastic R-curves to describe ductile fracture of Zr-2.5Nb pressure tube alloy. Mcdonald, on the other hand, used plastic stress singularity strength to correlate fracture data of A36 and HSLA structure steel connections and Merkle used an empirical equation to analyze nozzle corner cracks. Notch root plasticity was used by Hammonda, et al., to study fatigue crack growth, and Brose, et al., and Mowbray correlated fatigue crack growth of 304 stainless steel and chromium-molylodenum-vanadium steel, respectively, with cyclic J.

The excellent summary by Landes and Clarke could have been reproduced here in place of this review if it would have not been for its length. As Landes so rightly stated in the Introduction, . . . "The variety of topics covered should be of interest to a large number of researchers working in the elastic-plastic area. This publication represents the first major collection of papers devoted solely to the topic of elastic-plastic fracture."

Turbulent Shear Flows I. Edited by F. Durst, B. E. Launder, F. W. Schmidt, and J. H. Whitelaw. 1979. Springer-Verlag, New York/Heidelberg, Berlin. Pages 415. Price $29.80

REVIEWED BY P. A. LIBBY[7]

This book contains the contributions to the First International Symposium on Turbulent Shear Flows held in 1977 at the Pennsylvania State University. This July, the Second Symposium was held in London; thus this series appears to be well founded and due for a long life. The successful initiation of a new series of international scale meetings and the proceedings resulting therefrom on turbulent shear flows indicates the interest this specialized topic attracts among engineering scientists throughout the world.

The proceedings include 26 papers within the framework of five chapters with the following titles: Free Flows, Wall Flows, Recirculating Flows, Developments in Reynolds Stress Closures, and New Directions in Modeling. Of considerable novelty and value are introductions to each chapter written by an expert and placing the in-

[5] Professor, Department of Mechanical Engineering, University of California, Berkeley, Calif.

[6] Professor, Department of Mechanical Engineering, University of Washington, Seattle, Wash. 98195.

[7] Professor of Fluid Mechanics, Department of AMES, University of California, La Jolla, Calif. 92093.

dividual contributions in perspective relative to the broader topic. The editors of subsequent volumes in this series and in fact of similar proceedings would be well advised to follow this practice; the literature of turbulent flows involves a variety and scope which makes it difficult for an "outsider" to make proper assessments of new contributions, of problems calling for attention, etc. Thus the introductory remarks add significantly to the value of this volume.

The contributions in the first three chapters are equally divided between experiment and theory while the subject of the last two chapters restricts their contents to developments in theory and numberical methods. It is the nature of current turbulence research that few papers deal with both experiment and theory.

Workers in turbulence research and engineers responsible for applications involving turbulent flows will find this volume a valuable addition to their reference library and will anticipate subsequent volumes in the series.

Advances in Analysis of Geotechnical Instabilities. Edited by J. C. Thompson. University of Waterloo Press. 1978. Pages 230. Price $15.

REVIEWED BY J. W. RUDNICKI[8]

This volume collects five invited papers which were contributed during September, 1976, to October, 1977, for a symposium on geotechnical instabilities. A sixth article which is included, "The Application of Mechanics to Rock Engineering," by C. Fairhurst, is reprinted from the *Proceedings of the Third Symposium on Engineering Applications of Solid Mechanics.*

This latter article provides a good overview of the subject of this volume and would be an appropriate introduction although it appeared fifth in the actual arrangement of papers. Fairhurst suggests that progress in geomechanics design has been hampered by the difficulties presented by natural materials, but he emphasizes the usefulness of theoretical analysis as a basis for good design even when material properties are not precisely known. Improvements in prediction of tensile failure of rock which have been made using the Griffith approach to fracture are discussed as an example. Fracture mechanics has, however, developed far beyond the analysis of Griffith and these developments, although not discussed, could perhaps lead to comparable improvements. This example illustrates one disappointing aspect of the volume: With the exception of a paper by I. Vardoulakis ("Equilibrium Bifurcation of Granular Earth Bodies"), which applies a bifurcation analysis to study the development of shear bands in sand, the articles describe modifications of standard approaches to problems in geomechanics. However, in view of the motivation for the symposium, which Thompson states in the editor's preface is the inadequate understanding of the mechanics of instability in geotechnical materials, I had hoped for the description of more novel approaches. In spite of my disappointment over this one feature, I did find the problems and variety of approaches which were discussed to be very interesting. This volume will be of interest to workers in geotechnical engineering as well as to those in other areas of mechanics who wish an introduction to this field.

"Instability" is a term which can have many interpretations, even within the confines of mechanics, and the following short synopsis of articles in this volume indicates a variety of approaches:

The first article by G. Gudehus discusses the application of an approach often taken in classical soil mechanics design: the deformation at failure is assumed to occur along discrete sufaces and instability is identified with the limiting state of static equilibrium. H. Lippman also uses this interpretation of instability in his article on "translatory rock bursting" but, after reducing the problem to one dimension, he employs an elastic-plastic analysis to identify the limiting state of equilibrium. I. Vardoulakis considers instability as the development of zones of localized shear deformation. An article by R. H. Fakunding and others describes the geology of the Clarendon-Linden fault system in western New York and surface features (e.g., faults, joints, "popups") which appear to reflect some process of mechanical instability. Although this article contains much terminology from structural geology which may be unfamiliar to many readers, it does make clear the difficulties which are faced in interpreting field data and infering mechanical processes from observations of the end state. The final article entitled "Discontinuity Models of Problems in Geomechanics," by A. M. Starfield summarizes and critically reviews computer methods for predicting the response of jointed rock masses.

The article by Vardoulakis illustrates the improvements which can result from more detailed analysis. The point-of-view that localization of deformation can be explained as a bifurcation from homogeneous deformation, has recently proven to be very fruitful in studying this phenomenon in a variety of materials (see, for example, the review by J. R., Rice, "The Localization of Plastic Deformation," *Proceedings of the 14th International Congress of Theoretical and Applied Mechanics,* Edited by W. T. Koiter, Delft, North Holland, Vol. 1, 1976, p. 207). Vardoulakis finds that this approach yields predictions for the orientation of shear bands which are in much better agreement with his experimental observations than are the standard Coulomb or Roscoe predictions.

Fracture of Composite Materials. Edited by G. C. Sih and V. P. Tamuzs. Sijthoff and Noordhoff, Alphen aan den Rijn—The Netherlands. 1979, Pages xvi–413. Price $35.

REVIEWED BY C. W. SMITH[9]

This volume constitutes the *Proceedings of the First U.S.A.–U.S.S.R. Symposium on Fracture of Composite Materials* which was held at the Hotel Jūrmala, Riga, U.S.S.R., September 4–7, 1978. The purpose of the meeting was to assemble a small group of researchers "to review fundamentals, discuss problem areas and display the current developments" pertaining to the fracture characteristics of polyphase materials.

The volume includes a total of 33 technical papers, 16 of which described studies conducted within the U.S.S.R., and 17 papers dealt with research conducted in the U.S.A. and in Europe. The volume is divided into five sections which may be briefly summarized as follows:

Section I (*Microfracture*) contains papers on micro and macrocracks (Mileiko), dispersed fracture (Tamuzs) microcrack enlargement criteria (Kuksenko, Frolov, and Orlov), and fracture kinetics (Regel, Leksovskii, and Pozdnyakov) which involved both analytical and experimental approaches.

Section II (*Statistical and Analytical Methods*) deals with stochastic models of fracture (Bolotin), computer simulation of fracture processes (Kopyov, Ovchinsky, and Bilsagayev), failure analysis (Wu), failure prediction (Chou), and interface crack analysis (Dunders and Comninou).

Section III (*Fracture Analysis*) contains a variety of papers which include both analytical and experimental aspects. Fracture mechanics (Sih), interaction of cracks (Vanin), implication of experimental observations (Smith), failure modes (Tarnopolskiy), finite-element analysis (Herrmann and Braun), multiple fracture (Kelly), polymer reinforcement (Knauss and Mueller), and fracture test results

[8] Professor, Department of Theoretical and Applied Mechanics, University of Illinois at Urbana-Champaign, Urbana, Ill. 61801.

[9] Professor of Engineering Science and Mechanics, Virginia Polytechnic Institute and State University, Blacksburg, Va. 24061.

(Wright, Welch, and Jollay), were described for a variety of polyphase materials.

Section IV (*Failure Analysis*) includes papers which focus upon criteria for predicting strength, fracture and/or failure of composite materials. Specifically, studies on strength criteria (Annin and Baev), failure of thin-walled structures under flexure (Nemirovsky), optimum design and strength (Obraztsov and Vasil'ev), fracture models (Rikards, Teters, and Upitis), influence of failure pecularities on strength (Perov, Skudra, Mashinskaja, and Bulavs), free edge induced failure analysis (Crossman), bone fracture (Knets), and fatigue life prediction (Parfeyev, Oldirev, Tamuzs) are presented.

Section V (*Experimental Methods*) contains papers on the experimentally behaviors in composite materials and various techniques for observing and testing them. Included are nondestructive study of damage (Latishenko, Matiss), test method development (Chamis), the nature of crack growth (Bunsell), optical methods (Rowlands and Stone), effect of high modulus fibers (Kalnin), interesting mechanical behaviors (Chiao), fracture characteristics (Lachman), and fracture initiation prediction (Mast, et al.).

The foregoing studies include both unidirectionally reinforced and crossply laminates and covered both common (glass-epoxy) and advanced (graphite-aluminum, etc.) materials as well as some more exotic (asbestos cement, bone tissue) of the polyphase materials.

Taken collectively, this volume presents a summary of current approaches and considerations involved in developing predictions of the failure by fracture and its associated mechanisms of a fairly wide variety of polyphase materials. Limitations and restrictions of the theories are noted and experimental methods are discussed and used to obtain results for comparison with analytical predictions. The volume should provide a window for viewing a "state of the art" in composite fracture (a developing but incomplete discipline) as seen collectively by the contributors. As such, it should be found of interest to workers in both composite materials and fracture mechanics.

Three-Dimensional Problems of the Mathematical Theory of Elasticity and Thermoelasticity. By V. D. Kupradze, T. G. Gegelia, M. O. Basheleishvili, and T. V. Burchuladze. Edited by V. D. Kupradze. North-Holland Publishing Co., New York. 1979. Pages 929. Price $158.50.

REVIEWED BY E. STERNBERG[10]

This voluminous tome is a translation into English of the 1976 second edition of a monograph originally published by the Tbilisi University Press in 1968. Although the individual contributions of the four authors involved are not identified, it is safe to surmise that the work of Kupradze, who also served as editor of the book, was predominant in determining its scope and character.

The present treatise is chiefly concerned with the classical linearized theory of homogeneous and isotropic elastic solids, elastostatic and elastodynamic considerations being given more or less equal attention. Further, a substantial amount of space is devoted to a linearized version of couple-stress theory for perfectly elastic, centrosymmetric-isotropic materials, as well as to linear thermoelasticity theory.

Notwithstanding its title, the book places relatively little emphasis on the treatment of specific physically important problems. Instead, the authors are heavily preoccupied with uniqueness and existence issues, and spend a major part part of their effort on the characterization of the relevant problem classes in terms of singular integral equations. Some background for this approach is supplied in preliminary chapters on basic singular solutions of the governing field equations, on the theory of singular integral equations, and on pertinent aspects of potential theory. Special mention should also be made of the three closing chapters, which pertain to contact problems for elastic media with inclusions, the use of generalized Fourier series, as well as to certain series and quadrature representations of solutions to half-space and quarter-space problems.

As ought to be apparent from the preceding all too cursory description, this is a rather unconventional treatise on elasticity theory, the choice of topics covered reflecting strongly the taste and bias of its authors. In particular, some readers—including the reviewer—may question whether couple-stress theory merits the emphasis it receives here.

There is also cause to wonder whether the authors have consistently achieved "the modern level of mathematical rigor" avowed in their preface. Indeed, the mathematical erudition affected in these pages is not always matched by an equal measure of conceptual clarity or genuine mathematical care.

A few examples drawn from the opening chapter on "Basic Concepts and Axiomatization" may serve to illustrate such misgivings. Here ordinary and couple-stresses are introduced (prior to any discussion of kinematics) through limit-definitions that are not made mathematically meaningful. The repeated allusions to molecules or particles seem neither helpful nor appropriate in the context of a continuum-mechanical exposition. In view of the authors' casualness in distinguishing material from spatial coordinates, their transition to the linearized theory will not bear scrutiny. Nor is the reader aided by the admonition (on p. 17) not to confuse the "vector of rigid rotation" with the "vector of internal rotation," despite the use of two different symbols, since both are defined as one-half the displacement-curl (see pp. 9, 16).

No credit is given to the translator of this volume, and not much credit is due in this connection. Sentences such as "One may have an infinite number of directions at each point of a medium" (p. 5), are apt to be attributable to faulty translation. So is the puzzling assertion (p. 2): "If the body . . . is deformed, . . . the parts of the body are no longer in mechanical equilibrium."

While this is hardly a treatise suitable for uninitiated students of elasticity theory, it renders accessible in English some valuable material of interest to specialists in this subject area.

Theoretical Kinematics. By D. Bottema and B. Roth. North-Holland Publishing Company, Amsterdam, New York, Oxford. 1979. Pages 558 + XIV. Price $87.75.

REVIEWED BY G. R. VELDKAMP[11]

This is a textbook in which kinematics is presented as a theory independent of any particular application, that is: as a fundamental science in its own right. The bulk of the book, 420 pages, is devoted to Euclidean kinematics of 3 and 2 dimensions. A characteristic feature of the treatment is the principle of starting with general concepts and problems and then specializing gradually to more simple cases. The first 22 pages of the text are accordingly written in terms of n-dimensional Euclidean space. The whole matter is in the main treated analytical accompanied by ample geometric interpretation. Synthetic reasoning however is not evaded in those places where it may contribute to a deeper understanding of the problem on hand. The mathematical tools are borrowed from elementary algebraic geometry, calculus, vector, and matrix algebra; mathematical concepts which

[10] Professor of Mechanics, California Institute of Technology, Division of Engineering and Applied Science, Pasadena, Calif. 91125.

[11] Department of Mathematics, Technical University Eindhoven, Eindhoven, The Netherlands.

are not generally known to the average reader are moreover explained in the text. The Chapters III, IV, and V contain a coherent account of three-dimensional positions theory for 2, 3, 4, or more positions, respectively, and for both finitely separated and consecutive positions. In slightly over 100 pages classical results are derived in a new way and others are either new or appear for the first time in an English textbook. The next chapter is devoted to the study of continuous spatial kinematics. The properties of the instantaneous tangents, principal normals and binormals are carefully exposed. The same can be said with regard to the developables of moving planes and the ruled surfaces generated by lines of the moving space. Here once more one sees many new aspects, both in the way of presentation and in regard to the results.

Chapter VII contains a neat survey of spherical kinematics, following the scheme: *finitely separated positions, consecutive positions,* and *time-dependent motions.* The next chapter deals with plane kinematics. It is a lucid self-contained treatise of about 90 pages, proceeding along the lines set by the scheme just mentioned.

Chapter IX is about special motions. The authors analyze such spatial motions as the Frenet-Serret motion, Darboux's, Mannheim's, Schoenflies' and Krames' motion. From plane kinematics they select the four-bar motion, the special cases thereof and the cycloidal motion. There follows a chapter on n-parameter motions. It contains among other things an outstanding treatment of the second-order properties of the general 2-parameter spatial motion. There is a nice section on two-parameter plane motion.

Chapter XI deals with a mapping of plane displacements on the points of a three-dimensional space, first introduced (1911) by Grünwald and by Blaschke. The mapping is treated in an elementary way. One of the applications given by the authors is to the four-bar motion. They show, seemingly effortless, how to obtain a parametrization of the coupler curve of a general four-bar by means of Jacobi elliptic functions. In addition it is shown how to parametricize the coupler curves of folding four-bars, these being, as is well-known, rational curves.

Chapter XII is devoted to kinematics in other geometries. Although emphasis is laid on equiform kinematics, affine, elliptic and hyperbolic kinematics are not neglected. A chapter on special mathematical methods in kinematics concludes the text.

An important feature of the book is the fact that the authors present some material without proof. This material is generally set in small print and denoted "Example." These examples are mainly formulated as exercises and must be regarded as an essential part of the text. There are somewhat over 800 examples. A careful student of the book will have no difficulty whatsoever in dealing with this material. There is an extensive bibliography up to 1977 of about 225 items and a reliable index. There are few misprints and the book is well produced. The authors must have done a great deal of preliminary work, before they could sit down to compose this outstanding book which is in the opinion of this reviewer a highly valuable asset to kinematic literature. As such it should be in the library of each researcher and advanced student in the field of theoretical kinematics and the closely connected theory of mechanisms. The scholarly merits of the book are matched by its didactical quality. It has the style of a classic.

Magnetohydrodynamic Flow in Ducts. By Herman Branover. John Wiley & Sons, Inc. (Halsted Press), New York. 1978. Pages xii–290.

REVIEWED BY J. S. WALKER[12]

Anyone who deals with liquid-metal flows in the presence of magnetic fields will find a wealth of invaluable information in this book which is not contained in any other book. This book is indispensable for both designers and basic researchers. The emphasis throughout the book is on the physical phenomena revealed by theoretical and experimental results, on comparison of all analytical and semiempirical predictions with experimental data, and on practical quantities, such as friction factors and velocity distributions. Equations are presented with emphasis on the physics behind the important terms and without prolonged derivations. In covering theoretical studies, the author presents the important results with emphasis on when the phenomena revealed will occur in actual practical situations and without all of the details of the mathematics behind the results. The latest theoretical and experimental studies are discussed and integrated to give an excellent picture of where the leading edge of the field has reached to date and of what lies just beyond. One lengthy chapter presents many practical suggestions on experimentation with liquid metals in magnetic fields. The author draws this information from his own 20 years of experience and from personal contacts with other MHD experimentalists throughout the world.

Over half of the book is devoted to three closely related topics: laminarization of turbulent flows by strong magnetic fields, semi-empirical formulas for turbulent MHD flows and the special anistropy of turbulence in MHD flows. This is the first unified presentation of this information on turbulent MHD flows, while most of the results are taken from papers in Russian, with many of these papers in proceedings which are not available outside of the U.S.S.R. This reflects the fact that the amount of research on MHD done in the U.S.S.R. during the past 15 years far exceeds that done in the U.S.A., and this book presents the results of much Soviet research in English for the first time.

Researchers concerned with turbulence in ordinary hydrodynamic flows should also find this book interesting. With an electrically conducting fluid, a magnetic field can be used to manipulate the characteristics of the turbulence in order to study otherwise unattainable phenomena, such as two-dimensional turbulence.

In summary, this book is a valuable contribution to the literature on turbulence and is the most important book on liquid-metal magnetohydrodynamics to appear since the basic textbooks published in the midsixties.

[12] Professor, Department of Theoretical and Applied Mechanics, University of Illinois, Urbana, Ill. 61801. Mem. ASME.